

WOMEN IN ANALYTICAL CHEMISTRY

EDITED BY: Nicole J. Jaffrezic-Renault, Ottavia Giuffrè, Eugenia Gallardo,
Camelia Bala and Quezia B. Cass

PUBLISHED IN: Frontiers in Chemistry and
Frontiers in Cellular and Infection Microbiology





frontiers

Frontiers eBook Copyright Statement

The copyright in the text of individual articles in this eBook is the property of their respective authors or their respective institutions or funders. The copyright in graphics and images within each article may be subject to copyright of other parties. In both cases this is subject to a license granted to Frontiers.

The compilation of articles constituting this eBook is the property of Frontiers.

Each article within this eBook, and the eBook itself, are published under the most recent version of the Creative Commons CC-BY licence.

The version current at the date of publication of this eBook is CC-BY 4.0. If the CC-BY licence is updated, the licence granted by Frontiers is automatically updated to the new version.

When exercising any right under the CC-BY licence, Frontiers must be attributed as the original publisher of the article or eBook, as applicable.

Authors have the responsibility of ensuring that any graphics or other materials which are the property of others may be included in the CC-BY licence, but this should be checked before relying on the CC-BY licence to reproduce those materials. Any copyright notices relating to those materials must be complied with.

Copyright and source acknowledgement notices may not be removed and must be displayed in any copy, derivative work or partial copy which includes the elements in question.

All copyright, and all rights therein, are protected by national and international copyright laws. The above represents a summary only. For further information please read Frontiers' Conditions for Website Use and Copyright Statement, and the applicable CC-BY licence.

ISSN 1664-8714

ISBN 978-2-83250-028-6

DOI 10.3389/978-2-83250-028-6

About Frontiers

Frontiers is more than just an open-access publisher of scholarly articles: it is a pioneering approach to the world of academia, radically improving the way scholarly research is managed. The grand vision of Frontiers is a world where all people have an equal opportunity to seek, share and generate knowledge. Frontiers provides immediate and permanent online open access to all its publications, but this alone is not enough to realize our grand goals.

Frontiers Journal Series

The Frontiers Journal Series is a multi-tier and interdisciplinary set of open-access, online journals, promising a paradigm shift from the current review, selection and dissemination processes in academic publishing. All Frontiers journals are driven by researchers for researchers; therefore, they constitute a service to the scholarly community. At the same time, the Frontiers Journal Series operates on a revolutionary invention, the tiered publishing system, initially addressing specific communities of scholars, and gradually climbing up to broader public understanding, thus serving the interests of the lay society, too.

Dedication to Quality

Each Frontiers article is a landmark of the highest quality, thanks to genuinely collaborative interactions between authors and review editors, who include some of the world's best academicians. Research must be certified by peers before entering a stream of knowledge that may eventually reach the public – and shape society; therefore, Frontiers only applies the most rigorous and unbiased reviews. Frontiers revolutionizes research publishing by freely delivering the most outstanding research, evaluated with no bias from both the academic and social point of view. By applying the most advanced information technologies, Frontiers is catapulting scholarly publishing into a new generation.

What are Frontiers Research Topics?

Frontiers Research Topics are very popular trademarks of the Frontiers Journals Series: they are collections of at least ten articles, all centered on a particular subject. With their unique mix of varied contributions from Original Research to Review Articles, Frontiers Research Topics unify the most influential researchers, the latest key findings and historical advances in a hot research area! Find out more on how to host your own Frontiers Research Topic or contribute to one as an author by contacting the Frontiers Editorial Office: frontiersin.org/about/contact

WOMEN IN ANALYTICAL CHEMISTRY

Topic Editors:

Nicole J. Jaffrezic-Renault, Université Claude Bernard Lyon 1, France

Ottavia Giuffrè, University of Messina, Italy

Eugenia Gallardo, Universidade da Beira Interior, Portugal

Camelia Bala, University of Bucharest, Romania

Quezia B. Cass, Federal University of São Carlos, Brazil

Citation: Jaffrezic-Renault, N. J., Giuffrè, O., Gallardo, E., Bala, C., Cass, Q. B., eds. (2022). Women in Analytical Chemistry. Lausanne: Frontiers Media SA.
doi: 10.3389/978-2-83250-028-6

Table of Contents

- 05 Editorial: Women in Analytical Chemistry**
N. J. Jaffrezic-Renault, O. Giuffrè, E. Gallardo, C. Bala and Q. B. Cass
- 09 Analysis of Milk Using a Portable Potentiometric Electronic Tongue Based on Five Polymeric Membrane Sensors**
C. Pérez-González, C. Salvo-Comino, F. Martin-Pedrosa, L. Dias, M. A. Rodriguez-Perez, C. Garcia-Cabazon and M. L. Rodriguez-Mendez
- 20 Co-Immobilized Capillary Enzyme Reactor Based on Beta-Secretase1 and Acetylcholinesterase: A Model for Dual-Ligand Screening**
Adriana Ferreira Lopes Vilela, Vitor Eduardo Narciso dos Reis and Carmen Lúcia Cardoso
- 30 Is a Lead Isotope Ratios in Wine Good Marker for Origin Assessment?**
Slađana Đurđić, Vesna Stanković, Slavica Ražić and Jelena Mutić
- 40 Combined Methodologies for Determining In Vitro Bioavailability of Drugs and Prediction of In Vivo Bioequivalence From Pharmaceutical Oral Formulations**
A. De Simone, L. Davani, S. Montanari, V. Tumiatti, S. Avanesian, F. Testi and V. Andrisano
- 53 Exploring the Thickness-Dependence of the Properties of Layered Gallium Sulfide**
Yael Gutiérrez, Maria M. Giangregorio, Stefano Dicorato, Fabio Palumbo and Maria Losurdo
- 61 Sensitive LC-MS/MS Methods for Amphotericin B Analysis in Cerebrospinal Fluid, Plasma, Plasma Ultrafiltrate, and Urine: Application to Clinical Pharmacokinetics**
Leandro Francisco Pippa, Maria Paula Marques, Anna Christina Tojal da Silva, Fernando Crivelenti Vilar, Tissiana Marques de Haes, Benedito Antônio Lopes da Fonseca, Roberto Martinez, Eduardo Barbosa Coelho, Lauro Wichert-Ana and Vera Lucia Lanchote
- 75 Targeted On-Demand Screening of Pesticide Panel in Soil Runoff**
Vikram Narayanan Dhamu, Suhashine Sukumar, Crisvin Sajee Kadambathil, Sriram Muthukumar and Shalini Prasad
- 85 Comparison of Three Complementary Analytical Techniques for the Evaluation of the Biosimilar Comparability of a Monoclonal Antibody and an Fc-Fusion Protein**
Alice Demellenne, Arij Ben Yahia, Delphine Lempereur, Jacques Crommen, Anne-Catherine Servais, Ines Fradi and Marianne Fillet
- 97 Diagnosis and Stratification of Pseudomonas aeruginosa Infected Patients by Immunochemical Quantitative Determination of Pyocyanin From Clinical Bacterial Isolates**
Barbara Rodriguez-Urretavizcaya, Nuria Pascual, Carme Pastells, Maria Teresa Martin-Gomez, Lluïsa Vilaplana and Maria-Pilar Marco

- 109 Development and Validation of a Bioanalytical UHPLC-MS/MS Method Applied to Murine Liver Tissue for the Determination of Indocyanine Green Loaded in H-Ferritin Nanoparticles**
Cristina Sottani, Elena Grignani, Danilo Cottica, Serena Mazzucchelli, Marta Sevieri, Arianna Chesi, Fabio Corsi, Sarah Galfrè, Francesco Saverio Robustelli della Cuna and Enrica Calleri
- 118 Highly Sensitive Water Detection Through Reversible Fluorescence Changes in a syn-Bimane Based Boronic Acid Derivative**
Apurba Pramanik, Joy Karmakar, Flavio Grynszpan and Mindy Levine
- 127 Single-Molecule Fluorescence Imaging Reveals GABAB Receptor Aggregation State Changes**
Fang Luo, GeGe Qin, Lina Wang and Xiaohong Fang
- 136 Asymmetrical Flow Field-Flow Fractionation Methods for Quantitative Determination and Size Characterization of Thiols and for Mercury Size Speciation Analysis in Organic Matter-Rich Natural Waters**
Isabelle A. M. Worms, Killian Kavanagh, Elodie Moulin, Nicole Regier and Vera I. Slaveykova
- 149 Spectroscopy, Morphology, and Electrochemistry of Electrospun Polyamic Acid Nanofibers**
Siyabulela Hamnca, Jessica Chamier, Sheila Grant, Timothy Glass, Emmanuel Iwuoha and Priscilla Baker
- 157 Aroma Clouds of Foods: A Step Forward to Unveil Food Aroma Complexity Using GC × GC**
Sílvia M. Rocha, Carina Pedrosa Costa and Cátia Martins
- 183 Speciation Study on O-Phosphorylethanolamine and O-Phosphorylcholine: Acid–Base Behavior and Mg²⁺ Interaction**
Donatella Aiello, Massimiliano Cordaro, Anna Napoli, Claudia Foti and Ottavia Giuffrè
- 198 Comprehending Cardiac Dysfunction by Oxidative Stress: Untargeted Metabolomics of In Vitro Samples**
Alan Gonçalves Amaral, Isabela Aparecida Moretto, Flávia da Silva Zandonadi, Hans Rolando Zamora-Obando, Isabela Rocha, Alessandra Sussulini, André Alexandre de Thomaz, Regina Vincenzi Oliveira, Aline Mara dos Santos and Ana Valéria Colnaghi Simionato
- 211 Chromatography Conditions Development by Design of Experiments for the Chemotype Differentiation of Four Bauhinia Species**
Amanda J. Aquino, Edenir R. Pereira-Filho, Regina V. Oliveira and Quezia B. Cass



Editorial: Women in Analytical Chemistry

N. J. Jaffrezic-Renault^{1*}, O. Giuffrè^{2*}, E. Gallardo^{3*}, C. Bala^{4*} and Q. B. Cass^{5*}

¹Université Claude Bernard Lyon 1, Villeurbanne, France, ²Dipartimento di Scienze Chimiche, Biologiche, Farmaceutiche ed Ambientali, Università di Messina, Messina, Italy, ³Centro de Investigação em Ciências da Saúde (CICS-UBI), Faculdade de Ciências da Saúde, Universidade da Beira Interior, Covilhã, Portugal, ⁴Department of Analytical Chemistry, University of Bucharest, Bucharest, Romania, ⁵Departamento de Química, Universidade Federal de São Carlos, São Carlos, Brazil

Keywords: analytical chemistry, clinical, food, agriculture, speciation, sensors

Editorial on the Research Topic

Women in Analytical Chemistry

This collection encompasses different areas of analytical chemistry and highlights the contribution and research work of women scientists from different parts of the world. The collection is composed of 18 articles and involves clinical applications, food and agricultural products analysis, speciation studies and analysis, semiconductors, and novel sensors developments.

OPEN ACCESS

Edited and reviewed by:

Alberto Salomone,
University of Turin, Italy

*Correspondence:

N. J. Jaffrezic-Renault
nicole.jaffrezic@univ-lyon1.fr

O. Giuffrè
ogiufrè@unime.it

E. Gallardo
egallardo@fcsaude.ubi.pt

C. Bala
camelia.bala@chimie.unibuc.ro

Q. B. Cass
qcass@ufscar.br

Specialty section:

This article was submitted to
Analytical Chemistry,
a section of the journal
Frontiers in Chemistry

Received: 21 May 2022

Accepted: 03 June 2022

Published: 11 August 2022

Citation:

Jaffrezic-Renault NJ, Giuffrè O,
Gallardo E, Bala C and Cass QB (2022)
Editorial: Women in
Analytical Chemistry.
Front. Chem. 10:949793.
doi: 10.3389/fchem.2022.949793

CLINICAL APPLICATIONS

The *in vitro* method for the prediction of drug bioavailability is of importance since it can save time, money, reduce chemical and biological waste, and when well-designed can be used for planning *in vivo* bioequivalence evaluation (BE). A dissolution/permeation model has herein been reported for 1.5 mg of levonorgestrel (LVN) as generic and brand-name tablets (Simone et al.). To meet this end, a standard dissolution test was combined with a parallel artificial membrane permeability assay (PAMPA). From this work, PAMPA has emerged as a complementary assay for predicting *in vivo* BE of drugs and explained the unsuccessful *in vivo* bioequivalence fallouts for these two tablets.

The ability to quantify amphotericin B (AmB) at any given time during the treatment of neurocryptococcosis is an analytical challenge, especially in cerebrospinal fluid (CSF). Lanchote and collaborators report on the development of a LC-MS/MS method for analysis of AmB in plasma, plasma ultrafiltrate, urine, and CSF (Francisco Pippa et al.). The developed method has been applied to a clinical pharmacokinetic study following the administration of the drug as a lipid complex in one patient. With that, a detailed description of the pharmacokinetic parameters has been obtained and created the conditions to investigate AmB in CSF at any time of the treatment.

The increased number of antibodies and derivatives on the market calls for methods development for analyzing biosimilars. Herein, capillary gel electrophoresis (CGE), liquid chromatography on the reversed elution mode (RPLC), and size-exclusion chromatography (SEC), all with UV detection, were used to analyze the monoclonal antibody (adalimumab), an Fc-fusion protein (etanercept) and to compare them to one of their biosimilars (Demelenne et al.). The three separation methods showed analytical complementarity for the biopharmaceuticals. While RPLC was useful for the separation of hydrophilic and hydrophobic degradation products, CGE showed selectivity for several adalimumab fragments, and SEC was worthwhile for the analysis of aggregates and certain fragments. LC-HRMS was also used to determine the exact mass of the intact protein of adalimumab while SEC with multiangle light scattering detection was used to measure the MW of etanercept (150 kDa) without

overestimation. The article meets the requirement of finding innovative analytical conditions especially for Fc-fusion proteins.

The GABAB receptor is a typical G protein-coupled receptor, and its functional impairment is related to a variety of diseases such as anxiety, depression, alcohol addiction, Parkinson, and cancer. While the premise of GABAB receptor activation is the formation of heterodimers, the receptor also forms a tetramer on the cell membrane. Thus, it is important to study the effect of the GABAB receptor aggregation state on its activation and signaling. In this study, Luo et al. have applied single-molecule photobleaching step counting and single-molecule tracking methods to investigate the formation and change of GABAB dimers and tetramers. A single-molecule stoichiometry assay of the wild-type and mutant receptors revealed the key sites on the interface of ligand-binding domains of the receptor for its dimerization. Moreover, they found that the receptor showed different aggregation behaviors under different conditions. The results offered new evidence for a better understanding of the molecular basis for GABAB receptor aggregation and activation.

Cardiovascular diseases have complex etiology and high mortality rates. Their main risk factors increase the formation of reactive oxygen species, normally produced by natural processes of cellular metabolism. Amaral et al. aim to perform an untargeted metabolomics investigation of cardiac cells (H9c2). The cells were divided into three groups: healthy cells, cells after simulated oxidative stress by H_2O_2 , and cells after recovery from oxidative stress. The purpose of this work was to identify changes in metabolism between groups. After some *in vitro* assays, the authors used liquid chromatography coupled with mass spectrometry (RPLC-MS and HILIC-MS) analyses to know metabolite annotation and pathway analysis. This multiplatform analysis in untargeted metabolomics approaches showed its importance in this field.

Enzymes immobilized on solid supports have received increasing attention as tools in clinical diagnosis because of their advantages like improved stability and the possibility of reusing proteins. Such screening assays are based on bioaffinity chromatography, which combines the specificity and sensitivity of an enzymatic reaction with the automation and reproducibility of a chromatographic system. Current approaches for high-throughput screening (HTS) are based on the search for compounds with efficacy toward single targets. However, a new paradigm is emerging in pharmacological research-exploration on the bioactivity of compounds at multiple targets. Lopes Vilela et al. developed an innovative, automated dual enzymatic system assay based on acetylcholinesterase and beta-secretase 1 co-immobilized on the inner surface of a fused silica capillary to screen ligands. To measure enzyme activities, liquid chromatography coupled to ion trap mass spectrometry was used. The proposed method was validated in order to confirm the standard inhibitors for both enzymes by determining half-maximum inhibitory concentrations. This

assay proved to be an excellent tool for multitarget-directed ligands in drug discovery for complex diseases, and an improvement on the HTS technique as well.

Concerning clinical imaging for diagnosis, staging, and therapy planning, there has been a great deal of attention concerning indocyanine green (ICG) dye. ICG is one of the most commonly used fluorophores in near-infrared fluorescence-guided techniques. However, the molecule forms aggregates in saline solution, presenting limited photostability and moderate fluorescence yield. Sottani et al. formulated ICG using protein-based nanoparticles of H-ferritin (HFn) to generate a more stable fluorophore (HFn-ICG). Ultrahigh performance liquid chromatography-tandem mass spectrometry was employed to determine ICG in liver samples from HFn-ICG-treated mice. The method was validated and applied successfully in bio-distribution studies to investigate the delivery of HFn-ICG.

Pseudomonas aeruginosa is a Gram-negative multidrug-resistant pathogen causing acute and chronic infections. L. Vilaplana et al. report on the development of a reliable, highly sensitive, and specific, immunochemical assay to detect pyocyanin (PYO), one of the main virulence factors (VFs) of *Pseudomonas aeruginosa* (Rodriguez-Urretavizcaya et al.). The ELISA developed allows researchers to achieve a limit of detection, LoD, in the low nM range. The strengths of this study are the potential of PYO as a biomarker of *P. aeruginosa* infection in clinical samples and the possibility of assessing the nature of the infection stage of the patients.

FOOD AND AGRICULTURAL PRODUCTS ANALYSIS

The chromatographic profile of the ethanolic extract of *Bauhinia forficata* leaves was developed as a model through a design of experiment (DoE) by modifying simultaneously multiple critical method parameters to find the appropriated chromatographic conditions (Aquino et al.). Then, they were used by LC-HRMS to identify the compounds that could differentiate the ethanolic extracts leaves of four Bauhinia Species: *B. forficata*, *B. variegata*, *B. longifolia*, and *B. affinis*. The MS data of the chemical profile evaluated by principal component and hierarchical cluster analysis was able to differentiate the species and, thus, be used for authentication of these herbal medicines. Furthermore, 55 molecules were inferred by dereplication. For that, manual comparison of the exact masses, MS/MS fragmentation patterns, and isotopic contribution patterns with those data either reported in the literature or deposited in spectral libraries online were carried out. The used analytical protocol has met the principles of green chemistry and has contributed to the phytochemical knowledge of the studied *Bauhinia* species and can be used for other natural product libraries.

Durđić et al. analyzed different samples of Serbian wine in order to detect lead isotope ratio patterns. The authors proposed that the lead isotope ratio is an excellent “fingerprint” to access

information on the geographical origin of wine as well as to identify potential sources of lead pollution. Through inductively coupled plasma mass spectrometry and multivariate methods of analysis, the authors were capable of comparing the levels of lead in Serbian wines with those of wines from different origins. Several anthropogenic sources are also shown to contribute to the total isotopic profile of lead. Taking into account the results obtained, it was possible to determine the authenticity and geographical origin of the wine using isotopic lead profiles.

Pérez-González et al. developed a portable potentiometric tongue (PE-tongue) and applied it to evaluate the quality of milk with different fat contents (skimmed, semi-skimmed, and whole) and with different nutritional content (classic, calcium-enriched, lactose-free, folic acid-enriched, and enriched in sterols of vegetal origin). The system consisted of a simplified array of five sensors based on PVC membranes, coupled to a data logger. Principal component analysis (PCA) and support vector machine (SVM) results indicated that the PE-tongue consisting of a five-electrode array could successfully discriminate and classify milk samples according to their nutritional content. SVM regression models were used to predict the physicochemical parameters classically used in milk quality control (acidity, density, % proteins, % lactose, and % fat). The prediction results were excellent and similar to those obtained with a much more complex array consisting of 20 sensors.

Finally, Rocha et al. performed a review in order to discuss the potential of the comprehensive two-dimensional gas chromatography methodologies, combined with a headspace solvent-free microextraction technique, in tandem with data processing and data analysis as a useful tool to the coverage of chemical aroma clouds of foods. Also due to the chemical complexity of aromas, the authors presented some challenges related to the characterization of volatile molecules and the perception of aromas as well as some examples reported in recent publications.

SPECIATION STUDIES AND ANALYSIS

The determination of Hg size speciation and the amount of Hg bound to dissolved organic matter (DOM) is crucial to assessing its fate and bioavailability in natural surface waters. Worms et al. describe a methodology combining thiol labeling by fluorescent monobromo(trimethylammonio)bimane bromide (qBBr) with asymmetrical flow field-flow fractionation and online fluorescence detection (AF4-FluoD), for separation of components, determination of size distribution and content of this in the macromolecular DOM in natural waters (Worms et al.). After enrichment with mercury, the quantification and the characterization of the size distributions of Hg bound to macromolecules and nano-sized inorganic particles were made using AF4-ICP-MS. The results of this study highlight new opportunities for determining the stability of the Hg-DOM complex.

The performance of biomaterials, such as O-phosphorylcholine (PPC) based materials, employed for

clinical applications, can be affected by electrolytes. Giuffrè et al. describe a multidisciplinary study useful to elucidate the interaction between O-phosphorylethanolamine (PEA) and PPC, compounds constituting the headgroups of biomembranes, with Mg^{2+} (Aiello et al.). The acid-base behavior, the complexation properties, the enthalpy changes, and the speciation were obtained by potentiometry and 1H -NMR spectroscopy. Spectra obtained by matrix-assisted laser desorption mass spectrometry (MALDI-MS) and MS/MS on these systems indicated an interaction mechanism *via* the phosphate group giving rise to a four-membered cycle. The purpose of the study was mainly to obtain thermodynamic information necessary to carry out simulations under real biological fluid conditions, and for evaluating the possible use of these compounds in several application fields.

SEMICONDUCTORS

In the field of semiconductors, gallium sulfide (GaS) is part of the new two-dimensional (2D) materials of significant interest for optoelectronic applications. A systematic study on the dependence of several properties on the thickness of layered GaS has been performed by Gutiérrez et al.. The GaS properties are structural from Raman spectra, photoluminescence, optical transmittance, resistivity, and work function (WF). More in detail, Raman spectra measured in layers show that the intensity increases with thickness. The resistivity decreases under visible and UV illumination showing a significant dependence on GaS thickness. The analysis of the WF shows an increase from Bulk GaS to monolayer. The results of this investigation may be useful for designing GaS-based optoelectronic devices.

NOVEL SENSORS

Electrochemical sensors and biosensors play a significant role in delivering data direct, in complex samples without prior separation of the target analyte, with applications in various fields ranging from the environment and food monitoring, clinical laboratory, and industrial applications. Shalini Prasad et al. (Narayanan Dhamu et al.) report a rapid response (10 min) sensors design and setup to screen two commonly used pesticides, glyphosate and atrazine, in soil. The reported sensor functions on the bio-affinity mechanism driven *via* an antibody receptor, specific towards the target pesticide. This development proves to be robust for a point-of-use (PoU) setting yielding LoD levels of 0.001 ng/ml for atrazine and 1 ng/ml for glyphosate.

The presence of antibiotic residues in various environmental samples, including water samples, represent an ecological risk. Herein, a notable contribution was done by Priscilla Baker's research group (Hamnca et al.) which reports a sensor modified with polyamic acid nanofibers to detect sulfonamides, classified as bacteriostatic antibiotics which can act as contaminants in the aquatic environment, for which there are no regulatory guidelines. The reported sensors succeed to perform real-time

detection of sulfonamides within a wider linear range and lower applied potential.

Water detection in organic solvents is of great interest in various fields, such as industrial, pharmaceutical, and chemical safety. In this context, Levine *et al.* report on a sensor with boronate ester-functionalized bimeane, which responds to the presence of water in organic solvents and water vapor in high humidity environments giving rise to a rapid and sensitive fluorescence quenching (Pramanik *et al.*). This response occurs both in the bimeane solution and on filter papers on which the bimeane is adsorbed, resulting in colorimetric and fluorimetric changes. This sensor has notable practical advantages, such as high sensitivity, non-toxicity, and ease of access.

AUTHOR CONTRIBUTIONS

All the authors listed have made a substantial, direct and intellectual contribution to the work, and approved it for publication.

ACKNOWLEDGMENTS

We thank all authors of the manuscripts for contributing to this research topic, as well as all reviewers for their rigorous and unbiased feedback.

Conflict of Interest: The authors declare that the research was conducted in the absence of any commercial or financial relationships that could be construed as a potential conflict of interest.

Publisher's Note: All claims expressed in this article are solely those of the authors and do not necessarily represent those of their affiliated organizations, or those of the publisher, the editors, and the reviewers. Any product that may be evaluated in this article, or claim that may be made by its manufacturer, is not guaranteed or endorsed by the publisher.

Copyright © 2022 Jaffrezic-Renault, Giuffrè, Gallardo, Bala and Cass. This is an open-access article distributed under the terms of the Creative Commons Attribution License (CC BY). The use, distribution or reproduction in other forums is permitted, provided the original author(s) and the copyright owner(s) are credited and that the original publication in this journal is cited, in accordance with accepted academic practice. No use, distribution or reproduction is permitted which does not comply with these terms.



Analysis of Milk Using a Portable Potentiometric Electronic Tongue Based on Five Polymeric Membrane Sensors

C. Pérez-González¹, C. Salvo-Comino^{1,2}, F. Martin-Pedrosa^{2,3}, L. Dias⁴,
M. A. Rodríguez-Pérez², C. García-Cabazon^{2,3*} and M. L. Rodríguez-Mendez^{1,2*}

¹Group UVASENS, Escuela de Ingenierías Industriales, Universidad de Valladolid, Valladolid, Spain, ²BioecoUVA Research Institute, Universidad de Valladolid, Valladolid, Spain, ³Dpt. of Materials Science, Universidad de Valladolid, Valladolid, Spain, ⁴Centro de Investigação de Montanha (CIMO), ESA, Instituto Politécnico de Bragança, Bragança, Portugal

OPEN ACCESS

Edited by:

Nicole J. Jaffrezic-Renault,
Université Claude Bernard Lyon 1,
France

Reviewed by:

Zouhair Haddi,
NVISION Systems and Technologies,
S.L., Spain
Antonio Riul Jr,
State University of Campinas, Brazil

*Correspondence:

C. García-Cabazon
crigar@eii.uva.es
M. L. Rodríguez-Mendez
mluz@eii.uva.es

Specialty section:

This article was submitted to
Analytical Chemistry,
a section of the journal
Frontiers in Chemistry

Received: 07 May 2021

Accepted: 11 June 2021

Published: 05 July 2021

Citation:

Pérez-González C, Salvo-Comino C,
Martin-Pedrosa F, Dias L,
Rodríguez-Pérez MA,
García-Cabazon C and
Rodríguez-Mendez ML (2021) Analysis
of Milk Using a Portable Potentiometric
Electronic Tongue Based on Five
Polymeric Membrane Sensors.
Front. Chem. 9:706460.
doi: 10.3389/fchem.2021.706460

A portable potentiometric electronic tongue (PE-tongue) was developed and applied to evaluate the quality of milk with different fat content (skimmed, semi-skimmed, and whole) and with different nutritional content (classic, calcium-enriched, lactose-free, folic acid-enriched, and enriched in sterols of vegetal origin). The system consisted of a simplified array of five sensors based on PVC membranes, coupled to a data logger. The five sensors were selected from a larger set of 20 sensors by applying the genetic algorithm (GA) to the responses to compounds usually found in milk including salts (KCl, CaCl₂, and NaCl), sugars (lactose, glucose, and galactose), and organic acids (citric acid and lactic acid). Principal component analysis (PCA) and support vector machine (SVM) results indicated that the PE-tongue consisting of a five-electrode array could successfully discriminate and classify milk samples according to their nutritional content. The PE-tongue provided similar discrimination capability to that of a more complex system formed by a 20-sensor array. SVM regression models were used to predict the physicochemical parameters classically used in milk quality control (acidity, density, %proteins, %lactose, and %fat). The prediction results were excellent and similar to those obtained with a much more complex array consisting of 20 sensors. Moreover, the SVM method confirmed that spoilage of unsealed milk could be correctly identified with the simplified system and the increase in acidity could be accurately predicted. The results obtained demonstrate the possibility of using the simplified PE-tongue to predict milk quality and provide information on the chemical composition of milk using a simple and portable system.

Keywords: potentiometric electronic tongue, milk, dairy, fat content, lactose, acidity

INTRODUCTION

Milk is a nutritious food containing significant components including fats, lactose, sugars, amino acids, vitamins, nucleotides, inorganic salts, and trace elements among many others. Milk composition and nutrient levels are usually assessed by classic analytical techniques such as gas chromatography/mass spectroscopy, high-performance liquid chromatography, and spectroscopy (Toldrá et al., 2021). However, there is a great interest in developing new methods for rapid detection, quantification, and evaluation of milk. Electrochemical sensors can be an alternative to classical

laboratory techniques because of their high sensitivity, low cost, and inherent portability (Zeng et al., 2018). However, electrochemical sensors have a lack of selectivity, and this can be a problem when dealing with complex samples such as milk.

An interesting approach to improve the performance of non-specific sensors consists in the use of arrays of sensors. According to the IUPAC definition, an electronic tongue (ET) is a multisensor system, which consists of a number of low-selective sensors and uses advanced mathematical procedures for signal processing based on pattern recognition and/or multivariate data analysis (Vlasov et al., 2005; Rodríguez-Méndez, 2016). Several types of sensors have been used in ETs dedicated to the analysis of milk and dairy products (Poghossian et al., 2019). These include voltammetric electrodes (Cetó et al., 2014; Wei et al., 2013; Bougrini et al., 2014; Salvo-Comino et al., 2018) or impedimetric sensors (Scagiona et al., 2016). However, most of the works in ETs applied to milk have been carried out using potentiometric sensor arrays. Since the pioneering work of Toko's group that developed an ET based on potentiometric electrodes (composed of several lipid/polymer membranes) (Hayaschi et al., 1995), the analysis of milk samples using ETs has been an active field of research. These instruments have been constantly progressing, and new improvements in sensor arrays, in data processing methods, and in applications are reported in the literature (Ciosek and Wroblewski, 2011; Ciosek and Wroblewski, 2015).

Potentiometric ETs have been used to analyze different aspects related to the quality of milk and dairy products. For example, they have been used for the discrimination and classification of milk based on fat content and brand (Ciosek and Wroblewski, 2008); for the classification of natural, fermented, and UHT milk (Tazi et al., 2018); to evaluate the organoleptic properties (Minghui et al., 2019); to detect flavor changes in bovine and goat milk (Tazi et al., 2017); in the detection of spoilage (Poghossian et al., 2019); and in the detection of adulterations of goat milk with bovine milk (Dias et al., 2009) or detection of water added to dairy products (Mabrook et al., 2006) among others. Only a few works have explored the possibility of using e-tongues to evaluate chemical parameters in milk. These works use partial least squares (PLS) models to establish correlations between the signals obtained with the sensor arrays and the chemical parameters obtained by classical techniques. For example, e-tongues have been used to determine the content of ethanol, acetaldehyde, lactic acid, acetic acid, and citric acid in probiotic fermented milk (Hruskar et al., 2010), or for the simultaneous detection of water-soluble ions (Torabi et al., 2020).

In many cases, potentiometric e-tongues consist of a large number of sensors (typically between 8 and 36) (Dias et al., 2009; Podražka et al., 2018; Torabi et al., 2020). The idea behind these large arrays is that a higher number of sensing units with different selectivity and sensitivity can provide a larger amount of information, improving the discrimination and prediction capability of the e-tongue. However, a large number of sensors imply a considerable number of variables to manage, and in many cases on-line. In addition, a large number of variables imply the presence of features containing irrelevant or redundant information. In addition, collinearity present in the variables

may affect the prediction results (Leardi, 1998). Finally, when models are built using a large number of variables, the training sample set must also be large. All these reasons make it interesting to reduce the number of variables by selecting only those that provide important information.

Several methods have been used to reduce the number of variables in e-tongues, including the wavelet transform (Holmin et al., 2002) or the kernel method (Salvo-Comino et al., 2018). Tools such as a genetic algorithm (GA) applied to PLS regression can be successfully used as a feature selection technique in voltammetric e-tongues (Prieto et al., 2013). The GA represents an efficient approach to non-linear optimization problems and has several advantages. For example, it does not require linear assumptions and is independent of the misfit criterion (Mirjalili, 2019; Reeves, 2010). The GA incorporates and exploits data collected during model space sampling, resulting in an incredibly efficient and robust optimization technique (Beg and Islam, 2016).

The main goal of this study was to develop a simplified and portable potentiometric electronic tongue (PE-tongue). To this end, the work has been carried out to 1) reduce the number of sensors forming the array using the GA; 2) investigate whether this simplified system could be used to discriminate milk with different fat content and nutritional composition using principal component analysis (PCA); 3) investigate whether acidity, density, %proteins, %lactose, and %fat could be accurately predicted using support vector machine (SVM) regression; and 4) evaluate the ability of the PE-tongue to detect spoilage of unsealed milk while exploring the possibility of predicting changes in physicochemical properties.

MATERIALS AND METHODS

All the reagents used in this work were of analytical degree and used as supplied. Standard solutions of KCl, CaCl₂, NaCl, lactose, glucose, galactose, citric acid, and lactic acid (Sigma-Aldrich, St. Louis, United States) were prepared in MilliQ deionized water (Merck KGaA, Darmstadt, Germany). Two sets of milk samples were used in the study. The first set was used to train the e-tongue and consisted of 13 types of milk samples (five replicas of each, total of 65 samples), including milk with different fat content (skimmed, semi-skimmed, and whole) and milk with different nutritional content (classic, calcium-enriched, lactose-free, folic acid-enriched, and enriched in sterols of vegetal origin) (Table 1). A second set of five samples was used as an external testing set to validate the results obtained with the e-tongue. The samples were stored at room temperature until used. Milk samples were analyzed by classical chemical methods: acidity (titration method ISO 22113:2012), density (hydrometer method ISO 2449:1974), fat (Röse-Gottlieb gravimetric method ISO 1211:2010), proteins (Kjeldahl method ISO 8968-1:2014), and lactose content (HPLC ISO 22662:2007). The averages of physicochemical parameters analyzed for each of the milk samples are collected in Table 1.

Sensors were based on polymeric membranes using high-density polyvinyl chloride (PVC) as the polymeric matrix

TABLE 1 | Types of milk samples included in the study and results of the chemical analysis.

Sample		Acidity (°D)	Density (g/ml)	Fat (%)	Proteins (%)	Lactose (%)
Training set						
C-S	Classic—skimmed	12.65	1033.55	0.32	3.3	5
C-SS	Classic—semi-skimmed	12.55	1031.6	1.56	3.27	4.91
C-W	Classic—whole	12.17	1029.38	3.56	3.21	4.85
CA-S	Calcium—skimmed	15.82	1039.47	0.29	3.93	5.59
CA-SS	Calcium—semi-skimmed	16.06	1037.29	1.55	3.9	5.49
CA-W	Calcium—whole	15.86	1035.71	3.55	3.91	5.54
L-S	Lactose-free—skimmed	12.67	1033.57	0.31	3.29	0.36
L-SS	Lactose-free—semi-skimmed	12.19	1032.09	1.59	3.31	0.42
L-W	Lactose-free—whole	11.98	1029.4	3.59	3.23	0.31
F-S	Folic acid—skimmed	12.57	1033.7	0.40	3.29	4.95
F-SS	Folic acid—semi-skimmed	12.95	1032.38	1.64	3.21	4.93
F-W	Folic acid—whole	12.72	1030.55	3.1	3.18	4.94
P-SS	Proactive—semi-skimmed	12.28	1031.48	1.91	3.16	4.88
External validation set						
V1	Skimmed calcium	15.94	1,039	0.35	3.89	5.49
V2	Semi-skimmed classic	12.36	1,032.14	1.58	3.34	4.97
V3	Semi-skimmed classic	12.45	1,032.45	1.65	3.35	4.96
V4	Whole acid folic	12.95	1,030.92	3.12	3.29	4.89
V5	Whole free lactose	12.45	1,029.92	3.58	3.33	0.52

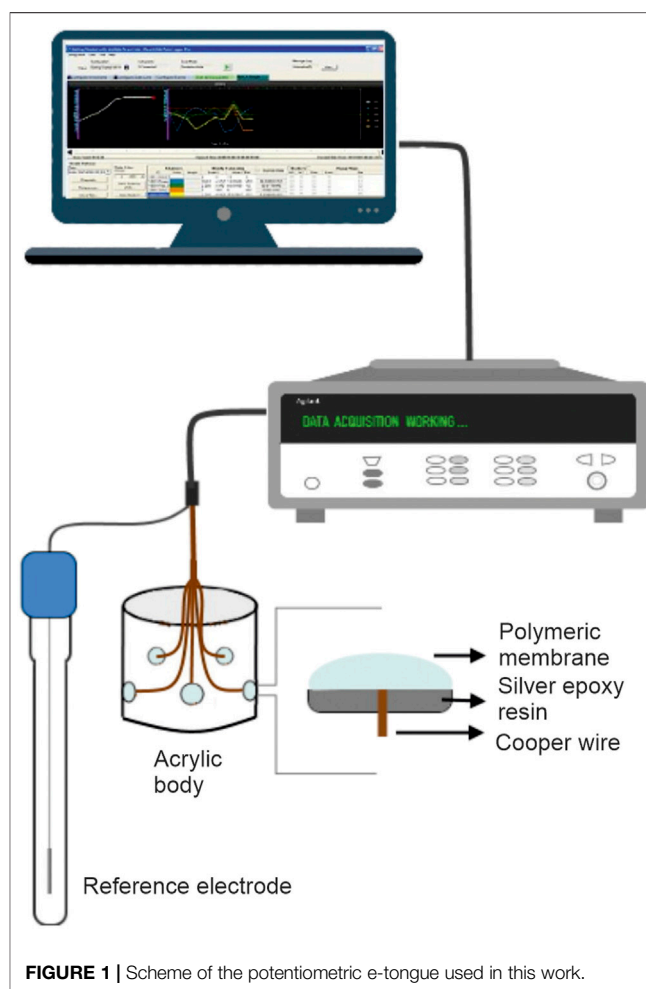
TABLE 2 | List of additives and plasticizers.

Component	Nomenclature	
Additives	Octadecylamine	1
	Oleyl alcohol	2
	Tridodecylmethylammonium chloride	3
	Oleic acid	4
Plasticizers	Bis(1-butylpentyl)adipate	A
	Tris(2-ethylhexyl)phosphate	B
	Dibutyl sebacate	C
	2-Nitrophenyl-octylether	D
	Diocetyl phenylphosphonate	F

(Sigma-Aldrich, St. Louis, United States). Additives and plasticizers were added to the polymeric matrix using tetrahydrofuran as the solvent (Sigma-Aldrich, St. Louis, United States). The final composition was 32% of PVC, 65% of the plasticizer compound, and 3% of the additive.

The additives and plasticizers are listed in **Table 2**. Five plasticizers (A–F) were combined with four additives (1–4) to obtain 20 different sensors that were named A1, A2, A3, A4; B1, B2, B3, B4; C1, C2, C3, C4; D1, D2, D3, D4; and F1, F2, F3, F4.

The body of the e-tongue consisted of an acrylic tube in which 20 holes of 0.3 cm diameter were drilled. Each hole was filled with a conductive silver epoxy resin (EPO-TEK, Billerica, United States) and connected to a multiplexer (Agilent Data Acquisition Switch Unit 34970A) via electrical copper wires. The outer surface of each hole was covered with one of the polymeric membranes described in **Table 2**. An Ag/AgCl electrode was used as the reference electrode for all measurements. **Figure 1** shows the schematic of the e-tongue system containing the working and reference electrodes connected to a multiplexer.

**FIGURE 1** | Scheme of the potentiometric e-tongue used in this work.

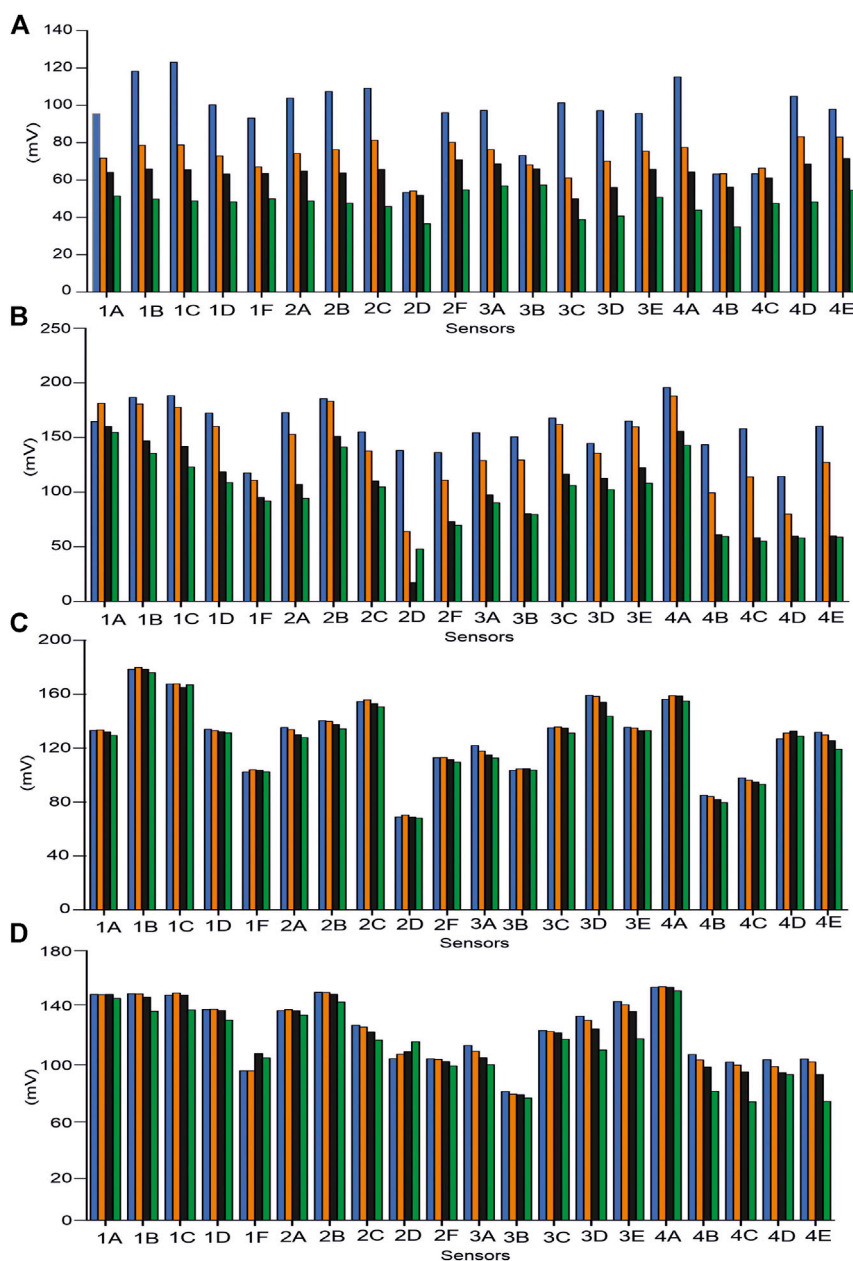


FIGURE 2 | Responses of the array of sensors to standard solutions of **(A)** CaCl_2 , **(B)** lactic acid, **(C)** lactose, and **(D)** galactose. Measures were carried out at four concentrations: 5×10^{-1} M (blue), 2×10^{-1} M (orange), 1×10^{-1} M (black), and 10^{-2} M (green) for ionic salts and 10^{-1} M (blue), 10^{-2} M (orange), 10^{-3} M (black), and 10^{-4} M (green) for lactic acid, lactose, and galactose.

The sensor array was immersed in a glass cell containing 100 ml of each sample (diluted 1:1 in deionized water). Potentiometric measurements were recorded for 5 min by registering the sensor signals every 3 s. All the samples were measured in quintuplicate. Throughout the experiment, the samples were kept at room temperature and under gentle agitation.

The statistical analysis was performed using RKWard 0.7.1 and Matlab R2014b (The Mathworks Inc., Natick, United States).

Data analysis included pre-processing of the potentiometric signals using the genetic algorithm and partial least squares (GA-PLS) procedure. Principal component analysis was used to assess the discrimination ability of the multisensor system. Support vector machine regression (SVMR) was used to establish correlations between the results obtained with the e-tongue and the chemical parameters given by chemical analysis. In addition, SVMR was used as a classification method to predict the quality of milk samples.

TABLE 3 | Sensitivity values obtained from the slopes of the calibration curves.

	NaCl	CaCl ₂	KCl	Lactose	Glucose	Galactose	Citric acid	Lactic acid
1A	81.30	78.37	58.06	16.13	18.62	10.23	35.98	46.24
1B	105.97	140.62	106.57	6.34	53.33	47.18	71.89	82.15
1C	133.63	128.83	118.81	15.08	58.38	47.18	38.40	88.65
1D	55.27	93.92	57.80	17.86	45.32	30.83	86.29	86.35
1F	75.25	64.44	32.41	-3.58	42.74	23.18	91.10	38.55
2A	86.73	98.96	81.74	46.61	62.42	-6.53	106.15	117.24
2B	69.79	109.17	76.80	27.60	35.56	15.69	100.90	75.27
2C	76.48	119.76	83.69	3.55	24.73	31.23	90.14	67.26
2D	80.30	37.77	70.35	0.37	26.92	56.74	114.94	123.56
2F	27.36	78.08	50.58	19.43	33.69	-12.14	85.45	86.45
3A	28.40	73.52	52.15	70.82	31.30	26.24	74.16	80.35
3B	18.37	29.75	15.46	8.06	87.40	72.91	96.37	115.37
3C	71.06	105.96	93.75	21.43	17.40	18.99	82.57	111.33
3D	65.93	109.58	86.87	76.46	86.20	81.04	36.42	64.25
3E	60.02	87.03	60.11	9.20	68.40	81.96	105.12	79.21
4A	102.35	127.67	105.21	-6.23	8.82	8.88	68.86	79.66
4B	65.80	63.98	24.07	40.01	39.74	78.39	101.56	83.27
4C	34.01	41.90	35.01	33.15	79.34	59.42	100.26	122.36
4D	113.37	105.73	64.77	-4.68	72.40	85.15	75.62	45.62
4E	34.85	86.26	57.28	79.23	84.50	80.32	97.65	126.32

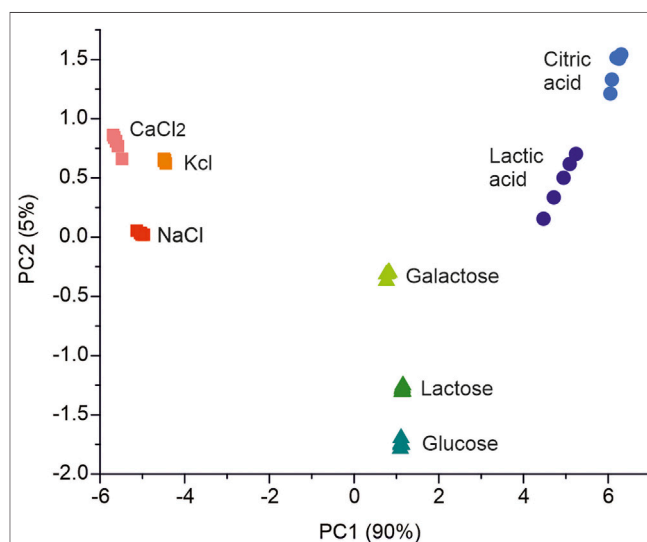
RESULTS

Characterization of the Individual Sensors

The performance of the 20 PVC membrane-based potentiometric sensors was evaluated using eight standard solutions of compounds commonly present in milk, including salts (KCl, CaCl₂, and NaCl), sugars (lactose, glucose, and galactose), and organic acids (citric acid and lactic acid), with concentrations ranging from 1×10^{-4} to 1×10^{-1} mol/L.

After immersing the electrodes in the corresponding solution, membrane potentials were recorded for 5 min every 3 s until stabilization of the signals. Signals were considered stable when an average variation of 1.6 mV/decade was observed between each reading. **Figure 2** illustrates the responses obtained when the sensors were immersed in standard solutions (figure shows the average of five replicas). This figure shows an example of salt (CaCl₂) and acid (lactic acid) of monosaccharide (galactose) and of disaccharide (lactose). The figure also includes the responses obtained at four different concentrations (5×10^{-1} M, 2×10^{-1} M, 1×10^{-1} M, and 10^{-2} M) for ionic salts and 10^{-1} M, 10^{-2} M, 10^{-3} M, and 10^{-4} M for the rest of the compounds. As shown in **Figure 2**, the sensors showed a variety of responses to the different components of milk. The sensitivity values shown in **Table 3** (measured as the slope of the calibration curves) were lower for sugars than for solutions containing ions and lactic acid, confirming the different reactivity of the sensors to components usually found in milk matrices. These differences confirm the cross-selectivity of the sensors and their suitability to be part of a multisensor system.

The signal repeatability and the reproducibility of the sensors against standard solutions were analyzed. Repeatability was evaluated by analyzing the responses of the sensors immersed in 0.1 M KCl solutions. Measurements were performed in

**FIGURE 3** | PCA score plot of the standard solutions of compounds present in milk.

quintuplicate, and coefficients of variation between 0.1 and 1.38% were obtained for all sensors. Reproducibility was calculated by analyzing the responses of two sets of identical sensors immersed in 0.1 M KCl solution. The responses of the sensors showed coefficients of variation between 0.57 and 7.76%. The lifetime was studied by calculating the coefficients of variation of the responses of the sensors immersed in 0.1 M KCl solution for a period of thirty days. The results showed coefficients of variation between 0.52 and 8.56%. The data collected with the set of 20 sensors were used as input variables for multivariate analysis. PCA was used to assess the

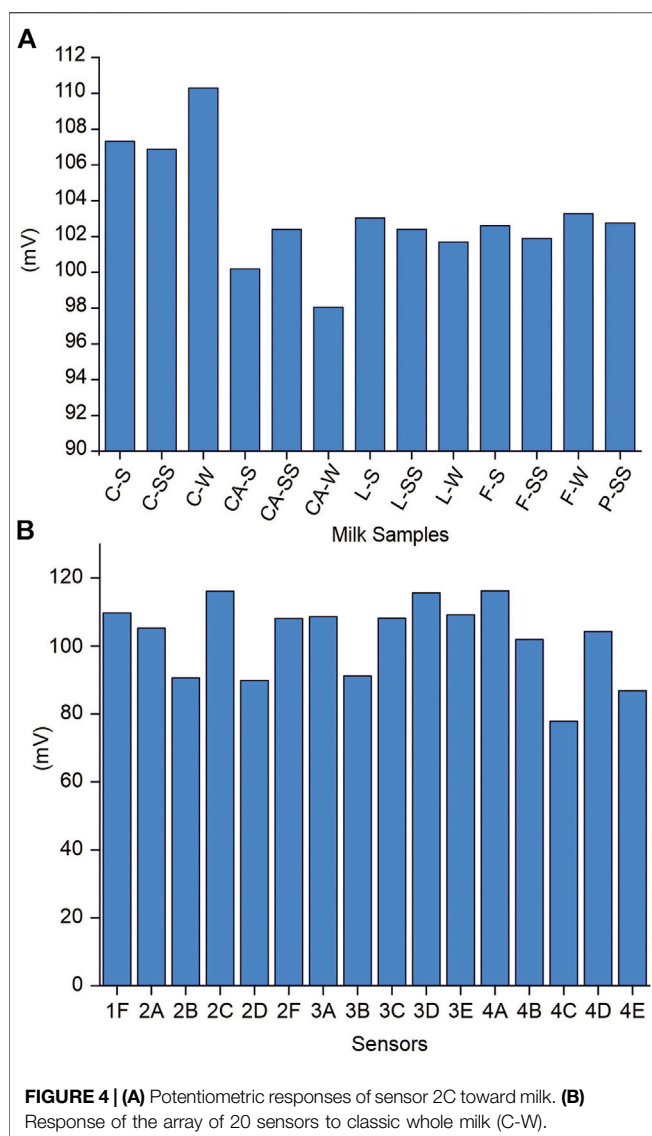


FIGURE 4 | (A) Potentiometric responses of sensor 2C toward milk. **(B)** Response of the array of 20 sensors to classic whole milk (C-W).

discrimination ability of the array. **Figure 3** shows the score plot of this analysis, in which the first two principal components explained 95% of the covariance of the data (90% by PC1 and 5% by PC2). The compounds analyzed were grouped according to their chemical nature. Ionic compounds appear on the left side of the graph, sugars in the middle, and organic acids in the right part of the diagram.

Analysis of Milk: Simplification of the Array of Sensors

The performance capabilities of the 20-sensor array were evaluated by registering the potentiometric signals obtained when the electrodes were immersed in milk samples of different qualities. **Figure 4** illustrates the responses of the sensors to the milk samples analyzed. As can be seen, each sensor shows distinct responses toward milk with different composition. For example, classic milk showed higher

potentials than calcium-enriched milk or lactose-free milk, regardless of their fat content. Moreover, all sensors showed significant differences between samples, confirming the cross-selectivity of the array.

The e-tongue developed here must operate in an industrial environment where time and cost are of paramount importance. For this reason, it is relevant to simplify the system by reducing the number of sensors included in the array but without losing information. A visual inspection of the sensor array responses indicated that some sensors could provide redundant information. For example, the responses of sensor 4A to different sugars were quite similar, and sensor 1F could barely detect sugars. To reduce the number of sensors in the array, the GA procedure was chosen to select the best sensors to be included in the array and build predictive regression models (Gendreau and Potvin, 2010). With GA, it is possible to get good solutions for the optimization problems. The GA was applied separately for the five chemical parameters (acidity, density, proteins, lactose, and fat). Fitting a PLS model (GA-PLS) to the sensor array for 13 milk samples and computing the performance by a leave-one-out cross-validation procedure was the way to optimize the problem. The chosen probability of initial variable selection was 0.5, the probability of crossover was 0.5, and the probability of mutation was 0.1. The selected variables were determined to be optimal after 500 GA-PLS evaluations with changing empirical parameter values. Ten iterations per evaluation were performed to avoid overfitting.

The response variable for each GA-PLS optimization was a vector of zeros and ones, corresponding to the thirteen milk types. In this way, the GA-PLS searches for the most relevant sensors in the electronic tongue to identify differences related to milk type. The sensors that provided a greater amount of information are indicated by showing higher responses in **Figure 5**. These sensors provided a better differentiation between samples according to the type of milk by nutritional content.

As can be seen, the sensors that include oleyl alcohol in their composition showed the best responses for each of the parameters studied. Therefore, these sensors were selected to form a new simplified e-tongue consisting of five sensors (2A, 2B, 2C, 2D, and 2F). The discrimination and prediction capability of the simplified e-tongue was studied.

Evaluation of the Performance of the 20-Sensor Array and the Simplified System Based on Five Sensors

1) Assessment of the discrimination capacity using PCA

In this section, the performance of the 20-sensor-based e-tongue was compared with that of the five-sensor-based system.

A PCA was performed to evaluate the discrimination ability of the array. **Figure 6A** shows the score plot of this analysis, in which the first three principal components jointly explained 88% of data variability (64% by PC1, 15% by PC2, and 9% by PC3). Surprisingly, discrimination between milk samples was not dominated by fat content. Instead, milk samples were grouped

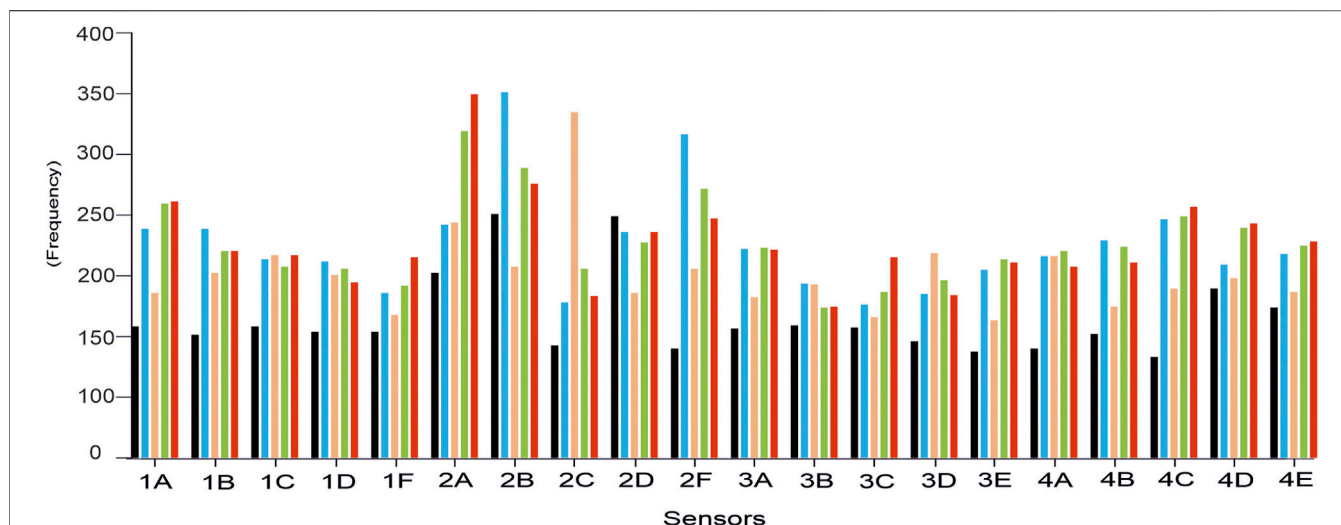


FIGURE 5 | Frequency of appearance of the sensors for 500 GA-PLS evaluations, for each of the empirical parameters: density (black), acidity (blue), fat (orange), protein (green), and lactose content (red).

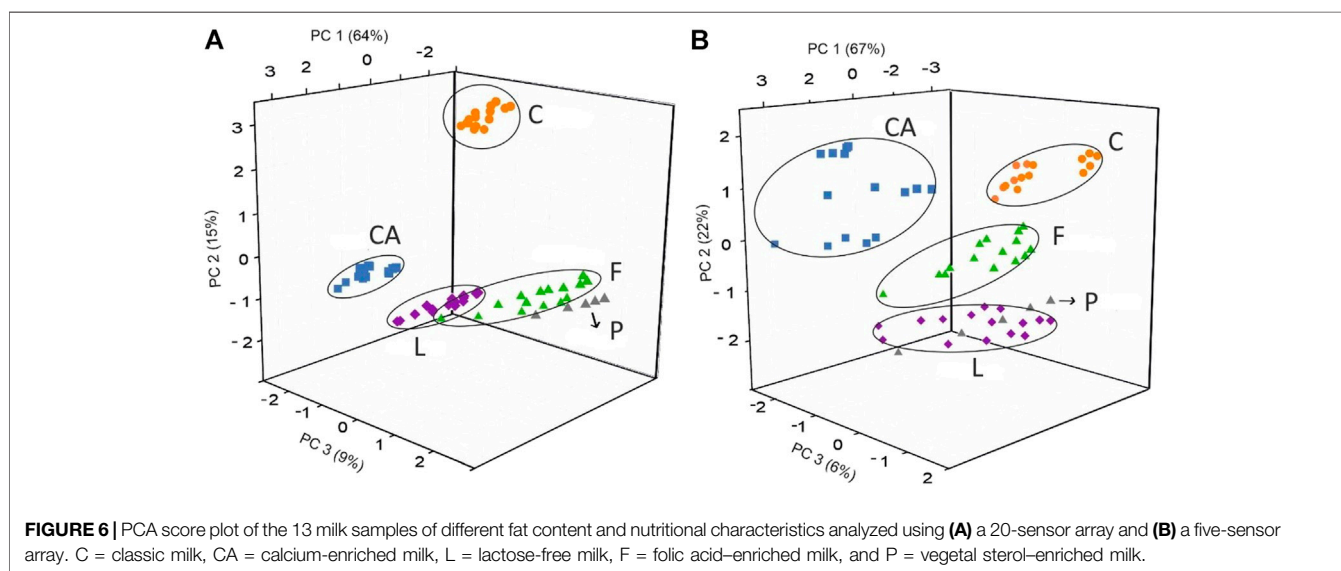


FIGURE 6 | PCA score plot of the 13 milk samples of different fat content and nutritional characteristics analyzed using (A) a 20-sensor array and (B) a five-sensor array. C = classic milk, CA = calcium-enriched milk, L = lactose-free milk, F = folic acid-enriched milk, and P = vegetal sterol-enriched milk.

according to added components (calcium or folic acid) or removed components (lactose). PC1 clearly discriminated classic milk (C: includes milk samples C-S, C-SS, and C-W) regardless of their fat content from the rest of the milk samples. PC2 discriminated calcium-enriched milk (CA: includes milk samples CA-S, CA-SS, and CA-W) from lactose-free milk (L: includes milk samples L-S, L-SS, and L-W) regardless of their fat content. Milk enriched in folic acid or in vegetal sterols appeared at the bottom of the diagram (F and P: include F-S, F-SS, F-W, and P-SS). The mixing of samples among some groups may be due to the sensitivity of the sensor device to other milk components such as fat content, which widely affect physicochemical aspects such as viscosity or density in the samples.

Figure 6B shows the score plot obtained from the responses to milk with different nutritional content obtained using the PE-tongue based on a five-sensor array. The first two PCs explain 89% of the total variance. As can be seen in **Figure 6B**, milk samples with similar nutritional content appeared in the same region of the graph. The first group contains milk with enhanced nutritional calcium content (CA: includes CA-S, CA-SS, and CA-W); the second group includes milk samples without any modification in terms of nutritional content (C: includes C-S, C-SS, and C-W); the third group contains milk that has been modified for low lactose content (L: includes L-S, L-SS, and L-W); finally, there is a mixed group with four types of milk samples with an increased amount of folic acid in their composition (F and P: include F-S, F-SS, F-W, and P-SS). The first and second

TABLE 4 | Results of the calibration and validation of SVMR for the 20-sensor e-tongue.

	Acidity	Density	%Proteins	%Lactose	%Fat
RMSE _c	0.1642	0.4575	0.0275	0.0239	0.3819
R _c ²	0.9915	0.9684	0.9912	0.9901	0.9287
RMSE _p	0.1988	0.6032	0.0341	0.0296	0.6102
R _p ²	0.9864	0.9452	0.9844	0.9844	0.7789

RMSE_c: root mean square error of calibration; R_c²: correlation coefficient in calibration; RMSE_p: root mean square error of prediction; R_p²: correlation coefficient in prediction.

groups, in the positive part of the second principal component, are separated by the first principal component (being in the positive and negative parts, respectively). The third, fourth, and fifth groups are separated by the second and third principal components (in the negative region) with a very low contribution of the first principal component.

This result indicates that the final subset of variables retained by GA-PLS presents the ability to discriminate milk classes according to their nutritional components, similar to that obtained with a complex system consisting of 20 sensors, although a complete discrimination has not been obtained.

2) Assessment of the classification capacity using SVM

The classification capability of the PE-tongue system was tested using SVM using the radial basis function (RBF) (Wu and Wang 2009) as a non-linear kernel, defined as follows:

$$K(x_i - x_j) = \exp(-\gamma \|x_i - x_j\|^2), \quad \gamma > 0,$$

where x_i and x_j are the training vectors of the input data and γ is the kernel parameter.

This kernel has been chosen since the number of instances is larger than the number of features, and therefore, it is recommended to use non-linear kernels (Hsu 2016).

In this study, the SVM model was trained with data obtained from 65 samples (corresponding to the thirteen types of milk samples with different fat content and nutritional characteristics). The same scaling factors were applied for the training and testing sets.

The optimal SVM regularization parameter (C, which is the penalty parameter of the error term) was set to the highest value (C = 100), implying that classification errors were not tolerated for the set of response patterns used for SVM training. Due to the relatively small number of available measurements, the leave-one-out cross-validation method was implemented to better estimate the true success rate that could be achieved with the SVM. This assumes that, with the given n measurements, the model was trained n times using n - 1 training vectors. This vector was then used for testing.

The results obtained for the 20-sensor array showed an accuracy of 99.87% for the classification of the 13 classes in training and 98.46% in validation. The results showed that the accuracy of the five-sensor array training set was 96.92%, and those of the validation set showed an accuracy of 90.76%, for the thirteen categories. Each of the problem samples was correctly

TABLE 5 | Results of the calibration and validation of SVMR for the five-sensor e-tongue.

	Acidity	Density	%Proteins	%Lactose	%Fat
RMSE _c	0.3908	0.9299	0.6018	0.0373	0.8866
R _c ²	0.9311	0.869	0.9372	0.9763	0.6350
RMSE _p	0.4522	1.0509	0.7005	0.0434	1.0286
R _p ²	0.9054	0.8316	0.9142	0.9666	0.3631

RMSE_c: root mean square error of calibration; R_c²: correlation coefficient in calibration; RMSE_p: root mean square error of prediction; R_p²: correlation coefficient in prediction.

classified according to its nutritional content. These results determine that the electronic tongue developed with five sensors was able to classify the milk samples according to their nutritional content and also by their fat content.

3) Prediction of chemical parameters by means of support vector machine regression (SVMR) models

One of the main challenges in the field of e-tongues is the implementation of models that can predict chemical parameters of importance in food quality control.

In this work, SVMR was used to predict acidity, density, and percentage of protein, lactose, and fat in milk. Sixty-five samples were used as the training set, and five samples (denoted V1, V2, V3, V4, and V5) were used as the external test set. The radial basis function, which could handle the non-linear relationships between the sensor signals and the target attributes, was chosen as the core function to predict acidity, density, and percentage of protein, lactose, and fat.

Although an electronic tongue has been shown to be able to perform classifications, the challenge for the reduced PE-tongue system is the implementation of regression models that can predict physicochemical parameters with adequate correlation values. For this purpose, SVMR has been applied to the 20-sensor array data.

Two data matrices have been built: the “X” matrix (predictors) constructed from the data recorded by the electronic tongue analyzing the milk samples and the “Y” matrix (responses) containing data of chemical parameters (acidity, density, protein, lactose, and fat) of the milk samples. Regression models were created using SVM regression (epsilon SVM, kernel type: radial basis function, C value: 1, cross-validation segment size: 15, and standard deviation weighting process in all cases).

The values obtained for the correlation coefficients and errors of calibration and prediction are shown in **Table 4**. In the case of acidity, protein content, lactose content, and density, the developed models achieved correlation values R^2 above 0.94 for both calibration and prediction, with low errors (RMSE) between 0.0239 and 0.9915. Lactose was the parameter with the lowest errors and highest correlation. In the case of fat, the correlation value only achieved 0.7789 for the prediction with a higher error of 0.6102.

The recognition capability of the five-sensor-based PE-tongue was tested by applying an SVM classification (SVMC) model. In this study, the model was trained with the data of 65 samples for

TABLE 6 | Results of the prediction of chemical parameters in a set of five external samples.

	Sample 1	Sample 2	Sample 3	Sample 4	Sample 5
Acidity predicted	16.113	12.594	12.661	13.095	12.532
Acidity by traditional methods	15.94	12.36	12.45	12.95	12.45
% Relative error	1.07	1.86	1.69	1.16	0.64
Density predicted	1,038.831	1,031.995	1,031.97	1,031.463	1,031.452
Density by traditional methods	1,039	1,032.14	1,032.45	1,030.92	1,029.92
% Relative error	0.02	0.01	0.48	0.05	0.15
Proteins predicted	3.914	3.375	3.369	3.338	3.368
Proteins by traditional methods	3.89	3.34	3.35	3.29	3.33
% Relative error	0.51	1.2	0.6	1.52	1.2
Lactose predicted	5.464	4.976	4.98	4.937	0.531
Lactose by traditional methods	5.49	4.97	4.96	4.89	0.52
% Relative error	0.55	0.2	0.4	1.02	0.2
Fat predicted	0.41	1.665	1.716	2.572	2.31
Fat by traditional methods	0.35	1.58	1.65	3.12	3.58
% Relative error	40.20	5.06	4.24	17.63	35.47

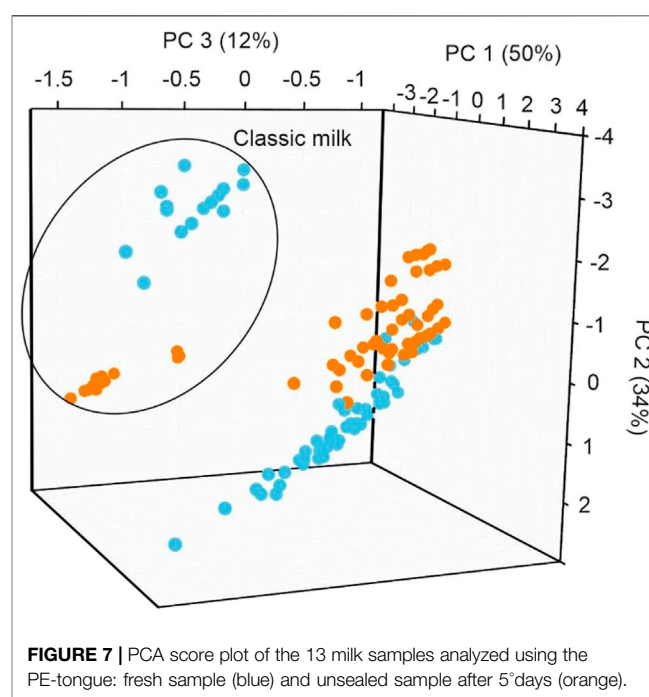
the training set (corresponding to 13 types of milk samples depending on their fat content and nutritional content), calibrated against the true type, and used to predict the classification of the problem samples (five milk samples with different nutritional content) for the test set.

The values obtained for the correlation coefficients and errors of calibration and prediction are shown in **Table 5**.

As can be seen, in the case of acidity, protein content, lactose content, and density, the developed models reached values above 0.85 for both calibration and prediction, with low errors between 0.0373 and 1.0509, lactose being the parameter with lowest errors (0.0373 for the calibration and 0.0434 for the prediction) and the highest correlation (0.9763 for the calibration and 0.9666 for the prediction). However, in the case of fat, it is observed that a good correlation between the data provided by an electronic tongue and the physical-chemical data was not achieved.

Once the SVMR model was built, as a verification of its applicability, regression models were used to predict the physicochemical parameters (acidity, density, proteins, lactose, and fat) of a set of five external samples that were not included in the creation of the model. The results are shown in **Table 6** vs. those obtained by traditional methods.

The results obtained showed that the SVM regression model was able to predict the physicochemical factors with values that showed low relative errors with respect to the values obtained by traditional analysis techniques, the lowest errors being reached for lactose content and density. However, in the case of fat content, as expected given its correlation parameters, the values obtained by prediction show a high error, with the highest value being 2.11% in the case of skim milk. These results show that the model developed is unable to predict the fat content. In spite of the number of research works dedicated to the analysis of milk with potentiometric electronic tongues, the effect of the interaction between fats and the sensor membranes has not been discussed (Ciosek, 2016; Poghossian et al., 2019; Rodríguez-Mendez et al., 2016). A possible explanation is that when sensors are immersed in milk, fats participate in the formation of the double layer that creates the membrane

**FIGURE 7 |** PCA score plot of the 13 milk samples analyzed using the PE-tongue: fresh sample (blue) and unsealed sample after 5 days (orange).

potential. Once the double layer is formed, the excess of lipids does not contribute to the signal.

Spoilage Monitoring

The capabilities of the simplified array were further evaluated by analyzing the capabilities to detect spoilage. For this purpose, tetrabrick packs were opened and stored at 5°C. Measurements were performed right after opening the packs and 5 days later.

PCA was used as a first approach to evaluate the ability of the PE-tongue to detect spoilage occurring in unsealed milk. As shown in **Figure 7**, the classic milk sample appeared clearly separated from the rest of the milk samples, and the simplified PE-tongue could detect compositional changes occurring during

storage. The reason why the classic milk samples (C-S, C-SS, and C-W) have a different aging behavior may be related to the fact that the rest of the milk samples have undergone various processes that can affect their composition. When examining the rest of the milk samples, a partial overlap between fresh and aged samples could be observed. This could be due to the fact that the degradation process does not occur at the same rate in all samples, as it can be affected by multiple factors such as milk composition and sample handling.

SVMC was used to classify between the two milk groups: fresh milk and aged milk. The classification results using the dataset showed that the sensor array achieved classification of the fresh and aged milk samples with an accuracy of 92.31% for the training set and 90.77% for the validation set. These results determine that the electronic tongue developed with five sensors was able to classify milk samples according to their state of preservation. Using SVMR, it has been demonstrated that the PE-tongue could be used to accurately predict physicochemical properties of the unsealed milk. After predicting the acidity of the aged samples, each of the samples showed an increase of approximately 1.20D in acidity. These results are consistent with the expected increase in milk acidity as a result of the increased microbiological activity in the unsealed samples.

CONCLUSION

In this work, a simplified and portable electronic tongue (PE-tongue) was developed and used to predict chemical characteristics of milk samples. The system used only five potentiometric sensors that were selected from an extended array of 20 sensors using the genetic algorithm. PCA showed that the PE-tongue showed similar discrimination capabilities to the extended ET consisting of 20 sensors, but with a substantial decrease in the number of variables

to be managed. The PE-tongue could be successfully used to classify milk with different nutritional characteristics and to predict acidity, density, %proteins, %lactose, and %fat, with low errors and high correlation coefficients. Potentiometric data acquired with the PE-tongue were successfully subjected to support vector machine (SVM) for classification of fresh and spoiled milk samples and to establish correlations with acidity of unsealed milk with excellent results.

DATA AVAILABILITY STATEMENT

The raw data supporting the conclusions of this article will be made available by the authors, without undue reservation.

AUTHOR CONTRIBUTIONS

MR-M, CG-C, and FM-P conceptualized the idea and supervised the work. CP-G and CS-C performed the experiment, curated the data, and wrote the original draft. FM-P involved in software design and development. CP-G, CS-C, MR-P, and LD involved in formal analysis. CG-C and MR-M acquired the funding. CP-G, CS-C, FM-P, MR-M, CG-C, and LD reviewed and edited the paper. All authors provided feedback.

FUNDING

We appreciate the financial support of MINECO-FEDER Plan Nacional (RTI 2018-097990-B-I00) and Junta de Castilla y León-FEDER (VA275P18) and “Infraestructuras Red de Castilla y León (INFRARED)” UVA01.

REFERENCES

- Beg, A. H., and Islam, M. Z. (2016). Advantages and Limitations of Genetic Algorithms for Clustering Records, Industrial Electronics and Applications (ICIEA), 2478–2483. doi:10.1109/iciea.2016.7604009
- Bougrini, M., Tahri, K., Haddi, Z., El Bari, N., Llobet, E., Jaffrezic-Renault, N., et al. (2014). Aging Time and Brand Determination of Pasteurized Milk Using a Multisensor E-Nose Combined with a Voltammetric E-Tongue. *Mater. Sci. Eng. C* 45, 348–358. doi:10.1016/j.msec.2014.09.030
- Cetó, X., Apetrei, C., Del Valle, M., and Rodríguez-Méndez, M. L. (2014). Evaluation of Red Wines Antioxidant Capacity by Means of A Voltammetric E-Tongue with an Optimized Sensor Array. *Electrochimica Acta* 120, 180–186. doi:10.1016/j.electacta.2013.12.079
- Ciosek, P. (2016). “Milk and Dairy Products Analysis by Means of an Electronic Tongue,” in *Electronic Noses and Tongues in Food Science*. Editor M. L. Rodriguez-Mendez. (Academic Press), 209–223. doi:10.1016/b978-0-12-800243-8.00021-4
- Ciosek, P., and Wróblewski, W. (2008). Miniaturized Electronic Tongue with an Integrated Reference Microelectrode for the Recognition of Milk Samples. *Talanta* 76, 548–556. doi:10.1016/j.talanta.2008.03.051
- Ciosek, P., and Wróblewski, W. (2015). Potentiometric and Hybrid Electronic Tongues for Bioprocess Monitoring - an Overview. *Anal. Methods* 7, 3958–3966. doi:10.1039/c5ay00445d
- Ciosek, P., and Wróblewski, W. (2011). Potentiometric Electronic Tongues for Foodstuff and Biosample Recognition-An Overview. *Sensors* 11, 4688–4701. doi:10.3390/s110504688
- Dias, L. A., Peres, A. M., Veloso, A. C. A., Reis, F. S., Vilas-Boas, M., and Machado, A. A. S. C. (2009). An Electronic Tongue Taste Evaluation: Identification of Goat Milk Adulteration with Bovine Milk. *Sensors Actuators B: Chem.* 136, 209–217. doi:10.1016/j.snb.2008.09.025L
- Gendreau, M., and Potvin, J. Y. (2010). Handbook of Metaheuristics. International Series in Operations Research & Management Science, Springer, Boston, MA.
- Hayaschi, K., Toko, K., Yamanaka, M., Yoshihara, H., Yamafuji, K., Ikazeki, H., et al. (1995). Electric Characteristics of Lipid-Modified Monolayer Membranes for Taste Sensors. *Sensors and Actuators B* 23, 55–61. doi:10.1016/0925-4005(94)01522-j
- Holmin, S., Björefors, F., Eriksson, M., Krantz-Rülcker, C., and Winqvist, F. (2002). Investigation of Electrode Materials as Sensors in a Voltammetric Electronic Tongue. *Electroanalysis* 14, 839–847. doi:10.1002/1521-4109(200206)14:12<839::aid-elan839>3.0.co;2-y
- Hruškar, M., Major, N., Krpan, M., and Vahčić, N. (2010). Simultaneous Determination of Fermented Milk Aroma Compounds by a Potentiometric Sensor Array. *Talanta* 82, 1292–1297. doi:10.1016/j.talanta.2010.06.048
- Hsu, C. W., Chang, C. C., and Lin, C. J. (2016). A Practical Guide to Support Vector Classification. *Tech. Rep.* https://www.csie.ntu.edu.tw/~cjlin/.
- Leardi, R., and Lupiáñez González, A. (1998). Genetic Algorithms Applied to Feature Selection in PLS Regression: How and when to Use Them. *Chemometrics Intell. Lab. Syst.* 41, 195–207. doi:10.1016/s0169-7439(98)00051-3
- Mabrook, M. F., Darbyshire, A. M., and Petty, M. C. (2006). Quality Control of Dairy Products Using Single Frequency Admittance Measurements. *Meas. Sci. Technol.* 17, 275–280. doi:10.1088/0957-0233/17/2/007

- Minghui, P., Lingjun, T., Xuelu, C., Nasi, A., Yungang, C., and Baoguo, S. (2019). Comparison of Sensory and Electronic Tongue Analysis Combined with HS-SPME-GC-MS in the Evaluation of Skim Milk Processed with Different Preheating Treatments. *Molecules* 24 (9), 1650. doi:10.3390/molecules24091650
- Mirjalili, S. (2019). “Genetic Algorithm,” in *Studies in Computational Intelligence* Springer, Cham, 780. Editors Evolutionary Algorithms, and Neural Networks. doi:10.1007/978-3-319-93025-1
- Podraška, M., Bącznyńska, E., Kundys, M., Jeleń, P., and Witkowska, E. (2018). Electronic Tongue—A Tool for All Tastes? *Biosensors* 8-1, 3. doi:10.3390/bios8010003
- Poghossian, A., Geissler, H., and Schoning, M. J. (2019). Rapid Methods and Sensors for Milk Quality Monitoring and Spoilage Detection. *Biosens. Bioelectron.* 140, 18–31. doi:10.1016/j.bios.2019.04.040
- Prieto, N., Oliveri, P., Leardi, R., Gay, M., Apetrei, C., Rodríguez-Méndez, M. L., et al. (2013). Application of a GA-PLS Strategy for Variable Reduction of Electronic Tongue Signals. *Sensors Actuators B: Chem.* 183, 52–57. doi:10.1016/j.snb.2013.03.114
- Rodríguez-Mendez, M. L., De Saja, J. A., Gonzalez-Anton, R., García-Hernández, C., Medina-Plaza, C., and García-Cabezón, C. (2016). Electronic Noses and Tongues in Wine Industry. *Front. Bioeng. Biotechnol.* 4, 81. doi:10.3389/fbioe.2016.00081
- Rodríguez-Mendez, M. L. (2016). Electronic Noses and Tongues in the Food Industry. *Elsevier-academic Press*.
- Salvo-Comino, C., García-Hernández, C., García-Cabezón, C., and Rodríguez-Méndez, M. (2018). Discrimination of Milks with a Multisensor System Based on Layer-By-Layer Films. *Sensors* 18 (8), 2716. doi:10.3390/s18082716
- Scagiona, V. P., Mercante, L. A., Sakamoto, K. Y., Oliveira, J. E., Fonseca, F. J., Mattoso, L. H. C., et al. (2016). An Electronic Tongue Based on Conducting Electrospun Nanofibers for Detecting Tetracycline in Milk Samples. *RSC Adv.* 6. doi:10.3740/103746
- Tazi, I., Choiriyah, A., Siswanta, D., and Triyana, K. (2017). Detection of Taste Change of Bovine and Goat Milk in Room Ambient Using Electronic Tongue. *Indones. J. Chem.* 17, 422–430. doi:10.22146/ijc.25288
- Tazi, I., Triyana, K., Siswanta, D., Veloso, A. C. A., Peres, A. M., and Dias, L. G. (2018). Dairy Products Discrimination According to the Milk Type Using an Electrochemical Multisensor Device Coupled with Chemometric Tools. *Food Measure* 12, 2385–2393. doi:10.1007/s11694-018-9855-8
- Toldrá, F., Leo, M. L., and Nollet, L. (2021). *Handbook of Dairy Foods Analysis*. CRC Press. ISBN: 9780367343132.
- Torabi, F., Ghasemi, J. B., Faridbod, F., and Ganjali, M. R. (2020). Simultaneous Quantification of Nine Major Water-Soluble Inorganic Ions Using a Potentiometric Electronic Tongue in Cheese Samples. *IEEE Sensors J.* 20, 10138–10144. doi:10.1109/jsen.2020.2990130
- Vlasov, Y., Legin, A., Rudnitskaya, A., Di Natale, C., and D’Amico, A. (2005). Nonspecific Sensor Arrays (“electronic Tongue”) for Chemical Analysis of Liquids (IUPAC Technical Report). *Pure Appl. Chem.* 77, 1965–1983. doi:10.1351/pac200577111965
- Wei, Z., Wang, J., and Zhang, X. (2013). Monitoring of Quality and Storage Time of Unsealed Pasteurized Milk by Voltammetric Electronic Tongue. *Electrochimica Acta* 88, 231–239. doi:10.1016/j.electacta.2012.10.042
- Wu, K.-P., and Wang, S.-D. (2009). Choosing the Kernel Parameters for Support Vector Machines by the Inter-cluster Distance in the Feature Space. *Pattern Recognition* 42, 710–717. doi:10.1016/j.patcog.2008.08.030
- Zeng, L., Wu, D., and Yang, B. (2018). “Electrochemical Methods of Analysis – Amperometry” in *Electrochemical Sensors for Food Safety*.

Conflict of Interest: The authors declare that the research was conducted in the absence of any commercial or financial relationships that could be construed as a potential conflict of interest.

The handling Editor declared a past co-authorship with the authors CS, MR.

Copyright © 2021 Pérez-González, Salvo-Comino, Martin-Pedrosa, Dias, Rodriguez-Perez, Garcia-Cabezón and Rodriguez-Mendez. This is an open-access article distributed under the terms of the Creative Commons Attribution License (CC BY). The use, distribution or reproduction in other forums is permitted, provided the original author(s) and the copyright owner(s) are credited and that the original publication in this journal is cited, in accordance with accepted academic practice. No use, distribution or reproduction is permitted which does not comply with these terms.



Co-Immobilized Capillary Enzyme Reactor Based on Beta-Secretase1 and Acetylcholinesterase: A Model for Dual-Ligand Screening

Adriana Ferreira Lopes Vilela, Vitor Eduardo Narciso dos Reis and Carmen Lúcia Cardoso*

Departamento de Química, Grupo de Cromatografia de Bioafinidade e Produtos Naturais, Faculdade de Filosofia, Ciências e Letras de Ribeirão Preto, Universidade de São Paulo, Ribeirão Preto, Brazil

OPEN ACCESS

Edited by:

Eugenia Gallardo,
Universidade da Beira Interior,
Portugal

Reviewed by:

Shouyu Wang,
Jiangnan University, China
Benjamin L. Oyler,
Vaccine Research Center (NIAID),
United States

*Correspondence:

Carmen Lúcia Cardoso
ccardoso@ffclrp.usp.br

Specialty section:

This article was submitted to
Analytical Chemistry,
a section of the journal
Frontiers in Chemistry

Received: 11 May 2021

Accepted: 23 June 2021

Published: 08 July 2021

Citation:

Vilela AFL, Narciso dos Reis VE and
Cardoso CL (2021) Co-Immobilized
Capillary Enzyme Reactor Based on
Beta-Secretase1 and
Acetylcholinesterase: A Model for
Dual-Ligand Screening.
Front. Chem. 9:708374.
doi: 10.3389/fchem.2021.708374

We have developed a dual enzymatic system assay involving liquid chromatography-mass spectrometry (LC-MS) to screen AChE and BACE1 ligands. A fused silica capillary (30 cm × 0.1 mm i.d. × 0.362 mm e.d.) was used as solid support. The co-immobilization procedure encompassed two steps and random immobilization. The resulting huAChE+BACE1-ICER/MS was characterized by using acetylcholine (ACh) and JMV2236 as substrates. The best conditions for the dual enzymatic system assay were evaluated and compared to the conditions of the individual enzymatic system assays. Analysis was performed in series for each enzyme. The kinetic parameters (K_{Mapp}) and inhibition assays were evaluated. To validate the system, galantamine and a β -secretase inhibitor were employed as standard inhibitors, which confirmed that the developed screening assay was able to identify reference ligands and to provide quantitative parameters. The combination of these two enzymes in a single on-line system allowed possible multi-target inhibitors to be screened and identified. The innovative huAChE+BACE1-ICER/MS dual enzymatic system reported herein proved to be a reliable tool to identify and to characterize hit ligands for AChE and BACE1 in an enzymatic competitive environment. This innovative system assay involved lower costs; measured the product from enzymatic hydrolysis directly by MS; enabled immediate recovery of the enzymatic activity; showed specificity, selectivity, and sensitivity; and mimicked the cellular process.

Keywords: co-immobilization procedure, dual enzymatic system assay, screening dual-target ligands, acetylcholinesterase, beta-secretase1

INTRODUCTION

Enzymes, play a fundamental role in cellular biochemical processes and are involved in many pathologies, have been investigated by researchers in the field of drug discovery and development. Investigations into the interaction of proteins and enzymes with target ligands provide essential information about biological systems, contributing to the design of new therapeutic interventions (Silber, 2010; Mignani et al., 2016; Cass et al., 2020).

Given that various small molecules are available for the production of new drugs and in view of the numerous biological targets known to date, new strategies must be adopted to develop relevant, reproducible, reliable, and robust moderate to high-throughput screening platforms for drug discovery (Janzen, 2014; Hage, 2017).

In this context, robust screening assays that employ enzymes immobilized on solid supports have received increasing attention because they offer advantages like improved stability and the possibility of proteins being reused (de Moraes et al., 2016). Such screening assays are based on bioaffinity chromatography, which combines the specificity and sensitivity of an enzymatic reaction with the automation and reproducibility of a chromatographic system (Acker and Auld, 2014; de Moraes et al., 2019).

Current approaches for high-throughput screening (HTS) are based on the search for compounds with efficacy toward a single target. However, a new paradigm is emerging in pharmacological research-exploration of the bioactivity of compounds at multiple targets (Mignani et al., 2016). This could enhance the therapeutic efficacy for diseases such as Alzheimer's disease (AD), which has heterogeneous etiology and complex mechanism and is the most common form of dementia leading to neurodegeneration (Anand et al., 2014; Hughes et al., 2016; Ramsay et al., 2018). Indeed, existing treatments for AD have shortcomings or result in failure, so researchers have been devoted to changing drug design strategies to investigate multitarget-directed ligands (Hughes et al., 2016; de Freitas Silva et al., 2018; Maramai et al., 2020; Uddin et al., 2021).

Because the enzymes acetylcholinesterase and beta-secretase are the main targets involved in AD progression, they have been widely studied, paving the way for future pharmacological treatment of the disease (Deardorff et al., 2015; Coimbra et al., 2018). Acetylcholinesterase (AChE, EC 3.1.1.7), a carboxyl transferase found in neuromuscular junctions and cholinergic brain synapses, occurs in all species belonging to the animal kingdom. AChE regulates the end of the transmission of the neurotransmitter acetylcholine (ACh) in cholinergic synapses (Fotiou et al., 2015). In turn, beta-secretase 1 (BACE1, EC 3.4.23.48), an aspartyl protease found in the brain, plays a pivotal part in the formation of the myelin sheath in peripheral nerve cells. BACE1 initiates the proteolytic cleavage of the amyloid precursor protein (APP) at the luminal end of the cell membrane, forming the C-terminal fragment that is subsequently cleaved by γ -secretase at the N-terminal end, to generate the amyloid peptide (A β peptide) (Willem et al., 2006). Regulating both AChE and BACE1 during the treatment of AD is important and has motivated the scientific community to search for molecules that can inhibit these enzymes more efficiently (Deardorff et al., 2015; Fotiou et al., 2015; Prati et al., 2018).

Ligand screening studies based on assays with AChE (Vanzolini et al., 2018; Seidl et al., 2019) and BACE (Ferreira Lopes Vilela and Cardoso, 2017; Schejbal et al., 2019; Ye et al., 2021) immobilized on solid supports have been reported. However, the modulating effect of the screened bioactive compound may present limitations in the entire biological system *in vivo*, so targeting a single target can produce undesirable dual or synergistic effects (Pang et al., 2012). Therefore, developing dual enzymatic system assays that can mimic cellular process has become relevant for better understanding of these mechanisms of action in biological systems and drug discovery research.

Immobilized enzymes are widely used in many other sectors such as the pharmaceutical, chemical, and cosmetic industries,

food processing, biofuel production, medical devices and biosensors, (Basso and Serban, 2019; Basso and Serban, 2020), and proteomic analyses by online protein digestion (Wang et al., 2016; Toth et al., 2017).

Multi-target systems can be developed by co-immobilization (Orrego et al., 2020) and have aroused interest due to their different applications, which include screening of ligands (Chen et al., 2017; Wu et al., 2020), syntheses of products (Betancor and Luckarift, 2010), design of biocatalyst cascades (Kang et al., 2014), and construction of biosensors to detect diseases (Zhang et al., 2012).

Given the inability of the one-target one-molecule strategy to develop efficient drugs for AD treatment over the last 20 years (Blaikie et al., 2019), we were motivated to develop a dual system assay to screen multitarget-directed ligands that are more fitting to AD treatment. To contribute to this field, here we report the development of an innovative, automated dual enzymatic system assay based on AChE and BACE1 co-immobilized on the inner surface of a fused silica capillary (30 cm \times 0.1 mm i.d. \times 0.362 mm e.d.) to screen ligands. Co-immobilization comprised two steps: first, the fused silica capillary was activated; then, the enzymes were covalently attached via amine-glutaraldehyde reaction. The resulting huAChE+BACE1-ICER was connected as a bioaffinity column to a liquid chromatographic system (LC) coupled to mass spectrometry (MS), to measure the activities of the enzymes. Comparisons with individual enzymatic systems were made. Next, the dual enzymatic system assay was validated, which allowed us to confirm standard inhibitors for both enzymes by determining the half-maximum inhibitory concentration (IC₅₀). The dual enzymatic system assay proved to be an improvement on the HTS technique and can aid the search for multitarget-directed ligands in drug discovery for complex diseases.

MATERIALS AND METHODS

Reagents and Solutions

The lyophilized powders of the enzymes β -secretase (BACE1, EC 3.4.23.48, human extracellular domain and recombinant C-terminal FLAG®-tagged expressed in HEK 293 cells) and acetylcholinesterase (huAChE EC 3.1.1.7, 1,000 units.mg⁻¹ from human recombinant, expressed in HEK 293 cells), the β -secretase inhibitor, acetylcholine iodide (ACh), and galantamine hydrobromide were obtained from Sigma-Aldrich (St. Louis, MO, United States). The peptide substrate *ortho*-aminobenzoyl (Abz)-(Asn⁶⁷⁰, Leu⁶⁷¹)-Amyloid β A4 Protein Precursor₇₇₀ (669–674) – ethylenediamine 2,4-dinitrophenol (EDDnp) trifluoroacetate salt (named JMV2236 hereafter) was acquired from Bachem AG (Bubendorf, Switzerland). Glutaraldehyde solution (25%), dimethyl sulfoxide (DMSO), solution components, and all the chemicals used during the immobilization procedure were of analytical grade and were supplied by Sigma-Aldrich (St. Louis, United States), Merck (Darmstadt, Germany), Synth (São Paulo, Brazil), or Acros (Geel, Belgium).

The water used in all the preparations was deionized in a Millipore Milli-Q® system (Millipore, São Paulo, Brazil). The

TABLE 1 | LC-MS conditions for measuring enzymatic activity in the huAChE+BACE1-ICER-LC-MS system.**LC-MS Conditions for dual and individual enzymatic assays**

	huAChE	BACE1
Substrate	ACh	JMV2236
Mobile phase	Pump A (isocratic mode): ammonium acetate solution, 15 mM, pH 4.5 Pump B (isocratic mode): methanol 100%	
Temperature	37°C	
Flow rate	0.02 ml min ⁻¹	
Injection volume	10 µL	
MS detection ^a	[M+H] ⁺ <i>m/z</i> 104	[M+H] ⁺ <i>m/z</i> 464.2 [M+H] ⁺ <i>m/z</i> 542.1
Stop flow	0 min	5 min
Analysis time	5 min	10 min

^amean error ± 0.5.

fused silica capillary (0.362 mm × 0.1 mm i.d.) was purchased from Polymicro Technologies (Phoenix, AZ, United States).

The mobile phases were prepared daily. The JMV2236 (1 mM) and β-secretase inhibitor (1 mM) stock solutions were prepared in DMSO and stored at -20°C. The ACh (1 mM) and galantamine (1 mM) stock solutions were prepared in ammonium acetate solution (15 mM, pH 4.5) and stored at -6°C.

Instrumentation and System Configuration for Analyses

The LC-MS analyses were conducted on an LC system Nexera XR HPLC (Shimadzu, Kyoto, Japan) equipped with two LC 20AD pumps, an SIL-20A autosampler, a DGU 20A degasser, a CTO-20A oven, and an interfaced CBM-20A system. The LC system was coupled to an AmaZon speed Ion Trap (IT) Mass Spectrometry (MS) (Bruker Daltonics, Bremen, Germany) equipped with an Electrospray Ionization (ESI) interface. Individual and dual enzymatic systems (30 cm × 0.1 mm i.d. × 0.362 mm e.d.) were placed in the LC system as the bioaffinity column for on-flow MS.

The ESI ionization parameters were as follows: capillary voltage = 4.000 V, end plate voltage = 500 V, drying gas flow = 6 L min⁻¹, drying temperature = 270°C, and nebulizer pressure = 18 psi. MS operating in the single ion-monitoring mode under positive ionization as follows: for huAChE (UltraScan 50–250 *m/z*), detection of the cations [M+H]⁺ *m/z* 146 (ACh) and [M+H]⁺ *m/z* 104 (Ch, the product of the enzymatic catalysis); for BACE1 (enhanced resolution 300–1,000 *m/z*), detection of the cations [M+H]⁺ *m/z* 987.5 (JMV2236) and [M+H]⁺ *m/z* 464.2 and *m/z* 542.1 (JMV2236 product of BACE1-catalyzed hydrolysis).

The LC analyses were performed at 37°C; 15 mM ammonium acetate solution pH 4.5 was used as mobile phase (pump A) at a flow rate of 20 µL min⁻¹, and a second pump (B) delivered methanol after the ICER and before the IT-MS throughout a “T” shaped connection, at the same flow rate as the mobile phase of pump A (See **Table 1**).

The data were collected with the Bruker Daltonics Data Analysis software (version 4.3).

A syringe pump model 11 Plus advanced single (Harvard Apparatus, Holliston, United States) was used to infuse all the solutions during the immobilization procedure.

Preparation and Evaluation of Individual Enzymatic Systems

huAChE or BACE1 Immobilization

huAChE (17 units.ml⁻¹ in 50 mM phosphate solution, pH 7.4) and BACE1 (942.8 units.ml⁻¹ in 50 mM phosphate solution, pH 7.4) were immobilized, separately, on the internal surface of an open tubular silica capillary (100 cm × 0.1 mm i.d. × 0.362 mm e.d.) by following previous protocols for individual enzyme immobilization as described in (Ferreira Lopes Vilela and Cardoso, 2017).

In each case, the 100-cm capillary was divided, to produce three 30-cm-long huAChE-ICERs or BACE1-ICERs.

Influence of the pH of the LC-MS System Mobile Phase

For huAChE-ICER and BACE1-ICER, 10-µL aliquots of ACh (70 µM) or JMV2236 (100 µM) solution at different pH values (from 4.0 to 6.0) were injected into the individual enzymatic system operating at 0.02 ml min⁻¹ and 37°C.

Apparent Kinetic Constant (*K*_{Mapp}) Studies

The *K*_{Mapp} constant of huAChE-ICER was obtained by using different ACh concentrations (25, 50, 75, 100, 125, 150, 250, or 1,000 µM) in ammonium acetate solution (15 mM, pH 4.5). To this end, 20 µL of each solution was further diluted to a final volume of 100 µL with ammonium acetate solution (15 mM, pH 8.0 or pH 4.5). The final solutions were vortex-mixed for 10 s, and 10-µL aliquots were injected into the huAChE-ICER-LC-MS system in triplicate.

The *K*_{Mapp} constant of BACE1-ICER was obtained. Briefly, 5-µL aliquots of JMV2236 solution at various concentrations (from 10 to 100 µM) were injected into the BACE1-ICER-MS system, in triplicate. The assayed solutions were obtained by addition of 25 µL of JMV2236 solution at different concentrations, completed to a final volume of 50 µL with ammonium acetate

solution (2 mM, pH 4.5) as described in Ferreira Lopes Vilela and Cardoso (2017).

The data were fitted by using nonlinear regression in a Michaelis-Menten plot, and the K_{Mapp} values were obtained with the software GraphPad Prism version 5.0.

Inhibition Studies

To determine the half-maximum inhibitory concentration (IC_{50}), galantamine and a β -secretase inhibitor were used as reference inhibitors for BACE1-ICER and huAChE-ICER, respectively (Andrau et al., 2003; Darvesh et al., 2003; Marques et al., 2011).

For huAChE-ICER, 10- μ L aliquots of solutions containing increasing galantamine (0.05–50 μ M) concentrations and ACh (70 μ M) were injected into the huAChE-ICER-LC-MS system, in triplicate. The assay solutions were obtained by using 20 μ L of a solution containing ACh (350 μ M) and 10 μ L of a solution containing different galantamine concentrations (0.05, 1.0, 2.5, 5.0, 7.0, 10, 15, 25, or 50 μ M). The final volume was completed to 100 μ L with ammonium acetate solution (15 mM, pH 4.5).

The product areas obtained in the presence (P_i) and absence (P_0) of the inhibitor were compared, and the percentage of inhibition was calculated by using Eq. 1:

$$\% \text{ Inhibition} = 100 - \left[\left(\frac{P_i}{P_0} \right) \times 100 \right] \quad (1)$$

For each standard inhibitor, an inhibition curve was constructed by plotting the % inhibition versus the concentration of the inhibitor. The software GraphPad Prism 5 was used to obtain the IC_{50} values by nonlinear regression analysis.

The IC_{50} for BACE1 was obtained by injecting 5 μ L aliquots of solutions containing increasing concentrations of the β -secretase inhibitor (from 0.05 to 10 μ M) and JMV2236 (5 μ M) into the BACE1-ICER-MS system, in triplicate. The assayed solutions were obtained by addition of 10 μ L of JMV2236 (50 μ M) and 10 μ L of a solution containing different concentrations of reference inhibitor, completed to a final volume of 50 μ L with ammonium acetate solution (2 mM, pH 4.5) (Ferreira Lopes Vilela and Cardoso, 2017).

Preparation and Evaluation of the Dual Enzymatic System

huAChE and BACE1 co-Immobilization

huAChE and BACE1 were co-immobilized on the internal surface of an open tubular silica capillary (100 cm \times 0.1 mm i.d. \times 0.362 mm e.d.) according to previous protocols described for individual enzymes (Vanzolini et al., 2013; Ferreira Lopes Vilela and Cardoso, 2017), with minor modifications.

A mixture of the enzymes was infused through the capillary at 50 μ L min^{-1} . The mixture consisted of 500 μ L of huAChE solution (17 units. mL^{-1} in 50 mM phosphate solution, pH 7.4) and 500 μ L of BACE1 solution at 942.8 units. mL^{-1} (20 μ L of BACE1 solution in 20 mM Hepes solution, pH 7.4, containing 125 mM NaCl, diluted to 500 mL with 50 mM phosphate solution, pH 7.4). The solution was collected, and this step was repeated five times by using the same solution.

The 100-cm capillary was divided, to give three 30-cm-long huAChE+BACE1-ICERs.

While huAChE+BACE1-ICER was not being used, it was maintained at 4°C, with both extremities immersed in 50 mM phosphate solution, pH 7.4.

Apparent Kinetic Constant (K_{Mapp}) Studies

The apparent kinetic constant (K_{Mapp}) was obtained independently for both substrates, ACh and JMV2236, by varying their concentrations.

For the huAChE, ACh stock solutions were prepared (25, 50, 75, 100, 125, 150, 250, and 1,000 μ M) in ammonium acetate solution (15 mM, pH 4.5), and 20 μ L of each solution was further diluted to a final volume of 100 μ L with the ammonium acetate solution (15 mM, pH 4.5). The final solutions were vortex-mixed for 10 s, and 10- μ L aliquots were injected into the huAChE+BACE1-ICER-LC-MS system, in triplicate.

For the BACE1, JMV2236 stock solutions were prepared (40, 60, 80, 100, 160, 200, 400, and 1,000 μ M) in DMSO, and 25 μ L of each solution was completed to a final volume of 50 μ L with ammonium acetate solution (15 mM, pH 4.5). The final solutions were vortex-mixed for 10 s, and 10- μ L aliquots were injected into the huAChE+BACE1-ICER-LC-MS system, in triplicate. The conditions are listed in Table 1.

The software GraphPad Prism 5 was used to obtain Michaelis-Menten plots by nonlinear regression analysis.

3) Inhibition Studies

To validate the assay, IC_{50} parameters were calculated for β -secretase inhibitor and galantamine, standard inhibitors for huAChE and BACE1, respectively (Andrau et al., 2003; Darvesh et al., 2003).

For each enzyme, fixed concentrations of their substrates with increasing concentrations of the standard inhibitors were employed.

For the huAChE, 10- μ L aliquots of solutions containing increasing galantamine concentrations (0.05–50 μ M) and ACh (70 μ M) were injected into the huAChE+BACE1-ICER-LC-MS system, in triplicate.

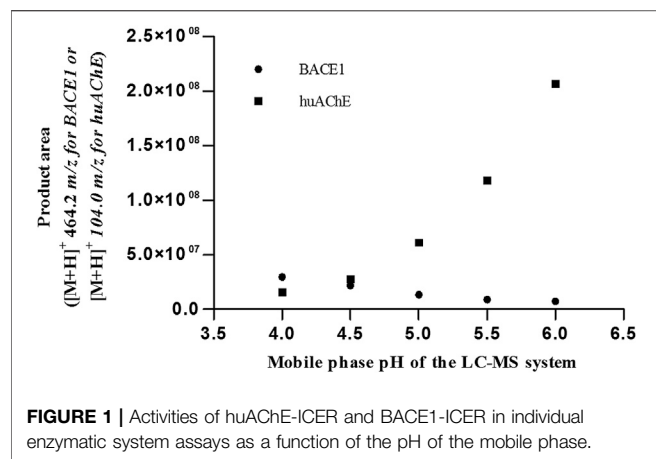
The assay solutions were obtained by adding 20 μ L of a solution containing ACh (350 μ M) and 10 μ L of a solution containing different galantamine concentrations (0.05, 1.0, 2.5, 5.0, 7.0, 10, 15, 25, or 50 μ M). The final volume was completed to 100 μ L with ammonium acetate solution (15 mM, pH 4.5).

For the BACE1, 10- μ L aliquots of solutions containing increasing concentrations of the β -secretase inhibitor (0.05–10 μ M) and JMV2236 (100 μ M) were injected into the huAChE+BACE1-ICER-LC-MS system, in triplicate.

The assay solutions were obtained by adding 10 μ L of a solution containing JMV2236 (1,000 μ M in DMSO) and 10 μ L of a solution containing different concentrations of the β -secretase inhibitor (0.05, 0.1, 0.25, 0.5, or 2.5 in DMSO). The final volume was completed to 50 μ L with ammonium acetate solution (15 mM, pH 4.5).

The assay conditions are described in Table 1.

The percentage of inhibition was calculated according to Eq. 1.



For each standard inhibitor, an inhibition curve was constructed by plotting the % inhibition versus the concentration of the inhibitor. The software GraphPad Prism 5 was used to obtain the IC_{50} values by nonlinear regression analysis.

RESULTS AND DISCUSSION

Individual Enzymatic System Assay

Before we developed the dual enzymatic system assay by co-immobilization of huAChE and BACE1, we studied the individual enzymes huAChE and BACE1 on the basis of previous works by Vanzolini et al. (2013), Ferreira Lopes Vilela and Cardoso (2017) to evaluate the best conditions for monitoring both enzymes in the dual enzymatic system assay by LC-MS.

We successfully immobilized huAChE and BACE1, individually, on the internal surface of an open tubular fused

silica capillary, to obtain huAChE-ICER and BACE1-ICER, respectively.

The pH study was crucial because the enzymes have optimal catalytic functions at different pH levels. BACE1 is an aspartyl protease with optimal activity in acidic pH, and AChE, an esterase, works best at pH between 7 and 8.5. On the basis of this information, we investigated the ideal pH for the dual enzymatic system assay.

The enzymatic activity can also be determined at a pH outside the optimum range, but smaller activity values must be accepted. In this way, a larger number of enzymes can be measured at one standardized pH (Bisswanger, 2014).

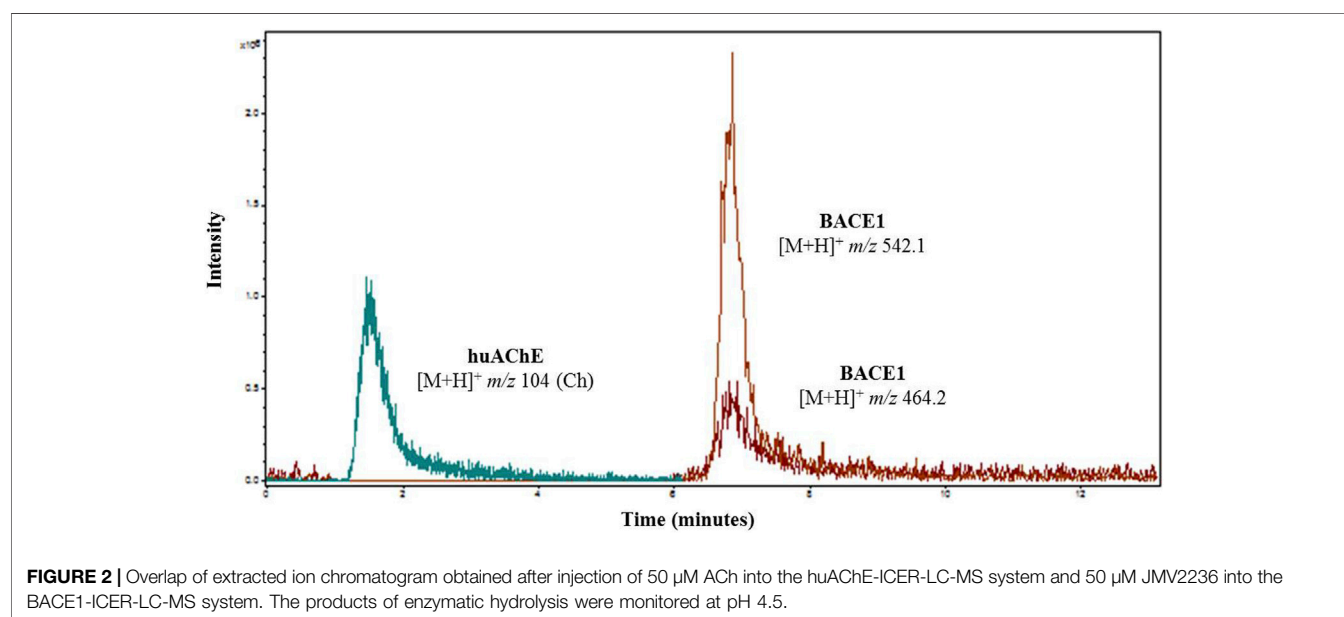
According to Figures 1, 2, at pH values above 5.5, BACE1-ICER does not function well. As for huAChE-ICER, we were able to evaluate its activity in a wide pH range. Our results showed that the ideal pH of the mobile phase for monitoring the dual enzymatic system should be 4.5.

On the basis of these studies, we standardized the mobile phase pH so as to measure the enzymatic catalysis for both enzymes in the dual enzymatic system assay.

The constant K_{Mapp} depends on the reaction medium conditions, so we investigated changes in this constant as a function of the conditions of the enzymatic reactions. BACE1-ICER had been previously studied, and its K_{Mapp} is described in Ferreira Lopes Vilela and Cardoso (2017). As for huAChE-ICER, K_{Mapp} studies were carried out for two mobile phase pH values, 8.0 (optimal for huAChE) and 4.5 (selected for monitoring of the dual enzymatic system assay).

K_{Mapp} was calculated as $51.5 \pm 2 \mu M$ at pH 4.5 and $23.3 \pm 1 \mu M$ at pH 8.0 (Figure 3). Compared to the value obtained at the optimal pH (8.0) for huAChE, K_{Mapp} at pH 4.5 was twice as large and will be used to carry out the ligand screening studies.

To validate the huAChE-ICER-LC-MS system for ligand screening, we used galantamine, a known inhibitor of cholinesterases (Darvesh et al., 2003). We also calculated the



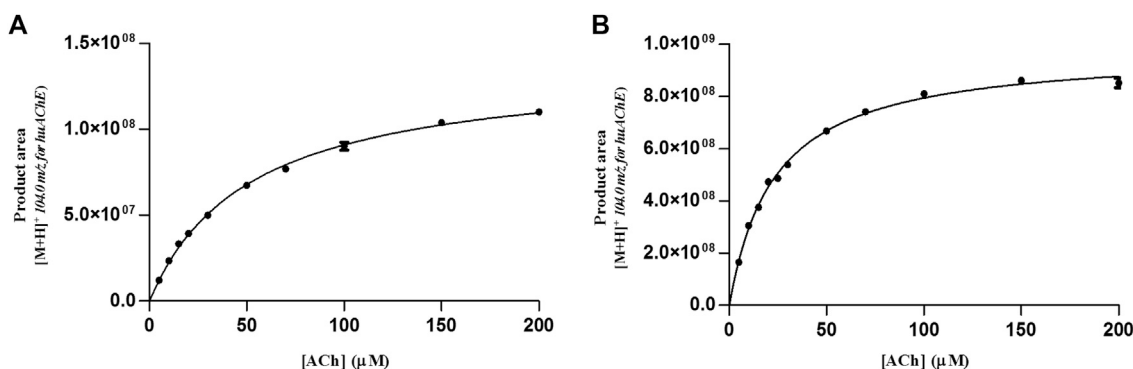


FIGURE 3 | Michaelis-plots of the product area obtained for huAChE-ICER by using ACh as the substrate. **(A)** mobile phase pH 4.5 and **(B)** mobile phase pH 8.0. See **Table 1** for conditions.

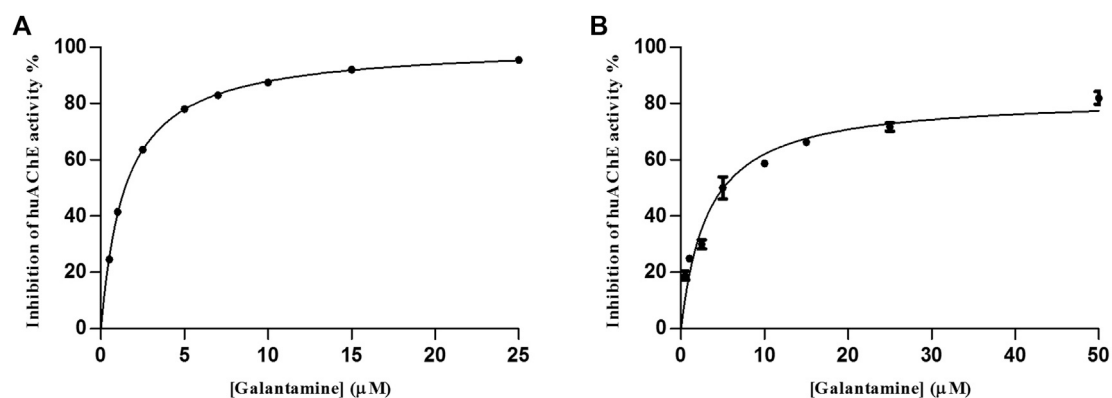


FIGURE 4 | Inhibitory potency curve obtained for huAChE-ICER by using ACh as a substrate. **(A)** mobile phase pH 4.5 and **(B)** mobile phase pH 8.0. See **Table 1** for conditions.

IC₅₀ values for huAChE-ICER at two mobile phase pH values, 8.0 (optimal for huAChE) and 4.5 (selected for monitoring of the dual enzymatic system assay). The IC₅₀ value for BACE1 has been described in (Ferreira Lopes Vilela and Cardoso, 2017).

We determined the IC₅₀ values as 3.29 ± 0.4 μM at pH 4.5 and 1.47 ± 0.03 μM at pH 8.0 (**Figure 4**), which showed that the huAChE-ICER-LC-MS system was able to identify the standard inhibitor on a micro-scale as compared to data previously reported for this inhibitor.

On the basis of these findings for the individual enzymatic system assays, we were able to establish the best conditions for the dual enzymatic system assay (**Table 1**).

Dual Enzymatic System Assay

The co-immobilization process used herein was successful: the activities of both enzymes were preserved after co-immobilization in the fused silica capillary. The random co-immobilization method (Schoffelen and van Hest, 2013) employed glutaraldehyde as linker, to produce covalent interactions with the mixture of enzymes on the support. The LC-MS system and the configuration used to monitor the enzymatic activities allowed us to measure the hydrolysis products by MS directly.

We analyzed both enzymes in series, BACE1 and huAChE, respectively. **Figure 5** illustrates the results.

We validated the assay according to guidelines for bioanalytical methods (Cassiano et al., 2009). The calibration curve revealed a linear relationship for JMV2236 concentrations ranging from 10 to 25 μM. For ACh, the calibration curve was linear (1.0–15 μM).

To evaluate the selectivity of the method, we carried out blank runs (15 mM ammonium acetate pH 4.5), where the target analytes were not present. These runs revealed no interference, demonstrating that no carry over occurred between analyses.

For ACh, the limit of quantification (LQ) was 1 μM (RSD = 2.4%, *n* = 3, and accuracy = 100.0%), and the limit of detection (LD) was 0.5 μM, calculated by the signal-to-noise ratio. For JMV2236, the limit of quantification (LQ) was 10 μM (RSD = 9.2%, *n* = 3, and accuracy = 100.6%), and the limit of detection (LD) was 5.0 μM, calculated by the signal-to-noise ratio.

We evaluated the K_{Mapp} constants for both enzymes in the dual enzymatic system, to verify whether the values changed due to co-immobilization. We found values of 19.25 ± 3 and 49.6 ± 4 μM for BACE1 and huAChE in the huAChE+BACE1-ICER-LC-MS system, respectively (**Figure 6**).

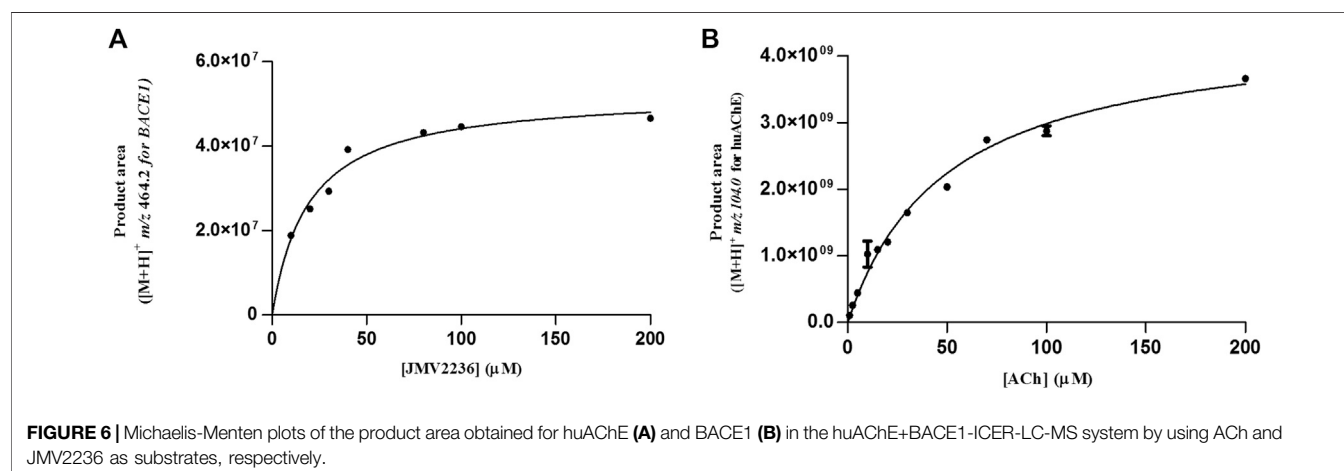
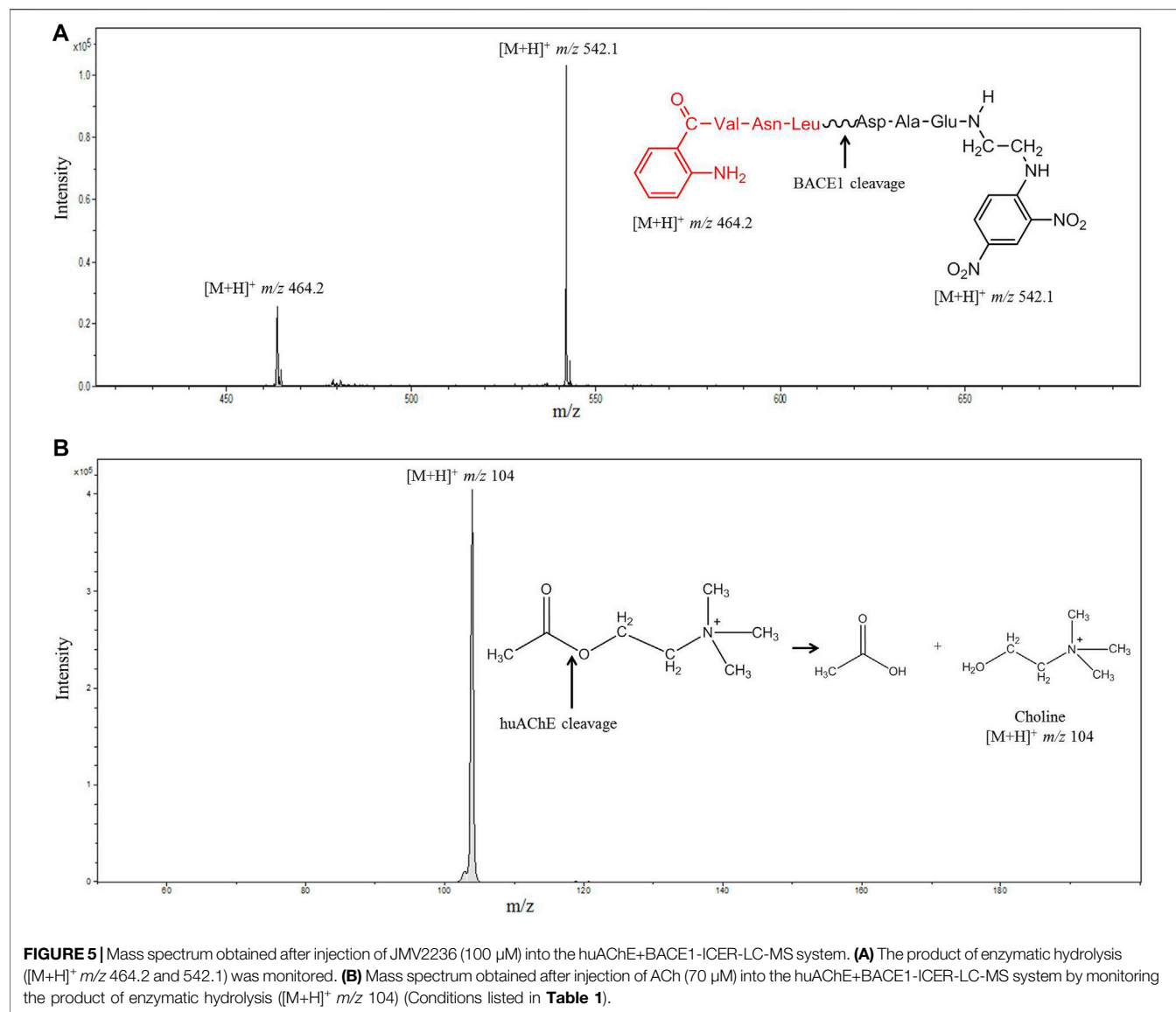


TABLE 2 | K_{Mapp} values obtained for the dual and individual system assays.

K_{Mapp} values (μM)	<i>huAChE</i>			<i>BACE1</i>		
	<i>huAChE-ICER</i> ^a	<i>huAChE+BACE1-ICER</i> ^b	Ratio ^c	<i>BACE1-ICER</i> ^{a,d}	<i>huAChE+BACE1-ICER</i> ^b	Ratio ^c
	51.5	49.6	0.96	17.2	19.2	1.1

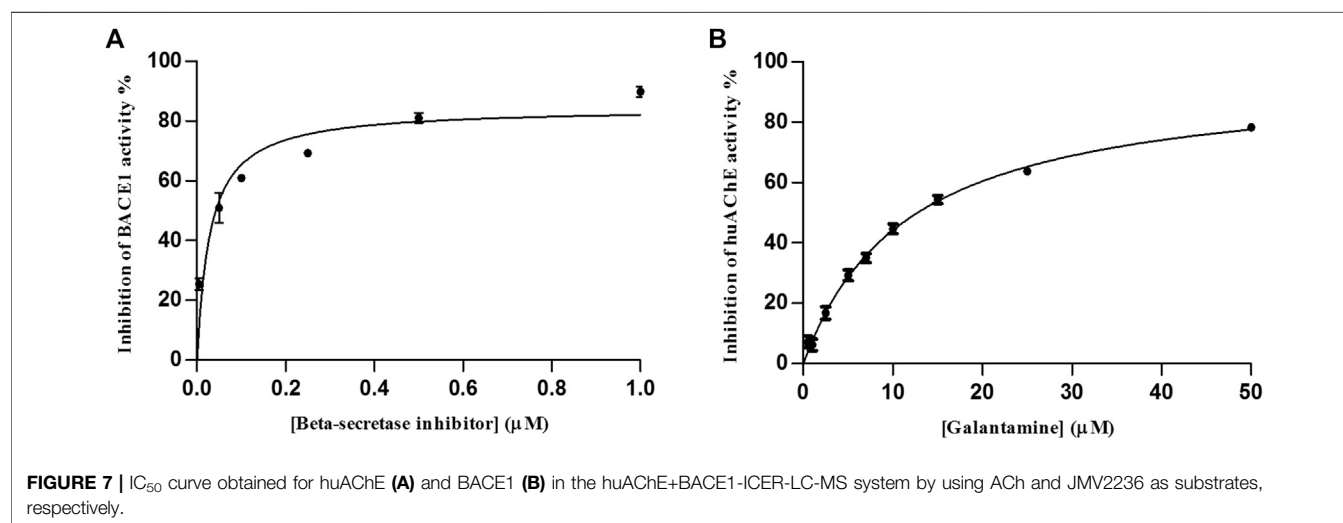
^aIndividual-system.^bDual-system.^cRatio between dual and individual-system.^dValue described in Ferreira Lopes Vilela and Cardoso (2017).

Table 2 compares the K_{Mapp} values obtained for the dual and individual system assays. There were no significant differences due to the random co-immobilization and immobilization process.

The individual and dual enzymatic systems developed herein showed that the enzymes catalyzed their substrates in a similar fashion in both systems; that is, their affinities and specificities were not affected. Therefore, we were able to mimic an *in vitro* cellular environment with two enzymes with distinct catalytic properties in a unique system. Other advantages of the proposed method include reduced costs of reagents and shorter preparation time. In addition, the same mobile phase and bioaffinity column can be used in the analyses, allowing ligands from synthetic or semi-synthetic combinatorial libraries and natural products or marine extracts to be identified and characterized, not to mention that the method can be applied to multi-target ligands. The proposed dual-enzymatic system assay did not allow the two substrates and products cleaved by the enzymes to be detected simultaneously due to the employed MS detector. However, the biocatalysis products were directly quantified in series by an MS detector.

Although the assay for *huAChE* was not performed under optimal catalysis conditions, we were able to evaluate its activity and selectivity with the same efficacy provided by individual enzymatic system. To validate the *huAChE+BACE1-ICER-LC-MS* system for the screening of ligands, we used galantamine and the β -secretase inhibitor as reference inhibitors of *BACE-1* and *huAChE*, respectively (Andrau et al., 2003; Darvesh et al., 2003).

The IC_{50} values were $11.6 \pm 0.8 \mu\text{M}$ for galantamine and $0.03 \pm 0.008 \mu\text{M}$ for the β -secretase inhibitor (**Figure 7**). On the basis of these values, the dual enzymatic system assay was able to identify the standard inhibitors on a micro-scale as compared to data previously reported for these inhibitors.

Each enzyme studied in the dual enzymatic system was selective and specific for its substrate and inhibitor without interference and/or problems during method development (30 days); the enzymatic activities were maintained for over 60 days. The K_{Mapp} and IC_{50} studies showed that co-immobilization did not alter the affinity of *BACE1* and *huAChE*, indicating that the approach used herein can be applied to screen multi-target-directed ligands in a competitive environment. This efficient system is a remarkable alternative to common single-enzyme screening methods at various levels during the drug discovery process.

CONCLUSION

We have described an innovative dual enzymatic system assay based on co-immobilization of *huAChE* and *BACE1* and on-flow LC-MS detection. This is the first time that a dual enzymatic system assay has been developed to screen ligands by a label-free automated screening system bearing two enzymes involved in AD etiology. We developed the novel dual enzymatic system assay by employing an effective random co-immobilization process that provided a system to evaluate the activities of *huAChE* and

BACE1 on-flow by LC-MS through a mobile phase with the same ionic strength and pH even though the enzymes have different kinetic properties.

DATA AVAILABILITY STATEMENT

The raw data supporting the conclusions of this article will be made available by the authors, without undue reservation.

AUTHOR CONTRIBUTIONS

AF: Methodology, Validation, Formal analysis, Investigation, Writing—Original Draft, Visualization. VN: Methodology, Validation. CC: Conceptualization, Funding acquisition,

Project administration, Resources, Validation, Visualization, Supervision, Writing—Review & Editing.

FUNDING

This investigation was supported by the National Council for Scientific and Technological Development (CNPq - Grants 145013/2019-7, and 303723/2018-1) and the São Paulo State Research Foundation (FAPESP - Grants 2019/05363-0; 2014/50249-8 and GSK). This study was partially financed by Coordenação de Aperfeiçoamento de Pessoal de Nível Superior, Brazil (CAPES), Finance Code 001. CC and AF acknowledge the São Paulo State Research Foundation (FAPESP) for the PhD scholarship (2016/02873-0) and CNPq (145013/2019-7).

REFERENCES

- Acker, M. G., and Auld, D. S. (2014). Considerations for the Design and Reporting of Enzyme Assays in High-Throughput Screening Applications. *Perspect. Sci.* 1, 56–73. doi:10.1016/j.pisc.2013.12.001
- Anand, R., Gill, K. D., and Mahdi, A. A. (2014). Therapeutics of Alzheimer's Disease: Past, Present and Future. *Neuropharmacology*. 76, 27–50. doi:10.1016/j.neuropharm.2013.07.004
- Andrau, D., Dumanchin-Njock, C., Ayral, E., Vizzavona, J., Farzan, M., Boisbrun, M., et al. (2003). BACE1- and BACE2-Expressing Human Cells. *J. Biol. Chem.* 278, 25859–25866. doi:10.1074/jbc.M302622000
- Basso, A., and Serban, S. (2019). Industrial Applications of Immobilized Enzymes—A Review. *Mol. Catal.* 479, 110607. doi:10.1016/j.mcat.2019.110607
- Basso, A., and Serban, S. (2020). Overview of Immobilized Enzymes' Applications in Pharmaceutical, Chemical, and Food Industry. *Methods Mol Biol.* 2100, 27–63. doi:10.1007/978-1-0716-0215-7_2
- Betancor, L., and Luckarift, H. R. (2010). Co-immobilized Coupled Enzyme Systems in Biotechnology. *Biotechnol. Genet. Eng. Rev.* 27, 95–114. doi:10.1080/02648725.2010.10648146
- Bisswanger, H. (2014). Enzyme Assays. *Perspect. Sci.* 1, 41–55. doi:10.1016/j.pisc.2014.02.005
- Blaikie, L., Kay, G., and Kong Thoo Lin, P. (2019). Current and Emerging Therapeutic Targets of Alzheimer's Disease for the Design of Multi-Target Directed Ligands. *Med. Chem. Commun.* 10, 2052–2072. doi:10.1039/c9md00337a
- Cass, Q. B., Massolini, G., Cardoso, C. L., and Calleri, E. (2020). Editorial: Advances in Bioanalytical Methods for Probing Ligand-Target Interactions. *Front. Chem.* 8, 8–10. doi:10.3389/fchem.2020.00378
- Cassiano, N. M., Barreiro, J. C., Martins, L. R. R., Oliveira, R. V., and Cass, Q. B. (2009). Validação em métodos cromatográficos para análises de pequenas moléculas em matrizes biológicas. *Quím. Nova* 32, 1021–1030. doi:10.1590/s0100-40422009000400033
- Chen, L., Wang, X., Liu, Y., and Di, X. (2017). Dual-target Screening of Bioactive Components from Traditional Chinese Medicines by Hollow Fiber-Based Ligand Fishing Combined with Liquid Chromatography-Mass Spectrometry. *J. Pharm. Biomed. Anal.* 143, 269–276. doi:10.1016/j.jpba.2017.06.001
- Coimbra, J. R. M., Marques, D. F. F., Baptista, S. J., Pereira, C. M. F., Moreira, P. I., Dinis, T. C. P., et al. (2018). Highlights in BACE1 Inhibitors for Alzheimer's Disease Treatment. *Front. Chem.* 6, 1–10. doi:10.3389/fchem.2018.00178
- Darvesh, S., Walsh, R., Kumar, R., Caines, A., Roberts, S., Magee, D., et al. (2003). Inhibition of Human Cholinesterases by Drugs Used to Treat Alzheimer Disease. *Alzheimer Dis. Associated Disord.* 17, 117–126. doi:10.1097/00002093-200304000-00011
- de Freitas Silva, M., Dias, K. S. T., Gontijo, V. S., Ortiz, C. J. C., and Viegas, C. (2018). Multi-Target Directed Drugs as a Modern Approach for Drug Design towards Alzheimer's Disease: An Update. *Curr Med Chem.* 25, 3491–3525. doi:10.2174/0929867325666180111101843
- de Moraes, M. C., Cardoso, C. L., and Cass, Q. B. (2019). Solid-Supported Proteins in the Liquid Chromatography Domain to Probe Ligand-Target Interactions. *Front. Chem.* 7, 1–16. doi:10.3389/fchem.2019.00752
- Deardorff, W. J., Feen, E., and Grossberg, G. T. (2015). The Use of Cholinesterase Inhibitors across All Stages of Alzheimer's Disease. *Drugs Aging*. 32, 537–547. doi:10.1007/s40266-015-0273-x
- Ferreira Lopes Vilela, A., and Cardoso, C. L. (2017). An On-Flow Assay for Screening of β -secretase Ligands by Immobilised Capillary Reactor-Mass Spectrometry. *Anal. Methods*. 9, 2189–2196. doi:10.1039/C7AY00284J
- Fotiou, D., Kaltsatou, A., Tsitsios, D., and Nakou, M. (2015). Evaluation of the Cholinergic Hypothesis in Alzheimer's Disease with Neuropsychological Methods. *Aging Clin. Exp. Res.* 27, 727–733. doi:10.1007/s40520-015-0321-8
- Hage, D. S. (2017). Analysis of Biological Interactions by Affinity Chromatography: Clinical and Pharmaceutical Applications. *Clin. Chem.* 63, 1083–1093. doi:10.1373/CLINCHEM.2016.262253
- Hughes, R. E., Nikolic, K., and Ramsay, R. R. (2016). One for All? Hitting Multiple Alzheimer's Disease Targets with One Drug. *Front. Neurosci.* 10. doi:10.3389/fnins.2016.00177
- Janzen, W. P. (2014). Screening Technologies for Small Molecule Discovery: The State of the Art. *Chem. Biol.* 21, 1162–1170. doi:10.1016/j.chembiol.2014.07.015
- Kang, W., Liu, J., Wang, J., Nie, Y., Guo, Z., and Xia, J. (2014). Cascade Biocatalysis by Multienzyme-Nanoparticle Assemblies. *Bioconjug. Chem.* 25, 1387–1394. doi:10.1021/bc5002399
- Maramai, S., Benckroun, M., Gabr, M. T., and Yahiaoui, S. (2020). Multitarget Therapeutic Strategies for Alzheimer's Disease: Review on Emerging Target Combinations. *Biomed. Res. Int.* 2020, 1–27. doi:10.1155/2020/5120230
- Marques, L. A., Maada, I., de Kanter, F. J. J., Lingeman, H., Irth, H., Niessen, W. M. A., et al. (2011). Stability-indicating Study of the Anti-alzheimer's Drug Galantamine Hydrobromide. *J. Pharm. Biomed. Anal.* 55, 85–92. doi:10.1016/j.jpba.2011.01.022
- Mignani, S., Huber, S., Tomás, H., Rodrigues, J., and Majoral, J.-P. (2016). Why and How Have Drug Discovery Strategies in Pharma Changed? what Are the New Mindsets? *Drug Discov. Today* 21, 239–249. doi:10.1016/j.drudis.2015.09.007
- Moraes, M. C., Cardoso, C., Seidl, C., Moaddel, R., and Cass, Q. (2016). Targeting Anti-cancer Active Compounds: Affinity-Based Chromatographic Assays. *Curr Pharm Des.* 22, 5976–5987. doi:10.2174/1381612822666160614080506
- Orrego, A. H., López-Gallego, F., Fernandez-Lorente, G., Guisan, J. M., and Rocha-Martín, J. (2020). Co-Immobilization and Co-localization of Multi-Enzyme Systems on Porous Materials. *Methods Mol. Biol.* 2100, 297–308. doi:10.1007/978-1-0716-0215-7_19
- Pang, M.-H., Kim, Y., Jung, K. W., Cho, S., and Lee, D. H. (2012). A Series of Case Studies: Practical Methodology for Identifying Antinociceptive Multi-Target Drugs. *Drug Discov. Today*. 17, 425–434. doi:10.1016/j.drudis.2012.01.003
- Prati, F., Bottegoni, G., Bolognesi, M. L., and Cavalli, A. (2018). BACE-1 Inhibitors: From Recent Single-Target Molecules to Multitarget Compounds for Alzheimer's Disease. *J. Med. Chem.* 61, 619–637. doi:10.1021/acs.jmedchem.7b00393

- Ramsay, R. R., Popovic-Nikolic, M. R., Nikolic, K., Uliassi, E., and Bolognesi, M. L. (2018). A Perspective on Multi-target Drug Discovery and Design for Complex Diseases. *Clin. Translational Med.* 7, 3. doi:10.1186/s40169-017-0181-2
- Schejbal, J., Šefraná, Š., Řemínek, R., and Glatz, Z. (2019). Capillary Electrophoresis Integrated Immobilized Enzyme Reactor for Kinetic and Inhibition Assays of β -secretase as the Alzheimer's Disease Drug Target*. *J. Sep. Sci.* 42, 1067–1076. doi:10.1002/jssc.201800947
- Schoffelen, S., and van Hest, J. C. (2013). Chemical Approaches for the Construction of Multi-Enzyme Reaction Systems. *Curr. Opin. Struct. Biol.* 23, 613–621. doi:10.1016/j.sbi.2013.06.010
- Seidl, C., Vilela, A. F. L., Lima, J. M., Leme, G. M., and Cardoso, C. L. (2019). A Novel On-Flow Mass Spectrometry-Based Dual Enzyme Assay. *Analytica Chim. Acta.* 1072, 81–86. doi:10.1016/j.aca.2019.04.057
- Silber, B. M. (2010). COMMENTARY Driving Drug Discovery: The Fundamental Role of Academic Labs. *Sci Transl Med*, 2, 1–7. doi:10.1126/scitranslmed.3000169
- Toth, C. A., Kuklenyik, Z., Jones, J. I., Parks, B. A., Gardner, M. S., Schieltz, D. M., et al. (2017). On-column Trypsin Digestion Coupled with LC-MS/MS for Quantification of Apolipoproteins. *J. Proteomics.* 150, 258–267. doi:10.1016/j.jprot.2016.09.011
- Uddin, M. S., Al Mamun, A., Kabir, M. T., Ashraf, G. M., Bin-Jumah, M. N., and Abdel-Daim, M. M. (2021). Multi-Target Drug Candidates for Multifactorial Alzheimer's Disease: AChE and NMDAR as Molecular Targets. *Mol. Neurobiol.* 58, 281–303. doi:10.1007/s12035-020-02116-9
- Vanzolini, K. L., da F. Sprenger, R., Leme, G. M., de S. Moraes, V. R., Vilela, A. F. L., Cardoso, C. L., et al. (2018). Acetylcholinesterase Affinity-Based Screening Assay on Lippia Gracilis Schauer Extracts. *J. Pharm. Biomed. Anal.* 153, 232–237. doi:10.1016/j.jpba.2018.02.035
- Vanzolini, K. L., Vieira, L. C. C., Corrêa, A. G., Cardoso, C. L., and Cass, Q. B. (2013). Acetylcholinesterase Immobilized Capillary Reactors-Tandem Mass Spectrometry: An On-Flow Tool for Ligand Screening. *J. Med. Chem.* 56, 2038–2044. doi:10.1021/jm301732a
- Wang, B., Shanguan, L., Wang, S., Zhang, L., Zhang, W., and Liu, F. (2016). Preparation and Application of Immobilized Enzymatic Reactors for Consecutive Digestion with Two Enzymes. *J. Chromatogr. A.* 1477, 22–29. doi:10.1016/j.chroma.2016.11.027
- Willem, M., Garratt, A. N., Novak, B., Citron, M., Kaufmann, S., Rittger, A., et al. (2006). Control of Peripheral Nerve Myelination by the β -Secretase BACE1. *Science.* 314, 664–666. doi:10.1126/science.1132341
- Wu, Z.-Y., Zhang, H., Yang, Y.-Y., and Yang, F.-Q. (2020). An Online Dual-Enzyme Co-immobilized Microreactor Based on Capillary Electrophoresis for Enzyme Kinetics Assays and Screening of Dual-Target Inhibitors against Thrombin and Factor Xa. *J. Chromatogr. A.* 1619, 460948. doi:10.1016/j.chroma.2020.460948
- Ye, L.-H., Zhang, R., and Cao, J. (2021). Screening of β -secretase Inhibitors from Dendrobii Caulis by Covalently Enzyme-Immobilized Magnetic Beads Coupled with Ultra-high-performance Liquid Chromatography. *J. Pharm. Biomed. Anal.* 195, 113845. doi:10.1016/j.jpba.2020.113845
- Zhang, H., Liu, R., and Zheng, J. (2012). Selective Determination of Cholesterol Based on Cholesterol Oxidase-Alkaline Phosphatase Bienzyme Electrode. *Analyst.* 137, 5363. doi:10.1039/c2an36075f

Conflict of Interest: The authors declare that the research was conducted in the absence of any commercial or financial relationships that could be construed as a potential conflict of interest.

Copyright © 2021 Vilela, Narciso dos Reis and Cardoso. This is an open-access article distributed under the terms of the Creative Commons Attribution License (CC BY). The use, distribution or reproduction in other forums is permitted, provided the original author(s) and the copyright owner(s) are credited and that the original publication in this journal is cited, in accordance with accepted academic practice. No use, distribution or reproduction is permitted which does not comply with these terms.



Is a Lead Isotope Ratios in Wine Good Marker for Origin Assessment?

Sladana Đurđić¹, Vesna Stanković², Slavica Ražić^{3*} and Jelena Mutić¹

¹Department of Analytical Chemistry, Faculty of Chemistry, University of Belgrade, Belgrade, Serbia, ²Department of Chemistry, Institute of Chemistry, Technology and Metallurgy, University of Belgrade, Belgrade, Serbia, ³Department of Analytical Chemistry, Faculty of Pharmacy, University of Belgrade, Belgrade, Serbia

Lead isotope ratio pattern ($^{206}\text{Pb}/^{207}\text{Pb}$, $^{208}\text{Pb}/^{206}\text{Pb}$, $^{206}\text{Pb}/^{204}\text{Pb}$, $^{207}\text{Pb}/^{204}\text{Pb}$, and $^{208}\text{Pb}/^{204}\text{Pb}$) was analyzed in 59 samples of Serbian wine, from four geographical regions. By utilization of powerful inductively coupled plasma mass spectrometry (ICP-QMS), lead isotope ratios were used as unique “fingerprint”, when combined with multivariate methods of analysis (Principal Component Analysis), provided information on the geographical origin of wine. In validation of ICP-QMS method and quantitative analysis, the certified reference material NIST SRM 981 was employed to test the mass-bias correction and thallium isotopes ^{203}Tl and ^{205}Tl (NIST SRM 997) as an internal standard. The obtained results were discussed in correlation with the corresponding values of LIRs of different European and Australian wines. In addition, the impact of anthropogenic Pb from different sources on the total Pb isotopic composition in Serbian wines was analyzed too. On the other side, the obtained values of Pb content were compared with the applicable health safety standards, according to the International Code of Oenological Practices.

Keywords: ICP-QMS, Serbian wines, principal component analysis, geographical origin, lead isotopes

OPEN ACCESS

Edited by:

Eugenia Gallardo,
Universidade da Beira Interior,
Portugal

Reviewed by:

Tea Zuliani,
Institut Jožef Stefan (IJS), Slovenia
Yanbei Zhu,
National Institute of Advanced
Industrial Science and Technology
(AIST), Japan

*Correspondence:

Slavica Ražić
slavica.razic@pharmacy.bg.ac.rs

Specialty section:

This article was submitted to
Analytical Chemistry,
a section of the journal
Frontiers in Chemistry

Received: 24 July 2021

Accepted: 21 September 2021

Published: 04 October 2021

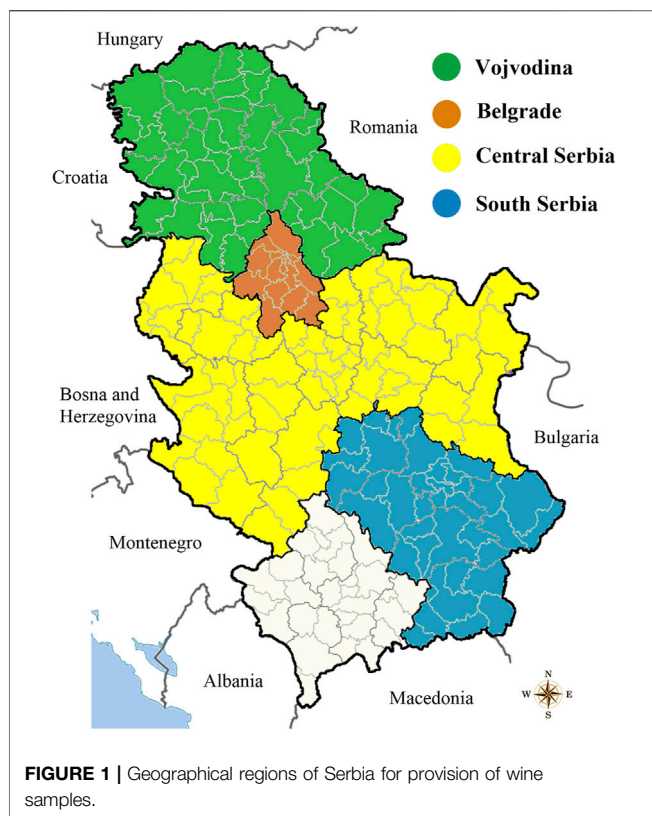
Citation:

Đurđić S, Stanković V, Ražić S and
Mutić J (2021) Is a Lead Isotope Ratios
in Wine Good Marker for Origin
Assessment?
Front. Chem. 9:746695.
doi: 10.3389/fchem.2021.746695

INTRODUCTION

Lead isotopic composition, based on different ratios of stable isotopes ($^{206}\text{Pb}/^{207}\text{Pb}$, $^{208}\text{Pb}/^{206}\text{Pb}$, $^{206}\text{Pb}/^{204}\text{Pb}$, $^{207}\text{Pb}/^{204}\text{Pb}$, and $^{208}\text{Pb}/^{204}\text{Pb}$), serves as a “fingerprint” for definition of different lead sources in the environment (Erel et al., 1997; Larcher et al., 2003; Komárek et al., 2008; Đurđić et al., 2020). Analysis of the lead isotope ratios (LIRs) in food and beverages has provided a powerful tool for determining the geographical origin and authenticity, most often, of wine (Medina et al., 2000; Tian et al., 2000; Barbaste et al., 2001; Mihaljević et al., 2006; Bora et al., 2018; Epova et al., 2020). In addition, LIRs can be used as a tool for elucidation of chemical environment in a mushrooms-soil system (Đurđić et al., 2020).

Primary, the presence of lead in wines originate from nature, where the vine reflected the isotopic signatures from the geological-pedological environment (natural lead; uncontaminated soli/bedrock). On the other side, lead in wines can also be found as a result of human activities. Anthropogenic lead in wines mainly originates from traffic, fertilizer, pesticide treatment, as well as from metallurgical and smelting activities (Almeida and Vasconcelos, 1999; Đurđić et al., 2020). LIRs might provide information on the origin of the wine assuming that sources of contamination do not distort the original isotope ratio pattern present in the local environment (Tian et al., 2000). $^{206}\text{Pb}/^{207}\text{Pb}$ and $^{206}\text{Pb}/^{208}\text{Pb}$ ratios could be significantly influenced by anthropogenic factors and may be used to differentiate natural and anthropogenic Pb contamination. On the other side, the chemical processes during winemaking have no significant influence on isotopic composition of wine



(Rosman et al., 1998). It was reported that the values of the isotope ratios between wines produced in a winery and laboratory were equivalent (Medina et al., 2000). However, the equipment used during the vinification can contribute substantially to the total lead content of the wine and Pb isotope ratios can deviate from those in the soil in the vineyard, which makes authentication rather difficult (Almeida and Vasconcelos, 2004). A precise and accurate lead isotope ratio measurements have been traditionally carried out by thermal ionization mass spectrometry (TIMS). The precision obtainable for isotope ratios determined by inductively coupled plasma mass spectrometry (ICP-QMS) is inherently worse than for many other types of mass spectrometers (Barbaste et al., 2001). For lead isotope ratio (LIR) measurements, the addition of thallium and the measurement of the $^{203}\text{Tl}/^{205}\text{Tl}$ ratio is good way to assess mass bias (Tian et al., 2000). ICP-QMS does not achieve the precision of TIMS but is considered as sufficient to differentiate the origin of wine (Almeida and Vasconcelos, 1999; Larcher et al., 2003; Mihaljević et al., 2006). Fingerprinting techniques based on chemical composition and multivariate statistical analysis can be used to distinguish the wine origin one from another and to classify them according to region, quality, and type (Kment et al., 2005; Lara et al., 2005; Paneque et al., 2010; Martin et al., 2012).

There are no available data about the LIRs in Serbian wines so, the aim of this paper was to conduct such study (LIRs), to contribute to the databases of LIRs for European wines and to investigate possibility of using it in the discrimination of wine from different regions in Serbia using ICP-QMS.

MATERIALS AND METHODS

Site Description

A sample collection of 59 red wines originates from four different regions of Serbia: Vojvodina, Belgrade, Central Serbia and South Serbia. Distribution of wine samples is shown on the map (Figure 1). All wines were supplied in glass bottles with cork stopper.

Reagents and Chemicals

The certified reference material NIST SRM 981 (Common lead isotopic standard, National Institute of Standards and Technology, United States) was employed to test the mass-bias correction and for standard solutions. As an internal standard used thallium isotopes ^{203}Tl and ^{205}Tl NIST SRM 997 (Isotope standard for Thallium, National Institute of Standards and Technology, United States). Mercury stock solution of $1,000 \pm 4 \mu\text{g/ml}$ (TraceCERT, Fluka, Dorset, United Kingdom) was used to study the isobaric interference, originating from ^{204}Hg , on ^{204}Pb measurements. All glassware was soaked in 10% HNO_3 for minimum 12 h and rinsed well with ultra-pure water. Ultra-pure water was prepared by passing doubly de-ionized water from Milli-Q system (Millipore Simplicity 185 System incorporating dual UV filters (185 and 254 nm) to remove carbon contamination). All chemicals were of analytical grade and were supplied by Merck (Darmstadt, Germany).

Instrumentations

Analytical measurements of Pb content and LIRs in wine samples were performed using an inductively coupled plasma mass spectrometer (ICP-MS iCAP Q, Thermo Scientific Xseries 2, United Kingdom) equipped with flat pole collision reaction cell, a micro-concentric nebulizer, nickel cones and a peristaltic sample delivery pump, running a quantitative analysis mode. The entire system controlled with Qtegra Instrument Control Software. The use of cooled spray chamber was found to be mandatory in order to minimize the effect of the ethanol matrix. Measured isotopes and instrument operating conditions for determination at ICP-QMS are given in Supplementary Table S1.

Optimization of Instrumental Parameters for LIRs Analysis

TIMS and ICP sector field multicollector mass spectrometry provides high precision and accuracy during isotope ratios analysis. On the other hand, isotope ratios measurements by ICP-QMS are considered as insufficiently accurate and precise (Vanhaecke et al., 2009), because of the “sequential” measuring approach. Therefore, it is necessary to optimize certain instrumental parameters in order to improve these crucial analytical parameters during the determination of LIRs by ICP-QMS.

The major goal in the isotope ratio measurements by ICP is to achieve constancy of the instrumental mass-bias with the time. Mass-bias effect (mass discrimination) is a feature of all ICP-QMS instruments and occurs due to differential ions transfer from the sample introduction system to the signal detection.

TABLE 1 | Validation of proposed method. Comparison of certified values of NIST SRM 981 with obtained LIRs by ICP-QMS using different correction protocols on mass-bias effect (Đurđić et al., 2020).

LIRs	Certified value \pm SD	Found value \pm SD ^a (the correction was performed with external standardization using NIST SRM 981)	Found value \pm SD ^a (the correction was performed with internal standardization using NIST SRM 997)
$^{207}\text{Pb}/^{206}\text{Pb}$	0.91464 ± 0.00033	0.9146 ± 0.0008	0.9191 ± 0.0007
$^{208}\text{Pb}/^{206}\text{Pb}$	2.1681 ± 0.0008	2.1679 ± 0.0009	2.1449 ± 0.0008
$^{204}\text{Pb}/^{206}\text{Pb}$	0.059042 ± 0.000037	0.058 ± 0.003	0.057 ± 0.002

^aSD—standard deviation ($n = 6$).

Accordingly, ICP-QMS has not the same sensitivity for different masses, due to differences in ion transmission and detection (Devulder et al., 2013). This phenomenon causes a difference between the true values and the obtained LIRs data (Đurđić et al., 2020; Marguí et al., 2007). Therefore, it is mandatory to correct the instrumental LIRs data on the mass-bias effect in order to improve accuracy in LIRs measurements. External and internal standardization can be used for data correction. External correction is based on the use of NIST SRM 981, while NIST SRM 997 was applied for internal standardization (Marguí et al., 2007; Vanhaecke et al., 2009). Also, for the correction of instrumental LIRs data, it is necessary to calculate the bias factor (K). For calculation of K , a linear, potential or exponential algorithm can be used (Đurđić et al., 2020; Marguí et al., 2007). In **Table 1**, the values of LIRs of the certified reference material NIST SRM 981 were compared with LIRs instrumental data after their correction to the mass-bias effect, using external and internal standardization with potential algorithm (Đurđić et al., 2020). As noted, external standardization ensured the best compliance of the obtained LIRs of NIST SRM 981 with the certified values of the standard material. Accordingly, this approach was applied to correct all obtained LIRs in wine samples. Finally, the correction of instrumental LIRs data for each wine sample was performed using “bracketing” sequences where the sample was analyzed between two runs of standard solution (Vanhaecke et al., 2009). “Bracketing” was done with standard solution of 5.12 $\mu\text{g/L}$ of lead. In addition, the matrix effect significantly contributes to the mass-bias effect. Matrix effect is dependent on the absolute concentration of matrix components and the most satisfactory methods to eliminate the matrix effect is to remove matrix elements. For that purpose, a large number of chromatographic techniques using chelating or ion exchange column can be used (Jones and Nesterenko, 1997). We tried overcoming matrix effects using the dilution approach due to sample dilution is an easy and effective method to reduce the severity of matrix effects. Several dilutions of the wine sample were tested in order to study the evolution of signal suppression. A dilution factor of 25 demonstrated to be enough to eliminate most of the matrix effects.

In addition to correction of LIRs for mass-bias effect, dwell time for each isotope and dead time of detector were optimized in order to increase precision and accuracy of measurements, respectively. These instrumental parameters were optimized by

NIST SRM 981 reference material. Standard solution of 5.12 $\mu\text{g/L}$ of lead, spiked with 2 $\mu\text{g/L}$ of thallium, was measured in six points per peak and five replicants, applying different dwell times. Dwell time for each isotope was optimized based on lowest relative standard deviation (RSD) between replicants (Encinar et al., 2001; Marguí et al., 2007). For majority of the analyzed isotopes, RSDs ranged from 0.10 to 0.15%, while RSD for ^{204}Pb was 0.32%. Finally, the optimized dwell time was 100 ms for ^{204}Pb , 5 ms for ^{208}Pb , while the dwell times for isotopes ^{206}Pb , ^{207}Pb , ^{208}Pb , ^{203}Tl and ^{205}Tl were set to 25 ms. In the case of dead time optimization, Nelms et al. (2001) presents several methods for optimizing this parameter. In this paper, $^{204}\text{Pb}/^{208}\text{Pb}$ was monitored as a function of different lead concentrations (10–30 $\mu\text{g/L}$), applying different dead times (25, 30, 35, 40 and 45 ns). Dead time of 40 ns was selected as optimal, after linear fitting of the regression line, where the slope of the regression line was close to zero (Nelms et al., 2001; Đurđić et al., 2020). Also, when discussing about the detector of ICP-QMS device, the mode in which the detector operates during LIRs measurements is essential. In this study, all LIRs were analyzed in pulse detector mode. The working range of lead concentration, which provides the operation of the detector of our ICP-QMS device in pulse mode, is up to 40 $\mu\text{g/L}$. Therefore, a dilution factor of 25 (*Sample preparation*) was sufficient to keep the lead concentration below the critical value, but at the same time, as stated, a dilution of 25 times was sufficient to minimize the matrix effect.

In the end, since ^{204}Pb is subject to isobaric interference of ^{204}Hg , a correction of ^{204}Pb intensity for ^{204}Hg was performed (Marguí et al., 2007; Đurđić et al., 2020).

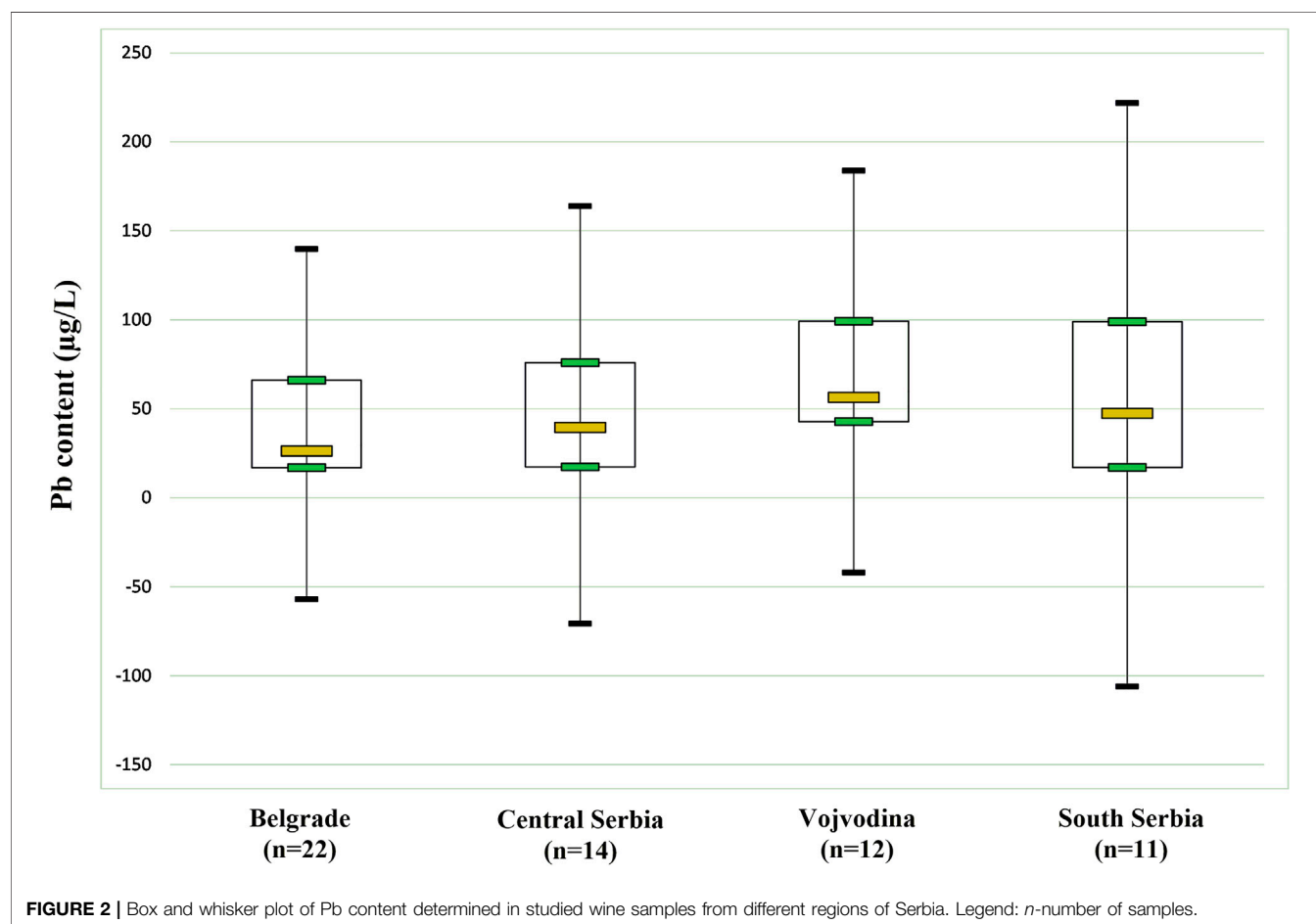
Sample Preparation

For determination of Pb content, all wine samples were diluted with ultra-pure water (1:10) and directly analyzed. All samples were contained HNO_3 in final concentration of 2% (v/v). Blank was prepared as standard solutions and wine samples with ultra-pure water and contained HNO_3 in concentration of 2% (v/v). Further presented Pb concentrations refer to values after blank correction.

For LIRs analysis in wine, samples were diluted with ultra-pure water. Depending of Pb concentration, dilution factor was 10 or 25. This dilution protocol was done in order to provide the pulse mode of the detector, which is mandatory in LIRs analysis. Thallium, as internal standard, was added to all samples in final concentration of 2 $\mu\text{g/L}$. All wine samples were contained HNO_3

TABLE 2 | Pb isotopic composition and Pb content in red wines from four Serbian regions.

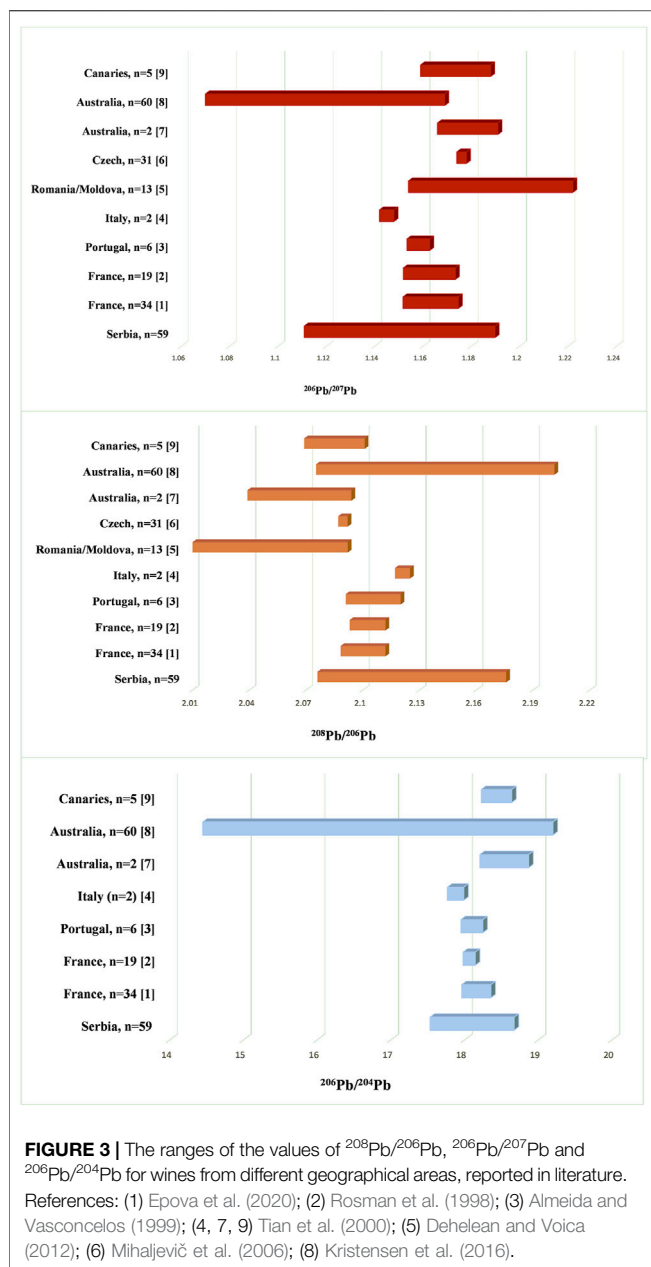
Regions of Serbia	Statistical parameters	Lead isotope ratios					Pb (µg/L)
		$^{206}\text{Pb}/^{204}\text{Pb}$	$^{208}\text{Pb}/^{206}\text{Pb}$	$^{207}\text{Pb}/^{204}\text{Pb}$	$^{208}\text{Pb}/^{204}\text{Pb}$	$^{206}\text{Pb}/^{207}\text{Pb}$	
Vojvodina	average \pm SD ^a	18.3 \pm 0.2	2.13 \pm 0.03	16.0 \pm 0.2	38.9 \pm 0.5	1.145 \pm 0.002	65.0 \pm 32.6
	Min	17.9	2.10	15.7	38.1	1.111	14.9
	Max	18.5	2.16	16.3	39.6	1.168	117.6
Belgrade	average \pm SD	18.3 \pm 0.4	2.14 \pm 0.03	16.0 \pm 0.2	38.7 \pm 0.7	1.141 \pm 0.003	44.4 \pm 29.6
	Min	17.6	2.10	15.6	37.4	1.112	12.6
	Max	18.6	2.17	16.2	39.8	1.170	100.3
Central Serbia	average \pm SD	18.3 \pm 0.4	2.14 \pm 0.03	16.0 \pm 0.3	39.0 \pm 0.7	1.145 \pm 0.002	48.8 \pm 35.1
	Min	17.5	2.10	15.6	37.6	1.112	11.5
	Max	18.6	2.17	16.3	39.9	1.171	114.5
South Serbia	average \pm SD	18.3 \pm 0.3	2.14 \pm 0.02	16.0 \pm 0.3	39.1 \pm 0.5	1.145 \pm 0.003	58.0 \pm 44.8
	Min	17.9	2.10	15.6	38.0	1.116	14.5
	Max	18.6	2.17	16.2	39.9	1.171	126.1

^aSD—standard deviation between samples.


in concentration of 2% (v/v). Blank was prepared as standard solutions and wine samples, with ultra-pure water, thallium solution and HNO₃. Final concentration of thallium and HNO₃ in blank were 2 µg/L and 2% (v/v), respectively. Blank correction has been done for each wine sample.

Statistical Analysis

Descriptive statistics, correlation analysis and Mann-Whitney *U* test were performed by NCSS software package, www.ncss.com (Hintze, 2001). All data produced were statistically treated to find possible statistically significant differences between the variables



with the aid of the nonparametric tests: Kruskal-Wallis and Mann-Whitney U. Principal component analysis (PCA) was carried out by PLS ToolBox, v.6.2.1, for MATLAB 7.12.0 (R2011a).

RESULTS AND DISCUSSION

Determination of Lead Content in Wine Samples

Basic statistical parameters of Pb analysis, for both of its total content and the isotopic ratios, are summarized in Table 2. The highest average content of Pb was recorded in samples from Vojvodina, while further Pb content decreases in the following

order: South Serbia > Central Serbia > Belgrade. In general, the lowest Pb content was $11.50 \pm 0.05 \mu\text{g/L}$ (Central Serbia), while the highest was $126.10 \pm 0.09 \mu\text{g/L}$ (South Serbia). Although a relatively high Pb content was found, it is important to point out that all tested wines are in accordance with the applicable health safety standards: The International Code of Oenological Practices (OIV code, 2019) defines a maximum Pb content in food and beverages of $150 \mu\text{g/L}$ (this value refers to wines produced since 2007).

Figure 2 represents the distribution of lead content in red wine samples from different Serbian regions. Vojvodina, Belgrade, Central Serbia and South Serbia, characterized by medians of 56.4, 26.3, 39.6, and 47.4, respectively. This non-parametric test demonstrates if there are significant differences between the regions.

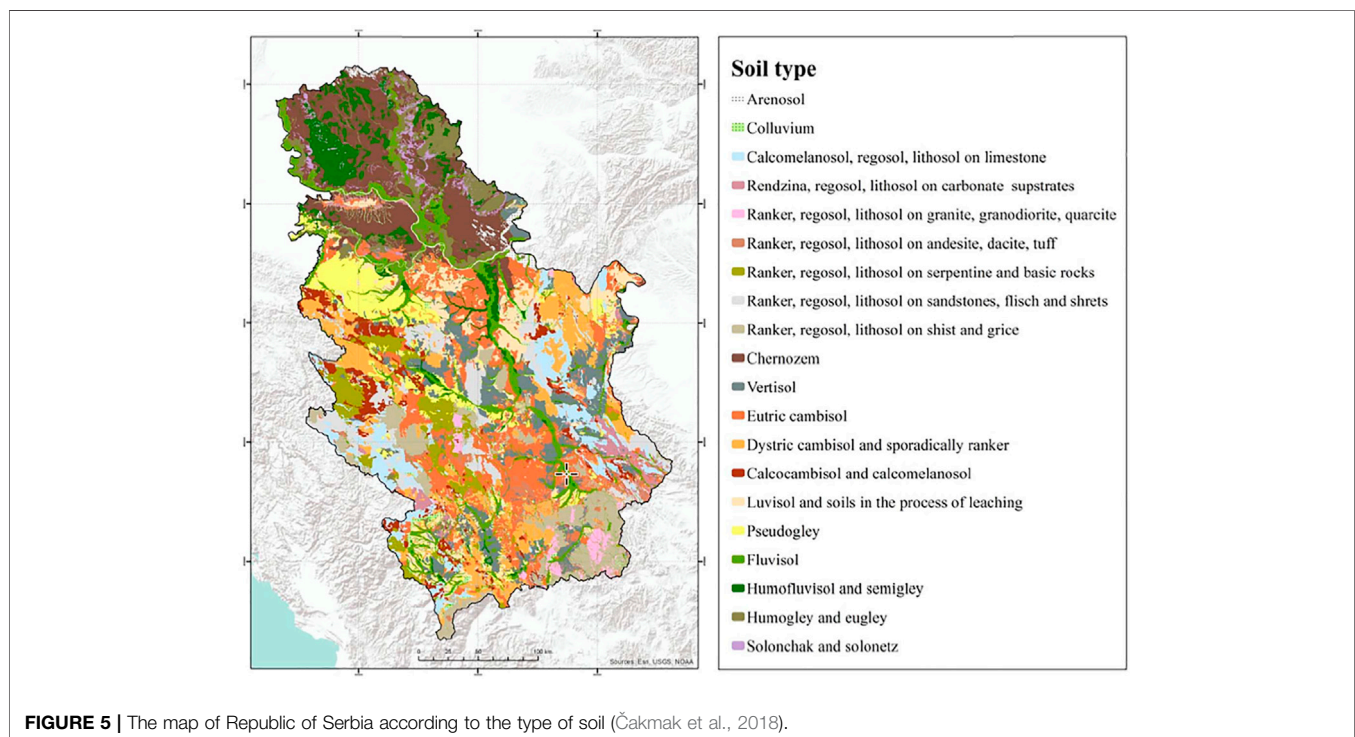
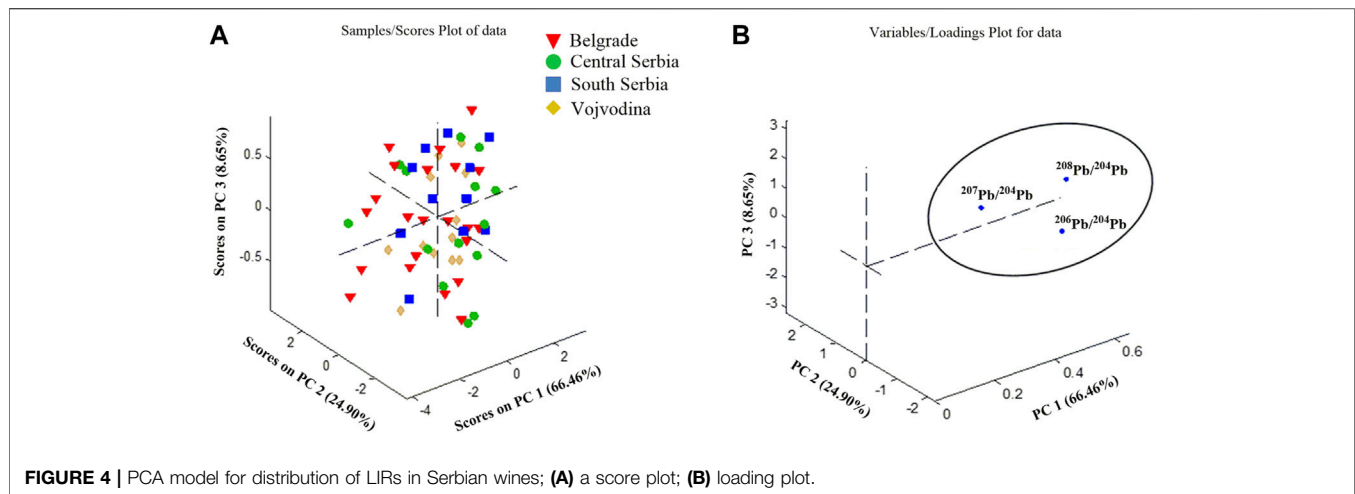
Lead Isotope Profile in Serbian Wines

According to our best knowledge, this is the first time that LIRs analysis in Serbian wines has been done. The average LIRs (average \pm SD) by their geographical origin are presented in Table 2. Small differences among the wines from the Serbian regions were observed for the $^{208}\text{Pb}/^{206}\text{Pb}$, $^{206}\text{Pb}/^{207}\text{Pb}$, and $^{208}\text{Pb}/^{204}\text{Pb}$ ratios. On another hand, average values of $^{207}\text{Pb}/^{204}\text{Pb}$ and $^{206}\text{Pb}/^{204}\text{Pb}$ were very similar in all Serbian regions. Minimal changes occur due to the fact that isotope ^{207}Pb changes slowly in time, in comparison with ^{208}Pb and ^{206}Pb isotopes, since ^{235}U generally decayed, while the abundance of ^{232}Th and ^{238}U is still relatively high on Earth (Komárek et al., 2008).

The obtained results showed that Serbian wines covered central part of the $^{208}\text{Pb}/^{206}\text{Pb}$, $^{206}\text{Pb}/^{207}\text{Pb}$ and $^{206}\text{Pb}/^{204}\text{Pb}$ ratios and are in concordance with LIRs of different European wines (Figure 3). In this case, ranges of $^{208}\text{Pb}/^{206}\text{Pb}$, $^{206}\text{Pb}/^{207}\text{Pb}$, and $^{206}\text{Pb}/^{204}\text{Pb}$ ratios were from 2.0760 to 2.1758, 1.1109 to 1.1898 and 17.53 to 18.67, respectively. Ranges of $^{208}\text{Pb}/^{206}\text{Pb}$ and $^{206}\text{Pb}/^{204}\text{Pb}$ ratios of Serbian wines were also within the wide ranges of Australian red wines ($^{208}\text{Pb}/^{206}\text{Pb}$ - from 2.0753 to 2.2013; $^{206}\text{Pb}/^{204}\text{Pb}$ —from 14.45 to 19.20) reported by Kristensen et al. (2016), while values of $^{206}\text{Pb}/^{207}\text{Pb}$ of our wines were slightly higher than reported ($^{206}\text{Pb}/^{207}\text{Pb}$ —from 1.0700 to 1.1690). On the other hand, Australian and Canaries wines reported by Tian et al. (2000) slightly coincide with the observed LIRs of Serbian wines. The different Pb isotopic composition of the mentioned wines in relation to Serbian wines potentially indicates a different source of Pb pollution in the observed regions (Komárek et al., 2008). On the other hand, Romanian/Moldavian wines were characterized by very low $^{208}\text{Pb}/^{206}\text{Pb}$ range (1.9961–2.0920) and a significantly high range of $^{206}\text{Pb}/^{207}\text{Pb}$ (1.1540–1.2220) compared to Serbian wines. Such Pb isotopic composition in Romanian/Moldavian wines is suspected to coal combustion whose isotope ratios values are similar to natural lead (Komárek et al., 2008; Dehelean and Voica, 2012).

Tracing the Geographical Origin of Wines by Non-Radiogenic ^{204}Pb Isotope

In order to define the geographical origin of wine, it is necessary to consider the geogenic ^{204}Pb . According to *a priori* knowledge



and environmental research, the ^{204}Pb isotope defines natural Pb-sources in environmental samples (Epova et al., 2020). In that sense, the content of ^{204}Pb in wines shows the isotopic composition in wine, and the corresponding soil, where the grape was grown, since the plant inherits isotopic signatures from the geological-pedological environment. In this way, the authenticity of the wine can be established (Martins et al., 2014; Bora et al., 2018; Epova et al., 2020).

For this purpose, the content of ^{204}Pb was discussed and correlated with the radiogenic isotopes ^{208}Pb , ^{207}Pb and ^{206}Pb . The corresponding LIRs of all four Serbian regions ($^{208}\text{Pb}/^{204}\text{Pb}$, $^{207}\text{Pb}/^{204}\text{Pb}$, and $^{206}\text{Pb}/^{204}\text{Pb}$) were subjected to the Principal Component Analysis (PCA). All data were autoscaled prior to

any multivariate analysis to bring values to compatible units. PCA was carried out as an exploratory data analysis by using a singular value decomposition algorithm and a 0.95 confidence level for Q and T2 Hotelling limits for outliers. The analysis was based on correlation matrix and factors with eigenvalues greater than one were retained. Sample scores and their loadings for the three PCs (PC1, PC2, and PC3), responsible for 100% of total variance, are presented in Figure 4. With a score plot (Figure 4A), the complete overlap of all regions of Serbia was obtained, while the loading graph (Figure 4B) clearly indicates the grouping according to all analyzed LIRs. It means that no relevant discrimination of wines according to their geographical origin was observed.

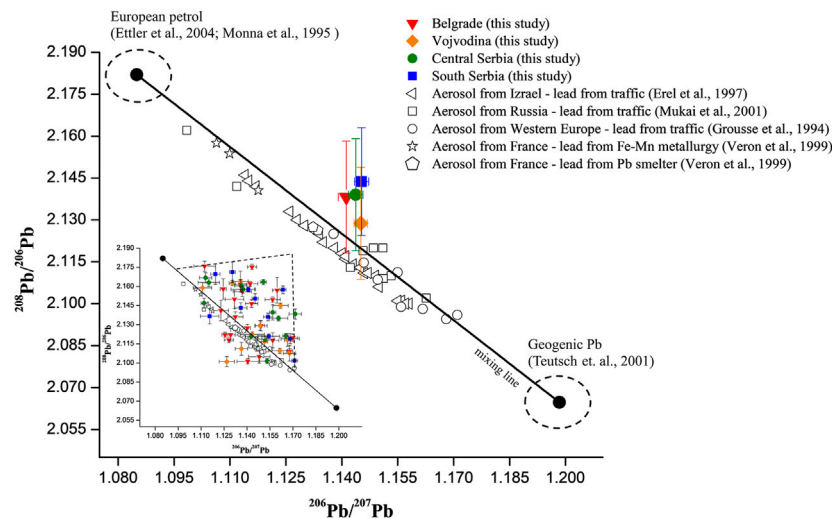


FIGURE 6 | Plot of average $^{208}\text{Pb}/^{206}\text{Pb}$ and average $^{206}\text{Pb}/^{207}\text{Pb}$ of analyzed Serbian wines. Error bars represent standard deviations between samples. Comparison with identical LIRs in aerosols from different European countries. Inset figure represent distribution of $^{208}\text{Pb}/^{206}\text{Pb}$ and $^{206}\text{Pb}/^{207}\text{Pb}$ for individual wine samples from four Serbian regions.

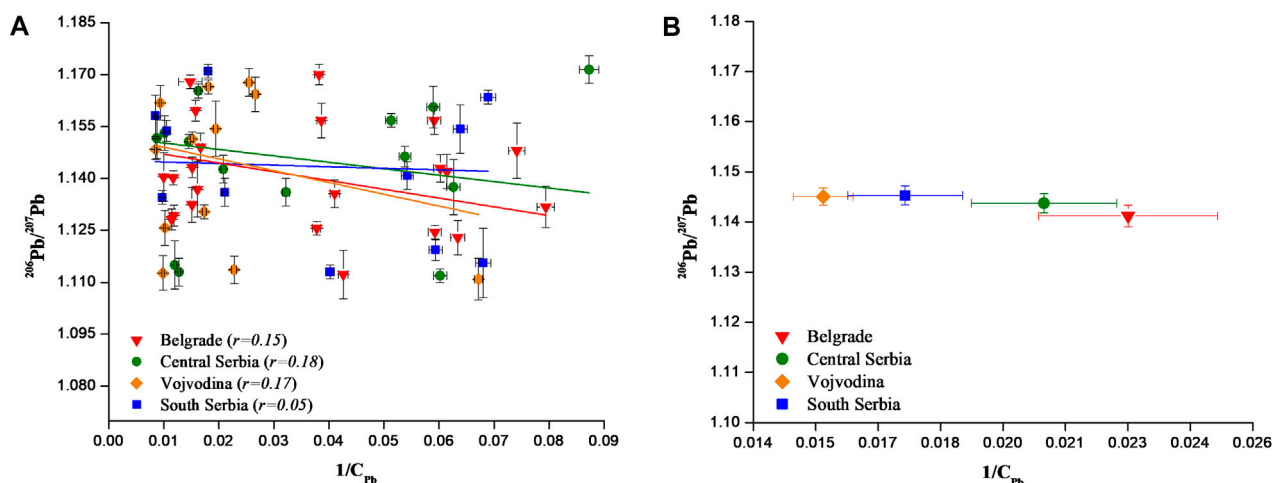


FIGURE 7 | (A) Possible isotopic signature of pollutant Pb sources in Serbian wines determined from $^{206}\text{Pb}/^{207}\text{Pb}$ ratio vs. $1/C_{\text{Pb}}$. **(B)** Plot of average $^{206}\text{Pb}/^{207}\text{Pb}$ ratio vs. average $1/C_{\text{Pb}}$ for four Serbian regions. Error bars represent standard deviations between samples.

The map of the Republic of Serbia (Čakmak et al., 2018) shows different soil profile in regions (Figure 5). It is clear that Vojvodina, as the largest Serbian plain, is characterized by chernozem and humofluvisol. In the area of Belgrade, eutric cambisol and luvisol soil types are dominant. Central and South Serbia, as a hilly and mountainous segment of Serbia, is characterized by diverse soil type such as vertisol, eutric cambisol, calcomelanosol and ranker. Among other factors, different soil types reflect different content of macro and micro elements (including Pb), as result of different processes in pedogenesis (Čakmak et al., 2018; Vukojević et al., 2019). Since the content of ^{204}Pb in wines (in combination with other LIRs) reflects the isotopic composition in the corresponding soil, the

recognition of Serbian regions is foreseen. However, anthropogenic sources can influence the Pb isotopic composition and should not be neglected.

Tracing Anthropogenic Influences Using $^{208}\text{Pb}/^{206}\text{Pb}$ and $^{206}\text{Pb}/^{207}\text{Pb}$

In environmental studies, plotting of $^{208}\text{Pb}/^{206}\text{Pb}$ vs. $^{206}\text{Pb}/^{207}\text{Pb}$ is used to identify different sources of Pb contamination such as natural, geogenic Pb (rock and soil formation) and anthropogenic (emissions from cars, industrial existence, metal activities, smelters ...) (Erel et al., 1997; Larcher et al., 2003; Komárek et al., 2008; Đurđić et al., 2020).

Lead particles emitted into the atmosphere are mostly retained in the atmosphere (atmospheric Pb), exhibiting Pb isotopic signature of atmospheric aerosol (Flament et al., 2002). It was reported that the average size of the anthropogenic Pb particle was about 0.9 μm , although the size of the emitted Pb particles varies depending on the source of pollution. The problem with contaminated aerosol occurs due to uncontrolled aerosol transport as a consequence of various climatic factors. This leads to difficulties to define Pb isotopic profile, as well as to identify sources of Pb pollution (Komárek et al., 2008). According to the reported data, the dust particles, originating from the Sahara, contribute significantly to the Pb isotopic composition in the European aerosol (Doucet and Carignan, 2001; Grousset et al., 1994). Erel et al. (2002), analyzing LIRs in atmospheric aerosol in Jerusalem (Israel), found a significant contribution of Pb that does not originate from a local source, but from other parts of the World (Eastern Europe, Turkey and Egypt). For example, LIRs in French wine from 19 different vintage (1950–1991), were influenced by contribution of Pb variations in aerosol (Rosman et al., 1998). Kristensen et al. (2016) defined the LIRs in Australian wines in correlation to leaded gasoline, especially during the 1960s and 1970s. The authors explained that influence of Pb in the atmospheric aerosol significantly contributed to the total Pb isotopic composition in wine. Besides, clearly separation from the LIRs obtained for the vineyard soil was observed (Kristensen et al., 2016). In this study, we compared average values of LIRs of Serbian wines from different regions with literature data (Erel et al., 1997; Grousset et al., 1994; Kristensen et al., 2016; Mukai et al., 2001; Véron et al., 1999) related to atmospheric aerosol containing Pb from different anthropogenic sources (leaded gasoline from different regions/countries, Fe-Mn metallurgy, Pb smelter) and presented on **Figure 6**. Three-isotopes “mixing line” ($^{208}\text{Pb}/^{206}\text{Pb}$ vs. $^{206}\text{Pb}/^{207}\text{Pb}$), obtained between the geogenic (Teutsch et al., 2001) and the anthropogenic LIRs, characterizes European petrol (as the most common anthropogenic source of Pb) (Ettler et al., 2004; Monna et al., 1995). The graph shows a very good accordance of the “mixing line” with LIRs characterized by Pb from traffic, Fe-Mn metallurgy and Pb smelter. LIRs of Serbian wines were distributed along the “mixing line” (inset **Figure 6**), what is in accordance with the literature data (Erel et al., 1997; Grousset et al., 1994; Kristensen et al., 2016; Mukai et al., 2001; Véron et al., 1999). From **Figure 6**, the average values of LIRs for four Serbian regions are proximately equivalent to one another and showed a typical value of the mixture of European petrol and geogenic Pb. This indicates that Pb in the aerosol from different sources significantly contributed to the total Pb isotopic composition in Serbian wines. On the other hand, a scattering of LIRs data of Serbian wines from “mixing line”, in the shape of an imaginary triangle, was observed (inset **Figure 6**). Such scattering was described by Vanhaecke et al. (2009), explaining that Pb isotopic composition in environmental samples is, in majority of cases, defined by more than two Pb sources. Unknown or uncategorized sources of pollution have to be considered as well.

The vinification process is also one of the important sources of lead contamination of wine. The vinification process begins with the grape harvest and continues with the transport of grapes to the winery, the crushing of grapes and the addition of pectolytic enzyme

preparations for maceration and antioxidants (ascorbic acid and tannin). These processes were followed by the addition of wine yeast to the must, filtration of the must, as well as sulfurization with certain doses of SO_2 -based compounds to final products in bottles. All these vinification steps represent potential sources of lead in wine (Almeida and Vasconcelos, 2003; Stockley et al., 2003). Recently, with the massive introduction of stainless-steel devices the contamination level was drastically reduced, but still, during traditional vinification protocol, a long contact of wine with Pb equipment significantly contributes to Pb isotope composition in wine (Almeida and Vasconcelos, 2003). This influence is especially pronounced in the preparation of red wine, since the maceration process is one of the main processes in its production. We believe that Pb from the vinification process, in addition to leaded gasoline, metallurgical activities/smelters, also contributed to the total Pb isotopic composition in wines. On the other side, this synergistic effect of all those influences cause difficulties to define Serbian wine regions.

In a final step, the isotope ratio $^{206}\text{Pb}/^{207}\text{Pb}$ was correlated with $1/C_{\text{Pb}}$ (C_{Pb} —Pb concentration) and the obtained results graphically presented on **Figure 7A**. When statistically reliable, the extrapolation of $1/C_{\text{Pb}}$ toward 0 provides the isotopic signature of the source of contamination, assuming it is a single source with a constant isotopic composition (Erel et al., 1997; Ndung'u et al., 2011). However, the Pearson correlation coefficient (r) for analyzed wines from four Serbian regions was from 0.05 to 0.18. Such a correlation indicates that there is no statistically significant difference between $^{206}\text{Pb}/^{207}\text{Pb}$ and $1/C_{\text{Pb}}$ due to the large variance of the data, indicating possible multiple sources of lead pollution (Ndung'u et al., 2011). This is also consistent with data discussed and presented on **Figure 6**. In addition, plot of average $^{206}\text{Pb}/^{207}\text{Pb}$ vs. average of $1/C_{\text{Pb}}$ for all Serbian regions (**Figure 7B**) showing that the LIRs are independent of Pb concentration.

CONCLUSION

In this work, systematic analysis of lead isotope profile in Serbian wines from four regions was conducted. The obtained results are discussed in order to identify potential sources of lead pollution and compared with those for European and Australian wines. The obtained values of the $^{208}\text{Pb}/^{206}\text{Pb}$, $^{206}\text{Pb}/^{207}\text{Pb}$, and $^{206}\text{Pb}/^{204}\text{Pb}$ ratios of Serbian wines are comparable to ratios reported for other European areas and contribute to the databases for lead isotope profiles of European wines. Further evaluation showed that, in addition to natural Pb, various anthropogenic sources such as leaded gasoline, Fe-Mn metallurgy, Pb smelter contribute to the total Pb isotopic profile of Serbian wines. Besides, the vinification process is also suspected to have a significant influence.

LIRs are powerful tool for tracing the origin of wine on condition that a single source of influence i.e., pollution is previously confirmed. In the case of multiple sources of influence isotopic signatures are not significantly different due to large variance of data. In any case, both fully validated ICP-QMS analysis and overall methodology, coupled with multivariate method of analysis (PCA) offer the best approach to answer the entitled question of tracing the origin of wine, determining the authenticity and geographical origin of wine.

DATA AVAILABILITY STATEMENT

The original contributions presented in the study are included in the article/**Supplementary Material**, further inquiries can be directed to the corresponding author.

AUTHOR CONTRIBUTIONS

SD and VS performed all the work, analysed, interpreted data and drafted this manuscript. SR and JM planned, designed, critically revised this paper and supervised all the work.

REFERENCES

- Almeida, C. M. R., and Vasconcelos, M. T. S. D. (1999). Determination of lead Isotope Ratios in Port Wine by Inductively Coupled Plasma Mass Spectrometry after Pre-treatment by UV-Irradiation. *Analytica Chim. Acta* 396, 45–53. doi:10.1016/s0003-2670(99)00356-6
- Almeida, C. M. R., and Vasconcelos, M. T. S. D. (2004). Does the Winemaking Process Influence the Wine $^{87}\text{Sr}/^{86}\text{Sr}$? A Case Study. *Food Chem.* 85, 7–12. doi:10.1016/j.foodchem.2003.05.003
- Almeida, C. M. R., and Vasconcelos, M. T. S. D. (2003). Lead Contamination in Portuguese Red Wines from the Douro Region: from the Vineyard to the Final Product. *J. Agric. Food Chem.* 51, 3012–3023. doi:10.1021/jf0259664
- Barbaste, M., Halicz, L., Galy, A., Medina, B., Emteborg, H., C. Adams, F., et al. (2001). Evaluation of the Accuracy of the Determination of lead Isotope Ratios in Wine by ICP MS Using Quadrupole, Multicollector Magnetic Sector and Time-Of-Flight Analyzers. *Talanta* 54, 307–317. doi:10.1016/s0039-9140(00)00651-2
- Bora, F. D., Donici, A., Rusu, T., Bunea, A., Popescu, D., and Bunea, C. I. (2018). Elemental Profile and $^{207}\text{Pb}/^{206}\text{Pb}$, $^{208}\text{Pb}/^{206}\text{Pb}$, $^{204}\text{Pb}/^{206}\text{Pb}$, $^{87}\text{Sr}/^{86}\text{Sr}$ Isotope Ratio as Fingerprints for Geographical Traceability of Romanian Wines. *Not. Bot. Horti Agrobot.* 46 (1), 223–239. doi:10.15835/nbha46110853
- Cakmak, D., Perovic, V., Kresovic, M., Jaramaz, D., Mrvic, V., Belanovic Simic, S., et al. (2018). Spatial Distribution of Soil Pollutants in Urban green Areas (A Case Study in Belgrade). *J. Geochem. Explor.* 188, 308–317. doi:10.1016/j.gexplo.2018.02.001
- Dehelean, A., and Voica, C. (2012). Determination of lead and Strontium Isotope Ratios in Wines by Inductively Coupled Plasma Mass Spectrometry. *Rom. Journ. Phys.* 57, 1194–1203.
- Devulder, V., Lobo, L., Van Hoecke, K., Degryse, P., and Vanhaecke, F. (2013). Common Analyte Internal Standardization as a Tool for Correction for Mass Discrimination in Multi-Collector Inductively Coupled Plasma-Mass Spectrometry. *Spectrochim. Acta B: At. Spectrosc.* 89, 20–29. doi:10.1016/j.sab.2013.08.009
- Doucet, F. J., and Carignan, J. (2001). Atmospheric Pb Isotopic Composition and Trace Metal Concentration as Revealed by Epiphytic Lichens. *Atmos. Environ.* 35, 3681–3690. doi:10.1016/s1352-2310(00)00510-0
- Encinar, J. R., Alonso, J. I. G., Sanz-Medel, A., Main, S., and Turner, P. J. (2001). A Comparison between Quadrupole, Double Focusing and Multicollector ICP-MS Instruments : Part I. Evaluation of Total Combined Uncertainty for lead Isotope Ratio Measurements. *J. Anal. Spectrom.* 16, 315–321. doi:10.1039/b006145j
- Epova, E. N., Bérail, S., Séby, F., Barre, J. P. G., Vacchina, V., Médina, B., et al. (2020). Potential of lead Elemental and Isotopic Signatures for Authenticity and Geographical Origin of Bordeaux Wines. *Food Chem.* 303, 125277. doi:10.1016/j.foodchem.2019.125277
- Erel, Y., Axelrod, T., Veron, A., Mahrer, Y., Katsafados, P., and Dayan, U. (2002). Transboundary Atmospheric lead Pollution. *Environ. Sci. Technol.* 36, 3230–3233. doi:10.1021/es020530q
- Erel, Y., Veron, A., and Halicz, L. (1997). Tracing the Transport of Anthropogenic lead in the Atmosphere and in Soils Using Isotopic Ratios. *Geochim. et Cosmochim. Acta* 61, 4495–4505. doi:10.1016/s0016-7037(97)00353-0

FUNDING

This research was financially supported by the Ministry of Education, Science and Technological Development of Republic of Serbia (contract numbers: 451-03-9/2021-14/200168 and 451-03-68/2020-14/200161).

SUPPLEMENTARY MATERIAL

The Supplementary Material for this article can be found online at: <https://www.frontiersin.org/articles/10.3389/fchem.2021.746695/full#supplementary-material>

- Ettler, V., Mihaljevic, M., and Komárek, M. (2004). ICP-MS Measurements of lead Isotopic Ratios in Soils Heavily Contaminated by lead Smelting: Tracing the Sources of Pollution. *Anal. Bioanal. Chem.* 378 (2), 311–317. doi:10.1007/s00216-003-2229-y
- Flament, P., Bertho, M.-L., Deboudt, K., Véron, A., and Puskaric, E. (2002). European Isotopic Signatures for lead in Atmospheric Aerosols: a Source Apportionment Based upon $^{206}\text{Pb}/^{207}\text{Pb}$ Ratios. *Sci. Total Environ.* 296, 35–57. doi:10.1016/s0048-9697(02)00021-9
- Grousset, F. E., Quétel, C. R., Thomas, B., Buat-Menard, P., Donard, O. F. X., and Bucher, A. (1994). Transient Pb Isotopic Signatures in the Western European Atmosphere. *Environ. Sci. Technol.* 28, 1605–1608. doi:10.1021/es00058a011
- Hintze, J. (2001). *NCSS and PASS Number Cruncher Statistical Systems*. Kaysville. Available at: www.ncss.com.
- Jones, P., and Nesterenko, P. N. (1997). High-Performance Chelation Ion Chromatography: A New Dimension in the Separation and Determination of Trace Metals. *J. Chromatogr. A* 789, 413–435. doi:10.1016/S0021-9673(97)00824-8
- Kment, P., Mihaljevič, M., Ettler, V., Šebek, O., Strnad, L., and Rohlová, L. (2005). Differentiation of Czech Wines Using Multielement Composition - A Comparison with Vineyard Soil. *Food Chem.* 91, 157–165. doi:10.1016/j.foodchem.2004.06.010
- Komárek, M., Ettler, V., Chrástný, V., and Mihaljevič, M. (2008). Lead Isotopes in Environmental Sciences: a Review. *Environ. Int.* 34 (4), 562–577. doi:10.1016/j.envint.2007.10.005
- Kristensen, L. J., Taylor, M. P., and Evans, A. J. (2016). Tracing Changes in Atmospheric Sources of lead Contamination Using lead Isotopic Compositions in Australian Red Wine. *Chemosphere* 154, 40–47. doi:10.1016/j.chemosphere.2016.03.023
- Lara, R., Cerutti, S., Salonia, J. A., Olsina, R. A., and Martinez, L. D. (2005). Trace Element Determination of Argentine Wines Using ETAAS and USN-ICP-OES. *Food Chem. Toxicol.* 43, 293–297. doi:10.1016/j.fct.2004.10.004
- Larcher, R., Nicolini, G., and Pangrazzi, P. (2003). Isotope Ratios of lead in Italian Wines by Inductively Coupled Plasma Mass Spectrometry. *J. Agric. Food Chem.* 51, 5956–5961. doi:10.1021/jf021064r
- Marguí, E., Iglesias, M., Queralt, I., and Hidalgo, M. (2007). Precise and Accurate Determination of lead Isotope Ratios in Mining Wastes by ICP-QMS as a Tool to Identify Their Source. *Talanta* 73, 700–709. doi:10.1016/j.talanta.2007.04.051
- Martin, A. E., Watling, R. J., and Lee, G. S. (2012). The Multi-Element Determination and Regional Discrimination of Australian Wines. *Food Chem.* 133, 1081–1089. doi:10.1016/j.foodchem.2012.02.013
- Martins, P., Madeira, M., Monteiro, F., Bruno de Sousa, R., Curvelo-Garcia, A. S., and Catarino, S. (2014). $^{87}\text{Sr}/^{86}\text{Sr}$ Ratio in Vineyard Soils from Portuguese Denominations of Origin and its Potential for Origin Authentication. *OENO One* 48 (1), 21–29. doi:10.20870/oeno-one.2014.48.1.1652
- Medina, B., Augagneur, S., Barbaste, M., Grousset, F. E., and Buat-Menard, P. (2000). Influence of Atmospheric Pollution on the lead Content of Wines. *Food Addit. Contam.* 17, 435–445. doi:10.1080/02652030050034019
- Mihaljevič, M., Ettler, V., Šebek, O., Strnad, L., and Chrástný, V. (2006). Lead Isotope Signatures of Wine and Vineyard Soils-Tracers of lead Origin. *J. Geochem. Explor.* 88, 130–133. doi:10.1016/j.gexplo.2005.08.025

- Monna, F., Benothman, D., and Luck, J. (1995). Pb Isotopes and Pb, Zn and Cd Concentrations in the Rivers Feeding a Coastal Pond (Thau, Southern France): Constraints on the Origin(s) and Flux(es) of Metals. *Sci. Total Environ.* 166 (1–3), 19–34. doi:10.1016/0048-9697(95)04514-2
- Mukai, H., Machida, T., Tanaka, A., Vera, Y. P., and Uematsu, M. (2001). Lead Isotope Ratios in the Urban Air of Eastern and central Russia. *Atmos. Environ.* 35, 2783–2793. doi:10.1016/s1352-2310(00)00341-1
- Ndung'u, K., Hibdon, S., Véron, A., and Flegal, A. R. (2011). Lead Isotopes Reveal Different Sources of lead in Balsamic and Other Vinegars. *Sci. Total Environ.* 409, 2754–2760. doi:10.1016/j.scitotenv.2011.04.001
- Nelms, S. M., Quétel, C. R., Prohaska, T., Vogl, J., and Taylor, P. D. P. (2001). Evaluation of Detector Dead Time Calculation Models for ICP-MS. *J. Anal. Spectrom.* 16, 333–338. doi:10.1039/b007913h
- OIV code (2019). International Code of Oenological Practices. Available at: <http://www.oiv.int/public/medias/6558/code-2019-en.pdf> (Accessed December 19, 2020).
- Paneque, P., Álvarez-Sotomayor, M. T., Clavijo, A., and Gómez, I. A. (2010). Metal Content in Southern Spain Wines and Their Classification According to Origin and Ageing. *Microchem. J.* 94, 175–179. doi:10.1016/j.microc.2009.10.017
- Rosman, K. J. R., Chisholm, W., Jimi, S., Candelone, J.-P., Bouchon, C. F., Teissedre, P.-L., et al. (1998). Lead Concentrations and Isotopic Signatures in Vintages of French Wine between 1950 and 1991. *Environ. Res.* 78, 161–167. doi:10.1006/enrs.1997.3812
- Stockley, C. S., Smith, L. H., Tiller, I. K. G., Gulson, B. L., Osborn, C. D. A., and Lee, T. H. (2003). Lead in Wine: a Case Study on Two Varieties at Two Wineries in South Australia. *Aust. J. Grape Wine Res.* 9, 47–55. doi:10.1111/j.1755-0238.2003.tb00231.x
- Teutsch, N., Erel, Y., Halicz, L., and Banin, A. (2001). Distribution of Natural and Anthropogenic lead in Mediterranean Soils. *Geochim. et Cosmochim. Acta* 65 (17), 2853–2864. doi:10.1016/s0016-7037(01)00607-x
- Tian, X., Emteborg, H. k., Barbaste, M., and Adams, F. C. (2000). Accuracy and Precision of lead Isotope Ratios in Wines Measured by Axial Inductively Coupled Plasma Time of Flight Mass Spectrometry. *J. Anal. Spectrom.* 15, 829–835. doi:10.1039/b001026j
- Vanhaccke, F., Balcaen, L., and Malinovsky, D. (2009). Use of Single-Collector and Multi-Collector ICP-Mass Spectrometry for Isotopic Analysis. *J. Anal. Spectrom.* 24, 863–886. doi:10.1039/b903887f
- Véron, A., Flament, P., Bertho, M. L., Alleman, L., Flegal, R., and Hamelin, B. (1999). Isotopic Evidence of Pollutant lead Sources in Northwestern France. *Atmos. Environ.* 33, 3377–3388. doi:10.1016/s1352-2310(98)00376-8
- Vukojević, V., Đurđić, S., Stefanović, V., Trifković, J., Čakmak, D., Perović, V., et al. (2019). Scandium, Yttrium, and Lanthanide Contents in Soil from Serbia and Their Accumulation in the Mushroom *Macrospora Procera* (Scop.) Singer. *Environ. Sci. Poll. Res.* 26, 5422–5434. doi:10.1007/s11356-018-3982-y
- Đurđić, S., Stanković, V., Ražić, S., and Mutić, J. (2020). Lead Isotope Ratios as Tool for Elucidation of Chemical Environment in a System of *Macrospora Procera* (Scop.) Singer - Soil. *Environ. Sci. Pollut. Res.* doi:10.1007/s11356-020-07947-6

Conflict of Interest: The authors declare that the research was conducted in the absence of any commercial or financial relationships that could be construed as a potential conflict of interest.

Publisher's Note: All claims expressed in this article are solely those of the authors and do not necessarily represent those of their affiliated organizations, or those of the publisher, the editors and the reviewers. Any product that may be evaluated in this article, or claim that may be made by its manufacturer, is not guaranteed or endorsed by the publisher.

Copyright © 2021 Đurđić, Stanković, Ražić and Mutić. This is an open-access article distributed under the terms of the Creative Commons Attribution License (CC BY). The use, distribution or reproduction in other forums is permitted, provided the original author(s) and the copyright owner(s) are credited and that the original publication in this journal is cited, in accordance with accepted academic practice. No use, distribution or reproduction is permitted which does not comply with these terms.



Combined Methodologies for Determining *In Vitro* Bioavailability of Drugs and Prediction of *In Vivo* Bioequivalence From Pharmaceutical Oral Formulations

A. De Simone¹, L. Davani², S. Montanari², V. Tumiatti², S. Avanesian³, F. Testi³ and V. Andrisano^{2*}

¹Department of Drug Science and Technology, University of Turin, Torino, Italy, ²Department for Life Quality Studies, University of Bologna, Rimini, Italy, ³Valpharma International S.p.A., Rimini, Italy

OPEN ACCESS

Edited by:

Quezia B. Cass,
Federal University of São Carlos, Brazil

Reviewed by:

Luiz Cláudio Rodrigues Pereira
da Silva,
Universidade Federal do Rio
de Janeiro, Brazil
Rafael Linden,
Feevale University, Brazil

*Correspondence:

V. Andrisano
vincenza.andrisano@unibo.it

Specialty section:

This article was submitted to
Analytical Chemistry,
a section of the journal
Frontiers in Chemistry

Received: 15 July 2021

Accepted: 15 September 2021

Published: 03 November 2021

Citation:

De Simone A, Davani L, Montanari S,
Tumiatti V, Avanesian S, Testi F and
Andrisano V (2021) Combined
Methodologies for Determining *In Vitro*
Bioavailability of Drugs and Prediction
of *In Vivo* Bioequivalence From
Pharmaceutical Oral Formulations.
Front. Chem. 9:741876.
doi: 10.3389/fchem.2021.741876

With the aim of developing an *in vitro* model for the bioavailability (BA) prediction of drugs, we focused on the study of levonorgestrel (LVN) released by 1.5 mg generic and brand-name tablets. The developed method consisted in combining a standard dissolution test with an optimized parallel artificial membrane permeability assay (PAMPA) to gain insights into both drug release and gastrointestinal absorption. Interestingly, the obtained results revealed that the tablet standard dissolution test, combined with an optimized PAMPA, highlighted a significant decrease in the release ($15 \pm 0.01 \mu\text{g min}^{-1}$ vs $30 \pm 0.01 \mu\text{g min}^{-1}$) and absorption ($19 \pm 7 \times 10^{-6} \pm 7 \text{ cm/s Pe}$ vs $41 \pm 15 \times 10^{-6} \text{ cm/s Pe}$) profiles of a generic LVN tablet when compared to the brand-name formulation, explaining unbalanced *in vivo* bioequivalence (BE). By using this new approach, we could determine the actual LVN drug concentration dissolved in the medium, which theoretically can permeate the gastrointestinal (GI) barrier. In fact, insoluble LVN/excipient aggregates were found in the dissolution media giving rise to non-superimposable dissolution profiles between generic and brand-name LVN tablets. Hence, the results obtained by combining the dissolution test and PAMPA method provided important insights confirming that the combined methods can be useful in revealing crucial issues in the prediction of *in vivo* BE of drugs.

Keywords: levonorgestrel, bioavailability, drug–excipient interaction, gastrointestinal passive permeability, PAMPA, bioequivalence, dissolution model

INTRODUCTION

The development of an *in vitro* method for the prediction of drugs' BA is an interesting challenge, mostly because of the possibility to save both time and money in the approval process of a given drug. The prediction of drugs' BA *in vitro* can be especially useful in those studies aimed at determining the BE of a generic and a brand-name drug. Indeed, despite the public concern in having access to generic drugs as quickly as possible due to their lower price, the regulatory process for their approval takes time like any other process related to this aspect (Chazin et al., 2020). However, if the chemical equivalence between two chemical entities is relatively easy to establish, it is more complex to prove

the BE between two or more formulations, with the same active pharmaceutical ingredients (APIs). The differences noticed in BE for the studied products can be mainly related to the physical properties of the excipients used in the compared formulations (Zarmpi et al., 2017). The ability of detecting the factors influencing the physicochemical properties, as well as drug delivery, will make it possible to thoroughly depict both its BA and BE profiles (Niazi, 2007).

Most of the studies comparing a generic drug to a brand-name product, in terms of BE, include the determination of active compounds or their metabolites in biological fluids. Other studies may involve comparative pharmacodynamic (PD) investigations in humans or comparative clinical trials. Nevertheless, it is not always possible or necessary to use *in vivo* human data for evaluating drug bioavailability, at least in the formulation optimization process (Chen et al., 2001a). A large number of physicochemical and physiologic factors that may influence the adsorption of drugs can indeed be monitored by applying some designed *in silico* (Mathias and Crison, 2012) and *in vitro* models. For all these reasons, the application of model-based drug development, as well as precise and accurate analytical methods supported by statistical considerations (Lalonde et al., 2007; Kim et al., 2018; Martinez and Zhao, 2018; Zhao et al., 2019), seems to offer a reliable approach for the *in vitro* characterization of a drug before *in vivo* BE studies. For these reasons, there is a great need to develop surrogate models able to provide information about the BA or BE profile for all the classes of studied drugs. Starting from the fact that the BA of a drug, released from a solid oral form, is influenced by dissolution, solubility, and intestinal permeability, the proposed methods should provide the characterization of both the dissolution and adsorption profiles. This is pivotal considering the need for pharmaceutical industries to develop and apply methods able to evaluate the bioavailability of a large fraction of poorly water-soluble drug compounds (Ku and Dulin, 2012; Sironi et al., 2017). Indeed, many *in vitro* models have been developed to evaluate the capacity of new drug delivery systems or formulations to enhance the permeability of poorly soluble drugs (Buyukozturk et al., 2010; Kanzer et al., 2010; Fischer et al., 2011a; Fischer et al., 2011b; Fischer et al., 2012). Despite the meaningful results obtained by these types of experiments, it is also essential to consider that, before any absorption can take place, the drug needs to be in solution. Indeed, such drugs can often exhibit an unreal high absorption rate if the experimental setup does not take into account the dissolution of the drug prior to membrane permeation. For this purpose, some combined dissolution/permeability models have been proposed (Ginski et al., 1999; Kobayashi et al., 2001; Kataoka et al., 2003; Kataoka et al., 2006; Motz et al., 2007; Kataoka et al., 2011; Kataoka et al., 2014). Some of the proposed models mimicking the *in vivo* environment were developed in order to forecast the oral absorption of pH-independent and -dependent drugs in a more and more reliable manner (Kobayashi et al., 2001; He et al., 2003; Kataoka et al., 2003; Noureddine et al., 2005; Sugawara et al., 2005; Kataoka et al., 2006). The application of these systems able to assess both the dissolution and the permeation process was found to be particularly suitable for poorly soluble drugs.

However, their application still remains very limited in the conventional drug discovery process because of the various drawbacks shown. In particular, for low aqueous solubility molecules, the precipitation of drugs in the aqueous buffer system may represent a critical step. At the same time, sufficient concentrations of the solubilized drug in both the donor and the receiver compartment must be guaranteed to carry out a permeability assay and ensure measurement sensitivity.

With all this in mind, the aim of this work was to validate an *in vitro* system combining dissolution and PAMPA for the assessment of both the dissolution and the *in vitro* oral adsorption profile of LVN from oral formulations. The designed method, combining both the tests, was intended to provide an integrated approach for BE prediction of the drug before moving on *in vivo* studies.

The dissolution test is routinely used for stability and quality control studies. The reliability of this kind of assay in predicting the *in vivo* performance of a drug product is related to its capability of reconstructing *in vitro* the distinctive conditions registered in the gastrointestinal (GI) tract (Dressman et al., 1998). Indeed, the FDA has now recognized the major role of this assay in reducing the regulatory burden in predicting the human studies in generic drug development (Anand et al., 2011). Moreover, according to the biopharmaceutics classification system (BCS) approach, which classifies drug substances into four primary groups (highly soluble/highly permeable, highly permeable/poorly soluble, highly soluble/poorly permeable, and poorly soluble/poorly permeable), the highly permeable/highly soluble drug substance formulated into a rapidly dissolving drug product may need only *in vitro* dissolution studies to establish its BA (Amidon et al., 1995; Dahan et al., 2009). As for the permeability (Pe) test, several methods such as *in situ* rat intestinal perfusion (Kim et al., 2006), the *ex vivo* rat intestinal tissue, the MDCK (Irvine et al., 1999) and Caco-2 (Artursson, 1990) cell monolayers, and the PAMPA (Avdeef, 2005) have been optimized to simulate drugs' absorption across biologic membranes, and it can be applied for permeability determination. These models are mostly suitable for the description of permeability across the GI membrane. Moreover, different cellular and non-cellular models combined with dissolution systems have been developed and adapted in order to evaluate the Pe even of poorly soluble drug entities (Buckley et al., 2012). With the intention to give mechanistic insights or evaluate the effect of different excipients on the performance of formulations, many approaches combining dissolution and Caco-2 permeation testing were suggested (Ginski et al., 1999; Kataoka et al., 2003; Kataoka et al., 2006; Motz et al., 2007). Since the application of the Caco-2 model unfortunately presents many drawbacks, more innovative approaches, employing non-cellular biomimetic barriers, were developed for the same purpose (Fischer et al., 2011b; Fischer et al., 2012; Gantzsche et al., 2014). Other methods affected the development of dialysis-based dissolution/permeation models (Lovering and Black, 1973;

Blanquet et al., 2004). Unfortunately, even these methods are partially flawed, mainly due to the interaction of amphiphilic weak basic and acidic drugs with such biomimetic membranes (Bibi et al., 2016). None of the suggested models specifically concerns the prediction of BE for two oral formulations containing the same API. Since the experimental setup, in this case as well, should predict the *in vivo* behavior of tested formulations, we combined the dissolution test previously described to the PAMPA one to achieve this objective. The PAMPA, using the phospholipid artificial membrane, is considered a suitable model for the detection of passive transport of epithelial cells. Due to its versatility, this method is more suitable for the detection of passive permeability than the Caco-2 model, even for poorly soluble drugs (Buckley et al., 2012). Moreover, it offers several features such as low cost and higher reproducibility that make it certainly more suitable for the high-throughput setup as a first approach than cellular models. The PAMPA model is now widely used for the assessment of passive transport of epithelial cells (Avdeef et al., 2007). Indeed, despite the real-life properties and reliable outcomes provided by cellular models applied to permeability studies (Borchardt et al., 2011), the PAMPA method is to be preferred for the determination of passive permeability, since it overcomes such issues as long cultivation time, high cost, high degree of variability and low capacity in characterizing poorly soluble drugs (Buckley et al., 2012; Berben et al., 2018). Indeed, the PAMPA model is described by Handbook of Bioequivalence Testing as a cost-effective and high-throughput method (Niazi, 2007). Moreover, due to its ability of providing the benefits of a more biologically relevant system, it is considered a very common assay nowadays (Avdeef, 2005).

The combination of the dissolution test and PAMPA method was applied to characterize and compare the BA of LVN released from a generic formulation (formulation A) to that of LVN released from the brand-name tablets (formulation B). This was done because *in vivo* BE failed after performing only a dissolution study. The idea is based on the awareness that the combination of the dissolution test with the PAMPA gives the opportunity to characterize the studied drugs in terms of solubility and absorption and to eventually point out some peculiarities that might influence these parameters in the studied formulations. The application of UV spectroscopy for the determination of LVN released and absorbed during the proposed assays was found to be more predictive of *in vivo* studies, since it guarantees the direct quantification of the real amount of analyte. Indeed, the direct UV analysis turned out to be appropriate for these studies, avoiding further modifications in the sample dissolution that might compromise the results, which may occur by using a reversed-phase HPLC method with the organic modifier.

Hence, starting from the necessity of understanding the different *in vivo* BE profiles shown by the two LVN oral formulations, the developed method was found to be able to provide a new set of information and recommendations useful for

resolving existing or emerging problems in BE studies of new oral formulations, more capable of predicting the *in vivo* behavior.

MATERIALS AND METHODS

Materials

HPLC-grade acetonitrile and ethanol (VWR, Radnor, Pennsylvania, United States) and water obtained from the Milli-RX apparatus (Millipore, Burlington, Massachusetts, United States) were used to prepare solutions and mobile phases. Sodium dodecyl sulfate (SDS) was purchased from Panreac Quimica (Barcelona, Spain). 37% hydrochloric acid (HCl) was obtained from VWR (Radnor, Pennsylvania, United States).

The water solution for dissolution studies was prepared by mixing 0.1% SDS in 0.1N HCl solution. The solutions were filtered through a 0.45 μm membrane filter and degassed before their use in HPLC.

UV Spectrophotometry

The spectrophotometric analyses were performed on a Jasco V-530 double beam spectrophotometer, using a 1 cm quartz cell. Suitable settings were a slide width of 2 nm, scan speed of 400 nm min^{-1} , and UV range of 210–450 nm. A stock solution was prepared by dissolving the appropriate amount of LVN in ethanol in order to obtain 1 mg/ml solution. LVN analytical solutions were obtained by diluting to volume with 0.1% SDS 0.1N HCl solution (0.37–6 $\mu\text{g}/\text{ml}$).

Calibration Graph

The zero-order UV spectra of LVN (0.375–6 $\mu\text{g}/\text{ml}$ in 0.1% SDS 0.1N HCl) were recorded using 0.1% SDS 0.1N HCl solution as the blank; the absorbance values at $\lambda_{\text{max}} = 245 \text{ nm}$ were plotted against the corresponding concentration to obtain the calibration graph.

HPLC Analysis

The HPLC Waters Alliance apparatus comprised a Waters Alliance 2489 UV detector, a Waters Alliance e2695 separation module, and a Waters column heater (Waters, Milford, MA, United States). The chromatographic separations were performed on a 2.5 μm C8 Luna (150 mm \times 4.6 mm i.d.) column (Phenomenex, Torrance, CA, United States) kept at 30°C, using a mobile phase consisting of acetonitrile: water at 60:40 (v/v) at a flow rate of 1.0 ml/min. UV detection at 247 nm was used.

Reference Solution

A 1.5 $\mu\text{g}/\text{ml}$ LVN solution was obtained by transferring about 30 mg of LVN working standard, exactly weighted, in a 200 ml volumetric flask. The powder was dissolved by sonication in 150 ml of ethanol. The solution was cooled down and brought to volume with the same solvent. 2 ml of the obtained solution was diluted to 200 ml with dissolution medium (0.1N HCl containing 0.1% SDS) in order to obtain 1.5 $\mu\text{g}/\text{ml}$ solution.

Calibration Graph

A stock solution of LVN (0.15 mg/ml) was prepared in the mobile phase of acetonitrile:water at 55:45 (v/v). This solution was then used to prepare standard solutions of LVN (0.3–3.0 µg/ml) by diluting to volume with 0.1N hydrochloric acid containing 0.1% sodium dodecyl sulfate. Each standard solution was injected in triplicate into the chromatograph; the peak areas were plotted against the corresponding LVN concentrations to obtain the calibration graph.

Samples Analysis

At least seven injections of the dissolution medium or as many as needed to obtain a good baseline were performed. Then, the standard solution was injected five times. The standard deviation of the areas was verified to be less than 2.0%. Then, the six dissolution samples derived from the dissolution test were analyzed.

Dissolution Test

In order to determine the LVN kinetics of release from formulations A and B in a time-course experiment, a dissolution experiment was carried out following the procedure reported in European Pharmacopoeia 9.0 (2.9.3. Dissolution Test for Solid Dosage Form). Apparatus 2 (paddle) described in European Pharmacopoeia 9.0 and a thermostatic bath regulated at $37 \pm 0.5^\circ\text{C}$ were used. The apparatus consisted of six vessels, each one equipped with a paddle. Three vessels for each tablet type were used. 0.1N hydrochloric acid containing 0.1% sodium dodecyl sulfate was adopted as the dissolution medium. The experiments were carried out under the following conditions: 1,000 ml dissolution medium volume, the rotation speed of the paddle of 75 ± 3 rpm, and the distance of the plate from the bottom of the vessel of 25 ± 2 mm. An equal volume of dissolution medium was poured in each of the six glass vessels. The liquid was kept at $37 \pm 0.5^\circ\text{C}$. Every single tablet obtained by two different manufacturers was transferred in the vessel before starting the test. 3 ml of solution was withdrawn from each vessel from an intermediate zone between the surface of the dissolution medium and the top of the paddle, and not less than 1 cm from the vessel wall. The solutions were then filtered through a 0.45 µm polypropylene (PP) filter and subjected to determination of LVN using the chromatographic conditions described above.

For the spectroscopic determination of LVN released during the dissolution test, the samples obtained as previously described were subjected to centrifugation at 1,500 rpm for 3 min. The collected samples were later analyzed by both RP-HPLC, as described in *HPLC Analysis*, and UV spectrophotometry (*UV Spectrophotometry*) in the wavelength range from 210 to 450 nm.

Dissolution Test in 100 ml Volumetric Flask

Both formulations A and B were left under constant stirring in 0.1N hydrochloric acid (Sigma-Aldrich) containing 0.1% sodium dodecyl sulfate (Sigma-Aldrich) solution at 37°C .

An aliquot of 1 ml of solution was withdrawn at different times from each flask. The UV spectra of the collected samples were

registered after centrifugation at 1,500 rpm for 3 min in the wavelength range from 210 to 450 nm.

PAMPA Test Validation

The quality control compounds atenolol, carbamazepine, coumarin, norfloxacin, and ranitidine hydrochloride (Sigma-Aldrich) of known intestinal permeability were used to validate the analysis set. Stock solutions of the reference drugs were prepared in DMSO (Sigma-Aldrich) at 10 mM and then diluted to reach the concentration of 500 µM in PBS of pH = 7.4, so that the concentration of DMSO does not exceed 5% of the total volume. The acceptor 96-well microplate (MultiScreen®, catalog no. MASSACCEPTOR from Millipore) was filled with 180 µl of pH = 7.4 PBS solution containing 5% of DMSO. The donor 96-well plate (MultiScreen® IP Sterile Plate PVDF membrane, pore size of 0.45 µm, catalog no. MAIPN4510 from Millipore) was coated with 5 µl fresh solution of L-α-phosphatidylcholine from egg yolk (Sigma-Aldrich) in dodecane (20 mg ml⁻¹) and left at 70°C for 5 min.

Then, it was filled with drug solution (180 µl per well). The obtained “sandwich” was left under constant slight shaking (50 rpm) overnight at 30°C .

LVN Stability Test

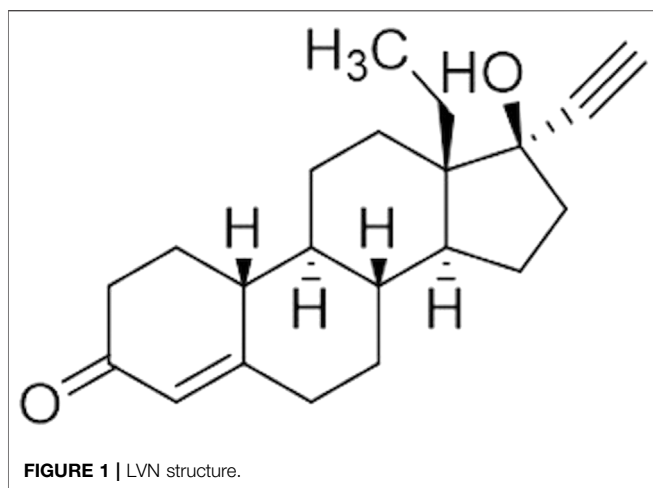
In order to investigate the stability of LVN in PAMPA conditions, the absorbance of the analyte was registered at different concentrations ranging from 6 to 30 µg/ml in 0.1% SDS 0.1N HCl. The parameters were set as reported in *UV Spectrophotometry*. The stability was monitored over 6 days.

PAMPA Test Applied to 1.5 mg LVN Tablets

An exact aliquot of 50 ml of the solutions obtained from 35' and 75' dissolution tests, performed in 100 ml flasks, was transferred to a Falcon tube and centrifuged for 10 min at 1,400 rpm at RT. Then, 10 ml of supernatant for each sample was transferred to a 15 ml Falcon tube and centrifuged under the described conditions. The acceptor 96-well microplate was filled with 180 µl of 0.1% SDS 0.1N HCl solution. The donor 96-well plate was prepared as previously described. Then, the wells were filled with 180 µl of drug solution (at least four wells for each sample). The “sandwich” was left for 1, 1.5, 2, and 4 h at 37°C under continuous slight shaking (50 rpm). After incubation, the solutions in the acceptor plate wells were collected for each sample, and the UV spectra were registered. A Jasco V-630Bio spectrophotometer (Jasco, Tokyo, Japan) was used for the UV measurements.

RESULTS AND DISCUSSION

This work was conceived after the failure of LVN *in vivo* bioequivalence studies, which were planned after only dissolution studies were carried out on the two formulations. In-house HPLC dissolution studies of generic and brand-name formulations did not show any differences in the LVN kinetics and equilibrium parameters. Therefore, the two formulations were considered “similar” and submitted to *in vivo* studies.



However, the application of *in vitro* models for the evaluation of excipient effects on API solubility and permeability is crucial in particular for drugs which exhibit poor aqueous solubility (Ku and Dulin, 2012). Indeed, especially for these kinds of compounds, the demand for fast and economical *in vitro* models able to appraise the effects of new formulations on drugs' BA is urgent. Since even BE may be affected by drug/excipient interactions, providing insights into dissolution and permeability profiles becomes crucial to predict and certify the BE of generic formulations compared to the corresponding brand-name ones. Moreover, the ability of predicting BA and BE profiles of a new drug gives the opportunity to avoid generic formulations which behave differently from the brand-name ones.

Both the definitions of BA and BE imply the use of pharmacokinetic measures to evaluate the rate of the drug released from the medicinal product and the amount of drug absorbed into the systemic circulation (Chen et al., 2001a). Hence, whatever the different approaches adopted in establishing the BE or BA profile of a drug are, the most important goal is to assess the rate and extent of drug absorption (el-Tahtawy et al., 1998; Chen et al., 2001b; Tozer et al., 1996; el-Tahtawy et al., 1994), since the obtained information will make it possible to consider the safety and the effectiveness of the studied drugs. So, the application of *in vitro* methodologies, able to predict the *in vivo* drug release and absorption from the solid oral formulation, has to be considered the key point to predict both the BA and the BE of oral products (Leslie, 1993).

All things considered, in order to offer new insights into a specific case, we developed a new approach whose scope may be extended to every oral formulation. Indeed, the new method was designed to be applied to the early detection of important formulation implications that might affect LVN BE *in vivo*.

In this regard, we focused on the optimization and development of a combined analytical approach for the *in vitro* characterization of dissolution and absorption profiles of LVN released by 1.5 mg generic and brand-name tablets. LVN is one of the most widely used progestogens (Figure 1), and

different dosage forms containing this API are on the market. The formulations we studied are classified as emergency contraceptive pills (ECPs) (Kitanova, 2019). According to the BCS (Amidon et al., 1995), LVN belongs to class I since it is considered a highly soluble [Guidance for industry, 2000; Multisource (generic) pharmaceutical products, 2000; Committee for Medicinal Products for Human Use, 2008] and highly permeable drug (Lindenberg et al., 2004). Indeed, it is characterized by a BA of almost 100%. This parameter is not influenced by a first-pass effect of the liver. LVN is rapidly and completely absorbed after oral administration. Indeed, with a single 1.5 mg tablet, a C_{\max} of 20 ng/ml with a T_{\max} of 1.4 h has been observed (Devoto et al., 2005).

In order to detect the reasons for the failure of the *in vivo* BE studies (data not shown) of these formulations, we combined a dissolution test following the criteria proposed by the European Pharmacopoeia and a PAMPA study to predict permeability. Indeed, once the rate of LVN time-course release by the dissolution test was established by UV spectroscopy, in comparison with the HPLC assay, the kinetics of permeation was measured by the PAMPA test, under optimized conditions, to identify any differences in LVN dissolution and absorption profiles. Indeed, what matters most is that the reliability of all these measurements regarding the release, along with the rate and extent of absorption of an active pharmaceutical ingredient (API), makes them applicable to studies intended to assure comparable therapeutic effects among different formulations.

Dissolution Test

The *in vivo* dissolution process is the first step on which the curative effect of a drug depends. The pharmaceutical products, in solid oral dosage forms, indeed have to undergo dissolution in the GI fluid, before being absorbed and reaching the systematic circulation. The results obtained from the dissolution test, in the field of BE studies, might be influenced by the physicochemical status of drugs and excipients and by the differences in applied manufacturing processes (Paus et al., 2015). In light of this, the dissolution assay can significantly reduce the number of *in vivo* studies, but it is also useful to assess batch-to-batch quality and support batch release, to provide process control and quality assurance and to assess the need for further BE studies. As mentioned before, in the case of such molecules as LVN, endowed with high solubility and absorption rate, the application of the dissolution test can be considered adequate for BA determination.

In the present study, the dissolution test was carried out for both 1.5 mg LVN formulations A and B, following the procedure reported by European Pharmacopoeia 9.0 (2.9.3. Dissolution Test for Solid Dosage Form. Apparatus 2) (Europe, 2016). The used apparatus consisted of six vessels equipped with a paddle which represents the stirring element. An equal number of three vessels were designed for each tablet type. The medium used for the dissolution test was 0.1N hydrochloric acid containing 0.1% sodium dodecyl sulfate (SDS). In order to obtain an LVN

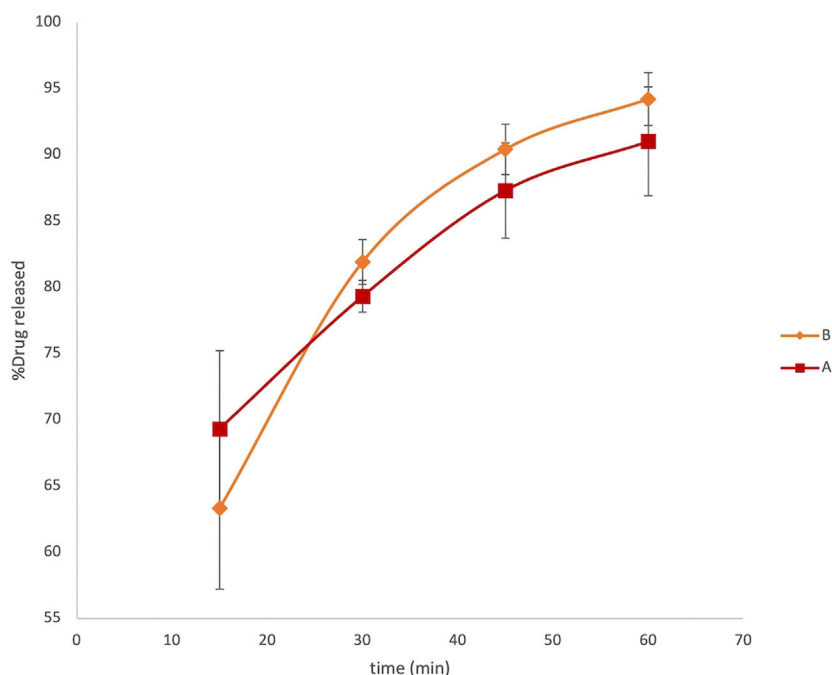


FIGURE 2 | LVN delivery profiles obtained by HPLC analysis. The graph shows the percentage of drug released vs time in minutes. Data are the mean of six replicates. RSD% ranged from 1.2 to 6.1%.

kinetics release plot from the dissolution test, HPLC and UV analyses were carried out.

HPLC Analysis

Different solutions were withdrawn from paddles at 15, 30, 45, and 60 min. The solutions containing LVN released by formulation A and formulation B were then analyzed by HPLC coupled with the UV detector (Görög, 2011). The method was validated by determining linearity, reproducibility, and specificity. Specificity was assessed by analysis under the same chromatographic conditions and the LVN and blank formulations, verifying no interferences eluting at the LVN retention time. The linearity of the method was assessed by a calibration curve obtained using standard solutions of LVN at different concentrations ranging from 0.30 to 3.00 µg/ml. The obtained equation was $y = 74,149.7x + 75.8$ ($R^2 = 1.000$). The samples withdrawn from paddles were replaced with an equal volume of dissolution media and injected in the HPLC system after being filtered. The obtained peak area for each sample was then compared to the standard average area obtained injecting five times a 1.5 µg/ml LVN standard solution (theoretical concentration). The percentage of the active ingredient released was calculated by the following formula:

$$\% = \frac{\text{SAMPLE AREA} \times W_s \times W_u}{\text{STANDARD AVERAGE AREA} \times 20 \times 1.5}$$

where W_s is the weight of the LVN standard, in mg; W_u is the assay percentage of the LVN standard; and 1.5 refers to the theoretical assay result of one tablet.

The graph reported in **Figure 2** describes a release profile very close to both the formulations. The original and generic formulations showed an extremely similar pattern of dissolution, both reaching the maximum released concentration equal to $1.36 \pm 0.05 \mu\text{g ml}^{-1}$ and $1.41 \pm 0.02 \mu\text{g ml}^{-1}$ in 1 h for formulations A and B, respectively. This analysis did not reveal any substantial evidence of different behavior between the generic and brand-name LVN formulations failing to explain the unsuccessful results obtained in *in vivo* BE studies. Moreover, we also calculate the fit factors f_1 (similarity factor) and f_2 (difference factor) applying the following equations:

$$f_1 = \left\{ \left[\sum_{t=1}^n |R_t - T_t| \right] \left[\sum_{t=1}^n R_t \right] \right\} \times 100,$$

$$f_2 = 50 \cdot \log \left\{ \left[1 + \frac{1}{n} \sum_{t=1}^n (R_t - T_t)^2 \right]^{-0.5} \right\} \times 100,$$

where R_t is the percentage of the dissolved product at time point t for the reference formulation (formulation B), T_t is the percentage of the dissolved product for the test batch, and n is the number of time points. The comparison of this value gives the opportunity to easily calculate and compare pairs of dissolution profiles. The values obtained were equal to 0.88 and 85.67 for f_1 and f_2 , respectively, indicating a very similar releasing profile for the two drugs (Anderson et al., 1998).

UV Spectroscopy Analysis

UV spectroscopy was used to detect and quantify LVN release kinetics during the dissolution test as an alternative to HPLC

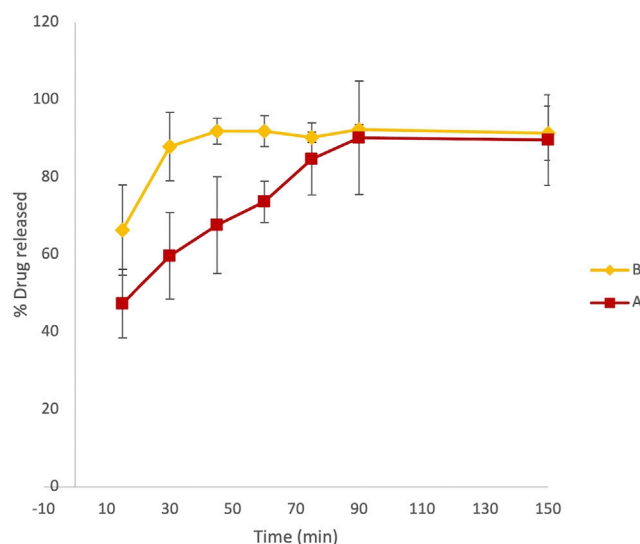


FIGURE 3 | Overlaid kinetic plots showing the percentage of LVN released by formulations A and B in time-course experiments. Data are the mean of six replicates. RSD% ranged from 1 to 15%. The graph clearly shows a difference in the dissolution trend for the two tablets.

analysis. The LVN standard solution UV spectrum, examined between 210 and 350 nm, shows one absorption band with a maximum at 245 nm. Therefore, the linearity of the method was assessed by a calibration curve obtained by using standard solutions of LVN at different concentrations (0.375–6 µg/ml). A linear calibration graph was obtained by plotting A_{245} against the LVN standard corresponding concentrations. The obtained equation was $y = 0.045 \pm 0.004x + 0.009 \pm 0.003$ ($n = 6$; correlation coefficient 0.9952). The LoD and LoQ were found to be 5.6 and 56 ng/ml. The UV method was found to be selective, since the excipients did not interfere at the LVN absorption maximum wavelength. The selectivity was proved by comparing the absorption spectra registered for LVN standard solution, LVN solution obtained after the dissolution test, and the one obtained after the dissolution of tablets without API.

At fixed time intervals, ranging from 15 to 150 min, aliquots of 3 ml samples were withdrawn from paddles and replaced with an equal volume of dissolution media. The absorbance of LVN in different samples was registered at 245 nm. Therefore, the application of the zero-order UV analyses to the LVN analytical solution was performed, which allowed for a selective determination of LVN in the dissolution experiments. The concentration of LVN expressed as µg/ml, for each sample, was calculated interpolating the absorbance values in the calibration curve. The results were then expressed as percentage of the LVN theoretical maximum concentration released from the tablet content, namely, 1.5 µg/ml. The time course of LVN release during the dissolution test, for both formulation A and formulation B, expressed as % of released drugs, is reported in **Figure 3**. Data points are the mean of three independent experiments, each repeated three times. RSD% was in the range from 1 to 15%. Unlike the results obtained by HPLC analysis, the graph reported in **Figure 3** shows that the kinetic profile for the release of LVN from both the tablets is quite

different. Indeed, the fit factors obtained were found to be equal to 16.18 and 63 for f_1 and f_2 , respectively, indicating a different releasing profile for the two drugs.

This difference is already significant in the first 30 min (**Figure 3**). Indeed, the LVN concentration values of 0.89 and 1.32 µg/ml were calculated for formulations A and B, respectively, by applying the equation obtained from the calibration curve and transforming the absorbance values registered for the two spectra of the solutions after 30 min dissolution. After 30 min, the percentage of LVN released by formulations A and B was 60 and 88%, respectively. The maximum amount of levonorgestrel released from formulation B is quickly obtained after 45 min following the results obtained by HPLC analysis (**Figure 2**). In contrast, at this time, the percentage of LVN released by formulation A is still 67%, lower than that detected by HPLC analysis. Afterward, at longer times, there is still a substantial difference between the amount of LVN released from the two tablets: the rate of LVN released from formulation A is 20% lower than the one from formulation B. In fact, for formulation A, the maximum amount of LVN released is stabilized after 90 min, twice as long as formulation B's. This result is in agreement with the high BA characterizing the studied drug and with the reported T_{max} equal to 1.4 h (Devoto et al., 2005). Despite that the equipment used to carry out this assay might present limitations in its ability to replicate the dynamic process of the oral forms in the complex GI luminal environment, the evaluation/prediction of bioequivalence of solid oral preparations can be considered reliable. Moreover, since the active compound studied belongs to class I of the BCS, it is reasonable to consider the obtained results as robust and reliable. Since the two formulations have the same qualitative and quantitative composition, the differences noticed in the release of LVN can be ascribed to the physicochemical difference, such as granulometry superficial areas, in excipient/drug

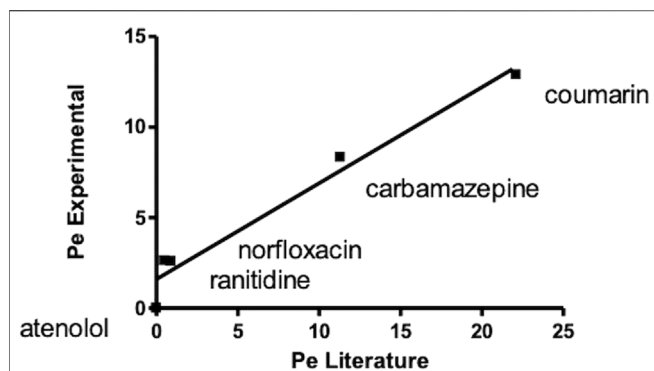


FIGURE 4 | Correlation graph for experimental and theoretical P_e of standard compounds obtained carrying out a PAMPA test for oral absorption assessment.

physicochemical status. LVN from formulation A might establish different stronger non-covalent interactions with excipients, causing a decreased solubility. The application of UV spectroscopy, as the detection method, made it possible to detect and quantify LVN solubility, excluding the possibility of false-positive results. Despite that the dissolution method was the same, analyzing the two LVN different samples by UV spectroscopy, the theoretical maximum drug concentration was not attained until 90 min, demonstrating the formation of insoluble LVN excipient aggregates. Instead, the application of HPLC analysis to the same study did not reveal any kinetics difference in the amount of LVN released by the two pharmaceutical products during the dissolution experiment. In this case, the percentage of LVN released in 60 min for both the formulations resulted to be the same and very close to 100%. This result can be related to the presence of an organic modifier in the mobile phase, which can solubilize drug/excipient aggregates caused by non-covalent interactions with excipients, hypothetically due to different solid-phase states between same excipients (Paus et al., 2015; Zarmpi et al., 2017). Other differences may arise in the morphology of more stable and less soluble LVN crystals used for the two formulations.

PAMPA Test Validation

Five standard compounds of known permeability were used to validate the permeability assay. Atenolol, carbamazepine, coumarin, norfloxacin, and ranitidine hydrochloride are indeed characterized by different oral permeability ranging from low to high values. The concentrations of drug solutions, before incubation, and of those collected from the acceptor wells, after incubation time, were determined by UV measurements in the wavelength range from 210 to 450 nm. The permeability coefficient (P_e) of each drug, in centimeter per second, was then calculated by applying the following formula (Avdeef et al., 2007):

$$P_e = \frac{V_d \cdot V_r}{(V_d + V_r) \cdot S \cdot t} \ln \frac{100 \cdot V_d}{100 \cdot V_d - \%T(V_d + V_r)}$$

$$\%T = \frac{V_r \cdot A_r}{A_{d_0} \cdot V_d} 100,$$

where V_d and V_r are the volume of the donor and the receptor solutions (0.18 cm^3), S is the membrane area (0.266 cm^2), t is the time of incubation expressed in seconds, A_r is the absorbance of the receptor plate after the experiment, and A_{d_0} is the initial absorbance in the donor compartment (Alex, 2012).

A correlation graph for experimental and theoretical P_e obtained for quality control compounds revealed a good correlation between the reported P_e (Zhu et al., 2002) and experimental ones ($R^2 > 0.95$) (Figure 4).

LVN Stability

As reported before (PAMPA Test Validation), the P_e value of substances determined by the PAMPA test is calculated taking into account the absorbance of analyte solutions in the receptor plate, after the experiment, and the initial absorbance of the analyte solutions in the donor compartment. The LVN solutions obtained by performing the dissolution test, as previously described, were not suitable for the PAMPA test since they showed A_{245} values corresponding to too low concentrations ($<1.35 \mu\text{g/ml}$) to get adequate analytical sensitivity. In order to determine the LVN P_e by the PAMPA test, we optimized the concentration for LVN solution suitable for the assay. The tested solution has indeed to be stable and has to ensure the assay sensitivity. Moreover, since the determination of P_e by the PAMPA requires long incubation time, ranging from few hours to more than 12 h, the stability of LVN in assay conditions was investigated. The absorbance of LVN at different concentrations ranging from 6 to $30 \mu\text{g/ml}$ in 0.1% SDS 0.1N HCl was monitored over 6 days. The obtained results showed a substantial decrease in the absorbance value, for the $30 \mu\text{g/ml}$ solution, during the first 24 h. At concentrations equal to 15 and $6 \mu\text{g/ml}$, the absorbance values registered over days did not change, demonstrating LVN stability.

For these results, the PAMPA test was applied to $15 \mu\text{g/ml}$ LVN standard solution since it represents the highest concentration at which LVN solutions are stable.

PAMPA Test Applied to LVN Tablets

Dissolution Assay in 100 ml Volumetric Flasks

Since the maximum concentration of LVN solution obtained by applying the paddle apparatus for the dissolution test was $1.35 \pm 0.18 \mu\text{g/ml}$ and $1.35 \pm 0.03 \mu\text{g/ml}$ for formulations A and B, respectively, we reproduced the dissolution test in a 100 ml flask in order to obtain solutions with concentrations close to $15 \mu\text{g/ml}$. Indeed, one of the most common experimental issues in carrying out a permeability assay is to provide sufficient concentration levels of the drug in order to easily evaluate the permeability value (Lakeram et al., 2008; Buckley et al., 2012). Thanks to the previously shown advantages, the use of UV spectroscopy as the detection method was applied also in this experiment. The kinetic profile obtained for formulations A and B was very similar to that achieved by the dissolution test carried out according to European Pharmacopoeia 9.0, described in paragraph 2.1.2. The results, expressed as percentage of LVN released over time, are quite similar to those obtained by using the dissolution test as reported in Figure 5, showing

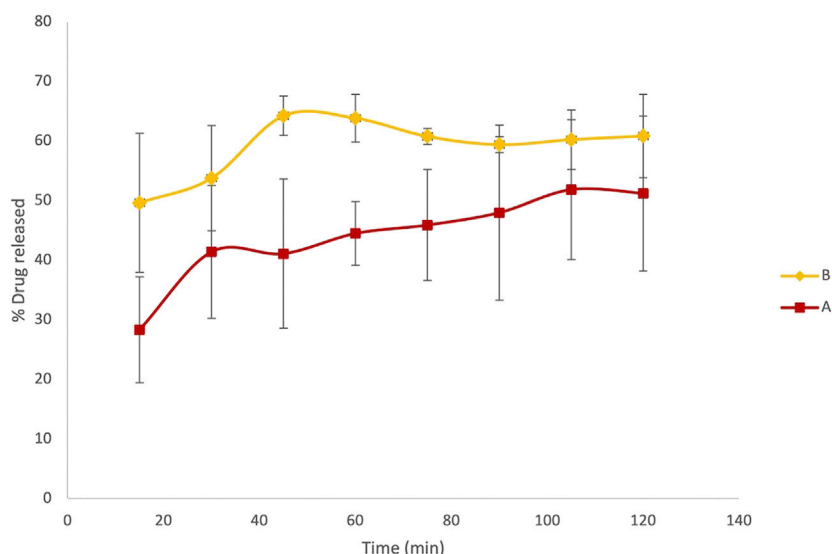


FIGURE 5 | Results referring to the dissolution test adjusted to obtain more concentrated LVN solutions, suitable for the PAMPA test. Overlaid kinetic plots show the percentage of the time-course LVN release from generic (A) and brand-name tablets (B).

T_{\max} at 45' and 105' for formulation B and formulation A, respectively.

PAMPA

We applied this method to understand the differences in BE that emerged in the *in vivo* studies of two LVN oral formulations. Since the aim of this work was to offer a dissolution/permeation model to apply for the BE study, we adopted the LVN solutions obtained from the dissolution test, performed as reported in *Dissolution Assay in 100 ml Volumetric Flasks*, in order to investigate the effect of drug/excipient interactions also on permeability in a time-course experiment. The use of solutions derived from the dissolution test

allowed to keep LVN in the dissolved state, thus avoiding the formation of supramolecular assemblies that could have altered the results by precipitation on the layer of the membranes (Flaten et al., 2008; Fischer et al., 2011a). Moreover, the application of solutions obtained as described in *Dissolution Assay in 100 ml Volumetric Flasks* allowed us to reach an optimal concentration level of the drug in the receiver compartment, overcoming analytical difficulties that may occur since the concentrations obtained may be lower than the limit of detection of the most common method of analysis such as HPLC (Liu et al., 2003). However, the choice and the pH of the medium used to carry out the assay are an essential step. They have to fulfill the criterion of

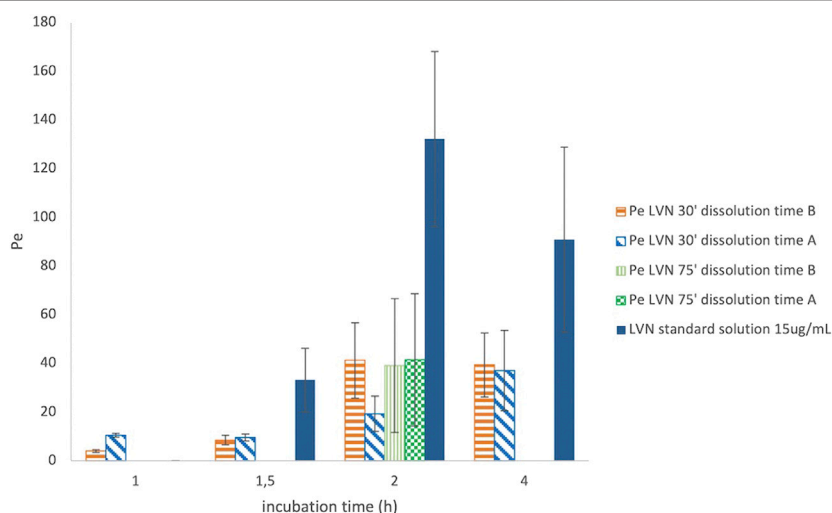


FIGURE 6 | Graph reporting the Pe values for LVN released from both formulations A and B after 30' and 75' dissolution time. The Pe values are plotted against different incubation time in hours. Data are the mean of at least four replicates. RSD% ranged from 7.70 to 70.23%.

TABLE 1 | Mean values and RSD% of the LVN Pe. The results were obtained by applying the equation reported in PAMPA test validation paragraph taking into account the different incubation times. The results refer to both the experiments carried out after 30' and 75' dissolution time. The reported values are the mean of four independent experiments.

Incubation time (h)	Formulation B 30' dissolution time		Formulation A 30' dissolution time		Formulation B 75' dissolution time		Formulation A 75' dissolution time	
	Pe mean value	RSD%	Pe mean value	RSD%	Pe mean value	RSD%	Pe mean value	RSD%
1	4.04	13.78	10.54	7.70				
1.5	8.54	12.89	9.53	15.00				
2	41.26	37.53	19.33	37.72	39.14	70.23	41.49	65.42
4	39.99	33.33	37.06	44.33				

analyte solubility and do not have to alter the test conditions. The membrane integrity indeed has to be preserved.

After PAMPA test validation carried out by using standard compounds of known Pe coefficient, the same system has been adopted for the characterization of LVN permeability released by both the 1.5 mg formulations A and B. Solutions containing LVN released by both the tablets at 30 and 75 min, during the dissolution test, carried out as reported in *Dissolution Assay in 100 ml Volumetric Flasks*, were used in the PAMPA test, in order to highlight the permeability when the extent of LVN released by the tablet is different. As shown before, 30' and 75' represent the times at which the maximum and minimum differences, for the amount of LVN released by formulations A and B, were obtained during the dissolution test. The permeability assay was then carried out at different incubation times, ranging from 30 min to 4 h. In parallel, a 15 µg/ml LVN standard solution was applied to the same procedure. The Pe values obtained for LVN released by both the tablets and LVN 15 µg/ml standard solution, at increasing times, are reported in **Figure 6**. In this graph, the Pe values are plotted against the PAMPA experiments' incubation times. The two formulation solutions, taken at 30 min from the release kinetic experiments, showed the most different Pe values. A Pe value of 19.33×10^{-6} cm/s was obtained for LVN from formulation A, significantly lower than and almost half of the formulation B Pe value of 41.26×10^{-6} cm/s. After 2 h, the results were very similar when the LVN solution was taken from the release at 75 min. The maximum Pe values of 39.14×10^{-6} and 41.49×10^{-6} cm/s are reached for LVN released by formulations B and A, respectively, presumably because at this time the maximum extent of release was reached by both the tablets. For the LVN standard solution, the maximum Pe value (132.14×10^{-6} cm/s) was reached after 2 h incubation time. This result could be ascribed to the absence of excipients that could interfere with the permeation of the drug.

The results are the mean value of four different experiments and are reported in **Table 1**. The RSD% value ranges from 8 to 70%. The results show a significant difference between formulations A and B at 30' dissolution time, 2 h incubation in the PAMPA, in agreement with the dissolution experiment UV data (**Figures 3, 5**). In contrast, the highest RSD% values were found for the experiments carried out on solutions derived from the 75' dissolution test and by applying 2 h incubation time. Despite the high RSD% value, the difference in Pe mean values obtained for LVN derived from both the tablets can be considered

not statistically significant ($p > 0.05$). This variability could be ascribed to the decrease in membrane stability probably due to the higher incubation time.

With that in mind, an incubation time of 2 h was found to be suitable for determining the LVN Pe value. The PAMPA data obtained after 2 h incubation time clearly show that LVN released from formulation B was able to reach the highest Pe value in half an hour. The obtained results underline the substantial difference, already highlighted in the dissolution test, in the amount of LVN released from the two tablets over time (almost half rate for formulation A vs formulation B). Therefore, PAMPA test results gave a clear picture of the absorption profile of LVN released from the two oral formulations and demonstrated that the LVN/excipient insoluble aggregates cannot pass through the GI tract.

CONCLUSION

With the intention of developing a new approach for the characterization of the *in vitro* BA profile of oral formulations, we focused on the case study of LVN. The determination of the dissolution and permeability profiles of two oral formulations, a generic and a brand-name one, was carried out to set up a reliable *in vitro* model to resolve or predict problems in *in vivo* BE studies.

By using a solvent simulating the intestinal fluid, a dissolution test was carried out in order to compare the LVN solubility and kinetics of release from the two oral formulations A and B. Interestingly, the UV spectroscopy direct determination of the LVN solutions obtained from the dissolution test in a time-course experiment was able to show different LVN kinetic releases in the two formulations, with a much slower dissolution profile for the generic formulation. In fact, it was found out that the presence of acetonitrile in the mobile phase of the HPLC system altered LVN solubility, increasing the dissolution of insoluble aggregates. As a consequence, by using the HPLC analysis, statistically equal LVN kinetics of release were determined for the two formulations, predicting a wrong equal behavior in *in vivo* experiments, which conversely failed to demonstrate *in vivo* BE.

Meanwhile, the optimization of the PAMPA for drug tablets allowed us to determine LVN permeability as an indication of passive oral absorption of LVN released by both formulations. This parameter was found to be statistically different for LVN generic and brand-name formulations, obtained after the 30' dissolution test ($p < 0.05$).

Thus, the combination of solubility and PAMPA methods demonstrated to be predictive of *in vivo* BE. Indeed, the capability of the *in vitro* model to predict the unmet BE studies among the two studied oral formulations was demonstrated. The obtained results explained and justified the unsuccessful results of the *in vivo* BE study. The studied case provided important insights into confirming that the new approach combining solubility and permeability studies can be useful in revealing crucial issues in the prediction of *in vivo* BE. Hence, during the formulation process, the two combined approaches can be recommended to analyze the drug performances resulting from dissimilar ingredient/drug interactions in generic formulations.

DATA AVAILABILITY STATEMENT

The raw data supporting the conclusions of this article will be made available by the authors, without undue reservation.

REFERENCES

- Alex, A. (2012). *Absorption and Drug Development: Solubility, Permeability, and Charge State*. 2nd Edition ed. Hoboken, NJ: Wiley.
- Amidon, G. L., Lennernäs, H., Shah, V. P., and Crison, J. R. (1995). A Theoretical Basis for a Biopharmaceutical Drug Classification: The Correlation of *In Vitro* Drug Product Dissolution and *In Vivo* Bioavailability. *Pharm. Res.* 12 (3), 413–420. doi:10.1023/a:1016212804288
- Anand, O., Yu, L. X., Conner, D. P., and Davit, B. M. (2011). Dissolution Testing for Generic Drugs: An FDA Perspective. *AAPS J.* 13 (3), 328–335. doi:10.1208/s12248-011-9272-y
- Anderson, N. H., Bauer, M., Boussac, N., Khan-Malek, R., Munden, P., and Sardaro, M. (1998). An Evaluation of Fit Factors and Dissolution Efficiency for the Comparison of *In Vitro* Dissolution Profiles. *J. Pharm. Biomed. Anal.* 17 (4–5), 811–822. doi:10.1016/s0731-7085(98)00011-9
- Artursson, P. (1990). Epithelial Transport of Drugs in Cell Culture. I: A Model for Studying the Passive Diffusion of Drugs over Intestinal Absorptive (Caco-2) Cells. *J. Pharm. Sci.* 79 (6), 476–482. doi:10.1002/jps.2600790604
- Avdeef, A., Bendels, S., Di, L. I., Faller, B., Kansy, M., Sugano, K., et al. (2007). PAMPA-critical Factors for Better Predictions of Absorption. *J. Pharm. Sci.* 96 (11), 2893–2909. doi:10.1002/jps.21068
- Avdeef, A. (2005). The Rise of PAMPA. *Expert Opin. Drug Metab. Toxicol.* 1 (2), 325–342. doi:10.1517/17425255.1.2.325
- Berben, P., Brouwers, J., and Augustjns, P. (2018). The Artificial Membrane Insert System as Predictive Tool for Formulation Performance Evaluation. *Int. J. Pharm.* 537 (1–2), 22–29. doi:10.1016/j.ijpharm.2017.12.025
- Bibi, H. A., Holm, R., and Bauer-Brandl, A. (2016). Use of Permeapad for Prediction of Buccal Absorption: A Comparison to *In Vitro*, *Ex Vivo* and *In Vivo* Method. *Eur. J. Pharm. Sci.* 93, 399–404. doi:10.1016/j.ejps.2016.08.041
- Blanquet, S., Zejdner, E., Beyssac, E., Meunier, J.-P., Denis, S., Havenaar, R., et al. (2004). A Dynamic Artificial Gastrointestinal System for Studying the Behavior of Orally Administered Drug Dosage Forms under Various Physiological Conditions. *Pharm. Res.* 21 (4), 585–591. doi:10.1023/b:pham.0000022404.70478.4b
- Borchardt, R. T., Hidalgo, I. J., Raub, T. J., and Borchardt, R. T. (2011). Hidalgo, I. J., Raub, T. J., and Borchardt, R. T.: Characterization of the Human Colon Carcinoma Cell Line (Caco-2) as a Model System for Intestinal Epithelial Permeability, Gastroenterology, 96, 736–749, 1989-The Backstory. *AAPS J.* 13 (3), 323–327. doi:10.1208/s12248-011-9283-8
- Buckley, S. T., Fischer, S. M., Fricker, G., and Brandl, M. (2012). *In Vitro* models to Evaluate the Permeability of Poorly Soluble Drug Entities: Challenges and Perspectives. *Eur. J. Pharm. Sci.* 45 (3), 235–250. doi:10.1016/j.ejps.2011.12.007
- Buyukozturk, F., Benneyan, J. C., and Carrier, R. L. (2010). Impact of Emulsion-Based Drug Delivery Systems on Intestinal Permeability and Drug Release Kinetics. *J. Controlled Release* 142 (1), 22–30. doi:10.1016/j.jconrel.2009.10.005
- Chazin, H., Woo, J., Han, J., Grosser, S., and Luan, J. (2020). FDA's Generic Drug Program: Decreasing Time to Approval and Number of Review Cycles. *Ther. Innov. Regul. Sci.* 54 (4), 758–763. Available at: <https://www.fda.gov/drugs/generic-drugs/what-approval-process-generic-drugs> (Accessed February 14, 2021). doi:10.1007/s43441-019-00016-2
- Chen, M.-L., Lesko, L., and Williams, R. L. (2001). Measures of Exposure versus Measures of Rate and Extent of Absorption. *Clin. Pharmacokinet.* 40 (8), 565–572. doi:10.2165/00003088-200140080-00001
- Chen, M. L., Shah, V., Patnaik, R., Adams, W., Hussain, A., Conner, D., et al. (2001). Bioavailability and Bioequivalence: an FDA Regulatory Overview. *Pharm. Res.* 18 (12), 1645–1650. doi:10.1023/a:1013319408893
- Committee for Medicinal Products for Human Use (2008). *Guideline on the Investigation of Bioequivalence (CPMP/EWP/QWP/1401/98 Rev. 1)*. London, UK: European Medicines Agency.
- Dahan, A., Miller, J. M., and Amidon, G. L. (2009). Prediction of Solubility and Permeability Class Membership: Provisional BCS Classification of the World's Top Oral Drugs. *AAPS J.* 11 (4), 740–746. doi:10.1208/s12248-009-9144-x
- Devoto, L., Fuentes, A., Palomino, A., Espinoza, A., Kohen, P., Ranta, S., et al. (2005). Pharmacokinetics and Endometrial Tissue Levels of Levonorgestrel after Administration of a Single 1.5-mg Dose by the Oral and Vaginal Route. *Fertil. Sterility* 84 (1), 46–51. doi:10.1016/j.fertnstert.2005.01.106
- Dressman, J. B., Amidon, G. L., Reppas, C., and Shah, V. P. (1998). Dissolution Testing as a Prognostic Tool for Oral Drug Absorption: Immediate Release Dosage Forms. *Pharm. Res.* 15 (1), 11–22. doi:10.1023/a:1011984216775
- el-Tahtawy, A. A., Jackson, A. J., and Ludden, T. M. (1994). Comparison of Single and Multiple Dose Pharmacokinetics Using Clinical Bioequivalence Data and Monte Carlo Simulations. *Pharm. Res.* 11 (9), 1330–1336. doi:10.1023/a:1018906931100
- el-Tahtawy, A. A., Tozer, T. N., Harrison, F., Lesko, L., and Williams, R. (1998). Evaluation of Bioequivalence of Highly Variable Drugs Using Clinical Trial Simulations. II: Comparison of Single and Multiple-Dose Trials Using AUC and C_{max}. *Pharm. Res.* 15 (1), 98–104. doi:10.1023/a:1011961006297
- Europe, C. O. (2016). *European Pharmacopoeia*. 9th ed. Strasbourg: European Directorate for the Quality of Medicines & HealthCare.
- Fischer, S. M., Buckley, S. T., Kirchmeyer, W., Fricker, G., and Brandl, M. (2012). Application of Simulated Intestinal Fluid on the Phospholipid Vesicle-Based Drug Permeation Assay. *Int. J. Pharm.* 422 (1–2), 52–58. doi:10.1016/j.ijpharm.2011.10.026
- Fischer, S. M., Brandl, M., and Fricker, G. (2011). Effect of the Non-Ionic Surfactant Poloxamer 188 on Passive Permeability of Poorly Soluble Drugs across Caco-2 Cell Monolayers. *Eur. J. Pharmaceutics Biopharmaceutics* 79 (2), 416–422. doi:10.1016/j.ejpb.2011.04.010
- Fischer, S. M., Flaten, G. E., Hagesæther, E., Fricker, G., and Brandl, M. (2011). *In-Vitro* Permeability of Poorly Water Soluble Drugs in the Phospholipid Vesicle-

AUTHOR CONTRIBUTIONS

VA and SA conceived and supervised the work and wrote the manuscript. FT and VT performed HPLC studies. SM, AD, and LD carried out UV spectroscopy and dissolution studies.

ACKNOWLEDGMENTS

The authors are grateful for financial support from UniRimini and the University of Bologna (CIRI-MAM funds), Italy.

SUPPLEMENTARY MATERIAL

The Supplementary Material for this article can be found online at: <https://www.frontiersin.org/articles/10.3389/fchem.2021.741876/full#supplementary-material>

- Based Permeation Assay: The Influence of Nonionic Surfactants. *J. Pharm. Pharmacol.* 63 (8), 1022–1030. doi:10.1111/j.2042-7158.2011.01301.x
- Flaten, G. E., Luthman, K., Vasskog, T., and Brandl, M. (2008). Drug Permeability across a Phospholipid Vesicle-Based Barrier 4. The Effect of Tensides, Co-solvents and pH Changes on Barrier Integrity and on Drug Permeability. *Eur. J. Pharm. Sci.* 34 (2–3), 173–180. doi:10.1016/j.ejps.2008.04.001
- Gantzsch, S. P., Kann, B., Ofer-Glaessgen, M., Loos, P., Berchtold, H., Balbach, S., et al. (2014). Characterization and Evaluation of a Modified PVPa Barrier in Comparison to Caco-2 Cell Monolayers for Combined Dissolution and Permeation Testing. *J. Controlled Release* 175, 79–86. doi:10.1016/j.jconrel.2013.12.009
- Ginski, M. J., Taneja, R., and Polli, J. E. (1999). Prediction of Dissolution-Absorption Relationships from a Continuous dissolution/Caco-2 System. *AAPS PharmSci.* 1 (2), E3. doi:10.1208/ps010203
- Görög, S. (2011). Advances in the Analysis of Steroid Hormone Drugs in Pharmaceuticals and Environmental Samples (2004–2010). *J. Pharm. Biomed. Anal.* 55 (4), 728–743. doi:10.1016/j.jpba.2010.11.011
- Guidance for industry (2000). *Waiver of in Vivo Bioavailability and Bioequivalence for Immediate Release Solid Oral Dosage Forms Based on a Biopharmaceutics Classification System*. Center for Drug Evaluation, USFDA.
- He, X., Sugawara, M., Kobayashi, M., Takekuma, Y., and Miyazaki, K. (2003). An *In Vitro* System for Prediction of Oral Absorption of Relatively Water-Soluble Drugs and Ester Prodrugs. *Int. J. Pharm.* 263 (1–2), 35–44. doi:10.1016/s0378-5173(03)00343-0
- Irvine, J. D., Takahashi, L., Lockhart, K., Cheong, J., Tolan, J. W., Selick, H. E., et al. (1999). MDCK (Madin-Darby Canine Kidney) Cells: A Tool for Membrane Permeability Screening. *J. Pharm. Sci.* 88 (1), 28–33. doi:10.1021/js9803205
- Kanzer, J., Tho, L., Flaten, G. E., Mägerlein, M., Hölig, P., Fricker, G., et al. (2010). *In-vitro* Permeability Screening of Melt Extrudate Formulations Containing Poorly Water-Soluble Drug Compounds Using the Phospholipid Vesicle-Based Barrier. *J. Pharm. Pharmacol.* 62 (11), 1591–1598. doi:10.1111/j.2042-7158.2010.01172.x
- Kataoka, M., Itsubata, S., Masaoka, Y., Sakuma, S., and Yamashita, S. (2011). *In Vitro* dissolution/permeation System to Predict the Oral Absorption of Poorly Water-Soluble Drugs: Effect of Food and Dose Strength on it. *Biol. Pharm. Bull.* 34 (3), 401–407. doi:10.1248/bpb.34.401
- Kataoka, M., Masaoka, Y., Sakuma, S., and Yamashita, S. (2006). Effect of Food Intake on the Oral Absorption of Poorly Water-Soluble Drugs: *In Vitro* Assessment of Drug Dissolution and Permeation Assay System. *J. Pharm. Sci.* 95 (9), 2051–2061. doi:10.1002/jps.20691
- Kataoka, M., Masaoka, Y., Yamazaki, Y., Sakane, T., Sezaki, H., and Yamashita, S. (2003). *In Vitro* system to Evaluate Oral Absorption of Poorly Water-Soluble Drugs: Simultaneous Analysis on Dissolution and Permeation of Drugs. *Pharm. Res.* 20 (10), 1674–1680. doi:10.1023/a:1026107906191
- Kataoka, M., Tsuneishi, S., Maeda, Y., Masaoka, Y., Sakuma, S., and Yamashita, S. (2014). A New *In Vitro* System for Evaluation of Passive Intestinal Drug Absorption: Establishment of a Double Artificial Membrane Permeation Assay. *Eur. J. Pharmaceutics Biopharmaceutics* 88 (3), 840–846. doi:10.1016/j.ejpb.2014.09.009
- Kim, J.-S., Mitchell, S., Kijek, P., Tsume, Y., Hilfinger, J., and Amidon, G. L. (2006). The Suitability of an *In Situ* Perfusion Model for Permeability Determinations: Utility for BCS Class I Biowaiver Requests. *Mol. Pharmaceutics* 3 (6), 686–694. doi:10.1021/mp060042f
- Kim, T. H., Shin, S., and Shin, B. S. (2018). Model-Based Drug Development: Application of Modeling and Simulation in Drug Development. *J. Pharm. Invest.* 48, 431–441. doi:10.1007/s40005-017-0371-3
- Kitanova, M. (2019). “Axiological Aspects of Some Models of Euphemisation in Bulgarian Language and Traditional Bulgarian Culture,” in *A View on Slavic Axiology*, 159–168. Available at: https://extranet.who.int/prequal/sites/default/files/documents/31%20BE_guidance_RH_medicines_March2019.pdf. doi:10.31168/0428-2.9
- Kobayashi, M., Sada, N., Sugawara, M., Iseki, K., and Miyazaki, K. (2001). Development of a New System for Prediction of Drug Absorption that Takes into Account Drug Dissolution and pH Change in the Gastro-Intestinal Tract. *Int. J. Pharm.* 221 (1–2), 87–94. doi:10.1016/s0378-5173(01)00663-9
- Ku, M. S., and Dulin, W. (2012). A Biopharmaceutical Classification-Based Right-First-Time Formulation Approach to Reduce Human Pharmacokinetic Variability and Project Cycle Time from First-In-Human to Clinical Proof-Of-Concept. *Pharm. Develop. Technol.* 17 (3), 285–302. doi:10.3109/10837450.2010.535826
- Lakeram, M., Lockley, D. J., Pendlington, R., and Forbes, B. (2008). Optimisation of the Caco-2 Permeability Assay Using Experimental Design Methodology. *Pharm. Res.* 25 (7), 1544–1551. doi:10.1007/s11095-008-9556-9
- Lalonde, R. L., Kowalski, K. G., Hutmacher, M. M., Ewy, W., Nichols, D. J., Milligan, P. A., et al. (2007). Model-based Drug Development. *Clin. Pharmacol. Ther.* 82 (1), 21–32. doi:10.1038/sj.cpt.6100235
- Leslie, Z. B. (1993). “The Role of Pharmacokinetics in the Drug Development Process,” in *Integration of Pharmacokinetics, Pharmacodynamics, and Toxicokinetics in Rational Drug Development*. (MA: Springer B), 115–123.
- Lindenberg, M., Kopp, S., and Dressman, J. B. (2004). Classification of Orally Administered Drugs on the World Health Organization Model List of Essential Medicines According to the Biopharmaceutics Classification System. *Eur. J. Pharmaceutics Biopharmaceutics* 58 (2), 265–278. doi:10.1016/j.ejpb.2004.03.001
- Liu, H., Sabus, C., Carter, G. T., Du, C., Avdeef, A., and Tischler, M. (2003). *In Vitro* Permeability of Poorly Aqueous Soluble Compounds Using Different Solubilizers in the PAMPA Assay with Liquid Chromatography/Mass Spectrometry Detection. *Pharm. Res.* 20 (11), 1820–1826. doi:10.1023/b:pham.0000003380.44755.5a
- Lovering, E. G., and Black, D. B. (1973). Drug Permeation through Membranes I: Effect of Various Substances on Amobarbital Permeation through Polydimethylsiloxane. *J. Pharm. Sci.* 62 (4), 602–606. doi:10.1002/jps.2600620412
- Martinez, M. N., and Zhao, X. (2018). A Simple Approach for Comparing the *In Vitro* Dissolution Profiles of Highly Variable Drug Products: A Proposal. *AAPS J.* 20 (4), 78. doi:10.1208/s12248-018-0238-1
- Mathias, N. R., and Crison, J. (2012). The Use of Modeling Tools to Drive Efficient Oral Product Design. *AAPS J.* 14 (3), 591–600. doi:10.1208/s12248-012-9372-3
- Motz, S. A., Schaefer, U. F., Balbach, S., Eichinger, T., and Lehr, C.-M. (2007). Permeability Assessment for Solid Oral Drug Formulations Based on Caco-2 Monolayer in Combination with a Flow through Dissolution Cell. *Eur. J. Pharmaceutics Biopharmaceutics* 66 (2), 286–295. doi:10.1016/j.ejpb.2006.10.015
- Multisource (generic) pharmaceutical products (2000). “Guidelines on Registration Requirements to Establish Interchangeability,” in *WHO Expert Committee on Specifications for Pharmaceutical Preparations, Fortieth Report* (Geneva: World Health Organization), 347–390.
- Niazi, S. K. (2007). *Handbook of Bioequivalence Testing*. CRC Press.
- Noureddine, N., Zerrouk, N., Nicolis, I., Allain, P., Sfar, S., and Chaumeil, J. C. (2005). Characterization of the Absorption of Theophylline from Immediate- and Controlled-Release Dosage Forms with a Numerical Approach Using the *In Vitro* Dissolution-Permeation Process Using Caco-2 Cells. *Drug Dev. Ind. Pharm.* 31 (4–5), 397–404. doi:10.1080/03639040500214589
- Paus, R., Prudic, A., and Ji, Y. (2015). Influence of Excipients on Solubility and Dissolution of Pharmaceuticals. *Int. J. Pharm.* 485 (1–2), 277–287. doi:10.1016/j.ijpharm.2015.03.004
- Sironi, D., Rosenberg, J., Bauer-Brandl, A., and Brandl, M. (2017). Dynamic Dissolution-/Permeation-Testing of Nano- and Microparticle Formulations of Fenofibrate. *Eur. J. Pharm. Sci.* 96, 20–27. doi:10.1016/j.ejps.2016.09.001
- Sugawara, M., Kadomura, S., He, X., Takekuma, Y., Kohri, N., and Miyazaki, K. (2005). The Use of an *In Vitro* Dissolution and Absorption System to Evaluate Oral Absorption of Two Weak Bases in pH-Independent Controlled-Release Formulations. *Eur. J. Pharm. Sci.* 26 (1), 1–8. doi:10.1016/j.ejps.2005.02.017
- Tozer, T. N., Bois, F. Y., Hauck, W. W., Chen, M. L., and Williams, R. L. (1996). Absorption Rate vs. Exposure: Which Is More Useful for Bioequivalence Testing. *Pharm. Res.* 13 (3), 453–456. doi:10.1023/a:1016061013606
- Zarmpi, P., Flanagan, T., Meehan, E., Mann, J., and Fotaki, N. (2017). Biopharmaceutical Aspects and Implications of Excipient Variability in Drug Product Performance. *Eur. J. Pharmaceutics Biopharmaceutics* 111, 1–15. doi:10.1016/j.ejpb.2016.11.004
- Zhao, L., Kim, M. J., Zhang, L., and Lionberger, R. (2019). Generating Model Integrated Evidence for Generic Drug Development and Assessment. *Clin. Pharmacol. Ther.* 105 (2), 338–349. doi:10.1002/cpt.1282
- Zhu, C., Jiang, L., Chen, T.-M., and Hwang, K.-K. (2002). A Comparative Study of Artificial Membrane Permeability Assay for High Throughput Profiling of Drug

Absorption Potential. *Eur. J. Med. Chem.* 37 (5), 399–407. doi:10.1016/s0223-5234(02)01360-0

Conflict of Interest: The authors SA and FT were employed by the company Valpharma International S.p.A.

The remaining authors declare that the research was conducted in the absence of any commercial or financial relationships that could be construed as a potential conflict of interest.

Publisher's Note: All claims expressed in this article are solely those of the authors and do not necessarily represent those of their affiliated organizations, or those of

the publisher, the editors, and the reviewers. Any product that may be evaluated in this article, or claim that may be made by its manufacturer, is not guaranteed or endorsed by the publisher.

Copyright © 2021 De Simone, Davani, Montanari, Tumiatti, Avanesian, Testi and Andrisano. This is an open-access article distributed under the terms of the Creative Commons Attribution License (CC BY). The use, distribution or reproduction in other forums is permitted, provided the original author(s) and the copyright owner(s) are credited and that the original publication in this journal is cited, in accordance with accepted academic practice. No use, distribution or reproduction is permitted which does not comply with these terms.



Exploring the Thickness-Dependence of the Properties of Layered Gallium Sulfide

Yael Gutiérrez, Maria M. Giangregorio, Stefano Dicorato, Fabio Palumbo and Maria Losurdo *

Institute of Nanotechnology, CNR-NANOTEC, c/o Dipartimento di Chimica, Università di Bari, Bari, Italy

Group III layered monochalcogenide gallium sulfide, GaS, is one of the latest additions to the two-dimensional (2D) materials family, and of particular interest for visible-UV optoelectronic applications due to its wide bandgap energy in the range 2.35–3.05 eV going from bulk to monolayer. Interestingly, when going to the few-layer regime, changes in the electronic structure occur, resulting in a change in the properties of the material. Therefore, a systematic study on the thickness dependence of the different properties of GaS is needed. Here, we analyze mechanically exfoliated GaS layers transferred to glass substrates. Specifically, we report the dependence of the Raman spectra, photoluminescence, optical transmittance, resistivity, and work function on the thickness of GaS. Those findings can be used as guidance in designing devices based on GaS.

Keywords: layered GaS, chalcogenides, work function, optical properties, photoresistivity

OPEN ACCESS

Edited by:

Ottavia Giuffrè,
University of Messina, Italy

Reviewed by:

Graziella Malandrino,
University of Catania, Italy
Manish Niranjana,
Indian Institute of Technology
Hyderabad, India

*Correspondence:

Maria Losurdo
maria.losurdo@cnr.it

Specialty section:

This article was submitted to
Analytical Chemistry,
a section of the journal
Frontiers in Chemistry

Received: 22 September 2021

Accepted: 15 October 2021

Published: 19 November 2021

Citation:

Gutiérrez Y, Giangregorio MM,
Dicorato S, Palumbo F and Losurdo M
(2021) Exploring the Thickness-
Dependence of the Properties of
Layered Gallium Sulfide.
Front. Chem. 9:781467.
doi: 10.3389/fchem.2021.781467

INTRODUCTION

Low-dimensional layered semiconductors are receiving increasing interest due to the possibility to tailor their light-matter interaction by varying their properties with the number of layers, especially in the few-layer regime. In this context, semiconducting gallium monochalcogenides such as gallium sulfide, selenide, telluride, GaX (X = S, Se, Te) are one of the latest additions to the two-dimensional (2D) materials family, and of particular interest for visible-UV optoelectronic applications due to their wide energy bandgap (Lu et al., 2020). Specifically, gallium monosulfide, GaS, in the bulk form, has an indirect bandgap of 2.35 eV corresponding to the electronic transition from $\Gamma \rightarrow M$ points in the band structure (Chen et al., 2015), whereas the bandgap of GaS monolayer has been calculated to be above 3 eV, with different values reported in the range 3.1–3.3 eV (Zhuang and Hennig, 2013; Jung et al., 2015). A direct bandgap ($\Gamma \rightarrow \Gamma$ transition) in the range 2.8–3.0 eV has also been reported for bulk GaS (Kepinska et al., 2001; Ho and Lin, 2006) and at 3.88 eV for the monolayer (Jung et al., 2015). Because of those bandgap values, GaS has potential to exhibit photoluminescence (PL) in the green-blue spectral region and to be exploited as a UV photodetector (Chen et al., 2019; Lu et al., 2020).

GaS crystallizes in a highly anisotropic layered structure of increasing interest due to its non-toxicity, high chemical and thermal stability, and resistance to oxidation. Specifically, the basal surface of the layered structure, shown in **Figure 1**, is extremely inert to chemisorption of contaminants as the sticking coefficient for contaminants on GaS has been reported to be undetectably small (Williams and McEvoy, 1972); consequently, contaminants are only loosely bound on GaS basal surface, and, hence, can easily be removed by heating in vacuum or exposure to an electron beam (Williams et al., 1972).

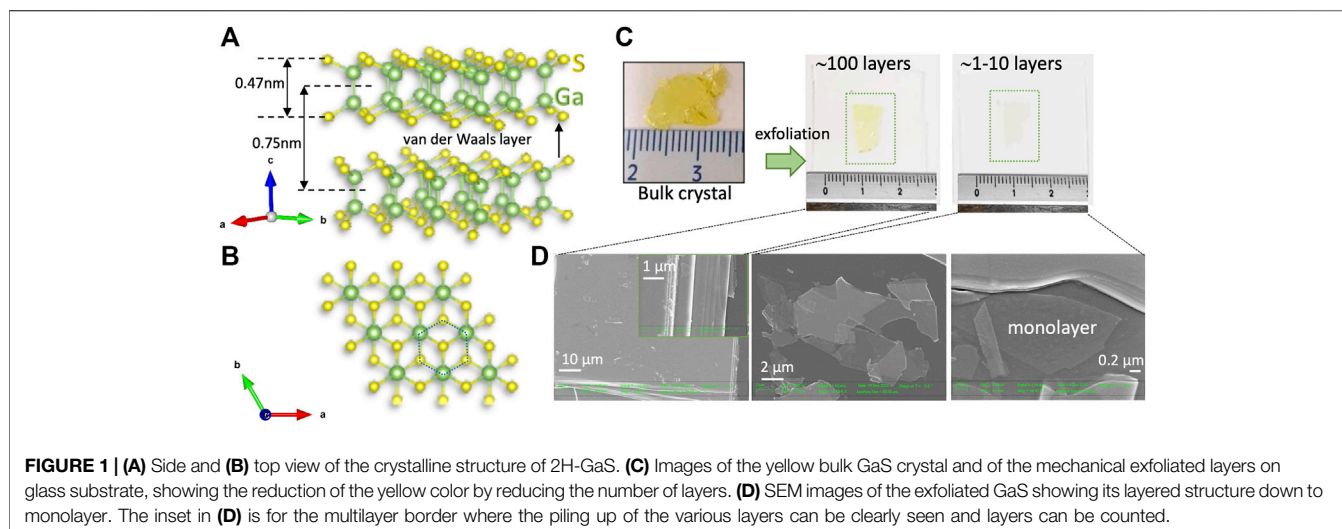


FIGURE 1 | (A) Side and (B) top view of the crystalline structure of 2H-GaS. (C) Images of the yellow bulk GaS crystal and of the mechanical exfoliated layers on glass substrate, showing the reduction of the yellow color by reducing the number of layers. (D) SEM images of the exfoliated GaS showing its layered structure down to monolayer. The inset in (D) is for the multilayer border where the piling up of the various layers can be clearly seen and layers can be counted.

Within the GaS layer, there is strong covalent binding, with two covalently bonded gallium, Ga, atoms between two layers of sulfur, S, atoms (see **Figure 1A**). Conversely, the inter-layers binding is of the Van der Waals type, classifying GaS as a 2D Van der Waals semiconductor. The unit cell of GaS is hexagonal, with the 2H-phase, β -GaS, crystal structure being the most energetically favorable polytype with lattice constants $a = b = 3.587 \text{ \AA}$, $c = 15.492 \text{ \AA}$. The interlayer separation of $\sim 0.75 \text{ nm}$ is shown in **Figure 1**. Interestingly, the formation energy of a monolayer of GaS has been calculated to be 0.06 eV/atom , which is even lower than that of MoS_2 (0.08 eV/atom) (Zhuang and Hennig, 2013), indicating that monolayer GaS can be obtained by mechanical exfoliation, as shown in **Figures 1C,D**.

In this work, we report a survey on the dependence of the main structural, optical, and electrical properties of mechanically exfoliated GaS on thickness, from bulk down to monolayer. This knowledge is relevant for designing devices and applications exploiting different thicknesses of GaS.

As Raman spectroscopy is the prime non-destructive characterization technique for layered materials, we report the Raman and PL data acquired at the same spot as a function of thickness from bulk GaS to monolayer. Furthermore, one of the most critical parameters in the design of novel electronic devices based on semiconducting layered materials is the work function (WF). This parameter is relevant for designing and understanding the band alignment at metal-semiconductor interfaces and in semiconducting heterostructures for photodetectors or phototransistors (Liu et al., 2021). For layered materials at the ultrathin regime, the WF is expected to critically depend on the number of layers of the material. For instance, it has been demonstrated that, for the prototypical transition metal dichalcogenide MoS_2 , the WF increases monotonically with the increase in the number of layers (Li et al., 2013; Choi et al., 2014). To the best of our knowledge, such study has not yet been performed on GaS; hence, we report the dependence of the GaS WF as a function of the GaS thickness as obtained by Kelvin probe force microscopy (KPFM). Moreover,

x-ray photoelectron spectroscopy analysis of the valence band (VB) has been used to analyze the position of the valence band maximum (VBM) with respect to the Fermi level (E_F) and corroborate the KPFM data for profiling bands as a function of thickness. To further guide the design of optoelectronic devices, we provide values of the resistivity and transmittance of GaS as a function of thickness in dark and under visible and UV illumination.

MATERIALS AND METHODS

Sample Fabrication

Few-layer GaS samples were obtained by mechanical exfoliation from commercially available bulk crystals purchased from 2D Semiconductors and HQ Graphene and transferred to glass and (285 nm) SiO_2/Si substrate by the thermal tape method. Several exfoliations were executed in order to obtain samples of decreasing thickness as inferred by the disappearing of the yellow color characteristics of GaS bulk crystal, as shown in **Figure 1**. Glass substrates were cleaned by diluted $\text{H}_2\text{O}:\text{H}_2\text{O}_2$ for 1 h at room temperature, followed by a water rinse to obtain an -OH terminated surface to improve adhesion with GaS.

Number of Layers and Thickness by Scanning Electron Microscopy

Scanning electron microscopy (SEM) was carried out for the morphological characterization of the samples with a Zeiss Supra 40 FEG SEM equipped with a Gemini field emission gun. Analyses were carried out at an extraction voltage of 3 kV and a 30- μm aperture.

Structure and Photoluminescence by Raman Spectroscopy

Raman spectroscopy (LabRam Horiba) was performed using a $\times 100$ microscope objective ($\text{NA} = 0.9$) and exciting wavelengths

of 633 and 473 nm. For the Raman measurements, performed with an excitation wavelength of 633 nm, the exfoliated flakes were deposited on glass substrates to avoid misinterpreting and overlapping of one of the GaS Raman modes with that at 303 cm^{-1} of conventionally used SiO_2/Si substrates. The 473-nm laser was used to excite the GaS above the bandgap and also acquire PL spectra.

Work Function and Morphology by Kelvin Probe and Atomic Force Microscopy

The WF of GaS flakes with different thicknesses was measured by Kelvin probe electrical force microscopy (KPFM) using the Autoprobe CP (Thermomicroscope) through the measurement of the local variation of the surface potential (SP). The sample topography and SP were recorded in a single-pass mode using gold-coated Si tips (their frequency is $\sim 80\text{ Hz}$) in non-contact mode. The oscillating potential, V_{ac} , applied to the tip is 5 V at a frequency ω of 13 kHz. The samples were electrically connected to the ground of the microscope (the sample stage).

For the Kelvin probe force microscopy experiments, the flakes were deposited on a reference Au/Si substrate, as the WF of gold at 4.75 eV (as measured by us on the same equipment and corroborated by x-ray photoelectron spectroscopy measurements) was used as reference. All measurements were collected in air at room temperature.

Valence Band Analysis by X-Ray Photoelectron Spectroscopy

For profiling the bands' energy levels, we determined the position of the VBM with respect to the Fermi level by x-ray photoelectron spectroscopy (XPS) using a Scanning XPS Microprobe (PHI 5000 Versa Probe II, Physical Electronics) equipped with a monochromatic Al $K\alpha$ x-ray source (1,486.6 eV), with a spot size of $200\text{ }\mu\text{m}$. Survey (0–1,200 eV) and high-resolution spectra (C 1s, O 1s, S2p, S2s, Ga2p3, Ga3d, and valence band region) were recorded in FAT mode at a pass energy of 117.40 and 29.35 eV, respectively. Spectra were acquired at a take-off angle of 45° with respect to the sample surface. Surface charging was compensated using a dual beam charge neutralization system, and the hydrocarbon component of C1s spectrum was used as internal standard for charging correction, and it was fixed at 285 eV.

Electrical Resistivity and Optical Transmittance Measurements

Electrical current–voltage, I – V , measurements were performed by the Keithley617 Programmable Electrometer. The voltage source has been used in conjunction with the electrometer section, to apply to the samples voltages from -2 to $+2\text{ V}$, where GaS has ohmic behavior. Contacts were made using silver. Current was measured in the dark whereas photoresponse was investigated in the visible range under a $100\text{ mW}\cdot\text{cm}^{-2}$ AM1.5 spectrum lamp and in the UV range using a 405-nm laser of 250 mW cm^{-2} as source.

UV–Vis transmittance spectra were measured on the same glass samples with a Perkin Elmer Lambda 900 spectrometer.

RESULTS

Colorimetry for Thickness Determination

Although mechanical exfoliation has become a widely used technique to achieve 2D layers, one of its main drawbacks is the difficulty in obtaining large area samples with homogeneous number of layers (as it can also be inferred by **Figure 1D**), and it generally results in randomly distributed flakes of different thickness. Consequently, there is a need for non-destructive, reliable, effective, and fast methods for inferring thickness. Interestingly, because of the contrast in the optical properties between GaS flake and its substrate, a full gamut of colors allows one to identify the thickness of mechanically exfoliated GaS transferred onto substrates, as shown in **Figure 2**. Optical microscopy methods relying on colorimetry can provide an effective solution to this problem. By calculating the reflectance of a system consisting of a GaS layer of variable thickness on an infinite substrate using a Fresnel laws-based model, and then its conversion to color coordinates using color matching functions, it is possible to predict the apparent color of a GaS flake of a specific thickness on a given substrate. Following this procedure, we have developed a methodology (Gutiérrez et al., 2021) and a code (Gutiérrez, 2021) that generates color rulers for the quick assessment of the thickness of GaS flakes on various substrates. As an example, **Figure 2** shows the color evolution of GaS as a function of thickness on glass and on $285\text{-nm SiO}_2/\text{Si}$ substrates as seen under an optical microscope when running a Raman measurement. By comparing the color of the flakes appearing under the microscope of the Raman system with those color rulers, it is possible to infer the thickness of the GaS flakes.

Raman and Photoluminescence Spectra

Figure 3 shows the thickness dependence of the Raman spectra of few-layer GaS samples. The Raman spectrum of bulk β -GaS (space group $P6_3/mmc$ and point group D_{6h}^4), as well as of thick layers, is characterized by six modes at 22.8 cm^{-1} (E_{2g}^2), 74.7 cm^{-1} (E_{1g}^1), 189 cm^{-1} (A_{1g}^1), 291.8 cm^{-1} (E_{1g}^2), 295.8 cm^{-1} (E_{2g}^1), and 360.9 cm^{-1} (A_{1g}^2). The most intense and investigated peaks are the A_{1g}^1 , A_{1g}^2 , and E_{2g}^1 (the latter often including the contribution of the nearby E_{1g}^2), whose vibrational modes are sketched in **Figure 3A**. Conversely, GaS monolayer (space group $P-6m2$ and point group D_{3h}^1) shows the E_{1g}^2 barely distinguishable as shown in **Figure 3B**. For a more accurate analysis, line-shape analysis for each Raman mode was performed by using one Lorentzian component. Central Raman shifts (ω) and the full width at half maximum FWHM (Γ) for each of the spectra recorded are shown in **Table 1**. No significant variation in the peaks position can be observed for all modes; similarly, the FWHM variation from thick layers to monolayer is within 1 cm^{-1} . This negligible dependence of Raman modes on thickness is mainly due to weak inter-layer interactions, and it is consistent with a previous work where it is reported a red-shift

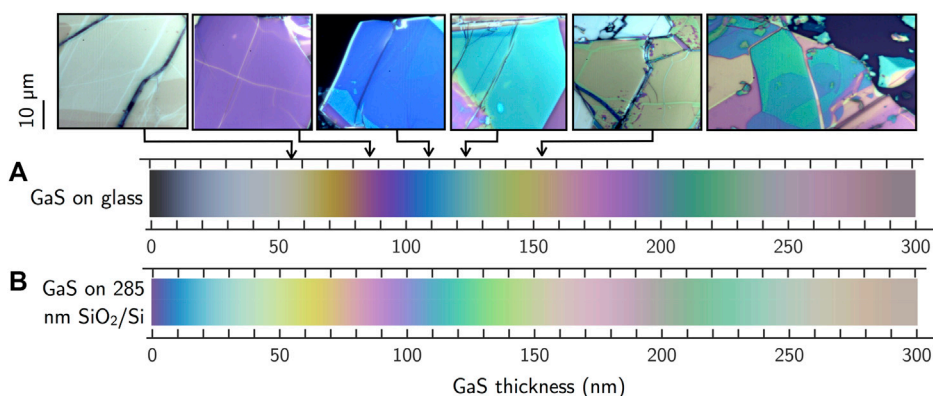


FIGURE 2 | Color evolution of GaS flakes as a function of their thickness on (A) glass and on (B) 285-nm SiO₂/Si substrates as determined according to the free-available code developed (Gutiérrez, 2021). The last image on the right is an example of an optical micrograph of a non-homogeneous exfoliated flake, with the different colors corresponding to different number of layers.

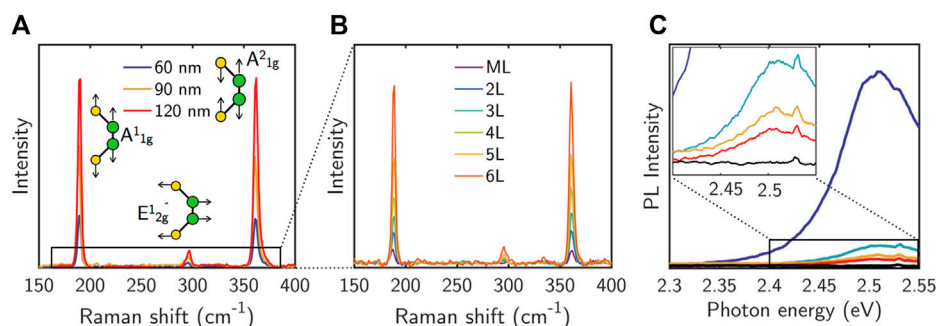


FIGURE 3 | Typical Raman spectra of (A) thick GaS and (B) few-layer GaS ranging from the monolayer (ML) to six layers transferred onto glass substrates (acquired using a 633-nm laser source). (C) PL spectra of same samples with different thickness acquired irradiating the sample with a 473-nm laser. The blue intense spectrum is for a >300-nm-thick sample; the black line is for the 1–6 L samples. Intermediate states are for layers with a thickness of ≈ 300 nm.

TABLE 1 | Raman shifts (ω) and FWHM (Γ) for the three modes A_{1g}^1 , E_{2g}^1 , and A_{1g}^2 measured for GaS layers with thickness ranging from monolayer to 120 nm. The 633-nm laser excitation was used.

	A_{1g}^1		E_{2g}^1		A_{1g}^2	
	Γ (cm ⁻¹)	ω (cm ⁻¹)	Γ (cm ⁻¹)	ω (cm ⁻¹)	Γ (cm ⁻¹)	ω (cm ⁻¹)
ML	3.4 ± 0.8	187.4 ± 0.8	—	—	3.1 ± 0.8	361.6 ± 0.8
2L	4.0 ± 0.5	188.4 ± 0.5	5.1 ± 0.8	296.5 ± 0.8	3.5 ± 0.5	361.5 ± 0.5
3L	3.2 ± 0.5	188.5 ± 0.5	4.6 ± 0.8	295.9 ± 0.8	4.2 ± 0.5	361.6 ± 0.5
4L	3.5 ± 0.5	188.4 ± 0.5	3.8 ± 0.5	296.1 ± 0.5	4.1 ± 0.5	361.4 ± 0.5
5L	2.7 ± 0.5	188.6 ± 0.5	3.9 ± 0.5	295.9 ± 0.5	3.7 ± 0.5	361.3 ± 0.5
6L	2.8 ± 0.5	188.6 ± 0.5	4.1 ± 0.5	295.3 ± 0.5	3.9 ± 0.5	361.1 ± 0.5
60 nm	2.9 ± 0.5	188.6 ± 0.5	3.6 ± 0.5	295.1 ± 0.5	4.1 ± 0.5	360.6 ± 0.5
90 nm	2.8 ± 0.5	188.8 ± 0.5	4.6 ± 0.5	295.1 ± 0.5	4.0 ± 0.5	361.3 ± 0.5
120 nm	2.8 ± 0.5	188.7 ± 0.5	4.4 ± 0.5	295.4 ± 0.5	4.0 ± 0.5	360.9 ± 0.5

in the A_{1g}^1 mode of only 1.4 cm⁻¹ when going from the monolayer (187.6 ± 0.3 cm⁻¹) to a 38-nm-thick layer (189.0 ± 0.1 cm⁻¹), whereas a constant position within the uncertainty was reported for A_{1g}^2 (Alencar et al., 2020). Similarly, the broadening of all Raman modes is within 1 cm⁻¹ going from monolayer to bulk. It is worth mentioning that for high-crystalline quality GaS, the 1:1

ratio between A_{1g}^1 and A_{1g}^2 is preserved in the range of thickness from bulk to monolayer, indicating that the stacking order of the layers is preserved during exfoliation.

Literature has given little attention to the PL of GaS. **Figure 3C** shows the PL spectra for samples of different thickness using a continuous-wave excitation from a 473-nm laser source.

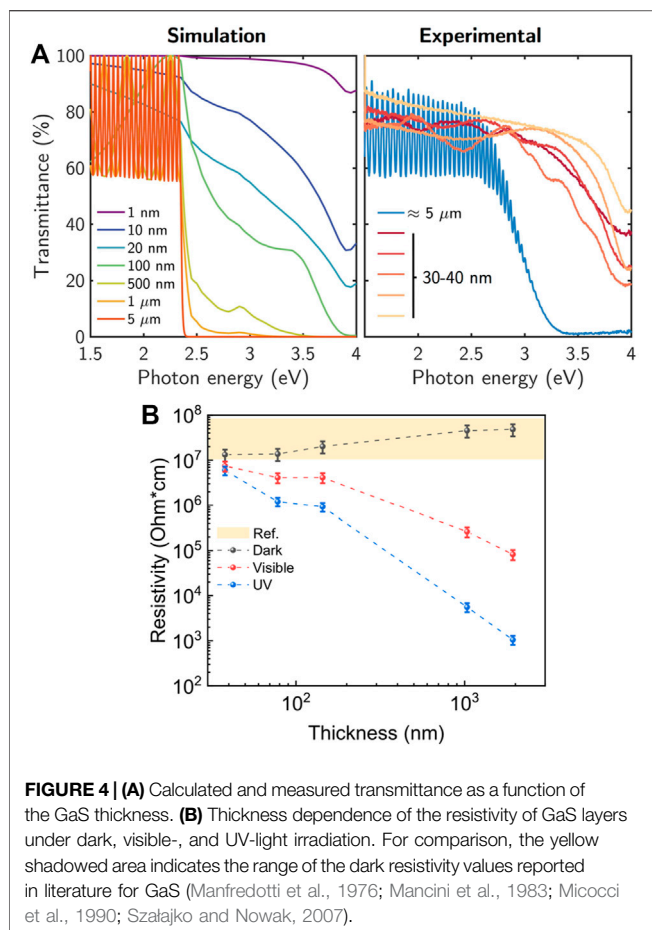


FIGURE 4 | (A) Calculated and measured transmittance as a function of the GaS thickness. **(B)** Thickness dependence of the resistivity of GaS layers under dark, visible-, and UV-light irradiation. For comparison, the yellow shadowed area indicates the range of the dark resistivity values reported in literature for GaS (Manfredotti et al., 1976; Mancini et al., 1983; Micocci et al., 1990; Szałajko and Nowak, 2007).

Noteworthy, the monolayer GaS as well as all the layered samples up to approximately 300 nm do not show any PL. A sharp PL peak at approximately 2.5 eV starts to be seen for thicknesses above 300 nm and increases with the increase in thickness, as shown in **Figure 3C**. This can be explained considering two main factors: 1) GaS is an indirect bandgap semiconductor requiring both photons and phonons for radiative recombination and defect-assisted recombination plays an important role, as due to the requirement of phonon momentum conservation, the radiative recombination on the indirect transition will be inefficient and sensitive to traps (Leonhardt et al., 2020). For monolayer and few layers, if the trap density is mainly localized at the substrate/GaS interface, traps result in the observed quenching of PL for the few-layer regime, as the substrate-interaction traps act as recombination centers in the bandgap. This is supported by literature (Shin et al., 2016), reporting that the surface roughness of the underlying substrate can result in inhomogeneous strain that leads to bandgap modifications in thin transition metal dichalcogenides causing the appearance of hole traps. The origin of these traps, however, is still under investigation. 2) By increasing the thickness, both the direct and indirect bandgaps are affected by the interlayer interactions along the *c*-axis and the appearance of new radiative recombination paths. This condition leads to the appearance of a distinct PL peak.

Optical and Electrical Properties

Figure 4 shows typical optical transmittance spectra measured on 30–40 nm and $\approx 5\text{-}\mu\text{m}$ -thick GaS. Simulated optical transmittance spectra are also shown as reference for different GaS thicknesses from 1 ML to 5 μm . The simulations were performed using the Transfer Matrix Method (Born et al., 1999) with the assumption of a flat interface multilayer GaS/glass system. The optical constants of GaS used in the simulations were experimentally measured by spectroscopic ellipsometry on a bulk crystal *c*-axis oriented. Interestingly, for a highly oriented defect-free GaS, the calculated spectra indicate a transmittance of 99.9% for the monolayer, 94.75% for approximately 10 layers, and 82.3% for approximately 20 nm (i.e., 20 layers), approaching the bulk 80% transmittance for a thickness higher than 20 nm. The measured optical transmittance line shape for the 30–40 nm GaS is in good agreement with the simulations performed for GaS layers with thickness in the range 10–50 nm. These spectra are characterized by a pronounced dip at $\approx 3.9\text{ eV}$ consistent with the interband critical point GS2 in the dielectric function as reported by Schlüter et al. (1976) and Isik et al. (2013). In the low-energy range, the lower measured transmittance as compared with simulation can be associated with phenomena not considered in the model such as surface roughness, scattering, as well as inhomogeneities in the sample. In the case of the $\approx 5\text{-}\mu\text{m}$ layer, the main difference between the measured and simulated spectra is in the onset and slope of the transmittance around the energy bandgap and the damped interference system. In this thick case, these differences can likely be attributed to polycrystallinity and defects or doping of the sample. This is supported by comparing the optical transmittance obtained by the model and that measured in a single crystal by Nakamura et al. (2021), in which the spectra also show a sharp step around the energy bandgap. These results provide evidence about the high density of defects introduced in the layers by the mechanical exfoliation process, which are also potentially the radiative traps causing the PL in **Figure 3C** for the thick GaS layers.

Furthermore, GaS has been demonstrated to be exploitable in blue-UV photodetectors (Chen et al., 2019; Lu et al., 2020). A critical parameter to be considered in the photodetector design is the resistivity of the active layer under light irradiation. Therefore, the photoresistivity of layered GaS with thickness ranging from ≈ 40 to 1900 nm transferred onto glass was also investigated. The calculated resistivity as a function of the GaS thickness with and without light irradiation is shown in **Figure 4B**.

In the dark state, GaS shows a typical resistivity of $\approx 10^7\text{ }\Omega\cdot\text{cm}$ independently of the thickness. This value is consistent with those reported by other authors (Manfredotti et al., 1976; Mancini et al., 1983; Micocci et al., 1990; Szałajko and Nowak, 2007). When illuminated, the GaS resistivity decreases for all the investigated thicknesses, consistently with an increase of the light absorption depth and generation of photocurrent in the GaS layers. Furthermore, the resistivity is lower when samples are illuminated by UV light than visible light. The lower resistivity values obtained under UV indicates a larger amount of free carriers generated due to the fact that all the excitation photons have an energy (405 nm/3.05 eV) above the GaS bandgap, making the electron–hole pair generation more

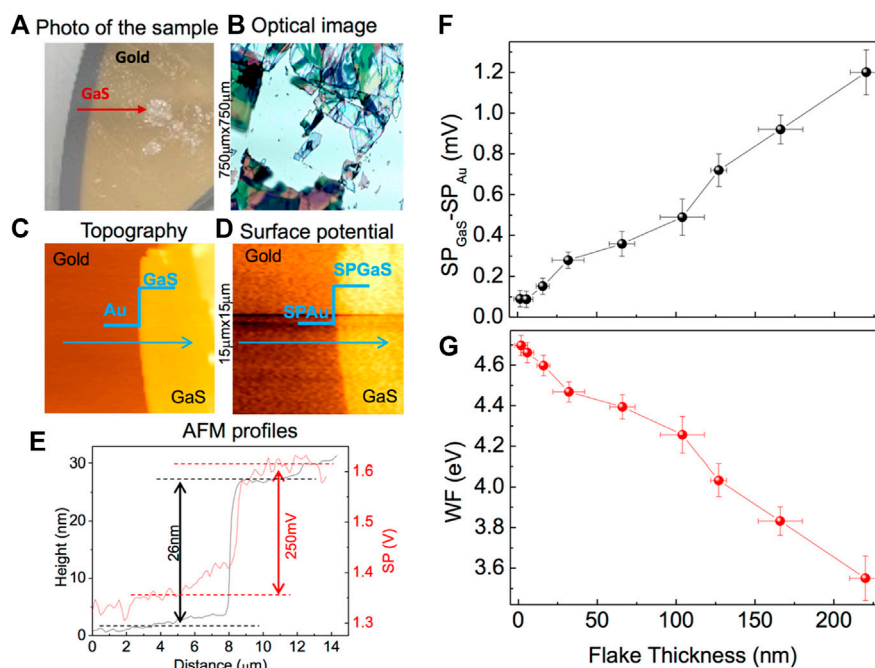


FIGURE 5 | (A) Picture of GaS flakes on gold; (B) optical image of a 750 μm × 750 μm area of GaS flakes (C,D) examples of 15 μm × 15 μm topographic and SP maps for a 26-nm-thick GaS flake. (E) Representative topographical (black line) and SP (red line) profiles for a GaS flake with 26-nm thickness against gold. (F) Thickness dependence of the difference in surface potential (SP) between gold and GaS. (G) Thickness dependence of the GaS work function (WF).

efficient than in the case of the visible light source, for which part of the emission spectrum contains photons below the GaS bandgap unable to generate photocarriers.

Thickness Dependence of the Work Function

Figure 5 illustrates the use of KPFM to determine the WF of GaS layers with different thickness, as it appears from the optical image (Figure 5B) of the sample, where the different colors correspond to flakes of different thickness, which have been mapped by atomic force topographies. The exfoliated GaS was deposited on a gold substrate, as shown in Figure 5A. A typical topography and corresponding surface potential SP map, 15 × 15 μm, are shown in Figures 5C,D, respectively. The difference between the SP of GaS flake, SP_{GaS}, and the SP of the gold, SP_{Au}, quantifies the difference in their Fermi levels according to the following relation:

$$\begin{aligned}\Delta SP &= SP_{\text{GaS}} - SP_{\text{Au}} = WF_{\text{tip}} - WF_{\text{GaS}} - WF_{\text{tip}} + WF_{\text{Au}} \\ &= WF_{\text{Au}} - WF_{\text{GaS}}\end{aligned}\quad (1)$$

where WF_{tip} is the tip work function, WF_{Au} is the gold work function, and WF_{GaS} is the work function of the GaS flake.

Figure 5E shows representative topographic and SP profiles obtained for a GaS flake with 26-nm thickness against gold. Specifically, the SP of the GaS flake is higher than the Au SP, i.e., $SP_{\text{GaS}} > SP_{\text{Au}}$, corresponding to a WF of the GaS flake 250 meV lower than that of the gold reference, which we previously calibrated to be 4.75 eV (Giangregorio et al., 2015).

By plotting the difference between the surface potential of the GaS flakes with a known thickness, SP_{GaS} , and the surface potential of gold, SP_{Au} , and the corresponding WF_{GaS} , as shown in Figures 5F,G, we found that GaS layers always have a SP higher than Au independently of their thickness. Moreover, the WF_{GaS} increases with the decrease in the GaS thickness from 3.55 ± 0.10 eV for GaS bulk to 4.70 ± 0.05 eV for GaS monolayer.

In order to explain this trend of the WF, we consider that 1) going from bulk to monolayer, the WF becomes more and more sensitive to the chemical and physical conditions at its surface, and 2) it depends on crystalline orientations, surface contamination, and surface roughness, which induce stress fluctuations affecting the Fermi level as well as the electrostatic potential in the vicinity of surface. It is worth pointing out that adsorption of atoms or molecules on GaS changes the surface dipole layer and hence the WF; e.g., electronegative adsorbates (e.g., O, C, and S) increase the WF. Oxygen adsorption involves localized orbital overlap and charge transfer between the adsorbate and surface atoms. The GaS bulk WF value is small compared with the oxygen ionization energy (13.618 eV), causing electron transfer from the GaS layer. Consequently, the WF increases as the negative pole of the adsorbed oxygen molecule points toward the vacuum, so the surface space charge or surface dipole presents an electrostatic field that causes an increase in the WF. The effect of adsorbates becomes more important with the decrease in the number of layers down to monolayer. The presence of those C and O adsorbates was confirmed by x-ray photoelectron spectroscopy (XPS).

These measurements of WF are useful to profile the bands and Fermi level variations as a function of GaS thickness. For

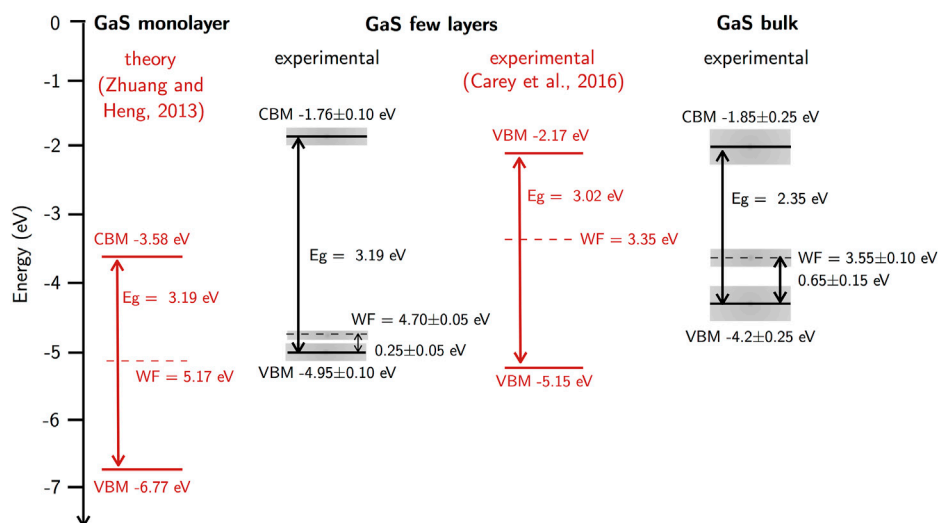


FIGURE 6 | Profiling of the valence band maximum (VBM), conduction band minimum (CBM), and Fermi level with respect to the vacuum level for GaS monolayer, few layers, and bulk considering theoretical (Zhuang and Hennig, 2013; Carey et al., 2017) and experimental values.

monolayer GaS, we consider as reference the values calculated by Zhuang and Hennig (2013) of the bandgap $E_g = 3.19$ eV, of the valence band maximum $VBM = -6.77$ eV and of the conduction band minimum $CBM = -3.58$ eV, as shown in **Figure 6**. In profiling the bands, the WF values were complemented with experimental values of the difference of the VBM with respect to Fermi level derived from the XPS valence band analysis. In the case of the few-layer GaS, we profiled the measured values of the WF and E_F of 4.70 ± 0.05 eV and of the VBM position with respect to Fermi level of 0.25 ± 0.05 eV. Assuming an energy bandgap similar to that of GaS monolayer, the VBM and CBM were set at -4.95 ± 0.10 and -1.76 ± 0.10 eV, respectively. For comparison, the values of VBM, CBM, and E_F reported by Carey et al. (2017) for few-layer GaS are also shown. In the case of bulk GaS, the measured WF = 3.55 ± 0.10 eV, the difference of 0.65 ± 0.15 eV for the VBM with respect to E_F , and the energy bandgap of 2.35 eV led to VBM and CBM at -4.2 ± 0.25 and -1.85 ± 0.25 eV, respectively. From these bands and Fermi level profiling, it can be inferred that the analyzed GaS samples are p-type semiconductors. This is consistent with other studies on GaS crystals grown by the Bridgman method (Lieth et al., 1969). As an example, for GaS monolayer, it has been reported that it becomes p-type under the gallium-poor and sulfur-rich conditions (Chen et al., 2015). The adsorbates mentioned above as well as the interface traps mentioned in **Figure 3C** could also contribute to the p-type doping of exfoliated GaS layers. The detailed identification of those radiative traps and p-type doping defects is in progress.

CONCLUSION

GaS layers of different thickness have been exfoliated and transferred to glass substrates. Different properties, such as structural properties from Raman spectra, PL, optical transmittance, resistivity, and WF have been investigated as a function of the number of layers. The

Raman spectra measured in layers with thickness ranging from the monolayer to 120 nm show no significant variation in the peak position and broadening, whereas their intensity is proportional to sample polarizability and, hence, increases with thickness. A model based on a planar stack of layers is able to reproduce the line shape of the optical transmittance spectra for few layers and micron-thick GaS layers. Phenomena of surface roughness, inhomogeneities, defects, or unintentional doping clearly decrease the transmittance. GaS dark resistivity is in the range of $\approx 10^7 \Omega \cdot \text{cm}$, independently of the thickness. Under visible and UV illumination, the resistivity decreases, and a pronounced dependence on GaS thickness is found. Finally, the analysis of the WF, using Kelvin probe force microscopy, shows an increase in the WF going from Bulk GaS down to monolayer. Accordingly, GaS bands have been profiled as a function of thickness. Although the study on this new 2D material is in progress, those trends can be useful to design optoelectronic devices based on GaS.

DATA AVAILABILITY STATEMENT

The original contributions presented in the study are included in the article/Supplementary Material, further inquiries can be directed to the corresponding author.

AUTHOR CONTRIBUTIONS

YG and SD prepared the samples. YG run the optical and structural characterization. MG contributed with the morphological and WF analysis. SD performed the electrical characterization. FP performed the XPS analysis. ML conceived the experiments and assisted in the discussions of all results. All authors discussed the data and results and agreed to the content of the work.

FUNDING

This research received funding from the European Union's Horizon 2020 research and innovation programme under grant agreement No. 899598—PHEMTRONICS.

REFERENCES

- Alencar, R. S., Longuinhos, R., Rabelo, C., Miranda, H., Viana, B. C., Filho, A. G. S., et al. (2020). Raman Spectroscopy Polarization Dependence Analysis in Two-Dimensional Gallium Sulfide. *Phys. Rev. B* 102, 1–10. doi:10.1103/PhysRevB.102.165307
- Born, M., Wolf, E., Bhatia, A. B., Clemmow, P. C., Gabor, D., Stokes, A. R., et al. (1999). *Principles of Optics*. Cambridge: Cambridge University Press. doi:10.1017/CBO9781139644181
- Carey, B. J., Ou, J. Z., Clark, R. M., Berean, K. J., Zavabeti, A., Chesman, A. S. R., et al. (2017). Wafer-scale Two-Dimensional Semiconductors from Printed Oxide Skin of Liquid Metals. *Nat. Commun.* 8, 1–10. doi:10.1038/ncomms14482
- Chen, H., Li, Y., Huang, L., and Li, J. (2015). Intrinsic Defects in Gallium Sulfide Monolayer: a First-Principles Study. *RSC Adv.* 5, 50883–50889. doi:10.1039/C5RA08329J
- Chen, T., Lu, Y., Sheng, Y., Shu, Y., Li, X., Chang, R.-J., et al. (2019). Ultrathin All-2D Lateral Graphene/GaS/Graphene UV Photodetectors by Direct CVD Growth. *ACS Appl. Mater. Inter.* 11, 48172–48178. doi:10.1021/acsami.9b11984
- Choi, S., Shaolin, Z., and Yang, W. (2014). Layer-number-dependent Work Function of MoS₂ Nanoflakes. *J. Korean Phys. Soc.* 64, 1550–1555. doi:10.3938/jkps.64.1550
- Giangregorio, M. M., Jiao, W., Bianco, G. V., Capezzuto, P., Brown, A. S., Bruno, G., et al. (2015). Insights into the Effects of Metal Nanostructuring and Oxidation on the Work Function and Charge Transfer of Metal/graphene Hybrids. *Nanoscale* 7, 12868–12877. doi:10.1039/C5NR02610E
- Gutiérrez, Y. (2021). *Code for Colorimetric 2D Materials Thickness Estimation*. doi:10.5281/zenodo.5116286
- Gutiérrez, Y., Santos, G., Giangregorio, M. M., Dicorato, S., Palumbo, F., Saiz, J. M., et al. (2021). Quick and Reliable Colorimetric Reflectometry for the Thickness Determination of Low-Dimensional GaS and GaSe Exfoliated Layers by Optical Microscopy. *Opt. Mater. Express* 11, 3697. doi:10.1364/OME.435157
- Ho, C. H., and Lin, S. L. (2006). Optical Properties of the Interband Transitions of Layered Gallium Sulfide. *J. Appl. Phys.* 100, 083508. doi:10.1063/1.2358192
- Isik, M., Gasanly, N. M., and Turan, R. (2013). Interband Transitions in Gallium Sulfide Layered Single Crystals by Ellipsometry Measurements. *Physica B: Condensed Matter* 408, 43–45. doi:10.1016/j.physb.2012.09.051
- Jung, C. S., Shojaei, F., Park, K., Oh, J. Y., Im, H. S., Jang, D. M., et al. (2015). Red-to-Ultraviolet Emission Tuning of Two-Dimensional Gallium Sulfide/Selenide. *ACS Nano* 9, 9585–9593. doi:10.1021/acs.nano.5b04876
- Kepinska, M., Nowak, M., Szalajko, M., and Murri, R. (2001). Temperature Dependence of Optical Parameters of Gallium Sulphide. *J. Wide Bandgap Mater.* 8, 241–249. doi:10.1106/152451102024667
- Leonhardt, A., Rosa, C. J. L., Nuytten, T., Banszerus, L., Sergeant, S., Mootheri, V. K., et al. (2020). Use of the Indirect Photoluminescence Peak as an Optical Probe of Interface Defectivity in MoS₂. *Adv. Mater. Inter.* 7, 2000413. doi:10.1002/admi.202000413
- Li, Y., Xu, C.-Y., and Zhen, L. (2013). Surface Potential and Interlayer Screening Effects of Few-Layer MoS₂ Nanoflakes. *Appl. Phys. Lett.* 102, 143110. doi:10.1063/1.4801844
- Lieth, R. M. A., Van Der Heijden, C. W. M., and Van Kessel, J. W. M. (1969). Preparation, Purity and Electrical Conductivity of Gallium Sulphide Single Crystals. *J. Cryst. Growth* 5, 251–258. doi:10.1016/0022-0248(69)90053-0
- Liu, R., Wang, F., Liu, L., He, X., Chen, J., Li, Y., et al. (2021). Band Alignment Engineering in Two-Dimensional Transition Metal Dichalcogenide-Based Heterostructures for Photodetectors. *Small Structures* 2, 2000136. doi:10.1002/sstr.202000136
- Lu, Y., Chen, J., Chen, T., Shu, Y., Chang, R. J., Sheng, Y., et al. (2020). Controlling Defects in Continuous 2D GaS Films for High-Performance Wavelength-Tunable UV-Discriminating Photodetectors. *Adv. Mater.* 32, 1906958. doi:10.1002/adma.201906958
- Mancini, A. M., Micocci, G., and Rizzo, A. (1983). New Materials for Optoelectronic Devices: Growth and Characterization of Indium and Gallium Chalcogenide Layer Compounds. *Mater. Chem. Phys.* 9, 29–54. doi:10.1016/0254-0584(82)90006-2
- Manfredotti, C., Murri, R., Rizzo, A., and Vasanelli, L. (1976). Hall Effect in N-type GaS. *Solid State. Commun.* 19, 339–342. doi:10.1016/0038-1098(76)91346-6
- Micocci, G., Rella, R., Siciliano, P., and Tepore, A. (1990). Investigation of Electronic Properties of Gallium Sulfide Single Crystals Grown by Iodine Chemical Transport. *J. Appl. Phys.* 68, 138–142. doi:10.1063/1.347105
- Nakamura, M., Nakamura, H., Shimamura, K., and Ohashi, N. (2021). Growth and Characterization of a Gallium Monosulfide (GaS) Single crystal Using the Bridgman Method. *J. Cryst. Growth.* 573, 126303. doi:10.1016/j.jcrysgro.2021.126303
- Schlüter, M., Camassel, J., Kohn, S., Voitchovsky, J. P., Shen, Y. R., and Cohen, M. L. (1976). Optical Properties of GaSe and GaSxSe1-x mixed Crystals. *Phys. Rev. B* 13, 3534–3547. doi:10.1103/PhysRevB.13.3534
- Shin, B. G., Han, G. H., Yun, S. J., Oh, H. M., Bae, J. J., Song, Y. J., et al. (2016). Indirect Bandgap Puddles in Monolayer MoS₂ by Substrate-Induced Local Strain. *Adv. Mater.* 28, 9378–9384. doi:10.1002/adma.201602626
- Szalajko, M., and Nowak, M. (2007). The Influence of Light Intensity on Surface Recombination in GaS Single Crystals. *Appl. Surf. Sci.* 253, 3636–3641. doi:10.1016/j.apsusc.2006.07.073
- Williams, R. H., Higginbotham, I. G., and Whitaker, M. A. B. (1972). Adsorption Anisotropy in Layer Chalcogenides. *J. Phys. C: Solid State. Phys.* 5, L191–L193. doi:10.1088/0022-3719/5/15/003
- Williams, R. H., and McEvoy, A. J. (1972). Surface Properties of the Gallium Monochalcogenides. *Phys. Stat. Sol. (A)* 12, 277–286. doi:10.1002/pssa.2210120130
- Zhuang, H. L., and Hennig, R. G. (2013). Single-Layer Group-III Monochalcogenide Photocatalysts for Water Splitting. *Chem. Mater.* 25, 3232–3238. doi:10.1021/cm401661x

ACKNOWLEDGMENTS

We acknowledge Dr. Giovanni Bruno for his helpful discussions during data analysis and our collaborator Sig. Alberto Sacchetti for his assistance in performing the experiments.

Conflict of Interest: The authors declare that the research was conducted in the absence of any commercial or financial relationships that could be construed as a potential conflict of interest.

Publisher's Note: All claims expressed in this article are solely those of the authors and do not necessarily represent those of their affiliated organizations, or those of the publisher, the editors and the reviewers. Any product that may be evaluated in this article, or claim that may be made by its manufacturer, is not guaranteed or endorsed by the publisher.

Copyright © 2021 Gutiérrez, Giangregorio, Dicorato, Palumbo and Losurdo. This is an open-access article distributed under the terms of the Creative Commons Attribution License (CC BY). The use, distribution or reproduction in other forums is permitted, provided the original author(s) and the copyright owner(s) are credited and that the original publication in this journal is cited, in accordance with accepted academic practice. No use, distribution or reproduction is permitted which does not comply with these terms.



Sensitive LC-MS/MS Methods for Amphotericin B Analysis in Cerebrospinal Fluid, Plasma, Plasma Ultrafiltrate, and Urine: Application to Clinical Pharmacokinetics

Leandro Francisco Pippa¹, Maria Paula Marques¹, Anna Christina Tojal da Silva², Fernando Crivelenti Vilar², Tissiana Marques de Haes³, Benedito Antônio Lopes da Fonseca², Roberto Martinez², Eduardo Barbosa Coelho⁴, Lauro Wichert-Ana⁵ and Vera Lucia Lanchote^{1*}

¹Department of Clinical Analyses, Toxicology and Food Science, School of Pharmaceutical Sciences of Ribeirão Preto, University of São Paulo, Ribeirão Preto, Brazil, ²Division of Infectious Diseases, Department of Internal Medicine, School of Medicine of Ribeirão Preto, University of São Paulo, Ribeirão Preto, Brazil, ³Department of Neurosciences and Behavioral Sciences, School of Medicine of Ribeirão Preto, University of São Paulo, Ribeirão Preto, Brazil, ⁴Division of Nephrology, Department of Internal Medicine, School of Medicine of Ribeirão Preto, University of São Paulo, Ribeirão Preto, Brazil, ⁵Division of Medical Images, Nuclear Medicine, Department of Medical, Imaging, Hematology and Oncology, School of Medicine of Ribeirão Preto, University of São Paulo, São Paulo, Brazil

OPEN ACCESS

Edited by:

Quezia B. Cass,
Federal University of São Carlos, Brazil

Reviewed by:

Cristina Sempio,
University of Colorado, United States
Elena Sánchez López,
Leiden University Medical Center,
Netherlands

*Correspondence:

Vera Lucia Lanchote
lanchote@fcrp.usp.br

Specialty section:

This article was submitted to
Analytical Chemistry,
a section of the journal
Frontiers in Chemistry

Received: 23 September 2021

Accepted: 26 October 2021

Published: 29 November 2021

Citation:

Pippa LF, Marques MP, Silva ACTd, Vilar FC, de Haes TM, Fonseca BAL, Martinez R, Coelho EB, Wichert-Ana L and Lanchote VL (2021) Sensitive LC-MS/MS Methods for Amphotericin B Analysis in Cerebrospinal Fluid, Plasma, Plasma Ultrafiltrate, and Urine: Application to Clinical Pharmacokinetics. *Front. Chem.* 9:782131. doi: 10.3389/fchem.2021.782131

Neurocryptococcosis, a meningoencephalitis caused by *Cryptococcus* spp, is treated with amphotericin B (AmB) combined with fluconazole. The integrity of the brain-blood barrier and the composition of the cerebrospinal fluid (CSF) may change due to infectious and/or inflammatory diseases such as neurocryptococcosis allowing for the penetration of AmB into the central nervous system. The present study aimed to develop LC-MS/MS methods capable of quantifying AmB in CSF at any given time of the treatment in addition to plasma, plasma ultrafiltrate, with sensitivity compatible with the low concentrations of AmB reported in the CSF. The methods were successfully validated in the four matrices (25 μ l, 5–1,000 ng ml⁻¹ for plasma or urine; 100 μ l, 0.625–250 ng ml⁻¹ for plasma ultrafiltrate; 100 μ l, 0.1–250 ng ml⁻¹ for CSF) using protein precipitation. The methods were applied to investigate the pharmacokinetics of AmB following infusions of 100 mg every 24 h for 16 days administered as a lipid complex throughout the treatment of a neurocryptococcosis male patient. The methods allowed for a detailed description of the pharmacokinetic parameters in the assessed patient in the beginning (4th day) and end of the treatment with AmB (16th day), with total clearances of 7.21 and 4.25 L h⁻¹, hepatic clearances of 7.15 and 4.22 L h⁻¹, volumes of distribution of 302.94 and 206.89 L, and unbound fractions in plasma ranging from 2.26 to 3.25%. AmB was quantified in two CSF samples collected throughout the treatment with concentrations of 12.26 and 18.45 ng ml⁻¹ on the 8th and 15th days of the treatment, respectively. The total concentration of AmB in plasma was 31 and 20 times higher than in CSF. The unbound concentration in plasma accounted for 77 and 44% of the respective concentrations in CSF. In conclusion, the present study described the most complete and sensitive method for AmB analysis in plasma, plasma ultrafiltrate, urine, and CSF

applied to a clinical pharmacokinetic study following the administration of the drug as a lipid complex in one patient with neurocryptococcosis. The method can be applied to investigate the pharmacokinetics of AmB in CSF at any given time of the treatment.

Keywords: amphotericin B, plasma, unbound fraction, urine, cerebrospinal fluid, LC-MS/MS, neurocryptococcosis, pharmacokinetics

1 INTRODUCTION

Neurocryptococcosis is a subacute meningoencephalitis caused by the inhalation of the fungus *Cryptococcus* spp. After a latency period in the pulmonary lymph nodes, it spreads throughout the body with tropism for the central nervous system (Coelho et al., 2014). Neurocryptococcosis is more prevalent in HIV and other immunosuppressed patients and less commonly in individuals considered immunocompetent (Jarvis et al., 2010; Durski et al., 2013; Pyrgos et al., 2013; Rolfes et al., 2015; Williamson et al., 2016).

The treatment for neurocryptococcosis aims to sterilize the central nervous system and reduce intracranial pressure to values below 200 mmH₂O considering that pressures above 350 mmH₂O are associated with papilledema, decreased visual acuity, decreased hearing capacity, headaches, and confusion. Symptoms resulting from increased cerebrospinal fluid (CSF) pressure can be controlled by lumbar punctures to reduce pressure to levels below 200 mmH₂O (Redmond et al., 2007).

Amphotericin B (AmB; C₄₇H₇₃NO₁₇) is a polyene derived from *Streptomyces nodosus*, a compound discovered in the 1950s that remains the first line of treatment for invasive fungal infections, although new triazole antifungal drugs with a broad spectrum of action and good distribution to the central nervous system, such as voriconazole and posaconazole are also available (Black and Baden, 2007; Lestner et al., 2010).

AmB is mainly eliminated unchanged via biliary secretion. There are no known AmB metabolites described either in preclinical or clinical studies. Tissue accumulation accounts for most of the drug's disposition. AmB can still be detected in the liver, spleen, and kidneys for up to 1 year after the end of therapy (Benson and Nahata, 1988). Based on experimental studies in mice, AmB is probably a substrate of P-glycoprotein (P-gp) (Wu et al., 2015) and breast cancer resistance protein (BCRP) (Stevens et al., 2015) drug transporters expressed in the brain-blood barrier (Cordon-Cardo et al., 1989; Schinkel et al., 1996).

The integrity of the brain-blood barrier and the composition of the CSF may change due to infectious and/or inflammatory diseases such as neurocryptococcosis (Shawahna, 2015) due to the high levels of pro-inflammatory cytokines and other inflammatory mediators (Williamson et al., 2016). *In vitro* studies indicate that the permeability of the brain-blood barrier for AmB is altered by TNF- α and lipopolysaccharide (Pyrgos et al., 2010). Considering that AmB is a Class 4 compound according to the Biopharmaceutics Drug Disposition Classification System (Shugarts and Benet, 2009; Hosey et al., 2016) and that central nervous system efflux and biliary secretion drug transporters play a significant role in the pharmacokinetics of this drug, adjustments to AmB dose may be necessary for neurocryptococcosis patients over the treatment evolution.

The first method for quantifying AmB in plasma dates from the late 1970s and reports the use of high-performance liquid chromatography (HPLC) with detection by UV or fluorescence (Nilsson-Ehle, 1977). Other methods applying HPLC or UHPLC (ultra-high-performance liquid chromatography) with detection by UV or fluorescence continue to be used over the years to date (Liu et al., 1995; Campanero et al., 1997; Echevarría et al., 1998; Groll et al., 2000; Lee et al., 2001; Wurthwein et al., 2005; Qu et al., 2017; Wirth et al., 2018).

The application of mass spectrometry (LC-MS/MS) to quantify was described for the first time by Lee et al. (Lee et al., 2001) in the assessment of four different biological matrices using 50 μ l of plasma, urine, and human fecal homogenate with lowest limits of quantification (LLOQ) of 2000, 50 and 40 ng ml⁻¹, respectively, and 200 μ l of human plasma ultrafiltrate with an LLOQ of 1 ng ml⁻¹. Other previous methods that apply LC-MS/MS (Lee et al., 2001; Deshpande et al., 2010; Strenger et al., 2014) have used larger volumes of biological matrices. In addition, these cited studies used the solid-phase extraction technique in the sample preparation, which makes the analysis of a large number of samples more expensive, a common scenario in clinical pharmacokinetics studies. LC-MS/MS was first used to analyze human CSF samples by Xiong et al. (2009), with 100 μ l samples and an LLOQ of 0.5 ng ml⁻¹.

The present study aimed to develop and validate LC-MS/MS methods for quantifying AmB total concentrations in plasma, urine, and CSF, as well as the unbound concentration in plasma using plasma ultrafiltrate. The investigation of the pharmacokinetics of AmB in patients with neurocryptococcosis requires the development and validation of methods with sensitivity compatible with the low concentrations of AmB reported in the CSF, taking into consideration the low volumes available for this matrix (Leenders et al., 1997; Wurthwein et al., 2005; Xiong et al., 2009; Hamill et al., 2010; Strenger et al., 2014; Stone et al., 2016). The methods described in the present study were successfully applied to quantify AmB in all available biological fluids including CSF samples from one patient with neurocryptococcosis up to the 16th day of treatment with AmB lipid complex.

2 MATERIALS AND METHODS

2.1 Standard Solutions and Reagents

A stock solution of AmB (88.6%, European Pharmacopeia Reference Standard, CRS, Strasbourg, France) was prepared in methanol:dimethylsulfoxide (1:1, v/v) at the concentration of

1 mg ml⁻¹. It was further diluted in methanol to obtain a concentration of 100 µg ml⁻¹. This solution was used to prepare the working solutions in methanol at 0.4–1,000 ng ml⁻¹. Piroxicam (C₁₅H₁₃N₃O₄S) (European Pharmacopeia Reference Standard, CRS, Strasbourg, France) used as the internal standard (IS) was prepared at the concentration of 1 mg ml⁻¹ of methanol and diluted to concentrations of 10 and 100 ng ml⁻¹ of methanol.

Since AmB is photosensitive (Beggs, 1978), all experiments were carried out under yellow light (sodium vapor lamps) as the only illumination source. Standard solutions were stored in BD Falcon® polypropylene tubes (BD, Franklin Lakes, NJ, United States), aliquoted in polypropylene microtubes, protected by aluminum foil, and stored at -20°C.

Acetonitrile, methanol (J. T. Baker, Phillipsburg, NJ, United States), isopropanol (Honeywell Riedel-de Haën®, Seelze, Germany), and dimethylsulfoxide (Merck, Darmstadt, Germany) were used at chromatographic grade. Formic acid (J. T. Baker, 90.1%) and ammonium acetate (J. T. Baker, 98.9%) were used at analytical grade. Water was obtained from the Milli Q Plus® purification system (Millipore, Bedford, MA, United States).

2.2 Chromatographic Analysis

AmB analysis was performed by liquid chromatography coupled to a tandem mass spectrometer (LC-MS/MS) consisting of a quaternary ACQUITY UPLC® H-Class pump, ACQUITY UPLC® Sample Manager—FTN automatic injector equipped with an ACQUITY Sample Organizer, TCM/CHM® column oven, and XEVO TQ-S® triple quadrupole mass spectrometer equipped with Zspray™ Electrospray Interface (ESI), all Waters Corp. (Milford, MA, United States).

The chromatographic analysis was conducted on a reverse-phase column LiChrospher® 60 RP-Select B 5 µm particles, 125 × 4.6 mm, protected by a guard column LiChrospher® 60 RP-Select B, 5 µm particles, 4 × 4 mm and kept at 25°C, all Merck (Darmstadt, Germany). The mobile phase consisted of an isocratic solvent system of 0.1% formic acid in water and 0.1% formic acid in acetonitrile in a ratio of 40:60 (v/v) for plasma or urine analysis and 50:50 (v/v) for plasma ultrafiltrate or CSF analysis, all at a flow rate of 0.8 ml min⁻¹. The wash solution was prepared with 0.25% formic acid in 50:20:15:15 (v/v/v/v) acetonitrile:isopropanol:methanol:water solution.

2.3 Mass Spectrometry

MS/MS analysis was performed in positive ionization mode. The capillary voltage at the ESI was set to 3.50 kV. The source and desolvation temperatures were kept at 120 and 400°C, respectively. Nitrogen was used as a nebulization gas at a flow rate of 600 L h⁻¹. Argon was used as the collision gas at a flow rate of 0.18 ml min⁻¹. The cone energy was 30 V for both AmB and IS. The collision energies were 20 eV for AmB and 30 eV for IS.

The MS/MS conditions were optimized by the direct infusions of AmB and IS solutions at the concentration of 100 ng ml⁻¹ prepared in a mixture of 0.1% formic acid in water and 0.1% formic acid in acetonitrile (1:1, v/v). The analysis was performed in the selected reaction monitoring mode. The protonated ions

[M + H]⁺ and their respective product ions were monitored in the transitions of m/z 906 → 743 for AmB for all the four matrices and m/z 332 → 95 for IS in plasma and urine analysis, and m/z 332 → 121 in plasma ultrafiltrate and CSF analysis. Data acquisition and sample quantification were performed using MassLynx® version 4.1 (Micromass, Manchester, United Kingdom).

2.4 Sample Preparation

2.4.1 Total Plasma and Urine Samples

Aliquots of 25 µl of plasma or urine were prepared by adding 25 µl of IS solution in methanol (piroxicam, 100 ng ml⁻¹), 25 µl of methanol, and further precipitated with 100 µl of the solution of 0.1% formic acid in acetonitrile. The tubes were shaken for 5 seconds and then centrifuged at 4°C for 15 min at 21,500 × g (refrigerated Himac CT15RE ultracentrifuge; Hitachi, Tokyo, Japan). Then, 100 µl of the supernatant were transferred to the injection vials and mixed with 100 µl of 0.1% formic acid in water, of which 20 µl of the final mixture were subjected to chromatographic analysis. The DQCs samples were diluted with the respective blank matrix in the proportion 1:4 (v/v) before the sample preparation process. Aliquots of 25 µl of the diluted DQC samples were transferred to a new microtube and processed following the same sample preparation procedure as a regular sample. Calibration curves were prepared similarly, enriching 25 µl of blank matrix (plasma or urine) with 25 µl of each working solution of AmB in methanol instead of 25 µl of methanol.

2.4.2 Plasma Ultrafiltrate Samples

Total plasma was ultrafiltered immediately before the sample preparation processes. Aliquots of 500 µl of plasma were added to Centrifree® Ultrafiltration Devices (Merck, Darmstadt, Germany) and centrifuged at 37°C for 30 min at 1875 × g in a fixed angle rotor centrifuge at an angle of 36° (Novatecnica, model NT 875), according to the manufacturer's indication. Aliquots of 100 µl of the obtained ultrafiltrate were processed by adding 25 µl of IS solution in methanol (100 ng ml⁻¹), 25 µl of methanol and further precipitated with 50 µl of the solution of 0.1% formic acid in acetonitrile. The tubes were shaken for 30 s and then centrifuged at 4°C for 15 min at 21,500 × g. An aliquot of 100 µl of the supernatant was transferred to the injection vials, mixed with 100 µl of 0.1% formic acid in water, and 30 µl of the final mixture was chromatographed. The DQCs samples were diluted blank plasma ultrafiltrate in the proportion 1:10 (v/v) before the sample preparation process. Aliquots of 100 µl of the diluted DQC samples were transferred to a new microtube and processed following the same sample preparation procedure as a regular sample. Calibration curves were also prepared similarly, enriching 100 µl of blank plasma ultrafiltrate with 25 µl of each working solution of AmB in methanol instead of 25 µl of methanol.

2.4.3 Cerebrospinal Fluid Samples

Aliquots of 100 µl of CSF at approximately 4°C were transferred to microtubes containing 25 µl of IS solution in methanol (piroxicam, 10 ng ml⁻¹), 25 µl of methanol, and further

precipitated with 50 μl of the solution of 0.1% formic acid in acetonitrile. The tubes were shaken for 30 s and then centrifuged at 4°C for 15 min at $21,500 \times g$. Then, 100 μl of the supernatant were transferred to the injection vials, and 50 μl of 0.1% formic acid in water were added, of which 20 μl of the final mixture were chromatographed. Calibration curves were also prepared similarly, enriching 100 μl of blank CSF with 25 μl of each working solution of AmB in methanol instead of 25 μl of methanol.

2.5 Method Validation

The analytical methods were developed and validated according to the Guideline on bioanalytical method validation of The European Medicines (European Medicines Agency, 2011). Blank plasma and urine samples were obtained from healthy volunteers after signing the prior informed consent form, and cerebrospinal fluid samples were provided by the Cerebrospinal Fluid Laboratory of the General Hospital of the Ribeirao Preto Medical School, University of São Paulo, according to the research project approved by the Research Ethics Committee of the School of Pharmaceutical Sciences of Ribeirão Preto, University of São Paulo and the Research Ethics Committee of the General Hospital of the Ribeirao Preto Medical School, University of São Paulo (Section 2.6 Clinical protocol).

2.5.1 Calibration Curves

Calibration curves for the analysis of plasma or urine concentrations were prepared in triplicates using aliquots of a blank matrix (25 μl of plasma, 25 μl of urine, 100 μl of plasma ultrafiltrate, or 100 μl of CSF) enriched with 25 μl of each working standard solutions of AmB to obtain different AmB concentrations in the ranges of 5–1,000 ng ml^{-1} for plasma and urine, 0.625–250 ng ml^{-1} for plasma ultrafiltrate, or 0.1–250 ng ml^{-1} for CSF. Blank, zero, and enriched samples were submitted to the process described in items 2.4.1 for plasma or urine, 2.4.2 for plasma ultrafiltrate, and 2.4.3 for CSF.

Linear regression equations were obtained for each matrix by plotting the ratios of the AmB/IS areas as a function of their respective concentrations. Calibration standards must present deviations less than or equal to 20% to the nominal value in the LLOQQC concentration and deviations less than or equal to 15% to the nominal value for the other concentrations. Calibration curves are accepted when at least 75% of the calibration standards meet these requirements, and they must include the concentrations of the LLOQ and ULOQ.

2.5.2 Quality Controls

Quality control (QC) solutions containing AmB were prepared in the respective biological matrix by adding the required volume of AmB standard in methanol, evaporating it under nitrogen flow, adding the necessary biological matrix and vigorously shaking (Phoenix Luferco solution shaker, model AP56, Araraquara, SP, Brazil) the solution for 3 min. The QC solutions for plasma and urine were prepared at final concentrations of 5 ng ml^{-1} (lowest limit of quantification quality control, LLOQQC); 10 ng ml^{-1} (low concentration quality control, LCQC); 500 ng ml^{-1} (medium concentration quality control, MCQC); 800 ng ml^{-1}

high concentration quality control, HCQC), and 2,000 ng ml^{-1} (dilution quality Control, DQC). The QC solutions for the quantifications in plasma ultrafiltrate were prepared at the concentrations 0.625 ng ml^{-1} (LLOQQC), 1.5625 ng ml^{-1} (LCQC), 125 ng ml^{-1} (MCQC), 200 ng ml^{-1} (HCQC), and 500 ng ml^{-1} (DQC).

2.5.3 Selectivity

The selectivities of the methods of analysis of AmB in plasma, plasma ultrafiltrate, urine, and CSF were evaluated in their respective blank matrices, eight for plasma and plasma ultrafiltrate (four normal, two hemolyzed, and two lipemic), six for urine (five normal and one obtained from a woman in the menstrual period) and eight for CSF (four normal, two yellowish-turbid, and two containing blood). The interfering peak areas at the same retention time of the AmB must be less than 20% of the area of the LLOQQC. The interfering peak areas near the IS retention time must be less than 5% of the IS area.

2.5.4 Carryover Effect

The carryover effects of the methods were evaluated by performing three injections of each processed blank sample (plasma, plasma ultrafiltrate, urine, and CSF), one before and two after the injection of the respective matrix in the concentration of the upper limit of quantitation (ULOQ, 1,000 ng ml^{-1} of plasma or urine; 250 ng ml^{-1} of plasma ultrafiltrate or CSF). The interfering peak areas at the same retention time of AmB must be less than 20% of the area originating from the LLOQQC. The interfering peak areas at the IS retention time should be less than 5% of the IS area.

2.5.5 Matrix Effect

The matrix effect (ME) was assessed at low and high concentration quality controls (LCQC and HCQC) levels in all three matrices. ME was assessed from eight plasma and plasma ultrafiltrate sources (four normal, two hemolyzed, and two lipemic), six urine sources (five normal and one from a woman in the menstrual period), eight CSF sources (four normal, two yellowish-turbid, and two containing blood). The samples were precipitated as described in items 2.4.1, 2.4.2, and 2.4.3, followed by the addition of the AmB and IS solutions to obtain the same concentrations as the LCQC and HCQC. The Matrix Factor Normalized by Internal Standard (MFNIS) was evaluated for each sample applying the equation below. The Coefficient of Variation (CV) for the group of samples from the same matrix must be less than 15%.

MFNIS =

$$\frac{(\text{analyte area in matrix}) / (\text{internal standard area in matrix})}{(\text{analyte area in solution}) / (\text{internal standard area in solution})}$$

MFNIS: Matrix Factor Normalized by Internal Standard.

Additionally, the matrix effect was also assessed by the classic post-column infusion test, injecting a processed sample from each biological matrix (plasma, urine, and CSF) with a combined infusion of the standard solution of AmB or the IS piroxicam,

both at a concentration of 250 ng/ml and at a flow rate of 5 $\mu\text{l min}^{-1}$. The same test was also performed by replacing the matrix (plasma, urine, and CSF) with water.

2.5.6 Precision and Accuracy

The precision and accuracy of the methods were assessed through within-run and between-run assays. The assays were performed at the concentrations of LLOQQC, LCQC, MCQC, and HCQC for each matrix (plasma, urine, plasma ultrafiltrate, and CSF) and DQC for the methods of plasma, urine, and plasma ultrafiltrate.

In order to assess within-run precision and accuracy, five replicates of each concentration (LLOQQC, LCQC, MCQC, HCQC, and DQC) in plasma, plasma ultrafiltrate, urine, and CSF were analyzed in a single analytical run. For assessing the precision and accuracy of the between-run assays, five aliquots of each concentration in the four matrices were analyzed in three different analytical runs.

The assessment of within-run and between-run precision was performed by calculating the CV of the results obtained. To be accepted as accurate, the CVs must be equal to or less than 15% for all the concentrations, except for the LLOQQC with an accepted CV of 20%. The accuracy is expressed by the Relative Error (RE, inaccuracy), with accepted values within the range of $\pm 15\%$ of the nominal value, except for the LLOQQC, with accepted values within the range of $\pm 20\%$ of the nominal value.

RE =

$$\frac{(\text{mean experimental concentration} - \text{nominal concentration})}{(\text{nominal concentration})} \times 100$$

RE: relative error (inaccuracy), %.

2.5.7 Stabilities

AmB stability assays were conducted using five replicate samples at concentrations of LCQC (10 ng ml^{-1} for plasma or urine, 1.5625 ng ml^{-1} for plasma ultrafiltrate, and 0.25 ng ml^{-1} for CSF) and HCQC (800 ng ml^{-1} for plasma or urine, and 200 ng ml^{-1} for plasma ultrafiltrate and CSF). Freeze and thaw stability was assessed by freezing samples at -70°C for at least 12 h and thawing at 25°C for 60 min. After three cycles of freezing and thawing, samples were analyzed using freshly prepared calibration curves. Freeze and thaw stability was not assessed for plasma ultrafiltrate since all samples were analyzed immediately after the ultracentrifugation process. Short-term stability was assessed after keeping the samples at 25°C for 4 h for plasma and urine, at 25°C for 2 h for plasma ultrafiltrate, and at 4°C for 2 h for CSF. All samples were analyzed using freshly prepared calibration curves. Post-processing stability was assessed after the LCQC and HCQC samples were kept for 24 h at the auto-injector temperature of 15°C for plasma, urine, and CSF, or for 20 h at 12°C for plasma ultrafiltrate. All samples were analyzed using freshly prepared calibration curves. The stability of AmB in biological matrices is accepted when the deviation from the nominal value is equal to or less than $\pm 15\%$.

2.5.8 Non-Specific Binding to Ultrafiltration Membrane
Solutions of AmB were prepared in water in the same concentrations of the LCQC and HCQC of the ultrafiltrate

QCs, respectively 1.5625 ng ml^{-1} and 200 ng ml^{-1} . Aliquots of 500 μl of each solution were added to Centrifree® Ultrafiltration Devices and centrifuged at 37°C for 30 min at $1875 \times g$, following the sample preparation protocol for plasma ultrafiltrate samples (2.4.2). Aliquots of 100 μl of both the obtained filtered solution or the unfiltered solution were prepared by adding 25 μl of the IS solution in methanol (piroxicam 100 ng ml^{-1}), 25 μl of methanol, 50 μl of the solution of 0.1% formic acid in acetonitrile and were subsequently transferred to the injection vials, of which 30 μl of the final mixture were chromatographed. Calibration curves were also prepared similarly, enriching 100 μl water with 25 μl of each working solution of AmB in methanol instead of 25 μl of methanol. The non-specific binding to the ultrafiltration membrane was assessed by quantifying five replicates of the filtered and unfiltered solutions prepared in both concentrations. CV and RE were calculated for all samples of each concentration, with accepted values within the range of $\pm 15\%$ of the nominal value.

2.6 Clinical Protocol

A 35-year-old white male admitted to the General Hospital of the Ribeirão Preto Medical School already under tuberculosis treatment was diagnosed with neurocryptococcosis. The subject was enrolled in this study previously approved by the Research Ethics Committee of the School of Pharmaceutical Sciences of Ribeirão Preto, University of São Paulo (CAAE: 96780618.7.0000.5403) and the Research Ethics Committee of the General Hospital of the Ribeirão Preto Medical School, University of São Paulo (CAEE: 96780618.7.3001.5440). As part of the treatment for neurocryptococcosis, the patient received daily doses of amphotericin B lipid complex (Abelcet® 100, Teva Pharmaceutical Industries Ltd., Brazil) and fluconazole. The subject was assessed at the beginning (Phase 1, 4th day) and the end (Phase 2, 16th day) of the treatment with AmB. In both phases, the patient was requested to empty his bladder and then received 100 mg in 500 ml saline in a four-hour i. v. infusion. The complete list of medications in use in both phases is described in **Table 1**. The sampling protocol is shown in **Figure 1**. Serial blood samples (4 ml) were collected in EDTA tubes immediately before AmB infusion and after 2, 4, 5, 6, 7, 10, 14, 18, 22, 23, and 24 h. Blood samples were centrifuged at 4°C for 15 min at $1875 \times g$. The plasma was transferred to polypropylene cryogenic tubes and stored at -80°C . Urine was collected in individual flasks at every spontaneous micturition, the volume was measured, and an aliquot of 5 ml was stored at -80°C . CSF samples were obtained from the exceeding volume of regular lumbar punctures performed by the medical team for fungal culture tests or to relieve increased intracranial pressure. CSF samples were collected in tubes containing no additives and stored at -80°C . A blood sample was collected immediately with each CSF sample in an EDTA tube, processed and stored as described above for plasma samples.

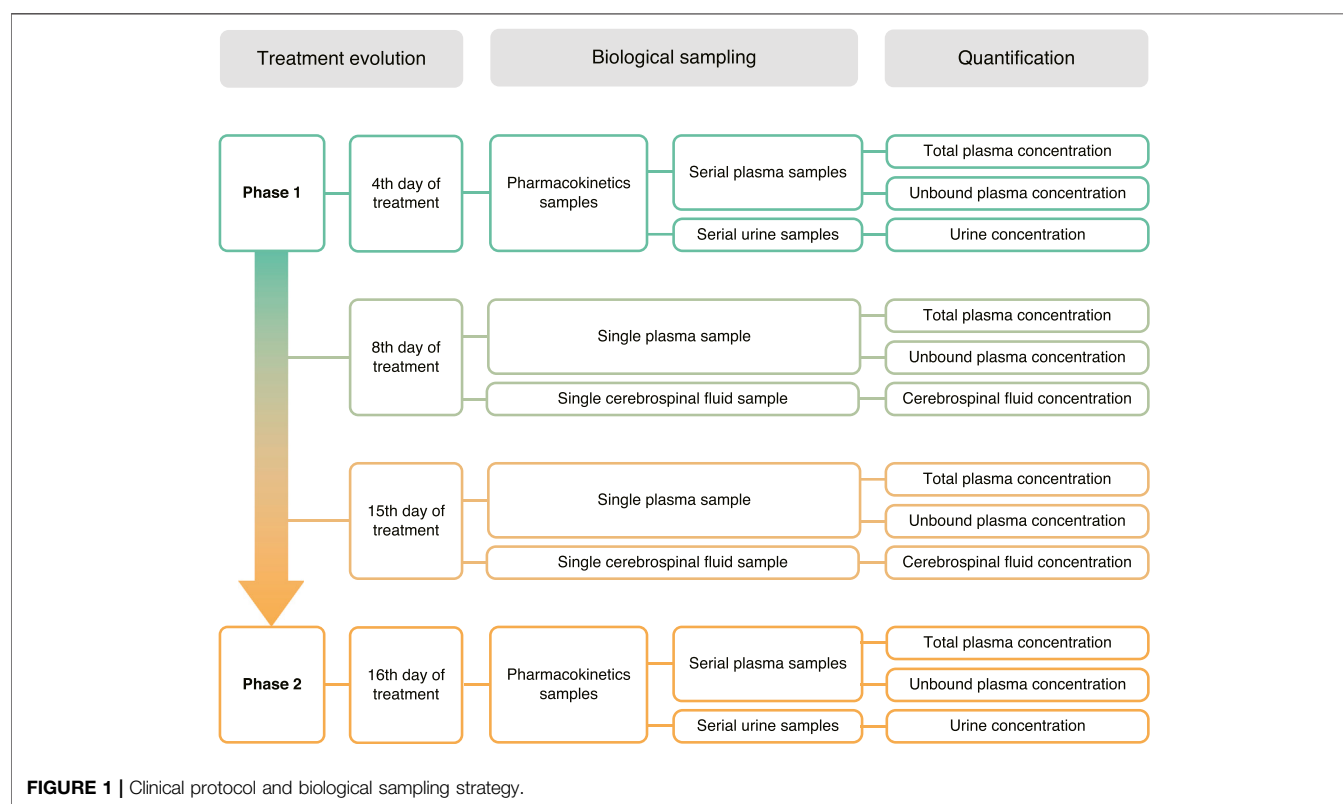
2.7 Pharmacokinetics Analysis

The pharmacokinetic parameters were calculated with Phoenix WinNonlin™, version 8.3.3.33 (Certara USA, Inc., Princeton, NJ, United States) based on the plasma concentration versus time

TABLE 1 | Anthropometric, biochemical, and hematological parameters of a male patient treated for neurocryptococcosis with a dosing regimen of 100 mg of amphotericin B lipid complex.

	References	Pretreatment	Phase 1	Phase 2
Age (years)		35		
Height (m)		1.75		
Weight (kg)		—	54.15	56.3
Amphotericin B dose (mg day ⁻¹)			100	100
Amphotericin B dose (mg kg ⁻¹ day ⁻¹)			1.85	1.78
Body mass index (kg m ⁻²)	18.50–24.90	—	17.68	18.38
Creatinine (mg dl ⁻¹)	0.74–1.35	0.87	0.84	—
Urea (mg dl ⁻¹)	5.00–20.00	29.29	43.87	33.95
Alkaline phosphatase (U L ⁻¹)	44.00–147.00	115.7	163.18	—
Alanine aminotransferase (U L ⁻¹)	7.00–55.00	52.72	—	71.13
Aspartate aminotransferase (U L ⁻¹)	8.00–48.00	34.92	531.08	61.44
Gamma-glutamyltransferase (U L ⁻¹)	8.00–61.00	128.14	190.07	—
Erythrocyte count (×10 ⁶ μl ⁻¹)	4.35–6.65	4.2	4.08	3.67
Leucocyte count (×10 ³ μl ⁻¹)	3.4–9.6	3.2	1.5	1.6
Lymphocyte count (×10 ³ μl ⁻¹)	0.9–8.0	0.6	0.5	0.5
Neutrophil count (×10 ³ μl ⁻¹)	1.6–8.0	2.1	0.7	0.7
Platelet count (×10 ³ μl ⁻¹)	135–317	163	174	128
List of co-administered drugs		1	1, 2, 3, 4, 5, 6, 7	1, 2, 3, 4, 5, 6, 8, 9, 10

(1) isoniazid + rifampicin; (2) amphotericin B lipid complex; (3) fluconazole; (4) enoxaparin sodium; (5) dipyrrone; (6) omeprazole; (7) vitamin B₆; (8) dexchlorpheniramine; (9) sulfamethoxazole + trimethoprim; (10) nicotine transdermal patch.

**FIGURE 1 |** Clinical protocol and biological sampling strategy.

curve. AmB was assessed by non-compartmental analysis (NCA) with the linear trapezoidal linear interpolation method. Unbound fractions (F_u) were analyzed on the last five samples from the pharmacokinetics curve of each phase as well as on the plasma samples obtained simultaneously as CSF samples.

The amount of AmB excreted (A_e) in each spontaneous micturition event was calculated by multiplying the urinary concentrations (C_u) by the respective volume of urine collected (V_u). The amount excreted in 24 h was obtained by the sum of A_e obtained from each interval. The fraction of the

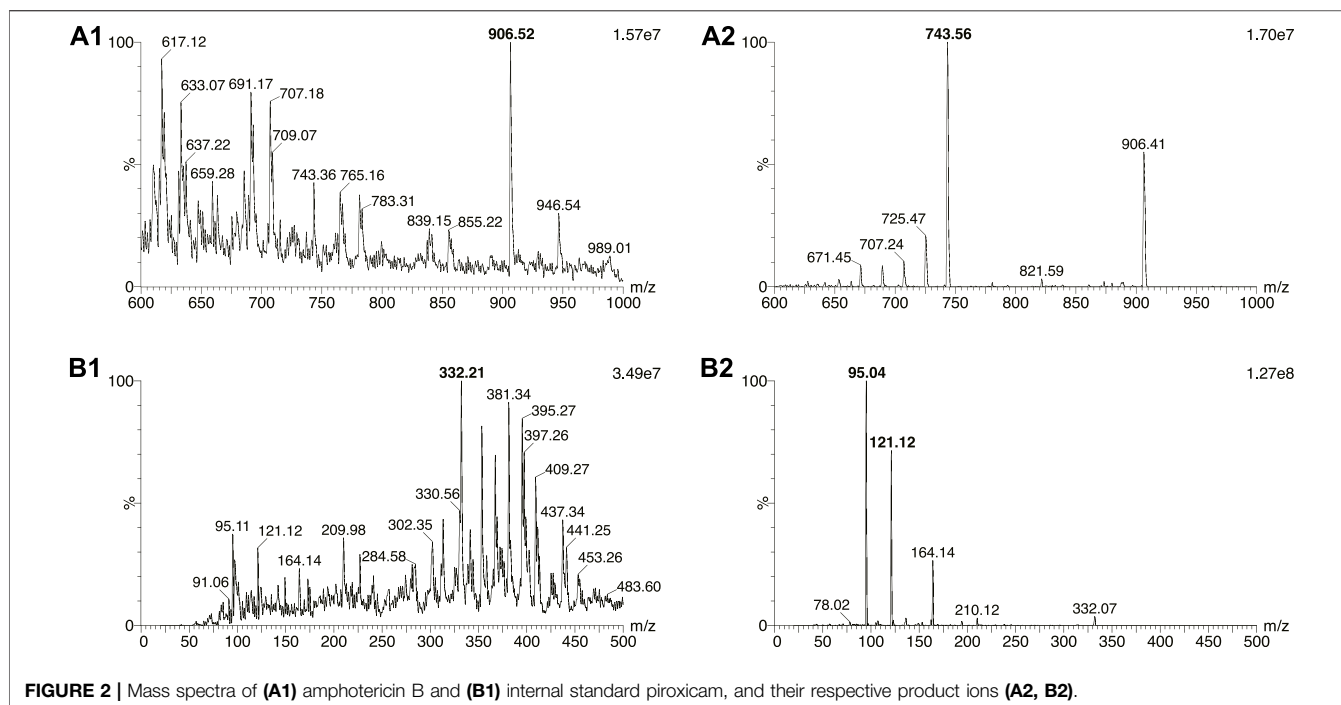


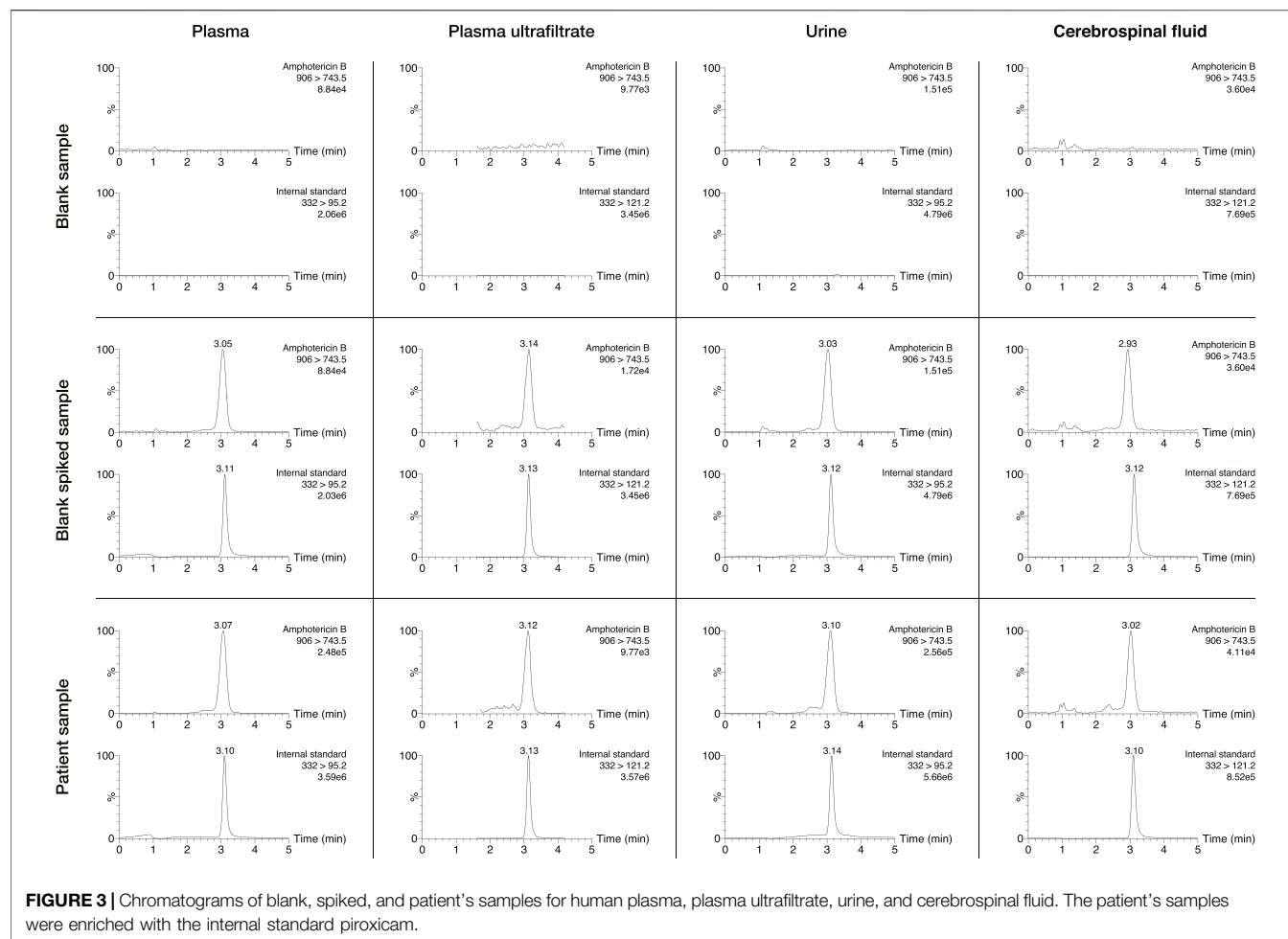
FIGURE 2 | Mass spectra of (A1) amphotericin B and (B1) internal standard piroxicam, and their respective product ions (A2, B2).

dose excreted into the urine (F_e) was calculated by dividing A_e by the dose (Ritschel and Kearns, 1999; Benet, 2010). The renal clearance (CL_{ren}) was calculated by multiplying the total clearance (CL) by the fraction of the dose excreted into the urine in 24 h (F_e). The hepatic clearance (CL_{hep}) was calculated by subtracting the renal clearance (CL_{ren}) from the total clearance (CL) (Benet, 2010).

3 RESULTS

The initial experiments of AmB analysis in plasma and urine were performed using the Micromass Quattro MicroTM triple quadrupole mass spectrometer (Waters Corporation, Milford, MA, United States). However, the equipment presented a lower sensitivity considering the expected AmB concentrations in biological samples. Thus, the methods were development using the system XEVO TQ-S[®] triple quadrupole mass spectrometer (Waters Corp., Milford, MA, United States) previously described. **Figure 2** shows the protonated ($[M + H]^+$) precursor ions and their respective product ions. AmB was monitored in the transition m/z 906 \rightarrow 743. The IS piroxicam was chosen in the absence of a commercially available deuterated standard for AmB. Piroxicam was a suitable IS for a sample preparation method applying protein precipitation and presented retention times similar to AmB (differences of 0.10–0.19 min depending on the biological matrix, **Figure 3**). The sequential analysis in plasma, plasma ultrafiltrate, urine, and CSF are presented in **Figure 3**. The methods for quantifying of AmB in the four biological matrices were applied to the investigation of the pharmacokinetics of AmB in a male patient treated for

neurocryptococcosis. The patient's anthropometric, biochemical, and hematological parameters, as well as a complete list of medications in use by the time of phases 1 and 2, are presented in **Table 1**. The validation parameters for the methods of quantification of AmB in plasma, plasma ultrafiltrate, urine, and CSF can be found in **Table 2**. All validation parameters relative errors were within the range of $\pm 15\%$ and coefficients of variation below 1%. The pharmacokinetic profiles of AmB in each phase of the study are shown in **Figure 4** for both plasma and urine. The unbound concentrations of AmB in plasma were determined in the last five samples comprising the terminal elimination phase and are presented in **Figure 4** and **Table 3**, with mean values of 3.25 (± 0.22) % in phase 1 and 2.99 (± 0.27) % in phase 2. Two CSF samples were obtained in the time between phases 1 and 2. The concentration of AmB in these samples and the relationships between the concentration in CSF and plasma as total and unbound concentrations collected simultaneously are described in **Table 4**. The ratios of total plasma concentration by CSF concentration ratios were 30.90 and 19.53, respectively at the 8th and 15th days of treatment with AmB. In contrast, the ratios of unbound plasma concentration by CSF concentration were 0.77 and 0.44, respectively at the 8th and 15th days, demonstrating the increasing concentrations of AmB in the CSF throughout the treatment. An overview of AmB concentrations determined in plasma as total and unbound concentrations and in CSF are shown in a comprehensive timeline in **Figure 5**. **Table 5** presents the pharmacokinetic parameters of AmB, the amount excreted into the urine in 24 h, and the renal and hepatic clearances. All datasets generated for this study are included in the article's Supplementary Material.



4 DISCUSSION

The present study aimed to develop a method capable of quantifying AmB in CSF at any given time of the treatment in addition to plasma, plasma ultrafiltrate, and urine. The quantification of AmB in CSF has been a methodological challenge from the last decades to the present day, with studies reporting a large number of CSF samples in which AmB concentrations are undetectable or below the LLOQ in a fraction of or all samples, despite the observation of clinical efficacy (Leenders et al., 1997; Wurthwein et al., 2005; Hamill et al., 2010; Strenger et al., 2014). Thus, the method developed for quantification of AmB in human CSF combines the convenience of a smaller sample volume (100 μ l) and lower LLOQ (0.1 ng ml⁻¹) compared to those reported in the literature, with sample volumes of 1,000 μ l (Liu et al., 1995), 500 μ l (Strenger et al., 2014), and 250 μ l (Wirth et al., 2018) and LLOQ's of 500 ng ml⁻¹ (Strenger et al., 2014), 1 ng ml⁻¹ (Liu et al., 1995), and 0.5 ng ml⁻¹ (Xiong et al., 2009).

The development of the chromatographic method was initially carried out following the method described by Su et al. (2018), which uses an Ascentis C18 reverse-phase column, 5 μ m particles,

50 \times 4.6 mm and applies a gradient of 0.2% formic acid and 5 mM ammonium acetate in water (solution A) and 0.2% formic acid in acetonitrile (solution B). During the parameters optimization step with an infusion of AmB, it was observed in our experiments that only 0.2% formic acid contributed to the increase in the signal of the analyte. The initial tests were performed using the reversed-phases columns Purospher RP-18e (123 \times 3 mm), RP-Select B (125 \times 4.6 mm), and RP-Select B (250 \times 4.6 mm), all with 5 μ m particles maintained at 40°C and protected by a guard column of the same specification. The columns were tested in different mobile phase combinations containing 0.1 and 0.2% formic acid in both water and acetonitrile in the proportions 70:30, 60:40, 50:50, 40:60 and 30:70 (v/v). The best chromatographic profile for the analysis of AmB in plasma and urine samples was observed in the RP-Select B reverse phase column (125 \times 4.6 mm) with a mobile phase consisting of a mixture of 0.1% formic acid in water and 0.1% formic acid in acetonitrile in a 40:60 (v/v) ratio. However, analysis of AmB in CSF and plasma ultrafiltrate samples required changing the proportion of mobile phase constituents (50:50, v/v) to obtain better shaped and more symmetrical chromatographic peaks (Figure 3). Initial tests were performed with the column maintained at 40°C (Su

TABLE 2 | Validation for the methods of quantification of amphotericin B in plasma, plasma ultrafiltrate, urine, and cerebrospinal fluid.

	Plasma		Plasma ultrafiltrate		Urine		Cerebrospinal fluid	
Matrix Effect								
Matrix factor normalized by IS (CV, %)	1.58 (8%)		1.41 (13%)		1.74 (9%)		1.14 (9%)	
Linearity (ng ml⁻¹)	5–1,000		0.625–250		5–1,000		0.1–250	
Linear equation	y = 0.00121752 · x + 0.00369099		y = 0.271171 · x – 0.0166566		y = 0.00139923 · x + 0.0026258		y = 0.058589 · x + 0.000938927	
<i>r</i> ²	0.996708		0.981444		0.997705		0.992380	
Non-specific binding to the membrane			CV	RE				
LCQC	—		11	–14	—		—	
HCQC	—		8	15	—		—	
Precision (CV, %) and Accuracy (RE, %)	CV	RE	CV	RE	CV	RE	CV	RE
Within-run								
LLOQQC	7	5	5	5	7	–1	5	7
LCQC	2	1	6	11	3	–2	1	6
MCQC	2	0	2	–6	3	1	2	–4
HCQC	2	–1	13	2	4	–5	1	–2
DQC (plasma 1:4, v/v; plasma ultrafiltrate 1:10, v/v; urine 1:4, v/v)	2	–4	4	–10	3	6	—	—
Between-run								
LLOQQC	9	–1	13	–1	7	3	7	0
LCQC	5	2	8	12	5	0	2	6
MCQC	6	0	11	1	4	4	3	–2
HCQC	4	–2	10	0	7	–4	5	–8
DQC (plasma 1:4, v/v; plasma ultrafiltrate 1:10, v/v; urine 1:4, v/v)	5	1	3	–9	4	6	—	—
Stabilities	CV	RE	CV	RE	CV	RE	CV	RE
Freeze and thaw	–70°C, 25°C		—		–70°C, 25°C		–70°C, 25°C	
LCQC	6	–9	—	—	5	–6	5	4
HCQC	4	–12	—	—	3	2	4	8
Short-term temperature	25°C, 4 h		25°C, 2 h		25°C, 4 h		4 °C, 2 h	
LCQC	2	6	6	0	5	–6	3	2
HCQC	3	2	3	–6	6	–1	1	–2
Post-preparative	15°C, 24 h		12°C, 20 h		15°C, 24 h		15°C, 24 h	
LCQC	6	–2	5	8	7	–1	3	–3
HCQC	2	–11	6	3	3	–2	2	–9

IS: internal standard; CV: coefficient of variation, expressed as percentage; RE: relative error (inaccuracy) expressed as percentage; LLOQQC: lowest limit of quantification quality control; LCQC: low concentration quality control, MCQC: medium concentration quality control; HCQC: high concentration quality control; DQC: dilution quality control.

et al., 2018), but considering that at 25°C the chromatographic profile remains constant, the lowest temperature was chosen.

Considering the absence of a commercially available deuterated standard for AmB, the search for an IS was based on previously published methods. Piroxicam, used in previous studies with spectrophotometric detection, proved to also be adequate for the protein precipitation process and mass spectrometry detection used in the present study (Campanero et al., 1997; Echevarria et al., 1998; Hope et al., 2012). It is noteworthy that piroxicam was monitored at transition *m/z* 332 → 95 in the analysis in plasma and urine, and at transition *m/z* 332 → 121 in the ana analysis in plasma ultrafiltrate and CSF to avoid interference with matrices components (Figure 3).

The methods for the chromatographic analysis of AmB in biological matrices use the solid-phase extraction technique, which makes the analysis of a large number of samples more expensive (Liu et al., 1995; Lee et al., 2001; Bekersky et al., 2002b;

Bellmann et al., 2003; Su et al., 2018; Van Daele et al., 2021). Sample preparation was initially tested with the intention of replacing solid-phase extraction by protein precipitation, aiming for lower costs of analysis and shorter times of sample preparations, key aspects of pharmacokinetic studies in which large numbers of samples are analyzed using sensitive methods. The best result was obtained by precipitating plasma, plasma ultrafiltrate, urine, and CSF samples with a 0.1% formic acid solution in acetonitrile, followed by dilution of the respective supernatants with a 0.1% formic acid solution in water.

The preparation of plasma, plasma ultrafiltrate, urine, and CSF samples with protein precipitation followed by dilution of the supernatants resulted in the absence of any significant matrix effect, evaluated as the observation of the coefficients of variation of matrix factor values normalized by the IS less than 10% (Table 2).

The linearity of the methods for the analysis of the concentration of AmB in plasma (5–1,000 ng ml⁻¹), plasma

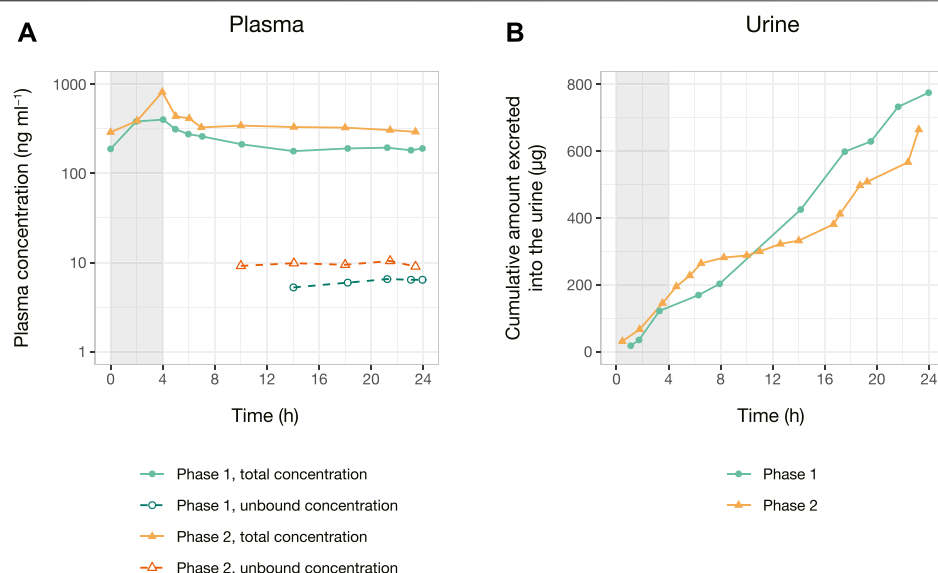


FIGURE 4 | Pharmacokinetics data of a patient treated for neurocryptococcosis with 100 mg of amphotericin B lipid complex as a 4 h i. v. infusion. Total and unbound plasma concentration versus time curve **(A)** is presented in ng ml⁻¹, and the cumulative amount excreted into the urine versus time curve **(B)** is presented in μg. Phase 1 was conducted on the 4th day of administration of amphotericin B, whereas phase 2 was conducted on the 16th day of treatment with the drug. The gray area indicates the length of the i. v. infusion (4 h) in both phases.

TABLE 3 | Unbound fraction of amphotericin B in plasma. The unbound concentration was determined in the last five plasma samples comprising the terminal elimination phase.

Phase 1 (4th day)	14 h	18 h	21 h	23 h	24 h	Mean (%)	SD	CV (%)
Total concentration (ng ml ⁻¹)	178.03	190.92	194.72	182.28	190.74			
Unbound concentration (ng ml ⁻¹)	5.25	5.94	6.51	6.40	6.40			
F _u (%)	2.95	3.11	3.34	3.51	3.36	3.25	0.22	6.83
Phase 2 (16th day)	10 h	14 h	18 h	21 h	23 h	Mean (%)	SD	CV (%)
Total concentration (ng ml ⁻¹)	344.72	331.94	326.86	306.94	293.45			
Unbound concentration (ng ml ⁻¹)	9.16	9.82	9.43	10.40	9.01			
F _u (%)	2.66	2.96	2.89	3.39	3.07	2.99	0.27	8.97

F_u: unbound fraction in plasma.

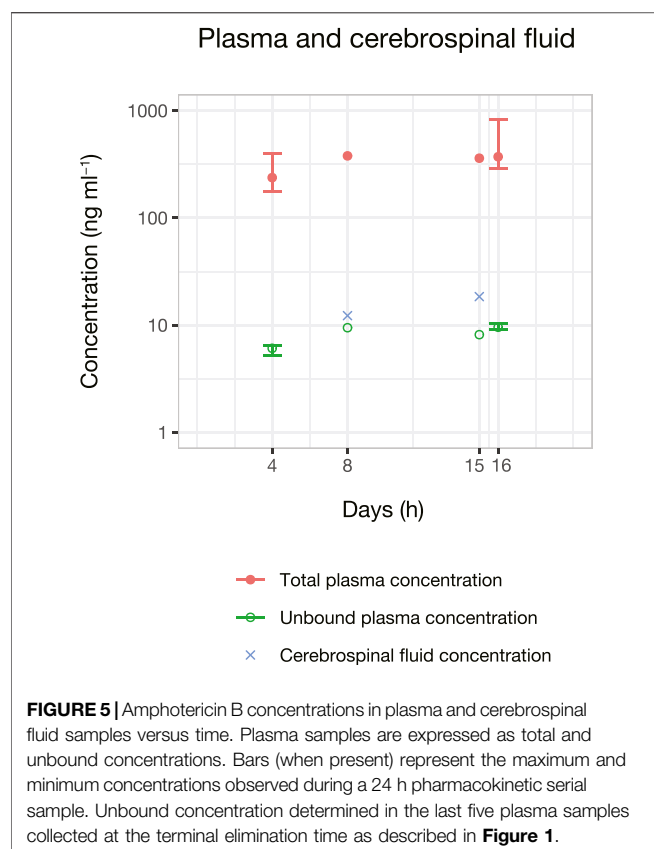
TABLE 4 | Total and unbound concentrations of amphotericin B in plasma and in cerebrospinal fluid samples.

	8th day	15th day
Total plasma concentration (ng ml ⁻¹)	378.83	360.25
Unbound plasma concentration (ng ml ⁻¹)	9.46	8.15
F _u (%)	2.50	2.26
CSF concentration (ng ml ⁻¹)	12.26	18.45
Total plasma concentration/CSF concentration ratio	30.90	19.53
Unbound plasma concentration/CSF concentration ratio	0.77	0.44

F_u: unbound fraction in plasma. CSF: cerebrospinal fluid.

ultrafiltrate (0.6–250 ng ml⁻¹), urine (5–1,000 ng ml⁻¹), and in CSF (0.1–250 ng ml⁻¹, **Table 2**) proved to be adequate for the application in clinical pharmacokinetics studies, with determination coefficients (r^2) greater than 0.98 for plasma ultrafiltrate and 0.99 for the other matrices. The wide linear range will enable the quantification of AmB in biological fluids

from patients treated with different AmB formulations, such as deoxycholate or lipid formulations (Ayestarán et al., 1996). The upper limit of quantification (ULOQ) values of 1,000 ng ml⁻¹ of plasma or urine and 250 ng ml⁻¹ of plasma ultrafiltrate and CSF were the highest within the linear ranges for which no carryover effect was observed. The methods developed and validated in this study using aliquots of 25 μl of human plasma or urine and 100 μl of human plasma ultrafiltrate and CSF, with LLOQ values of 5 ng ml⁻¹ for plasma or urine, 0.6 ng ml⁻¹ for plasma ultrafiltrate, and 0.1 ng ml⁻¹ for CSF can be considered the most sensitive ones described so far. Overall, the methods described here are 3.2–1,500 times more sensitive than the LC-MS/MS methods previously described in the literature (Lee et al., 2001; Bekersky et al., 2002a; Xiong et al., 2009; Deshpande et al., 2010; Qin et al., 2012; Al-Quadeib et al., 2014; Strenger et al., 2014; Su et al., 2018; Van Daele et al., 2021). Despite reaching the highest sensitivity in the literature, the methods could be further adjusted to use even lower sample volumes by adding a final concentration step, in



which the supernatants are evaporated and reconstituted in lower volumes. Even though undesirable for clinical pharmacokinetic studies, since it adds a new time-consuming step, this modification would allow for the methods to be applied to animal models, such as mice.

The methods of analysis of total concentrations of AmB in plasma, urine, and CSF and the unbound concentration in plasma proved to be precise and accurate, with coefficients of variation and relative error values below 12% (**Table 2**). The freeze and thaw, short-term temperature, and post-preparative stabilities studies showed coefficients of variation and relative error values equal to or less than 12% when quantified with freshly prepared calibration curves (**Table 2**).

AmB is a highly lipophilic drug administered parenterally due to its low oral absorption. The administration of AmB in lipid formulation results in faster AmB accumulation in peripheral tissues, in lower plasma concentrations, and minimizes adverse reactions compared to the deoxycholate formulation (Ayestarán et al., 1996). The methods validated in the present study were applied to investigate the pharmacokinetics of AmB following infusions of 100 mg every 24 h for 16 days administered as a lipid complex throughout the treatment of a neurocryptococcosis patient.

All collected biological samples (**Figure 1**) were quantified considering the high sensitivity of the method. It is important to highlight that AmB was successfully quantified in CSF samples collected on the 8th and 15th days of the treatment (**Figure 5**).

TABLE 5 | Pharmacokinetics parameters of amphotericin B in a patient with neurocryptococcosis at the beginning and at the end of the treatment.

	Phase 1	Phase 2
Amphotericin B dose (mg)	100	100
Amphotericin B dose (mg kg ⁻¹)	1.85	1.85
C _{max} (ng ml ⁻¹)	402.43	820.02
t _{1/2} λ _z (h)	29.89	35.07
λ _z (h ⁻¹)	0.023	0.020
AUC ₀₋₂₄ (h ng ml ⁻¹)	5642.79	8671.01
AUMC ₀₋₂₄ (h ² ng ml ⁻¹)	58,789.75	92,773.66
MRT (h)	8.42	8.70
A _e (μg)	775.17	664.70
F _{el} (%)	0.008	0.007
V _{ss} (L)	302.94	206.89
V _{ss} (L kg ⁻¹)	5.59	3.67
CL (L h ⁻¹)	7.21	4.25
CL (L h ⁻¹ kg ⁻¹)	0.133	0.076
CL _{ren} (L h ⁻¹)	0.056	0.028
CL _{ren} (L h ⁻¹ kg ⁻¹)	0.00103	0.00050
CL _{hep} (L h ⁻¹)	7.15	4.22
CL _{hep} (L h ⁻¹ kg ⁻¹)	0.077	0.047

C_{max}, maximum observed concentration; t_{1/2} λ_z, terminal elimination half-life; λ_z, terminal elimination rate constant; AUC₀₋₂₄, area under the plasma concentration versus time curve, from time zero to 24 h; AUMC₀₋₂₄, area under the first moment of the plasma concentration versus time curve, from time zero to 24 h; MRT, mean residence time; A_e, amount of the dose recovered in the urine; F_{el}, fraction of the dose excreted into the urine; V_{ss}, volume of distribution in the steady state; CL, total clearance; CL_{ren}, renal clearance; CL_{hep}, hepatic clearance.

Clinical pharmacokinetics of AmB lipid complex was previously reported in healthy volunteers (Kan et al., 1991) and in patients with systemic fungal infections (Adedoyin et al., 2000). The AmB pharmacokinetic parameters such as total clearance and volume of distribution at steady state are dose-dependent considering that the drug accumulates in the tissues. The cited authors observed total clearance values in healthy volunteers ranging from 0.07 to 0.09 L h⁻¹ kg⁻¹, values similar to those presented in **Table 5** for the patient with neurocryptococcosis (0.133 L h⁻¹ kg⁻¹ on the 8th day to 0.076 L h⁻¹ kg⁻¹ on the 15th day). However, the administration of AmB lipid complex at 5 mg kg⁻¹ day⁻¹ to patients with fungal infections resulted in higher total clearance values (17.8 ± 5.2 L h⁻¹) compared to the values presented in **Table 5** for the investigated patient with neurocryptococcosis treated with daily infusions of 100 mg (7.21 L h⁻¹ on the 8th day to 4.25 L h⁻¹ on the 15th day). However, when the different studies are dose-normalized, all the values are equivalent. Considering that in the present study AmB was also quantified in urine, it was possible to verify that total clearance values are very similar to hepatic clearance (0.077 L h⁻¹ kg⁻¹ on the 8th day and 0.047 L h⁻¹ kg⁻¹ on the 15th day) due to its elimination mainly by biliary secretion; **Table 5**.

AmB lipid complex is highly distributed. Volumes of distribution at steady state were also evaluated in healthy volunteers (1.7–3.9 L kg⁻¹) (Kan et al., 1991) and in patients with systemic fungal infections (865 ± 347 L) (Adedoyin et al., 2000). Volumes of distribution at steady state for the investigated patient were 5.59 (8th day) to 3.67 L kg⁻¹ (15th day) (**Table 5**); values close to the cited studies when dose-normalized.

AmB unbound fraction following the lipid formulation was evaluated in the investigated neurocryptococcosis patient. The

data reported in **Tables 3** and **4** show AmB unbound fraction values of 3.25 (4th day), 2.50 (8th day), 2.26 (15th day), and 2.99 (16th day). Although there are no reports in the literature about AmB unbound fraction following the lipid formulation, the administration of other formulations such as liposomal or deoxycholate also result in unbound fraction values of 4.5 and 20.6%, respectively (Bekersky et al., 2002b).

In the present study, total plasma concentration/CSF concentration ratios ranged from 30.90 (8th day) to 19.53 (15th day), whereas unbound plasma concentration/CSF concentration ratio ranged from 0.77 (8th day) to 0.44 (15th day), showing increasing concentrations of AmB in the CSF with the evolution of the treatment. Strenger et al. (2014) reported total plasma concentration/CSF concentration ratios ranging from 124 to 2,391 in haemato-oncological pediatric patients treated with liposomal AmB ($3 \text{ mg kg}^{-1} \text{ day}^{-1}$) in samples evaluated from 0 to 48 h after drug infusion. However, total plasma concentration/CSF concentration and unbound plasma concentration/CSF concentration ratios were not found in the available literature following the administration of lipid formulation.

In conclusion, the present study described the most complete and sensitive methods for AmB analysis in plasma, plasma ultrafiltrate, urine, and CSF applied to a clinical pharmacokinetic study following the administration of the drug as a lipid complex in one patient with neurocryptococcosis. Previous clinical studies failed to fully assess all biological matrices due to low sensitivity and higher matrices volumes, especially for CSF. The method can be applied to investigate the pharmacokinetics of AmB in CSF at any given time of the treatment.

DATA AVAILABILITY STATEMENT

The original contributions presented in the study are included in the article/**Supplementary Material**, further inquiries can be directed to the corresponding author.

REFERENCES

- Adedoyin, A., Swenson, C. E., Bolcsak, L. E., Hellmann, A., Radowska, D., Horwith, G., et al. (2000). A Pharmacokinetic Study of Amphotericin B Lipid Complex Injection (Abelcet) in Patients with Definite or Probable Systemic Fungal Infections. *Antimicrob. Agents Chemother.* 44, 2900–2902. doi:10.1128/aac.44.10.2900-2902.2000
- Al-Quadeib, B. T., Radwan, M. A., Siller, L., Mutch, E., Horrocks, B., Wright, M., et al. (2014). Therapeutic Monitoring of Amphotericin B in Saudi ICU Patients Using UPLC MS/MS Assay. *Biomed. Chromatogr.* 28, 1652–1659. doi:10.1002/bmc.3198
- Ayestarán, A., López, R. M., Montoro, J. B., Estibalez, A., Pou, L., Julià, A., et al. (1996). Pharmacokinetics of Conventional Formulation versus Fat Emulsion Formulation of Amphotericin B in a Group of Patients with Neutropenia. *Antimicrob. Agents Chemother.* 40, 609–612. doi:10.1128/AAC.40.3.609
- Beggs, W. H. (1978). Kinetics of Amphotericin B Decay in a Liquid Medium and Characterization of the Decay Process. *Curr. Microbiol.* 1, 301–304. doi:10.1007/BF02601687
- Bekersky, I., Fielding, R. M., Dressler, D. E., Lee, J. W., Buell, D. N., and Walsh, T. J. (2002a). Pharmacokinetics, Excretion, and Mass Balance of Liposomal

ETHICS STATEMENT

The studies involving human participants were reviewed and approved by the Research Ethics Committee of the School of Pharmaceutical Sciences of Ribeirão Preto, University of São Paulo (CAAE: 96780618.7.0000.5403) and the Research Ethics Committee of the General Hospital of the Ribeirão Preto Medical School, University of São Paulo (CAEE: 96780618.7.3001.5440). The patients/participants provided their written informed consent to participate in this study.

AUTHOR CONTRIBUTIONS

LP: Conceptualization, investigation, formal analysis; writing. MM: Investigation. AS: Investigation. FV: Investigation. TH: Resources. BF: Resources. RM: Resources. EC: Conceptualization, funding acquisition. LW-A: Conceptualization, investigation, funding acquisition. VL: Conceptualization, funding acquisition, project administration, writing.

FUNDING

This study was supported by the São Paulo Research Foundation (FAPESP, Brazil, Process 2018/0516-3, Brazil), the Coordination for the Improvement of Higher Education Personnel (CAPES, Brazil, Finance Code 001) and the Brazilian National Council for Scientific and Technological Development (CNPq, Brazil, Processes 303 142/2019-7 and 165620/2018-8).

SUPPLEMENTARY MATERIAL

The Supplementary Material for this article can be found online at: <https://www.frontiersin.org/articles/10.3389/fchem.2021.782131/full#supplementary-material>

- Amphotericin B (AmBisome) and Amphotericin B Deoxycholate in Humans. *Antimicrob. Agents Chemother.* 46, 828–833. doi:10.1128/AAC.46.3.828-833.2002
- Bekersky, I., Fielding, R. M., Dressler, D. E., Lee, J. W., Buell, D. N., and Walsh, T. J. (2002b). Plasma Protein Binding of Amphotericin B and Pharmacokinetics of Bound versus Unbound Amphotericin B after Administration of Intravenous Liposomal Amphotericin B (AmBisome) and Amphotericin B Deoxycholate. *Antimicrob. Agents Chemother.* 46, 834–840. doi:10.1128/AAC.46.3.834-840.2002
- Bellmann, R., Egger, P., Gritsch, W., Bellmann-Weiler, R., Joannidis, M., Kaneider, N., et al. (2003). Amphotericin B Lipid Formulations in Critically Ill Patients on Continuous Veno-Venous Haemofiltration. *J. Antimicrob. Chemother.* 51, 671–681. doi:10.1093/jac/dkg139
- Benet, L. Z. (2010). Clearance (Née Rowland) Concepts: a Downdate and an Update. *J. Pharmacokinet. Pharmacodyn.* 37, 529–539. doi:10.1007/s10928-010-9187-8
- Benson, J. M., and Nahata, M. C. (1988). Clinical Use of Systemic Antifungal Agents. *Clin. Pharm.* 7, 424–438. Available at: <http://www.ncbi.nlm.nih.gov/pubmed/3042267> (Accessed October 4, 2017).
- Black, K. E., and Baden, L. R. (2007). Fungal Infections of the CNS. *CNS Drugs* 21, 293–318. doi:10.2165/00023210-200721040-00004
- Campanero, M. A., Zamarreño, A. M., Diaz, M., Dios-Vieitez, M. C., and Azanza, J. R. (1997). Development and Validation of an HPLC Method

- for Determination of Amphotericin B in Plasma and Sputum Involving Solid Phase Extraction. *Chromatographia* 46, 641–646. doi:10.1007/BF02490525
- Coelho, C., Bocca, A. L., and Casadevall, A. (2014). The Tools for Virulence of *Cryptococcus Neoformans*. *Adv. Appl. Microbiol.* 87, 1–41. doi:10.1016/B978-0-12-800261-2.00001-3
- Cordon-Cardo, C., O'Brien, J. P., Casals, D., Rittman-Grauer, L., Biedler, J. L., Melamed, M. R., et al. (1989). Multidrug-resistance Gene (P-Glycoprotein) Is Expressed by Endothelial Cells at Blood-Brain Barrier Sites. *Proc. Natl. Acad. Sci.* 86, 695–698. doi:10.1073/pnas.86.2.695
- Deshpande, N. M., Gangrade, M. G., Kekare, M. B., and Vaidya, V. V. (2010). Determination of Free and Liposomal Amphotericin B in Human Plasma by Liquid Chromatography-Mass Spectroscopy with Solid Phase Extraction and Protein Precipitation Techniques. *J. Chromatogr. B* 878, 315–326. doi:10.1016/j.jchromb.2009.11.036
- Durski, K. N., Kuntz, K. M., Yasukawa, K., Virnig, B. A., Meya, D. B., and Boulware, D. R. (2013). Cost-Effective Diagnostic Checklists for Meningitis in Resource-Limited Settings. *JAIDS J. Acquir. Immune Defic. Syndr.* 63, e101–e108. doi:10.1097/QAI.0b013e31828e1e56
- Echevarría, I., Barturen, C., Renedo, M. J., and Dios-Viéitez, M. C. (1998). High-performance Liquid Chromatographic Determination of Amphotericin B in Plasma and Tissue. Application to Pharmacokinetic and Tissue Distribution Studies in Rats. *J. Chromatogr. A* 819, 171–176. doi:10.1016/S0021-9673(98)00425-7
- European Medicines Agency (2011). *Guideline on Bioanalytical Method Validation*. Available at https://www.ema.europa.eu/en/documents/scientific-guideline/guideline-bioanalytical-method-validation_en.pdf (Accessed September 2021).
- Groll, A. H., Giri, N., Petraitis, V., Petraitiene, R., Candelario, M., Bacher, J. S., et al. (2000). Comparative Efficacy and Distribution of Lipid Formulations of Amphotericin B in Experimental *Candida albicans* Infection of the Central Nervous System. *J. Infect. Dis.* 182, 274–282. doi:10.1086/315643
- Hamill, R. J., Sobel, J. D., El-Sadr, W., Johnson, P. C., Graybill, J. R., Javaly, K., et al. (2010). Comparison of 2 Doses of Liposomal Amphotericin B and Conventional Amphotericin B Deoxycholate for Treatment of AIDS-Associated Acute Cryptococcal Meningitis: A Randomized, Double-Blind Clinical Trial of Efficacy and Safety. *Clin. Infect. Dis.* 51, 225–232. doi:10.1086/653606
- Hope, W. W., Goodwin, J., Felton, T. W., Ellis, M., and Stevens, D. A. (2012). Population Pharmacokinetics of Conventional and Intermittent Dosing of Liposomal Amphotericin B in Adults: a First Critical Step for Rational Design of Innovative Regimens. *Antimicrob. Agents Chemother.* 56, 5303–5308. doi:10.1128/AAC.00933-12
- Hosey, C. M., Chan, R., and Benet, L. Z. (2016). BDDCS Predictions, Self-Correcting Aspects of BDDCS Assignments, BDDCS Assignment Corrections, and Classification for More Than 175 Additional Drugs. *AAPS J.* 18, 251–260. doi:10.1208/s12248-015-9845-2
- Jarvis, J. N., Meintjes, G., Williams, A., Brown, Y., Crede, T., and Harrison, T. S. (2010). Adult meningitis in a setting of high HIV and TB prevalence: findings from 4961 suspected cases. *BMC Infect. Dis.* 10, 67. doi:10.1186/1471-2334-10-67
- Kan, V. L., Bennett, J. E., Amantea, M. A., Smolskis, M. C., McManus, E., Grasela, D. M., and Sherman, J. W. (1991). Comparative safety, tolerance, and pharmacokinetics of amphotericin B lipid complex and amphotericin B desoxycholate in healthy male volunteers. *Journal of Infectious Diseases* 164, 418–421. doi:10.1093/INFDIS/164.2.418
- Lee, J. W., Petersen, M. E., Lin, P., Dressler, D., and Bekersky, I. (2001). Quantitation of Free and Total Amphotericin B in Human Biologic Matrices by a Liquid Chromatography Tandem Mass Spectrometric Method. *Therapeutic Drug Monitoring* 23, 268–276. doi:10.1097/00007691-200106000-00015
- Leenders, A. C. A. P., Reiss, P., Portegies, P., Clezy, K., Hop, W. C. J., Hoy, J., et al. (1997). Liposomal Amphotericin B (AmBisome) Compared with Amphotericin B Both Followed by Oral Fluconazole in the Treatment of AIDS-Associated Cryptococcal Meningitis. *AIDS* 11, 1463–1471. doi:10.1097/00002030-199712000-00010
- Lestner, J. M., Howard, S. J., Goodwin, J., Gregson, L., Majithiya, J., Walsh, T. J., et al. (2010). Pharmacokinetics and Pharmacodynamics of Amphotericin B Deoxycholate, Liposomal Amphotericin B, and Amphotericin B Lipid Complex in an *In Vitro* Model of Invasive Pulmonary Aspergillosis. *Antimicrob. Agents Chemother.* 54, 3432–3441. doi:10.1128/AAC.01586-09
- Liu, H., Davoudi, H., and Last, T. (1995). Determination of Amphotericin B in Cerebrospinal Fluid by Solid-phase Extraction and Liquid Chromatography. *J. Pharm. Biomed. Anal.* 13, 1395–1400. doi:10.1016/0731-7085(95)01566-4
- Nilsson-Ehle, I. (1977). High-pressure Liquid Chromatography as a Tool for Determination of Antibiotics in Biological Fluids. *Acta Pathol. Microbiol. Scand. Suppl.*, 61–66. Available at: <http://www.ncbi.nlm.nih.gov/pubmed/269648> [Accessed May 20, 2019].
- Pyrgos, V., Mickiene, D., Sein, T., Cotton, M., Fransesconi, A., Mizrahi, I., et al. (2010). Effects of Immunomodulatory and Organism-Associated Molecules on the Permeability of an *In Vitro* Blood-Brain Barrier Model to Amphotericin B and Fluconazole. *Antimicrob. Agents Chemother.* 54, 1305–1310. doi:10.1128/AAC.01263-09
- Pyrgos, V., Seitz, A. E., Steiner, C. A., Prevots, D. R., and Williamson, P. R. (2013). Epidemiology of Cryptococcal Meningitis in the US: 1997–2009. *PLoS One* 8, e56269. doi:10.1371/journal.pone.0056269
- Qin, W., Tao, H., Chen, Y., Chen, Z., and Wu, N. (2012). Sensitive, Accurate and Simple Liquid Chromatography-Tandem Mass Spectrometric Method for the Quantitation of Amphotericin B in Human or Minipig Plasma. *J. Chromatogr. Sci.* 50, 636–643. doi:10.1093/CHROMSCI/BMS049
- Qu, L., Qian, J., Ma, P., and Yin, Z. (2017). Utilizing Online-Dual-SPE-LC with HRMS for the Simultaneous Quantification of Amphotericin B, Fluconazole, and Fluorocytosine in Human Plasma and Cerebrospinal Fluid. *Talanta* 165, 449–457. doi:10.1016/j.talanta.2016.12.052
- Rajasingham, R., Rolfes, M. A., Tengsupakul, S., Mossel, E. C., Akampurira, A., Boulware, D. R., et al. (2015). Epidemiology of Meningitis in an HIV-Infected Ugandan Cohort. *Am. J. Trop. Med. Hyg.* 92, 274–279. doi:10.4269/ajtmh.14-0452
- Ritschel, W. A., and Kearns, G. L. (1999). *Handbook of Basic Pharmacokinetics*. 5th ed. Washington, DC, EUA: American Pharmaceutical Association.
- Schinkel, A. H., Wagenaar, E., Mol, C. A., and van Deemter, L. (1996). P-glycoprotein in the Blood-Brain Barrier of Mice Influences the Brain Penetration and Pharmacological Activity of many Drugs. *J. Clin. Invest.* 97, 2517–2524. doi:10.1172/JCI118699
- Shawahna, R. (2015). Physical and Metabolic Integrity of the Blood-Brain Barrier in HIV Infection: A Special Focus on Intercellular Junctions, Influx and Efflux Transporters and Metabolizing Enzymes. *Cdm* 16, 105–123. doi:10.2174/138920021602150713114715
- Shugarts, S., and Benet, L. Z. (2009). The Role of Transporters in the Pharmacokinetics of Orally Administered Drugs. *Pharm. Res.* 26, 2039–2054. doi:10.1007/s11095-009-9924-0
- Stevens, D. A., Clemons, K. V., Martinez, M., and Chen, V. (2015). The Brain, Amphotericin B, and P-Glycoprotein. *Antimicrob. Agents Chemother.* 59, 1386. doi:10.1128/AAC.04768-14
- Stone, N. R. H., Bicanic, T., Salim, R., and Hope, W. (2016). Liposomal Amphotericin B (AmBisome): A Review of the Pharmacokinetics, Pharmacodynamics, Clinical Experience and Future Directions. *Drugs* 76, 485–500. doi:10.1007/s40265-016-0538-7
- Strenger, V., Meintzer, A., Donnerer, J., Hofer, N., Dornbusch, H. J., Wanz, U., et al. (2014). Amphotericin B Transfer to CSF Following Intravenous Administration of Liposomal Amphotericin B. *J. Antimicrob. Chemother.* 69, 2522–2526. doi:10.1093/jac/dku148
- Su, C., Yang, H., Sun, H., Fawcett, J. P., Sun, D., and Gu, J. (2018). Bioanalysis of Free and Liposomal Amphotericin B in Rat Plasma Using Solid Phase Extraction and Protein Precipitation Followed by LC-MS/MS. *J. Pharm. Biomed. Anal.* 158, 288–293. doi:10.1016/j.jpba.2018.06.014
- Van Daele, R., de Beer, Y., Croes, S., Aarnoutse, R., Wauters, J., Maertens, J., et al. (2021). Ultra-performance Liquid Chromatography for Quantification of Amphotericin B Plasma Concentrations after Use of Liposomal Amphotericin B. *J. Antimicrob. Chemother.* 76, 961–966. doi:10.1093/JAC/DKAA515
- Williamson, P. R., Jarvis, J. N., Panackal, A. A., Fisher, M. C., Molloy, S. F., Loyse, A., et al. (2016). Cryptococcal Meningitis: Epidemiology, Immunology, Diagnosis and Therapy. *Nat. Rev. Neurol.* 13, 13–24. doi:10.1038/nrneurol.2016.167
- Wirth, F., de Azevedo, M. I., Pilla, C., Aquino, V. R., Neto, G. W., and Goldani, L. Z. (2018). Relationship between Intracranial Pressure and Antifungal Agents Levels in the CSF of Patients with Cryptococcal Meningitis. *Med. Mycol.* 56, 257–262. doi:10.1093/mmy/myx054
- Woods, M., Redmond, A., and Dancer, C. (2007). Fungal Infections of the central Nervous System: A Review of Fungal Pathogens and Treatment. *Neurol. India* 55, 251–259. doi:10.4103/0028-3886.35686

- Wu, J.-Q., Shao, K., Jiang, C., and Zhu, L.-P. (2015). Reply to "The Brain, Amphotericin B, and P-Glycoprotein". *Antimicrob. Agents Chemother.* 59, 1387. doi:10.1128/AAC.04774-14
- Würthwein, G., Groll, A. H., Hempel, G., Adler-Shohet, F. C., Lieberman, J. M., and Walsh, T. J. (2005). Population Pharmacokinetics of Amphotericin B Lipid Complex in Neonates. *Antimicrob. Agents Chemother.* 49, 5092–5098. doi:10.1128/AAC.49.12.5092-5098.2005
- Xiong, X., Zhai, S., and Liu, F. (2009). Determination of Amphotericin B in Human Cerebrospinal Fluid by LC-MS-MS. *Chroma* 70, 329–332. doi:10.1365/s10337-009-1112-1

Conflict of Interest: The authors declare that the research was conducted in the absence of any commercial or financial relationships that could be construed as a potential conflict of interest.

Publisher's Note: All claims expressed in this article are solely those of the authors and do not necessarily represent those of their affiliated organizations, or those of the publisher, the editors and the reviewers. Any product that may be evaluated in this article, or claim that may be made by its manufacturer, is not guaranteed or endorsed by the publisher.

Copyright © 2021 Pippa, Marques, Silva, Vilar, de Haes, Fonseca, Martinez, Coelho, Wichert-Ana and Lanchote. This is an open-access article distributed under the terms of the Creative Commons Attribution License (CC BY). The use, distribution or reproduction in other forums is permitted, provided the original author(s) and the copyright owner(s) are credited and that the original publication in this journal is cited, in accordance with accepted academic practice. No use, distribution or reproduction is permitted which does not comply with these terms.



Targeted On-Demand Screening of Pesticide Panel in Soil Runoff

Vikram Narayanan Dhamu¹, Suhashine Sukumar¹, Crisvin Sajee Kadambathil¹,
Sriram Muthukumar² and Shalini Prasad^{1*}

¹Department of Bioengineering, Biomedical Microdevices and Nanotechnology Laboratory, University of Texas at Dallas, TX, Richardson, United States, ²EnLiSense LLC, TX, Allen, United States

OPEN ACCESS

Edited by:

Camelia Bala,
University of Bucharest, Romania

Reviewed by:

Emmanuel Iheanyichukwu Iwuoha,
University of the Western Cape,
South Africa
Abhishek Mandal,
Indian Agricultural Research Institute
(ICAR), India

*Correspondence:

Shalini Prasad
Shalini.Prasad@utdallas.edu

Specialty section:

This article was submitted to
Analytical Chemistry,
a section of the journal
Frontiers in Chemistry

Received: 24 September 2021

Accepted: 11 November 2021

Published: 30 November 2021

Citation:

Dhamu VN, Sukumar S,
Kadambathil CS, Muthukumar S and
Prasad S (2021) Targeted On-Demand
Screening of Pesticide Panel in
Soil Runoff.
Front. Chem. 9:782252.
doi: 10.3389/fchem.2021.782252

Using pesticides is a common agricultural and horticultural practice to serve as a control against weeds, fungi, and insects in plant systems. The application of these chemical agents is usually by spraying them on the crop or plant. However, this methodology is not highly directional, and so only a fraction of the pesticide actually adsorbs onto the plant, and the rest seeps through into the soil base contaminating its composition and eventually leaching into groundwater sources. Electrochemical sensors which are more practical for *in situ* analysis used for pesticide detection in soil runoff systems are still in dearth, while the ones published in the literature are attributed with complex sensor modification/functionalization and preprocessing of samples. Hence, in this work, we present a highly intuitive electroanalytical sensor approach toward rapid (10 min), on-demand screening of commonly used pesticides—glyphosate and atrazine—in soil runoff. The proposed sensor functions based on the affinity biosensing mechanism driven via thiol cross-linker and antibody receptors that holistically behaves as a recognition immunoassay stack that is specific and sensitive to track test pesticide analytes. Then, this developed sensor is integrated further to create a pesticide-sensing ecosystem using a front-end field-deployable smart device. The method put forward in this work is compared and validated against a standard laboratory potentiostat instrument to determine efficacy, feasibility, and robustness for a point-of-use (PoU) setting yielding LoD levels of 0.001 ng/ml for atrazine and 1 ng/ml for glyphosate. Also, the ML model integration resulted in an accurate prediction rate of ~80% in real soil samples. Therefore, a universal pesticide screening analytical device is designed, fabricated, and tested for pesticide assessment in real soil runoff samples.

Keywords: field-deployable sensing platform, soil runoff sensor, pesticide screening, soil pollution analysis, environmental sensor, impedimetric biosensor

INTRODUCTION

There is a major requirement at present to address environmental sustainability in ecological and agricultural practices as highlighted by the United Nations “2030 Agenda for sustainable development” (Arduini et al., 2020). As a result of this proposition, there has been an influx in studies to develop biosensor technologies meant for green living and monitoring different areas in environmental and agri-food sectors. Despite these efforts, one particular vital component of the environment has been probed comparatively much more sparsely, namely, the soil ecosystem that directly and indirectly affects the agricultural health and throughput as well as ecosystem balance

(Bullock and Gregory, 2009). One specific problem is that the application of pesticides in crops and other plants often finds its way seeping into soil in large quantities, and there exists a leaching effect at the soil and groundwater sources (Kellogg et al., 2000). The effect caused by the pesticide residues in soil is two-fold: 1. There is a definite relationship between long-term, low-dose exposure of any kind either ingestion, inhalation, or through contact and human health effects such as immune suppression, hormone disruption, diminished intelligence, reproductive abnormalities, and cancer; 2. impact on the environment via surface/groundwater contamination and soil contamination-mediated damage to non-target species—soil biomass, and microorganisms causing decreased crop throughputs and food quality, affecting global food security (Aktar et al., 2009; Lo, 2010; Joko et al., 2017; Gunstone et al., 2021).

The potential for a sensor system that detects in field is given as follows: the levels of pesticide residues in soil runoff is immense and would be beneficial to understand the negative effect of mismanagement and overuse of pesticide agents on food safety and overall quality of life. This field-deployable sensor probe would help promote responsible agricultural practices and curb the overapplication of harmful agents to the soil (Ali et al., 2020). Currently, it is rare to quantify and test for pesticide residues in soil, and even if it is performed, it is done for mostly one analyte, while the field norm in assessing residue levels is reliant on mainly chromatographic techniques (LC-MS/MS, GC-HRMS) with the QuEChERS sample preparation methodology (Silva et al., 2019). Samples in the liquid state requiring complex preprocessing have been tested in different scientific studies and in some cases commercially available test kits utilizing different methods such as capillary electrophoresis (Chang and Liao, 2002), spectrophotometry (Catrinck et al., 2014), and liquid chromatography (Chamkasem and Harmon, 2016) which possess the desired sensitivity and selectivity. A comprehensive summary table has been created, detailing output metrics between different analytical methods versus the sensor performance as a function of processing steps involved, determination/detection time, and limit of detection (LoD), as given in the supplementary section (**Supplementary Table S1**). However, as mentioned previously, the cost of using these techniques is large overhead in terms of sample collection and transfer, need for sample processing, complex machinery, and reagents as well as the added costs associated with all these steps. Therefore, detection of these pesticides in trace levels in real time in the soil matrix (runoff water) is highly desirable with minimal or no pre-sample processing step involved.

Electroanalytical chemistry proves to be a viable choice of application for such a sensor to track pesticides in soil samples due to its feasibility for *in situ* analysis used as well as solving for the ASSURED criteria as given by the World Health Organization (WHO), wherein it denotes Affordable, Sensitive, Specific, User-friendly, Rapid, and robust, Equipment-free, and Deliverable to end-users (Lim and Bonanni, 2020). The proposed system would have to utilize minimally complex sensor modification/functionalization and no preprocessing of samples. By studying the levels of soil contaminant residues at the field

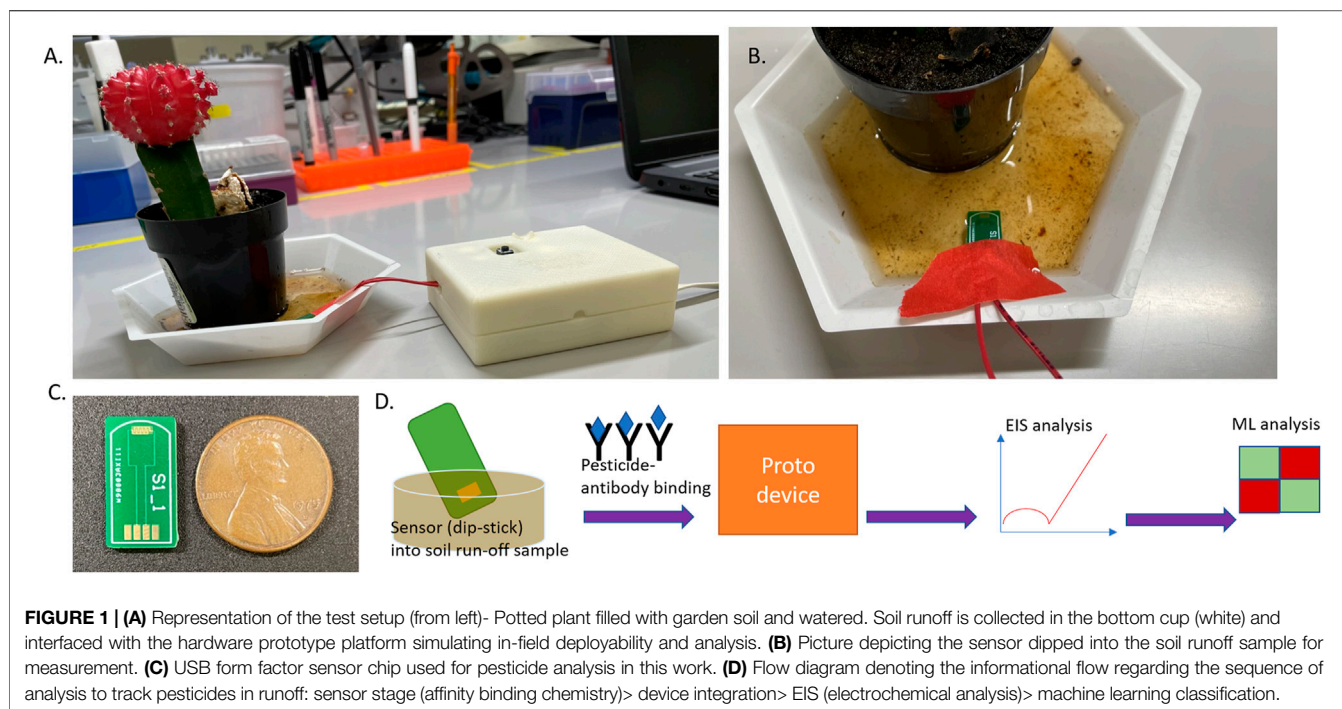
site, the sensor acts as a screening instrument for soil pollution levels.

Hence—citing all these factors and requirements—in this work, we evaluate an electroanalytical sensor approach toward rapid, on-demand screening of 2 commonly used pesticides in this proof-of-feasibility study—glyphosate and atrazine in soil runoff which have a half-life around 60 days¹ and 60–75 days (Hanson et al., 2020) in soil, respectively. The rationale behind testing these 2 particular pesticide groups is that recently with the agricultural and related developments and the introduction of genetically modified plants, the use of the pesticides such as glyphosate and atrazine has increased to a larger extend worldwide (Battaglin et al., 2009). Glyphosate [N-(phosphonomethyl)glycine] is a polar pesticide used to control the plant weeds by inhibiting the synthesis of amino acids required for the growth of the plants. The most commonly being used is genetically modified glyphosate-resistant crops such as corn, soybean, and cotton crops (Duke and Powles, 2008). Similarly, atrazine (2-chloro-4-ethylamino-6-isopropylamino-1,3,5-triazine) is another pesticide which is largely non-polar used for the pre- and post-emergence control of weeds, especially in sugarcane, maize, and sorghum crops (Oliveira et al., 2015). With the intense use of these two most used pesticides, several concerns have been raised due to the possible residue levels in the soil, water, and plants, a potential threat to the environment and human health (Van Bruggen et al., 2018). With the possible link to the human conditions such as the disruption of endocrine hormones, a potential cause of various cancers (Gillezeau et al., 2019), the U.S. Environmental Protection Agency (EPA) has set the maximum acceptable limit (MRL) of these pesticides in drinking water and various food commodities before they are being marketed (Ambrus, 2015).

In our previous work, we have shown a sensing methodology to test water and produce groups for glyphosate (Dhamu and Prasad, 2020; Dhamu et al., 2021) and atrazine (Pichetsurthorn et al., 2012), respectively, using an affinity-based biosensing mechanism that is highly specific to the target species. This sensor functions based on an affinity biosensing mechanism driven via thiol cross-linker and antibody receptors that holistically behaves as a recognition immunoassay stack that is specific and sensitive to track test pesticide analytes in the parts per billion (ppb) range for glyphosate and parts per trillion (ppt) range for atrazine. Herein, this universal sensor architecture and chemistry is built and optimized to survey atrazine and glyphosate pesticide panel in soil runoff samples. Here, the universal sensor panel refers to the ability to use and deploy the same 2-electrode design, hardware interface, electrochemical mode (electrochemical impedance spectroscopy; EIS), and similar affinity binding stack respective to each target analyte.

Then, this developed sensor is integrated further to create a pesticide-sensing ecosystem using a front-end field-deployable

¹Report-Technical factsheet on glyphosate by United States Environmental protection agency (US-EPA)



smart device that drives the electrochemical signal from a potentiostat and then performs computational regression modeling on-chip to denote the resultant trace pesticide level output. Therefore, a universal pesticide-screening analytical device is designed and fabricated for pesticide assessment in real soil runoff samples.

MATERIALS AND METHODS

All data graphs were plotted and analyzed using GraphPad Prism, with error bars as mean with the standard error of mean (SEM). All electrochemical experiments were performed using the Gamry Reference 600 potentiostat (GAMRY Instruments, United States).

The sensor design depicted in **Figure 1C** that was designed and tested in-house was then fabricated on a PCB substrate, manufactured by PCB Way (HK WEIKU Technology Company Limited, China). The fabrication was a single-layer (Top layer) deposition with the conductive layer (copper layer), solder mask, and overlay (silkscreen layer). Here, the conductive layer holds the immersion gold, which is an electroless nickel metal (ENIG) plating technique with a thin layer of gold finish. This provides the electrical connectivity required for the sensor, while the solder mask provides insulation to the rest of the sensor region. The silkscreen layer is added for functionality and depicts sensor chip boundary regions, thereby giving the necessary interfacing capability with the electronic reader (USB-Flash drive design to slot into reader port). The PCB substrate material type used is FR-4 TG-130, with a thickness of 1.6 mm (6/6 mil track/spacing), and the overall dimension of the sensor chip is 17.8×9.7 mm.

Preparation of Soil Runoff Samples

Garden soil used commonly for horticultural use was procured from a commercial source (Home Depot, GA, United States). A standard small cylindrical pot with a hole at the bottom was filled with this soil, and a common cactus was planted which acts as the sample setup for this study. Filtered RO (Reverse Osmosis) grade water was used to water the plant setup, and the excess water (runoff) was collected using a cup holding the pot within it, as shown in **Figure 1A**. This water was collected and was used as the stock dilution to serially dilute and create the pesticide (antigen) doses with atrazine and glyphosate, respectively. Then 1 mg of the solute (atrazine salt) was mixed into 2 ml of the runoff water and then sonicated for 1 h, following which this concentration of 500 $\mu\text{g/ml}$ was serially diluted down to the test range of 1 pg/ml –1 $\mu\text{g/ml}$. Similarly, with the glyphosate salt, 1 mg was mixed into 1 ml of the soil runoff and mixed. The difference with glyphosate was that the solution forms readily as it is a polar organic molecule which is dissoluble in water even under lower solvent volumes. Then this 1 mg/ml stock concentration of glyphosate soil runoff sample was diluted to the test range between 1 ng/ml and 10 $\mu\text{g/ml}$.

Electrochemical Immunoassay Protocol for Affinity Sensing Approach

Phosphate-buffered saline (PBS) (pH 7.4) was used as the solvent and diluent in this set of experiments. To record the binding events at the electrode region between the antibody and pesticide antigen (glyphosate and atrazine), a 10 mV AC bias was applied at the WE and impedance recorded by electrochemical impedance spectroscopy (EIS) to effectively polarize and

capture the electrode–electrolyte interfacial effects. Sensor chips were prepared by cleaning with isopropyl alcohol, followed by deionized water. The whole protocol was devised for one individual chip, and each chip was dosed serially from the lowest to the highest dose (ascending order). Experiments were conducted in triplicate, that is, 3 unique sensor chips.

Once the sensor was prepared, 5 μL of cross-linker dithiobis(succinimidyl propionate) (DSP) (Thermo Scientific, United States) made in dimethyl sulfoxide (DMSO) was dispensed onto the gold electrode-sensing region and incubated for 90 min, providing sufficient time for the DSP molecules to be immobilized onto the gold surface. The sensor surface was then coated with 5 μL of glyphosate antibody (chicken polyclonal) solution and atrazine antibody (sheep polyclonal) solution (Fitzgerald Antibodies, United States) of 500 $\mu\text{g}/\text{ml}$ and 100 $\mu\text{g}/\text{ml}$, respectively, and allowed to incubate for 30 min undisturbed. Next, 5 μL of superbloc (blocking buffer) (Thermo Scientific, United States) was dispensed to the electrode surface and incubated for 10 min to minimize unspecific binding by hydrolyzing the cross-linker functional sites.

The glyphosate antigen (Sigma Aldrich, United States) doses of the range of concentrations required between 1 ng/ml and 10 $\mu\text{g}/\text{ml}$ were prepared as described before using soil runoff. Similarly, for the atrazine pesticide (Sigma Aldrich, United States), it was serially dosed in the range of 1 pg/ml –1 $\mu\text{g}/\text{ml}$. Blank soil runoff with no detectable pesticide traces (baseline/negative control) was added to the sensor surface, incubated (10 min), and measured as zero dose (ZD). Then, the fluid was aspirated from the electrode surface, and this procedure was repeated for the next corresponding doses in increasing concentration for the same incubation interval to promote pesticide-antibody binding to take place. EIS measurements were taken after each incubation and dosing step of the immunoassay.

RESULTS AND DISCUSSION

EIS Methodology for Pesticide Residue Analysis

This section explains in detail the biosensing chemistry that is surveyed using impedimetric analysis that can be captured as a function of pesticide levels in the target sample: soil runoff matrix. Conjugation of the immunoassay stack to specifically recognize the pesticides-glyphosate (GLP) and atrazine (ATR) was implemented on the ENIG immersion-gold finish PCB (FR-4) interdigitated electrode. This stack effectively creates a double layer at the electrode-electrolyte interface that gets modulated due to the presence of increased target analytes in the solution. To explain this concept in detail, we point to the electrical double layer (EDL) structure (Munje et al., 2015; Munje et al., 2017) created when a conductive or semiconducting surface is in contact with a fluid matrix. The EDL consists of a chemically adsorbed layer of charged molecules followed by a layer of oppositely charged species held together via charge attraction (Coulomb forces). What follows is defined as the diffuse layer that

can be visualized as ions that move within the fluid under the influence of the applied electrical field and whose strength is proportional to the distance from the contact layer defined formerly.

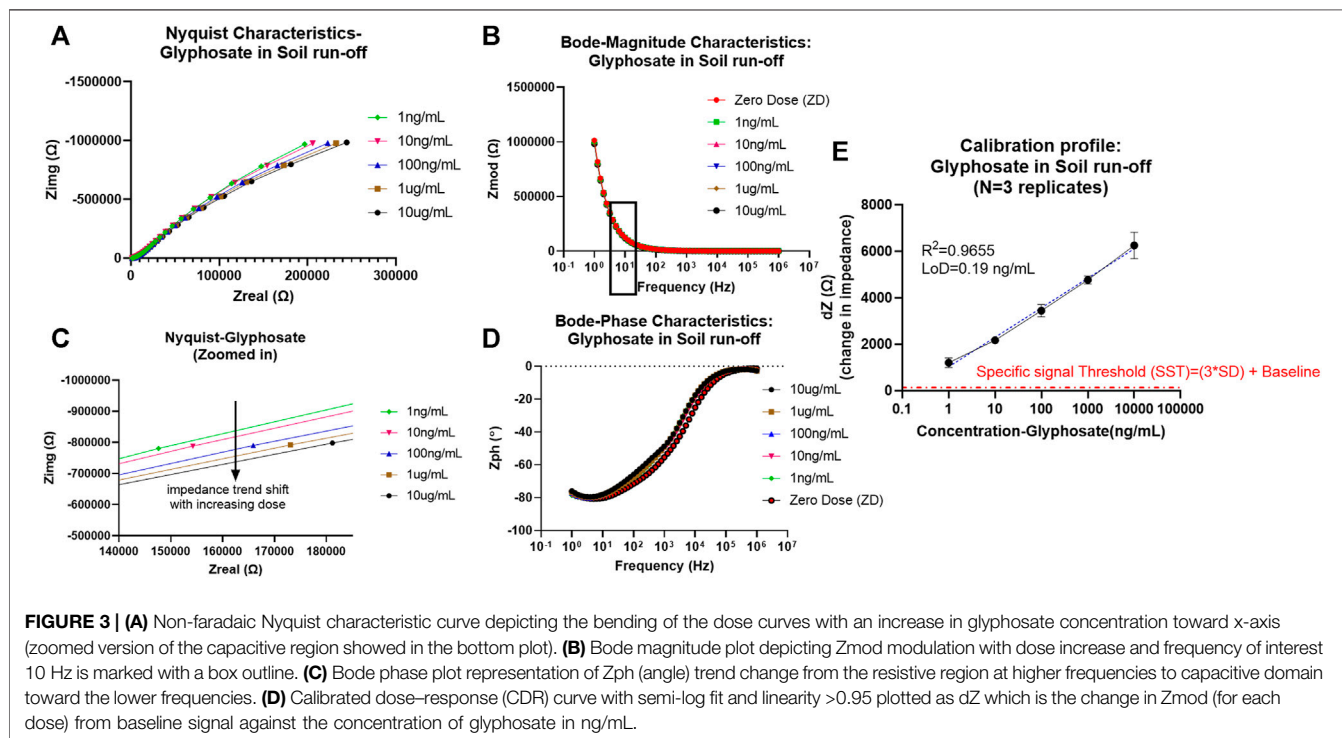
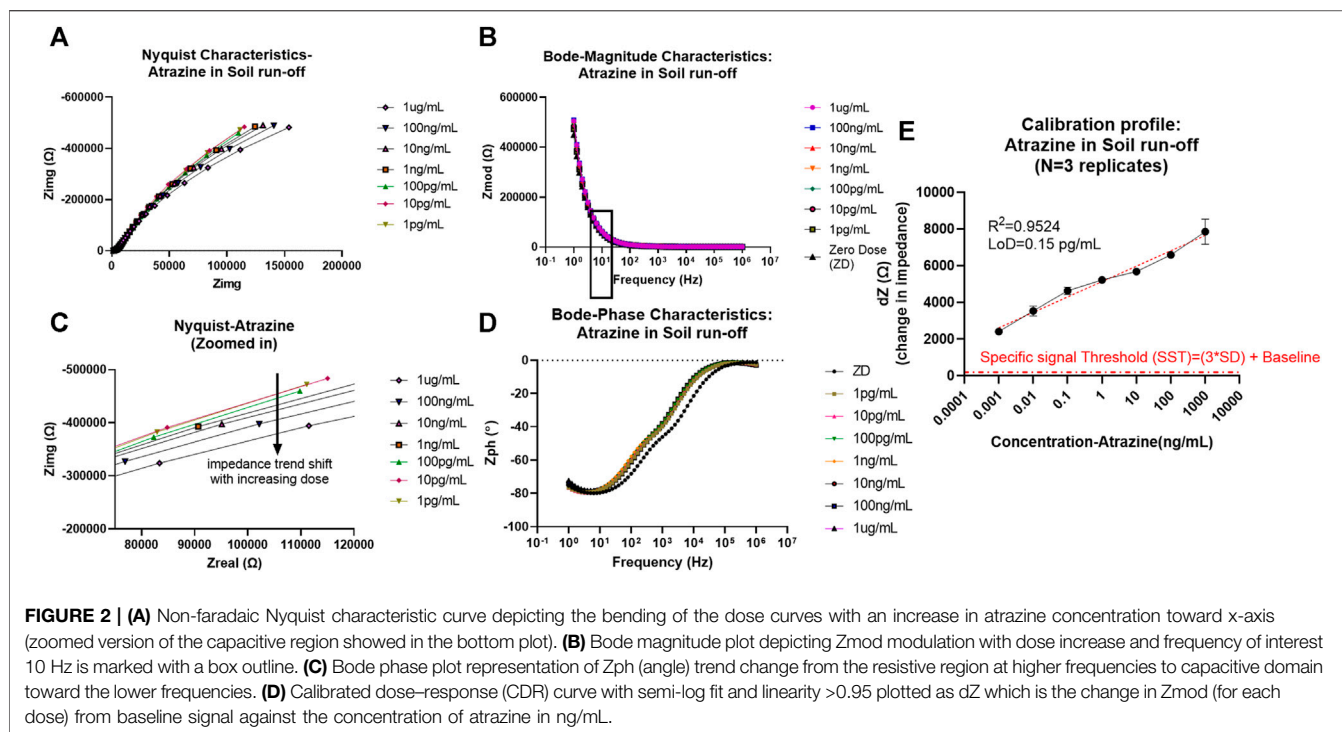
The detection strategy employed using affinity biosensing is reliant on the following concept: The gold electrode surface is dispensed and conjugated with a thiol cross-linker molecule dithiobis(succinimidyl propionate) (DSP) that binds to the gold layer by thiol–SH linkage, while the opposite end is the NHS ester group end (Xue et al., 2014; Kamakoti et al., 2018). Based on prior characterizations and studies into the design and building of a biosensor for atrazine and glyphosate, it was possible to obtain the optimum antibody parameters for the experimental protocol and determine suitable concentration; an antibody saturation study was conducted, based on results corresponding to a clearly noticeable linear increase in signal values as we increase the dose antibody concentration (Dhamu and Prasad, 2019). It was determined that based on signal saturation at a particular antibody dose, 500 $\mu\text{g}/\text{ml}$ for glyphosate and 100 $\mu\text{g}/\text{ml}$ for atrazine was the optimum concentration of antibody required with respect to this IDE sensor system. The specific antibody based on the sought-after target group is then functionalized onto the immunoassay that is confirmed by the breakage of the CO–NHS bond in the cross-linker layer and formation of amide bonds I and II, reiterating the binding of the antibody to the DSP cross-linker and thereby the sensor surface itself as understood and proven via Fourier transform infrared (FTIR) spectroscopy in the scientific literature that is relevant here to characterize standard antibody stack conjugation (Upasham et al., 2018).

After this stage, the sensing capture biochemistry is now ready for binding with the target species (pesticide groups GLP and ATR). These interactions are captured via capacitive modulations in the EDL using impedance analysis with EIS that is well-suited for studying and modeling complex systems as ours, which in this case is runoff from field soils.

Electrochemical Impedance Spectroscopy Enabled Pesticide Sensing

After confirmation of immunoassay functionalization on the gold sensor surface, pesticide levels in aqueous systems were determined using non-faradaic EIS. The non-faradaic method implies the ability to detect target analytes without the use of a redox tag or label. This enables the capability of the sensor to thereby be preprocessing-free and hence does not require additional reagents to act as indicators.

As described before, the changes to the analyte under test are observed as a function of capacitive modulations to the EDL. Therefore, non-faradaic EIS is best suited for this role as it is a thorough method to map the subtle chemistry effects at the electrode–electrolyte interface. So, it is possible to obtain high sensitivity by employing this interfacial probing mode (EIS). To explain this phenomenon in detail, the following is considered: When an AC voltage of 10 mV is applied to the electrode, it results in the perturbation of the solid–liquid interface. Furthermore, causing a capacitance (dielectric) modulation in



the double-layer structure due to binding between the antibody and the pesticide molecule, that is, EDL capacitance varies with respect to the antigen-antibody binding. The background behind capacitance change in this model has to do with the dielectric

permittivity of the system being modulated due to the double-layer structure and length being perturbed.

These variations are surveyed and then subsequently analyzed with the EIS results plotted as Nyquist (Z_{real} vs. Z_{img}), Bode phase

(Freq vs. Z_{ph}), and Bode magnitude (frequency vs. Z_{mod}) plots. This whole EDL structure and the impedance parameters associated with the EIS mode can be visualized and modeled using an equivalent electrical circuit called modified Randle's circuit (Saxena and Srivastava, 2019; Xu et al., 2019; MintahChurcher et al., 2020).

As can be seen from the EIS results later, the absence of charge transfer resistance R_{ct} (infinite) in the Nyquist plot denoted by incomplete semicircles is indicative of non-faradaic analysis (Tanak et al., 2019). Another indicative trend noticed from the Nyquist characteristics is that with increased pesticide doses of glyphosate and atrazine, there is an associated reduction in the radius of curvature in the incomplete semicircles. This is seen as the shift toward the x-axis with an increase in dose, as can be seen in the zoomed-in Nyquist plot in **Figure 2** (ATR) and **Figure 3** (GLY). One major observation made was that due to the presence of bulk molecules in the soil and water as such, the time needed for binding was increased to 10 min.

In addition to this, Bode plots shown for atrazine and glyphosate is representative of the antigen–antibody binding. The magnitude plot shows that with more binding relative to increases in the dose of pesticide, there is a correlated Z_{mod} modulation, while conversely, in the case of the phase plot, there is a change in phase angle values from more negative values (close to -90°) corresponding to more capacitive behavior toward zero phase values, indicative of more resistive nature as there are more antigen–antibody interactions.

The binding between the antibody and antigen drives the impedance modulations in this strategy. Probing further, we understand from utilizing EIS mapping at the electrode–electrolyte interface that the concentration of the analyte molecules drives the degree of binding between the antibody and antigen, which translates to the quantitative correlation and modulation in terms of the analyte-to-signal ratio, especially when looking at Randle's equivalent circuit, the C_{dl} (double-layer capacitance) or the CPE (pseudo-capacitance) components referring to the capacitive elements that drive this signal as a function of binding interactions that are translated to concentration-dependent responses (Munje et al., 2015).

Randle's equivalent circuit here refers to the electrical component model that is used to mimic the chemical stack at the electrode–electrolyte layer. This is previously simulated with the experimental results to fit and compare the values of the electrical components to determine the parameter that drives the molecular level reactions (Dhamu et al., 2021).

Thereby, EIS analysis was used to map the binding effects between the antigen and antibody occurring at the electrode interface while neglecting other bulk effects and non-specific binding effects that contribute to electrochemical noise. To model and extract sensing performance of the system, the Z_{mod} values were utilized at 10 Hz (capacitive binding dominant region), and the calibration curve was plotted each for atrazine and glyphosate and is explained later. To better visualize the change in signal in the Bode magnitude curves for each concentration of pesticide analyte, the graph was zoomed in to the 10 Hz region to better visualize the trend in Z_{mod} shift

with an increasing dose for both atrazine and glyphosate, as depicted in Figure S2.

Atrazine

From the calibrated dose–response (CDR) curve, the sensor response was measured/calibrated against the baseline or zero dose signal value. Thus, the resultant plot was between the dZ (change in impedance from baseline) signal on the y-axis versus the dose of atrazine (ng/ml) on the x-axis. The semi-log curve fitting was used to plot the sensor dose response and extract the parameters of limit of detection (LoD, measured based on a specific signal threshold (SST) as $3 \times$ standard deviation (SD) of baseline + baseline level) value of 0.15 pg/ml and sensitivity being $-838.6 \Omega/\log(\text{ppb})$. Also, the operable limit of quantification (LoQ) for confident tracking and sensor functionality was determined by experimental characteristics to be 1 pg/ml. The values of concentrations chosen in this study for the experimental cycle are in log scale. So, semi-log (x-axis concentration in log scale and y-axis signal in linear scale) fitting was best suited for our analysis, giving a desirable linearity factor of $R^2 = 0.9524$ (>0.95). EIS was consequently down-selected as the primary probing mode after comprehensive analysis to track pesticide levels in samples using an affinity biosensing approach. Additionally, the SST also showed that the signal-to-noise ratio (SNR) of this system was appreciable to keep all unspecific noise below its threshold level, and all the desirable concentration-dependent signals are captured efficiently.

Glyphosate

Similarly, the CDR curve was determined and plotted for glyphosate in an equivalent manner. The system showed improved performance from the atrazine case with linearity $R^2 = 0.9655$, partly attributed to its polar nature and thereby better binding and diffusion into the EDL. Operable LoQ obtained was 1 ng/ml (1ppb), which is sufficient based on MRL levels for most agricultural cases, while the LoD was calculated to be 0.19 ng/ml (ppb). The LoD was determined based on the SST in the same manner, as described before for atrazine ($3 \times$ SD of baseline + baseline impedance value). Additionally, the sensitivity score also got better with $1,271 \Omega/\log(\text{ppb})$.

It is possible for the system to capture a dynamic range of 1 pg/ml–1 $\mu\text{g/ml}$ (atrazine) which is in the ppt range and 1 ng/ml–10 $\mu\text{g/ml}$ (glyphosate) therein in the ppb range making it a sensitive, robust, and viable sensor. Additionally, the stability of this method was surveyed using EIS mode and results are denoted using an error bar with \pm standard error of mean (SEM).

Point-of-Use (PoU) Testing and Feasibility via Electroanalytical Sensing Device

The emstat pico module (PalmSens BV, Netherlands) was utilized as the core element of the circuit and interfaced for I/O operations to the MKR zero (Arduino, Somerville, MA, United States) microcontroller system. Together this constitutes the prototype device package used within this study for potted-plant soil runoff experiments. The software interface in use for data collection and subsequent analysis with this device is the PSTrace software

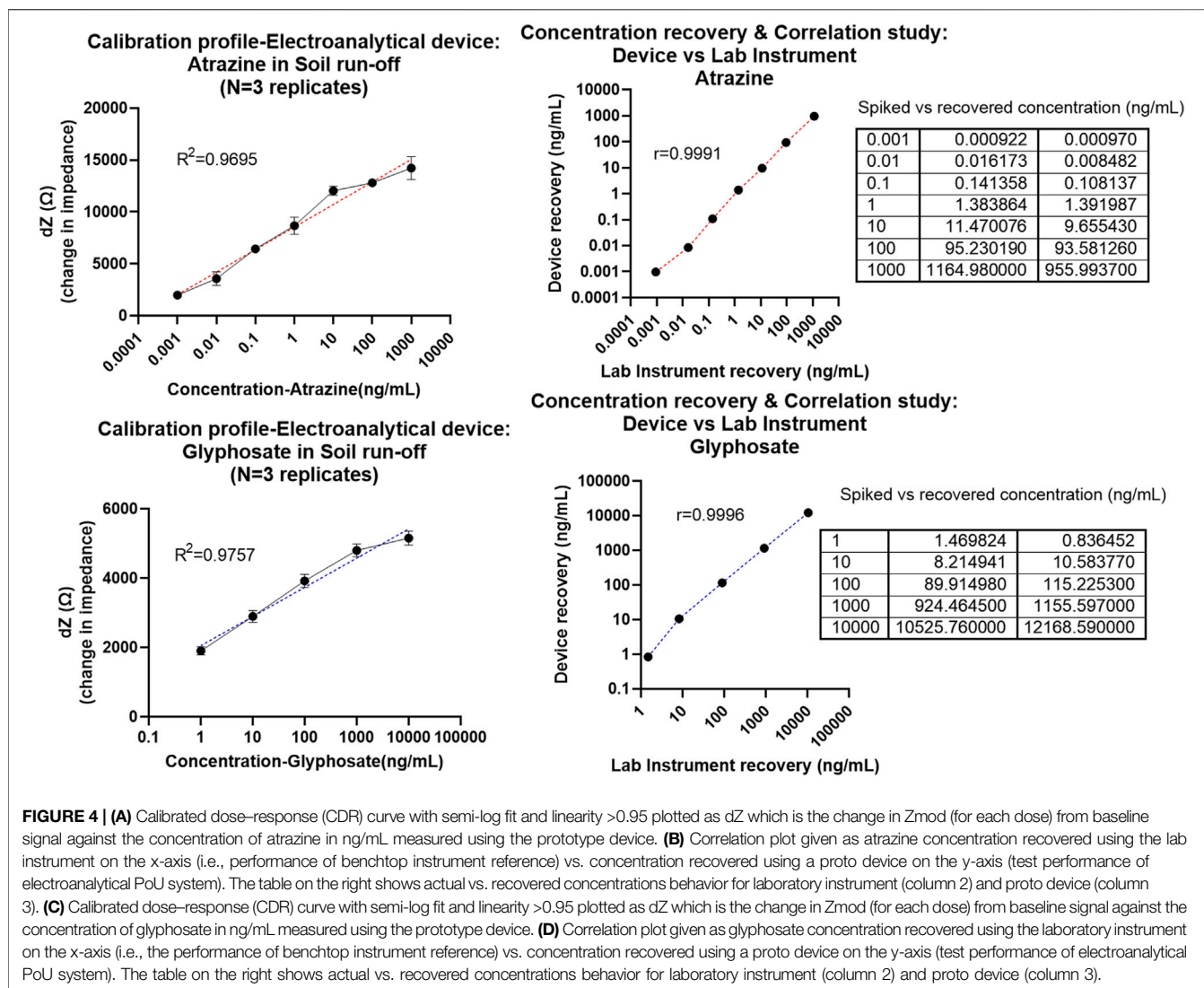


FIGURE 4 | (A) Calibrated dose–response (CDR) curve with semi-log fit and linearity >0.95 plotted as dZ which is the change in Z_{mod} (for each dose) from baseline signal against the concentration of atrazine in ng/mL measured using the prototype device. **(B)** Correlation plot given as atrazine concentration recovered using the lab instrument on the x-axis (i.e., performance of benchtop instrument reference) vs. concentration recovered using a proto device on the y-axis (test performance of electroanalytical PoU system). The table on the right shows actual vs. recovered concentrations behavior for laboratory instrument (column 2) and proto device (column 3). **(C)** Calibrated dose–response (CDR) curve with semi-log fit and linearity >0.95 plotted as dZ which is the change in Z_{mod} (for each dose) from baseline signal against the concentration of glyphosate in ng/mL measured using the prototype device. **(D)** Correlation plot given as glyphosate concentration recovered using the laboratory instrument on the x-axis (i.e., the performance of benchtop instrument reference) vs. concentration recovered using a proto device on the y-axis (test performance of electroanalytical PoU system). The table on the right shows actual vs. recovered concentrations behavior for laboratory instrument (column 2) and proto device (column 3).

under the PalmSens BV banner. A wired connector was used to interface the USB form factor-IDE sensor with the device as shown in **Figure 1**. This hardware platform was put together into a 3D printed housing construct and interfaced with a tablet/laptop computer for GUI analysis and experimental data collection by running EIS with similar settings as the lab instrument explained previously in the methods section (10 mV AC bias with a frequency sweep between 50000 and 5 Hz).

Similar to the previous section, calibration response curves extracted from the Bode magnitude (Z_{mod}) plot at 10 Hz were obtained for the atrazine and glyphosate analytes, as shown in **Figure 4**. All measurements and tests in this phase of the study were conducted in triplicates, that is, $N = 3$ independent sensor chips with 3 loops each acting as internal replicates.

The impedimetric response plotted as signal change (dZ) from baseline is fitted as a semi-log non-linear curve in **Figure 4** depicting a linearity coefficient R^2 of 0.9695 for atrazine (**Figure 4A**) and 0.9757 as in the case of glyphosate (**Figure 4C**). It was notable that the analytical

device system was able to capture the whole dynamic range of 0.001–1,000 ng/ml (atrazine) and 1–10,000 ng/ml (glyphosate) with the dotted line curves representative of the 95% CI line fit which lies on top of the dose–response curve. This is indicative of the feasibility and robustness of this sensor ecosystem. It was observed from the non-overlapping error bars that the PoU device can reliably distinguish between each dose and its subsequent concentration in a thorough manner. Furthermore, statistical ANOVA test of $p < 0.05$ (95% CI) yielded and cemented the hypothesis that different concentration doses are differentiable from each other with statistical significance. The system was able to effectively read concentrations as low as 0.001 ng/ml (LOD-atrazine) and 1 ng/ml (LOD-glyphosate) with respect to a $3 \times SD$ -specific signal threshold (SST) calculation.

Next, to determine the applicability and performance metrics of this PoU device, the dose–response results obtained from the laboratory reference instrument were compared to that evaluated using the fabricated prototype device. Herein, the laboratory instrument which was a Gamry potentiostat system is taken as the standard potentiostat to which the proto device output is compared.

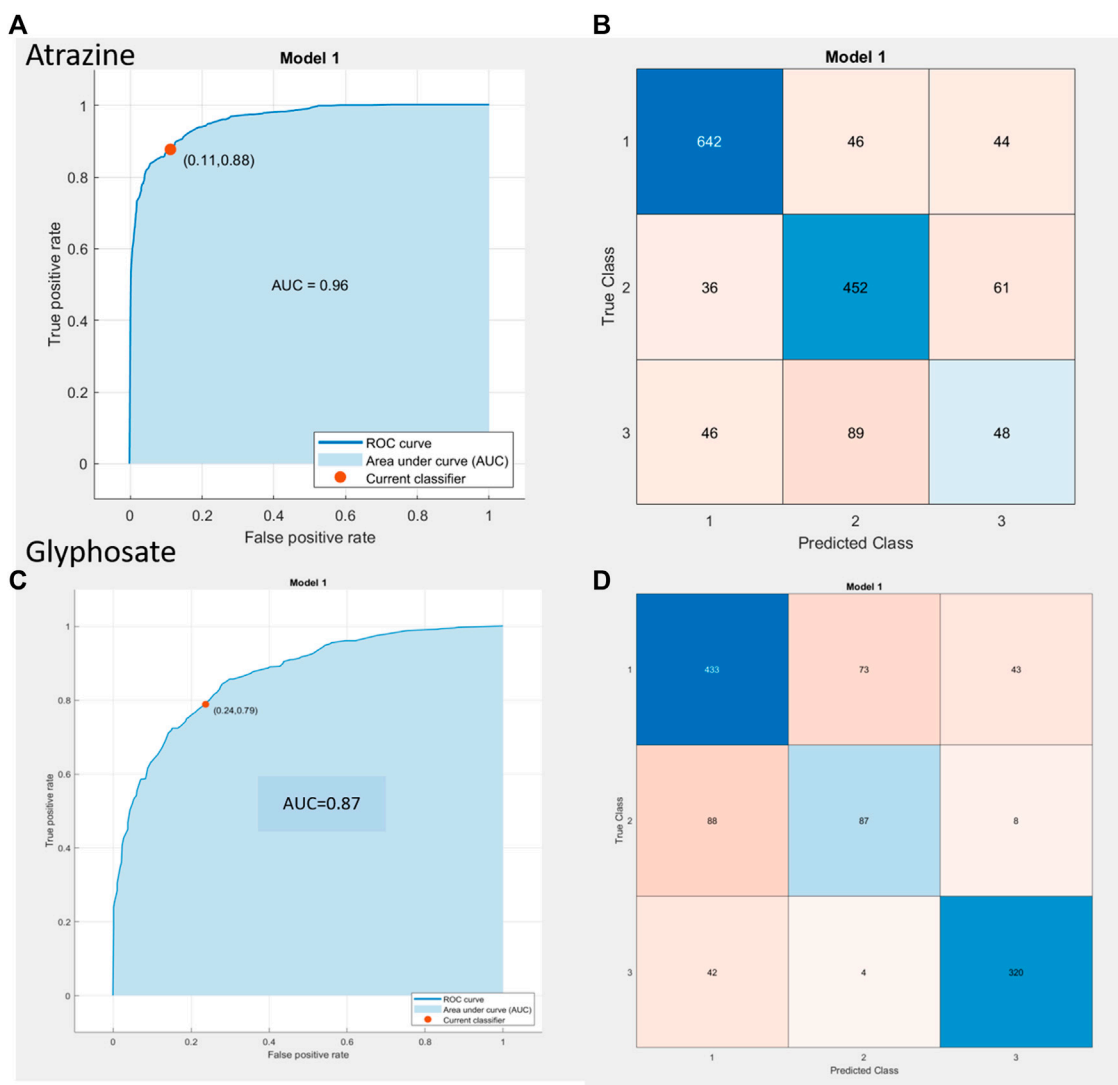


FIGURE 5 | (A,C) ROC curve results for atrazine **(A,B)** and glyphosate **(C,D)** inclusive of AUC value, TPR, and FPR value (represented as the red dot with values in parenthesis). **(B,D)** Confusion matrix depiction to determine true class vs predicted class behavior for ATR **(A,B)** and GLY **(C,D)**, respectively.

By applying the calibrated line equation model [$y = m \ln(x) + c$], the output signal (y-axis in CDR curve) was used to reverse calculate the concentration (x-axis on CDR curve) and “m” denotes the slope of the line and “c” represents the intercept value. Thus, the signal from the experiment is used to obtain the recovered concentrations against the standard curve fit. From this step, we obtain 2 key performance metrics: First, Pearson correlation analysis performed between the results from two devices (methods); laboratory instrument vs device is used to validate the feasibility of system toward in-field deployability. A linear matching between the recovered concentration dataset (plotted in y-axis as device results) and that of the laboratory instrument results (plotted in x-axis) is compared by determining Pearson’s correlation coefficient “r” of 0.9991 in the case of atrazine and 0.9996 for glyphosate. Therefore, the proposed system showed excellent correlation with the laboratory instrument sensor response data with a high r-value close to 1 (ideal).

Second, the efficacy of the sensor system in translating signal values to pesticide contamination levels was determined using the spike and recovery table seen on the right side of **Figures 4B,D**. Even with a complex system like the soil, the system was able to capture the pesticide levels (recovered concentration values) within $\pm 20\%$ error of the actual concentration present in the sample. This makes the proposed platform viable for in-field testing and broad-scale use.

Machine Learning Classifier Integration

The pesticide contamination machine learning (ML) classification model and application GUI (for use in Windows) were implemented using MATLAB (Natick, MA, United States)—Classification Learner application to create the training model and then perform subsequent testing. The model for the training dataset was tested using 5-fold cross-validation (Lakshmi and Rao, 2019), and the algorithm for ML processing was based on bagged trees logic

which is a commonly used method for classification purposes (Al-Barazanchi et al., 2017; Widasari et al., 2020).

The utility of the PoU platform is enhanced by the integration of the classifier algorithm and is used to segregate sample pesticide contamination into 3 output classes:

Atrazine.

- 1) 0–0.1 ng/ml (low)
- 2) 0.1–100 ng/ml (mid)
- 3) >100 ng/ml (high)

Glyphosate.

- 1) 0–10 ng/ml (low)
- 2) 10–100 ng/ml (mid)
- 3) >100 ng/ml (high)

Experimental output data collected from the proto device platform contain column-wise information as follows: Zreal, Zimg, Zph, Zmod, frequency, and dose within each measurement cycle. The novelty in this proposed classifier is the ability to obtain ML classification output into the aforementioned 3 classes by exporting this output data file directly into the computational system without any need for preprocessing or data consolidation. The factors, namely, frequency, Zreal, Zimg, and Zmod, together were seen to be optimized predictors for the model with the response as tertiary classes based on observations as described before: low, mid, and high contamination classes.

The data input is from $N = 3$ independent sensor replicates with 3 loops each for 8 concentration doses for atrazine and 6 concentration doses for glyphosate yielded 1,464 and 1,098 unique observations/sample points for the two pesticide compounds, respectively. This is the input used to build and test the ML model whose results are depicted in **Figure 5** as a receiver operating characteristic (ROC) curve plotted between the true-positive rate (TPR) on the x-axis and false-positive rate (FPR) on the y-axis. The choice was finalized following the review of output parameters such as accuracy in % and the ROC curve characteristics (i.e., maximum TPR and minimal FPR). From the ROC curve results for atrazine, it can be seen that the TPR/FPR ratio is sufficient taking into account the complex nature of soil along with the overall accuracy being 79.4% and area under the curve (AUC) value of 0.96. Additionally, on the right side of the figure, the confusion matrix is seen with the predicted class on x-axis versus the true class on y-axis. Classes 1, 2, and 3 refer to the low, mid, and high contamination levels, and from the heat map for atrazine, it is seen that the error is more prominent at the mid-high contamination level borders, while there is a good degree of confidence at the lower concentration ranges. For the case of glyphosate, the ROC curve yields the performance metrics of 76.5% overall accuracy and AUC value of 0.87; the error for

glyphosate was concentrated for the most part in the mid-level contamination region. It is the assumption of the authors that adding more data points from different soil types and an additional number of sensor results would cause the model to auto-resolve further and optimize the performance to yield even better results.

CONCLUSION

In this study, we have successfully put forward a sensing ecosystem to track a pesticide panel of different types—atrazine (non-polar) and glyphosate (polar)—using the same universal sensor design and setup. This solution holds the potential to be deployed *in situ* as a first response to screening and solving for soil pollution, food quality understanding, and thereby boosting food security.

It was possible to depict sensor performances in the range of parts-per-trillion detection limits for atrazine and parts-per-billion in the case of glyphosate with runoff from actual real field soil samples. A feasibility study was undertaken to cement the field deployability aspect by designing an electroanalytical device to run EIS on the samples in a portable setting and thereby obtaining the trace residue levels in an on-demand manner. The performance from the electroanalytical system was correlated to that obtained from the laboratory-grade benchtop instrument indicating the stability and robustness of the proposed platform for agricultural field tests in wet farms that grow paddy (rice), etc.

DATA AVAILABILITY STATEMENT

The raw data supporting the conclusion of this article will be made available by the authors, without undue reservation.

AUTHOR CONTRIBUTIONS

VD, SM, and SP conceptualized the theoretical framework of the study and methodology. VD, SM, and SP worked on the design of experiments. VD designed and assembled the sensing platform. VD and SS performed the experiments on the laboratory instrument and prototype device. CK and VD performed modeling of data. VD, SM, and SP analyzed the experimental data and wrote the manuscript.

SUPPLEMENTARY MATERIAL

The Supplementary Material for this article can be found online at: <https://www.frontiersin.org/articles/10.3389/fchem.2021.782252/full#supplementary-material>

REFERENCES

- Aktar, W., Sengupta, D., and Chowdhury, A. (2009). Impact of Pesticides Use in Agriculture: Their Benefits and Hazards. *Interdiscip. Toxicol.* 2, 1–12. doi:10.2478/V10102-009-0001-7
- Al-Barazanchi, K. K., Al-Neami, A. Q., and Al-Timemy, A. H. (2017). "Ensemble of Bagged Tree Classifier for the Diagnosis of Neuromuscular Disorders," in 2017 Fourth International Conference on Advances in Biomedical Engineering (ICABME), Beirut, Lebanon, 19–21 Oct. 2017. doi:10.1109/ICABME.2017.8167564

- Ali, M. A., Dong, L., Dhau, J., Khosla, A., and Kaushik, A. (2020). Perspective-Electrochemical Sensors for Soil Quality Assessment. *J. Electrochem. Soc.* 167, 037550. doi:10.1149/1945-7111/ab69fe
- Ambrus, A. (2015). International Harmonization of Food Safety Assessment of Pesticide Residues. *J. Agric. Food Chem.* 64, 21–29. doi:10.1021/JF505854W
- Arduini, F., Micheli, L., Scognamiglio, V., Mazzaracchio, V., and Moscone, D. (2020). Sustainable Materials for the Design of Forefront Printed (Bio)sensors Applied in Agrifood Sector. *Trac Trends Anal. Chem.* 128, 115909. doi:10.1016/J.TRAC.2020.115909
- Battaglin, W. A., Rice, K. C., Focazio, M. J., Salmons, S., and Barry, R. X. (2009). The Occurrence of Glyphosate, Atrazine, and Other Pesticides in vernal Pools and Adjacent Streams in Washington, DC, Maryland, Iowa, and Wyoming, 2005–2006. *Environ. Monit. Assess.* 155, 281–307. doi:10.1007/s10661-008-0435-y
- Bullock, P., and Gregory, P. J. (2009). Soils: A Neglected Resource in Urban Areas. *Soils Urban Environ.*, 1–4. doi:10.1002/9781444310603.CH1
- Catrinck, T. C. P. G., Dias, A., Aguiar, M. C. S., Silvério, F. O., Fidêncio, P. H., and Pinho, G. P. (2014). A Simple and Efficient Method for Derivatization of Glyphosate and AMPA Using 9-Fluorenylmethyl Chloroformate and Spectrophotometric Analysis. *J. Braz. Chem. Soc.* 25, 1194–1199. doi:10.5935/0103-5053.20140096
- Chamkasem, N., and Harmon, T. (2016). Direct Determination of Glyphosate, Glufosinate, and AMPA in Soybean and Corn by Liquid Chromatography/Tandem Mass Spectrometry. *Anal. Bioanal. Chem.* 408, 4995–5004. doi:10.1007/s00216-016-9597-6
- Chang, S. Y., and Liao, C.-H. (2002). Analysis of Glyphosate, Glufosinate and Aminomethylphosphonic Acid by Capillary Electrophoresis with Indirect Fluorescence Detection. *J. Chromatogr. A* 959, 309–315. doi:10.1016/S0021-9673(02)00453-3
- Dhamu, V. N., Poudyal, D. C., Muthukumar, S., and Prasad, S. (2021). A Highly Sensitive Electrochemical Sensor System to Detect and Distinguish between Glyphosate and Glufosinate. *J. Electrochem. Soc.* 168, 057531. doi:10.1149/1945-7111/AC00F7
- Dhamu, V. N., and Prasad, S. (2019). Electrochemsense : Electrochemical Real-Time Pesticide Sensing System. The University of Texas at Dallas. Available at: <https://utd-ir.tdl.org/handle/10735.1/9218> (accessed September 23, 2021).
- Dhamu, V. N., and Prasad, S. (2020). ElectrochemSENSE: A Platform Towards Field Deployable Direct On-Produce Glyphosate Detection. *Biosens. Bioelectron.* 170, 112609. doi:10.1016/j.bios.2020.112609
- Duke, S. O., and Powles, S. B. (2008). Glyphosate: A Once-In-A-Century Herbicide. *Pest Manag. Sci.* 64, 319–325. doi:10.1002/ps.1518
- Gillezeau, C., Van Gerwen, M., Shaffer, R. M., Rana, I., Zhang, L., Sheppard, L., et al. (2019). The Evidence of Human Exposure to Glyphosate: A Review. *Environ. Health* 18, 1–14. doi:10.1186/s12940-018-0435-5
- Gunstone, T., Cornelisse, T., Klein, K., Dubey, A., and Donley, N. (2021). Pesticides and Soil Invertebrates: A Hazard Assessment. *Front. Environ. Sci.* 9, 122. doi:10.3389/FENV.2021.643847
- Hanson, W., Strid, A., Gervais, J., Cross, A., and Jenkins, J. (2020). Atrazine Fact Sheet. Available at: <http://npic.orst.edu/factsheets/atrazine.html> (accessed September 23, 2021).
- Joko, T., Anggoro, S., Sunoko, H. R., and Rachmawati, S. (2017). Pesticides Usage in the Soil Quality Degradation Potential in Wanasari Subdistrict, Brebes, Indonesia. *Appl. Environ. Soil Sci.* 2017, 1–7. doi:10.1155/2017/5896191
- Kamakoti, V., Shanmugam, N. R., Tanak, A. S., Jagannath, B., and Prasad, S. (2018). Investigation of Molybdenum-Crosslinker Interfaces for Affinity Based Electrochemical Biosensing Applications. *Appl. Surf. Sci.* 436, 441–450. doi:10.1016/j.apsusc.2017.12.026
- Kellogg, R. L., Nehring, R., Grube, A., Goss, D. W., and Plotkin, S. (2000). “Environmental Indicators of Pesticide Leaching and Runoff from Farm Fields | NRCS Soils,” in *Agric. Product. Data, Methods, Meas.* (Washington DC: USDA). Available at: https://www.nrcs.usda.gov/wps/portal/nrcs/detail/soils/survey/?cid=nrcs143_014053 (accessed September 23, 2021).
- Lakshmi, J. M., and Rao, N. S. (2019). Effect of K-Fold Cross Validation on MRI Brain Images Using Support Vector Machine Algorithm. *Int. J. Recent Technol. Eng.* 7, 301–307. doi:10.35940/ijrte.2277-3878
- Lim, R. R. X., and Bonanni, A. (2020). The Potential of Electrochemistry for the Detection of Coronavirus-Induced Infections. *Trac Trends Anal. Chem.* 133, 116081. doi:10.1016/J.TRAC.2020.116081
- Lo, C.-C. (2010). Effect of Pesticides on Soil Microbial Community. *J. Environ. Sci. Health B* 45, 348–359. doi:10.1080/03601231003799804
- Mintah Churcher, N. K., Upasham, S., Rice, P., Bhadsavle, S., and Prasad, S. (2020). Development of a Flexible, Sweat-Based Neuropeptide Y Detection Platform. *RSC Adv.* 10, 23173–23186. doi:10.1039/d0ra03729j
- Munje, R. D., Muthukumar, S., Panneer Selvam, A., and Prasad, S. (2015). Flexible Nanoporous Tunable Electrical Double Layer Biosensors for Sweat Diagnostics. *Sci. Rep.* 5, 1–11. doi:10.1038/srep14586
- Munje, R. D., Muthukumar, S., and Prasad, S. (2017). Lancet-free and Label-free Diagnostics of Glucose in Sweat Using Zinc Oxide Based Flexible Bioelectronics. *Sensors Actuators B: Chem.* 238, 482–490. doi:10.1016/j.snb.2016.07.088
- Oliveira, H. C., Stolf-Moreira, R., Martinez, C. B. R., Grillo, R., De Jesus, M. B., and Fraceto, L. F. (2015). Nanoencapsulation Enhances the post-emergence Herbicidal Activity of Atrazine against Mustard Plants. *PLoS One* 10, e0132971. doi:10.1371/journal.pone.0132971
- Pichetsurthorn, P., Vattipalli, K., and Prasad, S. (2012). Nanoporous Impedimetric Biosensor for Detection of Trace Atrazine from Water Samples. *Biosens. Bioelectron.* 32, 155–162. doi:10.1016/j.bios.2011.11.055
- Saxena, R., and Srivastava, S. (2019). An Insight into Impedimetric Immunosensor and its Electrical Equivalent Circuit. *Sensors Actuators B: Chem.* 297, 126780. doi:10.1016/j.snb.2019.126780
- Silva, V., Mol, H. G. J., Zomer, P., Tienstra, M., Ritsema, C. J., and Geissen, V. (2019). Pesticide Residues in European Agricultural Soils - A Hidden Reality Unfolded. *Sci. Total Environ.* 653, 1532–1545. doi:10.1016/J.SCITOTENV.2018.10.441
- Tanak, A. S., Jagannath, B., Tamrakar, Y., Muthukumar, S., and Prasad, S. (2019). Non-faradaic Electrochemical Impedimetric Profiling of Procalcitonin and C-Reactive Protein as a Dual Marker Biosensor for Early Sepsis Detection. *Analytica Chim. Acta X* 3, 100029. doi:10.1016/j.acax.2019.100029
- Upasham, S., Tanak, A., Jagannath, B., and Prasad, S. (2018). Development of Ultra-Low Volume, Multi-Bio Fluid, Cortisol Sensing Platform. *Sci. Rep.* 8, 16745. doi:10.1038/s41598-018-35199-5
- US EPA (n.d.). *Technical Factsheet on: GLYPHOSATE*.
- Van Bruggen, A. H. C., He, M. M., Shin, K., Mai, V., Jeong, K. C., Finckh, M. R., et al. (2018). Environmental and Health Effects of the Herbicide Glyphosate. *Sci. Total Environ.* 616–617, 255–268. doi:10.1016/j.scitotenv.2017.10.309
- Widasari, E. R., Tanno, K., and Tamura, H. (2020). Automatic Sleep Disorders Classification Using Ensemble of Bagged Tree Based on Sleep Quality Features. *Electronics* 9, 512. doi:10.3390/ELECTRONICS9030512
- Xu, Y., Li, C., Mei, W., Guo, M., and Yang, Y. (2019). Equivalent Circuit Models for a Biomembrane Impedance Sensor and Analysis of Electrochemical Impedance Spectra Based on Support Vector Regression. *Med. Biol. Eng. Comput.* 57, 1515–1524. doi:10.1007/s11517-019-01970-7
- Xue, Y., Li, X., Li, H., and Zhang, W. (2014). Quantifying Thiol-Gold Interactions towards the Efficient Strength Control. *Nat. Commun.* 5, 1–9. doi:10.1038/ncomms5348

Conflict of Interest: SP and SM have a significant interest in EnLiSense LLC, a company that may have a commercial interest in the results of this research and technology. The potential individual conflict of interest has been reviewed and managed by the University of Texas at Dallas and played no role in the study design; in the collection, analysis, and interpretation of data; in the writing of the report; or in the decision to submit the report for publication.

The remaining authors declare that the research was conducted in the absence of any commercial or financial relationships that could be construed as a potential conflict of interest.

Publisher's Note: All claims expressed in this article are solely those of the authors and do not necessarily represent those of their affiliated organizations, or those of the publisher, the editors, and the reviewers. Any product that may be evaluated in this article, or claim that may be made by its manufacturer, is not guaranteed or endorsed by the publisher.

Copyright © 2021 Dhamu, Sukumar, Kadambathil, Muthukumar and Prasad. This is an open-access article distributed under the terms of the Creative Commons Attribution License (CC BY). The use, distribution or reproduction in other forums is permitted, provided the original author(s) and the copyright owner(s) are credited and that the original publication in this journal is cited, in accordance with accepted academic practice. No use, distribution or reproduction is permitted which does not comply with these terms.



Comparison of Three Complementary Analytical Techniques for the Evaluation of the Biosimilar Comparability of a Monoclonal Antibody and an Fc-Fusion Protein

Alice Demelenne^{1†}, Arij Ben Yahia^{1,2†}, Delphine Lempereur¹, Jacques Crommen¹, Anne-Catherine Servais¹, Ines Fradi² and Marianne Fillet^{1*}

¹Laboratory for the Analysis of Medicines, Center for Interdisciplinary Research on Medicines (CIRM), Quartier Hôpital, University of Liege, Liege, Belgium, ²Laboratory of Chemical, Pharmaceutical and Pharmacological Development of Drugs, Faculty of Pharmacy, University of Monastir, Monastir, Tunisia

OPEN ACCESS

Edited by:

Quezia B. Cass,
Federal University of São Carlos, Brazil

Reviewed by:

Vincent Dugas,
Université Claude Bernard Lyon 1,
France
Gabriella Massolini,
University of Pavia, Italy

*Correspondence:

Marianne Fillet
marianne.fillet@uliege.be

[†]These authors have contributed
equally to this work

Specialty section:

This article was submitted to
Analytical Chemistry,
a section of the journal
Frontiers in Chemistry

Received: 23 September 2021

Accepted: 28 October 2021

Published: 06 December 2021

Citation:

Demelenne A, Ben Yahia A,
Lempereur D, Crommen J, Servais AC,
Fradi I and Fillet M (2021) Comparison
of Three Complementary Analytical
Techniques for the Evaluation of the
Biosimilar Comparability of a
Monoclonal Antibody and an Fc-
Fusion Protein.
Front. Chem. 9:782099.
doi: 10.3389/fchem.2021.782099

In this work, a monoclonal antibody, adalimumab, and an Fc-fusion protein, etanercept, were studied and compared to one of their biosimilars. Samples submitted to stress conditions (agitation and high temperature) were used for method development. The developed methods were also applied to samples reduced by beta-mercaptoethanol to evaluate their capability to distinguish the expected species. Capillary gel electrophoresis (CGE), reversed-phase liquid chromatography (RPLC), and size-exclusion chromatography (SEC) methods coupled with UV detection were used to analyze the biopharmaceuticals. Their complementarity was investigated. For further molecular weight determination, SEC-multi angle light scattering and RPLC-quadrupole time-of-flight were occasionally used. For adalimumab, a larger amount of fragments and aggregates was observed in the biosimilar compared with the reference product. For etanercept, more related species were found in the reference product. Those three separation techniques showed good complementarity. Indeed, RPLC enabled the separation of hydrophilic and hydrophobic degradation products. CGE provided good selectivity for several adalimumab fragments, and SEC was useful for the analysis of aggregates and certain fragments that cannot be separated by the other approaches. Moreover, those formulations were submitted to mild stress conditions (30°C, 300 rpm for 4 h) that mimic shipping conditions. No additional peak was found under these conditions for the two studied biopharmaceuticals.

Keywords: adalimumab, etanercept, capillary gel electrophoresis, reversed-phase liquid chromatography, size-exclusion chromatography

1 INTRODUCTION

Over the last decade, biopharmaceuticals have represented one of the fastest growing classes of human therapeutics. According to the International Council for Harmonization of Technical Requirements for Pharmaceuticals for human use (ICH), biopharmaceuticals are defined as molecules that are produced in various biological systems and are used to diagnose, treat, or

prevent diseases. This category includes hormones, receptors, enzymes, cytokines, and monoclonal antibodies (mAbs) (ICH, 2021).

mAbs represent a major class among protein therapeutics. Indeed, around 80 therapeutic mAbs are currently approved by the European Medicines Agency (EMA) and around 100 by the Food and Drug Administration (FDA) (Antibody society, 2021). mAbs are now standard therapeutics in oncology, transplantation, and chronic inflammatory diseases (Davis et al., 2013). They are highly complex glycoproteins of approximately 150 kDa that belong to the immunoglobulin supergene family. They are composed of two identical heavy chains and two identical shorter light chains. These chains are interlinked by a variable number of disulfide bonds (Liddell, 2013).

New classes of proteins derived from mAbs are emerging, such as antibody–drug conjugates, bispecific antibodies, and Fc-fusion proteins (Davis et al., 2013). Fc-fusion proteins are molecules formed by the fusion of the crystallizable fraction (Fc) of the IgG antibody with different molecules, such as extracellular receptor domains, enzymes, or peptides, to increase their half-life and stability (Duivelshof et al., 2021). Among the biopharmaceuticals approved by the EMA or FDA, 13 are Fc-fusion proteins (Duivelshof et al., 2021).

With the expiration of the patents for those products, biosimilars have emerged on the market. Biosimilars are defined as products that are highly similar to the reference product (Gherghescu and Delgado-Charro, 2021). The first biosimilar was approved by the EMA in 2006 and by the FDA in 2015. By June 2021, 66 biosimilars had been approved by the EMA (European Medicines Agency, 2021) and 29 by the FDA (Food and Drug Administration, 2021). Among them, 38 are biosimilars of five mAbs (adalimumab, bevacizumab, infliximab, rituximab, and trastuzumab) and four are biosimilars of one Fc-fusion protein (etanercept) (European Medicines Agency, 2021; Food and Drug Administration, 2021). In the coming years, the number of biosimilars is expected to increase significantly.

To assess the biosimilar comparability between two products, comparability studies need to be performed. Those studies include the determination of physicochemical and immunochemical properties, biological activity, purity, and quantity. If differences are observed between the two products, further clinical and nonclinical evaluations are required to evaluate the impact of those changes on the final product (European Medicines Agency, 2014). Reliable analytical techniques are, thus, essential to demonstrate the biosimilar comparability.

A U.S. Pharmacopeia chapter provides the panel of analytical procedures for IgG mAb analysis. A size-exclusion chromatography (SEC) method is recommended for high-molecular-weight (MW) species assessment and a capillary gel electrophoresis (CGE) method under nonreduced and reduced conditions for fragments assessment. For the oligosaccharide analysis, capillary electrophoresis (CE) or high-performance liquid chromatography (HPLC) coupled with fluorescence detection is recommended for N-linked oligosaccharides analysis and HPLC with amperometric detection for sialic acid determination. The principles described in the chapter can be applied to other types of antibodies, such as Fc-fusion proteins (FDA, 2021).

In this work, three separation techniques [CGE, reversed-phase liquid chromatography (RPLC), and SEC] were used to analyze a monoclonal antibody (adalimumab) and an Fc-fusion protein (etanercept). CGE was used as a complementary technique to SEC for fragment analysis. Both drugs neutralize the tumor necrosis factor (TNF)- α , which is a pro-inflammatory cytokine (Goldenberg, 1999; Bang and Keating, 2004). They are used to treat diseases, such as rheumatoid arthritis and inflammatory bowel diseases (Mitoma et al., 2018).

Degraded samples using strong stress conditions and samples submitted to reducing conditions were used to optimize the separation conditions. Those methods were then applied to compare the reference products [Humira® (adalimumab) and Enbrel® (etanercept)] with their biosimilars [CinnoRA® (adalimumab) and Erelzi® (etanercept)] (see Table 1).

2 MATERIAL AND METHODS

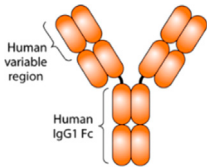
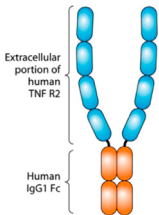
2.1 Chemicals

Trifluoroacetic acid (TFA) ULC-MS, and formic acid (FA) ULC-MS were acquired from Biosolve (Dieuze, France). Boric acid, sodium dihydrogen phosphate (NaH_2PO_4), sodium dodecyl sulfate (SDS), and hydrochloric acid (HCl) were purchased from Fisher (Loughborough, Leicestershire, United Kingdom). Sodium hydroxide pellets, ethylenediaminetetraacetic acid (EDTA), disodium hydrogen phosphate (Na_2HPO_4), potassium chloride (KCl), and glycerol were obtained from VWR (Leuven, Belgium). Ultrapure water was obtained from a Millipore Milli-Q Academic System from Merck (Darmstadt, Germany). Ultra Gradient HPLC-grade acetonitrile (ACN) was obtained from JT Baker (Deventer, Netherlands). Tris base Ultrol Grade was purchased from Merck. Polyethylene oxide (PEO) with an MW of 200,000, phosphoric acid (H_3PO_4), sodium chloride (NaCl), dextran from *Leuconostoc mesenteroides* (MW 1,500,000–2,800,000), beta-mercaptoethanol (BME), lysozyme, and iodoacetamide (IAM) were acquired from Sigma-Aldrich (St. Louis, MO, United States). SDS sample buffer and SDS-MW Size Standard (10, 20, 35, 50, 100, 150, and 225 kDa proteins) were purchased from Beckman Coulter (Fullerton, CA, United States). An mAb size variant standard was obtained from Waters (Milford, MA, United States). The formulations used in this study [Enbrel® (expiration date: 12/2020), Erelzi® (expiration date: 04/2021), Humira® (expiration date: 08/2020) and CinnoRA® (expiration date: 01/2020)] were provided by a partner.

2.2 Instrumentation

SEC was performed on an Agilent 1200 HPLC system (Agilent Technologies, Waldbronn, Germany). RPLC was performed on an Agilent 1100 HPLC system for method evaluation (section 3.1) and on an Agilent 1200 HPLC system for biosimilar comparability exercises (section 3.2). Detection was carried out with a diode-array detector. SEC multiangle light scattering (MALS) was performed on a 1260 Bio-Inert HPLC coupled with a Bio-Dual Angle LS/DLS (Agilent). CGE-UV separations were carried out on a G7100 CE system (Agilent) coupled to a diode-array detector. For RPLC quadrupole time-of-flight (QTOF) experiments, a UHPLC system coupled to a DTIMS-QTOF mass spectrometer

TABLE 1 | Studied biologics.

Molecule	Type	Structure Davies, (2016)	Molecular weight (kDa) Goldenberg, (1999); EMEA, (2003); Lee et al. (2019)	Reference product	Biosimilar
Adalimumab	A recombinant human IgG		148	Humira®	CinnoRA®
Etanercept	Fc-fusion protein		150	Enbrel®	Erelzi®

6,560 (Agilent) was used. A Dual Agilent Jet Stream ESI was used as electrospray ionization source.

2.3 Operational Conditions

2.3.1 CGE

An uncoated fused-silica capillary with a length of 33 cm (50 μ m ID, 24.5 cm effective length) was used to perform all separations (Polymicro Technologies, Phoenix, AZ, United States). Hydrodynamic injection was used for all samples by applying a pressure of 4 bars for 2 s at the inlet. During the run, the pressure was set at 2 bars at both ends. The separation voltage was set at 20 kV and the UV detection wavelength was set at 220 nm. The temperature of the cassette was maintained at 25°C. Instrument control and data acquisition were achieved by using the Agilent OpenLab CDS C.01.07 (27) software.

A new capillary was first conditioned by flushing water, followed by 1 M NaOH, 0.1 M NaOH, and water again for 5 min each. The capillary was then flushed with 1 M NaOH for 5 min followed by 1 M HCl for 10 min, water for 10 min, PEO 0.2% for 5 min, and finally water for 5 min. Between each run, the capillary was rinsed with water for 3 min, 0.1 M HCl for 3 min, 0.2% PEO for 5 min, and finally with the gel for 10 min at 4 bars for each fluid. The gel was made up of 0.6 M Tris-borate buffer (pH 8.1), 0.005 M EDTA, 10% dextran (w/v), 0.2% SDS (w/v), and 10% glycerol (v/v) (Liu et al., 2008).

2.3.2 RPLC

RPLC-UV: Three columns were used: BioResolve® Polyphenyl (2.1 \times 100 mm, 2.7 μ m particle size, 450 Å) (Waters), Biozen® intact C4 (2.1 \times 50 mm, 3.6 μ m particle size, 200 Å) (Phenomenex, Torrance, CA, United States), and Biozen® intact XB-C8 (2.1 \times 50 mm, 3.6 μ m particle size, 200 Å) (Phenomenex). The column compartment was set at 80°C for the three columns. The detection wavelength and the flow rate

were, respectively, set at 280 nm and 0.4 ml/min. The injection volume was set at 10 μ l. Agilent OpenLab CDS C.01.08 (210) software was used for system control and data acquisition. Mobile phase A consisted of water with 0.1% of TFA, and mobile phase B consisted of acetonitrile with 0.1% of TFA. The gradient started at 75% A and was carried out as follows: 0–20 min, from 75% to 55% A; 20–20.1 min, from 55% to 20% A.

RPLC-MS: For MS detection, the BioResolve® (polyphenyl) column was used. The same mobile phase, gradient, column temperature, and injection volume as for RPLC-UV were used. The reference masses (m/z 121.04 and 922.01) were infused at 0.1 ml/min. The Dual Agilent Jet Stream ESI source was set at a drying gas temperature and flow of 290°C and 13 L/min, respectively. The sheath gas temperature was set at 400°C and the corresponding flow at 12 L/min. The nebulizer was fixed at 20 psi. The capillary voltage was set at 5000 V and the nozzle voltage at 2000 V. The m/z range was set from 100 to 7000, and the scan rate was set at one spectrum/s. The spectra were deconvoluted using the maximum entropy algorithm in MassHunter BioConfirm software (Agilent).

2.3.3 SEC

SEC-UV: BioResolve® SEC mAb column (7.8 \times 300 mm, 2.5 μ m particle size, 200 Å) (Waters) with a BioResolve® SEC mAb Guard column (4.6 \times 30 mm, 2.5 μ m particle size, 200 Å) (Waters) were used. The column compartment was thermostated at 20°C, and the wavelength was set at 280 nm. The flow rate and injection volume were set at 0.5 ml/min and 10 μ l, respectively. Agilent OpenLab CDS C.01.08 (210) software was used for system control and data acquisition. The mobile phase was composed of 50 mM phosphate buffer (pH 7) and 200 mM KCl.

SEC-MALS: For MALS detection, the same column and mobile phase as for SEC-UV were used. The column compartment was

thermostated at 30°C, and the LS wavelength was set at 658 nm. The flow rate was set at 0.5 ml/min. The dn/dc ratio and UV extraction coefficient were found in the literature and were set at 0.185 ml/g and 1.42 ml/(mg.cm), respectively (Gokarn et al., 2015) for mAb size variant standard, at 0.185 ml/g and 1.39 ml/(mg.cm) for adalimumab, and at 0.172 ml/g and 0.912 ml/(mg.cm) (Miranda-hernández et al., 2015) for etanercept. Agilent Bio-SEC software was used for system control and data acquisition. The injection volume was 30 µl for mAb size variant standard, 40 µl for adalimumab, and 10 µl for etanercept.

2.3.4 Sample Preparation

2.3.4.1 CGE

CinnoRA®, Enbrel®, and Erelzi® formulations were diluted 20 times in Tris-HCl buffer at pH 9.0 with 1% of SDS (SDS sample buffer) containing 6 mM of iodoacetamide. Humira® was diluted 40 times in the same medium. All samples (at a final concentration of 2.5 mg/ml) were then heated at 70°C for 10 min. For the reduction, each formulation was diluted 50 times in a solution of 5% BME in SDS sample buffer and then heated for 15 min at 70°C.

2.3.4.2 RPLC

RPLC-UV: CinnoRA®, Enbrel®, and Erelzi® were diluted 100 times in 0.1% FA to obtain a concentration of 0.5 mg/ml. Humira® was diluted 200 times in the same solvent to reach the same concentration. For the reduction, 2 µl of CinnoRA®/Enbrel®, 10 µl of BME, and 188 µl of water were mixed. The samples were then heated for 15 min at 70°C.

RPLC-MS: CinnoRA® and Humira® were diluted 100 and 200 times in 0.1% FA, respectively, and 500 µl of samples were centrifuged in Vivaspin 500® Centrifugal Concentrator of 10 kDa (Sartorius, Goettingen, Germany) during 5 min at 12,000 rpm. Then, 20 µl of the nonfiltered liquid was collected, and 180 µl of water containing 1% FA was added.

2.3.4.3 SEC

SEC-UV: CinnoRA®, Enbrel®, and Erelzi® were diluted 100 times in water, and Humira® was diluted 200 times to achieve a final concentration of 0.5 mg/ml. For the reduction, 2 µl of formulation were diluted 100 times in a 10% BME solution and then heated for 15 min at 70°C.

SEC-MALS: CinnoRA® and Enbrel® were diluted 25 times in water to reach a concentration of 2 mg/ml.

2.3.4.4 Forced Degradation

For this, 350 µl of CinnoRA® and 200 µl of Enbrel® were subjected to stirring (600 rpm) at 60°C for 2 h. These samples were then prepared as mentioned above.

2.3.5 Calibration

2.3.5.1 CGE

Standard of MW preparation: 5 µl of the SDS-MW size standard (10, 20, 35, 50, 100, 150, and 225 kDa proteins) were mixed with 5 µl of BME and 70 µl of SDS-sample buffer. The standard was heated at 100°C for 3 min.

The waters mAb size variant standard preparation: The waters mAb size variant standard was diluted two times in SDS-sample buffer before injection.

CGE calibration curve: The curve was made using proteins from the standard of MW at 20 and 35 kDa and the main peak at 148 kDa from the waters mAb size variant standard (see **Supplementary Figure S1**).

2.3.5.2 SEC

The Waters mAb size variant standard was composed of main peak (148 kDa) low-MW species around 50 and 100 kDa, and high-MW species larger than 300 kDa were used for MW estimation.

2.4 Statistical Analysis

Statistical analyses were performed using GraphPad Prism 6 (GraphPad Software, Inc. La Jolla, CA). Two-way ANOVA tests were performed.

3 RESULTS AND DISCUSSION

3.1 Method Evaluation Using Samples Submitted to Stress and Reducing Conditions

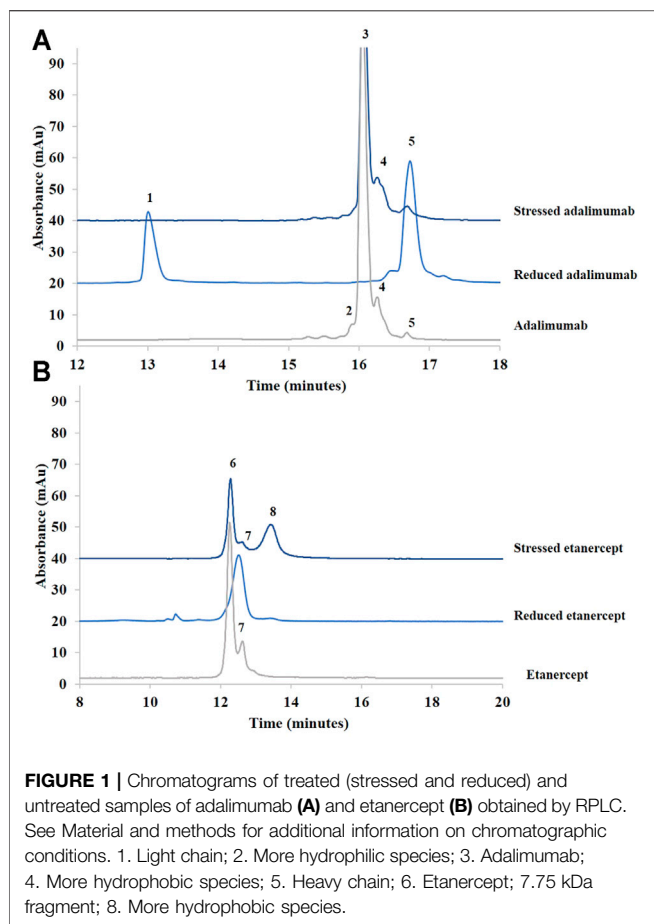
Adalimumab and etanercept were submitted to forced degradation conditions. Usually, forced degradation studies are performed to determine the degradation pathways of biopharmaceuticals and their stability (Venkataraman and Manasa, 2018). Here, we used degraded samples to assess the selectivity of the analytical methods (ICH, 1996). Each formulation was submitted to high temperature (60°C) and agitation (600 rpm) for 2 h. This process was expected to denature the proteins and generate aggregates, fragments, oxidation, and deamidation products (Tamizi and Jouyban, 2016; Nowak et al., 2017; Le Basle et al., 2020).

Moreover, BME, a reducing agent, was added to adalimumab and etanercept samples to cleave the disulfide bridges of the proteins (Müller and Winter, 2017). Intact adalimumab MW is approximately 148 kDa (EMEA, 2003; Lee et al., 2019). The treatment with BME was supposed to give two peaks for adalimumab corresponding to the light (25 kDa) and heavy (50 kDa) chains. Intact etanercept MW is approximately 150 kDa (Goldenberg, 1999). For etanercept, two fragments of about 75 kDa should be generated (see **Supplementary Figure S2**).

For method optimization, adalimumab biosimilar and etanercept reference product formulations were used. They were analyzed before and after stress conditions (temperature and agitation) and reduction by CGE, RPLC, and SEC.

3.1.1 RPLC

Three core-shell columns with a solid core and a porous outer layer were tested by RPLC. The stationary phases of the Biozen® columns (C4 and XB-C8; 3.6 µm particles) are grafted with alkyl groups and endcapped with trimethylsilyl groups. This reduces the interaction between the positive charges of adalimumab and etanercept and free silanols that may be negatively charged at a pH above 3. The BioResolve® column is functionalized with polyphenyl groups. This type of grafting has recently been used for the separation of antibodies and derived products (Bobály et al., 2018). The particles have a diameter of 2.7 µm. Moreover, the BioResolve®



column used in this study is two times longer than the Biozen® columns.

Gradient slope and flow rates were optimized (data not shown). Not surprisingly, the BioResolve® column offered the best performance. As shown in **Supplementary Figure S3**, the column was thermostated at 80°C as it is well known that a high temperature decreases the phenomenon of adsorption of monoclonal antibodies on the stationary phase (François and Guillaume, 2020). Working at 60°C was not high enough because an additional peak was still observed (**Supplementary Figure S3A**). At 80°C, this additional peak almost disappeared. This phenomenon was much less pronounced for etanercept samples (**Supplementary Figure S3B**).

Figure 1 shows the chromatograms obtained for adalimumab and etanercept under reducing and stress conditions. Under stress conditions, the small peaks already present in adalimumab (peaks 4 and 5) were still present, but the shoulder before the main peak (peak 2) corresponding to hydrophilic species disappeared.

After reduction, the chromatogram of adalimumab shows that the light (peak 1) and heavy chains (peak 5) are well separated (**Figure 1A**). The light chain, which is more hydrophilic, elutes first. The heavy chain elutes after the intact antibody (Bobály et al., 2018). This suggests that hydrophobic moieties in the heavy chain are hidden when the light chain is bound. Once the two chains are separated, these hydrophobic moieties could be

exposed, which might explain the higher retention of the heavy chain compared with the intact antibody.

Etanercept was analyzed under stress conditions as well. A major peak, more retained than the main peak of untreated etanercept, was generated (peak 8). For this recombinant protein, BME cleaves the disulfide bridges at the hinge region. The molecule should be divided into two identical fragments of about 75 kDa (see **Supplementary Figure S2**). Because there are intrachain disulfide bridges, the three-dimensional conformation of the fragments is also modified. As can be seen in **Figure 1B**, the generated peak is slightly more retained than the major peak observed in the nondegraded sample.

In sum, RPLC gave information on the hydrophobic character of recombinant proteins and their degradation products. Moreover, this technique was able to separate the species obtained after sample reduction. Further investigations concerning the identity of these species are discussed in **section 3.2** dedicated to the biosimilar comparability study.

3.1.2 CGE

An SDS-CGE method previously developed for the study of protein aggregation was used (Demelenne et al., 2019). The nature of the sample dilution solvent was optimized using adalimumab. This solvent appeared to have a tremendous impact on antibody peak shape (see **Figure 2**). Samples were first diluted in a Tris-HCl buffer at pH 9.0 with 1% of SDS and then heated. SDS is a denaturing agent that binds to the hydrophobic residues of the protein and disrupts noncovalent bonds and secondary and tertiary structures (Duivelshof et al., 2021). Covalent bonds, such as disulfide bridges or peptide bonds, remain intact (Schmid et al., 2017). SDS is used to give uniform charge to the molecules, allowing for a size-based separation in SDS-CGE.

Figure 2 shows the impact of the composition of the dilution solvent on adalimumab peak shape. As can be seen in this figure, it was necessary to block the free thiol groups of cysteine to analyze intact antibodies. Indeed, free thiol groups can reduce neighboring disulfide bonds, which can lead to the formation of unwanted species (Zhang et al., 2010). IAM is an alkylation agent that binds specifically to free thiol groups and blocks them. IAM prevents, thus, the formation of intermolecular disulfide bridges and the cleavage of existing disulfide bonds (Salas-Solano et al., 2006). Without IAM in the sample buffer, two

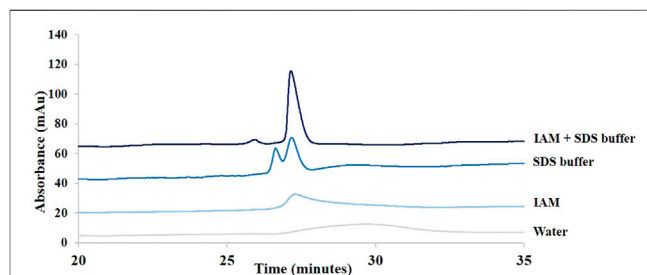


FIGURE 2 | Influence of the dilution solvent on adalimumab peak shape in SDS-CGE. Comparison of samples diluted 20 times in water, in 5 mM IAM, in SDS buffer, and in a mixture of SDS buffer and IAM. See Material and methods for additional information about CGE conditions.

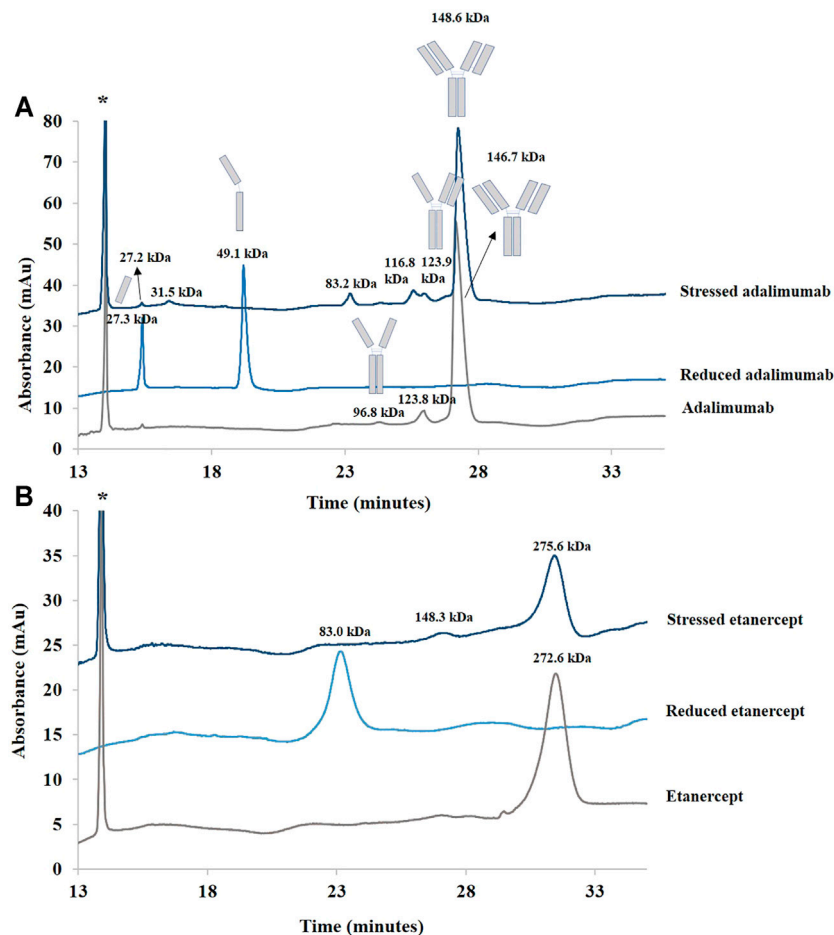


FIGURE 3 | Electropherograms of treated (stressed and reduced) and untreated samples of adalimumab **(A)** and etanercept **(B)** obtained by SDS-CGE. Molecular weights were estimated using a calibration curve. See Material and methods for additional information on the CGE conditions. *: lysozyme (internal standard).

peaks were detected, and with IAM in the buffer, one main peak was detected.

Adalimumab and etanercept were, thus, analyzed under those conditions. Lysozyme was used as an internal standard to correct peak areas and migration times. Adalimumab had a migration time of 27.2 min, and etanercept migrated at 31.5 min (see **Figure 3**). The MWs of the studied biopharmaceuticals were estimated using a calibration curve (see Material and methods). MWs of adalimumab and etanercept were estimated at 146.7 and 272.6 kDa, respectively. This is pretty close to the actual MW for adalimumab (148 kDa) but not for etanercept (150 kDa). This could be explained by the extended conformation of the sugar on etanercept. As etanercept is highly glycosylated, the protein could be not fully recovered by SDS, and the migration time is, thus, longer than for a molecule of similar MW with less glycosylation. This results in a biased MW determination (Wang et al., 2017). Moreover, etanercept appears as a broad peak due to the heterogeneity of the glycans that represent one third of its total MW.

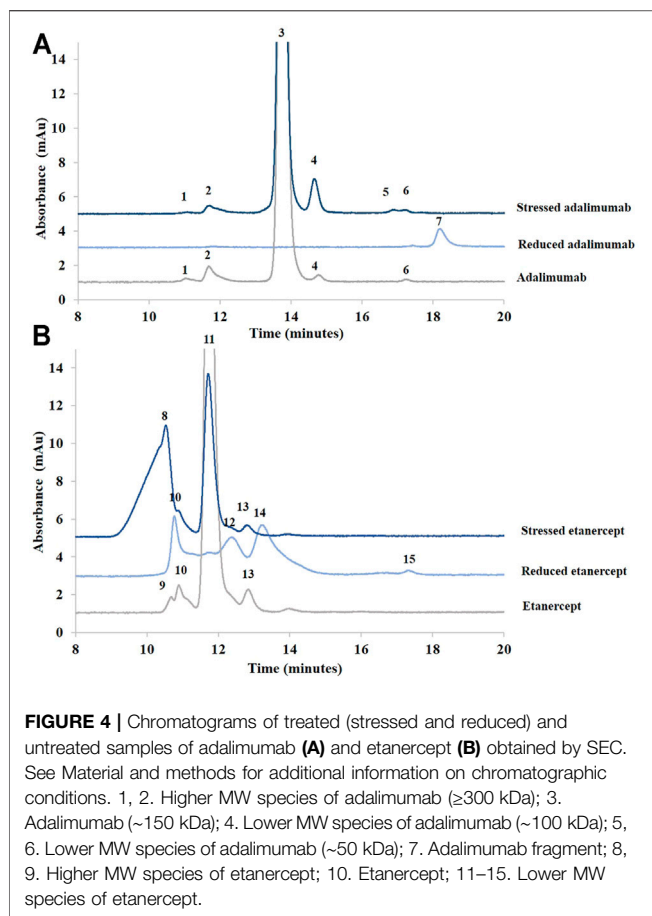
For the samples treated with BME, two peaks (at 15.5 and 19.5 min) were observed for adalimumab as expected. MWs for the light and heavy chains of adalimumab were estimated at 27.3

and 49.1 kDa, respectively. For etanercept, the treatment of the sample with BME provided only one peak estimated at 83.0 kDa.

As can also be seen in **Figure 3**, the sample of adalimumab submitted to stress generated species between 25 and 150 kDa (27.2, 31.5, 83.2, 116.8, and 123.9 kDa). The 27.2 kDa corresponds to the light chain of the antibody. The 123.9 kDa species could be related to the antibody without one of its light chains (theoretical value of 125 kDa).

In the untreated sample, the light chain of the antibody was found as well. Moreover, the 96.8 kDa species could correspond to the antibody with two heavy chains and no light chains (theoretical value of 100 kDa).

For etanercept, a peak estimated at 148.3 kDa was observed after agitation at 60°C for 2 h. Moreover, there is a loss of almost 50% of the normalized peak area (ratio of the peak area to its migration time corrected with the ratio of the peak area of the internal standard to its migration time). This low recovery suggests some precipitation of etanercept before injection (but a low recovery would also be observed with other techniques in that case), some adsorption of the high-MW species to the capillary wall, or some impossibilities for the high-MW species to enter into the gel.



No peak of higher MW than adalimumab or etanercept was found. Indeed SDS-CGE is not a suitable technique for the detection of noncovalent aggregates because they would be dissociated by SDS present in the buffer and in the sample (Duijvelshof et al., 2021). However, CGE was able to distinguish between species of various sizes in adalimumab and etanercept.

3.1.3 SEC

Adalimumab and etanercept were analyzed by SEC coupled to UV and MALS using a previously described method (Waters, 2020). The SEC analysis was performed on a BioResolve® SEC mAb column of 2.5 μm particle size and 200 \AA pore size of 30 cm with 7.8 mm internal diameter. The mobile phase was composed of 50 mM phosphate buffer (pH 7) and 200 mM KCl (Waters, 2020). An mAb standard was used for MW estimation by SEC-UV (see Section 2.3.5.2).

As can be seen in Figure 4, a difference in retention time between adalimumab and etanercept was observed. Adalimumab eluted in 13.7 min, and etanercept eluted after only 11.7 min. This suggests that etanercept is a larger protein than adalimumab although they have almost the same molecular weight (~ 150 kDa). Using a calibration curve obtained from mAb standard species, etanercept MW was estimated at 300 kDa. This is consistent with the value observed in CGE in which etanercept MW was estimated at 260 kDa, much larger than expected. It is described in the literature that sugars may have an

important effect on elution in SEC and, thus, that SEC-UV may not be suitable for MW determination of highly glycosylated proteins (Wen et al., 1996).

The analysis of the species obtained after BME reduction showed one single peak at 50 kDa, which corresponds to the heavy chain. The light chain could not be detected or coeluted with the heavy chain. For reduced etanercept, four peaks were observed instead of the expected single peak.

MALS was then used as an absolute approach to assess the MW of untreated adalimumab and etanercept and after stress conditions. Adalimumab (peak 3, corresponding to the intact product), has an estimated MW of 152 kDa. This is close to the expected MW of 148 kDa. The MW of the species related to peak 1 in the stressed solution could correspond to a complex of approximately 5 adalimumab molecules (819 kDa). Peak 2 species could correspond to a trimer (455 kDa). Peak 4 species could correspond to a mixture of antibodies that have lost at least one light chain (115 kDa). Peaks 5 and 6 species could correspond to the antibody that has lost its two light chains (109 kDa). As two peaks were observed, it should probably correspond to two populations of two heavy chain antibodies with small differences in their MW. It is interesting to note that peak 4 represents only 1% of the main peak in the untreated adalimumab sample but 6.6% of the main peak in the degraded sample. The percentage of high-MW species was almost identical in both samples (the sum of peaks 1 and 2 represents 3.3% of the main peak in the untreated sample and 3.2% of the main peak in the degraded sample).

For etanercept, the MW of peak 11 species, corresponding to intact etanercept, was estimated at 151 kDa. For etanercept submitted to stress conditions, a significant increase of the aggregated species (peak 8) was observed. Indeed, this peak represents 6.5% of the main peak (peak 11) in the reference product although it represents 166% of peak 11 in the stressed sample. The MW of this aggregate was found at 3451 kDa, which might correspond to the aggregation of 23 Fc-fusion proteins. In the untreated sample, peak 9 was estimated to correspond to a trimer (464 kDa), and peak 10 was estimated to correspond to a dimer (266 kDa). Peaks 12–15 species correspond to lower MW species.

In sum, aggregates could be nicely separated from adalimumab and etanercept fragments by SEC. For adalimumab, the light chain of the antibody could not be detected. MALS, which is an absolute approach, was necessary to estimate the MW of etanercept accurately.

3.2 Biosimilar Comparability Exercise

In the second part of this study, biosimilars of adalimumab and etanercept were compared with the reference products to evaluate their comparability. It should be noted that both the biosimilar and the reference product of adalimumab were outdated. However, they had expired less than a year previous to the time of analysis.

The formulations were compared in their initial state and after submission to a mild stress supposed to mimic biopharmaceuticals shipping conditions, i.e., agitation at 300 rpm for 4 h at 30°C.

3.2.1 Adalimumab

As can be seen in Figure 5A,D, few differences were observed in RPLC between the biosimilar and its reference product for the

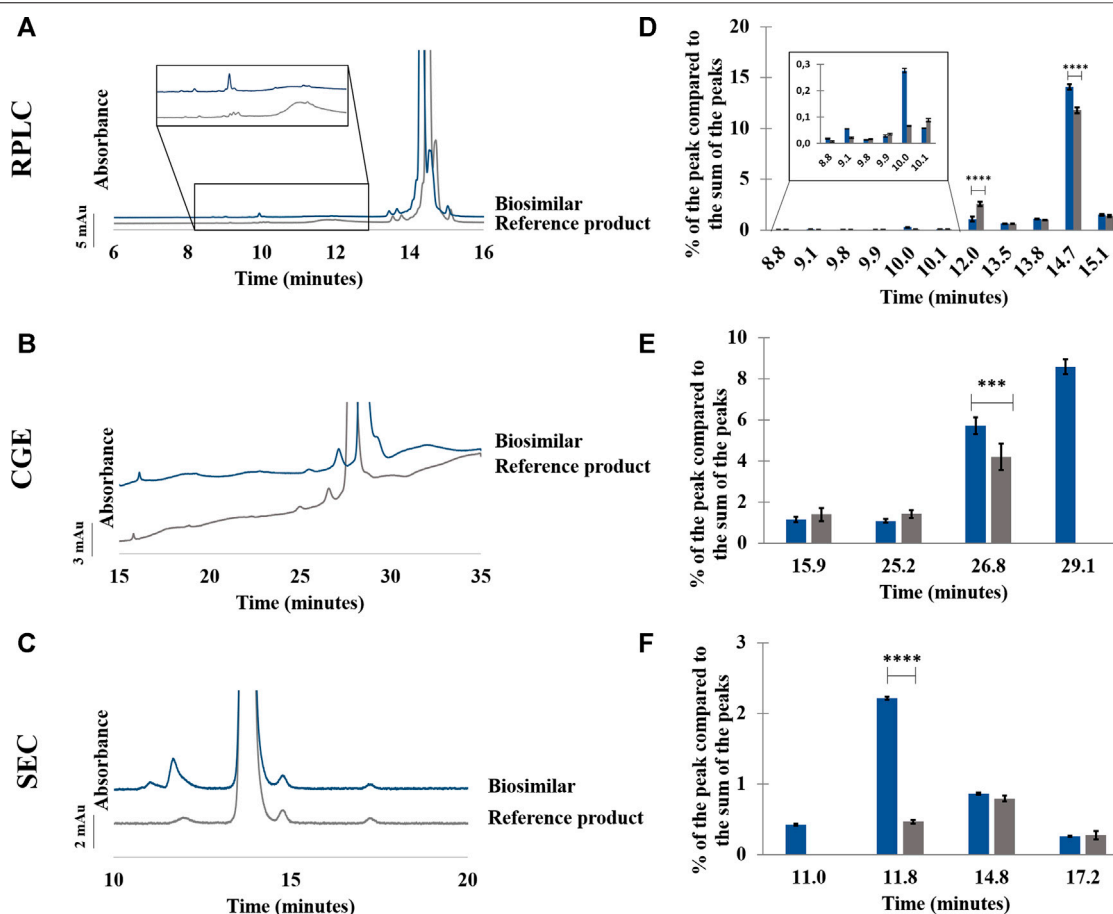


FIGURE 5 | Comparison between adalimumab reference product and its biosimilar by RPLC (A–D), CGE (B–E), and SEC (C–F). Chromatograms (A–C) and percentage of the peak compared to the sum of the peaks in function of the retention/migration time ($n = 3$) (D–F). For CGE, the peak areas of the peaks were corrected by their migration times. *** represents statistically different results with a p -value < 0.001 . **** represents statistically different results with a p -value < 0.0001 . See Material and methods for additional information on experimental conditions.

formulations in their initial state. The sum of the more hydrophilic impurities represents 3.3% of the sum of the peak areas for the biosimilar, and it represents 4.5% of the sum of the peak areas for the reference product. In particular, the peak at 10.1 min was more abundant in the biosimilar compared with the reference product, and the peak at 12.0 min was more abundant in the reference product than in the biosimilar (see **Supplementary Table S1**). Concerning the more hydrophobic impurities, they were slightly more abundant in the biosimilar as they represented 15.6% of the sum of the peak areas compared with 13.1% for the reference product. The repeatability of the method was evaluated from three injections of each product. RSDs below 0.3% were found for the retention time and peak area of the main peak for both the biosimilar and the reference product (see **Supplementary Table S2**).

Samples were also analyzed by RPLC-QTOF to determine the exact mass of the main peak of the reference product and that of the biosimilar. Antibodies are often characterized by their N-glycan composition. G0F glycoform is one of the most frequent types and represents oligosaccharides that contain fucose with no terminal galactosylation (Tebbey et al., 2015).

Moreover, adalimumab is present as three major isoforms depending on the number of C-terminal lysine (0, 1, or 2) carried by the molecule (EMA, 2003). The main peak for the reference product of adalimumab was detected at 148,092.25 Da and could be attributed to adalimumab G0F/G0F glycoform with no terminal lysine on the C terminal chain (Füssl et al., 2019). The main peak for the biosimilar of adalimumab was detected at almost the same MW (148,093.20 Da).

In CGE, a shoulder can be seen after the main peak in the biosimilar but not in the reference product. This shoulder represents around 8.6% of the sum of the peak areas. Moreover, the peak corresponding to the 125 kDa fragment was more abundant in the biosimilar than in the reference product (see **Figure 5B,E**; **Supplementary Table S1**). RSDs below 0.5% were found for migration times of the main peak. For peak area, 9.1% and 4.3% of variation were observed, respectively, for the reference product and the biosimilar (See **Supplementary Table S2**).

In SEC, a higher proportion of aggregates was found in the biosimilar than in the reference product (2.6% vs. 0.5%). Moreover, an aggregate was found at 11.0 min in the biosimilar that was

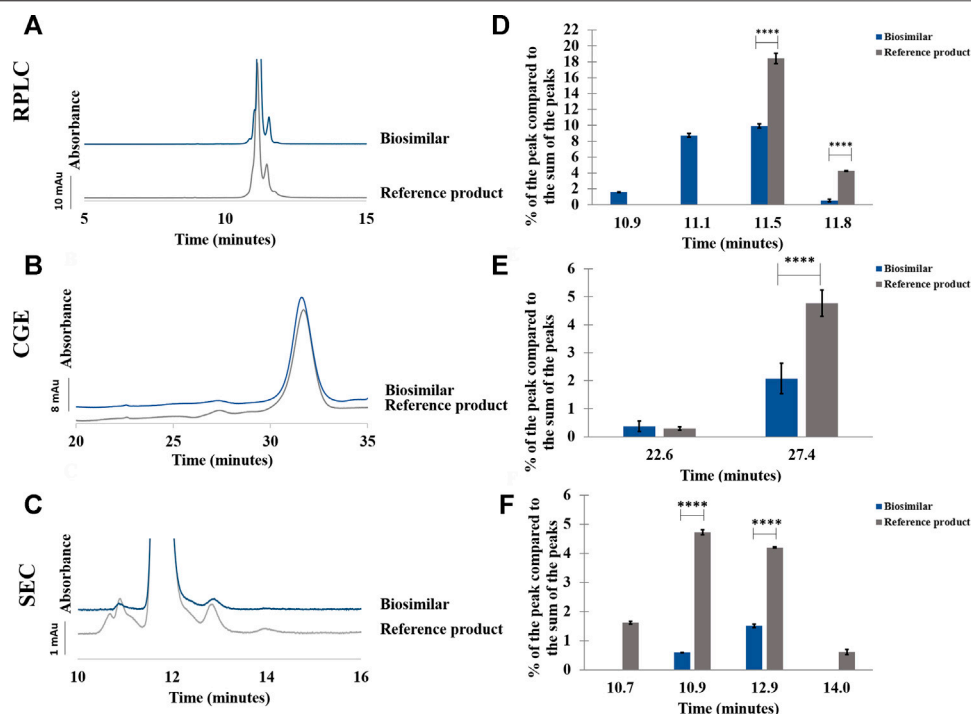


FIGURE 6 | Comparison between etanercept reference product and its biosimilar by RPLC (A–D), CGE (B–E), and SEC (C–F). Chromatograms (A–C) and percentage of the peak compared to the sum of the peaks in function of the retention/migration time ($n = 3$) (D–F). For CGE, the peak areas of the peaks were corrected by their migration times. **** represents statistically different results with a p -value < 0.0001 . See Material and methods for additional information on experimental conditions.

not present in the reference product. Concerning the fragments, there were no significant differences between the two biopharmaceuticals (see **Figure 5C,F**; **Supplementary Table S1**). RSDs on retention time and peak area of the main peak were below 0.1% for the reference product and the biosimilar (See **Supplementary Table S2**).

For samples of the reference product and biosimilar subjected to a temperature of 30°C and a stirring speed of 300 rpm for 4 h, no change in the chromatographic and electrophoretic profiles was observed (data not shown). This indicates a similar stability of the product under those conditions.

3.2.2 Etanercept

In RPLC, small differences were observed between the reference product and the biosimilar (see **Figure 6A,D**). A shoulder can be seen before the main peak in the biosimilar but not in the reference product. This shoulder corresponds to more hydrophilic species and represents 8.7% of the sum of the peak areas. Moreover, another hydrophilic species eluting just before the shoulder was also present only in the biosimilar and represented 1.6% of the sum of the peak areas. The percentage of the peak eluting just after the main peak (a 75-kDa fragment) was almost two times higher in the reference product than in the biosimilar (see **Supplementary Table S3**). RSDs below 0.1% were found for the retention time of the main peak and below 0.5% for its peak area for both the biosimilar and the reference product (see **Supplementary Table S4**).

Samples of etanercept were also analyzed by RPLC-QTOF to determine the exact mass of the main peak of the reference product and that of the biosimilar. Unfortunately, no exact mass measurement could be extracted from the acquired data. Indeed, the high heterogeneity of Fc-fusion proteins due to the presence of multiple glycosylation sites makes the analysis by MS particularly challenging (Duivelshof et al., 2021). The exact mass measurement of the protein is, thus, not possible without prior deglycosylation with an enzyme such as PNGase (Zhu et al., 2014).

In CGE, a higher percentage of the lower MW species was observed in the reference product compared to the biosimilar (4.8 vs. 2.1%) (see **Figure 6B,E**; **Supplementary Table S3**). The RSDs were below 0.2% for the migration time of the main peak and below 3.7% for its peak area (see **Supplementary Table S4**).

In SEC, a lower quantity of fragments and aggregates was found in the biosimilar compared with the reference product. Moreover, two groups of fragments and aggregates were observed for the reference product although there was only one group of fragments and aggregates for the biosimilar (see **Figures 6C,F**). A higher proportion of fragments (6.4% vs. 0.6%) and higher percentage of aggregates (4.8% vs. 1.5%) were observed in the reference product compared with the biosimilar (see **Supplementary Table S3**). RSDs below 0.1% were found for the retention time of the main peak and below 0.4% for its peak area (see **Supplementary Table S4**).

As in the case of adalimumab, no further degradation was observed for both samples subjected to a temperature of 30°C and a stirring at 300 rpm for 4 h (data not shown).

4 CONCLUSION AND PERSPECTIVES

With the increasing number of antibodies and derivatives on the market and the emergence of biosimilars, there is an important need for methods to study the comparability between the reference products and their biosimilars. The three analytical techniques (RPLC, SEC, and CGE) used herein to study adalimumab, etanercept, and their biosimilars were found to be very complementary.

The forced degradation applied to the studied biopharmaceuticals produced fragments and aggregates. It was shown that, although SEC is interesting for the detection of aggregates, CGE is able to distinguish between the fragments of adalimumab. However, it failed to give information about fragments for etanercept. RPLC provided information about the relative hydrophobicity of degradation products. RPLC and SEC were more repeatable than CGE. However, RSDs of retention/migration times were always lower than 0.5%.

The comparison between the biosimilars and their reference products showed that they are highly similar, but some slight differences were observed. A greater quantity of fragments and aggregates was observed in the adalimumab biosimilar compared with the reference product, but a smaller quantity of aggregates and fragments was observed in the etanercept biosimilar compared with the reference product. Similar results were obtained for the samples subjected to mild stress conditions.

In this work, complementary techniques to study size-variant products (SEC and CGE) and hydrophilic and hydrophobic impurities (RPLC) were used. Other chromatographic and electrophoretic techniques could also be used to evaluate comparability. Ion-exchange chromatography and capillary isoelectric focusing would be useful to study acidic and basic variants, and HILIC and CZE would help determine the glycosylation profile of the biopharmaceuticals (Berkowitz et al., 2012; Fekete et al., 2015; Pedersen-Bjergaard et al., 2019). All those variants need to be carefully controlled as they represent critical quality attributes that may affect product safety and efficacy (Oshinbolu et al., 2018).

Mass spectrometry was useful to determine the exact mass of the intact protein of adalimumab and could also be employed to determine the mass of the impurities. Due to the complexity of the glycosylation profile of etanercept, the use of an enzyme to cleave glycosidic bonds would be necessary to simplify the spectrum and enable analysis of the intact protein (Zhu et al., 2014).

Analysis by SEC and CGE showed a difference between the retention/migration times of these two biopharmaceuticals. The MW of etanercept was overestimated using both techniques knowing that the estimation of MW relies for both techniques on a calibration curve, including an IgG antibody standard. This difference is most probably due to the high glycosylation of etanercept which renders MW estimation inaccurate.

The combination of SEC with MALS detection was used to measure the MW of etanercept (150 kDa) without

overestimation. MALS has the advantage of determining the MW of proteins without the need for reference molecules having the same conformation. It is considered an absolute technique that determines the MW of compounds according to the amount of light scattered by them (Some et al., 2019).

Ion mobility spectrometry would also be an interesting additional technique to provide information on the three-dimensional conformation of adalimumab and etanercept. Moreover, collision-induced unfolding analysis could be applied to study how the molecules unfold when submitted to an accelerating electric field (Kerr et al., 2019).

Besides the analytical comparison of reference products with their related biosimilars, a biological activity comparison between these products must also be performed to demonstrate that they have similar pharmacological activity.

The analysis of monoclonal antibodies has been described in many publications due to the high number of mAbs on the market and the increasing number of biosimilars, but fewer articles dealing with Fc-fusion proteins can be found. Fc-fusion proteins are more complex molecules than mAbs as their structure depends on the structure of the ligand that is bound to the Fc fragment. As this ligand is different for every commercialized Fc-fusion protein, it is probably not possible to develop generic methods as is the case for mAbs. Moreover, Fc-fusion proteins present often more complex glycosylation profiles than those observed for mAbs, and innovative analytical methods are, therefore, required (Duivelshof et al., 2021).

DATA AVAILABILITY STATEMENT

The raw data supporting the conclusion of this article will be made available by the authors without undue reservation.

AUTHOR CONTRIBUTIONS

MF contributed to conception and design of the study. AD, AY, and DL performed the analysis. AD wrote the first draft of the manuscript. All authors contributed to manuscript revision, read, and approved the submitted version.

ACKNOWLEDGMENTS

The authors acknowledge the research grants from the Walloon Region of Belgium and EU Commission (project FEDER-PHARE) for the funding of the DTIMS-QTOF instrument.

SUPPLEMENTARY MATERIAL

The Supplementary Material for this article can be found online at: <https://www.frontiersin.org/articles/10.3389/fchem.2021.782099/full#supplementary-material>

REFERENCES

- Antibody society (2021). *An International Non-Profit Supporting Antibody-Related Research and Development. Antibody Therapeutics Approved or in Regulatory Review in the EU or US*. Available at: <https://www.antibodysociety.org/resources/approved-antibodies/> (Accessed June 27, 2021).
- Bang, L. M., and Keating, G. M. (2004). Adalimumab. *BioDrugs*. 18, 121–139. doi:10.2165/00063030-200418020-00005
- Berkowitz, S. A., Engen, J. R., Mazzeo, J. R., and Jones, G. B. (2012). Analytical Tools for Characterizing Biopharmaceuticals and the Implications for Biosimilars. *Nat. Rev. Drug Discov.* 11, 527–540. doi:10.1038/nrd3746
- Bobály, B., D'Atri, V., Lauber, M., Beck, A., Guillaume, D., and Fekete, S. (2018). Characterizing Various Monoclonal Antibodies With Milder Reversed Phase Chromatography Conditions. *J. Chromatogr. B*. 1096, 1–10. doi:10.1016/j.jchromb.2018.07.039
- Davies, H. D. (2016). Infectious Complications With the Use of Biologic Response Modifiers in Infants and Children. *Pediatrics*. 138, e20161209. doi:10.1542/peds.2016-1209
- Davis, J. D., Deng, R., Boswell, C. A., Zhang, Y., Li, J., Fielder, P., et al. (2013). *Monoclonal Antibodies: From Structure to Therapeutic Application*. Editors D. J. A. Crommelin, R. Sindelar, and B. Meibohm (Springer: Pharm. Biotechnol.), 1–544.
- Demelenne, A., Napp, A., Bouillenne, F., Crommen, J., Servais, A.-C., and Fillet, M. (2019). Insulin Aggregation Assessment by Capillary Gel Electrophoresis without Sodium Dodecyl Sulfate: Comparison With Size-Exclusion Chromatography. *Talanta*. 199, 457–463. doi:10.1016/j.talanta.2019.02.074
- Duivelshof, B. L., Murisier, A., Camperi, J., Fekete, S., Beck, A., Guillaume, D., et al. (2021). Therapeutic Fc-Fusion Proteins: Current Analytical Strategies. *J. Sep. Sci.* 44, 35–62. doi:10.1002/jssc.202000765
- EMA (2003). *Humira - Scientific Discussion*.
- European Medicines Agency, Medicines (2021). Available at: https://www.ema.europa.eu/en/medicines/field_ema_web_categories%253Aname_field/Human/ema_group_types/ema_medicine/field_ema_med_status/authorised-36/ema_medicine_types/field_ema_med_biosimilar/search_api_aggregation_ema_medicine_types/field_ema_med_biosim (Accessed June 26, 2021).
- European Medicines Agency (2014). Guideline on Similar Biological Medicinal Products Containing Biotechnology-Derived Proteins as Active Substance : Quality Issues. Available at: http://www.ema.europa.eu/docs/en_GB/document_library/Scientific_guideline/2015/01/WC500180219.pdf.
- FDA (2021). Available at: <https://www.fda.gov/> (Accessed April 22, 2021).
- Fekete, S., Beck, A., Veuthey, J.-L., and Guillaume, D. (2015). Ion-Exchange Chromatography for the Characterization of Biopharmaceuticals. *J. Pharm. Biomed. Anal.* 113, 43–55. doi:10.1016/j.jpba.2015.02.037
- Food and Drug Administration (2021). Biosimilar Drug Information. Available at: <https://www.fda.gov/drugs/biosimilars/biosimilar-product-information> (Accessed June 26, 2021).
- François, Y., and Guillaume, D. (2020). “Facing the Complexity of Biopharmaceuticals Characterization,” in 36th Int. Symp. Microscale Sep. Bioanal. 36.
- Füssli, F., Trappe, A., Cook, K., Scheffler, K., Fitzgerald, O., and Bones, J. (2019). Comprehensive Characterisation of the Heterogeneity of Adalimumab via Charge Variant Analysis Hyphenated On-Line to Native High Resolution Orbitrap Mass Spectrometry. *MAbs* 11, 116–128. doi:10.1080/19420862.2018.1531664
- Gherghescu, I., and Delgado-Charro, M. B. (2021). The Biosimilar Landscape: An Overview of Regulatory Approvals by the EMA and FDA. *Pharmaceutics*. 13, 1–16. doi:10.3390/pharmaceutics13010048
- Gokarn, Y., Agarwal, S., Arthur, K., Bepperling, A., Day, E. S., Filoti, D., et al. (2015). “Biophysical Techniques for Characterizing the Higher Order Structure and Interactions of Monoclonal Antibodies,” in *State-of-the-Art Emerg. Technol. Ther. Monoclon. Antib. Charact.* (ACS Symposium Series), 285–327. doi:10.1021/bk-2015-1201.ch006
- Goldenberg, M. M. (1999). Etanercept, a Novel Drug for the Treatment of Patients With Severe, Active Rheumatoid Arthritis. *Clin. Ther.* 21, 75–87. doi:10.1016/s0149-2918(00)88269-7
- ICH (1996). Q2B : Validation of Analytical Procedures: Methodology, n.D. Available at: www.ich.org.
- ICH (2021). *ICH Official Web Site*. ICH. Available at: <https://www.ich.org/> (Accessed January 24, 2021).
- Kerr, R. A., Keire, D. A., and Ye, H. (2019). The Impact of Standard Accelerated Stability Conditions on Antibody Higher Order Structure as Assessed by Mass Spectrometry. *MAbs*. 11, 930–941. doi:10.1080/19420862.2019.1599632
- Le Basle, Y., Chennell, P., Tokhadze, N., Astier, A., and Sautou, V. (2020). Physicochemical Stability of Monoclonal Antibodies: A Review. *J. Pharm. Sci.* 109, 169–190. doi:10.1016/j.xphs.2019.08.009
- Lee, N., Lee, J. J., Yang, H., Baek, S., Kim, S., Kim, S., et al. (2019). Evaluation of Similar Quality Attribute Characteristics in SB5 and Reference Product of Adalimumab. *MAbs*. 11, 129–144. doi:10.1080/19420862.2018.1530920
- Liddell, E. (2013). *Antibodies*. in *Immunoass. Handb.* (Elsevier), 245–265. doi:10.1016/b978-0-08-097037-0.00017-8
- Liu, Y., Parameswara, R., Ratnayake, C., and Koh, E. (2008). *Methods and Compositions for Capillary Electrophoresis*. Beckman Coulter Inc.
- Miranda-hernández, M. P., Valle-gonzález, E. R., and Ferreira-gómez, D. (2015). Theoretical Approximations and Experimental Extinction Coefficients of Biopharmaceuticals. *Anal. Bioanal. Chem.* 408 (5), 1523–1530. doi:10.1007/s00216-015-9261-6
- Mitoma, H., Horiuchi, T., Tsukamoto, H., and Ueda, N. (2018). Molecular Mechanisms of Action of Anti-TNF- α Agents - Comparison Among Therapeutic TNF- α Antagonists. *Cytokine*. 101, 56–63. doi:10.1016/j.cyt.2016.08.014
- Müller, T., and Winter, D. (2017). Systematic Evaluation of Protein Reduction and Alkylation Reveals Massive Unspecific Side Effects by Iodine-Containing Reagents. *Mol. Cell Proteomics*. 16, 1173–1187. doi:10.1074/mcp.m116.064048
- Nowak, C., K. Cheung, J., M. Dellatore, S., Katiyar, A., Bhat, R., Sun, J., et al. (2017). Forced Degradation of Recombinant Monoclonal Antibodies: A Practical Guide. *MAbs*. 9, 1217–1230. doi:10.1080/19420862.2017.1368602
- Oshinbolu, S., Wilson, L. J., Lewis, W., Shah, R., and Bracewell, D. G. (2018). Measurement of Impurities to Support Process Development and Manufacture of Biopharmaceuticals. *Trac Trends Anal. Chem.* 101, 120–128. doi:10.1016/j.trac.2017.10.026
- Pedersen-Bjergaard, S., Gammelgaard, B., and Gronhaug Halvorsen, T. (2019). *Introduction to Pharmaceutical Analytical Chemistry*. John Wiley & Sons Ltd.
- Salas-Solano, O., Tomlinson, B., Du, S., Parker, M., Strahan, A., and Ma, S. (2006). Optimization and Validation of a Quantitative Capillary Electrophoresis Sodium Dodecyl Sulfate Method for Quality Control and Stability Monitoring of Monoclonal Antibodies. *Anal. Chem.* 78, 6583–6594. doi:10.1021/ac060828p
- Schmid, M., Prinz, T. K., Stäbler, A., and Sänglerlaub, S. (2017). Effect of Sodium Sulfite, Sodium Dodecyl Sulfate, and Urea on the Molecular Interactions and Properties of Whey Protein Isolate-Based Films. *Front. Chem.* 4, 49–15. doi:10.3389/fchem.2016.00049
- Some, D., Amartely, H., Tsadok, A., and Lebendiker, M. (2019). Characterization of Proteins by Size-Exclusion Chromatography Coupled to Multi-Angle Light Scattering (SEC-MALS). *J. Vis. Exp.* 148, 1–9. doi:10.3791/59615
- Tamizi, E., and Jouyban, A. (2016). Forced Degradation Studies of Biopharmaceuticals: Selection of Stress Conditions. *Eur. J. Pharmaceutics Biopharmaceutics*. 98, 26–46. doi:10.1016/j.ejpb.2015.10.016
- Tebbey, P. W., Varga, A., Naill, M., Clewell, J., and Venema, J. (2015). Consistency of Quality Attributes for the Glycosylated Monoclonal Antibody Humira (Adalimumab). *MAbs*. 7, 805–811. doi:10.1080/19420862.2015.1073429
- Venkataraman, S., and Manasa, M. (2018). Forced Degradation Studies: Regulatory Guidance, Characterization of Drugs, and Their Degradation Products - A Review. *Drug Invent. Today*. 10, 137–146.
- Wang, G., De Jong, R. N., Van Den Bremer, E. T. J., Parren, P. W. H. I., and Heck, A. J. R. (2017). Enhancing Accuracy in Molecular Weight Determination of Highly Heterogeneously Glycosylated Proteins by Native Tandem Mass Spectrometry. *Anal. Chem.* 89, 4793–4797. doi:10.1021/acs.analchem.6b05129
- Waters (2020). *BioResolve SEC mAb Guard and Columns*.
- Wen, J., Arakawa, T., and Philo, J. S. (1996). Size-Exclusion Chromatography With On-Line Light-Scattering, Absorbance, and Refractive Index Detectors for Studying Proteins and Their Interactions. *Anal. Biochem.* 240, 155–166. doi:10.1006/abio.1996.0345

- Zhang, J., Burman, S., Gunturi, S., and Foley, J. P. (2010). Method Development and Validation of Capillary Sodium Dodecyl Sulfate Gel Electrophoresis for the Characterization of a Monoclonal Antibody. *J. Pharm. Biomed. Anal.* 53, 1236–1243. doi:10.1016/j.jpba.2010.07.029
- Zhu, L., Guo, Q., Guo, H., Liu, T., Zheng, Y., Gu, P., et al. (2014). Versatile Characterization of Glycosylation Modification in CTLA4-Ig Fusion Proteins by Liquid Chromatography-Mass Spectrometry. *MAbs.* 6, 1474–1485. doi:10.4161/mabs.36313

Conflict of Interest: The authors declare that the research was conducted in the absence of any commercial or financial relationships that could be construed as a potential conflict of interest.

Publisher's Note: All claims expressed in this article are solely those of the authors and do not necessarily represent those of their affiliated organizations, or those of the publisher, the editors and the reviewers. Any product that may be evaluated in this article, or claim that may be made by its manufacturer, is not guaranteed or endorsed by the publisher.

Copyright © 2021 Demelenne, Ben Yahia, Lempereur, Crommen, Servais, Fradi and Fillet. This is an open-access article distributed under the terms of the Creative Commons Attribution License (CC BY). The use, distribution or reproduction in other forums is permitted, provided the original author(s) and the copyright owner(s) are credited and that the original publication in this journal is cited, in accordance with accepted academic practice. No use, distribution or reproduction is permitted which does not comply with these terms.



Diagnosis and Stratification of *Pseudomonas aeruginosa* Infected Patients by Immunochemical Quantitative Determination of Pyocyanin From Clinical Bacterial Isolates

OPEN ACCESS

Edited by:

Costas C. Papagiannitsis,
University of Thessaly, Greece

Reviewed by:

Jianuan Zhou,
South China Agricultural University,
China

Marc Finianos,
Charles University, Czechia

*Correspondence:

Lluïsa Vilaplana
lluïsa.vilaplana@iqac.csic.es

Specialty section:

This article was submitted to
Clinical Microbiology,
a section of the journal
Frontiers in Cellular and
Infection Microbiology

Received: 08 October 2021

Accepted: 12 November 2021

Published: 14 December 2021

Citation:

Rodriguez-Urretavizcaya B,
Pascual N, Pastells C,
Martin-Gomez MT, Vilaplana L and
Marco M-P (2021) Diagnosis and
Stratification of *Pseudomonas*
aeruginosa Infected Patients by
Immunochemical Quantitative
Determination of Pyocyanin From
Clinical Bacterial Isolates.
Front. Cell. Infect. Microbiol. 11:786929.
doi: 10.3389/fcimb.2021.786929

Barbara Rodriguez-Urretavizcaya^{1,2}, Nuria Pascual^{1,2}, Carme Pastells^{1,2},
Maria Teresa Martin-Gomez³, Lluïsa Vilaplana^{1,2*} and Maria-Pilar Marco^{1,2}

¹ Nanobiotechnology for Diagnostics (Nb4D), Institute of Advanced Chemistry of Catalonia, Institute for Advanced Chemistry of Catalonia (IQAC)-Spanish National Research Council (CSIC), Barcelona, Spain, ² Centro de Investigación Biomédica en Red (CIBER) de Bioingeniería, Biomateriales y Nanomedicina (CIBER-BBN), Madrid, Spain, ³ Microbiology Department, Hospital Universitari Vall d'Hebron, Barcelona, Spain

The development of a highly sensitive, specific, and reliable immunochemical assay to detect pyocyanin (PYO), one of the most important virulence factors (VFs) of *Pseudomonas aeruginosa*, is here reported. The assay uses a high-affinity monoclonal antibody (mAb; C.9.1.9.1.1.2.2.) raised against 1-hydroxyphenazine (1-OHphz) hapten derivatives (PC1; a 1:1 mixture of 9-hydroxy- and 6-hydroxy-phenazine-2-carboxylic acids). Selective screening using PYO and 1-OHphz on several cloning cycles allowed the selection of a clone able to detect PYO at low concentration levels. The microplate-based ELISA developed is able to achieve a limit of detection (LoD) of 0.07 nM, which is much lower than the concentrations reported to be found in clinical samples (130 μM in sputa and 2.8 μM in ear secretions). The ELISA has allowed the investigation of the release kinetics of PYO and 1-OHphz (the main metabolite of PYO) of clinical isolates obtained from *P. aeruginosa*-infected patients and cultured in Mueller–Hinton medium. Significant differences have been found between clinical isolates obtained from patients with an acute or a chronic infection (~6,000 nM vs. ~8 nM of PYO content, respectively) corroborated by the analysis of PYO/1-OHphz levels released by 37 clinical isolates obtained from infected patients at different stages. In all cases, the levels of 1-OHphz were much lower than those of PYO (at the highest levels 6,000 nM vs. 300 nM for PYO vs. 1-OHphz, respectively). The results found point to a real potential of PYO as a biomarker of *P. aeruginosa* infection and the possibility to use such VF also as a biomarker for patient stratification[2] and for an effective management of these kinds of infections.

Keywords: quorum sensing, pyocyanin, ELISA, *Pseudomonas aeruginosa*, monoclonal antibody, diagnostic

1 INTRODUCTION

Pseudomonas aeruginosa is a common Gram-negative opportunistic multidrug-resistant pathogen that causes acute and chronic infections especially in immunocompromised patients (Barbier et al., 2013; Pieters et al., 2019). It is one of the main pathogens causing nosocomial infections such as hospital-acquired pneumonia (HAP), health care-associated pneumonia (HCAP), ventilator-associated pneumonia (VAP), and ventilator-associated tracheobronchitis (Williams et al., 2010), contributing to a high mortality and morbidity (Gaynes et al., 2005; Sadikot et al., 2005; Pang et al., 2019). It colonizes different parts of the body such as the skin, heart, urinary tract, ears, eyes, airways, and lung tissues, causing urinary infections, burn, respiratory infections, and septicemia (Yang et al., 2011; Ruffin and Brochiero, 2019). Moreover, it is one of the most predominant bacteria in the lungs of patients with cystic fibrosis (CF) (Maurice et al., 2019). CF is an autosomal recessive genetic disease frequent in the Caucasian population caused by mutations in the cystic fibrosis transmembrane conductance regulator (*CFTR*) gene. This gene codes for the CFTR protein that is responsible for maintaining epithelial surface hydration by regulating ion and water transport (De Boeck, 2020). Defective expression of CFTR induces mucus hypersecretion that obstructs airways and ultimately triggers morbidity and mortality in CF patients (Puchelle et al., 2002).

In the last years, as many other bacterial species (Blair et al., 2015), *P. aeruginosa* has developed resistance to antibiotics mainly due to its high adaptability and metabolic versatility (Breidenstein et al., 2011; Klockgether et al., 2011). Usually, *P. aeruginosa* infections are categorized as acute and chronic. The first is associated with a planktonic lifestyle, and it is frequent during early stages of infection. It shows a high virulence factor (VF) expression [as it is the case for pyocyanin (PYO) (Chandler et al., 2019)] and, in general, is susceptible to antibiotics. In contrast, chronic infections are characterized by low VF levels and are more resistant to antibiotics mainly due to biofilm formation (Heacock-Kang et al., 2017) and persistent cell generation (chronicity) (Van den Bergh et al., 2017), both characteristics of resistance mechanisms in *P. aeruginosa* (Taylor et al., 2014; Valentini et al., 2018; Lozano et al., 2018). Therefore, eradication therapies at early stages of the infection are recommended, since at this stage, bacterial strains are more susceptible to antibiotics (Zegans et al., 2002; Boucher et al., 2009; Hirsch and Tam, 2010; Park et al., 2012; Pang et al., 2019).

Plate cultures inoculated from swab samples continue to be the most common practice for *P. aeruginosa* identification, but it can take between 24 and 48 h (Sismaet et al., 2017), which usually results in a delay on the administration of the correct treatment, aggravating the symptoms and/or increasing resistance problems. Hence, the development of efficient tools for early diagnosis could significantly improve the management of *P. aeruginosa* infections. In this context, the identification of new biomarkers of infection has become an essential milestone. The development of pathogenesis and the transition between

acute and chronic infection stages are regulated by a bacterial gene regulation mechanism called quorum sensing (QS) system. QS coordinates the expression of a myriad of genes in response to the presence of small signal molecules known as autoinducers (AIs) (Valentini et al., 2018). When a threshold concentration of AIs is reached, the expression of genes that regulate the secretion of VFs and biofilm formation is triggered. Therefore, QS has attracted attention as a promising target to develop diagnostic and therapeutic approaches (Fong et al., 2018; Rehman and Leiknes, 2018).

Here, we focus on the main QS-regulated VF of *P. aeruginosa* called PYO, which is specific for this bacterium. PYO is a nitrogen-containing aromatic blue pigment belonging to the family of phenazines that presents unique redox properties (Dietrich et al., 2006; Jayaseelan et al., 2014; Hall et al., 2016). Phenazines exert a large number of effects on host cells such as cytokine production alteration [interleukin (IL)-8 and IL-6 increase], reactive oxygen species production (oxidative stress), cell signaling disruption, and ciliary motion inhibition (Ran et al., 2003; Hall et al., 2016). Moreover, phenazines can cause toxic effects or benefit other cells using electron transfer mechanisms (Costa et al., 2015). They are secreted at high concentrations during early colonization to establish infection (acute infections); however, during chronic infections, their levels are downregulated (D'Argenio et al., 2007; Mena et al., 2008). Apart from absorbance, electrochemical methods (Chen et al., 2015; Sismaet et al., 2017; Sakamoto et al., 2018) and surface-enhanced Raman spectroscopy studies (SERS) (Zukovskaja et al., 2017) are the most commonly used techniques for PYO detection in biological samples. Routine implementation of these technologies for biomedical and clinical analysis is difficult; in contrast, immunochemical analytical methods are positioned as reliable, efficient, and low-cost clinical diagnostic alternatives, reaching low limits of detection (LoDs) and excellent specificity (Krogsrud and Koivunen, 2006). These methods, based on the specific interaction between an antigen and an antibody (Ab), are widely implemented in clinical laboratories (Ma et al., 2019; Vatankhah et al., 2019; Zelini et al., 2019). Few years ago, we reported for the first time the development of polyclonal antibodies (pAbs) and microplate-based ELISA for 1-hydroxyphenazine (1-OHphz), the main metabolite of PYO, with an excellent detectability ($IC_{50} = 0.53$ nM) (Pastells et al., 2016). It has been reported that 1-OHphz also contributes to the virulence of *P. aeruginosa*. Besides the great structural similarities between PYO and 1-OHphz (**Figure 1**), the PYO cross-reacted only by a 0.1% ($IC_{50} > 800$ nM). Hence, PYO quantification required its complete transformation to 1-OHphz prior to the analysis, which was achieved by treating the samples with a strong base. Here, we report the development of monoclonal antibodies (mAbs) showing a much greater affinity for PYO, which have allowed direct quantification of this phenazine in culture broth of clinical isolates without prior transformation into 1-OHphz. The ELISA developed has been used to assess the potential of PYO and 1-OHphz as biomarkers of infection and patient stratification.

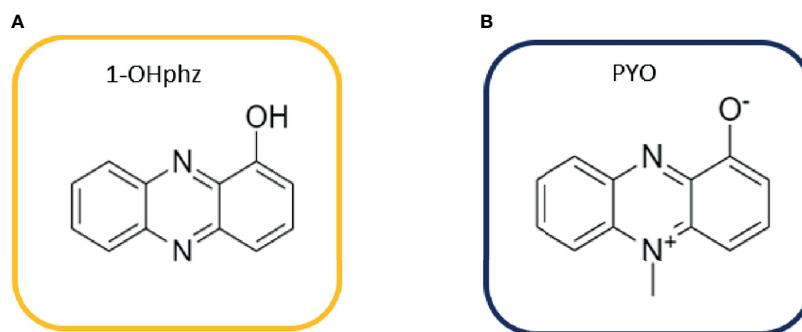


FIGURE 1 | Structures of **(A)** 1-hydroxyphenazine (1-OHphz) and **(B)** pyocyanin (PYO) phenazines. Both molecules are structurally similar having the PYO molecule just an extra methyl group at position 5.

2 MATERIALS AND METHODS

2.1 General Methods and Instruments

The pH and conductivity of all buffers and solutions were measured with a pH-meter pH 540 GLP and a conductimeter LF 340, respectively (WTW, Weilheim, Germany).

Polystyrene microtiter plates used for the ELISAs were purchased from Nunc (Maxisorp, Roskilde, Denmark). Dilution plates were purchased from Nirco (Barberà del Vallès, Spain). Washing steps performed during the ELISA were carried out on a Biotek ELx465 (Biotek Inc.). Absorbances were read on a Thermo Scientific MultiSkan GO (Thermo Fisher Scientific, Waltham, MA, USA) at 450-nm wavelength. The competitive curves shown were obtained using a four-parameter logistic equation using GraphPad Prism 7.0 (GraphPad Software Inc., San Diego, CA, USA). The presented results correspond to the average and standard deviation of at least two well replicates.

2.2 Buffers and Bacterial Growth Media

Phosphate-buffered saline (PBS) is 10 mM phosphate buffer with 0.8% saline solution, adjusting the pH to 7.5. PBST (assay buffer) is PBS with 0.05% Tween 20. Also, 10× PBS is PBS 10 times concentrated. Coating buffer is 50 mM carbonate-bicarbonate buffer pH 9.6. Citrate buffer is a 40-mM solution of sodium citrate pH 5.5. The substrate solution contains 0.01% TMB (3,3',5,5'-tetramethylbenzidine) and 0.004% H₂O₂ in citrate buffer. Mueller–Hinton (MH) broth (Ref. 70192, Sigma Aldrich) was prepared by diluting 21 g of the corresponding powder in 1 L of deionized water, as indicated by the manufacturer. The resulting liquid medium was subsequently autoclaved.

2.3 Chemicals and Immunochemicals

PYO was obtained from Sigma-Aldrich Co. (St. Louis, MO), and 1-OHphz was synthesized following the procedures (Vivian, 1956). The development of the anti-1-OHphz pAb As230 was described by Pastells et al. (2016). The preparation of the PYO mAb C.9.1.9.1.1.2.2. has been performed with the support of the U2 [Custom Antibody Service (CABS) of the ICTS “NANOBIOSIS”]. PC1-HCH and PC1-BSA bioconjugates were

obtained following the same synthetic route described in Pastells et al. (2016).

2.4 Preparation of Monoclonal Antibodies

BALB/c female mice (8–10 weeks old) were immunized with PC1-HCH maleic acid (MA). The first dose consisted of 100 µg of bioconjugate injected intraperitoneally as an emulsion of PBS and complete Freund's adjuvant. In addition, three booster injections were given at 3-week intervals using the same dose of immunogen emulsified in incomplete Freund's adjuvant. Mice selected as spleen donors for hybridoma production received a final injection of 100 µg of antigen in PBS 4 days prior to fusion.

P3-X63/Ag 8.653 murine myeloma cells (ATCC, Rockville, MD) were cultured in Dulbecco's Modified Eagle Medium (DMEM) (high-glucose DMEM with 2 mM alanylglutamine, 1 mM MEM nonessential amino acids, and 25 µg/ml gentamicin) supplemented with 10% (v/v) fetal bovine serum (FBS). Mouse spleen lymphocytes were fused with myeloma cells at a 4:1 ratio using PEG 1500 (Roche Applied Science, Mannheim, Germany) as a fusing agent. The fused cells were cultured in 96-well culture plates at a density of 2×10^5 cells/100 µl of 15% FBS-supplemented DMEM per well. After 24 h, Hypoxanthine-aminopterin-thymidine medium (HAT) selection medium [10% FBS-supplemented DMEM with 100 µM hypoxanthine, 0.4 µM aminopterin, 16 µM thymidine, 2% Hybridoma Fusion and Cloning Supplement (HFCS; Roche)] was added (100 µl/well). Subsequently, 10 days after cell fusion, culture supernatants were screened by performing indirect ELISA assays, coating the corresponding plates with 1.0 µg/ml PC1-BSA conjugate in order to select the hybridomas that were able to recognize PYO with high affinity. The chosen hybridomas were then cloned by the limiting dilution method using HT medium (HAT medium without aminopterin), supplemented with 15% FBS and 1% HFCS. Finally, stable antibody-producing clones were expanded and cryopreserved in liquid nitrogen, and the resulting supernatants containing mAbs were purified by protein G affinity chromatography.

Protocols and procedures have been approved by the CID-CSIC Ethical Committee (local institution), CSIC-CEEA: Ethics

Committee for Animal Experimentation of CSIC (CSIC animal experimentation ethical committee, evaluating procedures at the national level), and Catalanian authorities.

2.5 Two-Dimensional Experiments

The appropriate dilutions of mAb and PC1-BSA coating antigen required to perform indirect competitive ELISAs were established by carrying out a 2D checkerboard titration assay (Barcelo et al., 1997). This 2D experiment consists of testing serial dilutions of PC1-BSA bioconjugate and mAb in order to select their optimal combination to achieve high absorbance values without reaching the saturation levels of the curve.

2.6 Competitive Microplate-Based ELISA

2.6.1 Pyocyanin ELISA

Microtiter plates were coated with PC1-BSA ($0.125 \mu\text{g ml}^{-1}$ in coating buffer $100 \mu\text{l well}^{-1}$) and incubated overnight at 4°C . Then, the plates were washed four times with PBST ($4 \times 300 \mu\text{l}$) and serial dilutions of PYO (from 3,200 to 0 nM in PBST) or the samples, diluted with the assay buffer, were added ($50 \mu\text{l well}^{-1}$) followed by the solution of the mAb C.9.1.9.1.1.2.2. ($0.01575 \mu\text{g ml}^{-1}$ also in PBST, $50 \mu\text{l well}^{-1}$). After 30-min incubation shaking at room temperature (RT), the plates were washed as described above, and the anti-immunoglobulin G (anti-IgG)-horseradish peroxidase (HRP) solution ($1/2,000$ in PBST, $100 \mu\text{l well}^{-1}$) was added, waiting an additional 30-min incubation period. Subsequently, another cycle of washes was performed, and the substrate solution was added ($100 \mu\text{l well}^{-1}$). Finally, the enzymatic reaction was stopped after 30 min at RT with $2 \text{ M H}_2\text{SO}_4$ ($50 \mu\text{l well}^{-1}$). The absorbances were measured at 450 nm.

2.6.2 1-Hydroxyphenazine ELISA

Briefly, the procedure used was similar as the PYO ELISA described above but coating the microplates with PC1-BSA at $0.0625 \mu\text{g ml}^{-1}$ and using the pAb As230 ($1/6,000$ in PBST) and anti-IgG-HRP ($1/6,000$ in PBST) (Pastells et al., 2016).

2.7 Matrix Effect Studies

Nonspecific interferences produced by bacterial isolates medium were analyzed by preparing standard curves of PYO and 1-OHphz directly in MH broth diluted several times (0 and from $1/5$ to $1/20$) with PBST and measuring them with the PYO and 1-OHphz ELISAs to assess the parallelism with respect to the calibration curves prepared in the assay buffer.

2.8 Accuracy Studies

PYO blind spiked samples (ranging from 30 to 0 nM) were prepared in PBST and MH broth and measured with the PYO ELISA to assess assay accuracy.

2.9 Clinical Isolate Samples

Thirty-seven bacterial isolates collected at the Microbiology Department of the Vall d'Hebron University Hospital (VHUH, Barcelona, Spain) from patients diagnosed with *P. aeruginosa*

acute or chronic infections (Table 1) were tested. Well-isolated colonies from primary cultures were selected and stored frozen in glycerol at -20°C until use. PAO1 strain (ATCC 15692) was used as a reference strain.

The experimentation reported here has been approved by the CEIC (Ethical Committee for Clinical Research) of the Hospital Vall d'Hebron and the ethical committee of CSIC.

2.10 Bacterial Isolate Growth Medium and Inoculum Preparation

Bacterial clinical isolate frozen stocks from patients with proven infection by *P. aeruginosa* were inoculated onto Columbia agar plates supplemented with 5% sheep blood (Biomérieux Ref. 43041) and incubated overnight at 37°C . Next day, four or five colonies from each plated isolate were transferred using a sterile swab into 10-ml Falcon with 3-ml MH liquid media (initial suspension) and kept shaking (500 rpm) at 37°C . When turbidity

TABLE 1 | Description of the 37 bacterial isolates from patients infected with *P. aeruginosa*.

Number of patient	Isolate Nb4D	Underlying clinical situation
1	PAAI1	Acute nosocomial infection
2	PAAI2	Acute nosocomial infection
3	PAAI3	Intermittent colonization
4	PAAI4	Acute nosocomial infection
5	PAAI5	Acute nosocomial infection
6	PAAI6	Acute nosocomial infection
7	PAAI7	Acute nosocomial infection
8	PAAI8	Acute infection. Lung transplant recipient
9	PAAI9	Acute infection. Lung transplant recipient
20	PACI1	Chronic infection. Non-CF bronchiectasis
21	PACI2	Chronic infection. Non-CF bronchiectasis
22	PACI3	Chronic infection. Non-CF bronchiectasis
23	PACI4	Chronic infection. Non-CF bronchiectasis
24	PACI5	Chronic infection. CF bronchiectasis. Sinusitis episode
25	PACI6	Chronic infection. CF bronchiectasis
26	PACI7	Chronic infection. CF bronchiectasis
27	PACI8	Chronic infection. CF bronchiectasis
–	PAO1 ^a	Control strain
10	PAAI10	Acute nosocomial infection
11	PAAI11	Acute nosocomial infection
12	PAAI12	Acute infection. COPD
13	PAAI13	Acute nosocomial infection
14	PAAI14	Acute infection. Lung transplant recipient
15	PAAI15	Acute nosocomial infection
16	PAAI16	Acute nosocomial infection
17	PAAI17	Intermittent colonization. Reagudization
18	PAAI18	Acute infection
19	PAAI19	Acute infection
28	PACI9	Chronic infection. Non-CF bronchiectasis
29	PACI10	Chronic infection. Non-CF bronchiectasis
30	PACI11	Chronic infection. Non-CF bronchiectasis
31	PACI12	Chronic infection. Non-CF bronchiectasis. Hemoptysis
32	PACI13	Chronic infection. Non-CF bronchiectasis
33	PACI14	Chronic infection. CF-bronchiectasis
34	PACI15	Chronic infection. CF-bronchiectasis. Acute viral infection
35	PACI16	Chronic infection. CF-bronchiectasis
36	PACI17	Chronic infection. CF-bronchiectasis
37	PACI18	Chronic infection. CF bronchiectasis. Reagudization

^aPAO1 was used as a positive control strain.

reached values [measured as optical density (OD) at 600 nm] between 0.2 and 0.3 (equivalent to a McFarland turbidity containing approximately 1×10^8 CFUs ml^{-1}), sample aliquots (10 μl) were taken and diluted in MH broth (10 ml) at different time intervals (t_0 , start time point) to preserve the conditions and to avoid growth disruption due to changes in the temperature or other eventualities.

2.11 Bacterial Growth Measurements and Phenazine Production Kinetics

Bacterial suspension aliquots collected at different incubation times were used to plot bacterial growth curves and to build up PYO and 1-OHphz kinetic production curves. Bacterial growth studies were performed by measuring the turbidity at each time point in broth culture aliquots. Turbidity correlates with cell density during the logarithmic growth phase and was measured as OD at 600 nm. In addition, CFUs were counted by plating serial dilutions of each time point aliquot and counting the colonies after 24-h incubation.

The OD of each sample was measured at 600 nm at RT in a Multiskan GO spectrophotometer using High Precision Cell cuvette made of quartz (Hellma Analytics). CFUs were determined by carrying out serial 1:10 dilutions of each time point aliquot (10 μl) on 5% blood agar plates (37°C, 24 h). In each case, the corresponding dilutions plated were established according to turbidity values (dilutions ranged from 1/10 to 1/10⁸) (Sarkar et al., 2017).

Collected bacterial time point aliquots were centrifuged (500 G, 5 min) for PYO mAb/PC1-BSA ELISA measures. The resulting supernatant was diluted 20 times in assay buffer to avoid matrix effects. For 1-OHphz measurements, a 1/5 dilution in assay buffer was carried out (Pastells et al., 2016).

3 RESULTS

3.1 ELISA Assays for Phenazines: 1-Hydroxyphenazine and Pyocyanin

A few years ago, we reported the development of an immunochemical assay to quantify PYO in complex biological media (Pastells et al., 2016). For this purpose, we used a 1-OHphz hapten to raise antibodies with the expectation that would recognize also PYO due to the chemical difficulties to obtain a stable PYO hapten. Although PYO and 1-OHphz are structurally closely related molecules (**Figure 1**), the antisera obtained showed much higher avidity for 1-OHphz ($\text{IC}_{50} = 0.62$ nM) than that for PYO ($\text{IC}_{50} > 800$ nM; % CR < 0.1%). For this reason, PYO quantification required its complete transformation to 1-OHphz, which was achieved by treating the samples with a strong base (Pastells et al., 2016). Aiming at simplifying the procedure, we attempted to accomplish a high-affinity mAb against PYO using the hybridoma technology that allows selecting cell clones with tailored features based on a rational selective screening approach. With this aim, mice were immunized with PC1-HCH (1-OHphz hapten linked to HCH), and the hybridoma cells obtained after the fusion step were selectively screened during several cloning cycles to select those clones that best detected PYO on a competitive format using both phenazines, PYO and 1-OHphz. Afterward, bidimensional checkerboard experiments (2D-ELISAs) allowed to determine the most appropriate concentrations for the bioconjugate competitor PC1-BSA and each mAb to be used on the competitive ELISAs. **Table 2** shows the IC_{50} values of the best selected 14 clones for PYO and 1-OHphz using the developed ELISAs according to the abovementioned criteria. In all cases,

TABLE 2 | Features of the monoclonal antibodies (mAb) selected in this study and of the As230 with respect to the recognition of PYO and 1-OHphz.

Clone name ^b	IC_{50} (1-OHphz) ^c	IC_{50} (PYO) ^d	Relation [(IC_{50} (PYO)/ IC_{50} (1-OHphz))]
C.9.1.7.2.1.2.1	2.17	16.26	7.48
C.9.1.7.2.1.2.2	0.43	3.87	8.99
C.9.1.9.7.3.1.1	3.72	27.21	7.31
C.9.1.9.7.3.1.2	1.23	7.88	6.42
C.9.2.8.3.1.2.2	0.90	5.98	6.67
C.9.1.7.1.1.2.1	1.19	7.39	6.22
C.9.1.4.1.1.4.2	0.24	1.97	8.37
C.9.1.4.1.1.4.1	0.38	3.81	10.13
C.9.1.9.1.1.2.2	0.32	2.96	9.27
C.9.1.4.1.1.4.4	0.26	2.13	8.06
C.9.1.4.1.1.4.3	1.10	6.56	5.99
C.9.2.8.3.1.2.3	0.83	7.45	8.96
C.9.1.7.1.1.1.2	1.34	9.23	6.91
C.9.1.7.1.1.2.3	0.79	5.01	6.37
As 230 (Pastells et al., 2016)	0.62	> 800	1290.32

^a A_{max} values were between 0.8 and 1.2.

^bAntibody concentration used 0.008 $\mu\text{g}/\text{ml}$ for mAb122 and 1/3,000 dilution for As230.

^{c,d}Coating antigen concentration used 0.125 and 0.0625 $\mu\text{g}/\text{ml}$ for PYO mAb122/PC1-BSA and As230/PC1-BSA, respectively. The IC_{50} values were determined using the protocol of the PYO mAb122/PC1-BSA (see experimental section) and As230/PC1-BSA (Pastells et al., 2016) for the case of As230.

Green means that was the selected clone for developing the ELISA.

final clones presented a better detectability for 1-OHphz than for PYO. While some of them (C.9.1.9.7.3.1.1. and C.9.1.7.2.1.2.1.) showed much higher affinity for 1-OHphz than for PYO (IC_{50} values for PYO ranging 15–20 μ M), other clones (C.9.1.4.1.1.4.2. and C.9.1.4.1.1.4.4. C.9.1.9.1.1.2.2.) had more similar selectivities for both phenazines, with low IC_{50} values for PYO (<2 nM). From these three best clones, C.9.1.9.1.1.2.2. (from now on PYO mAb122) was selected to quantify PYO levels in clinical samples, as it showed better ELISA parameters such as slope and Abs_{max} (data not shown).

The analytical parameters of the PYO mAb122/PC1-BSA ELISA are summarized in **Table 3**. The low LoD (0.07 nM in the assay buffer and 0.15 nM in MH diluted 20 times) reached allowed contemplating the possibility to directly quantify PYO without the need to convert it to 1-OHphz. Even if this last metabolite was much better recognized (IC_{50} : 0.32 vs. 2.92 nM for 1-OHphz and PYO, respectively; **Table S2** and **Figure S3**), it was expected to find it at much lower levels. Hence, Wilson et al. (1988) reported 1-OHphz levels to be much lower (9-fold times lower) than PYO concentration in sputum samples. Nevertheless, in this work, the PYO concentrations measured have been expressed as PYO immunoreactivity equivalents (PYO IRequiv) to take this fact into consideration.

TABLE 3 | Features of the PYO mAb122/PC1-BSA ELISA in PBST and MH broth diluted 20 times.

	PBST	MH 1/20
A_{min}	0.07 ± 0.01	0.05 ± 0.01
A_{max}	1.08 ± 0.09	0.92 ± 0.14
Slope	-1.40 ± 0.49	-1.11 ± 0.21
IC_{50}/nM	0.68 ± 0.10	1.18 ± 0.24
Dynamic range	0.18 ± 0.08 and 2.18 ± 0.19	0.32 ± 0.10 and 4.13 ± 1.35
LoD	0.07 ± 0.04	0.15 ± 0.07
R^2	0.99 ± 0.01	0.99 ± 0.01

Assay conditions used were PC1-BSA at 0.125 μ g/ml and PYO mAb 122 at 0.008 μ g/ml in both cases. The data shown correspond to the average of the parameters of the calibration curves performed on three different days using at least three well replicates per concentration.

The robustness of the assay was demonstrated by measuring IC_{50} , slope, and Abs_{max} values during a year ($n = 13$). Thus, the obtained results followed a normal distribution (D'Agostino & Pearson normality test, Shapiro–Wilk normality test, and Kolmogorov–Smirnov (KS) normality test) showing values of 1.72 ± 0.79 , -1.28 ± 0.27 , and 0.97 ± 0.29 , respectively (**Figure S1**). Moreover, the low variability of the assay is demonstrated through the low dispersion of the obtained results, which are concentrated around the mean value. In this sense, IC_{50} values have only oscillated between 0.8 and 2.8, the slope between -0.9 and -1.7, and the Abs_{max} between 0.8 and 1.5 (outliers are not considered). In addition, the assay was able to work between 4.5 and 7.5 pH values, showing slightly better performance at 6.5 and 7.5 values (**Figure S2**) with acceptable IC_{50} values. At pH below 4.5 and over 7.5, there was a drastic decrease observed in the absorbance of the assay.

3.2 Implementation of Phenazine ELISAs to the Analysis of Bacterial Isolates

To investigate the release profile of both PYO and 1-OHphz by different clinical bacterial isolates obtained from patients infected with *P. aeruginosa* at different stage, clinical isolates were grown in MH broth. Sample aliquots were taken at different times to be measured with PYO mAb122/PC1-BSA ELISA reported here and with 1-OHphz As230/PC1-BSA ELISA already published (Pastells et al., 2016). Before, the potential nonspecific interferences caused by the MH broth in the ELISA were initially assessed. For this purpose, calibration curves of PYO and 1-OHphz were prepared in MH diluted at different ratios with PBST (from 1/5 to 1/20) and measured with the corresponding ELISA to compare their performance with the calibration curves run in buffer. As observed in **Figure 2**, PYO mAb122/PC1-BSA ELISA worked very well in MH broth after just a 1/5 dilution ($IC_{50} = 1.22$ nM), although the signal was significantly decreased under these conditions. However, considering that the detectability achieved by this ELISA was well below the values reported in clinical samples (μ M range) (Hall et al., 2016), we decided to attempt measuring the samples using a 1/20 dilution of MH in PBST to

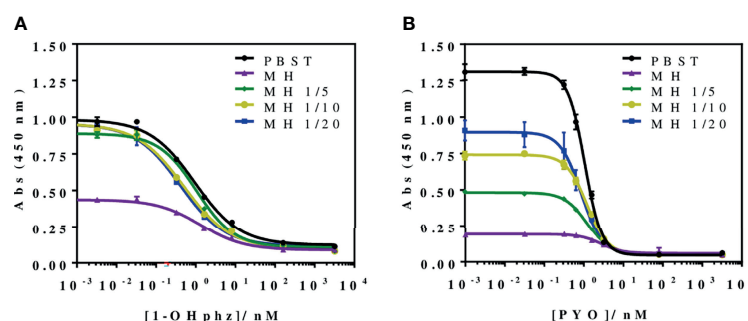


FIGURE 2 | Matrix effect of the Mueller–Hinton (MH) broth undiluted and diluted 5, 10, and 20 times with PBST on the (A) PYO mAb122/PC1-BSA and (B) As230/PC1-BSA ELISA. The calibration curves were run using the conditions established for the assay in PBST. The results demonstrate that it is possible to perform direct measurements in MH media diluted from 5 to 20 times in PBST for both phenazines (see **Table 3** for analytical parameters of the standard curves in PBST and in 1/20 MH on PYO mAb122/PC1-BSA and **Table 4** for analytical parameters of the standard curves in PBST and in 1/5 MH). The results shown are the average and standard deviations of analysis made by triplicates.

investigate the release profile of the abovementioned clinical bacterial isolates. As shown in **Table 3**, the analytical parameters of the ELISA run in 1/20 MH seemed to be suitable for our purposes ($IC_{50} = 1.18 \pm 0.24$, $LoD = 0.15 \pm 0.07$). Moreover, accuracy studies performed under these conditions supported this fact. As observed in **Figure 3**, the coefficient of correlation between concentrations of the blind spiked samples and the values measured with the ELISA was excellent ($R^2 = 0.997$), and the slope of the linear regression was close to 1 (slope = 1.08), showing almost a perfect match between spiked and measured concentration values. In the same line, calibration curves of 1-OHphz were prepared in different dilutions of MH in PBST (from 1/5 to 1/20; **Figure 2**) and evaluated using As230/PC1-BSA ELISA. The obtained results showed that the assay could be used to measure MH samples diluted just five times with the assay buffer ($IC_{50} = 1.02$ nM). The analytical parameters of the ELISA run in 1/5 MH are illustrated in **Table 4**.

3.3 Growth Curves and Phenazine Release Profile of *P. aeruginosa* Bacterial Isolates

Bacterial growth curves were built by culturing some clinical isolates from patients with acute and chronic infections (**Table 1**). These measurements were important to compare growth dynamics of the different clinical isolates and also to determine the time required to detect these phenazines in the media using the ELISA developed. Thus, in total, five *P. aeruginosa* isolates (using PAO1 as reference) were incubated in MH media to study their growth dynamics through the measurement of culture turbidity (OD 600 nm) and CFU counting (**Table S1**).

Recently, we have reported that the levels released by clinical isolates of *P. aeruginosa* AIs of the *pqs* QS system, such as PQS and HHQ, were significantly different depending on the stage of

TABLE 4 | Features of the As230/PC1-BSA ELISA in PBST and MH broth diluted five times.

	PBST	MH 1/5
A_{min}	0.12 ± 0.02	0.11 ± 0.02
A_{max}	0.99 ± 0.02	0.89 ± 0.02
Slope	-0.75 ± 0.07	-0.90 ± 0.11
IC_{50}/nM	0.93 ± 0.05	1.02 ± 0.06
Dynamic range	0.17 and 6.47	0.24 and 5.85
LoD	0.06	0.10
R^2	0.99 ± 0.03	0.99 ± 0.02

Assay conditions used were PC1-BSA at $0.0625 \mu g/ml$ and 1/6,000 dilution of As230 in both cases. The data shown correspond to the average of the parameters of the calibration curves performed on the same day using at least three well replicates per concentration.

the infection (Montagut et al., 2020; Montagut et al., 2021). Thus, for the case of bacterial isolates from patients with acute infection, quantifiable PQS levels could be measured after 5-h growth, while those belonging to patients with a chronic infection, levels could only be quantified after more than 12-h growth, which was correlated to the virulence and behavior of *P. aeruginosa* due to their high adaptability to the environment. With this scenario, we were expecting to find similar differences in terms of the release of a QS-regulated VF such as PYO.

Figure 4 shows the growth curves obtained when analyzing two representative bacterial isolates, PAACI18 and PAAI20, from patients with a chronic and an acute infection, respectively. As expected, a clear difference between them was observed. Thus, the PAAI20 isolate started its exponential growth phase after 6 h of incubation, whereas PAACI18 showed a longer lag phase, initiating its exponential division at 12 h of incubation, in agreement with the behavior observed for the QS signaling molecules of these same types of bacterial isolates. Moreover, the growth profile of both isolates reached

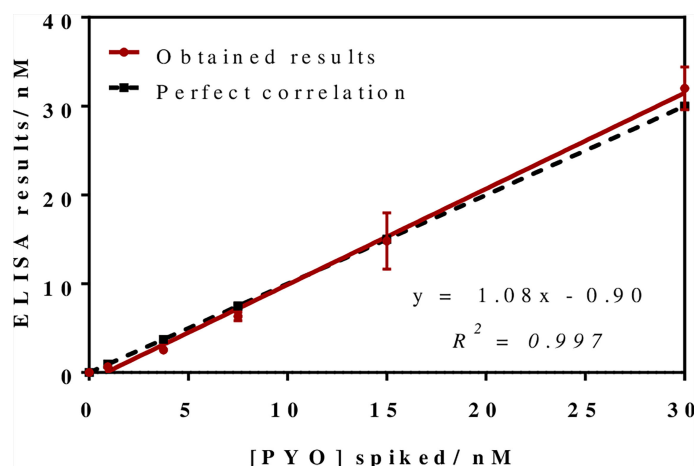


FIGURE 3 | Results from the accuracy study. The graph shows the linear regression analysis obtained representing the different pyocyanin (PYO) concentrations spiked in Mueller–Hinton (MH) broth against the concentration measured with the PYO mAb122/PC1-BSA ELISA. Assays were run in MH culture media diluted 1/20 using PBST. Each calibration point was measured in triplicates on the same ELISA plate and the results show the average and standard deviation of analysis made on three different days.

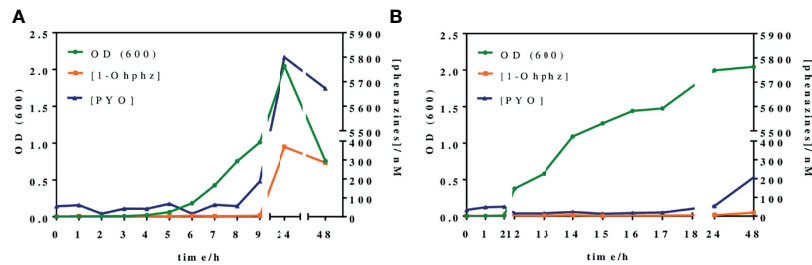


FIGURE 4 | Growth curves and phenazines kinetics production of two *P. aeruginosa* isolates grown for 48 h. The green line (OD 600) gives information about the bacterial growth. The blue and the orange lines indicate IRequiv. of pyocyanin (PYO) and 1-hydroxyphenazine (1-OHphz) production, respectively. Results obtained **(A)** from an isolate (PAAI20) of a patient undergoing an acute *P. aeruginosa* infection and **(B)** from an isolate (PACI18) of a patient suffering chronic infection. The data shown are the average and standard deviation of IRequiv. of PYO and 1-OHphz determinations performed with the corresponding ELISAs on the same day using three well replicates.

the stationary phase. However, in the case of PAAI20, after getting to the maximum growth levels, the curve showed a very steep drop caused by the cytotoxic effect of PYO high levels (it should be noticed that after 24 h of incubation, bacterial cultures corresponding to isolates from acute infections show a clear blue color) (D'Argenio et al., 2002; Hall et al., 2016). Focusing on CFU counting, both isolates reached a plateau on the number of viable cells, similar regarding the values obtained but the isolate PAAI20 yielded the maximum cell number at 7 h of incubation and, by contrast, the isolate PACI18 hit this point after 15 h of culturing time (Table S1).

In parallel, at the same time points, bacterial culture aliquots were also analyzed to determine the pattern of phenazine production kinetics of *P. aeruginosa* isolates obtained from acute and chronic infections. The results have been plotted in the same graphs of Figure 4. As observed, the release kinetics of the two phenazines studied are coherent with the results previously reported by Montagut et al. (2020, 2021) for the QS signaling molecules mentioned above. Thus, the bacterial isolate from the patient with an acute infection clearly shows much higher levels of both molecules (5,800 nM for PYO and 370 nM for 1-OHphz at 24 h) than the isolate obtained from a patient with chronic infection (54 nM for PYO and 5 nM for 1-OHphz at 24 h).

Focusing on the phenazine production kinetic patterns found, they remain constant when studying an isolate from a patient suffering from a chronic infection, just slightly increasing for PYO after 48 h of culturing. In contrast, the phenazine production profile of an isolate from a patient with an acute infection shows a marked increase in PYO levels, which reaches its maximum at 24 h of incubation, decreasing smoothly after 48 h of growth predictably due to the effects of PYO itself on bacterial viability causing autolysis (Meirelles and Newman, 2018; Ahmed et al., 2019). Furthermore, in all cases, both phenazines showed the same secretion profile, being the levels of the precursor 1-OHphz much lower than those determined for the VF PYO. As an example, at the highest point of the growth curve of the clinical isolate from the patient with an acute infection, PYO reached values near 6,000 nM, while the highest level of 1-OHphz achieved was around 400 nM.

In light of these results, we decided to expand our studies, analyzing the release of PYO and 1-OHphz from 37 bacterial isolates obtained from patients with different respiratory infections at different stages and with distinct symptom severity. The clinical isolates were grown for 16 h to ensure measurements, in case the isolates would belong to a patient with a chronic infection. As a reference control, the strain PAO1 was also cultured under the same conditions, and the phenazines produced by it were also quantified.

As shown in Figure 5, the data obtained confirmed the differences found in the behavior of clinical isolates from acute and chronic infections regarding the levels of PYO and 1-OHphz released. Moreover, with few exceptions, which could be due to clinical casuistry, the levels of both phenazines were remarkably higher. Most values found in the MH samples from clinical isolates from patients diagnosed with an acute infection caused by *P. aeruginosa* were between 6,000 and 200 nM for PYO and between 200 and 20 nM for 1-OHphz (Table S2). Conversely, they were much lower when the phenazine levels were determined in the culture broth samples of clinical isolates from patients suffering chronic infection. In this case, they were in the low nM range; most values found were between 15 and 1 nM for PYO and between 4 and 0.5 nM for 1-OHphz (Table S2). For all clinical isolates, it could be confirmed that the PYO levels are higher than those of the precursor 1-OHphz.

4 DISCUSSION

P. aeruginosa is considered one of the most threatening pathogens worldwide given its multidrug-resistant and adaptability behavior. It causes a wide variety of infections predominantly in individuals with other diseases. *P. aeruginosa* infections are commonly classified as acute and chronic infections according to the infection status and characteristics (Furukawa et al., 2006). Due to its highly adaptability, this bacterium can survive for long periods of time in the lungs of patients (chronicity) in the form of biofilm (mucoid phenotype). This causes resistance processes, making antibiotic therapies less

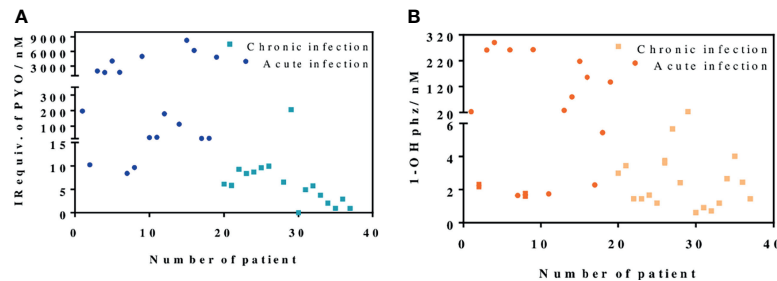


FIGURE 5 | PYO IRequiv. **(A)** and 1-hydroxyphenazine (1-OHphz) levels **(B)** (expressed in nM) found in the Mueller–Hinton (MH) media where clinical bacterial isolates obtained from patients infected with *P. aeruginosa* were growth during 16 h. Dark blue and orange dots correspond to levels from isolates of patients with acute infection and light blue and yellow dots from patients with chronic infection. Each data point represents the average and standard deviation of the results obtained on experiments performed on the same day using three well replicates. See **Table 1** for information on the clinical record of the patients.

effective. Therefore, it is essential to have appropriate diagnostic strategies to detect infections at early stages (acute infections). This early detection will allow applying more specific antibiotic treatments, preventing chronification of the infections and the appearance of resistant strains (Vilaplana and Marco, 2020).

It has been already reported that when *P. aeruginosa* changes to a mucoid phenotype (chronic infection), exopolysaccharide production is increased, whereas motility and VF production are decreased (Smith et al., 2006; D'Argenio et al., 2007; Ryall et al., 2014). The immunochemical assay described here has allowed the measurement of levels of the PYO VF in bacterial isolates obtained from patients undergoing different stages of *P. aeruginosa* infections with high sensitivity (LoD at low nM range). All the data obtained have reinforced the hypothesis of PYO as a potential biomarker for discerning among acute and chronic *P. aeruginosa* infections.

The most commonly used methods for PYO detection are based on its unique optical and electrical properties. In this sense, PYO can be detected by absorbance at different wavelengths (Reszka et al., 2004), UV-Vis or mass spectroscopy (MS) (Wilson et al., 1988), SERS (Polisetti et al., 2017), or electrochemical systems (Alatraktchi et al., 2018) reaching LoDs in the low μM and in the high nM range. However, some of these techniques lack specificity (i.e., UV-Vis), may take from 24 to 48 h to render results, or require expensive equipment and need time-consuming pretreatment steps. In contrast, the immunochemical assay described here achieves a very low LoD (low nM range) and does not require any sophisticated equipment. Previously, we reported a microplate-based ELISA (Pastells et al., 2016) able to detect PYO with an LoD of 0.01 nM in less than 90 min. However, this ELISA uses polyclonal antisera showing a much greater avidity for 1-OHphz than to PYO, which required prior transformation of PYO to 1-OHphz. In contrast, the immunochemical strategy reported in this paper is the result of using the hybridoma technology to select a mAb cell clone able to recognize PYO with a much higher affinity. This mAb has been obtained by immunizing mice with the same hapten described by Pastells et al. (2016) derived from the more stable 1-OHphz molecule. Performance of selective cloning rounds allowed to isolate 14 clones that were highly sensitive to PYO. Although all

those clones detected 1-OHphz with higher avidity than PYO, three clones showed similar IC_{50} for both phenazines. Hence, clone C.9.1.9.1.1.2.2. (mAb122) was selected to determine PYO levels on clinical isolates. Due to the specific interference caused by 1-OHphz, PYO concentrations are expressed as IRequiv of PYO. Moreover, with the aim of analyzing 1-OHphz quantity on the culture media and determine its contribution, As230/PC1-BSA ELISA was used (Pastells et al., 2016).

The low LoD (0.04 nM) achieved using mAb122 allowed the direct measurement of PYO in culture broth where bacterial isolates from patients infected with *P. aeruginosa* were grown after inoculation of bacteria. Furthermore, the obtained LoD and dynamic ranges may allow the direct quantification of PYO in different clinical samples such as ear secretions (up to 8.1 μM using HPLC-UV) (Reimer et al., 2000), wounds (up to 2.8 μM using chloroform and acid extraction) (Cruickshank and Lowbury, 1953), and sputa (up to 100 μM using HPLC-UV) (Wilson et al., 1988) without any previous treatment or chemical transformation step.

In this paper, we have used the PYO mAb122/PC1-BSA here reported and the As230/PC1-BSA (Pastells et al., 2016) ELISAs to quantify PYO and 1-OHphz levels released by bacterial isolates obtained from patients infected with *P. aeruginosa*. Both ELISAs, showing LoDs in the low nM range, have proven to be robust under different physicochemical conditions including the analysis of a complex biological sample such as the MH broth used to grow the clinical isolates. Thus, bacterial isolates from patients with acute infections released higher concentrations of PYO and 1-OHphz (from 100 to 6,000 nM and from 20 to 100 nM, respectively) than those with chronic infections (5–8 nM and 1–3 nM, respectively). In light of these results, it seems clear that the concentration of phenazines released is correlated with the type or stage of *P. aeruginosa* infection. Moreover, these results are consistent with previously reported studies (Heacock-Kang et al., 2017; Faure et al., 2018; Lozano et al., 2018; Chandler et al., 2019) that showed how, during early stages of *P. aeruginosa* infection, VF and exoproduct expression is increased (acute infections), whereas at chronic stages, *P. aeruginosa* adapts to the host environment by reducing bacterial invasiveness, which means decreasing the expression of toxins, VFs, and QS molecules. In that respect, the described PYO mAb122/PC1-BSA ELISA could

be a valuable technique to understand the stage of the disease and to provide patients with the most appropriate treatment strategy.

Bacterial cultures are confined systems where, in addition to the culture components, VFs, proteins, and other bacterial exoproducts are released. Therefore, these culture media are quite complex samples, which predict further successful implementation of the technology here reported to the direct analysis of clinical samples such as sputum, bronchoalveolar lavage (BAL), urine, or plasma. The preliminary data presented point out the possibility to use the reported PYO ELISA to diagnose *P. aeruginosa* infections in clinical samples and to help to stratify patients according to the nature of their infection stage (chronic or acute) based on PYO content. This positions PYO as a potential useful biomarker of *P. aeruginosa* infections. Further investigations may open new avenues of knowledge resulting from the possibility to monitor PYO levels in clinical samples, such as the possibility to predict exacerbations or to diagnose the infection at early stages of the diseases. Moreover, the early and rapid detection of *P. aeruginosa* could reduce the morbidity and mortality of infected patients by giving them a more specific treatment. This will avoid chronification, minimizing resistance to antibiotics and, in consequence, improving the patient's quality of life. In fact, the described immunochemical approach could be used on different analytical configurations, such as point-of-care (PoC) immunosensor devices, to rapidly detect *P. aeruginosa*.

In the same line, the ineffectiveness of classic antibiotics as a consequence of their inappropriate use has resulted in the rise of *P. aeruginosa* multidrug-resistant strains. However, patients are still treated with the same classical antibiotics, especially β -lactam antibiotics alone and in combination with other families of these compounds due to the lack of new therapeutic approaches (O'Donnell et al., 2020). Among the new emerging therapeutic techniques, mAbs are gaining importance as a consequence of their high affinity and specificity, which minimize possible side effects (Ducancel and Muller, 2012; Khan et al., 2017). Moreover, mAb market has doubled in size in the last 5 years (Grilo and Mantalaris, 2019). Thus, mAbs are increasingly used in different human diseases such as infectious diseases; currently, 4 mAbs are approved by the US Food and Drug Administration (FDA) for this purpose (Lu et al., 2020). In this sense, the here described mAb against PYO could also be tested as a therapeutic agent, since it could minimize or even avoid the cytotoxic effects produced by PYO VF (Ran et al., 2003; Hall et al., 2016) by specifically binding it.

DATA AVAILABILITY STATEMENT

The raw data supporting the conclusions of this article will be available by the authors without undue reservation if required.

ETHICS STATEMENT

The experimentation reported here has been approved by the CEIC (Ethical Committee for Clinical Research) of the Hospital

Vall d'Hebron and the Ethical Committee of CSIC. Written informed consent to participate in this study was provided by the participants' legal guardian/next of kin. Animal study protocols and procedures have been approved by the CID-CSIC Ethical Committee (local institution), CSIC-CEEA (CSIC animal experimentation ethical committee, evaluating procedures at national level), and Catalan authorities.

AUTHOR CONTRIBUTIONS

BR-U and LV planned and designed the experiments. BR-U carried out all the experiments, performed the analysis and statistics of the obtained results, and wrote the final article. PC designed the 1-OHphz hapten and developed the As230/PC1-BSA ELISA. NP helped in the synthesis of the here presented antibodies. MT-M provided the clinical isolates from patients infected with *P. aeruginosa*. LV and M-PM supervised all the work. All authors discussed the results and contributed to the final article. All authors contributed to the article and approved the submitted version.

FUNDING

This work has been funded by the Spanish Government to M-PM through the Ministry of Science and Innovation (SAF2015-67476-R, RTI2018-096278-B-C21, PI, M-PM) and by Fundació Marató de TV3 (201825-30-31, PI, M-PM). The Nb4D group is a consolidated research group (Grup de Recerca) of the Generalitat de Catalunya and has support from the Departament d'Universitats, Recerca i Societat de la Informació de la Generalitat de Catalunya (expedient: 2017 SGR 1441). CIBER Actions are financed by the Instituto de Salud Carlos III with assistance from the European Regional Development Fund (ERDF). Moreover, BR-U has an FI fellowship from the AGAUR (Agència de Gestió d'Ajuts Universitaris I de Recerca) of the Government of Catalonia (Generalitat de Catalunya) (2019FI_B00289). *El Fons social Europeu Inverteix en el teu futur*.

ACKNOWLEDGMENTS

The U2 [Custom Antibody Service (CAbs) of the ICTS "NANOBIOSIS"] is acknowledged for the assistance and support related to the immunoreagents used in this work and Vall d'Hebron Hospital for providing clinical isolates from positive infected patients.

SUPPLEMENTARY MATERIAL

The Supplementary Material for this article can be found online at: <https://www.frontiersin.org/articles/10.3389/fcimb.2021.786929/full#supplementary-material>

REFERENCES

- Ahmed, S., Rudden, M., Smyth, T. J., Dooley, J. S. G., Marchant, R., and Banat, I. M. (2019). Natural Quorum Sensing Inhibitors Effectively Downregulate Gene Expression of *Pseudomonas Aeruginosa* Virulence Factors. *Appl. Microbiol. Biotechnol.* 103, 3521–3535. doi: 10.1007/s00253-019-09618-0
- Alatraktchi, F. A., Noori, J. S., Tanev, G. P., Mortensen, J., Dimaki, M., Johansen, H. K., et al. (2018). Paper-Based Sensors for Rapid Detection of Virulence Factor Produced by *Pseudomonas Aeruginosa*. *PloS One* 13, e0194157. doi: 10.1371/journal.pone.0194157
- Barbier, F., Andreumont, A., Wolff, M., and Bouadma, L. (2013). Hospital-Acquired Pneumonia and Ventilator-Associated Pneumonia: Recent Advances in Epidemiology and Management. *Curr. Opin. Pulm. Med.* 19, 216–228. doi: 10.1097/MCP.0b013e32835f27be
- Barcelo, B., Ballesteros, D., Camps, F., and Marco, M.-P. (1997). Preparation of Antisera and Development of a Direct Enzyme-Linked Immunosorbent Assay for the Determination of the Antifouling Agentirgarol 1051. *Anal. Chim. Acta* 347, 139–147. doi: 10.1016/S0003-2670(97)00317-6
- Blair, J. M., Webber, M. A., Baylay, A. J., Ogbolu, D. O., and Piddock, L. J. (2015). Molecular Mechanisms of Antibiotic Resistance. *Nat. Rev. Microbiol.* 13, 42–51. doi: 10.1038/nrmicro3380
- Boucher, H. W., Talbot, G. H., Bradley, J. S., Edwards, J. E., Gilbert, D., Rice, L. B., et al. (2009). Bad Bugs, No Drugs: No ESCAPE! An Update From the Infectious Diseases Society of America. *Clin. Infect. Dis.* 48, 1–12. doi: 10.1086/595011
- Breidenstein, E. B., de la Fuente-Nunez, C., and Hancock, R. E. (2011). *Pseudomonas Aeruginosa*: All Roads Lead to Resistance. *Trends Microbiol.* 19, 419–426. doi: 10.1016/j.tim.2011.04.005
- Chandler, C. E., Horspool, A. M., Hill, P. J., Wozniak, D. J., Schertzer, J. W., Rasko, D. A., et al. (2019). Genomic and Phenotypic Diversity Among Ten Laboratory Isolates of *Pseudomonas Aeruginosa* PAO1. *J. Bacteriol.* 201, 1–18. doi: 10.1128/JB.00595-18
- Chen, W., Liu, X. Y., Qian, C., Song, X. N., Li, W. W., and Yu, H. Q. (2015). An UV-Vis Spectroelectrochemical Approach for Rapid Detection of Phenazines and Exploration of Their Redox Characteristics. *Biosens. Bioelectron.* 64, 25–29. doi: 10.1016/j.bios.2014.08.032
- Costa, K. C., Bergkessel, M., Saunders, S., Korlach, J., and Newman, D. K. (2015). Enzymatic Degradation of Phenazines Can Generate Energy and Protect Sensitive Organisms From Toxicity. *mBio* 6, e01520–e01515. doi: 10.1128/mBio.01520-15
- Cruikshank, C. N., and Lowbury, E. J. (1953). The Effect of Pyocyanin on Human Skin Cells and Leucocytes. *Br. J. Exp. Pathol.* 34, 583–587.
- D'Argenio, D. A., Calfee, M. W., Rainey, P. B., and Pesci, E. C. (2002). Autolysis and Autoaggregation in *Pseudomonas Aeruginosa* Colony Morphology Mutants. *J. Bacteriol.* 184, 6481–6489. doi: 10.1128/JB.184.23.6481-6489.2002
- D'Argenio, D. A., Wu, M., Hoffman, L. R., Kulasekara, H. D., Deziel, E., Smith, E. E., et al. (2007). Growth Phenotypes of *Pseudomonas Aeruginosa* lasR Mutants Adapted to the Airways of Cystic Fibrosis Patients. *Mol. Microbiol.* 64, 512–533. doi: 10.1111/j.1365-2958.2007.05678.x
- De Boeck, K. (2020). Cystic Fibrosis in the Year 2020: A Disease With a New Face. *Acta Paediatr.* 109, 893–899. doi: 10.1111/apa.15155
- Dietrich, L. E., Price-Whelan, A., Petersen, A., Whiteley, M., and Newman, D. K. (2006). The Phenazine Pyocyanin Is a Terminal Signalling Factor in the Quorum Sensing Network of *Pseudomonas Aeruginosa*. *Mol. Microbiol.* 61, 1308–1321. doi: 10.1111/j.1365-2958.2006.05306.x
- Ducancel, F., and Muller, B. H. (2012). Molecular Engineering of Antibodies for Therapeutic and Diagnostic Purposes. *MAbs* 4, 445–457. doi: 10.4161/mabs.20776
- Faure, E., Kwong, K., and Nguyen, D. (2018). *Pseudomonas Aeruginosa* in Chronic Lung Infections: How to Adapt Within the Host? *Front. Immunol.* 9, 2416. doi: 10.3389/fimmu.2018.02416
- Fong, J., Zhang, C., Yang, R., Boo, Z. Z., Tan, S. K., Nielsen, T. E., et al. (2018). Combination Therapy Strategy of Quorum Quenching Enzyme and Quorum Sensing Inhibitor in Suppressing Multiple Quorum Sensing Pathways of *P. Aeruginosa*. *Sci. Rep.* 8, 1155. doi: 10.1038/s41598-018-19504-w
- Furukawa, S., Kuchma, S. L., and O'Toole, G. A. (2006). Keeping Their Options Open: Acute Versus Persistent Infections. *J. Bacteriol.* 188, 1211–1217. doi: 10.1128/JB.188.4.1211-1217.2006
- Gaynes, R., Edwards, J. R., and National Nosocomial Infections Surveillance, S. (2005). Overview of Nosocomial Infections Caused by Gram-Negative Bacilli. *Clin. Infect. Dis.* 41, 848–854. doi: 10.1086/432803
- Grilo, A. L., and Mantalaris, A. (2019). The Increasingly Human and Profitable Monoclonal Antibody Market. *Trends Biotechnol.* 37, 9–16. doi: 10.1016/j.tibtech.2018.05.014
- Hall, S., McDermott, C., Anoopkumar-Dukie, S., McFarland, A. J., Forbes, A., Perkins, A. V., et al. (2016). Cellular Effects of Pyocyanin, a Secreted Virulence Factor of *Pseudomonas Aeruginosa*. *Toxins (Basel)* 8, 1–14. doi: 10.3390/toxins8080236
- Heacock-Kang, Y., Sun, Z., Zarzycki-Siek, J., McMillan, I. A., Norris, M. H., Bluhm, A. P., et al. (2017). Spatial Transcriptomes Within the *Pseudomonas Aeruginosa* Biofilm Architecture. *Mol. Microbiol.* 106, 976–985. doi: 10.1111/mmi.13863
- Hirsch, E. B., and Tam, V. H. (2010). Impact of Multidrug-Resistant *Pseudomonas Aeruginosa* Infection on Patient Outcomes. *Expert Rev. Pharmacoecon. Outcomes Res.* 10, 441–451. doi: 10.1586/erp.10.49
- Jayaseelan, S., Ramaswamy, D., and Dharmaraj, S. (2014). Pyocyanin: Production, Applications, Challenges and New Insights. *World J. Microbiol. Biotechnol.* 30, 1159–1168. doi: 10.1007/s11274-013-1552-5
- Khan, F. Y., AbuKamar, M., and Anand, D. (2017). Nosocomial *Pseudomonas Putida* Meningitis: A Case Report and Literature Review. *Oman Med. J.* 32, 167–169. doi: 10.5001/omj.2017.30
- Klockgether, J., Cramer, N., Wiehlmann, L., Davenport, C. F., and Tummler, B. (2011). *Pseudomonas Aeruginosa* Genomic Structure and Diversity. *Front. Microbiol.* 2, 150. doi: 10.3389/fmicb.2011.00150
- Krogsrud, R. L., and Koivunen, M. E. (2006). Principles of Immunochemical Techniques Used in Clinical Laboratories. *Labmedicine* 37, 491–497.
- Lozano, C., Azcona-Gutierrez, J. M., Van Bambeke, F., and Saenz, Y. (2018). Great Phenotypic and Genetic Variation Among Successive Chronic *Pseudomonas Aeruginosa* From a Cystic Fibrosis Patient. *PloS One* 13, e0204167. doi: 10.1371/journal.pone.0204167
- Lu, R. M., Hwang, Y. C., Liu, I. J., Lee, C. C., Tsai, H. Z., Li, H. J., et al. (2020). Development of Therapeutic Antibodies for the Treatment of Diseases. *J. BioMed. Sci.* 27, 1. doi: 10.1186/s12929-019-0592-z
- Maurice, N. M., Bedi, B., Yuan, Z., Goldberg, J. B., Koval, M., Hart, C. M., et al. (2019). *Pseudomonas Aeruginosa* Induced Host Epithelial Cell Mitochondrial Dysfunction. *Sci. Rep.* 9, 11929. doi: 10.1038/s41598-019-47457-1
- Ma, Z., Wang, T., Li, Z., Guo, X., Tian, Y., Li, Y., et al. (2019). A Novel Biotinylated Nanobody-Based Blocking ELISA for the Rapid and Sensitive Clinical Detection of Porcine Epidemic Diarrhea Virus. *J. Nanobiotechnology* 17, 96. doi: 10.1186/s12951-019-0531-x
- Meirelles, L. A., and Newman, D. K. (2018). Both Toxic and Beneficial Effects of Pyocyanin Contribute to the Lifecycle of *Pseudomonas Aeruginosa*. *Mol. Microbiol.* 110, 995–1010. doi: 10.1111/mmi.14132
- Mena, A., Smith, E. E., Burns, J. L., Speert, D. P., Moskowitz, S. M., Perez, J. L., et al. (2008). Genetic Adaptation of *Pseudomonas Aeruginosa* to the Airways of Cystic Fibrosis Patients Is Catalyzed by Hypermutation. *J. Bacteriol.* 190, 7910–7917. doi: 10.1128/JB.01147-08
- Montagut, E. J., Martin-Gomez, M. T., and Marco, M. P. (2021). An Immunochemical Approach to Quantify and Assess the Potential Value of the *Pseudomonas* Quinolone Signal as a Biomarker of Infection. *Anal. Chem.* 93, 4859–4866. doi: 10.1021/acs.analchem.0c04731
- Montagut, E. J., Vilaplana, L., Martin-Gomez, M. T., and Marco, M. P. (2020). High-Throughput Immunochemical Method to Assess the 2-Heptyl-4-Quinolone Quorum Sensing Molecule as a Potential Biomarker of *Pseudomonas Aeruginosa* Infections. *ACS Infect. Dis.* 6, 3237–3246. doi: 10.1021/acsinfectdis.0c00604
- O'Donnell, J. N., Bidell, M. R., and Lodise, T. P. (2020). Approach to the Treatment of Patients With Serious Multidrug-Resistant *Pseudomonas Aeruginosa* Infections. *Pharmacotherapy* 40, 952–969. doi: 10.1002/phar.2449
- Pang, Z., Raudonis, R., Glick, B. R., Lin, T. J., and Cheng, Z. (2019). Antibiotic Resistance in *Pseudomonas Aeruginosa*: Mechanisms and Alternative Therapeutic Strategies. *Biotechnol. Adv.* 37, 177–192. doi: 10.1016/j.biotechadv.2018.11.013
- Park, S. Y., Park, H. J., Moon, S. M., Park, K. H., Chong, Y. P., Kim, M. N., et al. (2012). Impact of Adequate Empirical Combination Therapy on Mortality

- From Bacteremic *Pseudomonas Aeruginosa* Pneumonia. *BMC Infect. Dis.* 12, 308. doi: 10.1186/1471-2334-12-308
- Pastells, C., Pascual, N., Sanchez-Baeza, F., and Marco, M. P. (2016). Immunochemical Determination of Pyocyanin and 1-Hydroxyphenazine as Potential Biomarkers of *Pseudomonas Aeruginosa* Infections. *Anal. Chem.* 88, 1631–1638. doi: 10.1021/acs.analchem.5b03490
- Pieters, A., Bakker, M., Hoek, R. A. S., Altenburg, J., van Westreenen, M., Aerts, J., et al. (2019). The Clinical Impact of *Pseudomonas Aeruginosa* Eradication in Bronchiectasis in a Dutch Referral Centre. *Eur. Respir. J.* 53, 1–5. doi: 10.1309/MV9RM1FDLWAUWQ3F
- Polisetti, S., Baig, N. F., Morales-Soto, N., Shrout, J. D., and Bohn, P. W. (2017). Spatial Mapping of Pyocyanin in *Pseudomonas Aeruginosa* Bacterial Communities Using Surface Enhanced Raman Scattering. *Appl. Spectrosc.* 71, 215–223. doi: 10.1177/0003702816654167
- Puchelle, E., Bajolet, O., and Abely, M. (2002). Airway Mucus in Cystic Fibrosis. *Paediatr. Respir. Rev.* 3, 115–119. doi: 10.1016/S1526-0550(02)00005-7
- Ran, H., Hassett, D. J., and Lau, G. W. (2003). Human Targets of *Pseudomonas Aeruginosa* Pyocyanin. *Proc. Natl. Acad. Sci. U.S.A.* 100, 14315–14320. doi: 10.1073/pnas.2332354100
- Rehman, Z. U., and Leiknes, T. (2018). Quorum-Quenching Bacteria Isolated From Red Sea Sediments Reduce Biofilm Formation by *Pseudomonas Aeruginosa*. *Front. Microbiol.* 9, 1354. doi: 10.3389/fmicb.2018.01354
- Reimer, A., Edvaller, B., and Johansson, B. (2000). Concentrations of the *Pseudomonas Aeruginosa* Toxin Pyocyanin in Human Ear Secretions. *Acta Otolaryngol. Suppl.* 543, 86–88. doi: 10.1080/000164800454062
- Reszka, K. J., O'Malley, Y., McCormick, M. L., Denning, G. M., and Britigan, B. E. (2004). Oxidation of Pyocyanin, a Cytotoxic Product From *Pseudomonas Aeruginosa*, by Microperoxidase 11 and Hydrogen Peroxide. *Free Radic. Biol. Med.* 36, 1448–1459. doi: 10.1016/j.freeradbiomed.2004.03.011
- Ruffin, M., and Brochiero, E. (2019). Repair Process Impairment by *Pseudomonas Aeruginosa* in Epithelial Tissues: Major Features and Potential Therapeutic Avenues. *Front. Cell Infect. Microbiol.* 9, 182. doi: 10.3389/fcimb.2019.00182
- Ryall, B., Carrara, M., Zlosnik, J. E., Behrends, V., Lee, X., Wong, Z., et al. (2014). The Mucoid Switch in *Pseudomonas Aeruginosa* Represses Quorum Sensing Systems and Leads to Complex Changes to Stationary Phase Virulence Factor Regulation. *PLoS One* 9, e96166. doi: 10.1371/journal.pone.0096166
- Sadikot, R. T., Blackwell, T. S., Christman, J. W., and Prince, A. S. (2005). Pathogen-Host Interactions in *Pseudomonas Aeruginosa* Pneumonia. *Am. J. Respir. Crit. Care Med.* 171, 1209–1223. doi: 10.1164/rccm.200408-1044SO
- Sakamoto, S., Putalun, W., Vimolmangkang, S., Phoolcharoen, W., Shoyama, Y., Tanaka, H., et al. (2018). Enzyme-Linked Immunosorbent Assay for the Quantitative/Qualitative Analysis of Plant Secondary Metabolites. *J. Nat. Med.* 72, 32–42. doi: 10.1007/s11418-017-1144-z
- Sarkar, S., Lund, S. P., Vyazasaty, R., Vanguri, P., Elliott, J. T., Plant, A. L., et al. (2017). Evaluating the Quality of a Cell Counting Measurement Process via a Dilution Series Experimental Design. *Cytotherapy* 19, 1509–1521. doi: 10.1016/j.jcyt.2017.08.014
- Sismaet, H. J., Pinto, A. J., and Goluch, E. D. (2017). Electrochemical Sensors for Identifying Pyocyanin Production in Clinical *Pseudomonas Aeruginosa* Isolates. *Biosens. Bioelectron.* 97, 65–69. doi: 10.1016/j.bios.2017.05.042
- Smith, E. E., Buckley, D. G., Wu, Z., Saenphimmachak, C., Hoffman, L. R., D'Argenio, D. A., et al. (2006). Genetic Adaptation by *Pseudomonas Aeruginosa* to the Airways of Cystic Fibrosis Patients. *Proc. Natl. Acad. Sci. U.S.A.* 103, 8487–8492. doi: 10.1073/pnas.0602138103
- Taylor, P. K., Yeung, A. T., and Hancock, R. E. (2014). Antibiotic Resistance in *Pseudomonas Aeruginosa* Biofilms: Towards the Development of Novel Anti-Biofilm Therapies. *J. Biotechnol.* 191, 121–130. doi: 10.1016/j.jbiotec.2014.09.003
- Valentini, M., Gonzalez, D., Mavridou, D. A., and Filloux, A. (2018). Lifestyle Transitions and Adaptive Pathogenesis of *Pseudomonas Aeruginosa*. *Curr. Opin. Microbiol.* 41, 15–20. doi: 10.1016/j.mib.2017.11.006
- Van den Bergh, B., Fauvart, M., and Michiels, J. (2017). Formation, Physiology, Ecology, Evolution and Clinical Importance of Bacterial Persisters. *FEMS Microbiol. Rev.* 41, 219–251. doi: 10.1093/femsre/fux001
- Vatankhah, M., Beheshti, N., Mirkalantari, S., Khoramabadi, N., Aghababa, H., and Mahdavi, M. (2019). Recombinant Omp2b Antigen-Based ELISA Is an Efficient Tool for Specific Serodiagnosis of Animal Brucellosis. *Braz. J. Microbiol.* 50, 979–984. doi: 10.1007/s42770-019-00097-z
- Vilaplana, L., and Marco, M. P. (2020). Phenazines as Potential Biomarkers of *Pseudomonas Aeruginosa* Infections: Synthesis Regulation, Pathogenesis and Analytical Methods for Their Detection. *Anal. Bioanal. Chem.* 412, 5897–5912. doi: 10.1007/s00216-020-02696-4
- Vivian, D. L. (1956). The Practical Synthesis of 1-Phenazinol. *Nature* 178, 753. doi: 10.1038/178753a0
- Williams, B. J., Dehnhostel, J., and Blackwell, T. S. (2010). *Pseudomonas Aeruginosa*: Host Defence in Lung Diseases. *Respirology* 15, 1037–1056. doi: 10.1111/j.1440-1843.2010.01819.x
- Wilson, R., Sykes, D. A., Watson, D., Rutman, A., Taylor, G. W., and Cole, P. J. (1988). Measurement of *Pseudomonas Aeruginosa* Phenazine Pigments in Sputum and Assessment of Their Contribution to Sputum Sol Toxicity for Respiratory Epithelium. *Infect. Immun.* 56, 2515–2517. doi: 10.1128/iai.56.9.2515-2517.1988
- Yang, L., Jelsbak, L., Marvig, R. L., Damkiaer, S., Workman, C. T., Rau, M. H., et al. (2011). Evolutionary Dynamics of Bacteria in a Human Host Environment. *Proc. Natl. Acad. Sci. U. S. A.* 108, 7481–7486. doi: 10.1073/pnas.1018249108
- Zegans, M. E., Becker, H. I., Budzik, J., and O'Toole, G. (2002). The Role of Bacterial Biofilms in Ocular Infections. *DNA Cell Biol.* 21, 415–420. doi: 10.1089/10445490260099700
- Zelini, P., Fornara, C., Furione, M., Sarasini, A., Klemens, J., Arossa, A., et al. (2019). Determination of Anti-P52 IgM and Anti-gB IgG by ELISA as a Novel Diagnostic Tool for Detection of Early and Late Phase of Primary Human Cytomegalovirus Infections During Pregnancy. *J. Clin. Virol.* 120, 38–43. doi: 10.1016/j.jcv.2019.09.006
- Zukovskaja, O., Jahn, I. J., Weber, K., Cialla-May, D., and Popp, J. (2017). Detection of *Pseudomonas Aeruginosa* Metabolite Pyocyanin in Water and Saliva by Employing the SERS Technique. *Sensors (Basel)* 17, 1–11. doi: 10.3390/s17081704

Conflict of Interest: The authors declare that the research was conducted in the absence of any commercial or financial relationships that could be construed as a potential conflict of interest.

Publisher's Note: All claims expressed in this article are solely those of the authors and do not necessarily represent those of their affiliated organizations, or those of the publisher, the editors and the reviewers. Any product that may be evaluated in this article, or claim that may be made by its manufacturer, is not guaranteed or endorsed by the publisher.

Copyright © 2021 Rodriguez-Urretavizcaya, Pascual, Pastells, Martin-Gomez, Vilaplana and Marco. This is an open-access article distributed under the terms of the Creative Commons Attribution License (CC BY). The use, distribution or reproduction in other forums is permitted, provided the original author(s) and the copyright owner(s) are credited and that the original publication in this journal is cited, in accordance with accepted academic practice. No use, distribution or reproduction is permitted which does not comply with these terms.



OPEN ACCESS

Edited by:

Eugenia Gallardo,
Universidade da Beira Interior,
Portugal

Reviewed by:

Christian Fernandes,
Federal University of Minas Gerais,
Brazil
Alvaro Jose Dos Santos Neto,
University of São Paulo, Brazil
Andras Szeitz,
University of British Columbia, Canada
Tanveer A. Wani,
King Saud University, Saudi Arabia

*Correspondence:

Cristina Sottani
Cristina.sottani@icsmaugeri.it
Enrica Calleri
enrica.calleri@unipv.it

Specialty section:

This article was submitted to
Analytical Chemistry,
a section of the journal
Frontiers in Chemistry

Received: 27 September 2021

Accepted: 19 November 2021

Published: 03 January 2022

Citation:

Sottani C, Grignani E, Cottica D,
Mazzucchelli S, Sevieri M, Chesi A,
Corsi F, Galfre S,
Robustelli della Cuna FS and Calleri E
(2022) Development and Validation of
a Bioanalytical UHPLC-MS/MS
Method Applied to Murine Liver Tissue
for the Determination of Indocyanine
Green Loaded in H-
Ferritin Nanoparticles.
Front. Chem. 9:784123.
doi: 10.3389/fchem.2021.784123

Development and Validation of a Bioanalytical UHPLC-MS/MS Method Applied to Murine Liver Tissue for the Determination of Indocyanine Green Loaded in H-Ferritin Nanoparticles

Cristina Sottani^{1*}, Elena Grignani¹, Danilo Cottica¹, Serena Mazzucchelli², Marta Sevieri², Arianna Chesi², Fabio Corsi^{2,3}, Sarah Galfre⁴, Francesco Saverio Robustelli della Cuna⁴ and Enrica Calleri^{4*}

¹Environmental Research Center, Istituti Clinici Scientifici Maugeri IRCCS, Pavia, Italy, ²Nanomedicine Laboratory, Department of Biomedical and Clinical Sciences "Luigi Sacco", Milano University, Milan, Italy, ³Breast Unit, Istituti Clinici Scientifici Maugeri IRCCS, Pavia, Italy, ⁴Department of Drug Sciences, University of Pavia, Pavia, Italy

Indocyanine green (ICG) is one of the most commonly used fluorophores in near-infrared fluorescence-guided techniques. However, the molecule is prone to form aggregates in saline solution with a limited photostability and a moderate fluorescence yield. ICG was thus formulated using protein-based nanoparticles of H-ferritin (HFn) in order to generate a new nanostructure, HFn-ICG. In this study, an ultrahigh performance liquid chromatography-tandem mass spectrometry (UHPLC-MS/MS) system was employed to develop and validate the quantitative analysis of ICG in liver tissue samples from HFn-ICG-treated mice. To precipitate HFn, cold acetone in acidic solution at pH 5.0 was used. The processed liver samples were injected into the UHPLC-MS/MS system for analysis using the positive electrospray ionization mode. Chromatographic separation was achieved on a Waters Acquity UPLC[®] HSS T3 Column (1.8 μ m, 2.1 \times 100 mm) with 0.1% formic acid and acetonitrile as the mobile phase with gradient elution. The selected reaction monitoring transitions of m/z 753 \rightarrow m/z 330 and m/z 827 \rightarrow m/z 330 were applied for ICG and IR-820 (the internal standard, IS), respectively. The method was selective and linear over a concentration range of 50–1,500 ng/ml. The method was validated for sensitivity, accuracy, precision, extraction recovery, matrix effect, and stability in liver tissue homogenates. ICG extraction recoveries ranged between 85 and 108%. The intra- and inter-day precisions were less than 6.28%. The method was applied to a bio-distribution study to compare the amount of ICG levels from mice treated with HFn-ICG and free ICG. The analyses of the homogenate samples from the two types of treatment showed that the concentration levels of ICG is approximately six-fold higher than those of free ICG (1,411 \pm 7.62 ng/ml vs. 235 \pm 26.0 ng/ml) at 2 h post injection.

Keywords: indocyanine green, liver tissue, UHPLC-MS/MS, FDA validation, biodistribution study

INTRODUCTION

Indocyanine green (ICG) (**Figure 1**) is a fluorescent dye which belongs to the family of cyanine dyes. ICG is an amphiphilic molecule, and this characteristic allows its dissolution in both aqueous and lipophilic solvents (Desmettre et al., 2000). Over the past decade, the molecule has become decisive as an *in vivo* imaging agent for different clinical applications (Reinhart et al., 2016; Ferrucci et al., 2018; Shen et al., 2018; Spinoglio et al., 2018; Sevieri et al., 2020). Moreover, as there is a growing interest in clinical imaging for diagnosis, staging, and therapy planning, this fluorescent dye has been investigated to develop a fluorescent probe with sufficient sensitivity in complex environments at deep-tissue penetration (Dang et al., 2019). The availability of an FDA-approved agent combined with a highly sensitive second near-infrared window fluorophore has promoted studies for detection and treatment of various cancers (Bhavane et al., 2018; Wang et al., 2018; Egloff-Juras et al., 2019).

However, ICG suffers from a high instability as the chemical degradation of this dye depends on the nature of solvents, concentration, temperature, and light exposure. In addition, the molecule tends to form aggregates in high concentrations (Desmettre et al., 2000). In order to increase its chemical stabilization, the amphiphilic nature of ICG has been used to generate nanostructures. In a recent study, ICG was loaded into nanocages of H-ferritin (HFn), a biocompatible protein, with the aim of studying a new nanotracer (HFn-ICG) in comparison to free ICG (Sitia et al., 2020). The accumulation of HFn-ICG in different organs of a breast cancer murine model was determined by using IVIS[®] Lumina II *in-vivo* Imaging System (Sevieri et al., 2021). For fluorescence pharmacokinetic rates of ICG in mouse liver, within the *in vivo* imaging techniques, diffusive fluorescence tomography has been also used (Zhang et al., 2018).

High performance liquid chromatography (HPLC) with ultraviolet, fluorescence, and tandem mass spectrometry (HPLC-MS/MS) have been used for determining the levels of

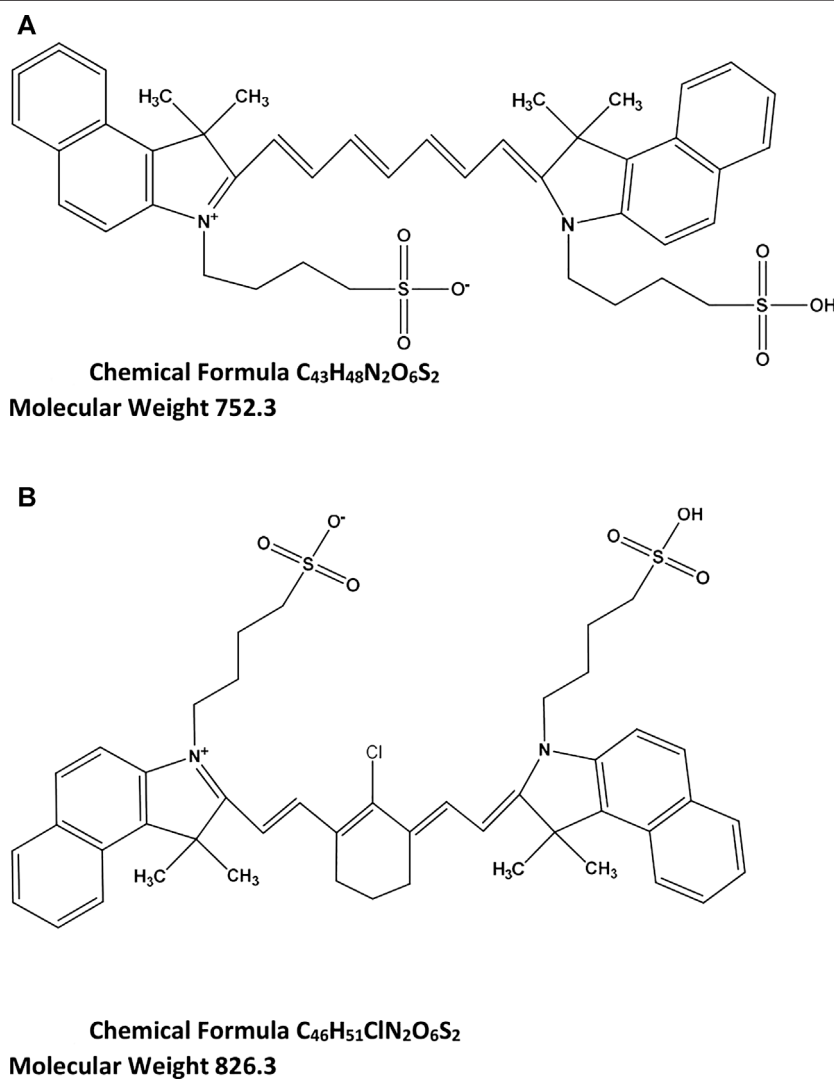
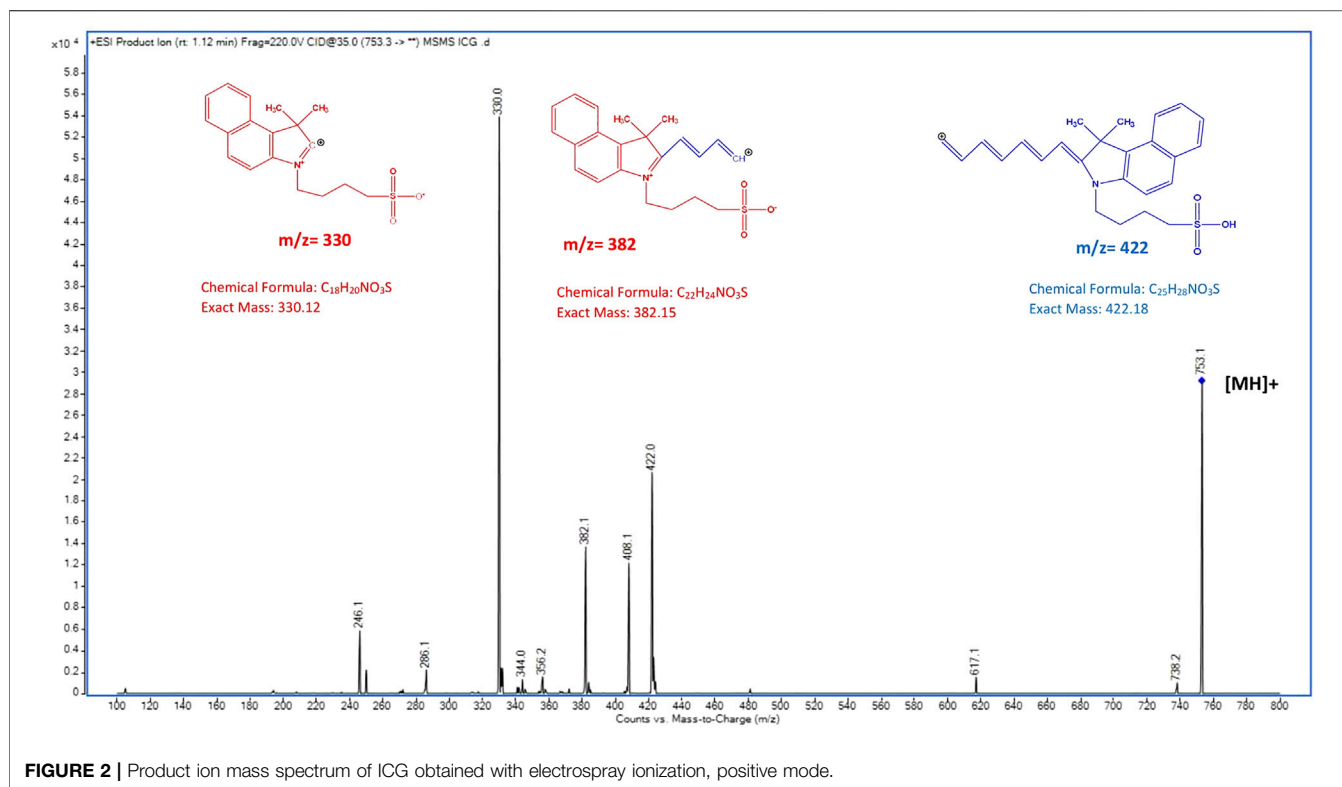


FIGURE 1 | Chemical structure and formula of ICG (**A**) and IR-820 (IS) (**B**).



free ICG in animal plasma and bile samples (Chen et al., 2015; Chen et al., 2008).

However, as ICG fluorescence varies, because of the dye concentration (i.e., the fluorescence quenches above 0.5 $\mu\text{g/ml}$), the clinical results are affected by incorrectly low fluorescence responses (Desmettre et al., 2000; Mindt et al., 2018). To measure ICG in both fluids and tissues, liquid chromatography tandem mass spectrometry (LC-MS/MS) technique has become the method of choice due to the high selectivity of mass spectrometric detector.

To our best knowledge, it is the first time that ultrahigh performance liquid chromatography tandem mass spectrometry (UHPLC-MS/MS) has been used to quantify HFn-ICG in mouse liver. More precisely, in our study, to analyze ICG encapsulated in the cavity of HFn, a simple and rapid sample clean-up procedure has been developed at the isoelectric point of HFn. Therefore, the accuracy of measuring ICG was achieved by first removing the protein-based interferences commonly present in biological samples. Moreover, the UHPLC-MS/MS assay used throughout the study was effective in the detection of ICG because not subject to impurities caused by a degradation phenomenon occurring in aqueous solution and followed by a rapid dimerization of ICG (Mindt et al., 2018).

The aim of the present study was to determine ICG levels in liver samples from mice treated with free ICG and ICG loaded in nanocages of HFn. The determination of ICG levels in tissues is essential for studying the tissue distribution of this compound.

In the present study, an accurate, specific, and reliable method with UHPLC-MS/MS was employed to quantify HFn-ICG using IR-820 as an internal standard (IS) **Figure 1**.

The developed procedure was also validated and applied to a bio-distribution study in liver homogenates from HFn-ICG-treated mice.

MATERIALS AND METHODS

Chemicals and Reagents

Indocyanine green (90%, reference substance) and IR-820 dye (80%) powders were obtained from Ultra Scientific Analytical Solutions s.r.l. (Bologna, Italy). H-ferritin nanocages were produced as recombinant protein in *E. coli* as previously described (Bellini et al., 2014). For chromatography, acetonitrile (ACN) (LC-MS-grade), formic acid, and ammonium formate (LC-MS-grade) were purchased from Merck House, Poole, United Kingdom; acetone (99.9%) and hydrochloric acid (37%) were from Merck KGaA 64271 Darmstadt, Germany; and water was deionized and purified on a Milli-Q system (Millipore, Marlborough, MA, United States).

UHPLC-MS/MS Conditions

ICG quantification was performed using the UHPLC-MS/MS system consisting of an Agilent 1,290 Infinity Binary Pump, a 1,290 Infinity Sampler, a 1,290 Infinity Thermostat, and a 1,290 Infinity Thermostatted Column Compartment connected to an

Agilent 6,460 triple quadrupole mass spectrometer (Agilent Technologies, Lexington, CA, United States). Mass Hunter workstation was used for data acquisition and analysis (Version 10.1 2006–2020). The instrument was operated in electrospray ionization, positive mode (ESI+) using Agilent Jet Stream. Ion source parameters were as follows: 11 ml/min, 300°C vaporizer temperature, 300 °C sheath gas, 600 V nozzle voltage, and 3000 V capillary voltage. Nitrogen was used as the nebulizer gas set at 45 psi with a flow rate of 5 L/min. ICG was quantitated at the selected reaction monitoring (SRM) transition of m/z 753 \rightarrow m/z 330, and IR-820 was monitored at m/z 827 \rightarrow m/z 330. The buffer was prepared by adding 1 ml 0.1% formic acid to 10 mM ammonium formate solution, pH 3.5. Several attempts were made to increase the ICG y -axis intensity by varying the ratio between the organic solvent and the aqueous solution (data not shown). Mobile phase A consisted of ACN: buffer, 20:80 (v/v), and mobile phase B ACN:buffer, 80:20 (v/v). ICG and IR-820A were separated using a Waters Acquity UPLC HSS T3 column (1.8 μ m, 2.1 mm \times 100 mm, Waters, Milford, MA, United States) maintained at 40°C with a flow rate of 0.3 ml/min.

The gradient programming started with mobile phase B 50% that was followed by a linear increase to 100% in 2.5 min, and maintained until 4 min. The system was allowed to return to initial conditions in 2 min. The total run time was 6 min.

Sample Collection and ICG Encapsulation

The ICG was nano-formulated exploiting the ability of HF_n nanocages to disassemble and reassemble its quaternary structure in response to changes in pH as previously reported (Sitia et al., 2020). A mixture of HF_n (0.5 mg/ml) dissolved in 0.15 M NaCl was brought to pH 2.0 adding 0.5 M HCl. HF_n was incubated at pH 2.0 for 15 min at room temperature by shaking at 100 rpm (OS-20 orbital shaker, BioSan, Italy) to disassemble the protein cage. Then, the pH was brought back to neutrality (pH 7.5) with the addition of 0.1 M NaOH. In the meantime, ICG powder Verdyne (25 mg; Diagnostic Green GmbH, Aschheim-Dornach, Germany) was solubilized in bidistilled deionized water (5 ml; 5 mg/ml) and added to the HF_n solution at a final dye concentration of 1.0 mg/ml. The mixture was incubated for 2 h at room temperature (RT) and shaking at 180 rpm to allow complete refolding of the HF_n quaternary structure.

The obtained HF_n–ICG nanoparticles were then concentrated by using Amicon Ultra-4 centrifugal filter devices (Merck S.p.a., Milan, Italy), and the non-encapsulated ICG has been removed by gel filtration using a Zeba Spin Desalting column (Thermo Fisher Scientific, Monza, Italy).

Tissue Homogenization

Liver tissues from treated and untreated mice were explanted, accurately weighed, and homogenized in water (10% w/v) with potter homogenizer (Glas-Col homogenizer, IKA, China). Tissues were kept in the ice-bath during the process and stored at –0°C until use.

Preparation of Standards and Quality Control Samples

Accurately weighed ICG powder was dissolved in methanol to prepare the stock standard solution at the concentration of 1 mg/

ml and stored at –80°C in dark conditions. The IS IR-820 stock solution was prepared in methanol as well (1 mg/ml). Stock solutions in methanol were brought to 4°C to prepare the working standard solutions in methanol at the concentrations of 0.4, 0.8, 1.2, 3.2, 8.0, and 12.0 μ g/ml for the calibration curve and 1.0, 2.0, 4.0, and 10 μ g/ml for the quality control (QC) samples. Similarly, IS was prepared in methanol at the concentration of 4.0 μ g/ml. Subsequently, each standard sample was prepared by adding 50 μ l of each working standard solution and 50 μ l of IS to a polypropylene tube. The aliquots were brought to dryness, and then 400 μ l of blank liver tissue homogenate was added. A six-point calibration curve (50, 100, 150, 400, 1,000, and 1,500 ng/ml) with four QC levels at the concentrations of 125, 250, 500, and 1,250 ng/ml was obtained. The concentration level of IR-820 was 500 ng/ml.

Extraction of ICG and IS was performed using a cold protein precipitation (PP) solution according to a procedure previously described (Sottani et al., 2020). To each standard sample, an 8-fold volume (3,200 μ l) of 1 mM PP solution was added. PP solution was prepared at pH 5.0 by addition of 10 μ l 37% HCl to 120 ml of cold acetone. PP solution was kept at –80°C before use. For protein precipitation, the samples were vortexed for 1 min and centrifuged (14,000 rpm for 15 min, 4°C) to separate the supernatant from the pellet. For each sample, the supernatant was filtered with a 0.45 μ m, 25 mm PTFE syringe filter and then dried under a gentle stream of N₂. The dry residues were reconstituted with 100 μ l of methanol, and 5 μ l was injected in the UHPLC-MS/MS system.

Assay Validation

The UHPLC-MS/MS method was validated according to Food and Drug Administration (FDA) Guidance on Bioanalytical Method Validation (Food and Drug Administration, 2018). The liver tissue homogenates from six animals were spiked with the IS only and with both ICG and IS. The selectivity of the assay was assessed comparing chromatograms of blank liver tissue to blank liver tissue spiked with the analyte.

Linearity and Sensitivity

The linearity of the assay was evaluated using the standard samples prepared with ICG in homogenate of murine liver tissue over the concentration range of 50–1,500 ng/ml. Calibration curves were constructed by plotting the concentrations of ICG on the x -axis vs. the chromatographic peak area ratios of ICG to IS on the y -axis. Using the $y = mx + b$ equation, the y -intercept (b), slope (m), and the coefficient of determination (R^2) were calculated. The calibration curves were weighted using the weighting factor of $1/x$. $R^2 \pm$ SD values were used to evaluate the linearity of the assay using the criteria of ≥ 0.990 .

The lower limit of quantification (LLOQ) was determined when the accuracy was between 80 and 120% and the precision \leq 20%. The signal-to-noise ratio criterion of 10:1 was used to assess the LLOQ value.

Accuracy and Precision

The accuracy and precision of the method were assessed by intra- and inter-day validation over three non-consecutive days. The intraday accuracy and precision were evaluated by processing QC samples in six replicates ($n = 6$) at four concentration levels. The

concentration of the QC samples was calculated vs. the daily calibration curves. The inter-day accuracy and precision were determined by analyzing QC samples in 18 replicates of each concentration. Accuracy was determined as the ratio between the back-calculated concentration and the nominal value and expressed as a percentage. For precision, the mean ratio of ICG peak area/IS peak area was used. The coefficient of variation (CV%) was employed as a measure of precision.

Recovery and Matrix Effect

The percentage extraction recovery (RE) was calculated at the lower level of quantification for ICG and at the liver tissue concentrations of the four QC samples (125, 250, 500, and 1,250 ng/ml) that were prepared as six replicates. The mean integration ratio (area of the analyte/area of IS) for ICG and IS spiked before PP extraction (Set C) was compared to that of ICG and IS spiked in the matrix of extracted blank homogenate of liver tissue (Set B). The mean peak area of IS prepared at the concentration of 500 ng/ml was used to assess its recovery from liver samples.

Matrix effect (ME) was assessed by comparing the mean ratio of the peak areas (ICG/IS) spiked in blank liver tissue after PP procedure to that of ICG standard solutions prepared in methanol (Set A). The potential for the relative matrix effect was also evaluated using six independent sources of extracted blank homogenates of murine liver tissues. ICG was therefore spiked at the QC levels in six blank liver tissue samples. The mean integration ratio of ICG for the four QC samples of Set B was compared to that of the QC standard solutions at the same concentrations (Matuszewski et al., 2003).

Stability

The stability of ICG in homogenate liver samples was assessed by analyzing QC samples at two concentration levels (125 and 500 ng/ml) during storage and handling. Bench-top stability was determined at room temperature after 8 h of the handling of ICG samples. Stability in the autosampler was also assessed at RT by reanalyzing the processed QC samples 48 h after the first injection. Freeze-thaw stability was studied by analyzing QC samples that were frozen overnight, at normal storage temperature (-80°C), and thawed at 4°C . When completely thawed, the samples were frozen again at the same temperature for 24 h and thawed. This freeze-thaw cycle was repeated two more times. After the third cycle (4 days), the samples were analyzed. To check freeze-thaw stability, an aliquot of each QC sample concentration was freshly prepared, processed, and analyzed. The analyte was considered stable at each concentration when the differences between the freshly prepared samples and the stability testing samples did not vary more than $\pm 15\%$ from the nominal concentrations.

Application to Bio-Distribution Studies in Liver Homogenates

The animals were managed according to procedures approved by the Italian Ministry of Health (Protocol Number 611/2019-PR, August 6, 2019). All procedures involving animals and their health were conducted in accordance with the 3R principles to

minimize the number of mice used and their collateral suffering. The animals were housed in specific pathogen-free conditions and were kept in cages with free access to water and food. In this study, a total of 32 seven-week-old female BALB/c mice (average weight of 20 g) were recruited and randomly divided in four groups (blank, 2, 6, and 24 h). For the method development, six animals were used as blank controls. Animals were intravenously injected in the tail vein with ICG or HFn-ICG at a dose of 3.8 mg/kg. Thus, the number of murine tissue samples was as follows: $n = 8$ at 0 and $n = 8$ at 2 h, $n = 8$ at 6 h, and $n = 8$ at 24 h. For each group, four animals were treated with free ICG and four animals treated with ICG loaded in HFn nanoparticles. Subsequently, the mice were sacrificed by cervical dislocation and the collected liver samples were stored at -80°C until use. Two way ANOVA was used, where time and the two types of treatment, and the interaction between them, have been applied using the R software tool (www.r-project.org). This study was part of a more complete and thorough investigation about ICG and HFn-ICG distribution in different murine tissues. The outcomes of this research will be reported in detail in another specific paper.

RESULTS AND DISCUSSION

Method Development and Validation Mass Spectrometry

The chemical structures of ICG and IR-820 are shown as ionized forms in **Figure 1**. With ESI+, ICG showed a protonated molecular ion $[\text{MH}]^{+}$ at m/z 753.2, and the IS at m/z 827 (not shown in **Figure 2**). In **Figure 1**, the molecular structure of ICG is presented as a combination of red and blue colours. **Figure 2** shows the product ion mass spectrum of ICG where red represents the main fragment ion of ICG at m/z 330, and blue at m/z 422. Other fragment ions are m/z 382 and m/z 408 (**Figure 2**).

In the product ion spectra of ICG reported in **Figure 2**, other fragment ions are m/z 382 and m/z 408. As the molecular structure of ICG is symmetric and is composed of two polycyclic parts (benzoindotricarbocyanin) linked by an alkene chain, the fragment ions such as those at m/z 382 and m/z 408 are observed indicating a fragmentation at the unsaturated chain of ICG.

Thereafter, the selected reaction monitoring (SRM) for quantitative and qualitative analyses was performed using the following transitions: m/z 753 \rightarrow 330, m/z 753 \rightarrow 422 for ICG, and m/z 827 \rightarrow 330 for IS.

Selectivity, Linearity, and LLOQ

Figure 3 shows the SRM channels of ICG (A1) and IR-820 (A2) in blank murine liver tissue. No interferences were found at the retention times of ICG and IR-820. **Figure 3B1** represents a murine tissue sample spiked with ICG (50 ng/ml) showing a retention time (Rt) 2.6 min, and (B2) spiked with IR-820 (500 ng/ml) showing a Rt 3.3 min.

The PP procedure carried out at the isoelectric point of HFn (pH 5.0) with cold acetone was effective in the selective recovery

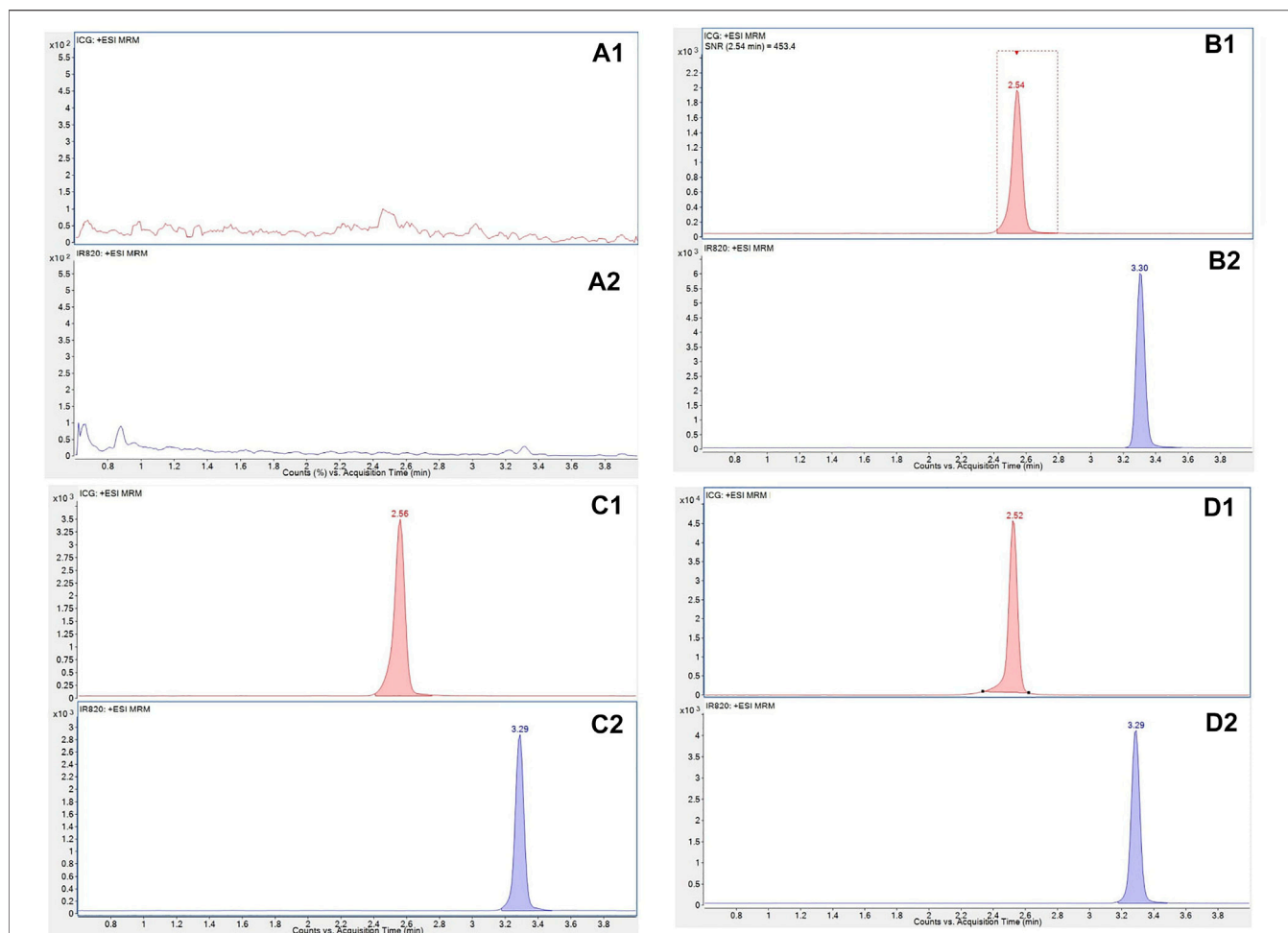


FIGURE 3 | Representative SRM chromatograms of ICG (A1) and IR-820 (A2) in blank murine liver tissue; in murine liver tissues samples spiked with (50.0 ng/ml) showing a reaction time (RT) 2.6 min (B1); and with IR-820 (500 ng/ml) showing a RT 3.3 min (B2). Representative SRM chromatograms of tissue samples obtained 2 h post injection from mice treated with free ICG (C1) and HFn-ICG (D1). For the two types of treatment, the SRM chromatograms for IR-820 are presented in (C2) and (D2).

of an amphiphilic molecule like ICG from homogenate samples of liver tissue.

The analytical conditions used to extract the target molecule from omopolymers of H-ferritin were therefore considered adequate as symmetrical and well baseline-separated peaks of ICG and the IS were obtained.

In addition, in order to show the different concentration levels of ICG in murine liver tissue, typical SRM chromatograms of ICG from mice treated with free ICG and HFn-ICG are presented in **Figures 3C1,D1**. In this figure, the concentrations of the fluorescent dye at 2 h post injection are reported. The level of ICG delivered by nanoparticles was higher (1,411 ng/ml) (C1) than that of free ICG (206 ng/ml) (D1). The SRM signals of IR-820 obtained with the two types of dosing are presented in **Figures 3C2,D2**.

The concentration levels detected from mice treated with free ICG and HFn-ICG decreased over time and detectable levels of ICG were determined up to 24 h. The lowest concentration value of ICG at 24 h was 56.7 ng/ml. For this reason, the calibration curves (integration ratio values vs. concentration values) for ICG in murine liver tissue were studied over a range of 50–1,500 ng/ml. The calibration equation

is represented by $y = (m \pm SD) x - (b \pm SD)$ where y is the relative response (peak area ratios ICG-to-IS) and x is ICG concentration in murine tissue. R^2 is the coefficient of determination \pm SD. The calibration equations prepared in triplicate over the 3 days of the validation process showed to be linear under the developed analytical conditions using the weighted ($1/x$) least squares regression analysis. The mean calibration equation for ICG was $y = (0.00741 \pm 0.000282) x - (0.0918 \pm 0.0585)$, with $R^2 = 0.996 \pm 0.000245$. As shown in **Figure 3** (panel B1), the high signal-to-noise ratio (≥ 400) of ICG obtained by injecting the lowest calibration standard spiked in blank liver tissue samples allowed a good sensitivity of the UHPLC-MS/MS assay with the LLOQ at 50 ng/ml which is around the expected concentrations of HFn-ICG in the matrix. The LLOQ response satisfied the acceptance criteria as the inter-day accuracy was 101% and the precision was 4.32%. Intra-day accuracy and precision are reported in **Table 1**.

Accuracy and Precision

QC samples were analyzed in six replicates over three different days to determine the intra-day accuracy and precision. Four QC

TABLE 1 | Accuracy and precision intra- and inter-day of ICG in murine tissue samples.

Nominal concentration (ng/ml)	Liver tissue					
	Accuracy (%)			Precision (CV, %)		
Intra-day (n = 6)						
	Day 1	Day 2	Day 3	Day 1	Day 2	Day 3
50.00	100	99.8	104	3.29	2.17	5.67
125.00	108	106	108	4.78	10.1	2.67
250.00	91.2	92.3	97.8	7.29	5.87	2.80
500.00	91.2	93.1	89.1	4.90	6.50	2.09
1,250.00	98.9	103	107	1.15	2.03	1.69
Inter-day (n = 18)						
50.00		101			4.32	
125.00		107			6.28	
250.00		93.8			5.80	
500.00		91.2			5.12	
1,250.00		103			3.99	

TABLE 2 | Extraction recovery and matrix effect of ICG in murine liver tissue samples.

Concentration (ng/ml)	Set B	Set C	Recovery (%)	Precision (CV%)
	Mean int. ratio \pm SD	Mean int. ratio \pm SD		
ICG				
50.0	0.280 \pm 0.020	0.306 \pm 0.036	107	11.8
125	0.852 \pm 0.070	0.920 \pm 0.097	108	10.6
250	1.90 \pm 0.066	1.64 \pm 0.074	87.0	4.47
500	3.83 \pm 0.253	3.25 \pm 0.255	84.8	7.85
1,250	9.66 \pm 0.716	9.52 \pm 0.254	98.6	2.67
IR-820 (ISTD)	Mean area	Mean area		
500	32,976 \pm 5,088	31,396 \pm 4,010	95.2	12.8
Concentration (ng/ml)	Set A	Set B	Matrix effect (ME%)	Precision (CV%)
	Mean int. ratio \pm SD	Mean int. ratio \pm SD		
ICG				
125	1.11 \pm 0.140	0.852 \pm 0.070	77.0	8.36
250	2.07 \pm 0.270	1.90 \pm 0.066	91.7	1.82
500	3.98 \pm 0.572	3.83 \pm 0.253	96.2	6.61
1,250	9.37 \pm 1.35	9.66 \pm 0.716	103	7.42

levels of ICG in murine liver tissues were investigated. **Table 1** summarizes the accuracy and precision for the obtained concentrations at the QC levels. Accuracy and precision for ICG determination in liver samples were within the acceptable limits recommended by the FDA bioanalytical method validation guideline. Hence, inter-day accuracy ranged from 91.2 to 107% and the intra-day precision was included between 3.99 and 6.28% for ICG detected in liver tissue samples.

Recovery and Matrix Effect

The results of recovery and matrix effect are presented in **Table 2**. The recovery of ICG from homogenate liver samples was evaluated by comparing the peak area ratio of ICG/IS QC samples (Set C) with that of blanks spiked with the analyte after PP procedure at the same concentrations. The extraction recovery values were similar

at the LLOQ level and over the concentrations of the four quality control samples (50–1,250 ng/ml). They ranged from 84.8 to 108% with a precision that met the requirements of FDA guideline (**Table 2**). For the absolute matrix effect, the mean integration ratio values of ICG QC samples extracted (Set B) were compared with those of the standard solutions (Set A) at the same concentrations. The absolute matrix effect in murine liver tissue for ICG ranged from 77.0 to 103% (**Table 2**). There was no significant effect of the matrix for the analysis of ICG in liver tissue samples using the developed UHPLC-MS/MS method.

Stability

The results of stability are presented in **Table 3**. At short-term storage conditions (48 h, at -80°C), stock solutions of ICG showed the stability of 80.2 and 78.2% compared to fresh-prepared solutions prepared at

TABLE 3 | Stability of ICG in standard solutions and in murine liver tissue samples.

Storage condition	Concentration (ng/ml)	Stability (%)
Stock solution (48 h, -80°C)	50.0	80.2
	1,250	78.2
Working standard (72 h, -20°C)	50.0	85.1
	1,250	91.4
Storage condition	Concentration (ng/ml)	Liver tissue stability (%)
Bench-top (6 h, 25°C)	50.0	85.1
	1,250	87.2
Processed sample stability (48 h, 25°C)	50.0	90.1
	1,250	88.1
Freeze-thaw (3 cycles)	50.0	81.1
	1,250	85.3

TABLE 4 | HFN-ICG and free ICG concentrations in murine tissue samples.

Treatment	Time (h)	Conc.	Treatment	Time (h)	Conc.	<i>p</i> Value
HFN-ICG		(ng/ml \pm SD)	ICG		(ng/ml \pm SD)	
	2	1,411 \pm 7.62		2	235 \pm 26.0	$p = <0.001$
	6	89.6 \pm 22.5		6	71.8 \pm 8.75	
	24	68.8 \pm 17.2		24	56.7 \pm 4.20	

the concentration of 50.0 ng/ml and 1,250 ng/ml. It is important to underline that stock solutions of ICG in methanol showed concentration levels less than 60% up till 48 h at -80°C if compared to those freshly prepared. Therefore, they have to be prepared freshly every day and stored in dark conditions. The working standard solutions in methanol are stable for up to 72 h at -20°C within 85.1% at the lowest levels of the QC samples. The working standard solutions have to be freshly prepared every 3 days over the development of the validation procedure. The stability of ICG was investigated also in liver samples. For bench top stability, the concentration values of ICG decreased by 15% during the handling of ICG homogenates of liver tissues when the samples were maintained in lab at RT (approximately 6 h). The stability of extracted samples stored in autosampler was measured up to 48 h (room temperature) and showed approximately 11% drop in the ICG levels.

After three freeze and thaw cycles, changes in responses of ICG spiked in the liver samples were in acceptable ranges (Table 3).

Applicability to Bio-Distribution Studies

The validated analytical method was used to determine the concentrations of ICG formulated as HFN-ICG. In this study, we compared the ICG concentrations obtained from the liver tissue samples of four mice treated with HFN-ICG and free ICG at three different time points. For each point (2, 6, 24 h), four animals were treated with HFN-ICG and four animals with free ICG. The average results were obtained for the two different types of treatments. The maximum concentration of ICG was obtained at 2 h post injection showing that the concentrations of ICG in liver from mice treated with HFN-ICG were approximately six-fold higher than those from mice treated with free ICG. As an example, the concentrations of ICG

observed at 2 h are presented in Figures 3C1,D1. Indeed, the results indicated a significant difference in the concentration values between ICG quantified by analyzing liver samples from mice treated with HFN-ICG and mice treated with free ICG (1,411 \pm 7.62 ng/ml vs. 235 \pm 26.0 ng/ml). The significant difference became negligible at 6 h. The analyses of liver tissue samples from mice treated with HFN-ICG and free ICG showed that the mean concentration values were 89.6 \pm 22.5 ng/ml and 71.8 \pm 8.75 ng/ml, respectively. Furthermore, this study revealed that the concentrations of ICG slowly dropped to 68.8 \pm 17.2 ng/ml at 24 h for mice, group 1, treated with HFN-ICG and to 56.7 \pm 4.20 ng/ml at 24 h for mice of the same group treated with free ICG. The present method enabled the determination of HFN-ICG up to 24 h in liver samples of the studied murine model. The results are summarized in Table 4. Two way ANOVA where time (in hours) and the two types of treatment, and the interaction between them, have been used as the explanatory variables and concentration (ng/ml) as the response variable confirmed a statistically significant interaction between time and treatment in modulating concentration ($p < 0.001$), assuming a significance level corresponding to $\alpha = 0.05$. Due to the small sample size and the limited number of observations, because the bio-distribution study is in its early stage, the results should be cautiously interpreted.

CONCLUSION

In this study, an UHPLC-MS/MS bioanalytical method was successfully developed and validated for the determination of ICG levels in murine liver tissue. The sample preparation

required PP procedure for ICG extraction. This method exhibited adequate selectivity, linearity, and sensitivity to obtain accurate and precise measurements of ICG in homogenate samples prepared from mice treated with free ICG and ICG loaded in protein-based nanoparticles. The UHPLC-MS/MS method can be applied in bio-distribution studies to investigate the delivery of this new formulated fluorescent dye (HFN-ICG).

DATA AVAILABILITY STATEMENT

The original contributions presented in the study are included in the article/Supplementary Material. Further inquiries can be directed to the corresponding authors.

REFERENCES

- Bellini, M., Mazzucchelli, S., Galbiati, E., Sommaruga, S., Fiandra, L., Truffi, M., et al. (2014). Protein Nanocages for Self-Triggered Nuclear Delivery of DNA-Targeted Chemotherapeutics in Cancer Cells. *J. Controlled Release* 196, 184–196. doi:10.1016/j.jconrel.2014.10.002
- Bhavane, R., Starosolski, Z., Stupin, I., Ghaghada, K. B., and Annapragada, A. (2018). NIR-II Fluorescence Imaging Using Indocyanine green Nanoparticles. *Sci. Rep.* 8, 14455. doi:10.1038/s41598-018-32754-y
- Chen, C. Y., Fancher, R. M., Ruan, Q., Marathe, P., Rodrigues, A. D., and Yang, Z. (2008). A Liquid Chromatography Tandem Mass Spectrometry Method for the Quantification of Indocyanine green in Dog Plasma and Bile. *J. Pharm. Biomed. Anal.* 47, 351–359. doi:10.1016/j.jpba.2008.01.007
- Chen, Y., Chen, D., Hu, W., Lin, G., and Huang, S. (2015). Pharmacokinetic Study of Indocyanine Green after Intravenous Administration by UPLC-MS/MS. *Int. J. Clin. Exp. Med.* 8 (9), 15482–15489.
- Dang, X., Bardhan, N. M., Qi, J., Gu, L., Eze, N. A., Lin, C.-W., et al. (2019). Deep-tissue Optical Imaging of Near Cellular-Sized Features. *Sci. Rep.* 9, 3873. doi:10.1038/s41598-019-39502-w
- Desmettre, T., Devoisselle, J. M., and Mordon, S. (2000). Fluorescence Properties and Metabolic Features of Indocyanine Green (ICG) as Related to Angiography. *Surv. Ophthalmol.* 45, 15–27. doi:10.1016/S0039-6257(00)00123-5
- Egloff-Juras, C., Bezdetnaya, L., Dolivet, G., and Lassalle, H.-P. (2019). NIR Fluorescence-Guided Tumor Surgery: New Strategies for the Use of Indocyanine green. *IJN* 14, 7823–7838. doi:10.2147/IJN.S207486
- Ferrucci, M., Franceschini, G., and Douek, M. (2018). New Techniques for sentinel Node Biopsy in Breast Cancer. *Transl. Cancer Res.* 7, S405–S417. doi:10.21037/tcr.2018.02.07
- Food and Drug Administration (2018). Bioanalytical Method Validation Guidance for Industry. Available at: <https://www.fda.gov/files/drugs/published/Bioanalytical-Method-Validation-Guidance-for-Industry.pdf> (Accessed October 28, 2021).
- Matuszewski, B. K., Constanzer, M. L., and Chavez-Eng, C. M. (2003). Strategies for the Assessment of Matrix Effect in Quantitative Bioanalytical Methods Based on HPLC-MS/MS. *Anal. Chem.* 75, 3019–3030. doi:10.1021/ac020361s
- Mindt, S., Karampinis, I., John, M., Neumaier, M., and Nowak, K. (2018). Stability and Degradation of Indocyanine green in Plasma, Aqueous Solution and Whole Blood. *Photochem. Photobiol. Sci.* 17, 1189–1196. doi:10.1039/C8PP00064F
- Reinhart, M. B., Huntington, C. R., Blair, L. J., Heniford, B. T., and Augenstein, V. A. (2016). Indocyanine Green: Historical Context, Current Applications, and Future Considerations. *Surg. Innov.* 23, 166–175. doi:10.1177/1553350615604053
- Sevieri, M., Silva, F., Bonizzi, A., Sitia, L., Truffi, M., Mazzucchelli, S., et al. (2020). Indocyanine Green Nanoparticles: Are They Compelling for Cancer Treatment? *Front. Chem.* 8, 535. doi:10.3389/fchem.2020.00535
- Sevieri, M., Sitia, L., Bonizzi, A., Truffi, M., Mazzucchelli, S., and Corsi, F. (2021). Tumor Accumulation and Off-Target Biodistribution of an Indocyanine-Green Fluorescent Nanotracer: An *Ex Vivo* Study on an Orthotopic Murine Model of Breast Cancer. *IJMS* 22, 1601. doi:10.3390/ijms22041601
- Shen, C., Wang, X., Zheng, Z., Gao, C., Chen, X., Zhao, S., et al. (2018). Doxorubicin and Indocyanine green Loaded Superparamagnetic Iron Oxide Nanoparticles with PEGylated Phospholipid Coating for Magnetic Resonance with Fluorescence Imaging and Chemotherapy of Glioma. *IJN* 14, 101–117. doi:10.2147/IJN.S173954
- Sitia, L., Sevieri, M., Bonizzi, A., Allevi, R., Morasso, C., Foschi, D., et al. (2020). Development of Tumor-Targeted Indocyanine Green-Loaded Ferritin Nanoparticles for Intraoperative Detection of Cancers. *ACS Omega* 5, 12035–12045. doi:10.1021/acsomega.0c00244
- Sottani, C., Grignani, E., Mazzucchelli, S., Bonizzi, A., Corsi, F., Negri, S., et al. (2020). Development and Validation of a Simple and Versatile Method for the Quantification of Everolimus Loaded in H-Ferritin Nanocages Using UHPLC-MS/MS. *J. Pharm. Biomed. Anal.* 191, 113644. doi:10.1016/j.jpba.2020.113644
- Spinoglio, G., Bertani, E., Borin, S., Piccioli, A., and Petz, W. (2018). Green Indocyanine Fluorescence in Robotic Abdominal Surgery. *Updates Surg.* 70, 375–379. doi:10.1007/s13304-018-0585-6
- Wang, H., Li, X., Tse, B. W.-C., Yang, H., Thorling, C. A., Liu, Y., et al. (2018). Indocyanine green-incorporating Nanoparticles for Cancer Theranostics. *Theranostics* 8, 1227–1242. doi:10.7150/thno.22872
- Zhang, Y., Zhang, L., Yin, G., Ma, W., and Gao, F. (2018). Assessing Indocyanine green Pharmacokinetics in Mouse Liver with a Dynamic Diffuse Fluorescence Tomography System. *J. Biophotonics* 11, e201800041. doi:10.1002/jbio.201800041

ETHICS STATEMENT

The animal study was reviewed and approved by the Italian Ministry of Health (Protocol Number 611/2019-PR, August 6, 2019).

AUTHOR CONTRIBUTIONS

CS and EC share the authorship and contributed to the final revision of the article. CS had conceived the idea of the present study and wrote the article. EC contributed to financial support. EG and DC contributed to lab management. SG and FR contributed to the UHPLC-MS/MS development and validation of the method. SM, MS, AC, and FC prepared the homogenates of liver tissue.

Conflict of Interest: The authors declare that the research was conducted in the absence of any commercial or financial relationships that could be construed as a potential conflict of interest.

Publisher's Note: All claims expressed in this article are solely those of the authors and do not necessarily represent those of their affiliated organizations, or those of the publisher, the editors and the reviewers. Any product that may be evaluated in this article, or claim that may be made by its manufacturer, is not guaranteed or endorsed by the publisher.

Copyright © 2022 Sottani, Grignani, Cottica, Mazzucchelli, Sevieri, Chesi, Corsi, Galfre, Robustelli della Cuna and Calleri. This is an open-access article distributed under the terms of the Creative Commons Attribution License (CC BY). The use, distribution or reproduction in other forums is permitted, provided the original author(s) and the copyright owner(s) are credited and that the original publication in this journal is cited, in accordance with accepted academic practice. No use, distribution or reproduction is permitted which does not comply with these terms.



Highly Sensitive Water Detection Through Reversible Fluorescence Changes in a *syn*-Bimane Based Boronic Acid Derivative

Apurba Pramanik[†], Joy Karmakar[†], Flavio Grynszpan^{*} and Mindy Levine^{*}

Department of Chemical Sciences, Ariel University, Ariel, Israel

OPEN ACCESS

Edited by:

Ottavia Giuffrè,
University of Messina, Italy

Reviewed by:

Jinsong Han,
China Pharmaceutical University,
China
Ugo Caruso,
University of Naples "Federico II", Italy

*Correspondence:

Flavio Grynszpan
flaviog@ariel.ac.il
Mindy Levine
mindyl@ariel.ac.il

[†]These authors have contributed
equally to this work

Specialty section:

This article was submitted to
Analytical Chemistry,
a section of the journal
Frontiers in Chemistry

Received: 24 September 2021

Accepted: 09 December 2021

Published: 17 January 2022

Citation:

Pramanik A, Karmakar J, Grynszpan F
and Levine M (2022) Highly Sensitive
Water Detection Through Reversible
Fluorescence Changes in a *syn*-
Bimane Based Boronic Acid Derivative.
Front. Chem. 9:782481.
doi: 10.3389/fchem.2021.782481

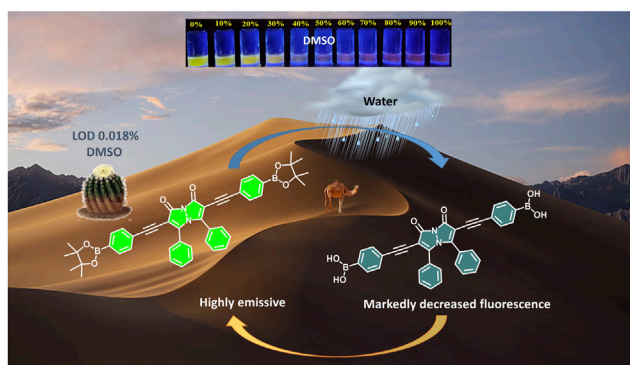
Reported herein is a fluorometric and colorimetric sensor for the presence of trace amounts of water in organic solvents, using *syn*-bimane based boronate ester **1**. This sensor responds to the presence of water with a highly sensitive turn-off fluorescence response, with detection limits as low as 0.018% water (v/v). Moreover, analogously high performance was observed when compound **1** was adsorbed on filter paper, with the paper-based sensor responding both to the presence of liquid water and to humid atmospheres. Reusability of the paper-based sensor up to 11 cycles was demonstrated, albeit with progressive decreases in the performance, and ¹H NMR and mass spectrometry analyses were used to explain the observed, hydrolysis-based sensor response.

Keywords: bimane, fluorescence, water sensor, boronate ester, paper-based sensing

INTRODUCTION

The detection of water in organic solvents is of significant interest from a variety of industrial, pharmaceutical, and chemical safety perspectives (Mishra and Singh 2021). From an industrial perspective, even minute quantities of water in organic solvents can rapidly contaminate chemical reactions, leading to deactivation of catalysts, a reduction in reaction efficiencies, and the generation of undesired side products (Lin et al., 2012). From a pharmaceutical perspective, the presence of water in organic solvents can dramatically affect the optimized syntheses of pharmaceutically active agents, with significant financial consequences particularly for large-scale syntheses (Thenrajan et al., 2021). From a chemical safety perspective, the incompatibility of a variety of molecules with water is well-known (Zor et al., 2021), and inadvertent exposure to water found as a contaminant in organic solvents can lead to the violent decomposition of water-incompatible reagents, resulting in chemical explosions and/or other undesired highly exothermic reactions (Yang et al., 2019).

Current methods for the detection of water in organic solvents tend to rely on spectral monitoring of the solvent to detect signals that correspond to the presence of water, and include the use of FTIR (Saleh and Tripp 2021), Raman (Yeung and Chan 2010), UV-visible (Mohar 2019), and fluorescence spectroscopy (Zhou et al., 2019; Kumar et al., 2016). Other methods, including gas chromatography (Kay et al., 2021) and electrochemical methods (Marecek and Samec 2020), have also been reported. These methods, which rely either on the detection of water directly or on the detection of signal changes corresponding to other molecules that interact with water, generally lead to extremely high sensitivity and selectivity (Wang et al., 2021). Nonetheless, ongoing challenges in using such methods include the need for costly and non-portable laboratory-grade instruments to monitor such spectral



GRAPHICAL ABSTRACT |

changes, as well as the fact that many of these methods are not reversible. Moreover, toxicity concerns remain around the use of water-detection materials that contain heavy metals, such as mercury and cadmium (Othong et al., 2020); around the use and responsible disposal of sensors composed of graphene oxide (Chi et al., 2021), carbon dots (Lee et al., 2019), and other carbon-based materials (Liu et al., 2020); and around sensors that rely on relatively weak noncovalent interactions in the sensor construction (Wu et al., 2020), and the potential for the degradation of such sensors to lead to environmental contamination (Gao et al., 2010).

Recent reports from one of our research groups have demonstrated the development of high-performance fluorometric (Haynes and Levine 2020) and colorimetric (Haynes et al., 2019) sensors for a variety of organic and inorganic analytes. Moreover, recent successes in novel sensor development have been reported in joint publications from our research groups, and demonstrate that bimane-based supramolecular constructs act as highly effective sensors for cobalt (II) ions (Pramanik et al., 2020) and for molecular iodine (Pramanik et al., 2021). These sensors, which operate in both solution-state and on filter papers to provide fluorometric and colorimetric analyte detection, have notable practical advantages, including their high sensitivity, ease of access, and non-toxicity of both the bimane transducing element and supramolecular cyclodextrin scaffold. The lack of toxicity of both cyclodextrin (Kfoury et al., 2019) and bimane (MSDS 38369) has been well-established in the literature, and has led to the use of both of these components in a variety of biologically-relevant applications (Barbosa et al., 2019; Lapidot et al., 2016; Lavis and Raines 2008). Moreover, an additional report from one of our research groups has demonstrated a streamlined approach to access bimane derivatives, which facilitates practically attainable access to a variety of these highly fluorescent structures (Szumski et al., 2021). This straightforward access, combined with our already demonstrated ability to use bimanes as components of effective sensors (Roy et al., 2018), prompted us to investigate the use of bimane derivatives as high impact fluorescent sensors for water contamination. Moreover, a recent theoretical report indicated that bimane is expected to

demonstrate significant water-induced fluorescence quenching, although experimental evidence in support of these calculations was not provided (Maillard et al., 2021).

Reported herein are the results of our investigations, which demonstrate that bimane **1** responds to the presence of liquid water in organic solvents and water vapor in high humidity environments, and that such a response occurs both in solution of bimane **1** and on filter papers to which bimane **1** had been adsorbed, leading to colorimetric and fluorimetric changes. Although water sensing via a similar boronate hydrolysis mechanism has been demonstrated using other fluorophores (Selvaraj et al., 2019), it has not yet been demonstrated using the bimane scaffold and represents a significant step towards the establishment of bimanes as a viable option in the tool-box of available fluorophores (Kosower et al., 1979). Determining the linear relationship between the sensor response (either colorimetric or fluorometric) and the amount of water provides a method for its straightforward quantitation. Finally, good reversibility of the paper-based sensors was also demonstrated, as were detailed mechanistic investigations that explain the basis of the sensor response.

MATERIALS AND METHODS

Synthesis of Bimane 1

Compound **1** was synthesized from compounds **3** and **4**. Bis(triphenylphosphine) palladium (II) chloride (20 mg, 0.028 mmol, 0.10 equiv) and cuprous iodide (2.7 mg, 0.014 mmol, 0.05 equiv) were added to a solution of 4-ethynylphenylboronic acid pinacol ester **4** (140 mg, 0.61 mmol, 2.2 equiv), diisopropylethylamine (0.48 ml, 2.8 mmol, 10 equiv), and compound **3** (150 mg, 0.28 mmol, 1.0 equiv) in CH₃CN (200 ml). The mixture was stirred at 80 °C for 1 hour under a nitrogen atmosphere. After 1 hour, the solvent was evaporated under reduced pressure, and the resulting crude product was purified *via* flash chromatography over silica gel eluting with 5% ethyl acetate: 95% dichloromethane. The product was isolated as a reddish-yellow colored solid in 67% yield (138 mg). ¹H NMR

(CDCl₃): 7.72–7.70 (*d*, *J* = 8 Hz, 2H, Ar-H), 7.36–7.34 (*d*, *J* = 8 Hz, 2H, Ar-H), 7.32–7.28 (*m*, 2H, Ar-H), 7.24–7.23 (*d*, *J* = 4 Hz, 1H, Ar-H), 7.17–7.13 (*m*, 2H, Ar-H), 1.33 [*s*, 12 H, 2(-Me)₂] ppm; ¹³C NMR (CDCl₃): 134.64, 131.24, 130.89, 129.31, 128.29, 84.15, 25.01 ppm; DEPTQ: 134.96, 131.20, 129.63, 128.61, 126.12, 25.32 ppm; HRMS *m/z* [M + H]⁺ calculated: 741.3322, found: 741.3332.

UV-Visible Spectroscopy Procedures

UV-Visible absorption spectroscopy was used in two different situations: 1) to study the solvent dependent properties of the bimane-based boronate compound **1**; and 2) to investigate the detection of water using bimane-based boronate compound **1**. Procedures for each of these situations are detailed below.

To Study the Solvent Dependent Properties of Compound 1

The effects of 13 different solvent systems were investigated by measuring the UV-visible absorption spectra of bimane **1** (from 200 to 700 nm) at a concentration of 10 μM in each of the solvent systems (see **Supplementary Table S1**).

To Investigate the Detection of Water Using Compound 1

The changes of the UV-visible absorbance spectrum of compound **1** upon the addition of varying concentrations of water was measured in a variety of water-miscible solvents. These experiments were conducted in HPLC grade solvents, with the concentration of compound **1** held constant at 10 μM, and with increasing concentrations of Milli-Q purified water added to the solution.

Fluorescence Spectroscopy Procedures

Fluorescence spectroscopy was used to investigate two different situations: 1) to study the solvent dependent fluorescence properties of compound **1**; and 2) to investigate the detection of water using compound **1** in a variety of solvents. In all cases, the excitation of bimane **1** occurred at 450 nm, and the excitation and emission slit widths were both 5.0 nm. The procedures used in each of these situations are discussed in detail below:

To Study the Solvent Dependent Fluorescence Properties of Compound 1

The concentration of compound **1** was held constant at 10 μM in acetonitrile, acetonitrile-water (1:1 vol: vol), methanol, ethanol, tetrahydrofuran, ethyl acetate, dichloromethane, chloroform, acetone, diethyl ether, *N,N*-dimethylformamide (DMF), dimethylsulfoxide (DMSO), and water. The fluorescence emission of compound **1** in each solvent was recorded via excitation at 450 nm. Changes in the fluorescence emission of bimane **1** were quantified by integrating the fluorescence emission vs. wavenumber on the X-axis (using OriginPro 2020).

To Investigate the Detection of Water Using Compound 1

Increasing concentrations of water were added to solutions of compound **1** in organic, water-miscible solvents, with the

concentration of bimane **1** held constant at 10 μM. The concentration of water in these experiments ranged from 0 to 43.16 μM. In all cases, changes in the fluorescence emission of compound **1** under these conditions were quantified by integrating the fluorescence emission vs. wavenumber on the X-axis using OriginPro 2020.

Experimental Procedures for Paper-Based Studies

Whatman #1 filter papers with dimensions of 3.5 cm × 0.9 cm were coated with a solution of compound **1** by submerging the filter papers in an acetonitrile solution of compound **1** [(**1**) = 10 μM] for 60 min at room temperature. After 60 min, the papers were carefully removed from the solution using tweezers and were then placed on a Petri dish and allowed to dry for 3 hours in an open-air environment. After that, varying amounts of water (100, 150, 200, 250, 300, or 350 μL) were added via pipette to the top of the paper, and the paper was allowed to dry for 4 h at room temperature on a benchtop. The dried papers were then visualized under a long-wave, hand-held TLC lamp (365 nm excitation) and the results of these studies are reported herein.

RESULTS AND DISCUSSION

The fluorescent sensor for water reported herein relies on bimane **1**, which was synthesized via the Sonogashira coupling of diiodobimane **3** with two equivalents of acetylene **4** (**Figure 1**). This diiodobimane was in turn accessed from 5-phenyl-4,4-dihydropyrazol-3-one **2** in a one-pot, three-step sequence in 68% overall yield, representing a marked improvement over multi-step, literature-reported methods that require the use of toxic chlorine gas and provide low overall yields (Kosower et al., 1982). The relative quantum yield of bimane **1** (0.17) and its extinction coefficient ($1.23 \times 10^4 \text{ L M}^{-1} \text{ cm}^{-1}$) are somewhat lower than values reported for other bimane structures (i.e., 0.83 for an unsymmetrically substituted bimane containing one chlorine substituent) (Szumski et al., 2021), but are in line with Kosower's observation that electron-donating alkyl and aryl substituents on the *syn*-bimane structure lead to noticeable reductions in the quantum yield (Kosower et al., 1983).

Interestingly, compound **1** displayed mild solvatochromism in its steady-state photophysical measurements, with slight solvent-induced differences in the absorbance (**Figure 2A**) and emission (**Figure 2B**) spectra observed. These changes were markedly more pronounced in a fully aqueous solvent, with water leading to a strong decrease in the visible absorbance band of compound **1**, and an even more pronounced decrease in the fluorescence emission. Interestingly, compound **1** in the solid-state also displayed a strong fluorescence emission, which decreased markedly upon the addition of water.

This water-induced quenching displayed a strong solvent-dependent response (**Figure 3**), with the addition of water to acetonitrile displaying the greatest degree of water-induced fluorescence quenching (**Figure 3A**, 53% decrease in the

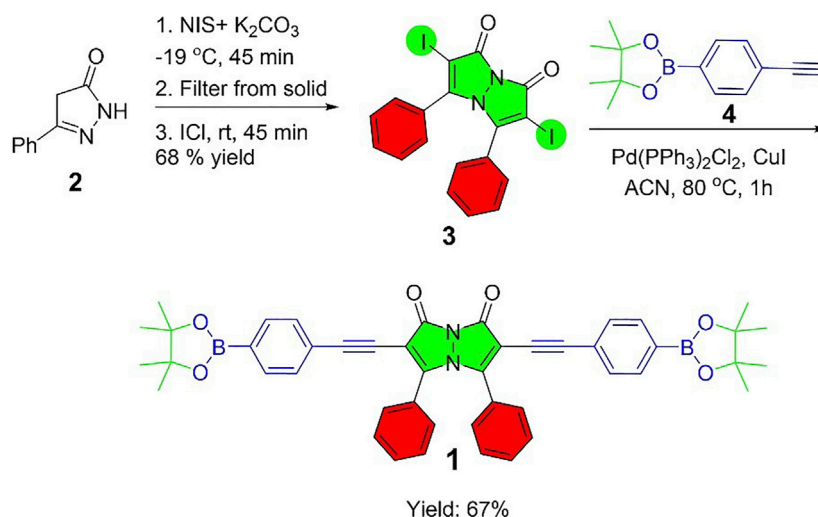


FIGURE 1 | A streamlined synthesis of diboronate ester functionalized bimane **1**.

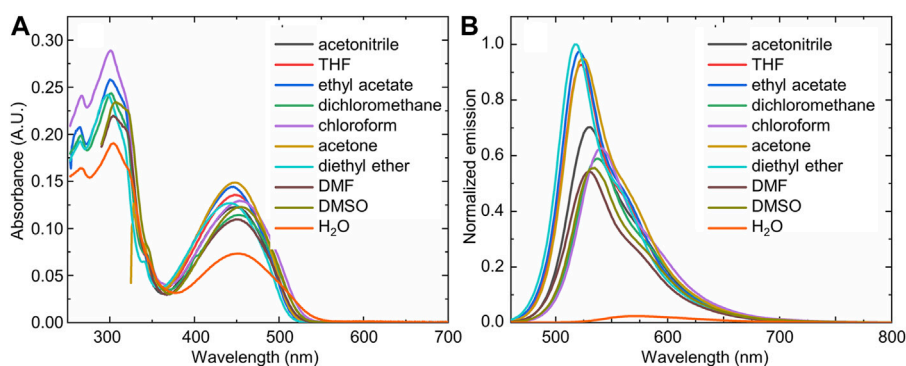


FIGURE 2 | The (A) UV-visible and (B) fluorescence emission spectra of compound **1** in a variety of solvents, highlighting the marked difference in spectra observed in water (orange trace) compared to the organic solvents [(**1**) = 10 μM; λ_{ex} = 450 nm].

integrated fluorescence emission compared to the emission in the absence of water). Extremely high sensitivity for low concentrations of water was also demonstrated (Table 1), with the lowest detection limit for water of 0.018% (v/v) calculated in DMSO. This detection limit is in line with the limits of the most sensitive sensors for water in organic solvents reported to date (Huang et al., 2021), and indicates that the sensor reported herein represents a highly sensitive detection method (Kumar et al., 2021). Of note, all aqueous studies were conducted in double deionized water, so that no interference and/or fluorescence quenching occurred due to residual metal ions. Such ions, in particular palladium (Das et al., 2016), sodium (Roy et al., 2018), and cobalt (Pramanik et al., 2020), have been shown to complex effectively to the bimane core, leading to marked changes in the bimane's photophysical properties. Also of note, the existence of trace amounts of water even in the "0%" water is likely, based on

literature precedent (Son et al., 2001), but this trace amount of water is accounted for as part of the baseline for our fluorescence quenching experiments, in accordance with literature precedent (Porter and Markham 1970).

Moreover, this highly sensitive fluorescence-based quenching response was accompanied by noticeable changes in the color of bimane **1** solutions in varying solvents with increasing percentages of water, which were particularly visible using 365 nm excitation of the bimane **1** solutions. Examples of such dramatic color changes are shown for water added to acetonitrile, THF, and DMSO (Figure 4, top). The quantitative blue values changed as a result of the addition of increasing percentages of water in a manner that was linear for a broad range of water percentages (Figure 4, bottom, Table 2); such linearity, in turn, directly enables the ability to detect unknown water concentrations within such solvent systems. Finally, general

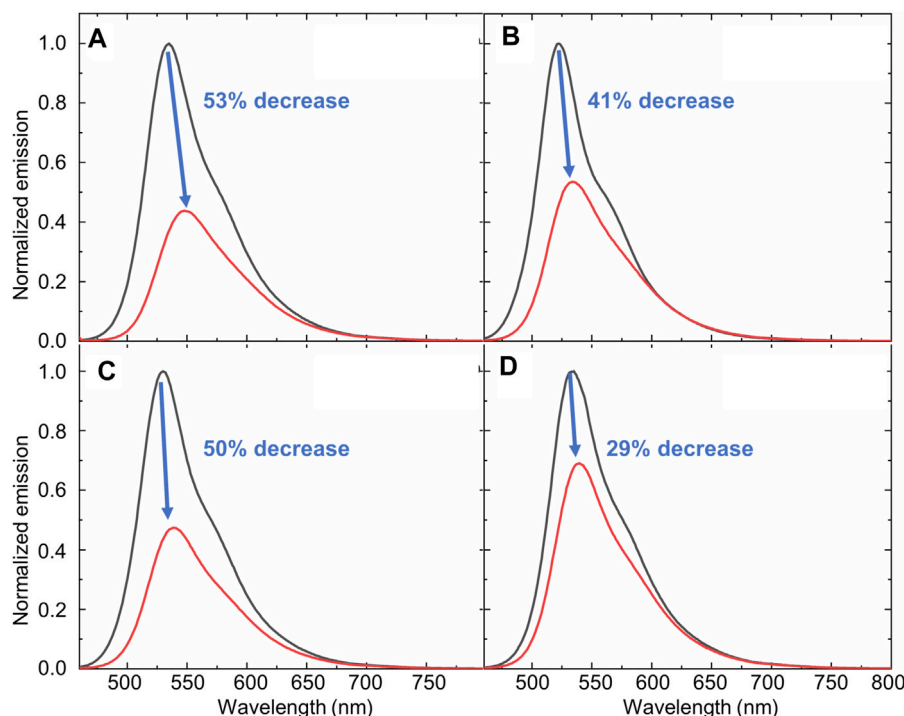


FIGURE 3 | An illustration of the changes in the fluorescence emission of compound **1** that occurs in the absence (black line) or presence (red line) of water in water-miscible organic solvents: **(A)** Acetonitrile; **(B)** THF **(C)** DMF; and **(D)** DMSO. [**1**] = 10 μ M; λ_{ex} = 450 nm].

TABLE 1 | Limits of detection and quantification of water in organic, water-miscible solvents, calculated as the percentage of water by volume.^a

Solvent	Limit of detection (v/v)	Limit of quantification (v/v)
Acetonitrile	0.57 \pm 0.003%	0.96 \pm 0.007%
THF	5.74 \pm 0.014%	6.05 \pm 0.014%
DMF	0.17 \pm 0.007%	0.60 \pm 0.014%
DMSO	0.018 \pm 0.001%	0.19 \pm 0.007%
Acetone	0.76 \pm 0.001%	1.08 \pm 0.002%

^aLimits of detection and quantification were calculated as percentage of water by volume in the solvent system, and results reported herein represent the average of at least three trials. The text in bold highlights the solvent with lowest LOD

applicability for the system was also demonstrated, with both purified milli-Q water and aqueous buffer solutions between pH 5 and pH 7.5 inducing identical colorimetric responses (see ESI for more details).

The mechanism by which the addition of water induces the fluorescence quenching of bimane **1** is likely via the water-induced hydrolysis of the boronate ester moieties on compound **1** to form the hydrolyzed boronic acid **5** (Figure 5). The formation of compound **5** was confirmed by ¹H NMR titrations and high-resolution mass spectrometry (see ESI for more details). Moreover, an analogous hydrolysis reaction occurred in methanol, resulting in the formation of methyl ester-substituted boronate moieties in lieu of the pinacol boronates.

The fact that changing the hybridization of boron-containing moieties from tetrahedral to trigonal planar induces such marked fluorescence decreases has been previously reported in the literature (Samaniego Lopez et al., 2015; Williams et al., 2021), and is fully consistent with the results reported herein. Notably, this fluorescence quenching occurs rapidly (within seconds), and remains stable (with less than 5% additional quenching) up to 20 min after the initial contact between compound **1** and water.

Gratifyingly, moving from solution-state water sensing to sensing on a solid-support resulted in analogous water-induced photophysical changes, with the addition of water to filter paper onto which bimane **1** had been adsorbed causing a marked change in the color and fluorescence of the system (Figure 6A). Notably, the procedure by which water is added to these paper sensors (dropping *via* pipette onto the functionalized paper) is done by design to ensure that we control the amount of water that the paper contacts, but we recognize that such a procedure will require further optimization before real-world device development and deployment. These changes were quantified by RGB color analysis (Figure 6B), which shows that the system becomes rapidly saturated with water, resulting in minimal changes in the RGB values after 100 μ L of water were added. Even more significantly, bimane **1**-functionalized filter papers responded to the presence of water vapor with an analogously strong sensor response, with exposure of the functionalized paper to a high humidity chamber (99% relative humidity) resulting in analogous changes in the sensor's

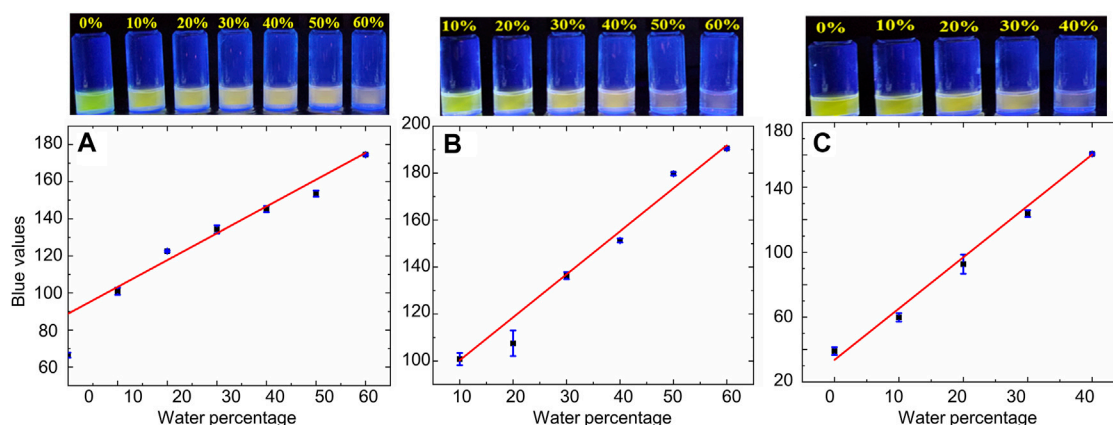


FIGURE 4 | Top: Naked eye color changes induced by the addition of increasing percentages of water to water-miscible solvents. Bottom: The linear relationship between the added water percentage and the quantitative blue value of the solution, measured from photographs taken under 365 nm excitation. **(A)** Acetonitrile solutions; **(B)** DMF solutions; and **(C)** DMSO solutions (other solvents are shown in the ESI; blue bars represent the calculated standard deviations for each data point).

TABLE 2 | The linear relationship between the percentage of water added to solutions of bimane **1** in water-miscible solvents and the quantitative blue value of the resulting solution when imaged under 365 nm excitation.^a

Solvent	Linear range	Equation	R^2 value
Acetonitrile	0–60% water	$y = 15.864x + 64.5$	0.9509
THF	0–60% water	$y = 115.75x + 71.518$	0.9207
DMF	10–60% water	$y = 198.15x + 73.953$	0.9841
DMSO	0–40% water	$y = 313.7x + 30.98$	0.9897
Acetone	0–100% water ^b	$y = -190.15x + 221.16$	0.9249

^aData were obtained from photographs of the bimane **1** solution under long-wave TLC, light irradiation (365 nm), with processing using random sampling of data points with Microsoft Paint (>10 random points/sample) and linear curve fitting using Microsoft Excel; (**1**) = 10 μ M.

^bGreen values were used as the blue values gave a poor linear fit.

photophysical (colorimetric and fluorometric) profile (Figure 6C).

Finally, the bimane **1**-functionalized filter papers demonstrated strong reversibility in the sensing of water in

both the liquid and vapor phase. Liquid water, which induced noticeable photophysical changes of the bimane **1**-functionalized paper (see Figure 6A, above), was effectively removed by drying the papers under ambient conditions followed by brief heating (80 °C for 10 min). This drying allowed for the introduction of water again to the paper, followed by re-drying of the paper under the aforementioned conditions. Overall, 11 cycles of sensing followed by drying were demonstrated, albeit with progressive decreases in the performance observed. This reusability was visible by naked eye detection (Figure 7A), and could also be quantified by measuring the saturation values for each of the papers (Figure 7B). Similarly, the reusability of bimane **1**-functionalized papers as humidity sensors was also demonstrated, with 7 cycles of exposure to 99% relative humidity, followed by drying and reuse of the same sensor with comparable performance results (Figure 7C). Of note, at this stage we cannot say with full certainty that in the dry state the original bimane **1** is regenerated. Reaction of bimane **5** with free OH groups in the surface of the paper would also lead to

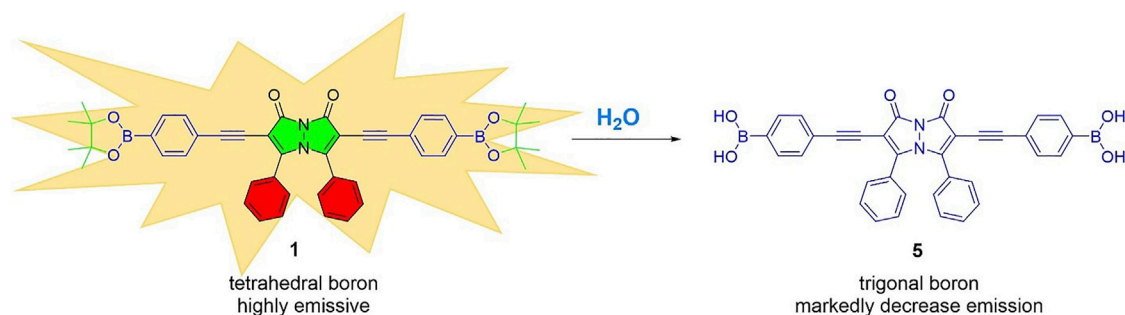


FIGURE 5 | The hydrolysis of boronate ester **1** to boronic acid **5**, which likely is responsible for water-induced fluorescence decreases.

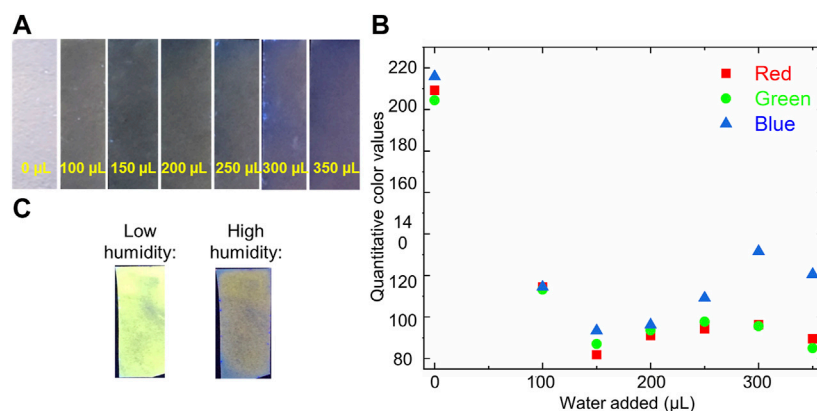


FIGURE 6 | (A) Photograph of bimane **1**-functionalized filter paper after the addition of water via micropipette (left-to-right: 0, 100, 150, 200, 250, 300, and 350 μL) (B) Quantitative RGB values of the bimane **1**-functionalized filter paper as a function of the addition of increasing amounts of water (calculated via ImageJ analysis); (C) Photographs of bimane **1**-functionalized filter paper under low humidity and high humidity conditions, imaged under 365 nm excitation.

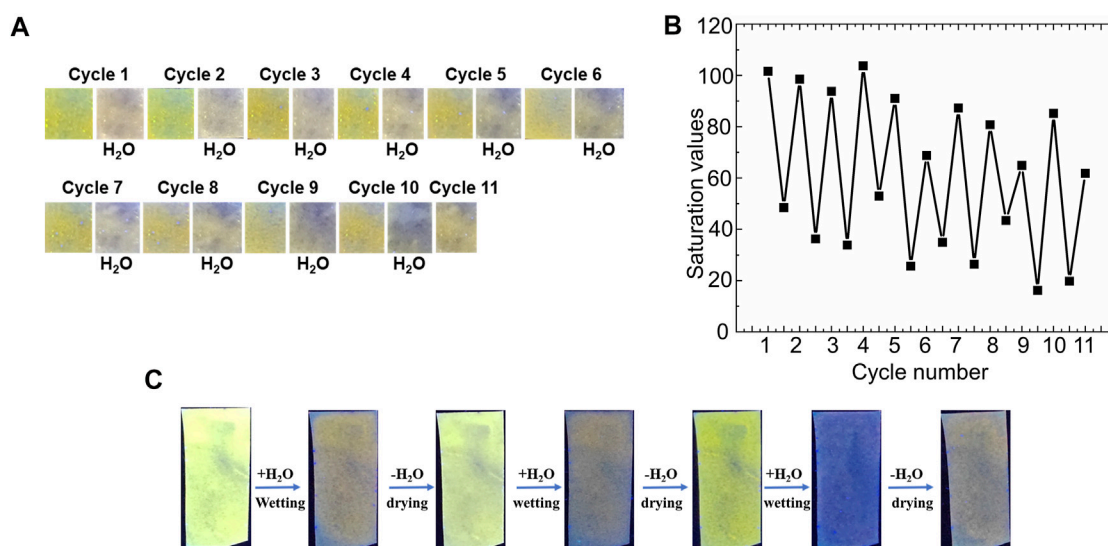


FIGURE 7 | An illustration of the regeneration and reusability of bimane **1**-functionalized filter papers: (A) The detection of liquid water droplets over 11 cycles of exposure followed by drying; (B) Quantitative green values of the papers plotted as a function of cycle number, with each cycle representing an exposure to water followed by drying; and (C) Reusability of the paper sensors for the detection of humidity through exposing the papers to 99% relative humidity, followed by drying under ambient humidity conditions and re-exposure.

fluorescent bimane based boronate esters, which means that the observed partial reversibility may be a result of the generation of new fluorescent bimane-based boronate esters on the paper support.

CONCLUSION

The development of methods for the rapid, sensitive, and generally applicable detection of water represents a high priority research area due to its significant applications in chemical safety and industry. The work reported herein

represents an important step towards addressing this issue, by reporting that a boronate ester-functionalized bimane, compound **1**, undergoes rapid and sensitive fluorescence quenching in the presence of trace quantities of water, both in solution and in the vapor phase. The successful access to this structure due to recent advances in synthetic methodology for *syn*-bimanes represents an additional important advance, and the reusability of paper-based sensors with compound **1** highlights the strong practical applicability of this system. Future work will be directed towards demonstrating the broad applicability of this sensor in real-world samples, and results of these and other investigations will be reported in due course.

DATA AVAILABILITY STATEMENT

The original contributions presented in the study are included in the article/**Supplementary Material** and further inquiries can be directed to the corresponding authors.

AUTHOR CONTRIBUTIONS

JK optimized the synthesis of the bimane boronate ester, conducted detailed analyses of the intermediates and final products along the synthetic pathway, and did fluorescence analytical work. AP optimized the sensing component of the work reported herein, including the work of the sensor in solution and on paper, using both fluorescence and colorimetric analysis. ML and FG assisted in the design of experiments and the interpretation of results. All authors contributed to the writing of the manuscript, with ML and FG providing final edits as needed. All authors give approval to the submission of this work, and all authors agree to be accountable for the work reported herein.

REFERENCES

- Barbosa, P. F. P., Cumba, L. R., Andrade, R. D. A., and do Carmo, D. R. (2019). Chemical Modifications of Cyclodextrin and Chitosan for Biological and Environmental Applications: Metals and Organic Pollutants Adsorption and Removal. *J. Polym. Environ.* 27, 1352–1366. doi:10.1007/s10924-019-01434-x
- Chi, H., Ze, L. J., Zhou, X., and Wang, F. (2021). GO Film on Flexible Substrate: An Approach to Wearable Colorimetric Humidity Sensor. *Dyes Pigm.* 185, 108916. doi:10.1016/j.dyepig.2020.108916
- Das, P. J., Diskin-Posner, Y., Firer, M., Montag, M., and Grynszpan, F. (2016). syn-Bimane as a Chelating O-Donor Ligand for Palladium(II). *Dalton Trans.* 45, 17123–17131. doi:10.1039/C6DT02141G
- Gao, Q., Xiu, Y., Li, G.-D., and Chen, J.-S. (2010). Sensor Material Based on Occluded Trisulfur Anionic Radicals for Convenient Detection of Trace Amounts of Water Molecules. *J. Mater. Chem.* 20, 3307–3312. doi:10.1039/b925233a
- Haynes, A., Halpert, P., and Levine, M. (2019). Colorimetric Detection of Aliphatic Alcohols in β -Cyclodextrin Solutions. *ACS Omega* 4, 18361–18369. doi:10.1021/acsomega.9b02612
- Haynes, A. Z., and Levine, M. (2020). Detection of Anabolic Steroids via cyclodextrin-Promoted Fluorescence Modulation. *RSC Adv.* 10, 25108–25115. doi:10.1039/d0ra03485a
- Huang, J., Liang, Y., Liu, H.-B., Zhang, X., and Wang, J. (2021). N-Hydroxypropyl Substituted 4-Hydroxynaphthalimide: Differentiation of Solvents and Discriminative Determination of Water in Organic Solvents. *Spectrochimica Acta A: Mol. Biomol. Spectrosc.* 253, 119559. doi:10.1016/j.saa.2021.119559
- Kay, J., Thomas, R., Gruenhagen, J., and Venkatramani, C. J. (2021). Simultaneous Quantitation of Water and Residual Solvents in Pharmaceuticals by Rapid Headspace Gas Chromatography with thermal Conductivity Detection (GC-TCD). *J. Pharm. Biomed. Anal.* 194, 113796. doi:10.1016/j.jpba.2020.113796
- Kfoury, M., Auezova, L., Greige-Gerges, H., and Fourmentin, S. (2019). Encapsulation in Cyclodextrins to Widen the Applications of Essential Oils. *Environ. Chem. Lett.* 17, 129–143. doi:10.1007/s10311-018-0783-y
- Kosower, E. M., Bernstein, J., Goldberg, I., Pazhenchevsky, B., and Goldstein, E. (1979). Configuration and Planarity of Fluorescent and Nonfluorescent 1,5-diazabicyclo[3.3.0]octadienediones (9,10-dioxabimanes) by X-ray Crystallography. *J. Am. Chem. Soc.* 101, 1620–1621. doi:10.1021/ja00500a055
- Kosower, E. M., Faust, D., Ben-Shoshan, M., and Goldberg, I. (1982). Bimanes. 14. Synthesis and Properties of 4,6-bis(carbalkoxy)-1,5-diazabicyclo[3.3.0]octa-3,6-Diene-2,8-Diones [4,6-Bis(carbalkoxy)-9,10-Dioxo-Syn-Bimanes].

FUNDING

Ariel University is acknowledged for providing start-up funding to ML, FG and a postdoctoral research fellowship for AP. FG is the incumbent of the Cosman endowment for organic chemistry research.

ACKNOWLEDGMENTS

The authors gratefully acknowledge Dr. Vered Marks for her assistance with ^1H NMR titration experiments and Dr. Itay Pitussi for his assistance with high resolution mass spectrometry. Dr. Rami Krieger is thanked for his role in maintaining all departmental instruments used for these experiments.

SUPPLEMENTARY MATERIAL

The Supplementary Material for this article can be found online at: <https://www.frontiersin.org/articles/10.3389/fchem.2021.782481/full#supplementary-material>

- Preparation of the Parent Syn-Bimane, Syn-(hydrogen,hydrogen)bimane. *J. Org. Chem.* 47, 214–221. doi:10.1021/jo00341a007
- Kosower, E. M., Kanety, H., and Dodiuk, H. (1983). Bimanes VIII: Photophysical Properties of Syn- and Anti-1,5-diazabicyclo[3.3.0] Octadienediones (9,10-dioxabimanes). *J. Photochem.* 21, 171–182. doi:10.1016/0047-2670(83)80020-3
- Kumar, P., Ghosh, A., and Jose, D. A. (2021). Chemical Sensors for Water Detection in Organic Solvents and Their Applications. *ChemistrySelect* 6, 820–842. doi:10.1002/slct.202003920
- Kumar, P., Kaushik, R., Ghosh, A., and Jose, D. A. (2016). Detection of Moisture by Fluorescent OFF-ON Sensor in Organic Solvents and Raw Food Products. *Anal. Chem.* 88, 11314–11318. doi:10.1021/acs.analchem.6b03949
- Lapidot, I., Baranes, D., Pinhasov, A., Gellerman, G., Albeck, A., Grynszpan, F., et al. (2016). α -Aminoisobutyric Acid Leads a Fluorescent Syn-Bimane LASER Probe across the Blood-Brain Barrier. *Mc* 12, 48–53. doi:10.2174/1573406411666150518105010
- Lavis, L. D., and Raines, R. T. (2008). Bright Ideas for Chemical Biology. *ACS Chem. Biol.* 3, 142–155. doi:10.1021/cb700248m
- Lee, H. J., Jana, J., Thi Ngo, Y.-L., Wang, L. L., Chung, J. S., and Hur, S. H. (2019). The Effect of Solvent Polarity on Emission Properties of Carbon Dots and Their Uses in Colorimetric Sensors for Water and Humidity. *Mater. Res. Bull.* 119, 110564. doi:10.1016/j.materresbull.2019.110564
- Lin, W., Cheng, H., Ming, J., Yu, Y., and Zhao, F. (2012). Deactivation of Ni/TiO₂ Catalyst in the Hydrogenation of Nitrobenzene in Water and Improvement in its Stability by Coating a Layer of Hydrophobic Carbon. *J. Catal.* 291, 149–154. doi:10.1016/j.jcat.2012.04.020
- Liu, X., Zhou, Z., Wang, T., Deng, P., and Yan, Y. (2020). Visual Monitoring of Trace Water in Organic Solvents Based on Ecofriendly B/r-CDs Ratiometric Fluorescence Test Paper. *Talanta* 216, 120958. doi:10.1016/j.talanta.2020.120958
- Maillard, J., Klehs, K., Rumble, C., Vauthey, E., Heilemann, M., and Fürstenberg, A. (2021). Universal Quenching of Common Fluorescent Probes by Water and Alcohols. *Chem. Sci.* 12, 1352–1362. doi:10.1039/d0sc05431c
- Mareček, V., and Samec, Z. (2020). Electrochemical Study of the Anomalous Salt Extraction from Water to a Polar Organic Solvent. *J. Solid State. Electrochem.* 24, 2173–2174. doi:10.1007/s10008-020-04656-5
- Mishra, S., and Singh, A. K. (2021). Optical Sensors for Water and Humidity and Their Further Applications. *Coord. Chem. Rev.* 445, 214063. doi:10.1016/j.ccr.2021.214063
- Mohar, M. (2019). A Metallogel Based on a Zwitterionic Spirocyclic Meisenheimer Complex: Sensing of Fluoride Ions in Water and Moisture Content in Organic Solvents. *ChemistrySelect* 4, 5308–5314. doi:10.1002/slct.201900939

- Othong, J., Boonmak, J., Kielar, F., and Youngme, S. (2020). Dual Function Based on Switchable Colorimetric Luminescence for Water and Temperature Sensing in Two-Dimensional Metal-Organic Framework Nanosheets. *ACS Appl. Mater. Inter.* 12, 41776–41784. doi:10.1021/acsami.0c12014
- Porter, L. J., and Markham, K. R. (1970). The Unsuitability of Ethanol as a Solvent for the Spectroscopic Detection of Functional Groups in Hydroxyflavones with Aluminium Chloride. *Phytochemistry* 9, 1363–1365. doi:10.1016/S0031-9422(00)85333-9
- Pramanik, A., Amer, S., Grynszpan, F., and Levine, M. (2020). Highly Sensitive Detection of Cobalt through Fluorescence Changes in β -Cyclodextrin-Bimane Complexes. *Chem. Commun.* 56, 12126–12129. doi:10.1039/d0cc05812b
- Pramanik, A., Karmakar, J., Grynszpan, F., and Levine, M. (2021). Facile Iodine Detection via Fluorescence Quenching of β -Cyclodextrin-Bimane-Ditriazole Inclusion Complexes. *Isr. J. Chem.* 61, 253–260. doi:10.1002/ijch.202000092
- Roy, A., Das, P. J., Diskin-Posner, Y., Firer, M., Grynszpan, F., and Montag, M. (2016). Quenching of syn-Bimane Fluorescence by Na^+ Complexation. *New J. Chem.* 42, 15541–15545. doi:10.1039/c8nj01945b
- Saleh, S. H., and Tripp, C. P. (2021). Measurement of Water Concentration in Oils Using CaO Powder and Infrared Spectroscopy. *Talanta* 228, 122250. doi:10.1016/j.talanta.2021.122250
- Samaniego Lopez, C., Lago Huvelle, M. A., Uhrig, M. L., Coluccio Leskow, F., and Spagnuolo, C. C. (2015). Recognition of Saccharides in the NIR Region with a Novel Fluorogenic Boronolectin: *In Vitro* and Live Cell Labeling. *Chem. Commun.* 51, 4895–4898. doi:10.1039/C4CC10425K
- Sekharan, T. R., Katari, O., Ruhina Rahman, S. N., Pawde, D. M., Goswami, A., Chandira, R. M., et al. (2021). Neoteric Solvents for the Pharmaceutical Industry: An Update. *Drug Discov. Today* 26, 1702–1711. doi:10.1016/j.drudis.2021.03.005
- Selvaraj, M., Rajalakshmi, K., Nam, Y.-S., Lee, Y., Kim, B. C., Pai, S. J., et al. (2019). Rapid-response and Highly Sensitive Boronate Derivative-Based Fluorescence Probe for Detecting H_2O_2 in Living Cells. *J. Anal. Methods Chem.* 2019, 5174764. doi:10.1155/2019/5174764
- Son, H. S., Roh, J., Shin, S. K., Park, J. W., and Ku, J. K. (2001). Luminescence Spectroscopy of Eu^{3+} (Bis-Tris) Complexes in Anhydrous DMF [Bis-Tris = 2,2-Bis(hydroxymethyl)-2,2',2''-Nitrilotriethanol]: Luminescence Quenching Rate Constants for the $^5\text{D}_0$ State of Eu^{3+} by DMF and Polyalcoholic OH Groups. *J. Chem. Soc. Dalton Trans.*, 1524–1528. doi:10.1039/b100566i
- Szumski, O., Karmakar, J., and Grynszpan, F. (2021). Re-enter the syn-(Me,I) Bimane: A Gateway to Bimane Derivatives with Extended π -Systems. *Synlett* 32, 1141–1145. doi:10.1055/s-0040-1706045
- Wang, Y., Zhou, Y., Xie, G., Li, J., Wang, Y., Liu, X., et al. (2021). Dual Resistance and Impedance Investigation: Ultrasensitive and Stable Humidity Detection of Molybdenum Disulfide Nanosheet-Polyethylene Oxide Hybrids. *ACS Appl. Mater. Inter.* 13, 25250–25259. doi:10.1021/acsami.1c02119
- Williams, G. T., Kedge, J. L., and Fossey, J. S. (2021). Molecular Boronic Acid-Based Saccharide Sensors. *ACS Sens.* 6, 1508–1528. doi:10.1021/acssensors.1c00462
- Wu, Y., Ji, J., Zhou, Y., Chen, Z., Liu, S., and Zhao, J. (2020). Ratiometric and Colorimetric Sensors for Highly Sensitive Detection of Water in Organic Solvents Based on Hydroxyl-Containing Polyimide-Fluoride Complexes. *Analytica Chim. Acta* 1108, 37–45. doi:10.1016/j.aca.2020.02.043
- Yang, Q., Sheng, M., Henkelis, J. J., Tu, S., Wiensch, E., Zhang, H., et al. (2019). Explosion Hazards of Sodium Hydride in Dimethyl Sulfoxide, N,N-Dimethylformamide, and N,N-Dimethylacetamide. *Org. Process. Res. Dev.* 23, 2210–2217. doi:10.1021/acs.oprd.9b00276
- Yeung, M. C., and Chan, C. K. (2010). Water Content and Phase Transitions in Particles of Inorganic and Organic Species and Their Mixtures Using Micro-Raman Spectroscopy. *Aerosol Sci. Technology* 44, 269–280. doi:10.1080/02786820903583786
- Zhou, L., Liao, J. F., Huang, Z. G., Wei, J. H., Wang, X. D., Li, W. G., et al. (2019). A Highly Red-Emissive Lead-Free Indium-Based Perovskite Single Crystal for Sensitive Water Detection. *Angew. Chem. Int. Ed.* 58, 5277–5281. doi:10.1002/anie.201814564
- Zor, C., Subaşı, Y., Hacı, D., Somer, M., and Afyon, S. (2021). Guide to Water Free Lithium Bis(oxalate) Borate (LiBOB). *J. Phys. Chem. C* 125, 11310–11317. doi:10.1021/acs.jpcc.1c01437

Conflict of Interest: The authors declare that the research was conducted in the absence of any commercial or financial relationships that could be construed as a potential conflict of interest.

Publisher's Note: All claims expressed in this article are solely those of the authors and do not necessarily represent those of their affiliated organizations, or those of the publisher, the editors, and the reviewers. Any product that may be evaluated in this article, or claim that may be made by its manufacturer, is not guaranteed or endorsed by the publisher.

Copyright © 2022 Pramanik, Karmakar, Grynszpan and Levine. This is an open-access article distributed under the terms of the Creative Commons Attribution License (CC BY). The use, distribution or reproduction in other forums is permitted, provided the original author(s) and the copyright owner(s) are credited and that the original publication in this journal is cited, in accordance with accepted academic practice. No use, distribution or reproduction is permitted which does not comply with these terms.



Single-Molecule Fluorescence Imaging Reveals GABAB Receptor Aggregation State Changes

Fang Luo^{1,2}, GeGe Qin^{1,2}, Lina Wang^{1,2} and Xiaohong Fang^{1,2*}

¹ CAS Key Laboratory of Molecular Nanostructure and Nanotechnology, Beijing National Research Center for Molecular Science, Institute of Chemistry, Chinese Academy of Science, Beijing, China, ² Department of Chemistry, University of the Chinese Academy of Sciences, Beijing, China

OPEN ACCESS

Edited by:

Nicole J. Jaffrezic-Renault,
Université Claude Bernard Lyon 1,
France

Reviewed by:

Xin Su,
Beijing University of Chemical
Technology, China
Fei Fang,
Michigan State University,
United States

*Correspondence:

Xiaohong Fang
xfang@iccas.ac.cn

Specialty section:

This article was submitted to
Analytical Chemistry,
a section of the journal
Frontiers in Chemistry

Received: 20 September 2021

Accepted: 28 October 2021

Published: 19 January 2022

Citation:

Luo F, Qin G, Wang L and Fang X
(2022) Single-Molecule Fluorescence
Imaging Reveals GABAB Receptor
Aggregation State Changes.
Front. Chem. 9:779940.
doi: 10.3389/fchem.2021.779940

The GABAB receptor is a typical G protein-coupled receptor, and its functional impairment is related to a variety of diseases. While the premise of GABAB receptor activation is the formation of heterodimers, the receptor also forms a tetramer on the cell membrane. Thus, it is important to study the effect of the GABAB receptor aggregation state on its activation and signaling. In this study, we have applied single-molecule photobleaching step counting and single-molecule tracking methods to investigate the formation and change of GABAB dimers and tetramers. A single-molecule stoichiometry assay of the wild-type and mutant receptors revealed the key sites on the interface of ligand-binding domains of the receptor for its dimerization. Moreover, we found that the receptor showed different aggregation behaviors at different conditions. Our results offered new evidence for a better understanding of the molecular basis for GABAB receptor aggregation and activation.

Keywords: GABAB receptor, single-molecule imaging, single-molecule tracking, stoichiometry, heterodimer, tetramer

INTRODUCTION

G protein-coupled receptors (GPCRs) are a large family of cell surface signaling proteins which play a central physiological role and represent more than one-third of current drug targets (Cornwell and Feigin, 2020; Wang et al., 2021). Although GPCRs can be generally activated as monomers, recent studies have shown that GPCRs form aggregates to regulate their signaling activity, especially for the class C GPCRs which are characterized by large extracellular ligand-binding domains (LBDs) (Gurevich and Gurevich, 2008; Yong et al., 2013; Lambert and Javitch, 2014; Vischer et al., 2015; Levitz et al., 2016). The metabotropic γ -aminobutyric acid B (GABAB) receptor is a typical C-type GPCR. It is widely expressed in the central and peripheral nervous systems, and its dysfunction is associated with a variety of diseases, such as anxiety, depression, alcohol addiction, Parkinson, and cancer (Hyland and Cryan, 2010; Evensen et al., 2020; Fritzius and Bettler, 2020; Sanchez-Vives et al., 2021; Shaye et al., 2021). A GABAB receptor consists of two subunits: GABAB₁ (GBR1) and GABAB₂ (GBR2). GBR1 is retained in the endoplasmic reticulum after expression. Once it binds with GBR2 to form a heterodimer, the GBR1-GBR2 complex docks to the cell membrane for signaling. Upon ligand stimulation, the GABAB receptor dimer (GBR1-GBR2 complex) recruits G proteins and activates the downstream pathway. Besides, GABAB receptors are also able to assemble into stable higher order oligomers. These oligomers are believed to play an important role in controlling the functional activation of the GABAB receptor (Pin et al., 2004). Therefore, it is of great interest to study the aggregation states and their dynamic changes of GABAB receptors under different conditions.

It has been confirmed by *in vitro* biochemical assays that GABAB receptors form a heterodimer GBR1–GBR2 in the cell (Burmakina et al., 2014). According to the studies of the GABAB receptor crystal structure, each of the receptor subunits, GBR1 and GBR2, consists of three domains: N-terminal LBD, seven helix transmembrane domains (TMDs), and cysteine-rich domain (CRD) connecting LBD and TMD. The heterodimerization of GBR1 and GBR2 for GABAB signaling is mediated by two interaction interfaces in their LB1 and LB2 regions of LBDs (Monnier et al., 2011; Geng et al., 2012; Ellaithy et al., 2020; Kim et al., 2020). However, the dimerization mechanism and the role of dimer interface in receptor function are still unclear. On the other hand, Comps-Agrar et al. (Comps-Agrar et al., 2012) found that GBR1–GBR2 could further form heterotetramers on the cell membrane. Their study was based on the fluorescence resonance energy transfer (FRET) analysis of association and exchange between two populations of the GBR1–GBR2 complex, one is the donor fluorophore–labeled GBR1–GBR2 population presented at the cell surface, and the other is acceptor fluorophore–labeled GBR1–GBR2 population originally retained in the endoplasmic reticulum (ER) but targeted to the plasma membrane after drug application. Several studies demonstrated that the assembly of higher order GABAB receptors resulted in a limited number of signaling protein binding (e.g., one tetramer only binds to 1 G protein), suggesting that the formation of a GABAB tetramer may reduce the receptor activation sensitivity, thus exerting an inhibitory effect (Schwenk et al., 2010; Comps-Agrar et al., 2011; Calebiro et al., 2013). However, the formation of a receptor tetramer has not been observed for other C-class GPCRs. Meanwhile, the aggregation states of GABAB receptors and the A-class GPCR $\beta 1$ and $\beta 2$ -adrenergic receptors have been reported to be unchanged after ligand stimulation (Calebiro et al., 2013). Therefore, the effect of GABAB dimer aggregation on receptor activation needs to be further studied.

In this study, single-molecule stoichiometry assay is carried out to investigate the formation and change of GABAB dimers and tetramers. Photobleaching event counting and diffusion characterization based on single-molecule fluorescence imaging is an effective approach to protein stoichiometry determination under physiological conditions (Zhang et al., 2009; Peterson and Harris, 2010; Xia et al., 2013; Hu and Zhang, 2014; Li et al., 2017; Xu et al., 2017; Li et al., 2019; Xu et al., 2019). With the imaging of the GABAB receptor on the cell membrane by using a total internal reflection fluorescence microscope (TIRFM), we revealed the key sites on the hydrophobic interface for GABAB receptor heterodimerization. Furthermore, we found that the receptors can form tetramers in both resting and activated states, and the ligand-induced tetramer population change depends on the receptor expression level and ligand concentration. Our results elucidate the molecular base for GABAB receptor dimerization and its influencing factors, providing new reference for a deeper understanding of GABAB receptor signaling under different conditions.

MATERIALS AND METHODS

Cell Culture

HEK293 cells were cultured in Dulbecco's modified Eagle medium (DMEM, Gibco) supplemented with 10% fetal bovine serum

(Hyclone) and antibiotics (50 mg/ml streptomycin, 50 U/mL penicillin) at 37°C in 5% CO₂.

Plasmids, Transfection, and Ligand Treatment

Mutant GBR1 and mutant GBR2 were obtained by mutating Y113 and Y117 of GBR1 and K112, Y118, and D119 of GBR2 into alanine, respectively. The LB2 mutant plasmid was constructed by deleting the sequence encoding the LB2 region in both GBR1 and GBR2 (Geng et al., 2012). Transfection was performed using Lipofectamine 3000 (Invitrogen). In order to obtain low-level GABABR-expressing cells, cells grown in 35-mm glass-bottom culture dish (Shengyou Biotech, China) were transfected with 0.3 µg/ml GBR1-EGFP and GBR2 plasmids in serum-free and phenol red-free DMEM for 6 h. High-level GABABR-expressing cells were transfected with 0.6 µg/ml GBR1-EGFP and GBR2 plasmids for 12 h. After the transfected cells were washed with PBS, the cells were fixed with 4% paraformaldehyde/PBS solution for 30 min or directly used for TIRFM fluorescence imaging in phenol red-free DMEM. For ligand-stimulated cells, the transfected cells were treated with 1 mM gamma-aminobutyric acid (GABA) (Sigma) in phenol red-free DMEM at 37°C for 15 min.

Single-Molecule Fluorescence Imaging

Single-molecule imaging was performed using a homemade objective-type total internal reflection fluorescence microscope (TIRFM) based on an Olympus IX71 inverted microscope (Zhang et al., 2009; Zhang et al., 2010). The sample was excited by a solid laser (a 488 nm laser), and the emitted light was collected by the oil immersion objective (100x, 1.45na, Olympus) and then separated by the dual-view assembly (Optical Insights). After being filtered by a band-pass filter (525/50 for EGFP), it was projected on to an electron multiplying charge coupled camera (EMCCD, Andor technology du-897 d-bv). The gain of EMCCD was set to 300. The power of excitation light measured after objective lens was modulated to 1 and 2 MW in the epifluorescence mode, respectively, for living cell imaging and fluorescence bleaching step experiments. Andor IQ software and the z-axis negative feedback equipment (MFC-2000) were used to control image acquisition. Movies of 300 frames were acquired for each sample at a frame rate of 10 Hz. Fixed cells were also imaged with a confocal microscope (FluoView FV1000-IX81, Olympus, Japan) equipped with a 100x, 1.40NA objective.

Single-Molecule Tracking and Photobleaching Steps Analysis

Time-lapse image sequences were used to extract the motion information of fluorescent points, and d U-track methods (Jaqaman et al., 2008) were used to track the information. The global optimal tracking algorithm was used to connect the single molecular points between adjacent frames into a complete trajectory. In the first step of the algorithm, the single molecular points between frames were connected; an objective matrix based on lap (linear task allocation) was

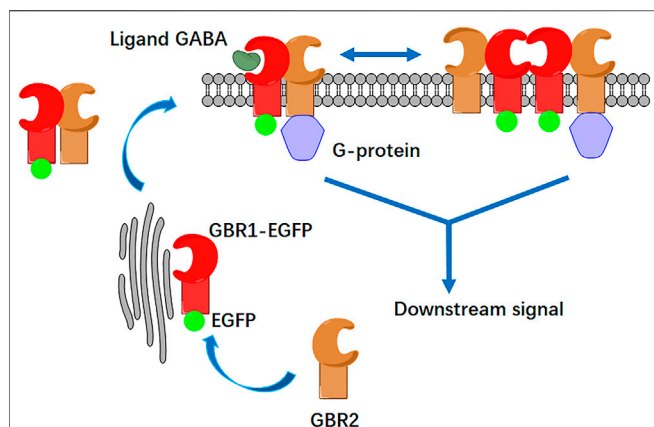


FIGURE 1 | Schematic illustration of GABAB receptor activation and its aggregation at cell membrane. The GABAB receptor consists of two subunits: GBR1 and GBR2. GBR1 carries the endoplasmic reticulum (ER) retention signal (RSRP); thus, it is retained in the endoplasmic reticulum. When GBR1 binds with GBR2 to form a heterodimer, GBR2 blocks the RSRP of GBR1, and both of them could dock to the membrane. On the cell membrane, the heterodimer can also be associated to form a tetramer. After GABA ligand stimulation, heterodimers and tetramers bind to Gi/o proteins to activate the downstream signaling pathway. Either receptor dimer or tetramer only binds with 1 G protein.

established; free diffusion or free diffusion plus linear motion was selected according to the motion behavior of the molecules to be tracked; and the points between adjacent frames were connected to segments using the optimal spatiotemporal algorithm. Then, considering the three possible connections of fragments (connection gap, fusion, and separation), the fragments were connected by a global optimal algorithm to form a complete single-molecule tracking trajectory. For the accuracy of fitting, only fluorescence trajectories lasting more than five consecutive frames were collected for a 2D mean square displacement (MSD) calculation. MSD was calculated as follows:

$$\text{MSD}(n\delta t) = \frac{1}{N-1-n} \sum_{i=1}^{N-1-n} \{ [x(i\delta t + n\delta t) - x(i\delta t)]^2 + [y(i\delta t + n\delta t) - y(i\delta t)]^2 \}$$

In the formula, Δt ($\Delta t = n\delta t$, with $\delta t = 100$ ms) is the elapsed time a single GBR1-EGFP molecule from position $x(i\delta t)$, $y(i\delta t)$ moves to $x(i\delta t + n\delta t)$, $y(i\delta t + n\delta t)$. Here, n and i are integers, and n determines the time increment. N is the total number of image frames before the molecule disappears. According to $\text{MSD} = 4D\Delta t$, using least squares fitting, the diffusion coefficient D could be calculated based on the slope of the first four points (100 ms). The histogram of the diffusion coefficient was obtained through multiple experiments, and the most possible D -average could be obtained by fitting these histograms with Gaussian distribution. Photobleaching steps of single GABABR molecules on the HEK293 cell membrane were analyzed according to the method we reported previously (Zhang et al., 2009).

cAMP Analysis

Intracellular cAMP levels were measured using GloSensor cAMP Assay (GloSensor kit, Promega) (Buccioni et al., 2011). The effects of GABA were calculated from signal change relative to the signal obtained with the origin group without GABA.

Statistics Analysis

Student's *t*-tests were performed using GraphPad Prism (GraphPad Software) to compare kinetic data. The nonparametric Mann-Whitney U test was performed using GraphPad Prism (GraphPad Software) to compare the robust data for single-molecule analysis. A *p*-value less than 0.05 was considered statistically significant.

RESULTS AND DISCUSSION

Single-Molecule Imaging of GABAB Receptor Dimer and Tetramer on Cell Surface

According to the activation mode of the GABAB receptor shown in **Figure 1**, GBR1 and GBR2 could dock on the cell surface only after they form a heterodimer (1:1 ratio) (Pin and Bettler, 2016). Single-molecule fluorescence imaging, based on total internal reflection fluorescence microscopy (TIRFM), was first applied to display single receptor molecules on the cell membrane of HEK293 cells. HEK293 cells, which have few endogenous GABAB receptors, are commonly used to study GABABR signaling with the receptor transfection. C-terminal EGFP-labeled GBR1 (GBR1-EGFP) and unlabeled GBR2 were co-expressed in the cells. The results showed that there were a large number of dispersed EGFP fluorescent spots on the cell membrane (**Figure 2A**). Because GBR1 stayed in the endoplasmic reticulum after expression and it could only dock on the membrane as a heterodimer after binding with GBR2, each single fluorescent spot on the cell membrane would represent a GABAB receptor heterodimer or its aggregates.

Two control experiments were conducted to confirm the fluorescent spots of GBR1-GBR2. When EGFP-labeled GBR1 was expressed alone in HEK293 cells, no fluorescent molecules were observed on the cell membrane by TIRFM. In contrast, the fluorescence signals were found to be concentrated in the cytoplasm by changing TIRFM to epifluorescence mode. This was consistent with the view that the GBR1 would stay in the endoplasmic reticulum (Pin and Bettler, 2016). On the other hand, when GBR2-EGFP was expressed alone at low expression level, dispersed fluorescent spots were observed on the cell membrane, and most of them were bleached in one or two steps. This indicated that GBR2 itself could be docked on the membrane and formed a homodimer. Therefore, GBR2-EGFP is not suitable to co-express with GBR1-EGFP for the judgment of a receptor heterodimer.

Our results proved that the GABAB receptor could be docked on the membrane normally as GBR1-EGFP/GBR2. Next, the individual fluorescent spots on the cell membrane were analyzed by counting fluorescent bleaching steps. Because GBR1-EGFP

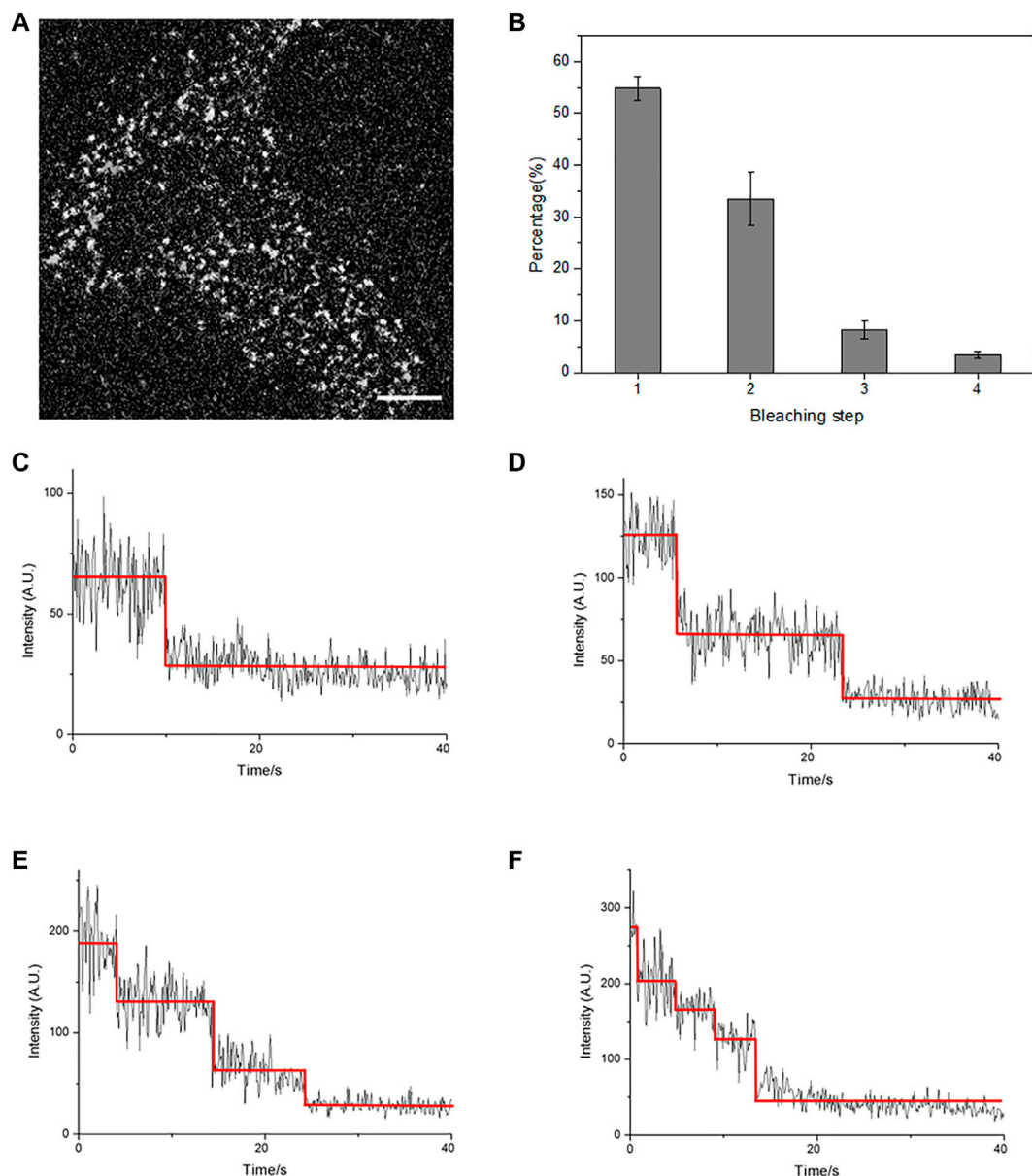


FIGURE 2 | Total internal reflection fluorescence microscopy (TIRFM) imaging revealed a membrane-docked GABAB receptor. **(A)** A typical single-molecule fluorescence image of individual receptor molecules on the HEK293 cell membrane in the absence of GABA. Scale bars: 5 μ m. **(B)** The population of bleaching steps of GABAB receptor, GBR1-EGFP/GBR2, on the cell membrane. **(C–F)** Four representative time courses of GBR1-EGFP/GBR2 emission showed one-(C), two-step (D), three-step (E), and four-step (F) bleaching, respectively. The red lines denote the automatically estimated bleaching steps. The results in (B) were calculated from 20 cells with more than 2000 single fluorescent molecules.

formed a heterodimer with GBR2 at a ratio of 1:1 when appeared on the cell membrane, the fluorescent spots bleached in one step represented the receptor heterodimer, GBR1-EGFP/GBR2, and the fluorescent spots bleached in two steps represented the tetramer formed by the association of two heterodimers, etc. In the resting state, most of the fluorescent spots were found to show a one-step bleaching (Figure 2C), accounting for about 50% population, while those with two-step bleaching (Figure 2D) accounted for about 30% receptors. These results indicated that the receptor mainly existed in the form of heterodimer on the cell

membrane before ligand stimulation, and a considerable part of the receptors formed a tetramer or higher aggregation complex (Figure 2B). Thus, the formation of a heterodimer and tetramer of the GABAB receptor by TIRFM was successfully observed.

Structural Basis for GABAB Receptor Heterodimer Formation

To investigate the structure basis for receptor dimerization, GBR1-EGFP was truncated by removing LBD or the entire

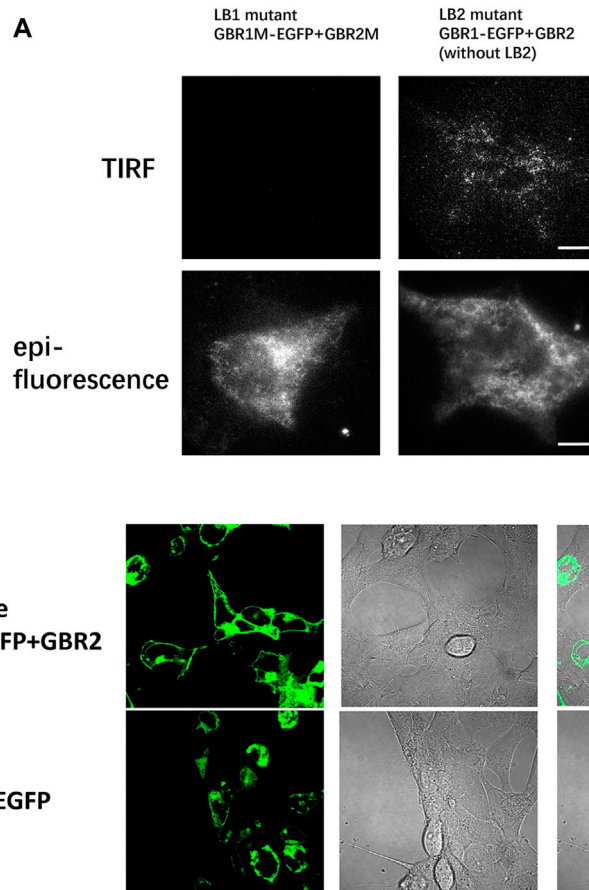


FIGURE 3 | Mutation in the LB1 region effectively prevented receptor dimerization. **(A)** In HEK293 cells, GBR1M-EGFP and GBR2M (with LB1 mutation) were transfected at the same time (**left**). GBR1M-EGFP remained in the endoplasmic reticulum, and no fluorescent spots were observed on the cell membrane due to the inhibition of dimerization. For the cell transfected with mutant GBR1-EGFP and mutant GBR2 that removed the LB2 region (**right**), they could still form a heterodimer and dock on the membrane. **(B)** Confocal microscopy was used to observe HEK293 cells transfected with GBR1-EGFP and GBR2 (**upper row**) or mutant GBR1M-EGFP, and GBR2M (**lower row**). Scale bars: 10 μ m.

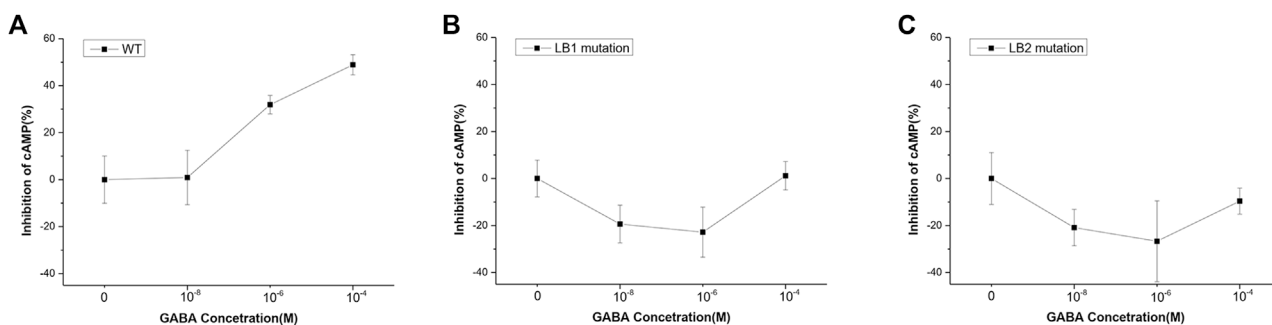
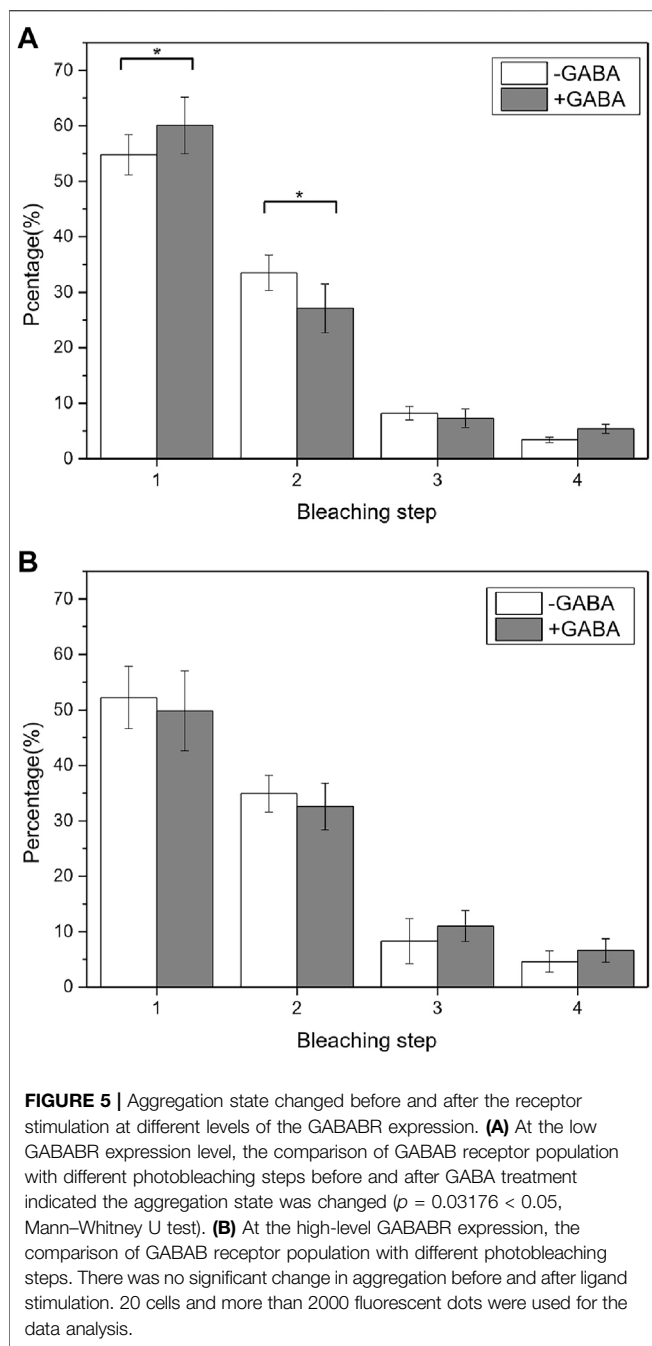


FIGURE 4 | Mutant GBR1M and GBR2M inhibited receptor activation. **(A)** The inhibition effect of HEK293 cells transfected with wild-type GBR1 and GBR2, or **(B)** GBR1M and GBR2M **(B)**, or **(C)** GBR1 and GBR2 with LB2 mutation under different concentration of GABA. Both mutations in LB1 **(B)** and LB2 **(C)** could seriously affect the function of the receptor. The ligand concentrations used in the experiment were (**from high to low**) 10^{-4} , 10^{-5} , 10^{-6} , 10^{-7} , 10^{-8} , and 10^{-9} M.



extracellular domain. In both cases, the fluorescence spots on the cell membrane disappeared, indicating that the extracellular domain, especially LBD, was necessary for an effective formation of GBR1-GBR2.

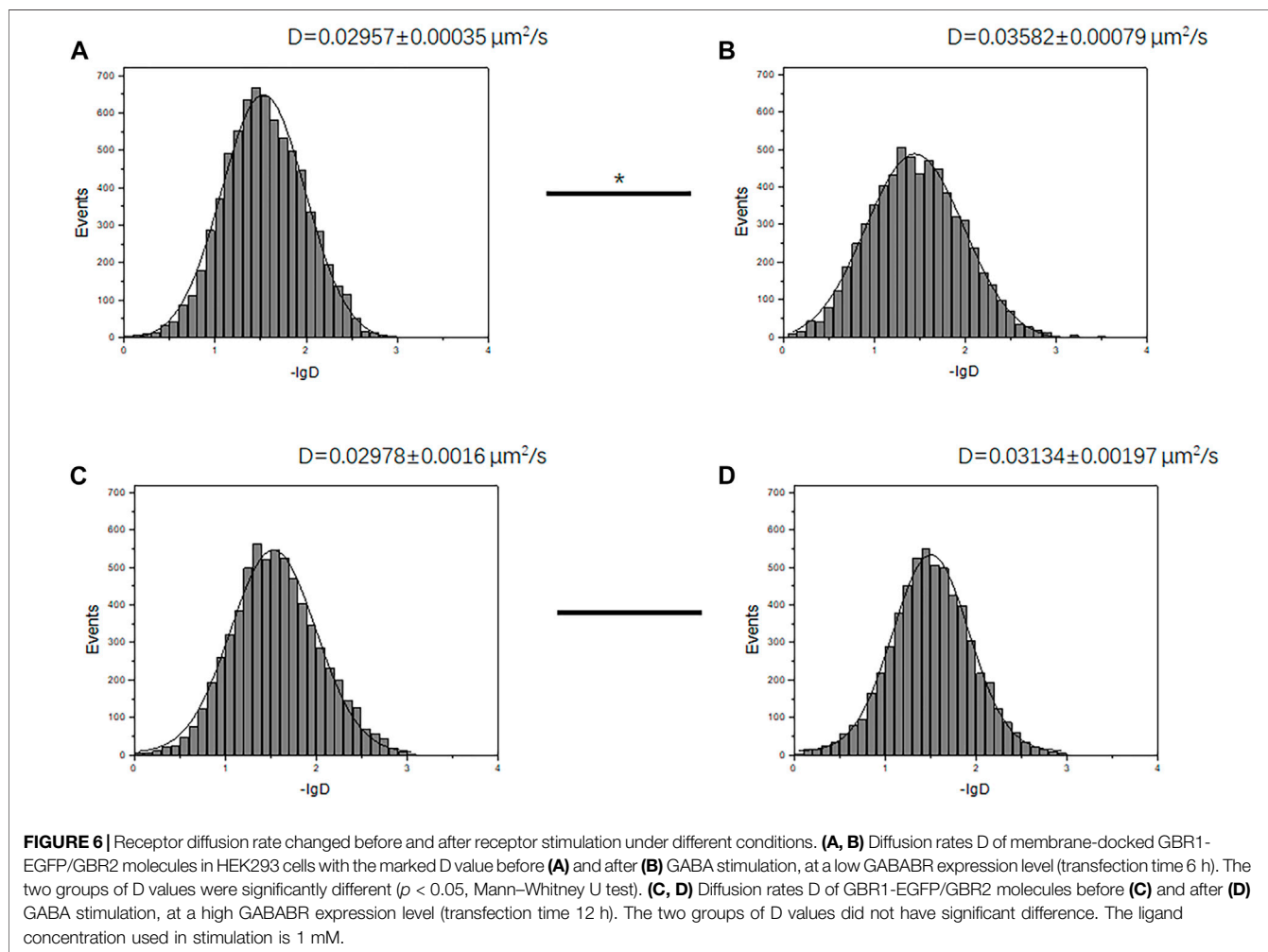
Then the dimer interface between the LBDs of GBR1 and GBR2 was further studied by examining the LBD crystal structure of GABAB receptor (Yong et al., 2013). The GABAB LBD crystal structure showed that it consists of two lobe-shaped domains (LB1 and LB2) which are connected by three short loops. LB1 is located in the upper lobe of LBD, and LB2 is located in the lower one. There are basically two interaction interfaces in LB1 and

LB2, respectively, for each receptor. In both resting state and the active state, there are a cluster of conserved hydrophobic residues at the interface in LB1. A total of five residues were chosen to mutate in this cluster, two in the LB1 domain of GBR1 (Y113A and Y117A) and three in the LB1 domain of GBR2 (K112A, Y118A, and D119A), to construct the mutant GBR1M-EGFP and mutant GBR2M-EGFP. In previous studies (Vischer et al., 2015), it has been proved that these sites are related to the function of the receptor, but their effect on receptor dimerization is unknown.

After single-molecule imaging, the HEK293 cells are co-transfected with either GBR1M-EGFP and wild-type GBR2, or wild-type GBR1-EGFP and GBR2M. The number of fluorescence spots on the cell membrane decreased significantly compared to that shown in **Figure 2A**. If both mutant GBR1-EGFP and mutant GBR2 were transfected at the same time, almost no fluorescence spots were found in the plasma membrane (**Figure 3A**), indicating that dimerization was completely inhibited. This is further confirmed by the confocal imaging results (**Figure 3B**). In the cells that transfected with GBR1-EGFP and GBR2, the fluorescent spots were mainly located on the cell membrane, while in the cells transfected with the mutant plasmids, most of the fluorescent spots remained in the cell interior, indicating that the heterodimerization of the GABAB receptor was inhibited.

The effect of LB1 mutation on GABAB receptor function was tested with the GloSensor kit cAMP assay, which is a biosensor based assay intended to measure cAMP accumulation in cells. Basically, GABABR activation by ligand stimulation inhibited cAMP production and the less cAMP was, the weaker the GloSensor signal we measured, and the percentage of inhibition increases. As shown in **Figure 4A,B**, the amount of cAMP decreased with the increase of GABA concentration in HEK293 cells transfected with wild-type GBR1 and GBR2, but remained unchanged in the cells which transfected with the mutant GBR1M and GBR2M. It indicated that the GABAB receptor with LB1 mutation has lost the function of activating downstream signal pathway. For the GABAB receptor with LB2 domain truncation (LB2 mutation), although we found its aggregation state was similar to that of wild type, the lower inhibition ratio suggested it did affect the receptor activation and function (**Figure 4C**).

According to the study on the crystal structure of the GABAR receptor, the interface of GBR1 and GBR2 dimerization is located in the LB1 region at the resting state, and a new interface at LB2 would form after ligand binding (Yong et al., 2013). Our single-molecule imaging data supported that the association of GBR1-GBR2 at the resting state is dependent on LB1 but not on LB2, with the new *in situ* characterization results on the cell membrane. In addition, we found that under the condition of LB2 domain deletion, the GBR1-GBR2 dimer could be still formed (**Figure 3A**), although GABAR signaling was reduced. Moreover, for the previous key five amino acids at the LB1 interface, previous work reported that each single amino acid mutation led to the reduction of the GABAR signal. Our results revealed that these five sites are the key sites of receptor dimerization, with the



mutation of all the five single amino acids, both GBR1-GBR2 dimerization and receptor signaling were fully inhibited.

Changes of GABAB Receptor Aggregation State After Ligand Stimulation

After the analysis of GABA receptor stoichiometry at the resting state, its aggregation state change after activation was explored. Previous studies showed that the GABAB receptor could be activated by a dimer and tetramer, and no change was found in its aggregation state after ligand stimulation (Calebiro et al., 2013; Pin and Bettler, 2016). In this study, it is interesting to find that the receptor showed different aggregation behaviors at different conditions.

We first checked the GABABR aggregation state change at different expression levels by controlling the receptor transfection time. The transfection time of 6 h resulted in a very low-level GABABR expression, while the transfection time of more than 12 h resulted in a relatively high-level GABABR expression but still suitable for single-molecule imaging. When the expression of EGFP-GBR1/GBR2 was relatively high (the density of the dispersed

fluorescent spots was about $0.87 \text{ particle}/\mu\text{m}^2$), the results from the single-molecule photobleaching counting showed no change in the dimer/tetramer population after 1 mM GABA stimulation (Figure 5B). In contrast, when the expression level was low ($0.15 \text{ particle}/\mu\text{m}^2$), the proportion of one-step bleaching molecule increased and that of two-step bleaching molecule decreased after ligand stimulation (Figure 5A) ($p < 0.05$).

It is known that the downstream pathway can be also activated by the formation of a GABA tetramer, but one heterotetramer can only bind to 1 G protein, so its activation efficiency is lower than that of a heterodimer (Pin and Bettler, 2016). Therefore, we expected that at a low GABABR expression level, GABA stimulation could reduce the number of tetramers and increase the number of dimers on the surface of the cell membrane, which is beneficial to improve the activation efficiency of the receptor. At a high GABABR expression level, when the density of receptors on the cell membrane is high enough to activate downstream pathways, the receptor activation efficiency no longer needs to be enhanced, thus no tetramer-to-dimer change.

Analysis of Diffusion Changes by Single-Molecule Tracking

To verify the previous observation on GABAR tetramer and dimer aggregation state change, we further evaluated the diffusion rate of GABABR on the cell membrane with living cells. It is known that the diffusion rate (D) of molecules on the cell membrane surface is affected by molecular volume. With the increase in molecular volume, the diffusion rate will decrease. In the case of low-level GABABR expression, the average diffusion rate of the receptor increased after ligand stimulation (**Figures 6A and B**) (D value changed from $0.02957 \pm 0.00035 \mu\text{m}^2/\text{s}$ to $0.03582 \pm 0.00079 \mu\text{m}^2/\text{s}$, $p < 0.05$, t -test). This is consistent with the change in the aggregation state we found in **Figure 5**. Since tetramers and higher order oligomers are not beneficial to the activation of receptors, GABABRs turn from tetramers to more efficient dimers after ligand stimulation, resulting in a faster diffusion rate due to the reduction in volume. In the case of high-level GABABR expression, GABA stimulation did not change the movement state of most receptors (D value changed from $0.02978 \pm 0.0016 \mu\text{m}^2/\text{s}$ to $0.03134 \pm 0.00197 \mu\text{m}^2/\text{s}$, $p > 0.05$, t -test) due to the excessive number of receptor dimers on the membrane (**Figure 6 C**, and **D**) and no tetramer–dimer population change was observed.

In conclusion, we have used the single-molecule imaging method to reveal the molecule basis for GABAB receptor dimerization and aggregation state change. Moreover, we

found that ligand stimulation can result in the change of receptor tetramer into dimer at a low receptor expression level, in order to improve the activation efficiency. Our results provide new reference for the understanding of the regulation of GABAB receptor aggregation and activation.

DATA AVAILABILITY STATEMENT

The original contributions presented in the study are included in the article/Supplementary Material, and further inquiries can be directed to the corresponding author.

AUTHOR CONTRIBUTIONS

FL and XF wrote the manuscript. GQ and LW helped with imaging experiment. All authors contributed to the article and approved the submitted version.

FUNDING

This work was supported by the National Natural Science Foundation of China (Nos. 21735006, 21890742, and 91939301) and the Chinese Academy of Sciences.

REFERENCES

- Buccioni, M., Marucci, G., Dal Ben, D., Giacobbe, D., Lambertucci, C., Soverchia, L., et al. (2011). Innovative Functional cAMP Assay for Studying G Protein-Coupled Receptors: Application to the Pharmacological Characterization of GPR17. *Purinergic Signal*. 7 (4), 463–468. doi:10.1007/s11302-011-9245-8
- Burmakina, S., Geng, Y., Chen, Y., and Fan, Q. R. (2014). Heterodimeric Coiled-Coil Interactions of Human GABAB Receptor. *Proc. Natl. Acad. Sci.* 111 (19), 6958–6963. doi:10.1073/pnas.1400081111
- Calebiro, D., Rieken, F., Wagner, J., Sungkaworn, T., Zabel, U., Borzi, A., et al. (2013). Single-molecule Analysis of Fluorescently Labeled G-Protein-Coupled Receptors Reveals Complexes with Distinct Dynamics and Organization. *Proc. Natl. Acad. Sci.* 110 (2), 743–748. doi:10.1073/pnas.1205798110
- Comps-Agrar, L., Kniazeff, J., Nørskov-Lauritsen, L., Maurel, D., Gassmann, M., Gregor, N., et al. (2011). The Oligomeric State Sets GABAB Receptor Signalling Efficacy. *EMBO J.* 30 (12), 2336–2349. doi:10.1038/emboj.2011.143
- Comps-Agrar, L., Kniazeff, J., Brock, C., Trinquet, E., and Pin, J. P. (2012). Stability of GABAB Receptor Oligomers Revealed by Dual TR-FRET and Drug-Induced Cell Surface Targeting. *FASEB J.* 26 (8), 3430–3439. doi:10.1096/fj.12-203646
- Cornwell, A. C., and Feigin, M. E. (2020). Unintended Effects of GPCR-Targeted Drugs on the Cancer Phenotype. *Trends Pharmacol. Sci.* 41 (12), 1006–1022. doi:10.1016/j.tips.2020.10.001
- Ellaithy, A., Gonzalez-Maeso, J., Logothetis, D. A., and Levitz, J. (2020). Structural and Biophysical Mechanisms of Class C G Protein-Coupled Receptor Function. *Trends Biochem. Sci.* 45 (12), 1049–1064. doi:10.1016/j.tibs.2020.07.008
- Evenseth, L. S. M., Gabrielsen, M., and Sylte, I. (2020). The GABAB Receptor-Structure, Ligand Binding and Drug Development. *Molecules* 25 (13), 3093. doi:10.3390/molecules25133093
- Fritzius, T., and Bettler, B. (2020). The Organizing Principle of GABA B Receptor Complexes: Physiological and Pharmacological Implications. *Basic Clin. Pharmacol. Toxicol.* 126, 25–34. doi:10.1111/bcpt.13241
- Geng, Y., Xiong, D., Mosyak, L., Malito, D. L., Kniazeff, J., Chen, Y., et al. (2012). Structure and Functional Interaction of the Extracellular Domain of Human GABAB Receptor GBR2. *Nat. Neurosci.* 15 (7), 970–978. doi:10.1038/nn.3133
- Gurevich, V. V., and Gurevich, E. V. (2008). GPCR Monomers and Oligomers: it Takes All Kinds. *Trends Neurosciences* 31 (2), 74–81. doi:10.1016/j.tins.2007.11.007
- Hu, J., and Zhang, C.-y. (2014). Multiplex Detection of Lung Cancer Cells at the Single-Molecule Level. *Chem. Commun.* 50 (88), 13581–13584. doi:10.1039/c4cc06460g
- Hyland, N. P., and Cryan, J. F. (2010). A Gut Feeling about GABA: Focus on GABAB Receptors. *Front. Pharmacol.* 01, 124. doi:10.3389/fphar.2010.00124
- Jaqaman, K., Loerke, D., Mettlen, M., Kuwata, H., Grinstein, S., Schmid, S. L., et al. (2008). Robust Single-Particle Tracking in Live-Cell Time-Lapse Sequences. *Nat. Methods* 5 (8), 695–702. doi:10.1038/nmeth.1237
- Kim, Y., Jeong, E., Jeong, J.-H., Kim, Y., and Cho, Y. (2020). Structural Basis for Activation of the Heterodimeric GABAB Receptor. *J. Mol. Biol.* 432 (22), 5966–5984. doi:10.1016/j.jmb.2020.09.023
- Lambert, N. A., and Javitch, J. A. (2014). CrossTalk Opposing View: Weighing the Evidence for Class A GPCR Dimers, the Jury Is Still Out. *J. Physiol.* 592 (12), 2443–2445. doi:10.1113/jphysiol.2014.272997
- Levitz, J., Habrian, C., Bharill, S., Fu, Z., Vafabakhsh, R., and Isacoff, E. Y. (2016). Mechanism of Assembly and Cooperativity of Homomeric and Heteromeric Metabotropic Glutamate Receptors. *Neuron* 92, 143–159. doi:10.1016/j.neuron.2016.08.036
- Li, L., Yu, Y., Wang, C., Han, Q., and Su, X. (2019). Transient Hybridization Directed Nanoflare for Single-Molecule miRNA Imaging. *Anal. Chem.* 91 (17), 11122–11128. doi:10.1021/acs.analchem.9b01766
- Li, N., Zhao, R., Sun, Y., Ye, Z., He, K., and Fang, X. (2017). Single-molecule Imaging and Tracking of Molecular Dynamics in Living Cells. *Natl. Sci. Rev.* 4 (5), 739–760. doi:10.1093/nsr/nww055
- Monnier, C., Tu, H., Bourrier, E., Vol, C., Lamarque, L., Trinquet, E., et al. (2011). Trans-activation between 7TM Domains: Implication in Heterodimeric

- GABAB Receptor Activation. *EMBO J.* 30 (1), 32–42. doi:10.1038/emboj.2010.270
- Peterson, E. M., and Harris, J. M. (2010). Quantitative Detection of Single Molecules in Fluorescence Microscopy Images. *Anal. Chem.* 82 (1), 189–196. doi:10.1021/ac901710t
- Pin, J.-P., and Bettler, B. (2016). Organization and Functions of mGlu and GABAB Receptor Complexes. *Nature* 540 (7631), 60–68. doi:10.1038/nature20566
- Pin, J.-P., Kniazeff, J., Binet, V., Liu, J., Maurel, D., Galvez, T., et al. (2004). Activation Mechanism of the Heterodimeric GABAB Receptor. *Biochem. Pharmacol.* 68 (8), 1565–1572. doi:10.1016/j.bcp.2004.06.035
- Sanchez-Vives, M. V., Barbero-Castillo, A., Perez-Zabalza, M., and Reig, R. (2021). GABAB Receptors: Modulation of Thalamocortical Dynamics and Synaptic Plasticity. *Neuroscience* 456, 131–142. doi:10.1016/j.neuroscience.2020.03.011
- Schwenk, J., Metz, M., Zolles, G., Turecek, R., Fritzius, T., Bildl, W., et al. (2010). Native GABAB Receptors Are Heteromultimers with a Family of Auxiliary Subunits. *Nature* 465 (7295), 231–235. doi:10.1038/nature08964
- Shaye, H., Stauch, B., Gati, C., and Cherezov, V. (2021). Molecular Mechanisms of Metabotropic GABAB Receptor Function. *Sci. Adv.* 7 (22), eabg3362. doi:10.1126/sciadv.abg3362
- Vischer, H. F., Castro, M., and Pin, J. P. (2015). G Protein-Coupled Receptor Multimers: A Question Still Open Despite the Use of Novel Approaches. *Mol. Pharmacol.* 88 (3), 561–571. doi:10.1124/mol.115.099440
- Wang, W., Bian, J., and Li, Z. (2021). Internalized Activation of Membrane Receptors: From Phenomenon to Theory. *Trends Cel Biol.* 31, 428. doi:10.1016/j.tcb.2021.03.008
- Xia, T., Li, N., and Fang, X. (2013). Single-molecule Fluorescence Imaging in Living Cells. *Annu. Rev. Phys. Chem.* 64, 459–480. doi:10.1146/annurev-physchem-040412-110127
- Xu, F., Zhang, M., He, W., Han, R., Xue, F., Liu, Z., et al. (2017). Live Cell Single Molecule-Guided Bayesian Localization Super Resolution Microscopy. *Cell Res* 27 (5), 713–716. doi:10.1038/cr.2016.160
- Xu, J., Qin, G., Luo, F., Wang, L., Zhao, R., Li, N., et al. (2019). Automated Stoichiometry Analysis of Single-Molecule Fluorescence Imaging Traces via Deep Learning. *J. Am. Chem. Soc.* 141 (17), 6976–6985. doi:10.1021/jacs.9b00688
- Yong, G., Bush, M., Mosyak, L., Feng, W., and Fan, Q. R. (2013). Structural Mechanism of Ligand Activation in Human GABAB Receptor. *Nature* 504 (7479), 254. doi:10.1038/nature12725
- Zhang, W., Jiang, Y., Wang, Q., Ma, X., Xiao, Z., Zuo, W., et al. (2009). Single-molecule Imaging Reveals Transforming Growth Factor- β -Induced Type II Receptor Dimerization. *Pnas* 106 (37), 15679–15683. doi:10.1073/pnas.0908279106
- Zhang, W., Yuan, J., Yang, Y., Xu, L., Wang, Q., Zuo, W., et al. (2010). Monomeric Type I and Type III Transforming Growth Factor- β Receptors and Their Dimerization Revealed by Single-Molecule Imaging. *Cel Res* 20 (11), 1216–1223. doi:10.1038/cr.2010.105

Conflict of Interest: The authors declare that the research was conducted in the absence of any commercial or financial relationships that could be construed as a potential conflict of interest.

Publisher's Note: All claims expressed in this article are solely those of the authors and do not necessarily represent those of their affiliated organizations, or those of the publisher, the editors, and the reviewers. Any product that may be evaluated in this article, or claim that may be made by its manufacturer, is not guaranteed or endorsed by the publisher.

Copyright © 2022 Luo, Qin, Wang and Fang. This is an open-access article distributed under the terms of the Creative Commons Attribution License (CC BY). The use, distribution or reproduction in other forums is permitted, provided the original author(s) and the copyright owner(s) are credited and that the original publication in this journal is cited, in accordance with accepted academic practice. No use, distribution or reproduction is permitted which does not comply with these terms.



Asymmetrical Flow Field-Flow Fractionation Methods for Quantitative Determination and Size Characterization of Thiols and for Mercury Size Speciation Analysis in Organic Matter-Rich Natural Waters

Isabelle A. M. Worms*, Killian Kavanagh, Elodie Moulin, Nicole Regier and Vera I. Slaveykova*

Environmental Biogeochemistry and Ecotoxicology, Department F.-A. Forel for Environmental and Aquatic Sciences, School of Earth and Environmental Sciences, Faculty of Science, University of Geneva, Genève, Switzerland

OPEN ACCESS

Edited by:

Ottavia Giuffrè,
University of Messina, Italy

Reviewed by:

Mélanie Davranche,
University of Rennes 1, France
Chad Cuss,
Memorial University of Newfoundland,
Canada

*Correspondence:

Isabelle A. M. Worms
isabelle.worms@unige.ch
Vera I. Slaveykova
vera.slaveykova@unige.ch

Specialty section:

This article was submitted to
Analytical Chemistry,
a section of the journal
Frontiers in Chemistry

Received: 23 October 2021

Accepted: 05 January 2022

Published: 16 February 2022

Citation:

Worms IAM, Kavanagh K, Moulin E,
Regier N and Slaveykova VI (2022)
Asymmetrical Flow Field-Flow
Fractionation Methods for Quantitative
Determination and Size
Characterization of Thiols and for
Mercury Size Speciation Analysis in
Organic Matter-Rich Natural Waters.
Front. Chem. 10:800696.
doi: 10.3389/fchem.2022.800696

Asymmetrical flow field-flow fractionation (AF4) efficiently separates various macromolecules and nano-components of natural waters according to their hydrodynamic sizes. The online coupling of AF4 with fluorescence (Fluo) and UV absorbance (UV) detectors (FluoD and UVD, respectively) and inductively coupled plasma-mass spectrometry (ICP-MS) provides multidimensional information. This makes it a powerful tool to characterize and quantify the size distributions of organic and inorganic nano-sized components and their interaction with trace metals. In this study, we developed a method combining thiol labeling by monobromo(trimethylammonio) bimeane bromide (qBBr) with AF4-FluoD to determine the size distribution and the quantities of thiols in the macromolecular dissolved organic matter (DOM) present in highly colored DOM-rich water sampled from Shuya River and Lake Onego, Russia. We found that the qBBr-labeled components of DOM (qB-DOM) were of humic type, characterized by a low hydrodynamic size ($d_h < 2$ nm), and have concentrations $< 0.3 \mu\text{M}$. After enrichment with mercury, the complexes formed between the nano-sized components and Hg were analyzed using AF4-ICP-MS. The elution profile of Hg followed the distribution of the UV-absorbing components of DOM, characterized by slightly higher sizes than qB-DOM. Only a small proportion of Hg was associated with the larger-sized components containing Fe and Mn, probably inorganic oxides that were identified in most of the samples from river to lake. The size distribution of the Hg-DOM complexes was enlarged when the concentration of added Hg increased (from 10 to 100 nM). This was explained by the presence of small iron oxides, overlapping the size distribution of Hg-DOM, on which Hg bound to a small proportion. In addition, to provide information on the dispersion of macromolecular thiols in colored DOM-rich natural water, our study also illustrated the potential of AF4-FluoD-UVD-ICP-MS to trace or quantify dynamic changes while Hg binds to the natural nano-colloidal components of surface water.

Keywords: AF4, DOM, reduced thiols, humic substances, colloids, mercury

1 INTRODUCTION

Dissolved organic matter (DOM) is known to control the physicochemical speciation and, thus, the transport and bioavailability of Hg in aquatic environments (Ravichandran, 2004; Lavoie et al., 2019; Demarty et al., 2021). The binding of Hg to heterogeneous pedogenic DOM such as humic substances is expected to have a protective effect on aqueous organisms. However, Hg bioaccumulation has been shown to increase together with the concentrations of humic substances for copepods living in surface water of lakes with low dissolved organic carbon (DOC) (French et al., 2014). The binding of ionic Hg^{II} or its reduced form, Hg^0 , to humic substances has been shown to depend on the time of interaction (Wang et al., 2020). This kinetic limitation has significant consequences on the bioavailability of Hg to bacteria (Chiasson-Gould et al., 2014). Additionally, the presence or generation of inorganic particles may impact the transport and the bioavailability of Hg (Smith et al., 2002; Ravichandran, 2004). The formation of HgS , for example, is well recognized to depend on the sulfide/DOM ratio in anoxic soils or sediments and largely immobilized Hg (Liem-Nguyen et al., 2017; Liem-Nguyen et al., 2021), but the generation of nano- HgS was also pointed out to occur under oxic conditions (without sulfide) when DOM is present (Manceau et al., 2015a), and probably available for fish (Bourdineaud et al., 2019). Additionally, Hg can bind to various inorganic particle surfaces (Tiffreau et al., 1995; Bonnissel-Gissingier et al., 1999). Found as nano-colloidal species, particles are more likely to remain in surface waters and control the reactivity of trace metals bound to them despite their low concentrations (Lead and Wilkinson, 2006; Waeber et al., 2012; Cuss et al., 2020). Therefore, determination of the physicochemical speciation of Hg and the amount of Hg bound to DOM is of high relevance to understand its fate and bioavailability in surface waters.

As measurements of total dissolved Hg concentrations (<450 nm) were shown to be a poor indicator of Hg bioavailability, in particular when Hg is bound to humic substances or present in/associated with particulate forms (Ndu et al., 2018), different analytical techniques, such as diffusive gradient in thin films (DGT) and voltammetric sensor, were developed to measure labile Hg species *in situ* (Pelcova et al., 2014; Pham et al., 2015; Bratkic et al., 2019; Tercier-Waeber et al., 2021). For example, DGT labile Hg species were used as a proxy to assess the Hg accumulated by fish (Pelcova et al., 2017). Similarly, Hg measured by DGT was a valuable proxy for Hg bioavailability to bacteria under anoxic conditions, when Hg was bound to amorphous FeS , humic substances, or was present as nano- HgS (Ndu et al., 2018). A voltammetric sensor for *in situ* measurements of the dynamic Hg fraction was very recently used to measure low concentrations of Hg found in natural water (Tercier-Waeber et al., 2021). Unfortunately, the measurement of Hg species associated with the nano-sized components of DOM and small inorganic colloids was outside of the analytical windows.

The measurement of Hg bound to DOM can be performed using ion exchange, liquid–liquid extraction, or solid-phase extraction (Gasper et al., 2007). The latter was shown to be the most promising to determine Hg binding in aquatic systems under kinetic constraints (Miller et al., 2009). The use of stable isotopes for monitoring the exchange kinetics of Hg can also be used to estimate the kinetics of formation/dissociation of Hg complexes with DOM or at inorganic surfaces (Jiskra et al., 2014; Zhang et al., 2021). Recent developments using stepwise reduction of Hg combined with ligand exchanges and measured by cold vapor atomic fluorescence spectrometer (CVAFS) have provided information on the relative stability of Hg complexes and illustrated the kinetic limitation of Hg complexation by the strong binding sites of DOM (Liang et al., 2019). These techniques provided important information on the dynamics of Hg complexes under ambient conditions with implications on the bioavailability of bound Hg (Zhang et al., 2019; Zhao et al., 2019; Tang et al., 2020). However, they could not identify which specific component is involved in Hg binding, especially if nano-sized components of DOM and small inorganic colloids are present in complex mixtures.

Among the different functional groups present in DOM, thiols are considered as the strongest binding sites for metallic ions despite their low contents (Smith et al., 2002; Skyllberg et al., 2006; Catrouillet et al., 2015). Considering the importance of thiols and the sulfide phase in the speciation of soft metallic cations, such as Hg, their stability constants have been implemented in thermodynamic models (Liem-Nguyen et al., 2017; Liem-Nguyen et al., 2021; Smith et al., 2021). These studies highlighted the necessity to measure the thiol concentrations in the aqueous phase, at low concentrations. Currently available data on thiol contents in heterogeneous DOM were obtained by combining Hg LIII-edge extended X-ray absorption fine structure (EXAFS) and sulfur speciation obtained by X-ray absorption near edge structure (XANES) (Skylberg et al., 2006; Manceau et al., 2015a; Manceau et al., 2015b; Song et al., 2018; Manceau and Nagy, 2019; Skyllberg et al., 2021). However, these techniques were not enough sensitive and required high amounts of DOM, making them inappropriate for use under commonly found conditions of surface waters. Nevertheless, these techniques revealed that the binding of Hg to the thiols present in heterogeneous DOM can be kinetically limited by the formation of other complexes involving carboxylate or amine groups (Jiang et al., 2015). Despite the improvements made in the measurement of the total thiol contents in surface water samples using fluorescent probes or mass spectrometry (Joe-Wong et al., 2012; Huynh et al., 2020; Liem-Nguyen et al., 2021), they do not discriminate the thiols present specifically in humic substances, for which the reactivity differed when compared to low-molecular-mass (LMM) thiols (Liang et al., 2019).

To date, the relationship between the thiols present in macromolecular DOM and the dynamics of Hg complexes formed with organic and inorganic nano-components has not been investigated in ambient water. This relays the difficulty of estimating the role of colloidal thiols involved in Hg binding

(Richard et al., 2016b). Considering the analytical windows of the currently available techniques, the reactivity of inorganic small colloids can also be difficult to estimate because of the dynamic processes involved in their generation and their low occurrence in surface waters (Richard et al., 2016a; Hochella et al., 2019; Montano et al., 2019).

Asymmetrical flow field-flow fractionation (AF4) coupled online with fluorescence detection (FluoD), UV-visible detection (UVD), and inductively coupled plasma-mass spectrometry (ICP-MS) allows separating, according to their hydrodynamic size, and characterizing the composition of the nano-sized components. It can be used in complex environmental settings to follow changes in the size distribution of nano-colloids and the associated changes in the size speciation of trace metals (Stolpe et al., 2010; Stolpe et al., 2013; Neubauer et al., 2013b; Neubauer et al., 2013c; Cuss et al., 2018). For example, AF4 coupled online with FluoD, UVD and ICP-MS was successfully employed to quantify the size speciation of Hg, for instance, its binding to humic substances and the dynamics of the formation of Hg nanoparticles (1–100 nm) in pore waters, both involved in Hg mobilization from a contaminated soil subjected to flooding and redox oscillation (Gfeller et al., 2021). AF4 coupled online with UVD and ICP-MS was also used to follow the kinetics of Cd and Zn exchange by Ag in the 7-kDa peptide metallothionein (Liu et al., 2017). AF4 coupled with FluoD was also successfully employed to measure the molecular mass (MM) distribution of thiols produced by microalgae and naturally present in surface waters following fluorescent labeling (Mangal and Gueguen, 2015).

In this study, we thus explored the capability of AF4 coupled online with multi-detectors to: 1) measure the concentrations and size distribution of thiol groups in macromolecular DOM using monobromo(trimethylammonio)bimane bromide (qBBr) fluorescent labeling (referred to as qB-DOM) and 2) determine the Hg size speciation in the size range 1–450 nm for natural surface waters rich in humic substances and iron (**Supplementary Figure S1**). A methodology involving AF4–UVD–FluoD for the quantification of thiols was developed considering the potential interferences due to the fluorescence of humic substances on the determination of qB-DOM. We evaluated how the MM or size (hydrodynamic diameter, d_h) distribution of qB-DOM can be influenced considering the retention of LMM fluorescent components during their injection due to membrane rejection and the potential inner-filtering effect of humic substances on fluorescence detection. Then, using AF4–UVD–ICP-MS, the size speciation of Hg was determined and related to the size distribution of other metals such as Fe, Mn, and Cu; the quantification of Hg–DOM species was also performed. Considering the very low Hg concentrations present in natural waters (Efremova et al., 2019), the samples were artificially enriched with Hg.

2 MATERIALS AND METHODS

2.1 Chemicals and Reagents

Cysteine (Cys), glutathione (GSH), and qBBr were purchased from Sigma-Aldrich (St. Louis, MO, USA) as powders and used

without further purification. All stock solutions (~1 mM) were prepared from powders in deoxygenated Milli-Q water in a N₂-purged tent and then preserved frozen at –20°C until use. Suwannee River natural organic matter (SRNOM, 1R101N), containing all the organic components isolated by reverse osmosis, was purchased from the International Humic Substances Society (IHSS, St. Paul (MN)) and stored at –20°C. A 500-mg L^{–1} stock solution of Suwannee River DOM (SRDOM) was prepared by dissolving the powder in Milli-Q water, slightly basified by the addition of saturated NaOH. Then, the solution was left to equilibrate in the dark at room temperature overnight and filtered on a 0.2-μm pore size filter (polyester sulfone; Millipore, Burlington, MA, USA). The SRDOM solution was preserved at 4°C in the dark.

The Hg analytical standard solution (1-mg L^{–1} of mercury in 5% nitric acid; TraceCERT® CRM for AAS) was purchased from Sigma-Aldrich. Intermediate Hg solutions of 10 mg L^{–1} (49.9 μM) were prepared by dilution in 1% HNO₃/0.5% HCl and used for ICP-MS calibration. The solution used for Hg enrichment of the DOM-rich water samples was prepared in 1% HNO₃. Diluted acid solutions were prepared from Suprapur 67% HNO₃, 35% HCl (Merck, Darmstadt, Germany), and Milli-Q water.

Ammonium nitrate (NH₄NO₃) and 2-[4-(2-Hydroxyethyl)piperazin-1-yl]ethane-1-sulfonic acid (HEPES), used as eluents for AF4, were obtained from Sigma-Aldrich, both prepared in Milli-Q water at 10 mM, pH 7.0. Before use, the solutions were filtered on 0.1-μm pore size polyvinylidene fluoride filters (Postnova Analytics, Landsberg am Lech, Germany). Sodium poly(styrene sulfonate) (PSS) standards of known MM, employed for the MM calibration of AF4 elution, were purchased from Postnova Analytics, dissolved in Milli-Q water at 1 g L^{–1}, filtered with 0.1-μm pore size polyester sulfone filters (Millipore), and stored at 4°C. They were diluted in the eluent to 2–5 mg L^{–1} before use. Ultra-uniformed gold nanoparticles (UUGNPs) with a 10-nm core size (d_h = 19 nm) were used to determine the channel thickness in order to convert the retention time (t_r) into hydrodynamic diameters. Stock suspension was purchased from NanoComposix (San Diego, CA, USA) and stored at 4°C. The suspension was diluted in proper eluent at a concentration of 0.5 mg L^{–1} after 30 s of homogenization using a vortex mixer.

2.2 Studied Area, Sample Description, and Preparation

2.2.1 Natural Water Samples

Brown-colored DOM-rich natural waters were sampled in different locations of the transect River Shuya–Petrozavodsk Bay–Lake Onego (Karelia, Russia) during two field campaigns in March and June 2017. Detailed description of the sampling sites can be found in our previous study (Worms et al., 2019). The samples were filtered on site on a 0.45-μm regenerated cellulose filter before being transported and stored in the dark at 4°C for further analysis. The water samples are characterized by a high iron content and DOM was predominantly of fulvic type (**Supplementary Table S1**), as shown previously (Worms

et al., 2019). The samples selected for analysis here corresponded to water taken from the Shuya River mouth and from the middle of the Petrozavodsk Bay at 3 different depths during the field campaigns in March and at 3 different locations but the same depth for June 2017. Lake Onego was sampled in June 2017. These samples are represented in gray in **Supplementary Table S1**.

2.2.2 Labeling of Thiols by qBBR

The samples were spiked to reach 10 μM qBBR using small volumes of the qBBR stock solution and allowed to react for 2 h at 20°C. The reaction was stopped by decreasing the temperature of the samples to 4°C. To assess the membrane rejection of the adducts formed with low-molecular-weight thiols and of the unreacted qBBR on qB-DOM size distribution, qB-Cys and qB-GSH formed after the addition of an excess of cysteine or glutathione (20 μM) to qBBR solutions of different concentrations were used. SRDOM prepared in HEPES was also labeled and analyzed for its qB-DOM size distribution and quantity to validate the labeling procedure. Unlabeled samples were analyzed to determine the MM distribution of intrinsic fluorescent and absorbing components of DOM present in natural waters and to estimate how they can interfere with the qB-DOM signals.

2.2.3 Mercury Addition and Total Mercury Measurements in the Samples

Mercury binding on the different nano-sized components was determined following Hg enrichment of natural samples using the 49.9- μM Hg stock solution prepared in 1% HNO_3 and equilibration for 24 h in the dark at room temperature (20°C). The maximum concentration allowed for inorganic mercury by the European Environmental Quality Standard is 2.5 nM for drinking water (EU Directive 2013/39, line 226). This concentration is closed to conditions where Hg-DOM detection using AF4-ICP-MS could be limited (Gfeller et al., 2021). Thus, a slightly higher concentration of 10 nM and another one of 100 nM, more representative of highly contaminated waters, were adopted. A solution of SRDOM at 10 mg L^{-1} spiked with 100 nM Hg was also analyzed.

The total Hg remaining in solution after 1 and 24 h of equilibration (Hg_{tot}) was determined with cold vapor atomic fluorescence spectrometer (CVAFS) coupled with a purge and trap system (MERX-T model III, Brooks Rand, Seattle, WA, USA). All samples were prepared following the Environmental Protection Agency (EPA) 1631 method in 40-ml glass vials with Teflon-lined septa caps. The stock calibration standard was purchased from Brooks Rand Instruments (4.9 μM Hg^{II} in 2% HNO_3). The standards were prepared directly in glass vials and the samples diluted 25 times in Milli-Q water in glass vials. Both standards and samples were spiked with 100 μl of 2% BrCl and allowed to react overnight in the dark. Before the measurements, the excess of BrCl was reduced by the addition of 100 μl of hydroxylamine hydrochloride. The samples were then treated with 100 μl SnCl_2 to convert all the Hg^{II} to elemental Hg^0 , capped, and directly analyzed using CVAFS. ORMS-5 water (National Research Council of Canada) was used as certified material. The

obtained concentrations of Hg_{tot} are reported in **Supplementary Table S1**.

2.3 Determination of the Size Distribution of qB-DOM and Absorbing/Fluorescent Components by AF4-UVD-FluoD

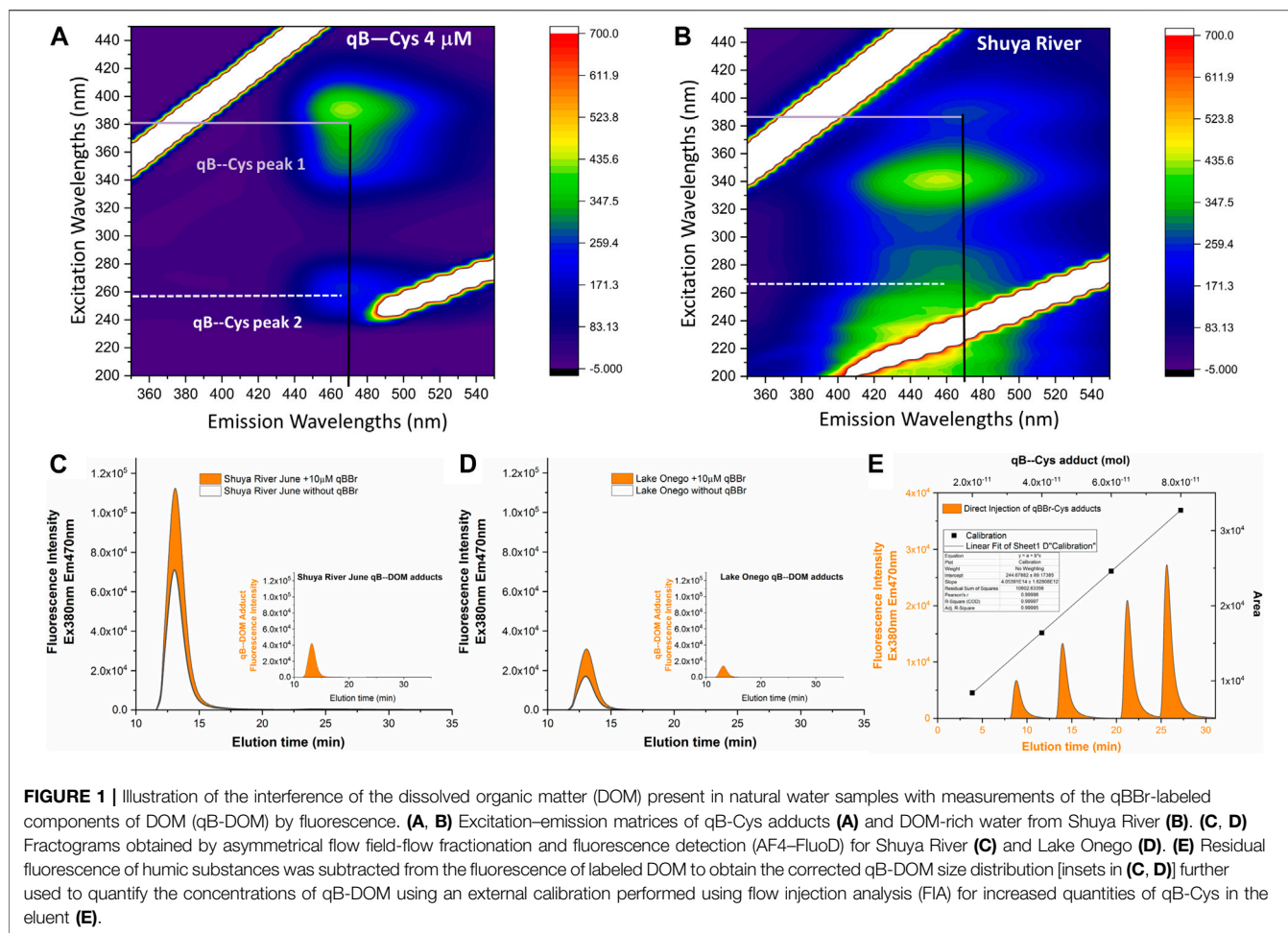
Fractionation of the samples was carried out with AF2000 Focus (Postnova Analytics) coupled online to UVD and FluoD (Postnova Analytics). System control and data collection were performed using the AF2000 Control software (version 1.1.011, Postnova Analytics) and LC solution workstation software (Shimadzu, Kyoto, Japan). The trapezoidal channel was made of a 500- μm -thick spacer and a 300-Da cutoff polyethersulfone membrane (Postnova Analytics) as the accumulation wall. Samples were injected using a 1-ml sample loop at $V_{\text{inj}} = 0.2 \text{ ml min}^{-1}$ for 10 min. During this step, the sample was simultaneously injected, concentrated, and focused using $V_{\text{foc}} = 3.4 \text{ ml min}^{-1}$, $V_{\text{xf}} = 2.7 \text{ ml min}^{-1}$, and $V_{\text{out}} = 0.7 \text{ ml min}^{-1}$. After 1 min transition time, an elution step of 15 min at $V_{\text{xf}} = 1.5 \text{ ml min}^{-1}$ was followed by a 2-min linear gradient to $V_{\text{xf}} = 0 \text{ ml min}^{-1}$. The runs ended with a 10-min elution at $V_{\text{xf}} = 0 \text{ ml min}^{-1}$ to release the unfractionated material.

For the analysis of the qB-labeled samples, the fluorescence detector was tuned to $\lambda_{\text{ex}} = 380 \text{ nm}/470 \text{ nm}$, selective for qB-DOM adducts, and to $\lambda_{\text{ex}} = 260 \text{ nm}/470 \text{ nm}$, selective for the fluorescent components of humic substances (Fluo Humic). These wavelengths were adopted after the analysis of qB-Cys adducts and our samples with excitation–emission matrix (EEM) recorded on an LS 55 luminescence spectrometer (Perkin-Elmer, Waltham, MA, USA) using a 3-ml, 1-cm path length quartz cuvette. EEMs were generated by recording the emission spectra from 300 to 550 nm with 0.5-nm steps for excitation wavelengths that varied between 200 and 450 nm with 5-nm steps and corrected by subtraction of the EEMs obtained for Milli-Q water. For the size distribution of the absorbing components of humic substances (Abs Humic), $\lambda_{\text{abs}} = 254 \text{ nm}$ was selected.

The molecular masses of qB-DOM and humic substances were determined following the calibration of the AF4 elution with PSS standards. To this end, sodium PSS standards with MMs ranging from 1.1 to 10.6 kDa (Postnova Analytics) were injected and the log–log relationship between the retention time (t_r) at peak maximum of the 254-nm fractograms and MMs was derived [$\log(\text{MM}) = 1.38 \log(t_r) + 0.21$, $R^2 = 0.995$] and used to convert the t_r at peak maximum to MM for each sample. The AF4 elution theory was used to derive the relationship between t_r and hydrodynamic diameters ($d_h = 1.065 t_r$) using UUGNPs to correct the channel thickness.

2.4 Characterization of the Association of Hg with Natural DOM Components by AF4-ICP-MS

To characterize Hg binding by the components of natural DOM and by the small inorganic colloids, AF4-FluoD-UVD was coupled online with ICP-MS (7700x model; Agilent Technologies, Santa Clara, CA, USA) as previously described



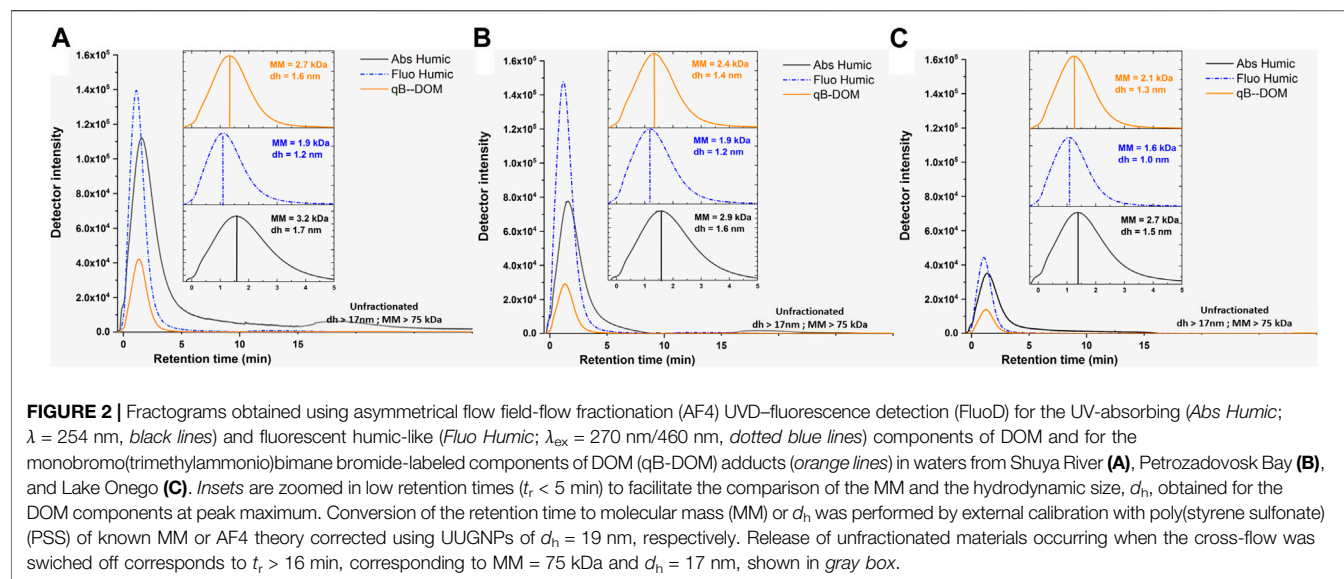
using a He collision cell (ORS3) to reduce polyatomic interferences (Dublet et al., 2019; Worms et al., 2019; Gfeller et al., 2021). Fractograms were recorded in time-resolved analysis (TRA) mode using MassHunter software (Agilent Technologies) with a 0.5-s acquisition time for each isotope (^{63}Cu , ^{56}Fe , ^{55}Mn , and ^{202}Hg). The quantitative treatment for the Hg fractograms was performed by converting counts per second (cps) into parts per billion (ppb) using an external calibration of the ICP-MS instrument made of appropriate dilutions of the intermediate solution of $49.85\ \mu\text{M}$ Hg, ranging from 0.5 to 10 nM, in the eluent containing 1% HNO_3 /0.5% HCl . A solution made in Milli-Q water and containing the same proportions of the different acids was used to rinse the tubing of the instrument between each measurement (Gfeller et al., 2021). The ICP-MS external calibrations were validated using digested phytoplankton certified reference material (IAEA-450, platinum in algae). Inter-batch calibrations were shown to be stable over several months, and our procedure showed less than 1% of deviation compared to the certified value. After the conversion of t_r into retention volume (V_r , in liters), baseline correction and integration of the signals were performed using Origin[®]Pro 2019 (OriginLab, Northampton, MA, USA). Deconvolution of the Fe and Hg signals was performed using the same software in

order to qualitatively relate the different forms of colloidal iron present in our samples and their interaction with Hg.

3 RESULTS AND DISCUSSION

3.1 Evaluation of the Size Distribution and Quantification of the Thiol Groups in Natural DOM

Previous strategies using a titration of thiols by qBBr measured by batch fluorescence had limits of detection in the micromolar range for highly absorbing DOM, although the concentration of small (non-absorbing) thiols can be determined with a detection limit of $0.05\ \mu\text{M}$ (50 nM) (Joe-Wong et al., 2012). The high detection limit for the determination of thiols present in DOM of pedogenic origin was due to the high fluorescence background of humic substances overlapping with the fluorescence of the qB adducts formed. Comparison of the EEMs of the qB-Cys adducts (**Figure 1A**) and the Shuya River water (**Figure 1B**) showed that the two E_x/E_m wavelengths of qB-Cys overlapped with those of DOM, suggesting possible interferences of the fluorogenic materials present in our samples, indeed. The emission peak



of qB-Cys adducts was shown to be less prone to interference of the humic fluorescent components than the one occurring in the UV region, where the fluorescence of humic substances was predominant. This second peak may refer to the one previously observed for the size distribution of qB-DOM, with $\lambda_{ex} = 230$ nm/470 nm, which was successfully used for the determination of thiols in algal growth media stripped of humic substances (Mangal and Gueguen, 2015).

Before qBBr labeling, the fractograms of the DOM-rich water samples exhibited a residual fluorescence at wavelengths corresponding to those used for the detection of qB adducts (Figures 1C, D, black lines). After the addition of qBBr, a significant increase in the intensity of the fluorescence signal was recorded, which can be attributed to the formation of qB-DOM adducts (Figures 1C, D, orange areas). Thus, the fractograms corresponding to the qB-DOM adducts (Figures 1C, D, insets) were obtained by subtracting the DOM fractograms obtained in the absence of qBBr from those recorded after the labeling of DOM with qBBr.

The qB-DOM adduct fractograms of the standard SRDOM and our samples were compared with those of the UV-absorbing (*Abs Humic*) or fluorescent (*Fluo Humic*) components (Figure 2). The MMs and size distributions of SRDOM (Supplementary Figure S2) were in the same range as those of the DOM-rich water samples ($MM < 11$ kDa, $d_h < 4.3$ nm; represented in the insets of Figure 2). Values at peak maximum were 2.5 kDa for the absorbing and 2.0 kDa for the fluorescent components of humic substances for SRDOM, thus a difference between absorbing and fluorescent components of $\Delta_{MMabs-MMFluo} = 0.5$ kDa. The MM corresponding to the peak of distribution of the qB-SRDOM components (1.5 kDa) was lower than that corresponding to the fluorescent and absorbing components of DOM. For natural samples, similarly to SRDOM, higher values of MM were found for the absorbing ($MM = 3.2$ – 2.7 kDa) compared to the fluorescent ($MM = 1.9$ – 1.6 kDa) components: the $\Delta_{MMabs-MMFluo}$ were

higher (from 1.3 to 1.1 kDa), suggesting a higher heterogeneity or agglomeration state of the humic components in our natural samples in comparison to SRDOM. Additionally, the MMs at the peak maximum of qB-DOM for natural samples were always intermediate between those corresponding to the fluorescent and absorbing components and varied from 2.7 to 2.1 kDa. The above results illustrated the heterogeneity in composition and size of the DOM components with different properties, from one environment to another. The evaluated hydrodynamic diameters at the peak maximum were always below 2 nm, as expected for humic substances, and it is encouraging that the qB-DOM measured here were part of this heterogeneous macromolecular pool of nano-sized DOM.

A comparison of the UV absorbance and fluorescence fractograms of DOM in all the studied samples revealed larger MMs and sizes for the absorbing components of DOM than fluorescent ones. Such a shift could be due to the impairment of fluorescence emission by an inner filtering effect, due to the shading of the excitation–emission lights by the absorbance of bigger-sized humic components (Senesi et al., 1991; Ohno, 2002). Similar considerations can apply to the fluorescence detection of qB-DOM. To verify whether the fluorescence intensities of $1.6 \mu\text{M}$ qB-Cys and $0.8 \mu\text{M}$ qB-GSH were altered by the presence of 10 mg L^{-1} SRDOM, we performed flow injection analysis (FIA) (Supplementary Figure S3). The results showed less than 5% error in the estimation of the qB adducts, implying that fluorescence detection was unaffected by the presence of the humic components in SRDOM.

Additionally, the shift toward apparent smaller-sized distribution parameters can be due to the contribution of the LMM components present as unreacted qBBr or as qB-DOM adducts and retained in the AF4 channel by membrane rejection. The retention of $8 \mu\text{M}$ qBBr ($MM = 409.12$ Da), qB-Cys ($MM = 449.82$ Da), or qB-GSH ($MM = 635.54$ Da) adducts was measured using two different eluents (Supplementary Figure S4). When HEPES was used as the eluent, low fluorescent peaks at

retention times just after those corresponding to the void volume were found. These results showed that the small thiols labeled by qBBR and unreacted qBBR passed to a large degree through the AF4 channel membrane and were below the limit of size resolution under our conditions, but could contribute to an increase in the signal used for qB-DOM measurements. When NH_4NO_3 was used as the eluent, the fluorescence signals were identical to the eluent itself. Therefore, we concluded that, in this case, the fluorescence signal of qB-DOM was not influenced by the retention of LMM components. In addition, analysis of 13.3 mg L^{-1} SRDOM in the presence or absence of $4 \mu\text{M}$ of qB-GSH provided only a slight increase in the signal intensity (**Supplementary Figure S4**), showing that qB-GSH passed through the membrane even in the presence of macromolecular DOM. Thus, the retention of the LMM components could not account for the shift toward lower MM and size distribution of qB-DOM as compared with the MM and size distribution of the UV-absorbing components. Considering that the MMs of the qB-LMM used here were higher than that of the AF4 channel membrane cutoff (300 Da), the present results were consistent with those obtained by Zhou and Guo (2015), who reported an effective pore size cutoff of 1.9 kDa for this membrane.

Overall, the increase in fluorescence signal observed after the addition of qBBR in the samples was due to the reaction of qBBR with the thiol groups of the natural DOM components and can be used to estimate the thiols specifically contained in the pool of humic substances of macromolecules.

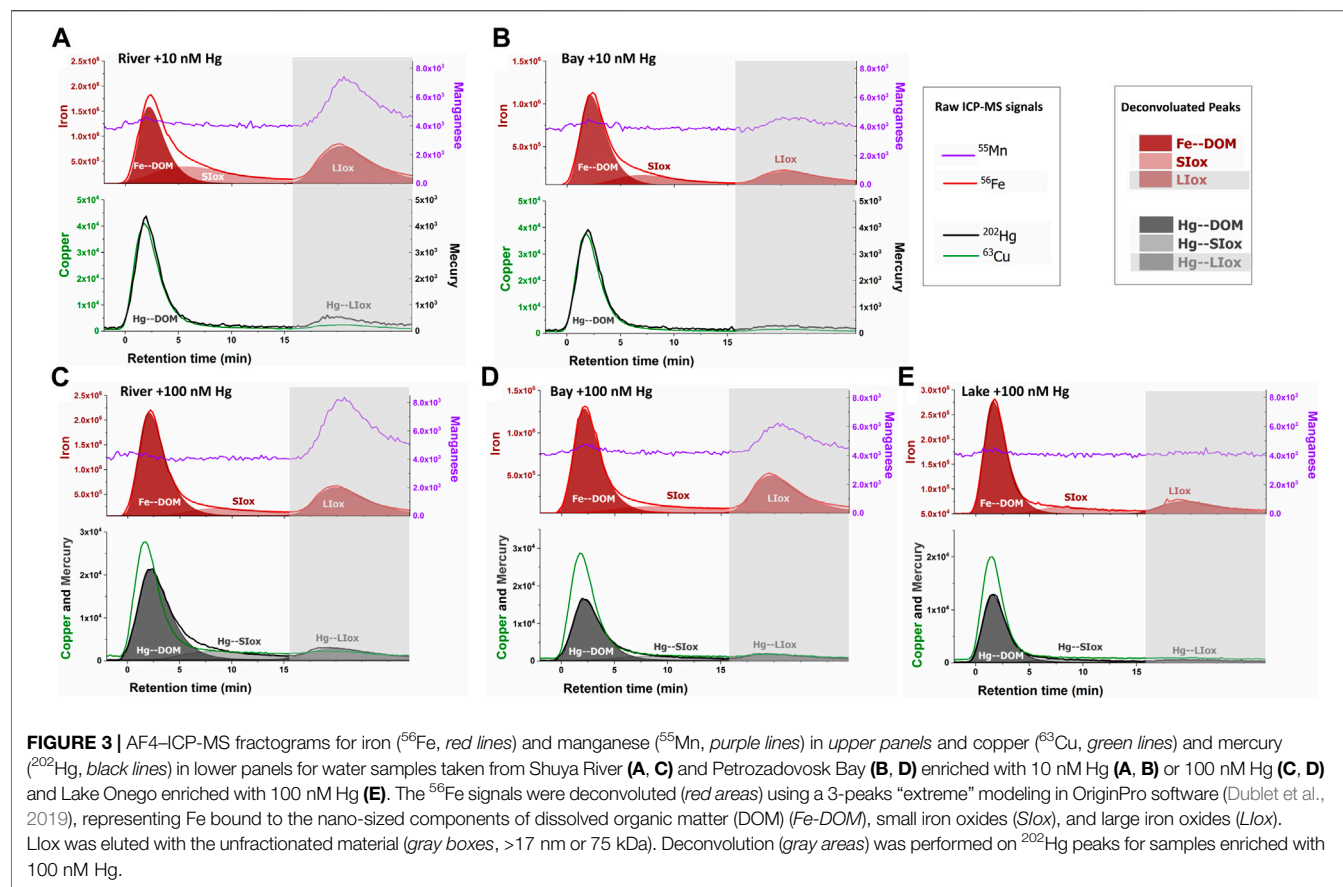
The qB-DOM fractograms were then integrated using OriginLab software and the area found were converted to qB-DOM quantities using external area-based calibration obtained by FIA of $100 \mu\text{l}$ qB-Cys standards (**Figure 1**). The calibration solutions were prepared by adding increasing concentrations of qBBR on a fixed cysteine concentration ($20 \mu\text{M}$) and diluted 10 times in the eluent to match the level of qB-DOM intensities of the samples. Under comparable conditions, a published study demonstrated that all the qBBR was converted to qB adducts when natural samples or standards presenting reduced thiols were in excess over the qBBR (Huynh et al., 2020). Maintaining an excess of thiols over qBBR decreased the possibility that unreacted qBBR may interfere with the measurement of the fluorescence signal.

Using qBBR labeling with the AF4-FluoD methodology, we found a thiol content of $4.8 \pm 1.5 \mu\text{mol g}^{-1}$ ($9.2 \pm 2.7 \mu\text{mol g}^{-1} \text{C}$) for SRDOM. Using titration with the ThioGlo-1 fluorescent probe, a value of $0.7 \pm 0.1 \mu\text{mol g}^{-1}$ was calculated for SRDOM (Rao et al., 2014), although using a commercial kit, the content of thiols was estimated at $120 \pm 9 \mu\text{mol g}^{-1} \text{C}$ (Smith et al., 2021). In both cases, the measurements were performed at a relatively high concentration of SRDOM ($\sim 100 \text{ mg L}^{-1}$). Thus, the large range in thiol content measured for this standard material can be attributed to the difficulties encountered in performing quantitative analysis of fluorescence measurements, when inner filtering and/or interferences of humic materials were not considered. Our methodology gave a thiol concentration closer but slightly lower than previously reported values using either X-ray absorption spectroscopy

(XAS) or thiol titration by MS detection of residual qBBR, which both converged to $7.5 \pm 0.4 \mu\text{mol g}^{-1}$ (Song et al., 2018; Huynh et al., 2020).

The loss of the LMM components of organic matter through (or on) the separation channel membrane was unavoidable for AF4 analysis, even for the lower cutoff membrane of 300 Da, as used in the present study (Zhou and Guo, 2015). The SRDOM recovery—estimated as a ratio between the peak area obtained after fractionation to the peak area found with FIA—was of 68% using Abs Humic as a surrogate of the DOM content. This contradicts the fact that most of the SRDOM [67% based on organic carbon (OC) measurements] was found to be of $\text{MM} > 3 \text{ kDa}$ using centrifugal filtration unit (CFU) (Song et al., 2018). However, in this specific study, the pH was lower than that in our study. Such lower pH could favor the aggregation of SRDOM components increasing in the same way as their retention by the filtration membrane. Similar experiments done with this CFU at neutral pH indeed showed lower DOC recovery (60%) (Bland et al., 2020). By considering the loss of the different components in the AF4 channel, a qB-DOM value of $7.0 \mu\text{mol g}^{-1}$ was derived for SRDOM using our methodology. This value, consistent with the literature (Huynh et al., 2020), indicated that the colloidal components of DOM contained similar thiol contents to the entire Suwannee River standard organic matter (OM) isolated by reverse osmosis.

The concentrations obtained for the qB-DOM adducts in natural water samples were below $0.5 \mu\text{M}$, indicating the low thiol contents of natural DOM. Comparable concentrations of qB-DOM adducts in Shuya River samples, $0.25 \pm 0.06 \mu\text{M}$ (March) and $0.35 \pm 0.2 \mu\text{M}$ (June), were found. The concentrations of the qB-DOM adducts in samples from Petrozavodsk Bay were even lower: $0.09 \pm 0.02 \mu\text{M}$ (March) and $0.14 \pm 0.02 \mu\text{M}$ (June). In the open lake, the concentrations of the qB-DOM adducts fell further down to $0.05 \mu\text{M}$. This decreasing trend in the concentration of qB-DOM adducts was consistent with the dilution process of DOM occurring in the river-lake transect. The thiol concentrations in natural DOM determined in the present study were lower than those reported in boreal aquatic environments, i.e., $1.16 \mu\text{M}$ in water from a stream and $0.96 \mu\text{M}$ in wetland dissolved fraction of pore water obtained by residual qBBR titration and mass spectrometry (Huynh et al., 2020). Such lower thiol concentrations were consistent with the rather limited biological activity found in Petrozavodsk Bay and Lake Onego during the sampling periods (Suarez et al., 2019). Much higher thiol concentrations have been reported in waters with higher microbial activity, leading to a larger production of LMM thiols (Mangal and Gueguen, 2015; Adediran et al., 2019; Mangal et al., 2020). For example, the thiol concentrations in high flowing water and marsh catchment of the Churchill River obtained by batch qBBR titration were much higher: 5.03 ± 1.94 and $21.0 \pm 0.7 \mu\text{M}$, respectively (Mangal and Gueguen, 2015). Furthermore, we did not expect freshly bio-produced reduced thiols to be preserved in our samples given their oxidation at neutral pH by organic matter (Chu et al., 2016). Finally, the low thiol concentrations found by AF4-FluoD could be due to the low amount of recovered material, as exemplified for



SRDOM previously. Indeed, the recovery of the UV-absorbing components in our samples was of $36 \pm 3\%$ of the UV signal obtained by FIA. This latter can be overestimated due to the presence of iron oxides (Dublet et al., 2019), leading thus to an overestimation of material loss and cannot be directly used to correct the thiol-to-colloidal DOC ratios.

In natural samples, the thiol-to-DOC ratios were thus estimated using the humic contents determined by liquid chromatography–organic carbon detection (LC-OCD) (Worms et al., 2019) (Supplementary Table S1). The thiol content was $11.0 \pm 1.4 \mu\text{mol g}^{-1} \text{C}$ independently of the sampling seasons or locations. Such low variability in the thiol/DOC ratio strongly suggest a similar source of a nano-sized ($d_h = 1.4\text{--}1 \text{ nm}$) pool of thiols in the DOM. This suggestion is supported by the good correlation of qB-DOM with either the DOC or humic contents of the natural water samples (Supplementary Figure S5). The obtained thiol-to-DOC ratios were about twice lower than those found in boreal stream, $25.2 \mu\text{mol g}^{-1} \text{C}$, but about 3.3 times higher than the one found in wetland pore water, $3 \mu\text{mol g}^{-1} \text{C}$ (Huynh et al., 2020). The obtained results implied that the nano-sized DOM could represent a “stable” pool of reduced thiols in DOM-rich surface water, and their role of Hg complexation should be considered.

Another aspect that should be considered is that the waters sampled were characterized by relatively high Fe/DOC ratios, $40.0 \pm 4.3 \mu\text{g Fe mg}^{-1} \text{C}$ for Shuya River and

$26.9 \pm 4.3 \mu\text{g Fe mg}^{-1} \text{C}$ for Petrozavodsk Bay, whereas this ratio was $4.5 \pm 0.2 \mu\text{g Fe mg}^{-1} \text{C}$ for Lake Onego (Supplementary Table S1). The Fe species recovered by AF4-ICP-MS (colloidal iron) corresponded to $60 \pm 17\%$ of the total dissolved iron measured by FIA, with lower values obtained in samples from Petrozavodsk Bay in June (35%). The nano-sized iron species in all the samples consisted of Fe-DOM complexes, small iron oxide nanoparticles (SIox), probably enrobed by humic substances and larger unfractionated iron colloids (LIox) using a deconvolution procedure (Figure 3, upper fractograms). The ^{63}Cu peaks occurred with the absorbing DOM components and followed their size distribution (Worms et al., 2019). The recoveries for Cu were lower but less variable ($42 \pm 6\%$) than for iron, in agreement with the small size of the components complexing Cu, with optimized conditions for the elution of macromolecular DOM components. For the samples taken from Shuya River and Petrozavodsk Bay, Mn oxides co-eluted with LIox in the releasing peak ($d_h > 17 \text{ nm}$) (Figure 3), but no co-elution of Mn was observed with DOM or SIox.

3.2 Distribution of Hg in the Nano-Sized Pool of DOM-Rich Natural Waters

To obtain insights into the MM and size distributions of Hg bound to the nano-sized components present in DOM-rich natural waters, the samples were enriched with 10 or 100 nM

of Hg, equilibrated for 24 h, and then analyzed by AF4–UVD–FluoD–ICP–MS.

In the samples spiked with 10 nM Hg (**Figures 3A,B**), most of the eluted Hg ($82 \pm 9\%$) followed the elution profiles of Cu, a metal known to preferentially bound to humic substances. Hg also co-eluted with the UV-absorbing components with hydrodynamic size corresponding to $d_h = 1.7$ nm at peak maximum, but the peak shifted toward a higher size in comparison with the qB-DOM components (**Supplementary Figure S6**), showing the preferential association of Hg with DOM components of humic type (Hg–DOM). A low proportion of Hg ($18 \pm 9\%$) was associated with the unfractionated LIOx material. In the samples spiked with 100 nM Hg to mimic the conditions in a highly polluted environment, a similar proportion of Hg bound to LIOx ($17 \pm 4\%$) was measured. The percentages of Hg bound to small-sized components of DOM were comparable ($83 \pm 4\%$), but an increase of the retention of the Hg–DOM components was observed in samples with high DOC contents (Shuya River and Petrozavodsk Bay) (**Figures 3C, D**). In these samples, a higher hydrodynamic size at peak maximum ($d_h = 2.2$ nm) than that in Lake Onego ($d_h = 1.7$ nm) was found and larger size distributions of Hg components were observed (**Supplementary Figure S6**). These shifts in size distribution suggested that: 1) inter-macromolecular binding of the DOM components could occur in the presence of Hg (Worms et al., 2015) and/or 2) Hg could bind to small iron oxide (SIOx) components co-eluting with Hg–DOM. The deconvolution of ^{202}Hg signals revealed that Hg was distributed among the 3 main fractions: Hg–DOM and Hg bound to SIOx and to LIOx, indeed (**Figures 3C–E**). Based on our deconvolution procedure, the proportion of Hg–DOM accounted for $63 \pm 7\%$ of the fractionated Hg due to the binding of Hg to SIOx.

It is worth noting that the addition of Hg resulted in changes in the size distribution of Fe species, especially SIOx due to the slight acidification of the samples (**Supplementary Figure S7**). Additionally, the concentration of Hg measured by FIA indicated a loss of $61 \pm 4\%$ of Hg in the AF4 system for samples spiked with 100 nM Hg *versus* only $6 \pm 14\%$ when 10 nM was added. A decrease in the pH could favor the formation of large inorganic aggregates, which bind Hg, and could not be eluted from the AF4 channel and, thus, contribute to the loss of Hg (Neubauer et al., 2013a). However, since no significant change in the Fe recoveries in the samples was observed ($\pm 9\%$) (**Supplementary Figure S7**), we supposed that this could have only a minor contribution to Hg losses. To obtain further information on the Hg losses for samples spiked with 100 nM Hg, we performed measurements of the total dissolved Hg in water samples before injection in the AF4 channel (Hg_{tot}) (**Supplementary Table S1**). The measurements revealed that only $32 \pm 4\%$ and $14 \pm 9\%$ of the initial Hg_{tot} concentrations were lost after 24 h of equilibration for the samples spiked with 100 and 10 nM Hg, respectively. These results demonstrated high Hg losses during the equilibration period, which were more pronounced at high Hg concentrations. A possible reason for such losses could be the reduction of Hg^{II} to volatile Hg^0 by the DOM, which was shown to be kinetically controlled and

dependent on the Hg/DOM ratio (Miller et al., 2009; Jiang et al., 2015). It could be suggested that part of the Hg^0 produced by dark reduction over 24 h remained in our samples, measured by CVAFS, but did not elute from the AF4 channel.

Nevertheless, further optimizations would be needed, especially for an in-depth evaluation on how the largest inorganic colloidal species could account for Hg binding and how Hg^0 could account for Hg speciation in artificially enriched natural samples.

When the losses during the equilibration of Hg with DOM after spiking were considered, the Hg recoveries after fractionation for samples spiked with 100 and 10 nM were in the same range, with $27 \pm 7\%$ and $30 \pm 3\%$, respectively. The quantity of the measured Hg thus increased proportionally to the Hg added, with 10 times more Hg bound to the nano-sized components in samples from Petrozavodsk Bay and Shuya River at 100 nM than at 10 nM (**Figure 4A**). In addition, a good correlation between the concentrations of the Hg–DOM and qB-DOM measured for the samples enriched with 100 nM Hg was found (**Figure 4B**). Based on the available literature, we could expect that $\text{Hg}-(\text{S-DOM})_2$ complexes could be predominantly formed and that the reactive thiols of DOM can be saturated (Skjellberg et al., 2006). The Hg/DOM ratios ($1.9\text{--}0.6$ and $0.1\text{--}0.06 \mu\text{g Hg mg}^{-1}\text{C}$ at high and low Hg concentrations, respectively) used here were low enough to sustain the binding of Hg to high-affinity sites for isolated DOM (Haitzer et al., 2002; Miller et al., 2009). Consequently, the quantity of the Hg–DOM should correspond to about 50% of the values of qB-DOM, used as a measure of the reduced thiol contents in DOM; however, it only accounted for $27 \pm 6\%$ in our case.

Therefore, we suggest working under conditions where no saturation of macromolecular thiols by Hg is observed. The lower than expected proportion of Hg–DOM could be due to the following: 1) the presence of various dissolved components with higher affinity for Hg or with higher concentration, which were lost in the AF4 separation channel, for example considering the low pH of our samples and the formation of complexes between Hg and chlorides (the Cl^- concentration was 0.130 mM) (**Supplementary Table S1**). 2) The significant interaction of Hg–S-DOM species with the AF4 channel membrane preventing their elution. The binding of Hg to DOM components could change their charge or properties, which may favor the interaction with the membrane of the AF4 channel and result in a decrease of Hg recovery. A similar nonspecific interaction for AF4 fractionation was found at high Ag loading to the peptide metallothionein (Liu et al., 2017), leading to a decrease in the recovered metal. 3) The binding of Hg to inorganic colloid or Hg^0 production and related losses, as discussed above.

Finally, the formation of $\text{Hg}-(\text{S-DOM})_2$ complexes should depend on the availability of proximal thiols within the macromolecular structure of humic substances or their capacity to promote inter-macromolecular binding. The measurement of the quantity of reduced thiols with the assumption that they formed $\text{Hg}-(\text{S-DOM})_2$ with high stability can be impaired by the formation of mixed Hg

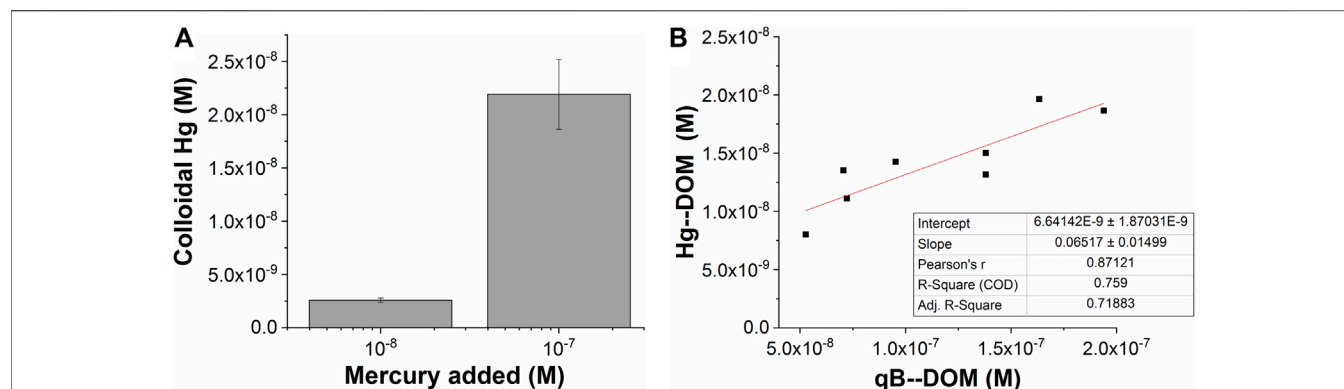


FIGURE 4 | AF4-ICP-MS measurements of mercury recovered as a function of the total mercury added (A) and binding to dissolved organic matter (DOM) (Hg--DOM) related to qB--DOM adducts measured using AF4 with fluorescence detection (FluoD) when 100 nM Hg was added (B).

complexes involving carboxylates or amines, which were less stable but prone to be displaced during our analysis (Liang et al., 2019). Such type of mixed complexes was shown to be more sensitive to protonation, which entered in competition with Hg complexation (Haitzer et al., 2003).

3.3 Stability of Hg Bound to the Nano-Sized Components of Standard SRDOM

Since the DOM-rich natural waters contained a high proportion of colloidal Fe and their pH could be altered by Hg addition, we complemented our study by analyzing standard SRDOM samples prepared in HEPES buffer at pH 7.0. The samples were enriched with 100 nM Hg to give a ratio of 2 µg Hg mg⁻¹ C sufficient to saturate thiols.

The measured Hg--DOM by AF4-ICP-MS (Supplementary Figure S8) corresponded to 44.2 ± 0.2% of the Hg added, corresponding to more than half of the qB--DOM content, measured to be 48 nM by AF4-FluoD in this case. To provide more complete information on the influence of the eluent type on the equilibrium of Hg binding with the DOM components during AF4 analysis, we compared the results obtained when HEPES instead of NH₄NO₃ was used as the eluent. High concentrations of NH₄NO₃ (10 mM) could be expected to favor the mobilization of Hg from low-affinity sites of SRDOM, as observed previously for carbonate-based ligands (Liang et al., 2019). The use of 10 mM HEPES as the mobile phase resulted in an increase in the proportion of Hg--DOM to 67.2 ± 1.7% of the added Hg. The partition coefficients (K_d) of Hg obtained by the ultrafiltration of individual size fractions <30 kDa of the SRDOM were shown to be relatively comparable (Bland et al., 2020). Such lack of a clear size dependence of the Hg binding affinity could be explained by the presence of small-sized components (LMM of <3 kDa) with the same properties as the larger ones. This can rely on the isolation procedure of this standard. This supports our results showing that the values of thiol/C for macromolecular SRDOM components were identical to those of unfractionated DOM. Thus, considering that the recovery of SRDOM components (68%) was identical to the one of Hg (67.2 ± 1.7%) when HEPES was used as the eluent, it can be suggested that most

of the Hg added was complexed by DOM, but that the use of NH₄NO₃ as the eluent displaced Hg from sites of low affinity during the analysis.

The results we obtained here for SRDOM are thus in line with the existing consensus that, after the saturation of thiols, other functional groups are involved in Hg complexation by DOM at neutral pH (Haitzer et al., 2003; Skjellberg et al., 2006). This provided evidence that the presence of other components or processes have affected the binding of Hg to the macromolecular thiols in our natural samples. This also suggested that the Hg--DOM we measured using AF4-ICP-MS for natural samples corresponded to the Hg bound to the relatively high-affinity sites of DOM. The fact that only a slight increase in the measured Hg--DOM was observed between 1 h when low-affinity sites must be involved (Jiang et al., 2015) and 24 h of equilibration in natural samples, but t_0 (Supplementary Figure S9), also supported these hypotheses.

The influence of the type of eluent for Hg--DOM complexation could be used to design experiments that allow accessing the relative lability/stability of Hg--DOM complexes. The lability of metal--DOM complexes, together with their hydrodynamic size, is an important parameter for the evaluation of the bioavailability of toxic metals (Ndu et al., 2018; Bland et al., 2020); however, it is difficult to determine, in particular for heterogeneous samples. Given the heterogeneous nature of DOM with respect to size, the composition of its different components, and their reactivities, further in-depth studies regarding the relative lability of Hg--DOM complexes under fractionation conditions will be highly sought. No stand-alone technique is available to date for the assessment of the lability of Hg--DOM complexes. Therefore, the use of AF4-UVD-FluoD-ICP-MS, together with techniques providing the relative binding strength and the redox state of Hg (e.g., Liang et al., 2019), and determining the thiol components and their Hg binding capacity in the size range uncovered by AF4 (e.g., Kozymatnyk et al., 2016; Adediran et al., 2019) will be of high relevance. Additionally, the proportions of nano-HgS must be assessed as they can account for stable and small-sized mercury species certainly formed before 24 h, as recently discussed in Bourdineaud et al. (2019). This structural information could not be obtained by online elemental detection using ICP-MS. Combining size fraction collection with complementary

techniques for material identification (iron or mercury nanoparticle composition) has been purposed (Dublet et al., 2019; Gfeller et al., 2021), but was limited by the low concentration of nanoparticles collected after AF4 fractionation.

4 CONCLUSION

In this study, we presented a methodology allowing the quantification of thiol groups in oxic water under the influence of a pedogenic DOM source. A combination of thiol labeling by fluorescent qBBR, separation of components by AF4, and online fluorescence detection was optimized for its uses to quantify the thiol contents in nano-sized macromolecular DOM together with their size distribution using Suwanee River DOM standard solutions. Neither the quantities of qB-DOM nor their size distribution was affected by the inner filtering properties of humic substances or by the presence of residual LMM fluorescent components. This methodology can be used to measure thiols under oxic/neutral conditions at relatively low concentrations (50 nM). The quantification and the characterization of the size distributions of Hg bound to macromolecules and nano-sized inorganic particles were obtained using AF4-ICP-MS. Using a signal deconvolution procedure, it was found that the spiked Hg was preferentially bound to macromolecular humic substances, with only a small proportion of Hg associated with inorganic nano-colloids. The measured Hg-DOM concentrations correlated well with the reduced thiol contents determined using AF4-FluoD. However, they were lower than those based on thiol contents. This result was explained by the potential reduction of Hg and the presence of other ligands in our samples impairing the binding of Hg to the thiols of macromolecules. We also showed that some Hg-DOM complexes can be displaced during their analysis by the NH_4NO_3 present in our eluent. These latter results open new opportunities to accessing the relative stability of the Hg-DOM complex when analyzed by AF4. The Hg-DOM contents we measured in DOM-rich natural waters using AF4-ICP-MS thus corresponded to Hg complexed to the high-affinity sites of nano-sized DOM.

REFERENCES

- Adediran, G. A., Liem-Nguyen, V., Song, Y., Schaefer, J. K., Skjellberg, U., and Björn, E. (2019). Microbial Biosynthesis of Thiol Compounds: Implications for Speciation, Cellular Uptake, and Methylation of Hg(II). *Environ. Sci. Technol.* 53 (14), 8187–8196. doi:10.1021/acs.est.9b01502
- Bland, G. D., Rao, B., and Reible, D. (2020). Evaluating the Transport of Hg(II) in the Presence of Natural Organic Matter through a Diffusive Gradient in a Thin-Film Passive Sampler. *Sci. Total Environ.* 749, 141217. doi:10.1016/j.scitotenv.2020.141217
- Bonnissel-Gissinger, P., Alnot, M., Lickes, J.-P., Ehrhardt, J.-J., and Behra, P. (1999). Modeling the Adsorption of Mercury(II) on (Hydr)oxides II: α -FeOOH (Goethite) and Amorphous Silica. *J. Colloid Interf. Sci.* 215 (2), 313–322. doi:10.1006/jcis.1999.6263
- Bourdineaud, J.-P., Gonzalez-Rey, M., Rovezzi, M., Glatzel, P., Nagy, K. L., and Manceau, A. (2019). Divalent Mercury in Dissolved Organic Matter Is

DATA AVAILABILITY STATEMENT

The raw data supporting the conclusion of this article will be made available by the authors, without undue reservation.

AUTHOR CONTRIBUTIONS

IW and VS developed the scientific concept and design of the study. KK carried out the EEM and AF4-FluoD measurements. EM and NR performed sample preparations for Hg doping and Hg measurements by MERX, respectively. IW performed the AF4-FluoD and AF4-MD-ICP-MS measurements. IW performed data processing and result interpretation, and wrote the first draft of the article. VS obtained funding and took part in the writing, reviewing, and editing of the text. All authors agreed on the submission of the final version.

FUNDING

The work was supported by the International Project “Lake Ladoga: Life Under Ice—Interplay of Under-Ice Processes by Global Change” and the Swiss National Science Foundation grant nos. 166089 and 183292.

ACKNOWLEDGMENTS

The authors want to thank Arin Kantarciyan and M. Kevin Trindade for fruitful discussion regarding the stability of qBBR and its reactivity in natural water. The authors wish to thank the two reviewers involved for their constructive comments, which have greatly ameliorate the quality of the manuscript.

SUPPLEMENTARY MATERIAL

The Supplementary Material for this article can be found online at: <https://www.frontiersin.org/articles/10.3389/fchem.2022.800696/full#supplementary-material>

Bioavailable to Fish and Accumulates as Dithiolate and Tetrathiolate Complexes. *Environ. Sci. Technol.* 53 (9), 4880–4891. doi:10.1021/acs.est.8b06579

- Bratkich, A., Klun, K., and Gao, Y. (2019). Mercury Speciation in Various Aquatic Systems Using Passive Sampling Technique of Diffusive Gradients in Thin-Film. *Sci. Total Environ.* 663, 297–306. doi:10.1016/j.scitotenv.2019.01.241
- Catrouillet, C., Davranche, M., Dia, A., Bouhnik-Le Coz, M., Pédrot, M., Marsac, R., et al. (2015). Thiol Groups Controls on Arsenite Binding by Organic Matter: New Experimental and Modeling Evidence. *J. Colloid Interf. Sci.* 460, 310–320. doi:10.1016/j.jcis.2015.08.045
- Chiasson-Gould, S. A., Blais, J. M., and Poulain, A. J. (2014). Dissolved Organic Matter Kinetically Controls Mercury Bioavailability to Bacteria. *Environ. Sci. Tech.* 48 (6), 3153–3161. doi:10.1021/es4038484
- Chu, C., Erickson, P. R., Lundeen, R. A., Stamatelatos, D., Alaimo, P. J., Latch, D. E., et al. (2016). Photochemical and Nonphotochemical Transformations of Cysteine with Dissolved Organic Matter. *Environ. Sci. Technol.* 50 (12), 6363–6373. doi:10.1021/acs.est.6b01291

- Cuss, C. W., Donner, M. W., Grant-Weaver, I., Noernberg, T., Pelletier, R., Sinnatamby, R. N., et al. (2018). Measuring the Distribution of Trace Elements Amongst Dissolved Colloidal Species as a Fingerprint for the Contribution of Tributaries to Large Boreal Rivers. *Sci. Total Environ.* 642, 1242–1251. doi:10.1016/j.scitotenv.2018.06.099
- Cuss, C. W., Glover, C. N., Javed, M. B., Nagel, A., and Shoty, W. (2020). Geochemical and Biological Controls on the Ecological Relevance of Total, Dissolved, and Colloidal Forms of Trace Elements in Large Boreal Rivers: Review and Case Studies. *Environ. Rev.* 28 (2), 138–163. doi:10.1139/er-2019-0014
- Demarty, M., Bilodeau, F., and Tremblay, A. (2021). Mercury Export from Freshwater to Estuary: Carbocentric Science Elucidates the Fate of a Toxic Compound in Aquatic Boreal Environments. *Front. Environ. Sci.* 9. ARTN 69756310. doi:10.3389/fenvs.2021.697563
- Dublet, G., Worms, I., Fruttschi, M., Brown, A., Zünd, G. C., Bartova, B., et al. (2019). Colloidal Size and Redox State of Uranium Species in the Porewater of a Pristine Mountain Wetland. *Environ. Sci. Technol.* 53 (16), 9361–9369. doi:10.1021/acs.est.9b01417
- Efremova, T. A., Sabylina, A. V., Lozovik, P. A., Slaveykova, V. I., Zobkova, M. V., and Pasche, N. (2019). Seasonal and Spatial Variation in Hydrochemical Parameters of Lake Onego (Russia): Insights from 2016 Field Monitoring. *Inland Waters* 9 (2), 227–238. doi:10.1080/20442041.2019.1568097
- French, T. D., Houben, A. J., Desforges, J. P. W., Kimpe, L. E., Kokelj, S. V., Poulain, A. J., et al. (2014). Dissolved Organic Carbon Thresholds Affect Mercury Bioaccumulation in Arctic Lakes. *Environ. Sci. Tech.* 48 (6), 3162–3168. doi:10.1021/es403849d
- Gasper, J. D., Aiken, G. R., and Ryan, J. N. (2007). A Critical Review of Three Methods Used for the Measurement of Mercury (Hg²⁺)-Dissolved Organic Matter Stability Constants. *Appl. Geochem.* 22 (8), 1583–1597. doi:10.1016/j.apgeochem.2007.03.018
- Gfeller, L., Weber, A., Worms, I., Slaveykova, V. I., and Mestrot, A. (2021). Mercury Mobility, Colloid Formation and Methylation in a Polluted Fluvial as Affected by Manure Application and Flooding-Draining Cycle. *Biogeosciences* 18 (11), 3445–3465. doi:10.5194/bg-18-3445-2021
- Haitzer, M., Aiken, G. R., and Ryan, J. N. (2003). Binding of Mercury(II) to Aquatic Humic Substances: Influence of pH and Source of Humic Substances. *Environ. Sci. Technol.* 37 (11), 2436–2441. doi:10.1021/es026291o
- Haitzer, M., Aiken, G. R., and Ryan, J. N. (2002). Binding of Mercury(II) to Dissolved Organic Matter: The Role of the Mercury-To-DOM Concentration Ratio. *Environ. Sci. Technol.* 36 (16), 3564–3570. doi:10.1021/es025699i
- Hochella, M. F., Mogk, D. W., Ranville, J., Allen, I. C., Luther, G. W., Marr, L. C., et al. (2019). Natural, Incidental, and Engineered Nanomaterials and Their Impacts on the Earth System. *Science* 363 (6434), 1414. doi:10.1126/science.aau8299
- Huynh, K., Liem-Nguyen, V., Feng, C., Lindberg, R., and Björn, E. (2020). Quantification of Total Concentration of Thiol Functional Groups in Environmental Samples by Titration with Monobromo(trimethylammonio) biman and Determination with Tandem Mass Spectrometry. *Talanta* 218, 121109. doi:10.1016/j.talanta.2020.121109
- IHSS, St. Paul (MN) (n.d.). Available at: <https://humic-substances.org>.
- Jiang, T., Skjellberg, U., Wei, S., Wang, D., Lu, S., Jiang, Z., et al. (2015). Modeling of the Structure-specific Kinetics of Abiotic, Dark Reduction of Hg(II) Complexed by O/N and S Functional Groups in Humic Acids while Accounting for Time-dependent Structural Rearrangement. *Geochimica Et Cosmochimica Acta* 154, 151–167. doi:10.1016/j.gca.2015.01.011
- Jiskra, M., Saile, D., Wiederhold, J. G., Bourdon, B., Björn, E., and Kretzschmar, R. (2014). Kinetics of Hg(II) Exchange between Organic Ligands, Goethite, and Natural Organic Matter Studied with an Enriched Stable Isotope Approach. *Environ. Sci. Technol.* 48 (22), 13207–13217. doi:10.1021/es503483m
- Joe-Wong, C., Shoenfelt, E., Hauser, E. J., Crompton, N., and Myneni, S. C. B. (2012). Estimation of Reactive Thiol Concentrations in Dissolved Organic Matter and Bacterial Cell Membranes in Aquatic Systems. *Environ. Sci. Technol.* 46 (18), 9854–9861. doi:10.1021/es301381n
- Kozyatnyk, I., Bouchet, S., Björn, E., and Haglund, P. (2016). Fractionation And Size-Distribution Of Metal And Metalloid Contaminants In A Polluted Groundwater Rich In Dissolved Organic Matter. *J. Hazardous Mater.* 318, 194–202. doi:10.1016/j.jhazmat.2016.07.024
- Lavoie, R. A., Amyot, M., and Lapierre, J. F. (2019). Global Meta-Analysis on the Relationship between Mercury and Dissolved Organic Carbon in Freshwater Environments. *J. Geophys. Res. Biogeosci.* 124 (6), 1508–1523. doi:10.1029/2018jg004896
- Lead, J. R., and Wilkinson, K. J. (2006). Aquatic Colloids and Nanoparticles: Current Knowledge and Future Trends. *Environ. Chem.* 3 (3), 159–171. doi:10.1071/En06025
- Liang, X., Lu, X., Zhao, J., Liang, L., Zeng, E. Y., and Gu, B. (2019). Stepwise Reduction Approach Reveals Mercury Competitive Binding and Exchange Reactions within Natural Organic Matter and Mixed Organic Ligands. *Environ. Sci. Technol.* 53 (18), 10685–10694. doi:10.1021/acs.est.9b02586
- Liem-Nguyen, V., Skjellberg, U., and Björn, E. (2021). Methylmercury Formation in Boreal Wetlands in Relation to Chemical Speciation of Mercury(II) and Concentration of Low Molecular Mass Thiols. *Sci. Total Environ.* 755, 142666. ARTN 14266610. doi:10.1016/j.scitotenv.2020.142666
- Liem-Nguyen, V., Skjellberg, U., and Björn, E. (2017). Thermodynamic Modeling of the Solubility and Chemical Speciation of Mercury and Methylmercury Driven by Organic Thiols and Micromolar Sulfide Concentrations in Boreal Wetland Soils. *Environ. Sci. Technol.* 51 (7), 3678–3686. doi:10.1021/acs.est.6b04622
- Liu, W., Worms, I. A. M., Herlin-Boime, N., Truffier-Boutry, D., Michaud-Soret, I., Mintz, E., et al. (2017). Interaction of Silver Nanoparticles with Metallothionein and Ceruloplasmin: Impact on Metal Substitution by Ag(I), corona Formation and Enzymatic Activity. *Nanoscale* 9 (19), 6581–6594. doi:10.1039/c7nr01075c
- Manceau, A., Lemouchi, C., Enescu, M., Gaillot, A.-C., Lanson, M., Magnin, V., et al. (2015a). Formation of Mercury Sulfide from Hg(II)-Thiolate Complexes in Natural Organic Matter. *Environ. Sci. Technol.* 49 (16), 9787–9796. doi:10.1021/acs.est.5b02522
- Manceau, A., Lemouchi, C., Rovezzi, M., Lanson, M., Glatzel, P., Nagy, K. L., et al. (2015b). Structure, Bonding, and Stability of Mercury Complexes with Thiolate and Thioether Ligands from High-Resolution XANES Spectroscopy and First-Principles Calculations. *Inorg. Chem.* 54 (24), 11776–11791. doi:10.1021/acs.inorgchem.5b01932
- Manceau, A., and Nagy, K. L. (2019). Thiols in Natural Organic Matter: Molecular Forms, Acidity, and Reactivity with Mercury(II) from First-Principles Calculations and High Energy-Resolution X-ray Absorption Near-Edge Structure Spectroscopy. *ACS Earth Space Chem.* 3 (12), 2795–2807. doi:10.1021/acsearthspacechem.9b00278
- Mangal, V., and Guéguen, C. (2015). Examining Concentrations and Molecular Weights of Thiols in Microorganism Cultures and in Churchill River (Manitoba) Using a Fluorescent-Labeling Method Coupled to Asymmetrical Flow Field-Flow Fractionation. *Anal. Bioanal. Chem.* 407 (15), 4305–4313. doi:10.1007/s00216-015-8599-0
- Mangal, V., Phung, T., and Guéguen, C. (2020). An Estimation of Sulfur Concentrations Released by Three Algae (*Chlorella Vulgaris*, *Chlamydomonas Reinhardtii*, *Scenedesmus Obliquus*) in Response to Variable Growth Photoperiods. *Environ. Sci. Pollut. Res.* 27 (11), 12491–12498. doi:10.1007/s11356-020-07812-6
- Miller, C. L., Southworth, G., Brooks, S., Liang, L., and Gu, B. (2009). Kinetic Controls on the Complexation between Mercury and Dissolved Organic Matter in a Contaminated Environment. *Environ. Sci. Technol.* 43 (22), 8548–8553. doi:10.1021/es901891t
- Montaño, M. D., von der Kammer, F., Cuss, C. W., and Ranville, J. F. (2019). Opportunities for Examining the Natural Nanogeochemical Environment Using Recent Advances in Nanoparticle Analysis. *J. Anal. Spectrom.* 34 (9), 1768–1772. doi:10.1039/c9ja00168a
- Ndu, U., Christensen, G. A., Rivera, N. A., Gionfriddo, C. M., Deshusses, M. A., Elias, D. A., et al. (2018). Quantification of Mercury Bioavailability for Methylation Using Diffusive Gradient in Thin-Film Samplers. *Environ. Sci. Technol.* 52 (15), 8521–8529. doi:10.1021/acs.est.8b00647
- Neubauer, E., Schenkeveld, W. D. C., Plathe, K. L., Rentenberger, C., von der Kammer, F., Kraemer, S. M., et al. (2013a). The Influence of pH on Iron Speciation in Podzol Extracts: Iron Complexes with Natural Organic Matter, and Iron mineral Nanoparticles. *Sci. Total Environ.* 461–462, 108–116. doi:10.1016/j.scitotenv.2013.04.076
- Neubauer, E., v.d. Kammer, F., and Hofmann, T. (2013c). Using FLOWFFF and HPSEC to Determine Trace Metal-Colloid Associations in Wetland Runoff. *Water Res.* 47 (8), 2757–2769. doi:10.1016/j.watres.2013.02.030

- Neubauer, E., von der Kammer, F., Knorr, K.-H., Peiffer, S., Reichert, M., and Hofmann, T. (2013b). Colloid-associated export of Arsenic in Stream Water during Stormflow Events. *Chem. Geology*. 352, 81–91. doi:10.1016/j.chemgeo.2013.05.017
- Ohno, T. (2002). Fluorescence Inner-Filtering Correction for Determining the Humification index of Dissolved Organic Matter. *Environ. Sci. Technol.* 36 (4), 742–746. doi:10.1021/es0155276
- Pelcová, P., Dočekalová, H., and Kleckerová, A. (2014). Development of the Diffusive Gradient in Thin Films Technique for the Measurement of Labile Mercury Species in Waters. *Analytica Chim. Acta* 819, 42–48. doi:10.1016/j.aca.2014.02.013
- Pelcová, P., Vičarová, P., Ridošková, A., Dočekalová, H., Kopp, R., Mareš, J., et al. (2017). Prediction of Mercury Bioavailability to Common Carp (*Cyprinus carpio* L.) Using the Diffusive Gradient in Thin Film Technique. *Chemosphere* 187, 181–187. doi:10.1016/j.chemosphere.2017.08.097
- Pham, A. L.-T., Johnson, C., Manley, D., and Hsu-Kim, H. (2015). Influence of Sulfide Nanoparticles on Dissolved Mercury and Zinc Quantification by Diffusive Gradient in Thin-Film Passive Samplers. *Environ. Sci. Technol.* 49 (21), 12897–12903. doi:10.1021/acs.est.5b02774
- Rao, B., Simpson, C., Lin, H., Liang, L., and Gu, B. (2014). Determination of Thiol Functional Groups on Bacteria and Natural Organic Matter in Environmental Systems. *Talanta* 119, 240–247. doi:10.1016/j.talanta.2013.11.004
- Ravichandran, M. (2004). Interactions between Mercury and Dissolved Organic Matter-Aa Review. *Chemosphere* 55 (3), 319–331. doi:10.1016/j.chemosphere.2003.11.011
- Richard, J.-H., Bischoff, C., Ahrens, C. G. M., and Biester, H. (2016a). Mercury (II) Reduction and Co-precipitation of Metallic Mercury on Hydrous Ferric Oxide in Contaminated Groundwater. *Sci. Total Environ.* 539, 36–44. doi:10.1016/j.scitotenv.2015.08.116
- Richard, J.-H., Bischoff, C., and Biester, H. (2016b). Comparing Modeled and Measured Mercury Speciation in Contaminated Groundwater: Importance of Dissolved Organic Matter Composition. *Environ. Sci. Technol.* 50 (14), 7508–7516. doi:10.1021/acs.est.6b00500
- Senesi, N., Miano, T. M., Provenzano, M. R., and Brunetti, G. (1991). Characterization, Differentiation, and Classification of Humic Substances by Fluorescence Spectroscopy. *Soil Sci.* 152 (4), 259–271. doi:10.1097/00010694-199110000-00004
- Skylberg, U., Bloom, P. R., Qian, J., Lin, C.-M., and Bleam, W. F. (2006). Complexation of Mercury(II) in Soil Organic Matter: EXAFS Evidence for Linear Two-Coordination with Reduced Sulfur Groups. *Environ. Sci. Technol.* 40 (13), 4174–4180. doi:10.1021/es0600577
- Skylberg, U., Persson, A., Tjerngren, I., Kronberg, R.-M., Drott, A., Meili, M., et al. (2021). Chemical Speciation of Mercury, Sulfur and Iron in a Dystrophic Boreal lake Sediment, as Controlled by the Formation of Mackinawite and Framboidal Pyrite. *Geochimica Et Cosmochimica Acta* 294, 106–125. doi:10.1016/j.gca.2020.11.022
- Smith, D. S., Bell, R. A., and Kramer, J. R. (2002). Metal Speciation in Natural Waters with Emphasis on Reduced Sulfur Groups as strong Metal Binding Sites. *Comp. Biochem. Physiol. C Toxicol. Pharmacol.* 133 (1-2), 65–74. doi:10.1016/S1532-0456(02)00108-4
- Smith, D. S., Nasir, R., Parker, W., Peters, A., Merrington, G., van Egmond, R., et al. (2021). Developing Understanding of the Fate and Behaviour of Silver in Fresh Waters and Waste Waters. *Sci. Total Environ.* 757, 14364810. doi:10.1016/j.scitotenv.2020.143648
- Song, Y., Jiang, T., Liem-Nguyen, V., Sparrman, T., Björn, E., and Skylberg, U. (2018). Thermodynamics of Hg(II) Bonding to Thiol Groups in Suwannee River Natural Organic Matter Resolved by Competitive Ligand Exchange, Hg LIII-Edge EXAFS and ¹H NMR Spectroscopy. *Environ. Sci. Technol.* 52 (15), 8292–8301. doi:10.1021/acs.est.8b00919
- Stolpe, B., Guo, L., Shiller, A. M., and Aiken, G. R. (2013). Abundance, Size Distributions and Trace-Element Binding of Organic and Iron-Rich Nanocolloids in Alaskan Rivers, as Revealed by Field-Flow Fractionation and ICP-MS. *Geochimica Et Cosmochimica Acta* 105, 221–239. doi:10.1016/j.gca.2012.11.018
- Stolpe, B., Guo, L., Shiller, A. M., and Hassellöv, M. (2010). Size and Composition of Colloidal Organic Matter and Trace Elements in the Mississippi River, Pearl River and the Northern Gulf of Mexico, as Characterized by Flow Field-Flow Fractionation. *Mar. Chem.* 118 (3-4), 119–128. doi:10.1016/j.marchem.2009.11.007
- Suarez, E. L., Tiffay, M.-C., Kalinkina, N., Tchekryzheva, T., Sharov, A., Tekanova, E., et al. (2019). Diurnal Variation in the Convection-Driven Vertical Distribution of Phytoplankton under Ice and after Ice-Off in Large Lake Onego (Russia). *Inland Waters* 9 (2), 193–204. doi:10.1080/20442041.2018.1559582
- Tang, W. L., Liu, Y. R., Guan, W. Y., Zhong, H., Qu, X. M., and Zhang, T. (2020). Understanding Mercury Methylation in the Changing Environment: Recent Advances in Assessing Microbial Methylators and Mercury Bioavailability. *Sci. Total Environ.* 714, 136827. ARTN 13682710. doi:10.1016/j.scitotenv.2020.136827
- Tercier-Waeber, M.-L., Abdou, M., Figuera, M., Kowal, J., Bakker, E., and van der Wal, P. (2021). In Situ Voltammetric Sensor of Potentially Bioavailable Inorganic Mercury in Marine Aquatic Systems Based on Gel-Integrated Nanostructured Gold-Based Microelectrode Arrays. *ACS Sens.* 6 (3), 925–937. doi:10.1021/acssensors.0c02111
- Tiffreau, C., Lützenkirchen, J., and Behra, P. (1995). Modeling the Adsorption of Mercury(II) on (Hydr)oxides 1. Amorphous Iron-Oxide And Alpha-Quartz. *J. Colloid Interf. Sci.* 172 (1), 82–93. doi:10.1006/jcis.1995.1228
- Waeber, M. L. T., Stoll, S., and Slaveykova, V. I. (2012). Trace Metal Behavior in Surface Waters: Emphasis on Dynamic Speciation, Sorption Processes and Bioavailability. *Arch. Des Sci.* 65, 119–142.
- Wang, Q. Y., Zhang, L. J., Liang, X. J., Yin, X. P., Zhang, Y. L., Zheng, W., et al. (2020). Rates and Dynamics of Mercury Isotope Exchange between Dissolved Elemental Hg(0) and Hg(II) Bound to Organic and Inorganic Ligands. *Environ. Sci. Tech.* 54 (23), 15534–15545. doi:10.1021/acs.est.0c06229
- Worms, I. A. M., Adenmatten, D., Miéville, P., Traber, J., and Slaveykova, V. I. (2015). Photo-transformation of Pedogenic Humic Acid and Consequences for Cd(II), Cu(II) and Pb(II) Speciation and Bioavailability to green Microalga. *Chemosphere* 138, 908–915. doi:10.1016/j.chemosphere.2014.10.093
- Worms, I. A. M., Chmiel, H. E., Traber, J., Tofield-Pasche, N., and Slaveykova, V. I. (2019). Dissolved Organic Matter and Associated Trace Metal Dynamics from River to Lake, under Ice-Covered and Ice-free Conditions. *Environ. Sci. Technol.* 53 (24), 14134–14143. doi:10.1021/acs.est.9b02184
- Zhang, L., Liang, X., Wang, Q., Zhang, Y., Yin, X., Lu, X., et al. (2021). Isotope Exchange between Mercuric [Hg(II)] Chloride and Hg(II) Bound to Minerals and Thiolate Ligands: Implications for Enriched Isotope Tracer Studies. *Geochimica Et Cosmochimica Acta* 292, 468–481. doi:10.1016/j.gca.2020.10.013
- Zhang, L., Wu, S., Zhao, L., Lu, X., Pierce, E. M., and Gu, B. (2019). Mercury Sorption and Desorption on Organo-Mineral Particulates as a Source for Microbial Methylation. *Environ. Sci. Technol.* 53 (5), 2426–2433. doi:10.1021/acs.est.8b06020
- Zhao, L., Li, Y., Zhang, L., Zheng, J., Pierce, E. M., and Gu, B. (2019). Mercury Adsorption on Minerals and its Effect on Microbial Methylation. *ACS Earth Space Chem.* 3 (7), 1338–1345. doi:10.1021/acsearthspacechem.9b00039
- Zhou, Z., and Guo, L. (2015). A Critical Evaluation of an Asymmetrical Flow Field-Flow Fractionation System for Colloidal Size Characterization of Natural Organic Matter. *J. Chromatogr. A* 1399, 53–64. doi:10.1016/j.chroma.2015.04.035

Conflict of Interest: The authors declare that the research was conducted in the absence of any commercial or financial relationships that could be construed as a potential conflict of interest.

Publisher's Note: All claims expressed in this article are solely those of the authors and do not necessarily represent those of their affiliated organizations, or those of the publisher, the editors, and the reviewers. Any product that may be evaluated in this article, or claim that may be made by its manufacturer, is not guaranteed or endorsed by the publisher.

Copyright © 2022 Worms, Kavanagh, Moulin, Regier and Slaveykova. This is an open-access article distributed under the terms of the Creative Commons Attribution License (CC BY). The use, distribution or reproduction in other forums is permitted, provided the original author(s) and the copyright owner(s) are credited and that the original publication in this journal is cited, in accordance with accepted academic practice. No use, distribution or reproduction is permitted which does not comply with these terms.



Spectroscopy, Morphology, and Electrochemistry of Electrospun Polyamic Acid Nanofibers

Siyabulela Hamnca^{1*}, Jessica Chamier², Sheila Grant³, Timothy Glass³, Emmanuel Iwuoha¹ and Priscilla Baker^{1*}

¹SensorLab, Chemistry Department, University of the Western Cape, Bellville, South Africa, ²HySA Catalysis, Department of Chemical Engineering, University of Cape Town, Rondebosch, Cape Town, South Africa, ³Chemistry Department, University of Missouri, Columbia, MO, United states

OPEN ACCESS

Edited by:

Camelia Bala,
University of Bucharest, Romania

Reviewed by:

Florence Lagarde,
Université Claude Bernard Lyon 1,
France
Mihaela Puiu,
University of Bucharest, Romania

*Correspondence:

Siyabulela Hamnca
3055982@myuwc.ac.za
Priscilla Baker
pbaker@uwc.ac.za

Specialty section:

This article was submitted to
Analytical Chemistry,
a section of the journal
Frontiers in Chemistry

Received: 24 September 2021

Accepted: 16 December 2021

Published: 16 February 2022

Citation:

Hamnca S, Chamier J, Grant S,
Glass T, Iwuoha E and Baker P (2022)
Spectroscopy, Morphology, and
Electrochemistry of Electrospun
Polyamic Acid Nanofibers.
Front. Chem. 9:782813.
doi: 10.3389/fchem.2021.782813

Polyamic acid (PAA) nanofibers produced by using the electrospinning method were fully characterized in terms of morphology and spectroscopy. A PAA nanofiber-modified screen-printed carbon electrode was applied to the detection of selected sulfonamides by following an electroanalytical protocol. The polyamic acid (PAA) nanofibers were characterized using Fourier transform infrared (FTIR) spectroscopy to study the integrity of polyamic acid functional groups as nanofibers by comparing them to chemically synthesized polyamic acid. A scanning electron microscope (SEM) was used to confirm the morphology of the produced nanofibers and 3D arrangement at the electrode interface. The Brunauer–Emmett–Teller (BET) method was used to determine the surface area of the nanofibers. Atomic force microscopy (AFM) was used to study the porosity and surface roughness of the nanofibers. Electrochemical evaluation based on diffusion-controlled kinetics was applied to determine the number of electrons transferred in the system, the surface concentration of the deposited PAA thin film ($2.14 \times 10^{-6} \text{ mol/cm}^2$), and the diffusion coefficient (D_e) for the PAA nanofiber-modified screen-printed carbon electrode ($9.43 \times 10^{-7} \text{ cm}^2/\text{s}$). The reported LODs for sulfadiazine and sulfamethazine detection are consistent with requirements for trace-level monitoring by early warning diagnostic systems.

Keywords: polyamic acid, nanofibers, screen-printed carbon electrodes, electrochemistry, electrospun (ES) nanofibers

INTRODUCTION

Electrospinning is an efficient and highly scalable method used for preparation and production of a variety of nanostructured polymer materials. The process of electrospinning requires the application of controlled voltage to produce fibers from charged polymer solutions producing fibers with diameters ranging from micron to nanometer size (Frenot and Chronakis, 2003; Valizadeh and Mussa Farkhani, 2013; Sapountzi et al., 2017; Chen et al., 2019). These polymer nanofibers exhibit unique properties such as high surface area-to-volume ratio, good structural and mechanical properties, extreme flexibility, low basic weight, and cost effectiveness (Machotová et al., 2016). Electrospinning works well for polymers with high molecular weight and good solubility to yield concentrated solutions. Additionally, polymers should also have good conductivity and viscosity. However, finding the correct mix of polymer solution properties for efficient spinning remains a challenging exercise. Researchers have adopted different approaches to improve the spinnability of

polymers and other non-polymer materials, employing carrier polymers or additives such as surfactants to impose spinning. Aduba et al. (2015) effectively used a carrier polymer method for producing electrospun nanocomposite fibers from PEGylated PAMAM dendrimers, blended with a small amount of high-molecular weight polyethylene oxide (PEO). Saquing et al. (2013) was able to produce high-quality spun fibers of alginate by blending it with high-molecular weight polyethylene oxide (PEO). The molecular weight of the polymer affects the polymer or polymer composite solution viscosity, surface tension, and conductivity (Machotová et al., 2016).

Polyamic acid (PAA) is a polyimide precursor polymer with amide and carboxylic functional groups. PAA is easy to synthesize and process due to its high solubility in aprotic solvents. PAA polymer thin films may easily be produced *in situ* at Au and glassy carbon electrode surfaces and functionalized in various ways to prepare very efficient electrochemical sensors (Andreescu et al., 2005; Noah et al., 2012; Hess et al., 2014; Hamnca et al., 2016). While electrochemical polymerization yields nanostructured PAA, no evidence of organized nanofibers produced from chemically synthesized PAA powder by any method has been reported yet. In this study, the semiconducting polymer, polyamic acid (PAA), was used to produce nanofibers by electrospinning PAA from a homogeneous blended polymer solution, using a minimal amount of high-molecular weight polyvinylpyrrolidone (PVP) for efficient nanofiber production, with good processability and yield.

Electrospinning of continuous fibers is improved by chemical cross-linkers, additives, and carrying polymers when spinning low-molecular weight polymers such as PAA (Wang et al., 2016). Polyvinylpyrrolidone (PVP) has been widely reported as an efficient carrier polymer in spinning of a wide range of materials, due to its high solubility in aprotic solvent such as dimethylformamide (DMF) and N,N-dimethylacetamide (DMAc). Lubasova et al. (2015) used PVP and PVP/poly (acrylic acid) blend to produce hydrogel nanofibers simply by heat treatment of the electrospun nanofibers without the inclusion of any toxic agent for cross-linking as reported by the authors. PVP has also been used as a carrying polymer in the fabrication of titania nanofibers (Chandrasekar et al., 2009). In this study, we present the spectroscopy, morphology, and electrochemistry of polyamic acid (PAA) nanofibers. The effect of carrier polymer loading, applied voltage, and flow rate on the efficacy of nanofiber formation was evaluated. Sulfonamides are a class of broad-spectrum synthetic bacteriostatic antibiotics which are usually administered in animal husbandry to prevent and control diseases. Sulfonamides are classified as the emerging contaminants in the aquatic environment, for which there are no regulatory guidelines. Therefore, it is important to develop tools that detect and report these antibiotics at trace concentrations. As contaminants of emerging concern, sulfonamides are frequently detected in all kinds of environmental water, surface water, ground water, and wastewater systems. Real-time detection of sulfonamides and other pharmaceuticals in the environment remains a global objective. Electrochemical sensors and biosensors play a

significant role in delivering data in a simple, portable, and cost-effective format.

EXPERIMENTAL

Chemicals and Reagents

The reagents 4, 4-oxydianiline (97%), 1, 2, 4, 5-benzenetetracarboxylic anhydride (97%), acetonitrile (99%), N,N-dimethylacetamide (DMAc), dimethylformamide (DMF), trizma-hydrochloric acid (Tris-HCl), polyvinylpyrrolidone (MW. 130000 g/mol), sulfadiazine (99%), and sulfamethazine (99%) were all obtained from Sigma-Aldrich, South Africa. All chemicals were of analytical grade and used without further purification. Deionized (ultra-pure) water purified at a resistivity of 18.2 MΩ/cm. A Milli-QTM system (Millipore) was used for preparation of all aqueous solutions.

Polyamic Acid Synthesis and Electrospinning of Polyamic Acid

Polyamic acid was synthesized from organic solvents, using 4, 4-oxydianiline and benzene 1,2,4,5-tetracarboxylic anhydride precursors, as previously described in the literature (Andreescu et al., 2005; Noah et al., 2012; Hamnca et al., 2016). A blend of polyamic acid (12% by wt.) and PVP (3% by wt.) was prepared using dimethylformamide (DMF) and dimethylacetamide (DMAc) as solvents, respectively. The electrospinning of polyamic acid (PAA) was carried out using a syringe of a diameter of 0.5 mm at an applied voltage of 16–16.8 kV, depending on humidity. The electrospinning experiments were performed at room temperature (typically 23°C) with atmospheric humidity in the range of 21–24%. The flow rate ranged between 99 and 150 µl/h, with the spinneret and collector distance set at 15 cm. The flow rate and spinning time had a direct effect on the amount of electrospun fibers produced. The deposited and freestanding nanofibers produced were dried and stored at room temperature. Freestanding PAA nanofibers were produced using a custom-designed electrospinning instrument in the biological engineering department (University of Missouri, Columbia, MO, United States). The freestanding nanofibers were characterized using microscopic and thermogravimetric techniques.

Instrumentation

An electrospinning instrument from IME technologies situated in the chemical engineering department (HySA) at the University of Cape Town was used to produce nanofibers. Fourier transform infrared spectroscopy was carried out using a PerkinElmer Spectrum 100 instrument. Thermal stability data for freestanding PAA nanofibers were obtained by using thermogravimetric analysis (TGA) Q500 V3.13 Build 261 in the temperature range of 10–475°C at a heating rate of 10°C/min in atmospheric nitrogen. The morphology studies were conducted on a Hitachi S3000N scanning electron microscope (SEM) and Zeiss Auriga high-resolution field emission gun (fegsem) scanning electron microscope (HRSEM) for samples

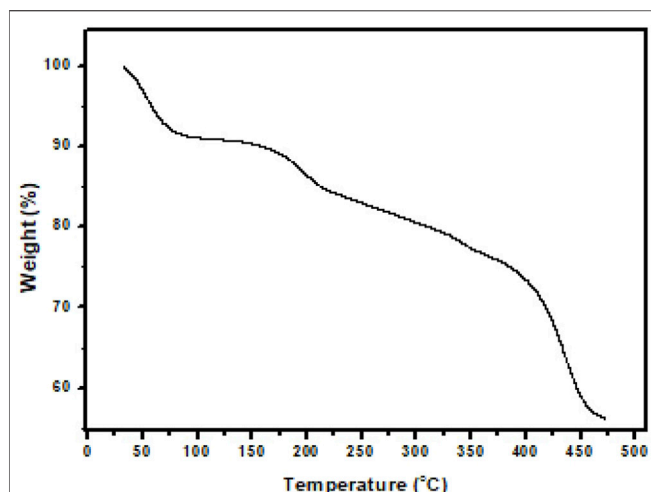


FIGURE 1 | Thermogravimetric analysis (TGA) curve of PAA nanofibers recorded under nitrogen atmosphere up to 475°C at 10°C/min.

deposited onto a carbon grid. Electrochemical deposition and evaluation were performed using a PalmSensPTrace 4.4 workstation (Bioanalytical Systems, United States). The electrodeposited thin films and electrospun nanofibers were prepared on screen-printed carbon electrodes from DropSens (DRP-C110, Spain). Nitrogen sorption experiments were performed on a Micromeritics TrisStar II 3020 version 2.0 instrument. The surface area was calculated from the Brunauer–Emmett–Teller (BET) equation. The Nanosurf EasyScan2 was used with highly doped silicon material probing tips with a resistivity of 0.01–0.02 (from NANOSENSORS™). Atomic force microscopy (AFM) was used to study the average height distribution of the screen-printed electrodes modified with polyamic acid nanofibers.

Electrochemical Evaluation

Scan rate-dependent cyclic voltammetry (CV) was used to evaluate the electrochemical integrity of the deposited PAA materials and, subsequently, its analytical response toward the quantification of a selection of sulfonamides. Scan rates ranged from 10 to 100 mV/s, with a potential window set between –1,000 and +1,000 mV vs. Ag/AgCl in a 0.1 M phosphate buffer (pH 7) electrolyte. The electrochemical determinations of sulfonamides were done in 0.1 M Tris–HCl (pH 8) using square wave voltammetry (SWV) at a scan rate of 50 mV/s, which was achieved by setting the frequency to 10 Hz and the step potential to 5 mV vs. Ag/AgCl. The electrochemical measurements were performed using the three-electrode screen-printed system cell, that is, working electrode (area = 0.13 cm²) and auxiliary (carbon) and reference electrodes (Ag/AgCl). The SPCE was inserted into 3 ml electrolyte solution which was bubbled with argon gas to remove dissolved oxygen. The working electrode surface was activated by five scans using the cyclic voltammetry technique at 50 mV/s, prior to data collection in electrochemical characterization of material and evaluation of the selected analyte. These

instrumental parameters were consistently applied to all electrochemical experiments.

RESULTS AND DISCUSSION

The solubility of PAA was tested in phosphate buffer, DMF, DMac, acetic acid, chloroform water, dimethyl sulfoxide (DMSO), acetone, NMP, acetonitrile (ACN), tetrahydrofuran (THF), methanol, chloroform, diethyl ether, and tetrahydrofuran/methanol (1:1 ratio) at concentrations 1, 5, 10, and 20% wt. PAA. However, polyamic acid was found to be completely soluble in DMF and DMac, which are high-boiling point aprotic solvents (153°C and 165.1°C, respectively) (see **Supplementary Table S1.1**).

Chemically synthesized PAA did not provide solutions in DMF and DMac for spinning on its own. Low concentrations of PVP (1, 2, 3, and 5% by wt.) were added to 12% by wt. PAA solutions using DMF and DMac, respectively. Each of these solutions were tested in terms of the quality of nanofibers that could be produced under the optimized instrumental parameters. The optimal spinning solution was produced from 12% by wt. PAA and 3% by wt. (see **Supplementary Table S1.2**). PVP dissolved in DMF yielded fine nanofibers with minimal beading. The morphology of freestanding PAA nanofibers produced from the custom-made electrospinning instrument (University of Missouri, United States) was determined by a scanning electron microscope (SEM), and thermogravimetric analysis (TGA) was used to study the thermal stability of the fibers. The diameters of the bead-free PAA fibers varied from 100 nm to 100 μm (see **Supplementary Figure S1.1**). The thermal degradation pathway showed a small change in weight percentage (3.57%) at 53°C which was attributed to water and solvent (DMF) evaporation. At a higher temperature (194°C), a further weight loss (12.76%) was observed and was assigned to water loss resulting in imidization of PAA. Above 300°C, no significant weight loss steps were observed (**Figure 1**).

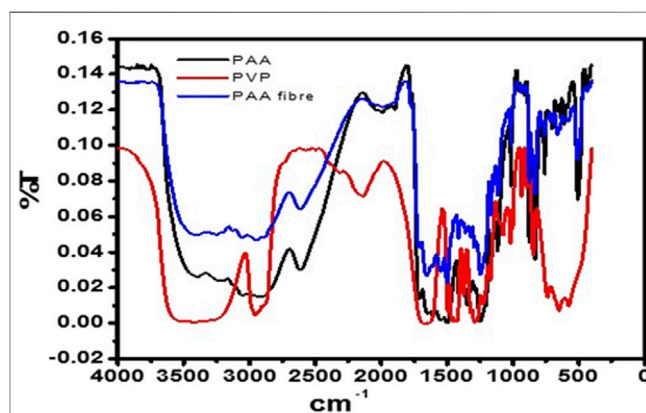


FIGURE 2 | FTIR spectrum of pure PAA powder, PVP, and PAA nanofibers.

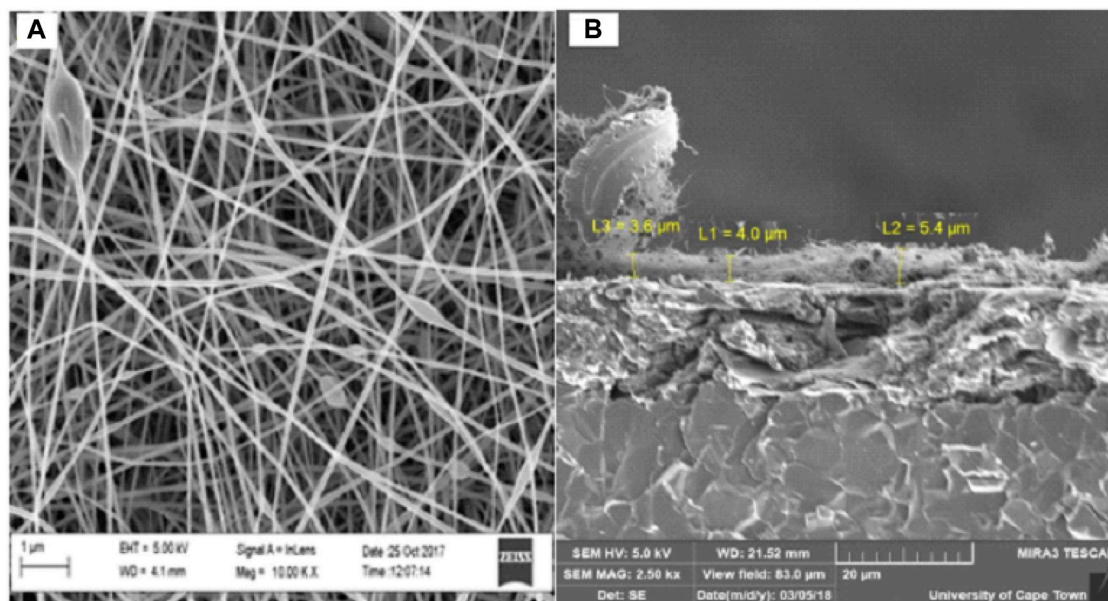


FIGURE 3 | HRSEM (A) at 100,00x and cross-sectional SEM (B) at 5,000x images of PAA nanofibers.

Fourier Transform Infrared Spectroscopy Characterization

The free-standing nanofibers were collected on aluminum foil. FTIR spectra (Figure 2) of PAA powder (chemically synthesized) and stand-alone nanofibers were recorded over the range of $4,000\text{ cm}^{-1}$ to $1,000\text{ cm}^{-1}$, from prepared potassium bromide (KBr) pellets. The FTIR spectra of the PAA nanofibers and chemically synthesized PAA were found to be in good agreement with literature reports (Noah et al., 2012; Hess et al., 2014; Aduba et al., 2015; Lubasova et al., 2015). The absorption bands that occur at around $3,254\text{ cm}^{-1}$, $1,649\text{ cm}^{-1}$, and $1,392\text{ cm}^{-1}$ indicate the presence of the amide group, whereas the bands occurring at around $2,612\text{ cm}^{-1}$ (broad) were assigned to the vibrational modes of carboxylic acid. A spike appearing at $3,049\text{ cm}^{-1}$ was assigned to the NH stretching vibration. The strong peak at around $1,239\text{ cm}^{-1}$ was indicative of the stretching vibrations of the ether group. The FTIR spectra confirmed the integrity of the PAA prepared as nanofibers from electrospinning, by comparison with literature reports as well as with the FTIR data obtained for the chemically synthesized PAA, also done in this work.

Scanning Microscopy Characterization

The high-resolution scanning electron microscope (HRSEM) provides electron backscattering images of the deposited spun nanofibers directly onto a screen-printed carbon electrode (SPCE). SEM images of the PAA nanofibers were identified as an entwined network of nanoscale dimension fibers (Figure 3A). The diameters of the nanofibers shown in these SEM images were estimated at 1–100 nm. The cross-sectional SEM in Figure 3B showed that nanofibers had an average layer thickness of $4.3\text{ }\mu\text{m}$ ($n = 4$). Average layer thickness for electrodeposited PAA films

was measured to be $17.63\text{ }\mu\text{m}$ ($n = 4$, five scans) and $26.54\text{ }\mu\text{m}$ ($n = 4$, 20 scans). The increased layer thickness is due to the space trapped within the nanofiber networks, resulting in a highly porous material with enhanced surface area and robustness. Thus, electrospinning is able to produce intact, mechanically stable, and high-surface area nanofiber networks spun directly onto the working electrode surface of the commercial SPCE. The efficient control over the nanomaterial structure and deposition demonstrated here with the electrospinning of PAA is a major advantage in the design of highly reactive electrocatalysts for a wide range of applications.

Atomic Force Microscopy

The atomic force microscopy (AFM) was used to obtain topographical images in the contact mode of PAA nanofibers (Figure 4), which reports the frequency shift ($df = f - f_0$) as a function of the X–Y variation in height without regulation in the z-direction (Zamfir et al., 2016). A sample with height and depth shows the distance variation between the tip–apex and the sample for a scan of the sample along the x–y direction without height regulation in the z-direction. The average height distribution of PAA nanofibers was measured as $6.02\text{ }\mu\text{m}$.

The AFM provides a top-down force sensing measurement of depth. The HRSEM provides surface imaging of the nanofibers in a similar top-down approach but with actual surface feature data generated from backscattered electron imaging. The HRSEM identified the structural arrangement of the nanofibers on the electrode and showed a controlled mesh of nanofibers. The cross-sectional SEM imaging of these nanofibers provided a deep distribution profile of the nanofibers and the entrapped pores between them, showing clearly that the nanofibers have a very dense packing close to the electrode surface, becoming porous as we move away from the electrode surface. This supports the

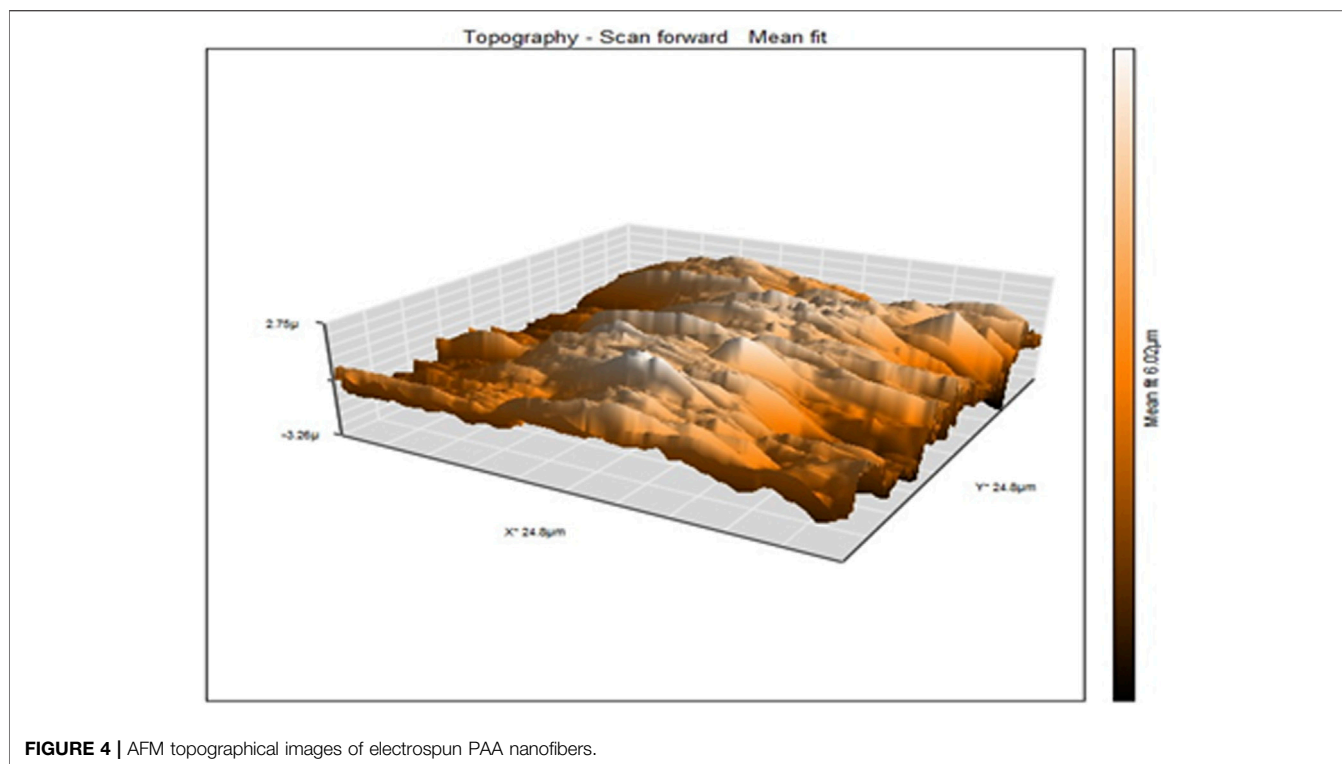


FIGURE 4 | AFM topographical images of electrospun PAA nanofibers.

characterization of the deposited nanofibers as a 3D network at the electrode surface from which diffusional properties were assessed.

Nitrogen Adsorption–Desorption

Isothermal N_2 measurements were used to study the surface structures of the freestanding polyamic acid (PAA) nanofibers. Based on the BET measurements [see **Supplementary Figure SI.3**], the surface area of the PAA nanofibers was found to be $13.9 \text{ m}^2/\text{g}$, comparable to the surface area of synthesized carbon-based nanomaterials such as multi-walled carbon nanotubes with BET surface area ranging from nine up to $500 \text{ m}^2/\text{g}$ (Lehman et al., 2011; Tetana et al., 2012).

Cyclic voltammetry of the PAA/SPCE prepared by electrospinning PAA nanofibers directly onto a screen-printed electrode (SPCE) was recorded at scan rates ranging from 10 to 100 mV/s . The redox behavior of PAA nanofibers observed from CV (see **Supplementary Figure SI.4**) was characteristic of PAA electrochemistry reported for PAA thin films and chemically synthesized PAA powders (Andreescu et al., 2005; Hamnca et al., 2017). PAA nanofiber electrodes showed two anodic peaks at 73 and 350 mV , respectively, with two cathodic peaks at 11 and 268 mV , vs Ag/AgCl. The peak currents reported for these peaks as a function of increasing scan rate between 10 and 100 mV/s showed a linear dependency, with a peak separation of 62 mV supporting a conclusion of a diffusion-controlled reversible process. The porous nature of the nanofiber arrangement, evidenced by cross-sectional SEM, allows for diffusion of ions into these spaces as well as electron diffusion within the polymer

nanofiber network. This supports the characterization of the deposited nanofibers as a 3D network at the electrode surface from which diffusional properties were assessed.

The PAA nanofibers displayed enhanced peak resolution in terms of peak shape and redox current intensity, attributed directly due to the high surface area and porosity of the spun fiber networks. The number of electrons transferred was calculated from peak a and a' in the CV data collected at PAA/SPCE using the following equation:

$$E_p - E_{p_{1/2}} = 2.20 RT/nF = 56.5/n, \quad (1)$$

where E_p is the maximum peak potential, $E_{p_{1/2}}$ is half maximum peak potential, R is the gas constant ($8.314 \text{ J}\cdot\text{mol}^{-1}\cdot\text{K}^{-1}$), T represents the absolute temperature (298 of the gas system), n is the number of electrons, and F is the Faraday constant ($96,584 \text{ C/mol}$). The a/a' redox chemistry was found to be a one-electron transfer process associated with the amine functionality of surface bound PAA/SPCE. The surface concentrations of physically adsorbed PAA nanofibers onto the SPCE was estimated from the plot of peak current vs potential at a scan of 50 mV/s (see **Supplementary Figure SI.5**) using the following equation (Brown–Anson model) (Brown and Anson, 1977):

$$I_p = n^2 F^2 I^* A v / 4RT, \quad (2)$$

where I_p is the cathodic/anodic peak current at a different scan rate, A was taken as the surface area of the unmodified electrode (0.13 cm^2), v is the scan rate (V/s), I^* is the surface concentration (mol cm^{-2}), and F , R , and T are the same as in **Eq. 1**. The surface

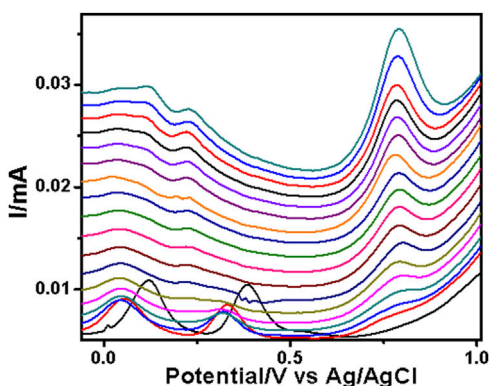


FIGURE 5 | SWV analysis of the sulfadiazine at the PAA nanofiber-modified screen-printed electrode (SPCE) in 0.1 M Tris-HCl with concentrations ranging from 25 to 250 μM at 50 mVs.

concentration was calculated to be $2.14 \times 10^{-6} \text{ mol/cm}^2$. The Randles-Sevcik plot (see **Supplementary Figure SI.4**) was used to calculate the diffusion coefficient (D_e) of the screen-printed carbon-PAA nanofiber electrode. The diffusion coefficient (D_e) of the SPCE-PAA nanofiber electrode was calculated to be $9.43 \times 10^{-7} \text{ cm}^2/\text{s}$. The values reported the literature for diffusion-controlled behavior of PAA thin film-coated electrode surfaces are $6.35 \times 10^{-7} \text{ cm}^2/\text{s}$ (electrodeposited using cyclic voltammetry onto a gold electrode between -500 and $1,000$ mV using 50 cycles at a scan rate of 50 mV/s), $7.10 \times 10^{-6} \text{ cm}^2/\text{s}$ (electrodeposited onto a glassy carbon electrode using 20 cycles between -400 mV and $+600$ mV at a scan rate of 50 mV/s), and $5.25 \times 10^{-6} \text{ cm}^2/\text{s}$ (electrochemically deposited onto a glass carbon electrode using five cycles between $-1,000$ mV and $+1,000$ mV at a scan rate of 50 mV/s (Noah et al., 2012; Hess et al., 2014; Ngema et al., 2019)). The diffusion coefficient calculated in this work falls in the range of the reported values for PAA-coated electrodes.

Electroanalytical Profiling of Sulfonamides

The PAA nanofiber modified screen-printed electrodes were used for the analytical reporting of sulfonamides in aqueous medium. A well-defined peak was observed at $0.79 \text{ V vs. Ag/AgCl}$ (**Figure 5**) for sulfadiazine oxidation and at $0.78 \text{ V vs. Ag/AgCl}$ (**Figure 6**) for sulfamethazine oxidation. The sulfonamide functionality typically reports an oxidation peak assigned to the oxidation of the para position $-\text{NH}_2$ group (Voorhies and Adams, 1958), at potentials ranging from 0.70 to $1.02 \text{ V vs. Ag/AgCl}$ (Fotouhi and Zabeti, 2014; Ebrahimi et al., 2017; Su and Cheng, 2018). The sulfonamides evaluated in this work showed oxidation peaks between 0.75 and $0.78 \text{ V vs. Ag/AgCl}$, depending on the specific sulfonamide drug investigated. The oxidation current is due to the para $-\text{NH}_2$ group, common to all of the sulfonamide drugs evaluated. The small shifts in potential are due to the polymer nanofibers, which attenuates the electron transfer.

The two peaks observed at $-0.03 \text{ V vs. Ag/AgCl}$ and $0.25 \text{ V vs. Ag/AgCl}$ were attributed to the porous electrospun polymer material. The sulfadiazine (**Figure 7**) and sulfamethazine

(**Figure 8**) showed excellent linear regression response for the concentration range evaluated, at the PAA nanofiber-modified electrodes, with R^2 values of 0.998 and 0.997 ($n = 3$), respectively. The limit of detection (LOD) of sulfadiazine and sulfamethazine was based on the oxidation of the para $-\text{NH}_2$ group observed at $0.78 \text{ V vs. Ag/AgCl}$. The LOD was found to be $8.26 \pm 2.07 \text{ }\mu\text{M}$ and $8.81 \pm 3.06 \text{ }\mu\text{M}$, respectively. The PAA nanofiber-modified screen-printed electrodes showed good sensitivity toward sulfadiazine ($0.05 \pm 0.01 \text{ }\mu\text{A Lmol}^{-1}$) and sulfamethazine ($0.07 \pm 0.02 \text{ }\mu\text{A }\mu\text{mol}^{-1}$), which we believe is due to the higher surface area and porosity of the nanofibers network enhancing the catalytic efficiency of the oxidation. However, the reproducibility of the repeated experiments for sulfamethazine was not as good as that for sulfadiazine. Sulfamethazine has methyl group substituents that may affect its alignment at the sensor interface and consequently impact reproducibility.

A comparison of the sensitivity of carbon-based nanomaterial electrodes toward sulfonamide detection showed that carbon nanotubes and PAA electrospun nanofibers outperformed nanoparticles, molecularly imprinted methods, and polymer blends used in the preparation of transducers for the detection of sulfonamides using the SWV method (Sadeghi and Motaharian, 2013; Fotouhi and Zabeti, 2014; Ebrahimi et al., 2017; Su and Cheng, 2018; Urzúa et al., 2018). The implication of the structure and size as opposed to size only, in efficiency of catalysis, is therefore substantiated. The major contribution of this work lies in the successful synthesis and characterization of PAA nanofibers onto SPCE, which to the best of our knowledge has been reported for the first time here. The analytical reporting parameters of LOD and sensitivity are not the lowest reported values but are still competitive compared to other carbon base materials and polymers as the tables demonstrate (**Supplementary Tables S1.3, S1.4**). In terms of analytical performance enhancement, in this particular application, the surface modification of the SPCE resulted in a wider linear range and lower potential for the analytical peak (**Supplementary Tables S1.5.1–3**). The sensors therefore

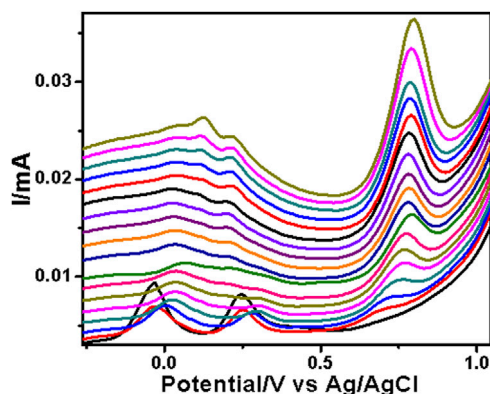


FIGURE 6 | SWV analysis of the sulfamethazine at the PAA nanofiber-modified screen-printed electrode (SPCE) in 0.1 M Tris-HCl with concentrations ranging from 25 to 250 μM at 50 mVs.

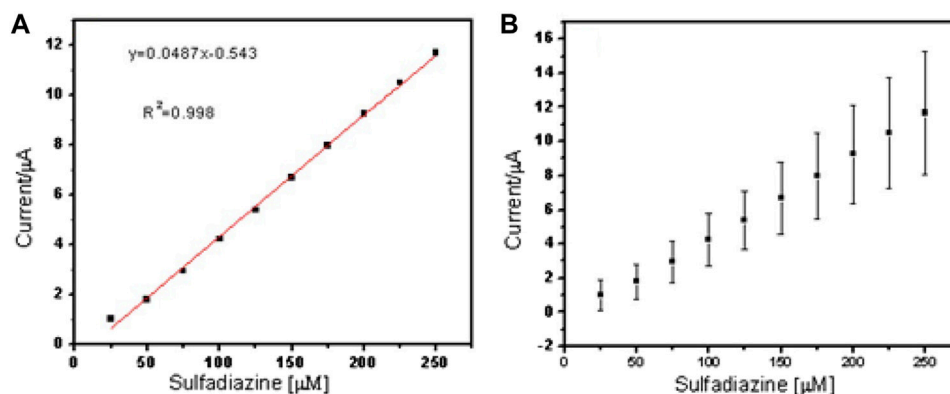


FIGURE 7 | Linear regression plot of current against concentration of sulfadiazine (A) and (B) standard error bar plot from the standard deviation ($n = 3$).

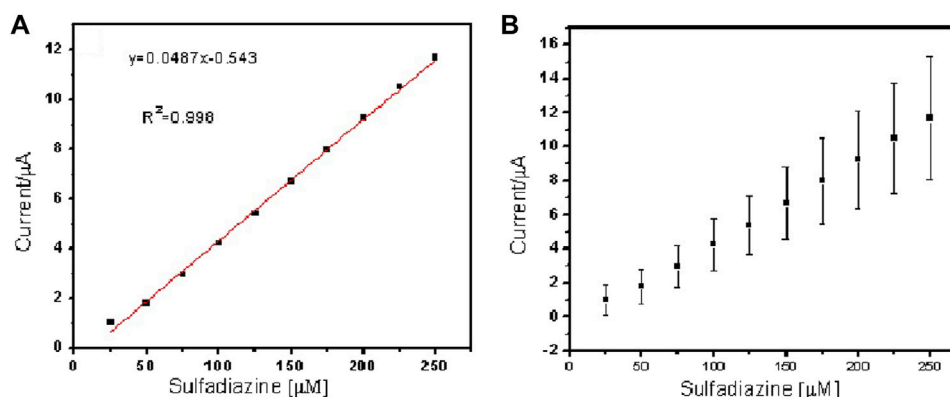


FIGURE 8 | Linear regression plot of current against concentration of sulfamethazine (A) and (B) standard error bar plot from the standard deviation ($n = 3$).

present a robust option for sulfonamide detection in aqueous systems.

CONCLUSION

The solubility behavior of polymers is crucial in its application as thin film devices such as sensors, photovoltaic cells, and interpenetrating network actuators. We have shown that PAA could be uniformly dispersed in two key organic solvents at relatively high-concentration loading. Subsequently, the critical mass for efficient electrospinning of PAA could be achieved by minimal incorporation of a carrier polymer, which resulted in highly dispersed, uniform nanofibers which could be deposited directly onto the working electrode area of commercial SPCE as well as freestanding nanofibers. The carrier polymer (PVP) did not influence the redox electrochemistry of the PAA as evidenced by the pronounced electrochemical reporting signals obtained. Quantitative analysis of selected sulfonamides corroborated the implication of size and structure on the performance of nano-electrocatalysts. The freestanding PAA nanofibers have potential

applications as robust portable electrodes in real-world sensor applications.

DATA AVAILABILITY STATEMENT

The original contributions presented in the study are included in the article/**Supplementary Material**; further inquiries can be directed to the corresponding authors.

AUTHOR CONTRIBUTIONS

All authors listed have made a substantial, direct, and intellectual contribution to the work and approved it for publication.

FUNDING

The research was funded by the University of the Western Cape and the National Research Foundation, South Africa.

ACKNOWLEDGMENTS

The authors would like to acknowledge the National Research Foundation (South Africa) and the University of Missouri South African Exchange Program (UMSAEP).

REFERENCES

- Aduba, D. C., Overlin, J. W., Frierson, C. D., Bowlin, G. L., and Yang, H. (2015). Electrospinning of PEGylated Polyamidoamine Dendrimer Fibers. *Mater. Sci. Eng. C* 56, 189–194. doi:10.1016/j.msec.2015.06.025
- Andreescu, D., Wanekaya, A. K., Sadik, O. A., and Wang, J. (2005). Nanostructured Polyamic Acid Membranes as Novel Electrode Materials. *Langmuir* 21 (15), 6891–6899. doi:10.1021/la050141k
- Brown, A. P., and Anson, F. C. (1977). Cyclic and Differential Pulse Voltammetric Behavior of Reactants Confined to the Electrode Surface. *Anal. Chem.* 49 (11), 1589–1595. doi:10.1021/ac50019a033
- Chandrasekar, R., Zhang, L., Howe, J. Y., Hedin, N. E., Zhang, Y., and Fong, H. (2009). Fabrication and Characterization of Electrospun Titania Nanofibers. *J. Mater. Sci.* 44 (5), 1198–1205. doi:10.1007/s10853-008-3201-1
- Chen, K., Chou, W., Liu, L., Cui, Y., Xue, P., and Jia, M. (2019). Electrochemical Sensors Fabricated by Electrospinning Technology: An Overview. *Sensors* 19 (17), 3676. doi:10.3390/s19173676
- Ebrahimi, M., Nikoofard, H., Faridbod, F., Dezfali, A. S., Beigzadeh, H., and Norouzi, P. (2017). A Ceria NPs Decorated Graphene Nano-Composite Sensor for Sulfadiazine Determination in Pharmaceutical Formulation. *J. Mater. Sci. Mater. Electron.* 28 (22), 16704–16712. doi:10.1007/s10854-017-7583-1
- Fotouhi, L., and Zabeti, M. (2014). Electrochemical Oxidation of Sulfamethazine on Multi-Walled Nanotube Film Coated Glassy Carbon Electrode. *J. Nanostructures* 4 (2), 161–166.
- Frenot, A., and Chronakis, I. S. (2003). Polymer Nanofibers Assembled by Electrospinning. *Curr. Opin. Colloid Interf. Sci.* 8 (1), 64–75. doi:10.1016/s1359-0294(03)00004-9
- Hamnca, S., Phelane, L., Iwuoha, E., and Baker, P. (2017). Electrochemical Determination of Neomycin and Norfloxacin at a Novel Polymer Nanocomposite Electrode in Aqueous Solution. *Anal. Lett.* 50 (12), 1887–1896. doi:10.1080/00032719.2016.1261876
- Hamnca, S., Ward, M., Ngema, X. T., Iwuoha, E. I., and Baker, P. G. L. (2016). Development of Graphenated Polyamic Acid Sensors for Electroanalytical Detection of Anthracene. *J. NanoR* 43, 11–22. doi:10.4028/www.scientific.net/jnanor.43.11
- Hess, E. H., Waryo, T., Sadik, O. A., Iwuoha, E. I., and Baker, P. G. L. (2014). Constitution of Novel Polyamic Acid/polypyrrole Composite Films by *In-Situ* Electropolymerization. *Electrochimica Acta* 128, 439–447. doi:10.1016/j.electacta.2014.01.038
- Lehman, J. H., Terrones, M., Mansfield, E., Hurst, K. E., and Meunier, V. (2011). Evaluating the Characteristics of Multiwall Carbon Nanotubes. *Carbon* 49 (8), 2581–2602. doi:10.1016/j.carbon.2011.03.028
- Lubasova, D., Niu, H., Zhao, X., and Lin, T. (2015). Hydrogel Properties of Electrospun Polyvinylpyrrolidone and Polyvinylpyrrolidone/poly(acrylic Acid) Blend Nanofibers. *RSC Adv.* 5 (67), 54481–54487. doi:10.1039/c5ra07514a
- Machotová, J., Zárybnická, L., Bačovská, R., and Černošková, E. (2016). Electrospinning of Styrene-Ethyl Acrylate Emulsion Copolymers: Exploring the Impact of Polymer Polarity and Glass Transition Temperature on Fiber Formation and Hydrophobicity. *Polymer-Plastics Tech. Eng.* 55 (4), 423–431.
- Ngema, X. T., Baker, P., Ajayi, F., Aubert, P.-H., and Banet, P. (2019). Polyamic Acid (PAA) Immobilized on Glassy Carbon Electrode (GCE) as an Electrochemical Platform for the Sensing of Tuberculosis (TB) Antibodies and Hydrogen Peroxide Determination. *Anal. Lett.* 53, 1–20. doi:10.1080/00032719.2019.1636058
- Noah, N. M., Omole, M., Stern, S., Zhang, S., Sadik, O. A., Hess, E. H., et al. (2012). Conducting Polyamic Acid Membranes for Sensing and Site-Directed Immobilization of Proteins. *Anal. Biochem.* 428 (1), 54–63. doi:10.1016/j.ab.2012.06.008
- Sadeghi, S., and Motaaharian, A. (2013). Voltammetric Sensor Based on Carbon Paste Electrode Modified with Molecular Imprinted Polymer for Determination of Sulfadiazine in Milk and Human Serum. *Mater. Sci. Eng. C* 33 (8), 4884–4891. doi:10.1016/j.msec.2013.08.001
- Sapountzi, E., Braiek, M., Chateaux, J.-F., Jaffrezic-Renault, N., and Lagarde, F. (2017). Recent Advances in Electrospun Nanofiber Interfaces for Biosensing Devices. *Sensors* 17 (8), 1887.
- Saquin, C. D., Tang, C., Monian, B., Bonino, C. A., Manasco, J. L., Alsberg, E., et al. (2013). Alginate-Polyethylene Oxide Blend Nanofibers and the Role of the Carrier Polymer in Electrospinning. *Ind. Eng. Chem. Res.* 52 (26), 8692–8704. doi:10.1021/ie302385b
- Su, Y.-L., and Cheng, S.-H. (2018). A Novel Electroanalytical Assay for Sulfamethazine Determination in Food Samples Based on Conducting Polymer Nanocomposite-Modified Electrodes. *Talanta* 180, 81–89. doi:10.1016/j.talanta.2017.12.026
- Sun, L., Chen, L., Sun, X., Du, X., Yue, Y., He, D., et al. (2009). Analysis of Sulfonamides in Environmental Water Samples Based on Magnetic Mixed Hemimicelles Solid-phase Extraction Coupled with HPLC-UV Detection. *Chemosphere* 77 (10), 1306–1312. doi:10.1016/j.chemosphere.2009.09.049
- Tetana, Z. N., Mhlana, S. D., Bepete, G., Krause, R. W. M., and Coville, N. (2012). The Synthesis of Nitrogen-Doped Multiwalled Carbon Nanotubes Using an Fe-Co/CaCO₃ Catalyst. *South Afr. J. Chem.* 65, 39–49.
- Urzúa, L., Pérez-Ortiz, M., and Álvarez-Lueje, A. (2018). Electrocatalytic Oxidation and Voltammetric Determination of Sulfamethazine Using a Modified Carbon Electrode with Ionic Liquid. *J. Chilean Chem. Soc.* 63 (1), 3914–3917.
- Valizadeh, A., and Mussa Farkhani, S. (2013). Electrospinning and Electrospun Nanofibers. *IET Nanobiotechnol* 8 (2), 83–92. doi:10.1049/iet-nbt.2012.0040
- Voorhies, J. D., and Adams, R. N. (1958). Voltammetry Solid Electrodes. Anodic Polarography of Sulfa Drugs. *Anal. Chem.* 30 (3), 346–350. doi:10.1021/ac60135a010
- Wang, X., Pellerin, C., and Bazuin, C. G. (2016). Enhancing the Electrospinnability of Low Molecular Weight Polymers Using Small Effective Cross-Linkers. *Macromolecules* 49 (3), 891–899. doi:10.1021/acs.macromol.5b02670
- Zamfir, L.-G., Rotariu, L., Marinescu, V. E., Simelane, X. T., Baker, P. G. L., Iwuoha, E. I., et al. (2016). Non-enzymatic Polyamic Acid Sensors for Hydrogen Peroxide Detection. *Sensors Actuators B: Chem.* 226, 525–533. doi:10.1016/j.snb.2015.12.026

SUPPLEMENTARY MATERIAL

The Supplementary Material for this article can be found online at: <https://www.frontiersin.org/articles/10.3389/fchem.2021.782813/full#supplementary-material>

Conflict of Interest: The authors declare that the research was conducted in the absence of any commercial or financial relationships that could be construed as a potential conflict of interest.

Publisher's Note: All claims expressed in this article are solely those of the authors and do not necessarily represent those of their affiliated organizations, or those of the publisher, the editors, and the reviewers. Any product that may be evaluated in this article, or claim that may be made by its manufacturer, is not guaranteed or endorsed by the publisher.

Copyright © 2022 Hamnca, Chamier, Grant, Glass, Iwuoha and Baker. This is an open-access article distributed under the terms of the Creative Commons Attribution License (CC BY). The use, distribution or reproduction in other forums is permitted, provided the original author(s) and the copyright owner(s) are credited and that the original publication in this journal is cited, in accordance with accepted academic practice. No use, distribution or reproduction is permitted which does not comply with these terms.



Aroma Clouds of Foods: A Step Forward to Unveil Food Aroma Complexity Using GC × GC

Sílvia M. Rocha*, Carina Pedrosa Costa and Cátia Martins

LAQV-REQUIMTE and Departamento de Química, Universidade de Aveiro, Campus Universitário Santiago, Aveiro, Portugal

OPEN ACCESS

Edited by:

Eugenia Gallardo,
Universidade da Beira Interior,
Portugal

Reviewed by:

Chiara Emilia Irma Cordero,
University of Turin, Italy
Henryk Jeleń,
Poznan University of Life Sciences,
Poland

*Correspondence:

Sílvia M. Rocha
smrocha@ua.pt

Specialty section:

This article was submitted to
Analytical Chemistry,
a section of the journal *Frontiers in
Chemistry*

Received: 23 November 2021

Accepted: 24 January 2022

Published: 01 March 2022

Citation:

Rocha SM, Costa CP and Martins C
(2022) Aroma Clouds of Foods: A Step
Forward to Unveil Food Aroma
Complexity Using GC × GC.
Front. Chem. 10:820749.
doi: 10.3389/fchem.2022.820749

The human senses shape the life in several aspects, namely well-being, socialization, health status, and diet, among others. However, only recently, the understanding of this highly sophisticated sensory neuronal pathway has gained new advances. Also, it is known that each olfactory receptor cell expresses only one type of odorant receptor, and each receptor can detect a limited number of odorant substances. Odorant substances are typically volatile or semi-volatile in nature, exhibit low relative molecular weight, and represent a wide variety of chemical families. These molecules may be released from foods, constituting clouds surrounding them, and are responsible for their aroma properties. A single natural aroma may contain a huge number of volatile components, and some of them are present in trace amounts, which make their study especially difficult. Understanding the components of food aromas has become more important than ever with the transformation of food systems and the increased innovation in the food industry. Two-dimensional gas chromatography and time-of-flight mass spectrometry (GC × GC-ToFMS) seems to be a powerful technique for the analytical coverage of the food aromas. Thus, the main purpose of this review is to critically discuss the potential of the GC × GC-based methodologies, combined with a headspace solvent-free microextraction technique, in tandem with data processing and data analysis, as a useful tool to the analysis of the chemical aroma clouds of foods. Due to the broad and complex nature of the aroma chemistry subject, some concepts and challenges related to the characterization of volatile molecules and the perception of aromas will be presented in advance. All topics covered in this review will be elucidated, as much as possible, with examples reported in recent publications, to make the interpretation of the fascinating world of food aroma chemistry more attractive and perceptive.

Keywords: foodstuff, beverages, aroma clouds, volatile organic compounds, SPME, GC × GC, data processing, data analysis

INTRODUCTION

Since the beginning of life on earth, smell has been known to allow communication between species, and recover or stimulate memory. The aromas have always fascinated mankind, even in prehistorical times. For instance, the use of scented materials, which were used to flavor various products and environments, mimicking nature's aromas, is documented since early history. The first odorous materials used were extracts obtained from natural products. The advent of organic chemistry and the advances in analytical instrumentation allowed the isolation and structural identification of odor-



FIGURE 1 | Aroma clouds of foods: a set of odorant volatile and semi-volatile molecules, released from foods, namely from liquid, solid, paste, or others, which are responsible for their aroma properties, here illustrated with white wine and espresso.

active compounds from natural extracts and their consequent syntheses made it possible to produce these compounds on an industrial scale for use in many applications (Pickenhagen, 2017). Nowadays, natural odorants or synthetic ones are largely used in perfumery, agri-food industries, as well as in textile, automobiles, and flavoring industries, among others. Particularly, the food aroma is of major concern for academics or industrials as it represents a significant factor influencing the public's food-buying decisions and has also been associated with food quality and safety.

Odorous compounds are typically volatile or semi-volatile in nature and have low relative molecular weight (i.e., the majority below 300). Despite this apparently limited range, odorous compounds embody a broad variety of substance classes that comprise diverse structural moieties, such as ester, alcohol, ketone, carboxylic acid, and aldehyde functions, among others; having aromatic or aliphatic forms; and may also include heteroatomic groups (Baldovini, 2017). Odorous molecules may be released from foods, namely from liquid, solid, paste, or others, constituting clouds surrounding them, and are responsible for their aroma notes (Figure 1). The qualitative and quantitative analyses of these molecules, as well as the knowledge of their origin and possible modifications, for instance, during ripening, processing, or storage, are crucial to understand and modulate the aroma properties of foods, and their perception by the consumers.

The aroma of food products is currently evaluated based on sensorial analysis, which translates information closer to what is perceived by humans. However, the implementation of classical sensorial assays is time consuming and expensive, and not all companies and research laboratories are able to maintain the regular functioning of panels. Innovative methodologies that combine sensorial and instrumental data have been developed, namely gas chromatography–olfactometry (GC-O) or electronic noses (Fuller et al., 1964; Delahunty et al., 2006; Giungato et al., 2018; Song and Liu, 2018). Although the chemical characterization by itself fails to reconstruct the final aroma perception that provides useful information about composition and mechanisms of aroma formation, there is nowadays a great interest in understanding the aroma clouds at the level of the molecules that compose them, which justifies the need for the use of robust and highly sensitive techniques. For instance, innovative enhancements, such as smell digitalization and sensomics, which are multi-step analytical approaches, are used to obtain the multipart odor picture of a food, including the identification and accurate quantitation of odorant molecules. Indeed, smell digitalization allows the measuring and chemically revealing of the smells to make them into a digital presentation, which represents cutting-edge research, and usually using artificial intelligence to interpret the odor signatures. Also, sensomics is an approach developed to help in the mapping of both aroma and taste key active molecules, which are perceived by humans'

chemosensory receptors and then integrated by the brain (Schieberle and Hofmann, 2011).

In the last decades, the development of highly sensitive equipment has catalyzed a growing interest in obtaining as detailed information as possible on the volatile composition of foods. These extremely sensitive equipment, as for instance comprehensive two-dimensional gas chromatograph coupled to mass spectrometer with time-of-flight analyzer (GC \times GC-ToFMS) or even high-resolution MS, enabled the study of complex samples, with hundreds of components and the measurement of volatile fraction of food products in quantities at the nanogram, picogram, and even lower levels. Also, the solid-phase microextraction (SPME) technique represents a highly efficient sample preparation step before chromatographic determination of volatiles and fulfills the requirements necessary for sustainable development and implementation of green chemistry principles in analytical laboratories (Spietelun et al., 2013; de Souza et al., 2018).

The main purpose of this review is to critically discuss the potential of the GC \times GC-based methodologies, combined with a headspace solvent-free microextraction technique (SPME), in tandem with data processing and data analysis, and as a useful tool to the coverage of the chemical aroma clouds of foods. Also because of the comprehensive and complex nature of the aroma chemistry subject, some concepts and challenges related to the characterization of volatile molecules, and the perception of aromas will be presented in advance. All topics covered in this review will be elucidated, as much as possible, with examples reported in recent publications, to make the interpretation of the fascinating world of food aroma chemistry more attractive and perceptive.

Food Aroma Chemistry: From Olfaction to the Odorant Molecules

Of all five senses, olfaction is the most complex molecular mechanism, as it comprises hundreds of receptor proteins enabling it to detect and discriminate thousands of odorant molecules (Menashe and Lancet, 2006). The understanding of this highly sophisticated sensory neuronal pathway has gained new advances. The sequencing of the human genome and the consequent advances on the associated genomic tools have opened new opportunities to better comprehend this multifaceted biological system.

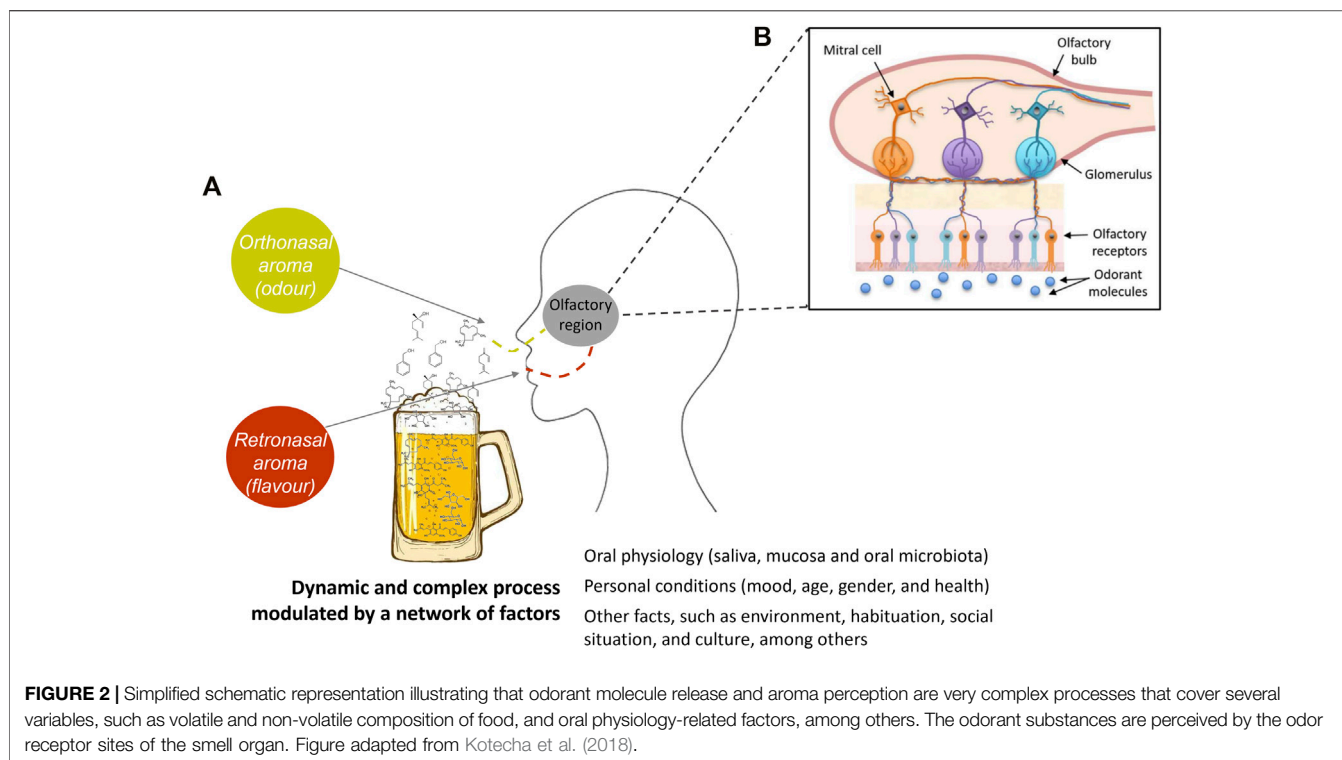
According to Buck and Axel (1991), 3% of our genes are used to code the different odorant receptors, which are located on the olfactory receptor cells in the nasal cavity (Figure 2). Each olfactory receptor cell expresses only one type of odorant receptor, and each receptor can detect a limited number of odorant substances. When an odorant receptor is activated by an odorant molecule, an electric signal is produced in the olfactory receptor cell and sent to the brain via nerve processes. Buck and Axel (1991) also showed that each odorant receptor first activates a G protein, to which it is coupled, and which in turn stimulates the formation of cAMP (cyclic adenosine monophosphate). This messenger molecule

activates ion channels, which are opened, and the cell is activated. The large family of odorant receptors belongs to the G protein-coupled receptors (GPCR) that differ in certain details, explaining why they are triggered by different odorant molecules (Buck and Axel, 1991; Menashe and Lancet, 2006).

The odorant substances are volatile compounds that are perceived by the odor receptor sites of the smell organ. This perception mechanism can be modulated by several factors associated to the individual, such as physiological characteristics, health condition, previous experiences, culture, and among others (Figure 2). Otherwise, the release of odorant compounds, i.e., their phase transfer from liquid, solid, paste, or other foods into the headspace surrounding, is also a huge element on this dynamic process and depends on numerous intrinsic factors of each molecule, such as interaction, and/or retention phenomena with non-volatile molecules, as well as the environmental conditions (pressure and temperature).

There are two routes of aroma perception: 1) orthonasal detection is when an individual smells food before eating it and the molecules enter the nose through the nostrils and reach the receptors; 2) retronasal detection is when an individual masticates and swallows food during eating (Figure 2). Mastication releases more aroma substances, and these molecules are carried to the throat when the food is swallowed, and then carried to the nose through breath out. Orthonasal or retronasal presentation of odorants evokes different responses, as the way odorant absorption occurs across the mucosa determines the way in which the olfactory epithelium responds (Negoias et al., 2008; Belitz et al., 2009a). The aroma perception, i.e., its recognition, depends on the characteristics of the odorant molecules and their respective concentration that reaches the human olfactory system, and on the nasal and oral physiology mucosa and microbiota. It also depends on the experiences and memories of the individual and their sensory acuity. For example, an individual who has never experienced a certain aroma will never recognize it and associate it with specific notes. Also, for each individual, changes in the thresholds of a given compound and perception of aromas may be observed with moods, time of the biorhythm, and with hunger or satiety, and even with age (Mobley et al., 2013).

More recently, innovative aroma-related initiatives have emerged such as the digital olfaction that mimics the way humans smell. As human sense of smell, digital olfaction mimics the process by which the brain identifies and differentiates odors, by involving a sensor, acting as the nose or receptor for aroma molecules, and associated software that interprets information from the sensor based on a database previously collected and analyzed, and then digitally presents them. It includes an initial advanced chromatographic analysis to chemically characterize the smells. New advances have been performed in this sense by design olfactory metamers—pairs of non-overlapping molecular compositions that generate identical odor percepts (Ravia et al., 2020). With the help of human volunteers (trained and untrained), accurate predictions of perceptual similarity were obtained, suggesting that a valid olfactory measure was achieved, and a step forward to the digitization of smell. The evolution of the digital smell goes



toward the digital scent technology (or olfactory technology) that is a technology to sense, transmit, and receive scent-enabled digital media (such as web pages, video games, movies, and music) (Viswanathan and Rajan, 2020).

It is notoriously difficult to study the molecules that produce aromas because a single natural aroma may contain hundreds or even thousands of volatile components, and some of them present in trace amounts. Understanding the components of food aromas has become more important than ever with the transformation of food systems and the increased innovation in the food industry. Indeed, the world has never produced or consumed so much food as in the current decade, which brings enormous challenges and opportunities in several fields. Also, current market trends are changing, namely it has been observed that there is an increasing demand for more natural and less processed products, which may result from the fact that several experts warned that increased consumption of ultra-processed foods has been linked to higher greenhouse gas emissions (da Silva et al., 2021). Otherwise, innovative technological developments in food processing and conservation, as for instance 3D-food printing, allow to obtain foods with novel sensorial characteristics. These products may offer novel consumer sensory experiences and disclose numerous challenges ahead in the aroma food comprehension. Indeed, thousands of foods' flavor compounds were reported in literature; nevertheless, the typical food aroma and taste is reflected by the combinatorial code of aroma and taste-active key components, considering their specific concentration and biological activity. However, for each food, it is estimated that only 3–40 are true key odorants (Dunkel et al., 2014). It is imperative to understand and deconvolute the puzzle behind

the food aroma, at the chemical level, and contribute to comprehend humans' olfaction sense.

It is common to observe some misconception between the characterization of the food volatile composition and an attempt to understand its aroma, as the study of a food chemistry aroma is much more than the analysis of its volatile composition. As previously reported, of all the food volatile components, only a limited number of them are important for its aroma. An odorous compound, also named aroma contributing substance or aroma-active compound, is primarily present in a higher concentration than its odor threshold (i.e., is the minimum concentration of a substance from which at least 50% of the test subjects can detect and identify a specific odor of a substance–aroma descriptor) (Meilgaard et al., 1999). The aroma potential of each compound may be assessed by calculating its odor active value ($OAV = c/s$), where c is the concentration of the compound in a food product and s is the olfactory perception threshold (OT) determined in the same type of product. Theoretically, compounds that exhibit $OAV > 1$ were considered to contribute individually to the food aroma and were designated as aroma-active compounds. Furthermore, when the concentration of specific volatile compound is at least 20% of its threshold unit (≥ 0.2), a sensorial contribution to the food overall aroma should also be considered (Meilgaard et al., 1999; Rocha et al., 2004). In general, the influence of the matrix is low on the aroma descriptors perceived but was high on their intensity (Belitz et al., 2009a). For instance, as illustrated in Table 1, dimethyl sulfide may contribute with a cooked cabbage and sulfury notes, in water or beer, but its threshold value is *ca.* 152 times higher in beer than in water.

TABLE 1 | Aroma descriptors and odor threshold values of a set of volatile compounds belonging to different chemical families, determined in water, beer, table wine, and lipidic matrices

	Log P ^a	Aroma descriptor	Threshold value (mg/kg)			
			Water	Beer (ca. 5–7.5% EtOH)	Table wine (ca. 10:90, v/v EtOH/H ₂ O)	Lipidic matrices
Butanoic acid	0.8	Cheese, rancid Franco et al. (2004)	0.204 Pino and Mesa (2006)	2.2 Meilgaard (1975)	2.2 Franco et al. (2004) 10 Guth (1997)	0.65—olive oil Kalua et al. (2007) 50—cream Belitz et al. (2009b)
Hexanoic acid	1.9	Sweaty Uselmann and Schieberle (2015)	3 Pino and Mesa (2006)	8 Meilgaard (1975)	0.42 Ferreira et al. (2000) 3 Guth (1997)	0.7—olive oil Kalua et al. (2007) 85—cream Belitz et al. (2009b)
Octanoic acid	3.1	Rancid, cheese, fatty Franco et al. (2004)	3 Pino and Mesa (2006)	13 Meilgaard (1975)	10 Franco et al. (2004)	3—olive oil Kalua et al. (2007) 200—cream Belitz et al. (2009b)
<i>n</i> -Butanol	0.9	Medicinal Franco et al. (2004)	0.50 Pino and Mesa (2006)	200 Belitz et al. (2009a)	150 Franco et al. (2004)	—
3-Methylbutanol	1.2	Alcoholic, banana Vanderhaegen et al. (2003a)	0.25 Belitz et al. (2009a) 0.30 Pino and Mesa (2006)	70 Meilgaard (1975)	30 Guth (1997)	0.1—olive oil Kalua et al. (2007)
3-Methylbutanal	1.2	Malty Uselmann and Schieberle (2015)	0.00050 Czerny et al. (2008)	0.6 Meilgaard (1975)	—	0.0054—olive oil Kalua et al. (2007)
(E)-2-Nonenal	3.6	Papery (cardboard) Vanderhaegen et al. (2003a)	0.00008 Belitz et al. (2009a)	0.00011 Meilgaard (1975)	—	0.9—sunflower oil van Gemert, (2011)
Ethyl hexanoate	2.8	Fruity Uselmann and Schieberle (2015)	0.001 Pino and Mesa (2006) 0.005 Schieberle (1991)	0.210 Vanderhaegen et al. (2003b)	0.005 Guth (1997)	—
Furfural	0.4	Sweet, cake, burnt, almond Franco et al. (2004)	3 Pino and Mesa (2006)	—	15 Franco et al. (2004)	—
2,3-Butanedione	−1.3	Butter Uselmann and Schieberle (2015)	0.001 Czerny et al. (2008)	0.15 Meilgaard (1975)	0.1 Franco et al. (2004)	0.003—sunflower oil van Gemert (2011) >2–4—butter van Gemert (2011)
γ-Butyrolactone	−0.6	Creamy, oily, fatty, caramel Li et al. (2021b)	20–50 van Gemert (2011)	—	20 Franco et al. (2004) 35 Escudero et al. (2007)	—
γ-Hexalactone	0.4	Herbal sweet tobacco peach apricot Li et al. (2021b)	0.26 Boonbumrung et al. (2001)	—	359 Franco et al. (2004)	—
δ-Octalactone	1.5	Sweet, coconut, dairy Li et al. (2021b)	0.200 Czerny et al. (2008)	—	0.386 Ferreira et al. (2000)	2.49—sunflower oil van Gemert (2011)
(E)-β-Damascenone	4.0	Cooked apple-like Uselmann and Schieberle (2015)	0.000004 Schieberle (1991) 0.000013 Czerny et al. (2008)	0.150 Vanderhaegen et al. (2003b)	0.00005 Guth (1997)	0.011—olive oil Kalua et al. (2007)
Linalool	3.0	Floral, lemon Thibaud et al. (2020)	0.006 Pino and Mesa (2006)	0.080 Meilgaard (1975)	0.015 Guth (1997)	—
Geraniol	3.6	Floral Thibaud et al. (2020)	0.0011 Czerny et al. (2008)	—	0.020 Escudero et al. (2007) 0.03 Guth (1997)	—
α-Terpineol	3.0	Lily, sweet, cake Franco et al. (2004)	1.2 Averbeck and Schieberle (2011)	414 Meilgaard (1975)	5 Franco et al. (2004)	—
Dimethyl sulfide	0.9	Cooked cabbage, sulfury Hui (2010)	0.00033 Belitz et al. (2009a)	0.05 Meilgaard (1975)	0.01 Guth (1997)	—
Guaiacol	1.3	Phenolic Uselmann and Schieberle (2015)	0.00084 Czerny et al. (2008)	0.00388 Sterckx et al. (2011)	0.01 Guth (1997)	0.016—olive oil Kalua et al. (2007) 0.019–0.050—sunflower oil van Gemert (2011)
4-Vinylguaiacol	1.8	Clove-like Uselmann and Schieberle (2015)	0.003 Pino and Mesa (2006)	0.119 Sterckx et al. (2011) 0.300 Meilgaard (1975)	0.04 Guth (1997)	—

^aData obtained from PubChem and FooDB Databases.

Table 1 systematizes the information related with the aroma descriptors and OT values from a set of volatile compounds, belonging to different chemical families, and which were determined in products presenting different physicochemical characteristics. Despite the reported publications, and different panels and methodologies that have been used to determine these sensorial parameters, the comparative analysis of the data from different publications shows that the lower OT values were mainly reported for water. The aroma intensity, expressed here by the OT, depends on several factors associated to the individual and/or panel performance, the physicochemical characteristics of each compound (namely its solubility in water, ethanol/H₂O or lipidic matrix, and volatility, among others), and on interaction phenomena (synergisms,

antagonistic, and/or others) that may occur between the analyte, and other volatile or non-volatile molecules present in the matrix. These last phenomena will be highly marked in alcoholic beverages and lipidic matrices, compared with water. Indeed, higher differences can be observed between OT in the lipidic matrices and the water or ethanol/H₂O matrices. For instance, the increase of the carbon skeleton in acid components promotes a raise of their log P (parameter to access molecular lipophilicity: butanoic acid—0.8, hexanoic acid—1.9, and octanoic acid—3.1), and compounds with higher log P present higher solubility in the lipidic matrices and consequent lower release to the headspace. This phenomenon may explain the higher OT values of these compounds in lipidic matrices. Butanoic and octanoic acids

showed OT values 245 and 67 times higher for cream than the OT reported for water (**Table 1**). Also, foods' viscosity has also a significant impact on OT values, as it may modulate the release of volatile compounds from the food product to the surrounding headspace. For example, the sunflower oil and butter present the viscosity at 20°C of 0.063 Pa s (Calligaris et al., 2014) and 427 Pa s (Glibowski et al., 2008), respectively. The lower viscosity from sunflower oil allows a faster gas phase diffusivity of the 2,3-butanedione (log P of -1.3, lipophobic compound) and consequently easier release to the headspace. Thus, 2,3-butanedione requires a lower OT (0.003 mg/kg) to be sensorially perceived in sunflower oil than the OT observed in butter (>2–4 mg/kg) (**Table 1**).

In fact, foodstuffs and beverages are highly complex matrices that are no longer regarded as a product themselves but as a food system that includes all the activities from the raw material(s) until its consumption. The food composition is the result of a set of factors, such as the raw material(s) composition and their conditions of cultivation, harvesting and storage, as well as the technological processes involved in its production, and subsequent conditions of distribution, storage, and finally the circumstances in which consumption occurs (The Future of Food and Farming: Challenges and choices for global sustainability, 2011; Galanakis, 2020). All these factors play an important role in the food's chemical composition, nutritional value, and sensory characteristics, including aroma. This holistic view of a food system is critical to comprehend and extract relevant chemical information from the food odorous compounds. On the other hand, information on the food volatile composition can provide key information for the control of raw materials and final products, technological processes, and conditions of transport or storage, among others.

The analytical coverage of the chemical clouds of food needs to be comprehensive and quantitative, and the use of a highly sensitive and high-throughput methodology such as the GC × GC-ToFMS seems to fulfill these requirements.

The Role of the SPME/GC × GC to Assess Chemical Characterization of Food Aromas

Capture of odorant molecules in a representative way, acquisition of chromatographic data, and its transformation into interpretable and useful information to the chemical characterization of food aromas involve many challenges, intrinsically linked to the peculiarities of volatile and semi-volatile compounds and matrix physicochemical characteristics, as well as of methodologies currently used. Some of these challenges can be listed to exemplify the inherent complexity of aroma chemistry field:

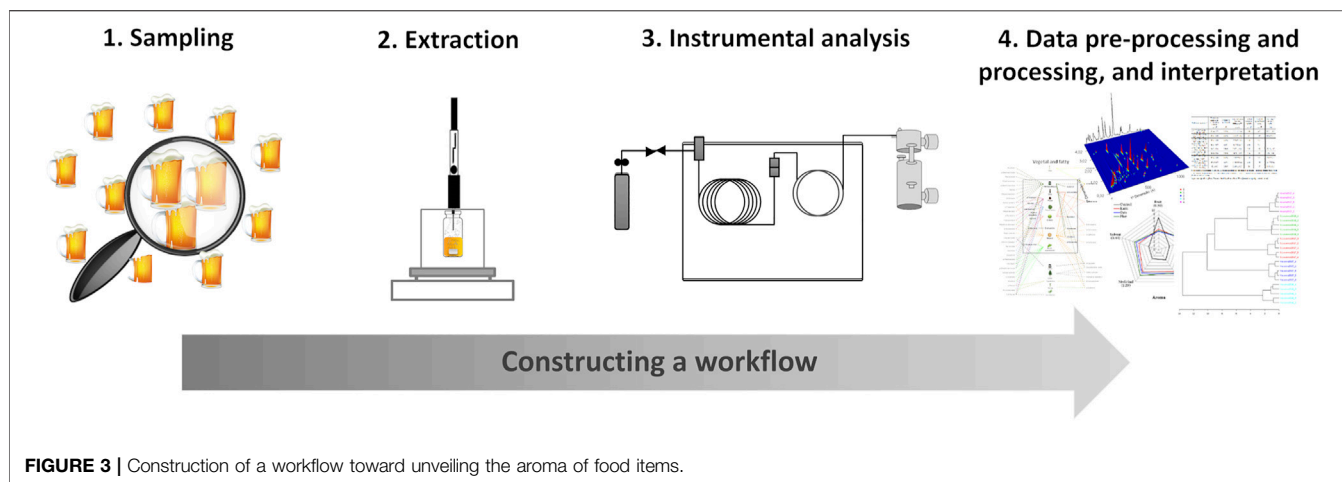
- High diversity of food and beverage products,
- Chemical diversity of volatile and semi-volatile molecules,
- Concentration in a wide dynamic range,
- Multiple sources of variability from sample, analysis methods (extraction and chromatographic ones), workflows, reagents, and so on,
- Lack of analytical standards, particularly due to the presence of unknown molecules,

- The need for robust, reliable data handling and bioinformatics,
- Throughput issues for preparing and analyzing large numbers of samples,
- Lack of information about aroma descriptors and OT values for the volatile and semi-volatile compounds present in a wide range of food products, namely for protected designation of origin products that are highly valued due to their distinctive sensory characteristics,
- Scarcity of information associated with antagonistic or synergistic effects between molecules, and their impact on different food products (matrix effect).

It is also important to point out that the odorant compounds are usually found in very low concentrations, ranging from nanograms to milligrams per liter or kilogram; many of them are highly reactive and thermally labile, and volatilize easily at room temperature (Chen and Ho, 2006; Belitz et al., 2009a). Another issue that also deserves to be highlighted is that, in general, it was observed that there was a higher complexity of the processed foods compared with the fresh ones. Indeed, several dozens or hundreds of volatile and semi-volatile compounds are reported in foodstuffs, as for instance fresh fruits and vegetables, but this number more than doubles when studying the volatile fraction of thermally processed foods, such as coffee, roasted beef, and distillate beverages, among others (Chen and Ho, 2006; Belitz et al., 2009a; Lopes et al., 2021). All these aspects make their analysis a stimulating task, and GC × GC-based methodologies have been considered a promising strategy to overcome these challenges (Amaral and Marriott, 2019; Biedermann and Grob, 2019; Cordero et al., 2019; Rasheed et al., 2021; Welke et al., 2021).

As a starting point to the implementation of a methodology, an appropriate workflow should be constructed, as schematically illustrated in **Figure 3**, which basically consists of four steps: 1) representative sampling; 2) extraction of the volatile and semi-volatile components; 3) data acquisition by chromatography-based methodology; 4) monitoring, pre-processing, and processing of signals, including data interpretation based on the relationship between odorants and sensory properties (Schieberle and Molyneux, 2012).

All the steps of the experiments should be carefully planned, namely the sampling to include sufficient samples representative of the whole population and to assure statistical significance of the results. Attempts to force statistical procedures to fit a data set after sampling can result in conclusions that are not meaningful. Solvent-free microextraction techniques such as SPME, in headspace mode, may represent a powerful tool for extraction of volatiles, including those that compose the aroma clouds (Kataoka et al., 2000; Bressanello et al., 2021). Analysis by GC is a long-established technique, particularly for the study of volatiles and/or aroma constituents (Schieberle and Molyneux, 2012). Advanced gas chromatographs, such as GC × GC, may represent a step further to overcome challenges due the complexity of aroma clouds, being well situated due to its high sensitivity, and chromatographic resolution. Finally, chromatographic data pre-processing and processing, and their



combination with sensorial data are crucial to mapping aroma-active compounds, clustering samples, establishing relationship between odorants and food aromas, and explaining formation mechanism of important odorants, among others.

Despite the huge importance of the sampling, in this review the primary attention will be devoted to the extraction, instrumental analysis, and data processing and interpretation steps (data analysis).

Solid-Phase Microextraction

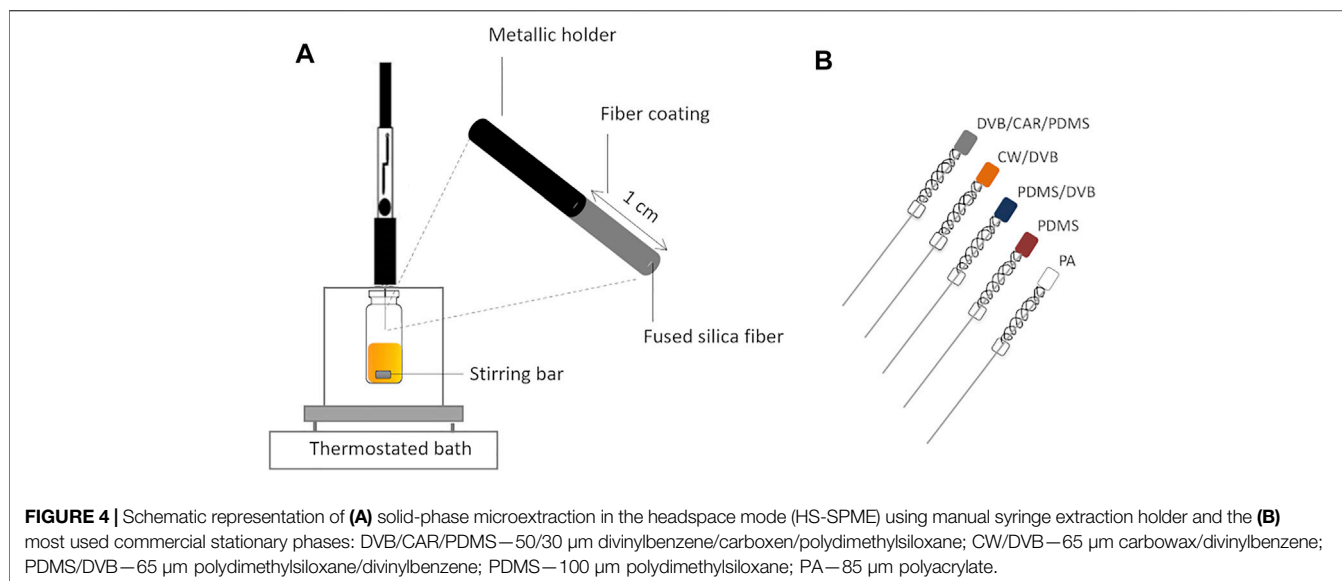
SPME is a rapid and simple sample preparation technique based on sorption of analytes (absorption and/or adsorption) into a stationary phase, allowing the simultaneous sampling, extraction, and pre-concentration. This technique was developed by Pawliszyn, in the beginning of the 1990 decade (Pawliszyn, 2009), and may be used to extract directly analytes from liquid, solid, and gaseous samples. SPME is a non-exhaustive extraction technique since it only extracts a small analyte fraction, which may be used to characterize the global composition of analytes in the free form (Vas and Vékey, 2004; Pawliszyn, 2009; Souza-Silva et al., 2015; Boyacı et al., 2018). These characteristics allow electing the SPME as a technique especially well positioned to extract the odorant molecules present in the food aroma clouds.

Several other advantages are associated with this technique, namely being a safe and user-friendly procedure, easily automated, and with potential to be miniaturized (Pawliszyn, 2009; Souza-Silva et al., 2015). It can be used routinely in combination with gas chromatography (GC) or liquid chromatography (LC) (Kataoka et al., 2000). Moreover, SPME has the ability to extract analytes at the level of nanograms or even picograms. It is also important to highlight that SPME represents a highly efficient one-step and solvent-free sample preparation technique, having each fiber a high durability, which fulfills the requirements necessary for sustainable development and implementation of green chemistry principles in analytical laboratories (Spiegel et al., 2013; de Souza et al., 2018). Also, considering the current state of SPME development, the price could become an advantage considering the low cost of

production. Principally with implementation of this technique in combination with high-throughput equipment, it could become an attractive feature as it can be used multiple times. These attributes are in line with the current concepts about the White Analytical Chemistry that is closer to the idea of sustainable development due to a more holistic view, considering a compromise that avoids an unconditional increase in greenness at the expense of functionality (Nowak et al., 2021).

In fact, SPME fibers can be reused hundreds of times without any compromise to their physicochemical properties and, consequently, extraction efficiency. Nevertheless, it is required to have a regular control of its performance, e.g., regularly a chemical standard with known concentration may be extracted and its concentration may be followed on time. Also, to avoid cross-over contaminations, thermal clean-ups between extractions have to be done. All the previously reported advantages are the justification for the fact that SPME has been successfully used as an extraction technique for a wide range of foodstuffs and beverages (Kataoka et al., 2000; Peñalver et al., 2000; Vesely et al., 2003; Vichi et al., 2003; Pawliszyn, 2009; Giri et al., 2010; Welke et al., 2014; Alves et al., 2015; Santos et al., 2015; Silva et al., 2015; Nunes et al., 2016; Salvador et al., 2016; Xu et al., 2016; Martins et al., 2018, 2020; Fonseca et al., 2020; Bressanello et al., 2021; Lopes et al., 2021; Rocha et al., 2021).

There are available various SPME geometries, namely fiber, miniaturized fiber (coated-tip), arrow, thin film, in-tube, magnetic nanoparticles, and in-tip (Piri-Moghadam et al., 2017). Nevertheless, fiber, which consists of a needle whose base is usually fused silica coated with a thin layer of a stationary phase inside a syringe, is the most commonly used configuration, and several fiber coatings are commercially available (**Figure 4A**). Using this configuration, two extraction modes can be performed: immersion or direct extraction (IM-SPME) and headspace extraction (HS-SPME). In the first mode, analytes are released directly from the sample to the fiber coating, once the coated fiber is placed into the sample, especially used for liquid samples. In the headspace extraction mode, the analytes are released from a liquid or solid matrix, being transported through



the air barrier, and the vaporized analytes are sorbed by the fiber stationary phase. Thus, no direct contact between fiber and sample occurs, which allows the preservation of the stationary phase against any damage resultant from matrix interferences (Pawliszyn, 2009). The headspace extraction mode is particularly appropriate for capturing volatile and semi-volatile compounds, which are the components of the aroma clouds surrounding foods and beverages (Figure 1).

After fiber exposition, a mass-transfer process takes place, and the analyte's amount that is sorbed by the stationary phase can be quantified by the following mathematical equation:

$$n = \frac{C_0 \times V_f \times V_s \times K}{K \times V_f + V_s}$$

where C_0 represents the sample's initial concentration; V_f and V_s are the volume of fiber and sample (or headspace), respectively; K represents $K_{fh} \times K_{hs}$, in which K_{fh} represents the partition coefficient between stationary phase and headspace, and K_{hs} is the partition coefficient between the headspace and the sample.

Several experimental parameters determine the extraction efficiency and reproducibility of SPME technique (Rocha et al., 2001; Vas and Vékey, 2004; Pawliszyn, 2009; Souza-Silva et al., 2015), namely:

- SPME fiber coating,
- Extraction temperature,
- Extraction time,
- Salt addition (salting-out effect, applicable specially in the case of aqueous-based samples),
- Stirring effect,
- Sample amount and chemical composition.

Thus, prior to the implementation of a SPME-based methodology, it is crucial to have generic information about the physicochemical characteristics of the sample to be analyzed,

and to optimize the previously reported experimental parameters. The matrix effect may have impact on the SPME extraction, i.e., the analytes' amount sorbed on the SPME fiber is determined by sorption kinetics and also by the analytes' coefficient distribution between the stationary coating and the food sample, which are intrinsically related with sample physicochemical properties (Rocha et al., 2001). Hence, the various experimental parameters with a relevant impact on the SPME process will be briefly addressed.

Different SPME stationary phases are commercially available, regarding polarity, types of analyte interaction (absorption and/or adsorption), and film thickness and length, although the most common are 1 cm in length (Figure 4B). For the fibers that extract via an adsorptive-type mechanism, such as DVB/CAR/PDMS (divinylbenzene/carboxen/polydimethylsiloxane) and PDMS/DVB (polydimethylsiloxane/divinylbenzene), the analytes interact primarily with the surface of the sorbent coating instead of partitioning into the entire coating and, therefore, the sensitivity of these fibers depends on other factors, such as the surface area and porosity of the material, among others (Shirey, 2012; Godage and Gionfriddo, 2019; Carriço et al., 2020). Lower extraction efficiency of volatile compounds may be observed for PDMS/DVB fiber due to the porosity properties of the DVB that represent some concerns about the analytes' displacement, and has difficulty to extract analytes with low molecular weight. The DVB/CAR/PDMS fiber, which combines three materials, was developed to overcome the limitations of the CAR/PDMS (carboxen/polydimethylsiloxane) in the desorption of higher molecular weight analytes and PDMS/DVB in difficulty of extracting analytes with low molecular weights. The DVB/CAR/PDMS coating contains both adsorbents that are layered to extend the molecular weight range of analytes extracted with one SPME fiber and the combination with the PDMS, an adsorptive-type fiber that also confers a bipolar character (Shirey, 2012; Godage and Gionfriddo,

2019; Carriço et al., 2020). This arrangement explains the high performance of the DVB/CAR/PDMS fiber for a wide range of chemical species and the fact that it is extensively used for profiling of volatile molecules released from various food items, such as table and fortified wine (Perestrelo et al., 2011; Santos et al., 2013; Welke et al., 2014; Whitener et al., 2016; Rocha et al., 2021), beer (Sterckx et al., 2010; Rodriguez-Bencomo et al., 2012; Romero-Medina et al., 2020), sea salt (Donadio et al., 2011; Silva et al., 2015), pear (Wang et al., 2019; Fonseca et al., 2020), distilled beverages (Thibaud et al., 2020), coffee (Ongo et al., 2020; Lopes et al., 2021), elderberry (Salvador et al., 2016), hazelnut (Cordero et al., 2010; Rosso et al., 2020), honey (Čajka et al., 2007; Siegmund et al., 2018), dairy products (Cardinali et al., 2021; Székelyhidi et al., 2021; Liu et al., 2022), virgin olive oil (Purcaro et al., 2014; Ros et al., 2019), and cereals (Buško et al., 2010). Indeed, DVB/CAR/PDMS fiber exhibited the highest sorption capacity for a wide range of VOCs released from honey, comparing with six other fiber coatings (Čajka et al., 2007). However, not always DVB/CAR/PDMS fiber is the best option to perform SPME in foods, as it was shown for instance in beer analysis (Martins et al., 2015): PDMS/DVB fiber had better reproducibility (expressed as RSD) than DVB/CAR/PDMS fiber (no significant differences in both peak area), using a set of analytes from several chemical families. Furthermore, the representativeness of different volatile extracts from French cider was compared, namely using IM-SPME, HS-SPME, purge and trap, and dynamic headspace (Villière et al., 2012). In this case, HS-SPME using CAR/PDMS as fiber coating was shown to produce the extracts with aroma characteristics, as near as possible, to those of the reference French cider.

Otherwise, diffusion of the analytes through the sorbent coating is a prevailing effect in fibers with absorptive-type mechanism such as PA (polyacrylate) and PDMS (Shirey, 2012) and the more recent fibers based on zwitterionic polymeric ionic liquids (Nan and Anderson, 2018; Pacheco-Fernández et al., 2019; Carriço et al., 2020). Consequently, analytes can freely partition into the sorbent, with little competition among analytes, and the concentration of each analyte at equilibrium is less affected by the presence of other analytes. Despite these fibers that were designed for more specific applications, i.e., for the extraction mainly of polar (PA and zwitterionic polymeric ionic liquids) or non-polar analytes (PDMS), their use can be very useful as they provide representative profiles of the headspace composition.

SPME extraction efficiency also depends on the extraction temperature since it influences the analytes' vapor pressure and solubility. This parameter interferes in the diffusion coefficients and Henry's law constants (K_H) of analytes, allowing to modulate the equilibrium time. With increasing extraction temperature, two phenomena can be promoted: the analytes' volatilization and their consequent transference from liquid or solid phase to the headspace; the analytes' solubility in the case of liquid matrices (Rocha et al., 2001; Pawliszyn, 2009). Thus, it is crucial to establish an extraction temperature that ensures the best compromise between both phenomena and consequently promote a high extraction efficiency, also ensuring that no sample degradation or artifact formation occurs (Pawliszyn,

2009). Particular care must be taken to prevent the formation of Maillard compounds, which may be produced during the extraction step (Villamiel et al., 2006). For instance, regarding beer volatile profiling, the SPME extraction temperature usually varied between 20 and 60°C. Particularly higher extraction temperatures (80°C) were used to improve the extraction efficiency in volatile phenols' determination, a chemical family with an important role for beer aroma profile (Martins et al., 2017). However, temperatures higher than 60°C can lead to artifact formation, through Maillard reactions (Villamiel et al., 2006), thus the extraction temperature of 80°C cannot be used for the global chemical characterization of beer's odorant molecules.

In addition to ensuring that no artifacts are formed, it is also important to study the samples under conditions like those in which they are consumed. Indeed, the creation of the aroma clouds containing the odorant compounds is modulated among other factors by the balance between the temperature and exposure time. Therefore, selection of the optimum extraction time is one of the critical steps in the SPME method development. Extraction time selection is always a compromise between the length, sensitivity, and repeatability of the method. Equilibrium extraction provides the highest sensitivity and repeatability, but in most SPME-GC applications, pre-equilibrium conditions are used since equilibrium extraction times tend to be longer and thus impractical. Both equilibrium and pre-equilibrium extractions need precise and perfectly repeatable timing, although for the latter condition, timing is more critical (Kudlejova et al., 2009; Pawliszyn, 2009). As illustrated in **Figure 5**, taking advantage of the versatility of the SPME technique, different extraction times may be used, and consequently, different types of information can be extracted. For instance, 3 min of SPME extraction time allows the detection of odorants present in espresso aroma clouds and under the regular conditions of its consumption. On the other hand, longer extraction time (30 min) may be applied for an in-depth characterization of espresso volatile components (Lopes et al., 2021), from which valuable information can be extracted for blend comparison or to predict the chemical aroma profile of an espresso brew based on the respective coffee powder composition.

Salt addition and stirring effect should also be considered as important factors in the extraction efficiency, particularly in aqueous-based matrices. The mass transfer of analytes from sample matrix to headspace can be improved with salt addition through the salting-out effect, where the reduction of analytes' solubility in the matrix occurs, while the boundary phase properties are changed (Kudlejova et al., 2009; Pawliszyn, 2009). The most used salt is high purity sodium chloride (NaCl, >99%) to avoid introduction of artifacts. First, the salting-out effect promotes the increase of extraction efficiency: hydration spheres, from water molecules, are formed around the ionic salt molecules, which leads to less free water molecules to dissolve the analytes, and consequently, analytes transfer to the headspace and then to SPME fiber coating. When saturation is achieved, the extraction efficiency may decrease because the salt ions in solution can participate in electrostatic interactions with analytes, blocking their transfer to the headspace, and consequently to SPME fiber coating (Pawliszyn, 2009). Regarding stirring effect, agitation

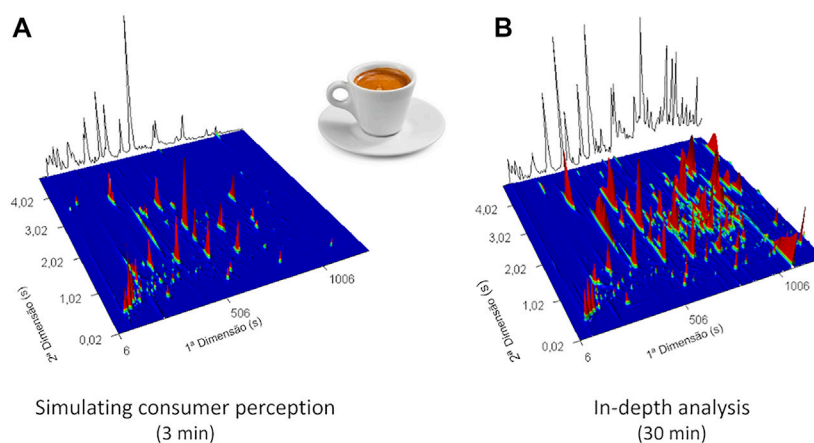


FIGURE 5 | 3D GC \times GC total ion chromatogram plot of **(A)** espresso using 3 min of SPME extraction time to simulate the consumption conditions of this product and **(B)** with 30 min of SPME extraction time for an in-depth characterization of volatile components (using a DVB/CAR/PDMS coating fiber, at 55°C of extraction temperature).

promotes an increase of extraction efficiency through the reduction of diffusion coefficients of analytes and decreases the depletion zone effect that occurs near the fiber as a result of fluid shielding. Agitation of the sample assists the mass transfer between the sample and the fiber coating, and the time required to achieve the equilibrium can be reduced by using an agitation method (Lord and Pawliszyn, 2000; Kudlejova et al., 2009). For instance, stirring (1,000 rpm) may increase up to 3 times the chromatographic signal of compounds associated with the wine aroma when compared with analysis performed without agitation. Also, a significant increase in SPME extraction efficiency was observed, up to 6 times, which was promoted by the addition of NaCl (Rocha et al., 2001).

Despite the importance of optimizing the SPME experimental parameters to ensure a high extractive efficiency and to obtain samples' headspace composition representativeness, innovative strategies were also developed to increase SPME performance, such as vacuum-assisted SPME and cumulative SPME. Vacuum-assisted SPME (Vac-HSSPME) consists in applying reduced pressure (usually 7 mbar, with a vacuum pump) inside a specific gas-tight sealed vial, which reduces the sampling pressure along the pre-equilibrium stage, decreasing the gas-phase resistance of analytes with low K_H values. Consequently, this procedure accelerates their extraction kinetics through the increasing of their diffusion and mass transfer to the headspace. The air-evacuation should be performed in the presence of solid matrices, while for liquid ones, the user may choose to evacuate the air before or after the introduction of the sample in the vial, which the latter option may promote the extraction of the less volatile compounds. After the sampling, SPME fiber is retracted, and then placed in the GC injector. Then, the pressure can be equilibrated to atmospheric pressure, and the vial can be opened. The main advantages of Vac-HSSPME are the requirement of shorter sampling times and lower extraction temperatures than conventional HS-SPME, thus maintaining the sample characteristics, and reducing artifact formation and compound

decomposition. Otherwise, the Vac-HSSPME requires the use of a home-made gas-tight sample container (Psillakis, 2017), as no commercial options are still available. This requirement may represent a relevant constraint, as not all laboratories will be able to build this accessory. Vac-HSSPME has been applied to explore the volatiles from extra virgin olive oil (Mascrez et al., 2020), in which it was possible to provide improved information of the olive oil aroma fingerprinting (namely by obtaining higher chromatographic area), particularly due to the extraction enhancement of semi-volatile analytes by Vac-HSSPME (comparing with conventional HS-SPME). The best analytical strategy to analyze this non-aqueous liquid sample required not only Vac-HSSPME but also the use of temperature for extraction (35°C after a full factorial central composite design (CCD) analysis) to increase analytes' diffusion through the liquid thin film (at the interface), and thus aiding their mass transfer. Another example is the use Vac-HSSPME to analyze cheese, particularly hard and semi-hard types (Sýkora et al., 2020). The main positive effects in Vac-HSSPME were achieved for the selected analytes, such as 1-pentanol, butanoic acid, 2,3-butanedione, and 2-heptanone, in water extraction; however, Vac-HSSPME only showed significant impact on butanoic acid extraction in cheese matrix. Sýkora et al. (2020) concluded that Vac-HSSPME will improve extraction of short- or medium-chain fatty acids that are present in cheese at low concentrations.

Cumulative SPME has been applied to enhance extraction performance by concentration of the volatiles through repeated sampling on the same vial, using different SPME fibers that are sequentially desorbed in the GC injector. The combination of different coatings and repeated extractions can be required once they needed to be put in the sample's headspace at desorption time intervals, each for the established extraction time, and then they are individually desorbed. For this, the installation of a cryotrap after the injector is required to allow the volatiles' cryofocusing (Chin et al., 2012). The main drawbacks, namely the use of different fibers, as well as the need to perform several

injections, make cumulative SPME a more time-consuming and more labor-intensive technique than conventional SPME. Cumulative SPME was used to enhance SPME performance in combination with GC-O, as it was showed for wine (Chin et al., 2012, 2015) and coffee (Chin et al., 2015) characterization. Indeed, the pre-concentration of wine volatiles (e.g., retention of apolar alkanes from C₁₀, and polar alcohols) improved the extract representativeness, compensating the sensitivity loss promoted by effluent splitting to two detectors (O-sensory detection, FID, or MS) (Chin et al., 2012). This effect was even more pronounced when cumulative SPME was coupled with multidimensional and comprehensive GC detection, which solved co-elutions that do not allow the proper analytes' identification and odorant recognition (Chin et al., 2015). For instance, 2-methoxy-3-isobutylpyrazine, associated to the capsicum odor, was identified in ground coffee, and had 5-fold S/N when data were acquired using a 6-time cumulative SPME sampling and comparing with conventional SPME. Mascres and Purcaro (2020) studied the impact of the number of cumulative SPME versus extraction time in the volatile characterization of olive oil. An improved burst level of information and overall sensitivity was achieved with shorter extraction time (10 min instead of 30 min) using 6-time cumulative SPME sampling once there was a decrease in the cumulative response using 30 min of extraction (Mascres and Purcaro, 2020).

Even with the potential interest of these strategies, there is still a need for some improvements to allow them to be easily implemented in common food analysis laboratories, namely the development of commercial accessories (e.g., with different volumes) to perform the Vac-HSSPME. Also, cumulative SPME still requires additional investigation regarding its efficiency and sensitivity, for instance the impact of the number of cumulative sampling versus extraction time into the time of the chromatographic analysis, and consequent improvement of the sample volatile's representativeness.

Comprehensive Two-Dimensional Gas Chromatography

Gas chromatography is the most common technique used for food products' and beverages' volatile characterization, specifically the one-dimensional gas chromatography (1D-GC). Significant improvements have been occurring, driven by the need for analytical tools that can analyze target and non-target components from complex samples, from a sensitive and/or selective point of view. Thus, several advances have been performed, namely the development of new stationary phases of GC columns, improvements of chromatographic equipment (e.g., development of pneumatics, microfluidic devices, and modulators, among others) and detection systems (selective and/or high-sensitivity detectors, with increasingly compact configuration and more user-friendly maintenance), improvements in the hardware and software (Wong et al., 2013), and also the recent advances in micro-GC systems (Qu and Duan, 2019). Consequently, the improvement on resolution and limits of detection (LOD), and reduction on the time of instrumental analysis and data processing have been contributing

to the deeper characterization of samples. Namely, advances on the multidimensional gas chromatography (MDGC), which was described as the process of selecting a region or zone of eluted compounds issuing from the end of one GC column, and subsequently subjecting this zone to a further GC displacement, have shown enormous advantages compared with the 1D-GC (Marriott et al., 2012; Seeley and Seeley, 2013; Prebihalo et al., 2018). MDGC are usually classified into two categories: heart-cutting 2D GC (in which only a small portion of the sample components is heart-cut and suffers both GC separations) or comprehensive two-dimensional gas chromatography (GC × GC, in which all sample components suffer heart-cutting). Both MDGC categories play an important role in aroma research of foods (Marriott et al., 2012; Seeley and Seeley, 2013; Prebihalo et al., 2018), particularly in the disclosure of aroma volatile compounds' characterization; nevertheless, GC × GC peculiarities will be the focus of this review.

This review is focused especially on the GC × GC, and for comparison purposes, **Figure 6** shows a schematic representation of the two configurations of GC systems that may be used for volatile determination: 1D-GC (**Figure 6A**) and GC × GC-ToFMS (**Figure 6B**). Chromatographic systems allow the separation of mixture's analytes through their partitioning between two phases: one large stationary surface (GC column) and a mobile phase (inert carrier gas), which is in contact with the first one. Dispersion and specific interactions between the stationary phase and the analytes are the main factors that contribute to analytes' elution. Chromatographic column housed in a temperature-programmable oven is connected within an injector and a detector.

Despite the MS detectors commonly used and combined with GC, conventional universal, element-selective, and structure-selective detectors may also be considered. These are classified by mechanism as ionization-based (flame ionization, thermionic ionization, electron capture, photoionization, and barrier discharge), bulk physical property (thermal conductivity), optical (flame photometric, chemiluminescence, atomic emission), and electrochemical (electrolytic conductivity) detectors (Poole, 2021). MS detectors were the most widely used ones, followed by flame ionization detector (FID), and the others were generally employed for specific applications. MS detectors allow the identification and quantification of analytes within complex mixtures and promote higher sensitivity than FID. For instance, quantification of hexanoic acid in beer was performed by HS-SPME, using sol-gel-derived TMSPMA-OH-TSO and DVB/CAR/PDMS coatings, combined with GC-FID and GC-MS, respectively, and the values of 0.27 (Liu et al., 2005) and 1.1 µg/L (Rodriguez-Bencomo et al., 2012) correspond, respectively, to the LOD obtained by GC-MS and GC-FID analysis. It is important to point out that, for target analysis, very low detection and quantification limits can be achieved using specific detectors, such as for example the flame photometric detector that allowed the detection of beer sulfur compounds in the order of nanograms per liter (Xiao et al., 2006). Volatile thiols, important aroma components of the edible rapeseed oil, were successfully determined via HS-SPME (using CAR/PDMS coating) combined with GC-sulfur

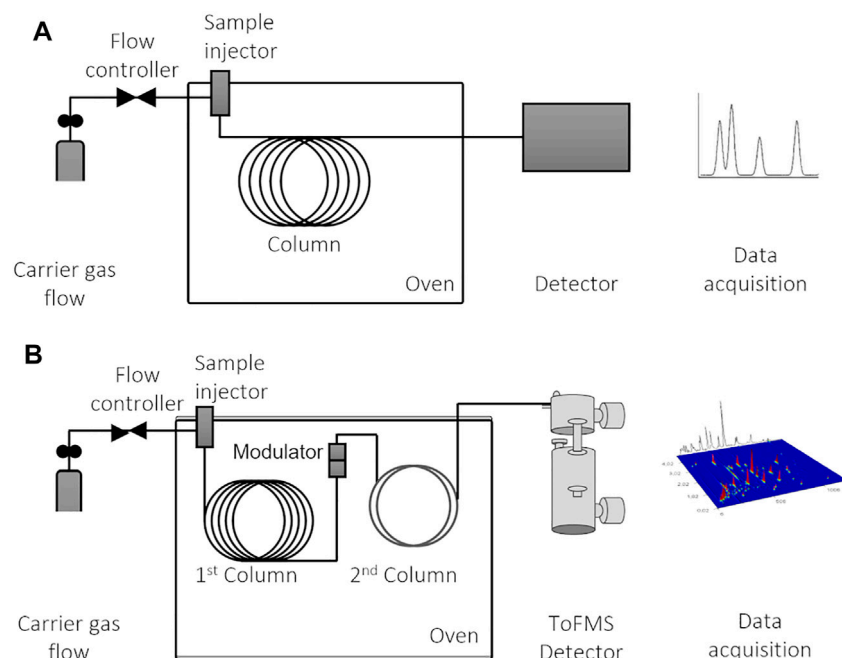


FIGURE 6 | Schematic illustrations of (A) one-dimensional gas chromatographic system (1D-GC), which can be coupled with various types of detectors; and (B) comprehensive two-dimensional (GC \times GC) gas chromatographic system coupled with ToFMS (time-of-flight mass spectrometry). Figure adapted from Martins et al. (2017).

chemiluminescence detection, with LODs ranging from 0.16 to 1.12 $\mu\text{g/kg}$ (Yang et al., 2021).

The complexity of foodstuffs and beverages usually implies long GC runs and overloaded chromatograms (with frequent co-elutions of two or more analytes), thus leading to difficulties in accurate analytes' identification and quantification. Therefore, considerable research has been developed toward the development of independent chromatographic separations, which allow to improve the resolving power, namely GC \times GC (Tranchida et al., 2004; Mondello et al., 2008; Marriott et al., 2012; Prebihalo et al., 2018). Indeed, short GC \times GC runs provided more chemical information regarding the volatile profiles of foods: for instance, in the study of Brazilian chamomile (*Matricaria recutita* L.), in which a substantial reduction of the chromatographic time from 93 to only 23 min was achieved, when the analysis was performed using GC-qMS and GC \times GC-ToFMS, respectively (Petronilho et al., 2011), significant improvement was observed regarding the analytes' detection (32 instead of the 7 sesquiterpenic compounds identified by GC-qMS). Moreover, this high-throughput technique not only allowed the reduction of the chromatographic time in wine analysis but also the number of detected components: from 110 min and 51 components using GC-MS, to 44 min and 317 components using GC \times GC-ToFMS (Lukić et al., 2020).

The separation efficiency of GC \times GC enables an in-depth characterization of complex samples. It implies the multiple sequential separation of a sample, using two columns with different stationary phases, connected by an interface that allows to preserve the individual analytes' retention,

i.e., orthogonal mechanisms (Tranchida et al., 2004; Marriott et al., 2012) (Figure 6B). The most common GC \times GC setup comprises two GC columns with different coating materials: first column (^1D) with a length of 30 m and with a non-polar stationary phase, which separates analytes by volatility; and a second column (^2D) short (1–2 m) and containing a polar stationary phase, which separates analytes by polarity.

This set of columns allows a relatively “slow” analytes' separation in ^1D column and then extremely “flash” high-resolution separation in the ^2D column. GC columns are connected in series by a modulator. There are different types of modulators, namely thermal, cryogenic, and valve-based modulators (Bahaghighat et al., 2019). In general, the cryo-modulator, which uses liquid nitrogen for cooling, is more efficient for the analysis of the highly volatile molecules. The cryo-modulator accumulates and traps small portions (usually 4–8 s) of the eluate from the ^1D column by cryo-focusing, and then re-injects them into the ^2D column. The ^1D separation is preserved once each peak is modulated several times. Moreover, the ^1D column separation is maintained once the collected fractions are no larger than one-fourth of the peak width, thus producing narrow peaks. These peaks are consequently “flash” separated before the subsequent modulation (Tranchida et al., 2004; Marriott et al., 2012).

The reverse combination of GC columns can also provide good results, depending on the analytes to be separated. In fact, the polar/non-polar set of columns is very appropriate for the analysis of polar analytes. The column set configuration comprising ^1D SolGel-Wax column (100% polyethylene glycol)

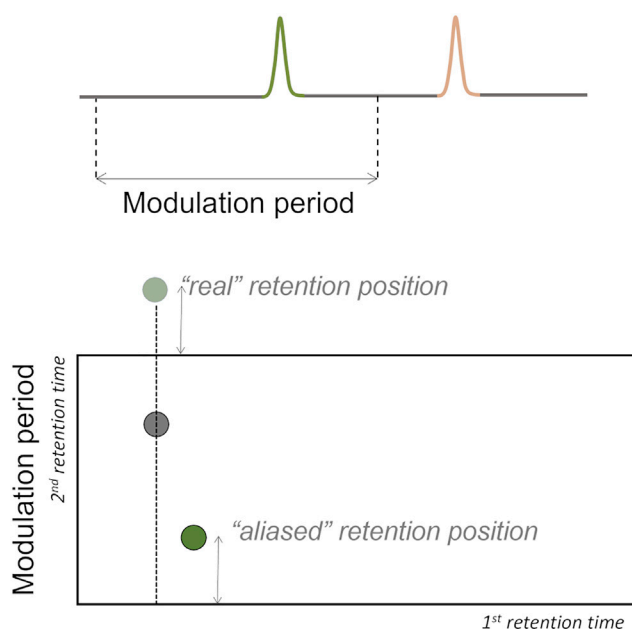


FIGURE 7 | Wrap-around phenomenon may occur if the separation on the 2nd dimension does not finish before the next modulation, i.e., the elution time of the analyte exceeds the modulation time.

coupled with a ^2D OV1701 column (86% polydimethylsiloxane, 7% phenyl, 7% cyanopropyl) were utilized for the combined untargeted and targeted fingerprinting of volatiles of olive oil, and a set of saturated (heptanal, octanal, and nonanal) and unsaturated ((E)-2-heptenal) aldehydes were monitored as they were well known to be correlated with specific sensory defects of olive oils (Magagna et al., 2016). Suitable chromatographic resolution and sensitivity were achieved for a set of polar analytes (log *P* ranging from -1.0 to 2.8 , for *N,N*-dimethylformamide and 3-octanol, respectively) using the column set configuration comprising Carbowax/BTR (ethylene glycol/siloxane copolymer) primary column coupled with Equity 5 (5% diphenyl/95% dimethyl siloxane) secondary column (Carriço et al., 2020). The use of a column set with the same diameter in primary and secondary columns yields a near-theoretical maximum in peak capacity gain, i.e., increases the number of components that the system can resolve (quantifiably and identifiably separate), and a better separation of the analytes was observed with smaller peak width.

If the ^2D separation of a certain analyte does not finish before the next modulation, the elution time of the analyte exceeds the modulation time, and wrap-around phenomenon occurs (Figure 7). This phenomenon can interfere in the accurate analytes' quantification if there are co-elutions with analytes of interest (Tranchida et al., 2004; Marriott et al., 2012), thus modulation time should be previously optimized to avoid this phenomenon.

The type of detectors to be used in GC \times GC depends on the requirements of rapid separation in the second dimension, i.e., the internal volume has to be small and the data acquisition rate high. For instance, the FID and electron-

capture detector (ECD) have been used; nevertheless, coupling with MS detectors, especially ToF analyzers, are the most widely used and offer greater advantages in terms of compound identification (Tranchida et al., 2016, 2018; Ruiz-Matute et al., 2018). The narrow peaks produced by GC \times GC (peak width at half height of 0.1 s or less) require a detector with high data acquisition speed (*ca.* hundred full-mass-range spectra per second), such as mass spectrometer, with ToF analyzer, thus providing sufficient data density (Tranchida et al., 2004; Marriott et al., 2012). Moreover, ToFMS allows the acquisition of full mass spectra at trace levels and mass spectral continuity, causing a reliable spectra deconvolution of overlapping peaks. Spectral continuity occurs when all the points of the chromatographic peak have the same ion abundance ratios for the different masses in the spectrum. More recently, progresses in the MS field go over and other MS analyzers, and more selective and sensitive ones have emerged, namely triple-quadrupole mass spectrometers, isotope ratio, and quadrupole time-of-flight mass spectrometer (Q-ToF). However, the use of low-cost GC \times GC instrumentation, such as the coupling with ToFMS, would be more acceptable for the determination of the overall odorant molecules (Tranchida et al., 2016). An example of the highest sensibility of GC \times GC-ToFMS can be observed, for instance in the LOD determination of eugenol, which was determined in wine matrices, with SPME (DVB/CAR/PDMS), being 0.002 and 0.01 $\mu\text{g/L}$ for GC \times GC-ToFMS (Welke et al., 2014) and GC-MS (Carrillo and Tena, 2006), respectively, which corresponds to a one magnitude order lower for GC \times GC-ToFMS.

GC \times GC produces structured chromatograms due to the orthogonal analytes' separation. For the case illustrated in Figure 8, the combination of a non-polar/polar columns

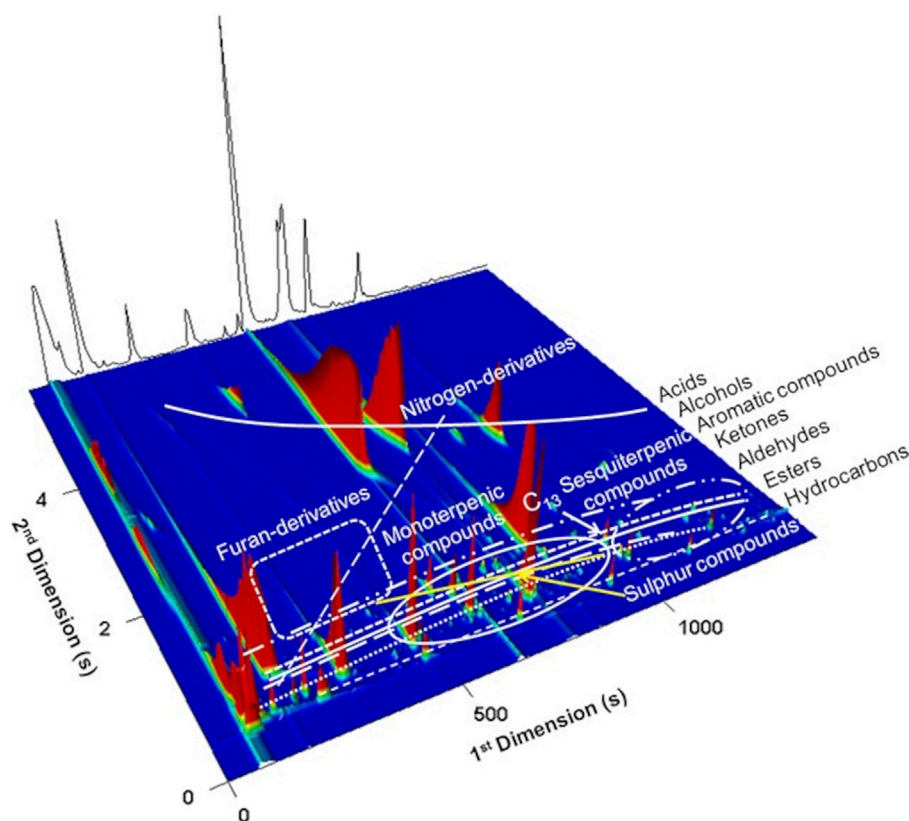


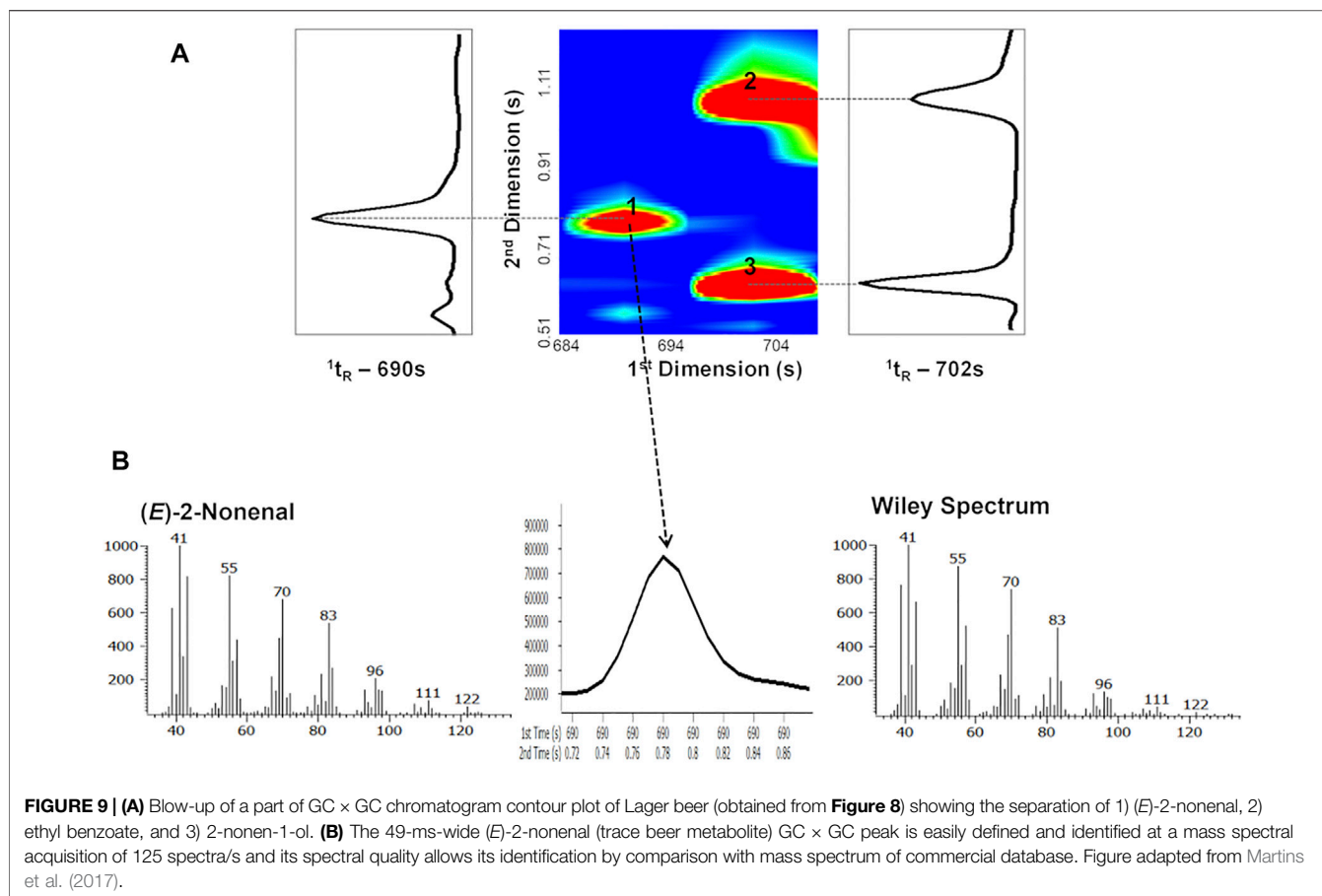
FIGURE 8 | 3D GC \times GC total ion chromatogram plot of a Lager beer highlighting its volatile chemical families. Bands and clusters formed by structurally related compounds are indicated. Reprinted with permission from Martins et al. (2015). Copyright 2021 John Wiley and Sons, Inc.

configuration was used, and consequently analytes with similar chemical properties display a specific spatial location in the 2D chromatographic space. Thus, chemically related analytes are easily recognized in the 2D “chemical map,” simplifying the data processing through the reduction of analysis time and helping to obtain reliable identifications (particularly if standards are not available) (Mondello et al., 2008). These structured chromatograms are possibly one of the most important features of GC \times GC, comparing with 1D-GC performance. **Figure 8** elucidates the principle of the structured chromatogram, where hydrocarbons, non-polar compounds, present the lower retention time for the second dimension (2t_R), and acids, with higher polarity, present higher 2t_R values. Due to the data complexity, specific software have been developed for GC \times GC-ToFMS equipment, such as the ChromaTOF that allows the acquirement, processing, and reporting data, through the True Signal Deconvolution, and automated peak find algorithms. ChromaTOF allows to generate and to visualize the GC \times GC chromatogram, either through a contour plot or a 3D plot. **Figure 8** shows a 3D plot obtained from a Lager beer (Martins et al., 2015).

Figure 9A represents a blow-up of a part of GC \times GC total ion contour plot presented in **Figure 8** and shows that compounds with similar volatility can be separated chromatographically by taking

advantage of the use of a second column with a different stationary phase. Indeed, ethyl benzoate (peak 2; $^1t_R = 702$ s, $^2t_R = 1.070$ s) and 2-nonen-1-ol (peak 3; $^1t_R = 702$ s, $^2t_R = 0.630$ s) presented the same 1t_R (similar volatility), thus co-eluted on the Equity-5 column (1D). However, they exhibited different polarity and, therefore, were separated on the DB-FFAP column (2D), once narrow fractions were cryo-focused and re-injected on the 2D column, allowing the separation of two compounds within only half of a second. Comparing the chemical structures of these compounds, the differences on polarity may be explained by the presence of an aromatic ring that increases the polarity of the molecules (higher 2t_R), using this non-polar/polar column set.

The determination of trace analytes raises additional challenges, which may also be overcome by using GC \times GC-ToFMS systems, where detection limits and spectral quality are particularly determinant. For instance, **Figure 9B** reveals that even with narrow peaks achieved for (*E*)-2-nonenal (ca. 49 ms), the spectral quality of the acquired spectrum is appropriate to compare it with MS commercial databases. Thus, the putative identification of (*E*)-2-nonenal can be achieved through the analysis of the retention times (1t_R and 2t_R), the mass spectrum and its similarity with commercial databases, the calculation of the RI, and its comparison with the literature for column equivalents with those used in the 1D .



To take advantage of the potentialities of the GC \times GC-ToFMS, it is important to properly define the conditions of acquisition and processing of the instrumental signal. Nowadays, robust software algorithms associated to the GC \times GC-ToFMS equipment allow an easier processing of the data, regarding both qualitative and quantitative purposes. MS data are acquired using full-scan mode (i.e., data acquisition using a wide m/z range, where ranges from 30 to 300 m/z were commonly used for volatiles' determination). In particular cases, ion extraction chromatography mode (IEC—data processing that uses data acquired in full-scan mode, and then the chromatograms may be reprocessed using specific m/z diagnostic ions) may be performed.

IEC may be performed by selecting a set of m/z diagnostic ions specific for some analytes or chemical families, allowing the definition of a two-dimensional chromatographic space containing these compounds, simplifying the data, and reducing the time of data processing. Thus, IEC contributes to increase the sensitivity and specificity, and consequently reduces the co-elution problems and increasing the GC area of specific analyte(s) (Tranchida et al., 2004). Moreover, a non-target and target analysis may be achieved with a single analysis by combining a full-scan acquisition mode with IEC data processing mode, selecting specific ions to highlight certain analyte(s) or chemical families. For instance, a HS-SPME/GC \times GC-ToFMS-based methodology was developed for the global

volatile analysis of Madeira wine, including age markers, with potential contribution for specific aromas of aged wines, and also allowed the quantification of ethyl carbamate (EC) (Perestrelo et al., 2010; Perestrelo et al., 2011). Under normal processing and/or storage conditions of Madeira wine, and with concentrations of urea in the range of 1–10 mg/L, a significant amount of EC may be produced. EC, known as urethane, is potentially toxic, and was re-classified in 2007 as “probably human carcinogenic compound” (Group 2A) by the International Agency for Research on Cancer, and it is recommended that its level in fortified wines should be under 100 $\mu\text{g/L}$. The reported methodology allows the EC quantification directly in Madeira wine, which provides significant reduction in time of analysis compared with the HPLC and 1D-GC methods reported in the literature (Perestrelo et al., 2010). In addition, it does not require a prior derivatization or any toxic solvent. The development of a methodology that allows the direct analysis of the sample without any previous handling is fundamental to avoid loss of analytes and the occurrence of artifacts. The use of GC \times GC-ToFMS full-scan acquisition mode combined with IEC mode allowed to achieve a simultaneous quantification of EC target analyte, increasing specificity and sensitivity, and to obtain data about the furans, lactones, volatile phenols, and acetals, defined as potential aged markers (Perestrelo et al., 2010; Perestrelo et al., 2011). From these, 103 volatile compounds were tentatively

identified, from which 71 have been reported for the first time in Madeira wines (Perestrelo et al., 2011). Indeed, due to the orthogonal separation, GC \times GC-ToFMS system offers a more useful approach to identify these compounds compared with previous studies using GC-qMS (gas chromatography–quadrupole mass spectrometry), reducing co-elutions, increasing peak capacity and mass selectivity, and contributing to the establishment of new potential Madeira wine age markers.

The analytes' identification must be confirmed through the co-injection of authentic standards. However, standards can be quite expensive, often unattainable in the time available for analysis, and sometimes not commercially available. Therefore, a strategy that combines several criteria is currently used to improve the identification confidence:

- Co-injection of standards (allows the construction of home-made databases),
- 1t_R and 2t_R values (structured chromatogram),
- Mass spectrum fragmentation pattern of each analyte and comparison with co-injected standards and MS from commercial databases (mass spectral similarity),
- Linear retention index (i.e., comparison between LRIs calculated and those available in the literature for columns like those used in the 1st dimension or equivalents).

Briefly, the analytes can be tentatively identified using home-made and commercial and/or open-source mass spectra databases, such as those widely used as the Wiley 275 and US National Institute of Science and Technology (NIST). In addition, the comparison of LRI values experimentally acquired and those obtained from literature, when available, may be performed. Therefore, an *n*-alkane is given a retention index value of 100 times its carbon number. The LRI of each analyte can be computed by van Den Dool and Kratz equation (van Den Dool and Kratz, 1963), in which the analyte's retention time is normalized with the adjacent eluting *n*-alkanes' retention times. An *n*-alkanes series (usually ranging from C₆ to C₂₀ for volatile and semi-volatile analytes) must be injected in the same GC column and program, and the LRI values calculated for each analyte may be compared with LRIs previously reported in the literature or in open-source LRI libraries, using a GC column like the one used experimentally in the 1^D. Indeed, different analytical laboratories can compare LRIs once they are independent of some instrumental variables of GCs (e.g., length and diameter of column, film thickness, pressure or carrier gas type, and velocity), contrary to retention times of the analytes (Babushok, 2015).

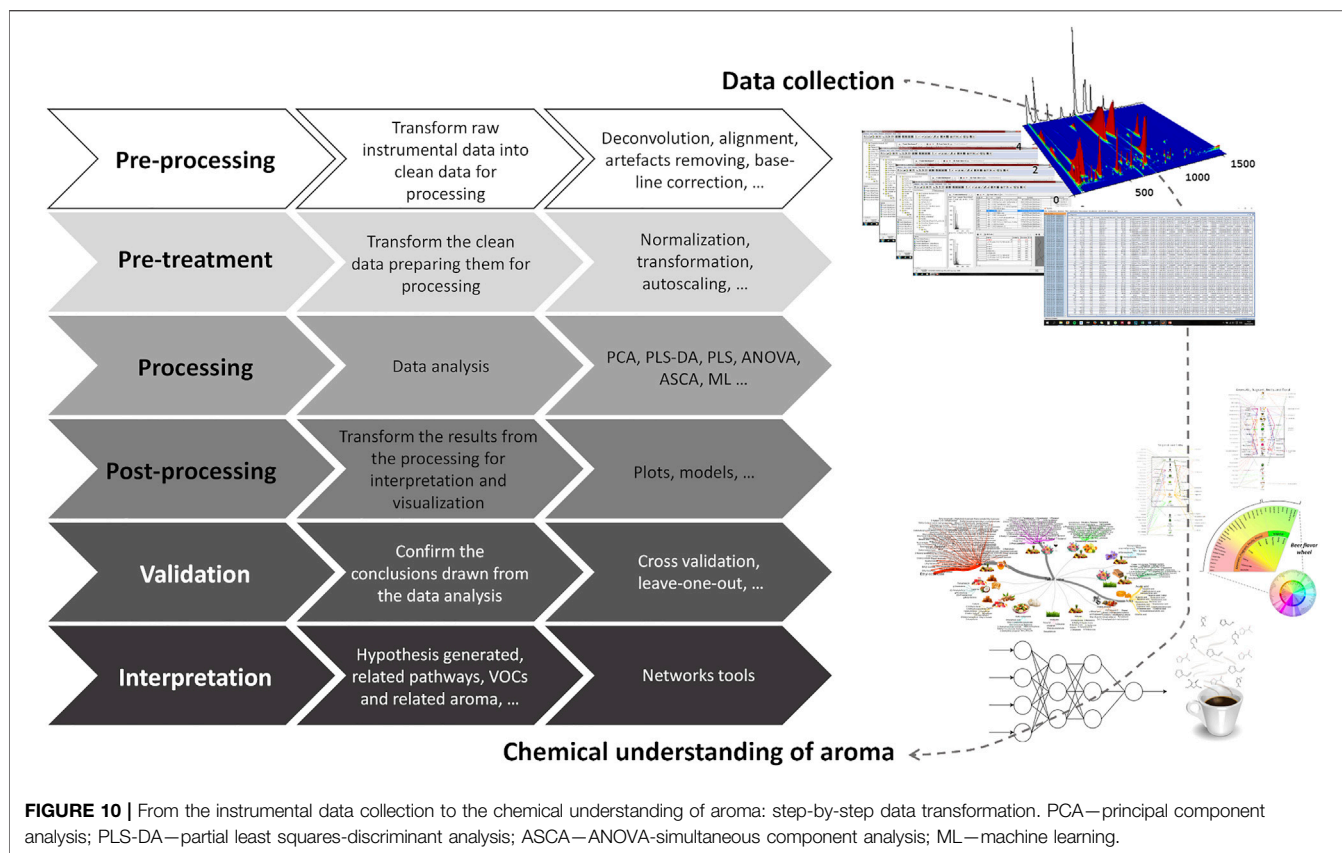
The amount of each analyte may be estimated through its chromatographic area. For target analysis, a set of methodologies may be implemented for the quantification purposes, namely construction of external calibration curves, including multiple calibration curves, and the use of isotopically labeled standards. Also, a standard addition method may be used to avoid the matrix effects. Despite providing highly accurate data, the costs associated with isotopically labeled standards have limited their use to very specific cases. On the other hand, a wide range of internal standards (IS) have been used depending on

the analytes and methodologies, and on this semi-quantification approach, for each analyte, and the results are expressed as equivalent of IS. The selection of the more appropriate method for each case depends on the purpose of the work and on the characteristics of the sample. For instance, for the quantification of EC in dry/medium dry and sweet/medium sweet Madeira wines, external calibration curves were performed for both types of wines using the IEC mode (*m/z* 62). Good linearity was obtained with a regression coefficient (*r*²) higher than 0.981. Low LODs were achieved for dry (4.31 µg/L) and sweet (2.75 µg/L) wines. The quantification limits (LOQ) and recovery for dry wines were 14.38 µg/L and 88.6%, whereas for sweet wines, these were 9.16 µg/L and 99.4%, respectively. The higher performance was attained for sweet wines since the higher glucose content improved the release of volatiles to the headspace. Moreover, better linearity, recovery, and precision was achieved (Perestrelo et al., 2010).

Nowadays, some drawbacks still remain regarding the use of the GC \times GC equipment, namely requiring operational expertise, complex instrumentation, and high costs of consumables (Tranchida et al., 2004; Marriott et al., 2012). However, the increase in sensitivity provided by the modulation process, together with the high chromatographic resolution power of GC \times GC combined with the ToFMS, makes this technique advantageous over 1D-GC for challenging food aroma chemistry assessments. Actually, this high-throughput technique has been used to assess several data associated with aroma characteristics of foodstuffs and beverages, and multiple uses covering target and/or non-target analysis have been reported. In particular, GC \times GC has been widely used in food applications, for instance for authenticity testing; search for differences between good and/or off odor, varieties or cultivars, and geographical origins; exploring for markers related with technological steps (e.g., ripening, postharvest conditions, fermentation), aroma, or aging; study of the key odorants, among others, as illustrated by the following studies: table, fortified and sparkling wines (Perestrelo et al., 2010, 2011; Weldegergis et al., 2011; Santos et al., 2013; Welke et al., 2014; Whitener et al., 2016; Rocha et al., 2021), beer (Inui et al., 2013; Martins et al., 2015, 2017, 2018), elderberry (Salvador et al., 2016), elderflower (Salvador et al., 2017), grape (Banerjee et al., 2008), aromatic plants (Shellie et al., 2002; Klimánková et al., 2008; Petronilho et al., 2011), sea salt (Silva et al., 2010, 2015), coffee (Bressanello et al., 2021; Lopes et al., 2021), hazelnut (Cordero et al., 2010; Kiefl et al., 2013; Kiefl and Schieberle, 2013; Rosso et al., 2020), honey (Čajka et al., 2007; Siegmund et al., 2018), milk (Hayward et al., 2010), cake (Rega et al., 2009), meat (Sekhon et al., 2010; Planche et al., 2015; Li W. et al., 2021), pear (Wang et al., 2019; Fonseca et al., 2020), and virgin olive oil (Peres et al., 2013; Purcaro et al., 2014; Ros et al., 2019).

From Instrumental Data to Chemical Aroma Comprehension

Considering the size and complexity of the data matrices generated by a single GC \times GC-ToFMS analysis, a strategy



should be carefully designed to transform the instrumental data into interpretable and useful information in understanding the aroma of food items. The main steps that may be considered on this challenging route are illustrated in **Figure 10**.

Data processing involves different steps from data pre-processing, pre-treatment, identification, quantification, and processing to data post-processing, validation, and interpretation. The chemical complexity of food matrices, the lack of reference mass spectra for all the compounds, and the inherent variability in each sample highlights the data processing importance. Instrumental signal data are currently used as an approach to estimate the relative content of each analyte, as it reports the response of the instrument to the analytes' abundances. Thus, the first steps, namely the pre-processing (deconvolution, alignment, artifact removal, baseline correction, etc.) and pre-treatment (normalization, transformation, autoscaling, ...), should be carefully performed before uni- and/or multivariate data analysis. Indeed, the decisions taken in these first 2 stages will have a crucial influence on the results.

Data analysis includes different possibilities, namely multivariate analysis that is intended to distinguish classes in complex datasets. Unsupervised multivariate analysis, such as principal component analysis (PCA), is often used as an exploratory technique, allowing to study the main sources of variability present in the data sets, as well as to detect clustering

formation, and to establish relationships between samples (objects) and analytes (variables) (Jolliffe, 2002; Berrueta et al., 2007). Clustering methods, such as heatmap hierarchical cluster analysis, an unsupervised clustering analysis, is highly applied to evaluate the similarities among samples. By using a chromatic scale, a visual and intuitive way of displaying the content of each analyte may be achieved.

Partial least squares (PLS) is a widely used procedure for both regression and classification purposes. Concerning the classification application of PLS, known as partial least squares-discriminant analysis (PLS-DA) (Eriksson et al., 2006), the most common approach is to use a Y matrix containing dummy variables, which defines sample memberships to pre-defined groups and allows extracting relevant information/variability that could describe the reasons for the observed patterns (clusters). This methodology allows to understand which variables (analytes) contribute the most for the observed distinction (Berrueta et al., 2007). PLS-DA may be also applied combined with VIP (variable importance in projection) values to identify the main analytes that contribute for the distinction between samples. The use of VIP values allows the reduction of the data set complexity and represents a huge approach for assessing relevant information in real time. For those supervised tools, classification model complexity (number of latent variables) and classification rate and Q^2 (quality-of-fit criterion) should be estimated by cross-validation. Thus, experiments must be carefully

designed to obtain a sufficient number of samples for the construction and validation of the model(s).

ANOVA-simultaneous component analysis (ASCA) can deal with complex multivariate datasets containing an underlying experimental design. It is a direct generalization of ANOVA for univariate data to the multivariate case. The method allows for easy interpretation of the variation induced by the different factors of the design. Validation is a crucial step, especially used for supervised statistical methods (e.g., leave-one-out validation), to guarantee the reliability of the applied model. Model validation process allows demonstrating that the models obtained by the supervised pattern recognition techniques are good enough to perform classification or discrimination of the samples (Berrueta et al., 2007).

Otherwise, univariate methods are also used to study one variable or chemical family that could characterize a sample or class of samples or may be altered among them. These methods are often used as a complement of the multivariate analysis. Depending on the data set and experimental design, a wide range of methods may be used. For instance, parametric methods for data are normally distributed, as the ANOVA may be applied as a *post hoc* test, as they allow evaluating one variable for more than two conditions (samples).

Taking advantages of the bioinformatics developments, it is possible to combine different domains of information and construct networks containing several underlying factors. For instance, data analysis combining chromatographic and sensorial data may generate a visual aroma network that represents an aroma snapshot and allows to estimate the role of the different volatiles to the aroma properties of foods (**Figure 10**) (Ahn et al., 2011; Martins et al., 2018).

More recently, innovative advances have been applied for data analysis, namely machine learning (ML), which is a subset of the artificial intelligence techniques, and that utilizes algorithms to extract patterns in a diversity of applications (Telikani et al., 2022). In this context, ML can be applied to unraveling the food aroma using the complex datasets resultant from the comprehensive fingerprinting and/or profiling of foods (for instance, as those obtained by GC × GC). ML techniques can use different domains as input (called units, nodes, or neurons), such as chromatographic data, sensorial data from literature (e.g., odor thresholds and aroma descriptors, among others), and/or data resultant from sensorial analysis, GC-O, and e-nose, among others. The pattern analysis is then applied to those inputs, using different algorithms (uses the weight of the link between two units), that can lead to the chemical understanding of aroma (**Figure 11A**). Several parameters should be optimized to achieve an accurate prediction model without over-fitting (i.e., good fitting results for the training dataset in the learning phase, however untrusty results with testing data), for instance the number of samples, hidden layers, and the number of iterations in the network's learning phase, among others (Hategan et al., 2021). If the dataset requires improvement of robustness (e.g., low number of samples), the data augmentation technique can be applied, for instance, to perform the convolutional neural network (CNN) based on deep chemometrics (Bjerrum et al., 2017).

ML has been applied to unveil the specific aroma attributes of different food matrices, such as wine and beer. Various ML

algorithms [namely linear discriminant analysis (LDA), linear support vector machines (SVM), and quadratic SVM] were applied to the comprehensive volatile fingerprinting extracted by GC×GC-ToFMS from 127 wines (Reichenbach et al., 2019). Those ML methods were able to classify wines according to grape varieties, grape-growing regions, vintage years, and wineries. For example, β -eudesmol presented higher Fisher ratio for a specific winery, and its presence in the wines may be linked to the closeness of the vineyards to *Eucalyptus* forests (this volatile compound is characteristic of *Eucalyptus* trees), whose leaves may take part accidentally in vinification. Furthermore, a rapid, non-destructive, and cost-effective tool was developed using 2 ML models based on artificial neural networks (ANNs) (Summerson et al., 2021a). The high accuracy regression models were constructed using e-nose outputs as inputs to predict the level of the volatile compounds and the smoke aroma intensity of Cabernet Sauvignon wines, thus creating a decision-making tool for winemakers (**Figure 11B**). The same approach was also used to access the effectiveness of smoke taint amelioration treatments in Pinot Grigio wines (Summerson et al., 2021b), and the more effective treatment was through the cleaving enzyme coupled with activated carbon, which can help delay the recovery of smoke aromas in wine's subsequent aging and glycoconjugate hydrolysis.

A highly accurate ML model ($R = 0.98$) based on ANN was developed to predict consumers' beer acceptability (Viejo et al., 2019). This model used the relative peak area of volatile data obtained as input; the aroma, flavor, and overall liking from sensorial analysis were used as targets from 24 analyzed beers. The ANN Bayesian regularization algorithm demonstrated to be a more appropriate analysis than multiple regression models once it included nonlinear correlations between the inputs and targets previously enumerated. The developed model allowed, for instance, to observe that 4-ethyguaiacol and *trans*- β -ionone contributed positively to beer, regarding aroma, flavor, and overall liking, while styrene contributed to the opposite effect. ML models can be also integrated with other technologies such as sensors and robotics, as it was demonstrated by the rapid and accurate evaluation of commercial beers using low-cost robotics and sensors—RoboBEER (Viejo and Fuentes, 2020). For this case, the absorbance of near-infrared (NIR) spectroscopy was used as input to predict the peak areas of volatiles and chemical parameters of beers; also, the same approach was used using robotics (RoboBEER) as input. Both achieved models were accurate; nevertheless, they still require improvement, such as complement the ML model with other robust data, including GC-MS, GC-O, and/or e-nose data.

Other pioneering approaches have attracted the attention of the food aroma specialists in recent years, namely the sensomics that is a reference procedure to characterize the key food odorants (KFOs), which includes the identification and accurate quantitation of KFOs, aroma reconstitution, and omission experiments (Schieberle and Hofmann, 2011). Different methodologies can be used for this purpose, such as solvent-assisted flavor evaporation (SAFE), to extract the food's volatiles; aroma extract dilution analysis (AEDA) to assign the aroma

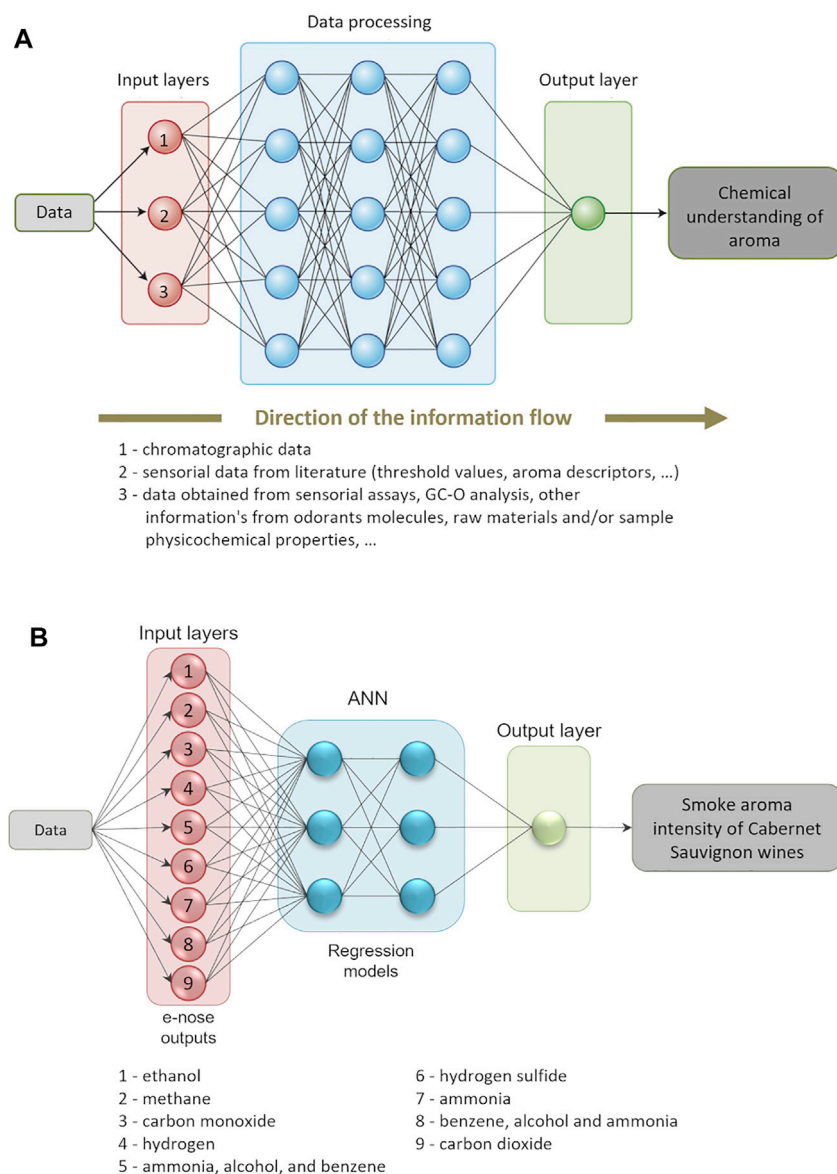


FIGURE 11 | (A) A symbiosis between advanced instrumental and bioinformatics with sensorial analysis or other data will represent a stream advance in chemical understanding of food aromas, taking advantage of the machine learning (ML) principles. Figure adapted from Topol (2019). **(B)** Assessment of volatile compounds in smoke-tainted Cabernet Sauvignon wines using a low-cost e-nose and machine learning modeling. The high accuracy regression models were constructed using e-nose outputs as inputs to predict smoke aroma intensity of Cabernet Sauvignon wines. ANN—artificial neural network. Figure adapted from Summerson et al. (2021a).

quality and volatiles' potency, through the preparation of different diluted extracts to be further analyzed by GC-O; and stable isotope dilution assays to quantify the volatile components with highest aroma potency, and consequently their OAV can be calculated. Model matrices are then spiked with the pure compounds of the identified KFOs (using the determined concentrations in the food itself) to prepare the aroma recombinates. These aroma recombinates are sensorially evaluated and compared with the original food, by a trained sensory panel, which validate the KFOs, considering their

accurate identification and quantitation (Schieberle and Hofmann, 2011; Nicolotti et al., 2019). Thus, KFOs are the food volatile components that, on one hand, exceed their OT in the food matrix and, on the other hand, have a determinant role to mimic the real food sensory profile, after the recombination and omission experiments.

Sensomics has been used to determine KFOs in a wide range of foods, for instance, black tea (Schieberle and Hofmann, 2011), cognac (Uselmann and Schieberle, 2015), truffles (Schmidberger and Schieberle, 2017), yeasted wheat dough (yeast dumpling)

(Sahin and Schieberle, 2019), pretzels' crust (Schoenauer and Schieberle, 2019), wine (Lyu et al., 2019), fried bread (Lasekan and Dabaj, 2020), garlic (Abe et al., 2020), bagels (Lasekan et al., 2021), fermented soybean product (Zhao et al., 2021), or cheese (Wang et al., 2021). However, some drawbacks can be pointed out, which makes this approach hard to be used as routine analysis, namely it is time consuming and globally complex, and it requires a wide range of different analytical instruments and techniques (Schieberle and Hofmann, 2011; Nicolotti et al., 2019).

Based on the sensomics approach, a single analytical platform was developed called sensomics-based expert system (SEBES) that foresees KFOs in an extract, through the combination of odor thresholds and quantification data in one software that automatically calculate the OAVs. This alternative and fast approach does not presuppose the use of human olfactory system, and the food odor codes are achieved by artificial intelligence smelling (Nicolotti et al., 2019), which gives a good alternative for routine analysis. Moreover, GC \times GC-ToFMS and GC Image software are recommended for SEBES approach: the former due to its high resolution and high sensitivity; the latter because of the software's capacity to perform automated quantitative data based on features and other custom functions (e.g., database construction of odor thresholds of KFOs in several matrices). SEBES was successfully applied to rum and Cabernet Sauvignon wines, once its performance was compared with the conventional sensomics approach (Nicolotti et al., 2019) and good agreement was observed between the two approaches (differences below 20%). Some instrumental drawbacks of SEBES are still required to overcome, e.g., shift to headspace over liquid techniques to detect highly volatile compounds; some odor thresholds are inferior to instrument's sensitivity and are not quantified as KFOs (Nicolotti et al., 2019). More recently, a headspace-based technique (MHS-SPME-GC \times GC-MS/FID) was proposed as artificial intelligence smelling machine using extra virgin oil as the studied matrix (Stilo et al., 2021), thus overcoming the drawback presented by Nicolotti et al. (2019). Despite the already respectable level of software automatization, there is still a great margin for future improvement, for instance developments presupposing the use of ML, which can lead to machine decision-making. Also, the construction of open access odor threshold databases will pursue the better development of SEBES approach (Nicolotti et al., 2019).

CONCLUDING REMARKS AND FUTURE PERSPECTIVES

This review provides the state-of-the-art and the technical know-how for young researchers and an extensive range of specialists from the food-related area and others who want to start studying aroma of food items at chemical level based on the use of advanced gas chromatographic methodologies. Indeed, increase in knowledge of aroma chemistry science was powered by advances in chemical analysis, being the gas

chromatography the central technique to characterize odorant compounds. Also, the vapor above a food—aroma cloud—holds the odorant molecules that may be perceived by the odor receptor sites of the smell organ. SPME is a sample preparation technique well suited to the extraction of these molecules.

As a capstone, it was considered important to highlight and/or systematize the main ideas addressed in this review:

- SPME, a solvent-free extraction technique, allows in a single step the sampling, extraction, and concentration of headspace volatile components, i.e., the aroma clouds components. Currently, there are several stationary phases and geometries on the market, and new solutions are under development. 3D printing will undoubtedly be one of the solutions that can open new opportunities in extracting representative headspace components,
- SPME/GC \times GC-based methodologies overcome a set of challenges previously reported for the analysis of volatile and semi-volatile food items; namely, it allows the detection of a high number of chemical structures of volatile and semi-volatile molecules, in a wide concentration range (from pg to mg),
- GC \times GC-ToFMS combined with SPME seems to be an appropriate combination to unveil food aroma complexity, as the modulation process (i.e., the cryofocusing of analytes between the two GC columns) and sensitivity achieved from ToFMS will compensate the non-exhaustive extraction provided by SPME,
- GC \times GC-based methodologies allow a simultaneous targeted and detailed study of the aroma clouds volatile composition within a single analysis, contributing to the detection of a huge number of analytes as never before achieved,
- This throughput issue is convenient for the analysis of large numbers of samples in a very convenient time (*ca.* 20 min of instrumental acquisition per sample),
- The generated instrumental raw data are compatible with the advanced data analysis tools, and some of them are free to access. Advanced artificial intelligence techniques may be used to interpret the volatile signatures and classify them based on data from collected smells, namely by combined chemical and sensorial data,
- The innovative strategies presented to transform the chromatographic data into useful information for aroma comprehension, although not replacing the sensorial assays, generate very important information for the understanding of the aroma at the level of the molecule and the phenomena related to its origin and/or open new approaches to modulate, modify, or even create new aromas.

Despite the enormous advantages covered by GC \times GC comparing with 1D-GC, such as improved resolution and peak capacity, faster run times, and improved detection limits, its use is still restricted to very specific applications. The new generations of GC \times GC are designed to reduce some drawbacks, namely making maintenance operations easier for the user, smaller equipment, more compact and easily integrated in

common laboratories, and advances in modulators to reduce the costs of consumables, among others. Due to the size and complexity of the data generated in a single analysis by GC \times GC, the data processing steps are time-consuming and tedious and there are some limitations that must be overcome to make this technique more appealing for the users. Also, to go further on the aroma chemistry comprehension, the combination of chromatographic data with other domains of information is crucial. Thus, the following are identified as very pertinent:

- Development of tools for the instrumental signal alignment, and in a relatively quick way to identify and quantify high numbers of analytes, in a large number of samples,
- Creation of open access databases with information about aroma potential of volatile and semi-volatile molecules (i.e., aroma descriptor and threshold value) in a wide range of food products, particularly for endogenous and unique products whose knowledge and valuation can have a high impact on the society and economy of local communities,
- Development of a bioinformatics platform that in an integrated way can allow the acquisition of instrumental signals and their processing, including interaction with databases of sensory information (when applicable). Indeed, in the future and after training, these tools will ingest and meaningfully process massive sets of data quickly, accurately, and inexpensively, and for machines that will see and do things that are not humanly possible.

For a holistic understanding of the aroma of foods, it is crucial to define a broad strategy, involving diverse techniques that can assess the multiple dimensions of the aroma perception, that are intrinsically associated with the multimodal perception concept, i.e., multimodal phenomena concern stimuli that generate simultaneous (or nearly simultaneous) information in more than one sensory modality (Chambers IV and Koppel, 2013; Bressanello et al., 2021). Certainly, the chemical aroma data are not enough, but crucial to move forward on this challenging topic, and GC \times GC-ToFMS seems to be a powerful technique for the analytical coverage of the chemical clouds of food. This technique seems to fulfill the requirements of the innovative

strategies in the field of the aroma chemistry such as the smell digitalization. Due to the huge significance of human olfaction in several fields, namely to improve nutritional health, diagnose and treat diseases, understand consumer preferences and consumption, measure and chemically reveal the smells, it represents cutting-edge research with an increase of such a tendency to be expected in the future.

Aroma chemistry is under an ever-increasing knowledge on chemical data driven by the latest equipment and bioinformation innovation. Although this review has been focused on the aroma of food, the concepts, methodologies, and challenges discussed in this context are perfectly transposable to the study of a wide range of non-food items. This information at the molecular level can be exploited in several dimensions beyond aroma, as these data may be useful to solve or understand issues related with product and process control, food safety, establishment of botanical markers, and understanding of the individual's response in health and disease condition, or in specific age range, among others.

AUTHOR CONTRIBUTIONS

SR: responsible for conceptualization, writing the original draft, review and editing the final version, preparation of illustrations, supervision, and funding acquisition. CC: editing the final version and preparation of illustrations. CM: writing and editing the final version and preparation of illustrations. All the authors contributed to the article and approved the submitted version.

FUNDING

Thanks are due to FCT/MEC for the financial support LAQV-REQUIMTE (UIDB/50006/2020) through national funds and when applicable co-financed by the FEDER, within the PT2020 Partnership Agreement. Thanks are also due to the project Cristal Eco Premium: Sustainable crystal glass line development (POCI-01-0247-FEDER-047101), funded by Incentive System for Research and Technological Development (SI IDT) |D Corporate, through FEDER, Compete2020 and PT 2020.

REFERENCES

- Abe, K., Hori, Y., and Myoda, T. (2020). Characterization of Key Aroma Compounds in Aged Garlic Extract. *Food Chem.* 312, 126081. doi:10.1016/j.foodchem.2019.126081
- Ahn, Y.-Y., Ahnert, S. E., Bagrow, J. P., and Barabási, A.-L. (2011). Flavor Network and the Principles of Food Pairing. *Sci. Rep.* 1, 196. doi:10.1038/srep00196
- Alves, Z., Melo, A., Figueiredo, A. R., Coimbra, M. A., Gomes, A. C., and Rocha, S. M. (2015). Exploring the *Saccharomyces cerevisiae* Volatile Metabolome: Indigenous versus Commercial Strains. *PLoS One* 10, e0143641. doi:10.1371/journal.pone.0143641
- Amaral, M. S. S., and Marriott, P. J. (2019). The Blossoming of Technology for the Analysis of Complex Aroma Bouquets-A Review on Flavour and Odorant Multidimensional and Comprehensive Gas Chromatography Applications. *Molecules* 24, 2080. doi:10.3390/molecules24112080
- Averbeck, M., and Schieberle, P. (2011). Influence of Different Storage Conditions on Changes in the Key Aroma Compounds of orange Juice Reconstituted from Concentrate. *Eur. Food Res. Technol.* 232, 129–142. doi:10.1007/s00217-010-1366-8
- Babushok, V. I. (2015). Chromatographic Retention Indices in Identification of Chemical Compounds. *Trac Trends Anal. Chem.* 69, 98–104. doi:10.1016/j.trac.2015.04.001
- Bahaghighat, H. D., Freye, C. E., and Synovec, R. E. (2019). Recent Advances in Modulator Technology for Comprehensive Two Dimensional Gas Chromatography. *Trac Trends Anal. Chem.* 113, 379–391. doi:10.1016/j.trac.2018.04.016
- Baldovini, N. (2017). "Natural Fragrant Raw Materials," in *Handbook of Odor*. Editor A. Buettner (Cham, Switzerland: Springer International Publishing AG), 39–62. doi:10.1007/978-3-319-26932-0_3
- Banerjee, K., Patil, S. H., Dasgupta, S., Oulkar, D. P., Patil, S. B., Savant, R., et al. (2008). Optimization of Separation and Detection Conditions for the Multiresidue Analysis of Pesticides in Grapes by Comprehensive Two-

- Dimensional Gas Chromatography-Time-Of-Flight Mass Spectrometry. *J. Chromatogr. A* 1190, 350–357. doi:10.1016/j.chroma.2008.03.017
- Belinato, J. R., Dias, F. F. G., Caliman, J. D., Augusto, F., and Hantao, L. W. (2018). Opportunities for green Microextractions in Comprehensive Two-Dimensional Gas Chromatography/Mass Spectrometry-Based Metabolomics - A Review. *Analytica Chim. Acta* 1040, 1–18. doi:10.1016/j.aca.2018.08.034
- Belitz, H.-D., Grosch, W., and Schieberle, P. (2009a). "Aroma Compounds," in *Food Chemistry* (Springer-Verlag Berlin Heidelberg), 340–402.
- Belitz, H.-D., Grosch, W., and Schieberle, P. (2009b). "Lipids," in *Food Chemistry* (Springer-Verlag Berlin Heidelberg), 158–247.
- Berrueta, L. A., Alonso-Salces, R. M., and Héberger, K. (2007). Supervised Pattern Recognition in Food Analysis. *J. Chromatogr. A* 1158, 196–214. doi:10.1016/j.chroma.2007.05.024
- Biedermann, M., and Grob, K. (2018). Advantages of Comprehensive Two-Dimensional Gas Chromatography for Comprehensive Analysis of Potential Migrants from Food Contact Materials. *Analytica Chim. Acta* 1057, 11–17. doi:10.1016/j.aca.2018.10.046
- Bjerrum, E. J., Glahder, M., and Skov, T. (2017). Data augmentation of spectral data for Convolutional Neural Network (CNN) based deep chemometrics. *arXiv Prepr.* arXiv:1710.01927, 1–10. Available at: <http://arxiv.org/abs/1710.01927>.
- Boonbumrung, S., Tamura, H., Mookdasanit, J., Nakamoto, H., Ishihara, M., Yoshizawa, T., et al. (2001). Characteristic Aroma Components of the Volatile Oil of Yellow Keaw Mango Fruits Determined by Limited Odor Unit Method. *Fstr* 7, 200–206. doi:10.3136/fstr.7.200
- Boyacı, E., Bojko, B., Reyes-Garcés, N., Poole, J. J., Gómez-Ríos, G. A., Teixeira, A., et al. (2018). High-throughput Analysis Using Non-depletive SPME: Challenges and Applications to the Determination of Free and Total Concentrations in Small Sample Volumes. *Sci. Rep.* 8, 1–10. doi:10.1038/s41598-018-19313-1
- Bressanello, D., Marengo, A., Cordero, C., Strocchi, G., Rubiolo, P., Pellegrino, G., et al. (2021). Chromatographic Fingerprinting Strategy to Delineate Chemical Patterns Correlated to Coffee Odor and Taste Attributes. *J. Agric. Food Chem.* 69, 4550–4560. doi:10.1021/acs.jafc.1c00509
- Buck, L., and Axel, R. (1991). A Novel Multigene Family May Encode Odorant Receptors: A Molecular Basis for Odor Recognition. *Cell* 65, 175–187. doi:10.1016/0092-8674(91)90418-X
- Busko, M., Jeleń, H., Góral, T., Chmielewski, J., Stuper, K., Szwajkowska-Michalek, L., et al. (2010). Volatile Metabolites in Various Cereal Grains. *Food Additives & Contaminants: A* 27, 1574–1581. doi:10.1080/19440049.2010.506600
- Čajka, T., Hajšlová, J., Cochran, J., Holadová, K., and Klimánková, E. (2007). Solid Phase Microextraction-Comprehensive Two-Dimensional Gas Chromatography-Time-Of-Flight Mass Spectrometry for the Analysis of Honey Volatiles. *J. Sep. Sci.* 30, 534–546. doi:10.1002/jssc.200600413
- Calligaris, S., Mirolo, G., Da Pieve, S., Arrighetti, G., and Nicoli, M. C. (2014). Effect of Oil Type on Formation, Structure and Thermal Properties of γ -oryzanol and β -sitosterol-Based Organogels. *Food Biophys.* 9, 69–75. doi:10.1007/s11483-013-9318-z
- Cardinali, F., Ferrocino, I., Milanović, V., Belleghia, L., Corvaglia, M. R., Garofalo, C., et al. (2021). Microbial communities and volatile profile of Queijo de Azeitão PDO cheese, a traditional Mediterranean thistle-curdled cheese from Portugal. *Food Res. Int.* 147, 110537. doi:10.1016/j.foodres.2021.110537
- Carrillo, J. D., and Tena, M. T. (2006). Determination of Volatile Oak Compounds in Aged Wines by Multiple Headspace Solid-phase Microextraction and Gas Chromatography-Mass Spectrometry (MHS-SPME-GC-MS). *Anal. Bioanal. Chem.* 385, 937–943. doi:10.1007/s00216-006-0446-x
- Carriço, Í. R., Marques, J., Trujillo-Rodríguez, M. J., Anderson, J. L., and Rocha, S. M. (2020). Sorbent Coatings for Solid-phase Microextraction Targeted towards the Analysis of Death-Related Polar Analytes Coupled to Comprehensive Two-Dimensional Gas Chromatography: Comparison of Zwitterionic Polymeric Ionic Liquids versus Commercial Coatings. *Microchemical J.* 158, 105243. doi:10.1016/j.microc.2020.105243
- Chambers, E., and Koppel, K. (2013). Associations of Volatile Compounds with Sensory Aroma and Flavor: The Complex Nature of Flavor. *Molecules* 18, 4887–4905. doi:10.3390/molecules18054887
- Chen, Y., and Ho, C.-T. (2006). "Flavor Analysis in Food," in *Encyclopedia of Analytical Chemistry*. Editor R. A. Meyers (John Wiley & Sons), 1–20. doi:10.1002/9780470027318.a1009
- Chin, S.-T., Eyres, G. T., and Marriott, P. J. (2015). Application of Integrated Comprehensive/multidimensional Gas Chromatography with Mass Spectrometry and Olfactometry for Aroma Analysis in Wine and Coffee. *Food Chem.* 185, 355–361. doi:10.1016/j.foodchem.2015.04.003
- Chin, S.-T., Eyres, G. T., and Marriott, P. J. (2012). Cumulative Solid Phase Microextraction Sampling for Gas Chromatography-Olfactometry of Shiraz Wine. *J. Chromatogr. A* 1255, 221–227. doi:10.1016/j.chroma.2012.03.084
- Cordero, C., Kiefl, J., Reichenbach, S. E., and Bicchi, C. (2019). Characterization of Odorant Patterns by Comprehensive Two-Dimensional Gas Chromatography: A challenge in Omic Studies. *Trac Trends Anal. Chem.* 113, 364–378. doi:10.1016/j.trac.2018.06.005
- Cordero, C., Liberto, E., Bicchi, C., Rubiolo, P., Schieberle, P., Reichenbach, S. E., et al. (2010). Profiling Food Volatiles by Comprehensive Two-Dimensional Gas Chromatography Coupled with Mass Spectrometry: Advanced Fingerprinting Approaches for Comparative Analysis of the Volatile Fraction of Roasted Hazelnuts (*Corylus avellana* L.) from Different Origins. *J. Chromatogr. A* 1217, 5848–5858. doi:10.1016/j.chroma.2010.07.006
- Czerny, M., Christlbauer, M., Christlbauer, M., Fischer, A., Granvogel, M., Hammer, M., et al. (2008). Re-investigation on Odour Thresholds of Key Food Aroma Compounds and Development of an Aroma Language Based on Odour Qualities of Defined Aqueous Odorant Solutions. *Eur. Food Res. Technol.* 228, 265–273. doi:10.1007/s00217-008-0931-x
- Da Ros, A., Masuero, D., Riccadonna, S., Brkić Bubola, K., Mulinacci, N., Mattivi, F., et al. (2019). Complementary Untargeted and Targeted Metabolomics for Differentiation of Extra virgin Olive Oils of Different Origin of purchase Based on Volatile and Phenolic Composition and Sensory Quality. *Molecules* 24, 2896. doi:10.3390/molecules24162896
- da Silva, J. T., Garzillo, J. M. F., Rauber, F., Kluczkowski, A., Rivera, X. S., da Cruz, G. L., et al. (2021). Greenhouse Gas Emissions, Water Footprint, and Ecological Footprint of Food Purchases According to Their Degree of Processing in Brazilian Metropolitan Areas: a Time-Series Study from 1987 to 2018. *Lancet Planet. Health* 5, e775–e785. doi:10.1016/s2542-5196(21)00254-0
- Delahunty, C. M., Eyres, G., and Dufour, J.-P. (2006). Gas Chromatography-Olfactometry. *J. Sep. Sci.* 29, 2107–2125. doi:10.1002/jssc.200500509
- Donadio, C., Bialecki, A., Valla, A., and Dufossé, L. (2011). Carotenoid-derived aroma compounds detected and identified in brines and specialty sea salts (fleur de sel) produced in solar salterns from Saint-Armel (France). *J. Food Compos. Anal.* 24, 801–810. doi:10.1016/j.jfca.2011.03.005
- Dunkel, A., Steinhaus, M., Kotthoff, M., Nowak, B., Krautwurst, D., Schieberle, P., et al. (2014). Nature's Chemical Signatures in Human Olfaction: A Foodborne Perspective for Future Biotechnology. *Angew. Chem. Int. Ed.* 53, 7124–7143. doi:10.1002/anie.201309508
- Eriksson, L., Johansson, E., Kettaneh, N., Wold, N., and Wold, S. (2006). *Multi and Megavariate Data Analysis, Part I: Principles and Applications*. Umea; Sweden: Umetrics Academy Publisher.
- Escudero, A., Campo, E., Fariña, L., Cacho, J., and Ferreira, V. (2007). Analytical Characterization of the Aroma of Five Premium Red Wines. Insights into the Role of Odor Families and the Concept of Fruitiness of Wines. *J. Agric. Food Chem.* 55, 4501–4510. doi:10.1021/jf0636418
- Ferreira, V., Lopez, R., and Cacho, J. F. (2000). Quantitative Determination of the Odorants of Young Red Wines from Different Grape Varieties. *J. Sci. Food Agric.* 80, 1659–1667. doi:10.1002/1097-0010(20000901)80:11<1659::aid-jfsa693>3.0.co;2-6
- Fonseca, A. M. A., Dias, C., Amaro, A. L., Isidoro, N., Pintado, M., Silvestre, A. J. D., et al. (2020). The Impact of Plant-Based Coatings in "ROCHA" Pear Preservation during Cold Storage: A Metabolomic Approach. *Foods* 9, 1299. doi:10.3390/foods9091299
- Franco, M., Peinado, R. A., Medina, M., and Moreno, J. (2004). Off-Vine Grape Drying Effect on Volatile Compounds and Aromatic Series in Must from Pedro Ximénez Grape Variety. *J. Agric. Food Chem.* 52, 3905–3910. doi:10.1021/jf0354949
- Fuller, G. H., Steltenkamp, R., and Tisserand, G. A. (1964). The Gas Chromatograph with Human Sensor: Perfumer Model. *Ann. NY Acad. Sci.* 116, 711–724. doi:10.1111/j.1749-6632.1964.tb45106.x
- Galanakis, C. M. (2020). The Food Systems in the Era of the Coronavirus (COVID-19) Pandemic Crisis. *Foods* 9, 523. doi:10.3390/foods9040523

- Giri, A., Osako, K., and Ohshima, T. (2010). Identification and Characterisation of Headspace Volatiles of Fish Miso, a Japanese Fish Meat Based Fermented Paste, with Special Emphasis on Effect of Fish Species and Meat Washing. *Food Chem.* 120, 621–631. doi:10.1016/j.foodchem.2009.10.036
- Giungato, P., Di Gilio, A., Palmisani, J., Marzocca, A., Mazzone, A., Brattoli, M., et al. (2018). Synergistic Approaches for Odor Active Compounds Monitoring and Identification: State of the Art, Integration, Limits and Potentialities of Analytical and Sensorial Techniques. *Trac Trends Anal. Chem.* 107, 116–129. doi:10.1016/j.trac.2018.07.019
- Glibowski, P., Zarzycki, P., and Krzepkowska, M. (2008). The Rheological and Instrumental Textural Properties of Selected Table Fats. *Int. J. Food Properties* 11, 678–686. doi:10.1080/10942910701622599
- Godage, N. H., and Gionfriddo, E. (2019). A Critical Outlook on Recent Developments and Applications of Matrix Compatible Coatings for Solid Phase Microextraction. *Trac Trends Anal. Chem.* 111, 220–228. doi:10.1016/j.trac.2018.12.019
- Gonzalez Viejo, C., and Fuentes, S. (2020). Beer Aroma and Quality Traits Assessment Using Artificial Intelligence. *Fermentation* 6, 56. doi:10.3390/fermentation6020056
- Gonzalez Viejo, C., Fuentes, S., Torrico, D. D., Godbole, A., and Dunshea, F. R. (2019). Chemical Characterization of aromas in Beer and Their Effect on Consumers Liking. *Food Chem.* 293, 479–485. doi:10.1016/j.foodchem.2019.04.114
- Guth, H. (1997). Quantitation and Sensory Studies of Character Impact Odorants of Different white Wine Varieties. *J. Agric. Food Chem.* 45, 3027–3032. doi:10.1021/jf970280a
- Hategan, A. R., Puscas, R., Cristea, G., Dehelean, A., Guyon, F., Molnar, A. J., et al. (2021). Opportunities and Constraints in Applying Artificial Neural Networks (ANNs) in Food Authentication. Honey-A Case Study. *Appl. Sci.* 11, 6723. doi:10.3390/app11156723
- Hayward, D. G., Pisano, T. S., Wong, J. W., and Scudder, R. J. (2010). Multiresidue Method for Pesticides and Persistent Organic Pollutants (POPs) in Milk and Cream Using Comprehensive Two-Dimensional Capillary Gas Chromatography–Time-Of-Flight Mass Spectrometry. *J. Agric. Food Chem.* 58, 5248–5256. doi:10.1021/jf100021p
- Inui, T., Tsuchiya, F., Ishimaru, M., Oka, K., and Komura, H. (2013). Different Beers with Different Hops. Relevant Compounds for Their Aroma Characteristics. *J. Agric. Food Chem.* 61, 4758–4764. doi:10.1021/jf3053737
- Jolliffe, I. T. (2002). *Principal Component Analysis*. 2nd editio. New York: Springer-Verlag.
- Kalua, C. M., Allen, M. S., Bedgood, D. R., Bishop, A. G., Prenzler, P. D., and Robards, K. (2007). Olive Oil Volatile Compounds, Flavour Development and Quality: A Critical Review. *Food Chem.* 100, 273–286. doi:10.1016/j.foodchem.2005.09.059
- Kataoka, H., Lord, H. L., and Pawliszyn, J. (2000). Applications of Solid-phase Microextraction in Food Analysis. *J. Chromatogr. A* 880, 35–62. doi:10.1016/S0021-9673(00)00309-5
- Kiefl, J., Pollner, G., and Schieberle, P. (2013). Sensomics Analysis of Key Hazelnut Odorants (*Corylus Avellana* L. 'Tonda Gentile') Using Comprehensive Two-Dimensional Gas Chromatography in Combination with Time-Of-Flight Mass Spectrometry (GC×GC-TOF-MS). *J. Agric. Food Chem.* 61, 5226–5235. doi:10.1021/jf400807w
- Kiefl, J., and Schieberle, P. (2013). Evaluation of Process Parameters Governing the Aroma Generation in Three Hazelnut Cultivars (*Corylus Avellana* L.) by Correlating Quantitative Key Odorant Profiling with Sensory Evaluation. *J. Agric. Food Chem.* 61, 5236–5244. doi:10.1021/jf4008086
- Klimánková, E., Holadová, K., Hajšlová, J., Čajka, T., Poustka, J., and Koudela, M. (2008). Aroma Profiles of Five Basil (*Ocimum basilicum* L.) Cultivars Grown under Conventional and Organic Conditions. *Food Chem.* 107, 464–472. doi:10.1016/j.foodchem.2007.07.062
- Kotecha, A., Corrêa, A., Fisher, K., and Rushworth, J. (2018). Olfactory Dysfunction as a Global Biomarker for Sniffing Out Alzheimer's Disease: A Meta-Analysis. *Biosensors* 8, 41. doi:10.3390/bios8020041
- Kudlejova, L., Risticic, S., and Vuckovic, D. (2009). "Solid-Phase Microextraction Method Development," in *Handbook of Solid Phase Microextraction*. Editor J. Pawliszyn (London: Chemical Industry Press), 173–214.
- Lasekan, O., and Dabaj, F. (2020). Characterization of the Key Aroma Constituents in Fry Breads by Means of the Sensomics Concept. *Foods* 9, 1129. doi:10.3390/foods9081129
- Lasekan, O., Dabaj, F., Muniandy, M., Juhari, N. H., and Lasekan, A. (2021). Characterization of the Key Aroma Compounds in Three Types of Bagels by Means of the Sensomics Approach. *BMC Chem.* 15, 1–13. doi:10.1186/s13065-021-00743-4
- Li, W., Chen, Y. P., Blank, I., Li, F., Li, C., and Liu, Y. (2021a). GC × GC-ToF-MS and GC-IMS Based Volatile Profile Characterization of the Chinese Dry-Cured Hams from Different Regions. *Food Res. Int.* 142, 110222. doi:10.1016/j.foodres.2021.110222
- Li, Y., Li, Q., Zhang, B., Shen, C., Xu, Y., and Tang, K. (2021b). Identification, Quantitation and Sensorial Contribution of Lactones in Brandies between China and France. *Food Chem.* 357, 129761. doi:10.1016/j.foodchem.2021.129761
- Liu, C., Yang, P., Wang, H., and Song, H. (2022). Identification of Odor Compounds and Odor-Active Compounds of Yogurt Using DHS, SPME, SAFE, and SBSE/GC-O-MS. *Lwt* 154, 112689. doi:10.1016/j.lwt.2021.112689
- Liu, M., Zeng, Z., and Xiong, B. (2005). Preparation of Novel Solid-phase Microextraction Fibers by Sol-Gel Technology for Headspace Solid-phase Microextraction-Gas Chromatographic Analysis of Aroma Compounds in Beer. *J. Chromatogr. A* 1065, 287–299. doi:10.1016/j.chroma.2004.12.073
- Lopes, G. R., Petronilho, S., Ferreira, A. S., Pinto, M., Passos, C. P., Coelho, E., et al. (2021). Insights on Single-Dose Espresso Coffee Capsules' Volatile Profile: From Ground Powder Volatiles to Prediction of Espresso Brew Aroma Properties. *Foods* 10, 2508. doi:10.3390/foods10102508
- Lord, H., and Pawliszyn, J. (2000). Evolution of Solid-phase Microextraction Technology. *J. Chromatogr. A* 885, 153–193. doi:10.1016/S0021-9673(00)00535-5
- Lukić, I., Carlin, S., and Vrhovsek, U. (2020). Comprehensive 2D Gas Chromatography with TOF-MS Detection Confirms the Matchless Discriminatory Power of Monoterpenes and Provides In-Depth Volatile Profile Information for Highly Efficient white Wine Varietal Differentiation. *Foods* 9, 1787. doi:10.3390/foods9121787
- Lyu, J., Ma, Y., Xu, Y., Nie, Y., and Tang, K. (2019). Characterization of the Key Aroma Compounds in Marselan Wine by Gas Chromatography-Olfactometry, Quantitative Measurements, Aroma Recombination, and Omission Tests. *Molecules* 24, 2978. doi:10.3390/molecules24162978
- Magagna, F., Valverde-Som, L., Ruiz-Samblás, C., Cuadros-Rodríguez, L., Reichenbach, S. E., Bicchì, C., et al. (2016). Combined Untargeted and Targeted Fingerprinting with Comprehensive Two-Dimensional Chromatography for Volatiles and Ripening Indicators in Olive Oil. *Analytica Chim. Acta* 936, 245–258. doi:10.1016/j.aca.2016.07.005
- Marriott, P. J., Chin, S.-T., Maikhunthod, B., Schmarr, H.-G., and Bieri, S. (2012). Multidimensional Gas Chromatography. *Trac Trends Anal. Chem.* 34, 1–21. doi:10.1016/j.trac.2011.10.013
- Martins, C., Almeida, A., and Rocha, S. M. (2017). "Recent Advances in Analytical Techniques Volume 1," in *Recent Advances in Analytical Techniques*. Editors R. A. Atta-ur-Rahman and S. A. Ozkan (Sharjah, U. A. E., AE: Bentham Science Publishers), 141–199. doi:10.2174/97816810844731170101
- Martins, C., Brandão, T., Almeida, A., and Rocha, S. M. (2020). Enlarging Knowledge on Lager Beer Volatile Metabolites Using Multidimensional Gas Chromatography. *Foods* 9, 1276. doi:10.3390/foods9091276
- Martins, C., Brandão, T., Almeida, A., and Rocha, S. M. (2015). Insights on Beer Volatile Profile: Optimization of Solid-phase Microextraction Procedure Taking Advantage of the Comprehensive Two-Dimensional Gas Chromatography Structured Separation. *J. Sep. Sci.* 38, 2140–2148. doi:10.1002/jssc.201401388
- Martins, C., Brandão, T., Almeida, A., and Rocha, S. M. (2018). Unveiling the Lager Beer Volatile Terpenic Compounds. *Food Res. Int.* 114, 199–207. doi:10.1016/j.foodres.2018.07.048
- Mascres, S., Psillakis, E., and Purcaro, G. (2020). A Multifaceted Investigation on the Effect of Vacuum on the Headspace Solid-phase Microextraction of Extra-virgin Olive Oil. *Analytica Chim. Acta* 1103, 106–114. doi:10.1016/j.aca.2019.12.053
- Mascres, S., and Purcaro, G. (2020). Exploring Multiple-cumulative Trapping Solid-phase Microextraction for Olive Oil Aroma Profiling. *J. Sep. Sci.* 43, 1934–1941. doi:10.1002/jssc.202000098
- Meilgaard, M. C., Carr, B. T., and Cville, G. V. (1999). in *Sensory Evaluation Techniques*. Editor M. C. Meilgaard. 3rd Editio (New York: CRC Press).
- Meilgaard, M. C. (1975). Flavor Chemistry of Beer Part II: Flavor and Threshold of 239 Aroma Volatiles. *MBAA Tech. Q.* 12, 151–168.

- Menashe, I., and Lancet, D. (2006). Signaling in the Chemosensory Systems. *Cell. Mol. Life Sci.* 63, 1485–1493. doi:10.1007/s00018-006-6111-x
- Mobley, A. S., Bryant, A. K., Richard, M. B., Brann, J. H., Firestein, S. J., and Greer, C. A. (2013). Age-dependent Regional Changes in the Rostral Migratory Stream. *Neurobiol. Aging* 34, 1873–1881. doi:10.1016/j.neurobiolaging.2013.01.015
- Mondello, L., Tranchida, P. Q., Dugo, P., and Dugo, G. (2008). Comprehensive Two-Dimensional Gas Chromatography-Mass Spectrometry: A Review. *Mass. Spectrom. Rev.* 27, 101–124. doi:10.1002/mas.20158
- Nan, H., and Anderson, J. L. (2018). Ionic Liquid Stationary Phases for Multidimensional Gas Chromatography. *Trac Trends Anal. Chem.* 105, 367–379. doi:10.1016/j.trac.2018.03.020
- Negoias, S., Visschers, R., Boelrijk, A., and Hummel, T. (2008). New Ways to Understand Aroma Perception. *Food Chem.* 108, 1247–1254. doi:10.1016/j.foodchem.2007.08.030
- Nicolotti, L., Mall, V., and Schieberle, P. (2019). Characterization of Key Aroma Compounds in a Commercial Rum and an Australian Red Wine by Means of a New Sensomics-Based Expert System (SEBES)-An Approach to Use Artificial Intelligence in Determining Food Odor Codes. *J. Agric. Food Chem.* 67, 4011–4022. doi:10.1021/acs.jafc.9b00708
- Nowak, P. M., Wietecha-Posluszy, R., and Pawliszyn, J. (2021). White Analytical Chemistry: An Approach to Reconcile the Principles of Green Analytical Chemistry and Functionality. *Trac Trends Anal. Chem.* 138, 116223. doi:10.1016/j.trac.2021.116223
- Nunes, C., Maricato, É., Cunha, Á., Rocha, M. A. M., Santos, S., Ferreira, P., et al. (2016). Chitosan-genipin Film, a Sustainable Methodology for Wine Preservation. *Green. Chem.* 18, 5331–5341. doi:10.1039/c6gc01621a
- Ongo, E. A., Montevecchi, G., Antonelli, A., Sberveglieri, V., and Sevilla III, F. (2020). Metabolomics Fingerprint of Philippine Coffee by SPME-GC-MS for Geographical and Varietal Classification. *Food Res. Int.* 134, 109227. doi:10.1016/j.foodres.2020.109227
- Pacheco-Fernández, I., Trujillo-Rodríguez, M. J., Kuroda, K., Holen, A. L., Jensen, M. B., and Anderson, J. L. (2019). Zwitterionic Polymeric Ionic Liquid-Based Sorbent Coatings in Solid Phase Microextraction for the Determination of Short Chain Free Fatty Acids. *Talanta* 200, 415–423. doi:10.1016/j.talanta.2019.03.073
- Pawliszyn, J. (2009). “Theory of Solid-phase Microextraction,” in *Handbook of Solid Phase Microextraction*. Editor J. Pawliszyn (London: Chemical Industry Press), 13–59.
- Peñalver, A., Pocurull, E., Borrull, F., and Marcé, R. M. (2000). Determination of Phthalate Esters in Water Samples by Solid-phase Microextraction and Gas Chromatography with Mass Spectrometric Detection. *J. Chromatogr. A* 872, 191–201. doi:10.1016/S0021-9673(99)01284-4
- Peres, F., Jeleń, H. H., Majcher, M. M., Arraias, M., Martins, L. L., and Ferreira-Dias, S. (2013). Characterization of Aroma Compounds in Portuguese Extra virgin Olive Oils from Galega Vulgar and Cobrançosa Cultivars Using GC-O and GC×GC-ToFMS. *Food Res. Int.* 54, 1979–1986. doi:10.1016/j.foodres.2013.06.015
- Perestrelo, R., Barros, A. S., Câmara, J. S., and Rocha, S. M. (2011). In-depth Search Focused on Furans, Lactones, Volatile Phenols, and Acetals as Potential Age Markers of Madeira Wines by Comprehensive Two-Dimensional Gas Chromatography with Time-Of-Flight Mass Spectrometry Combined with Solid Phase Microextraction. *J. Agric. Food Chem.* 59, 3186–3204. doi:10.1021/jf104219t
- Perestrelo, R., Petronilho, S., Câmara, J. S., and Rocha, S. M. (2010). Comprehensive Two-Dimensional Gas Chromatography with Time-Of-Flight Mass Spectrometry Combined with Solid Phase Microextraction as a Powerful Tool for Quantification of Ethyl Carbamate in Fortified Wines. The Case Study of Madeira Wine. *J. Chromatogr. A* 1217, 3441–3445. doi:10.1016/j.chroma.2010.03.027
- Petronilho, S., Maraschin, M., Delgadillo, I., Coimbra, M. A., and Rocha, S. M. (2011). Sesquiterpene Composition of the Inflorescences of Brazilian Chamomile (*Matricaria Recutita* L.): Impact of the Agricultural Practices. *Ind. Crops Prod.* 34, 1482–1490. doi:10.1016/j.indcrop.2011.05.005
- Pickenhagen, W. (2017). “History of Odors and Odorants,” in *Handbook of Odor*. Editor A. Buettner (Cham, Switzerland: Springer International Publishing AG), 1–10.
- Pino, J. A., and Mesa, J. (2006). Contribution of Volatile Compounds to Mango (*Mangifera indica* L.) Aroma. *Flavour Fragr. J.* 21, 207–213. doi:10.1002/ffj.1703
- Piri-Moghadam, H., Alam, M. N., and Pawliszyn, J. (2017). Review of Geometries and Coating Materials in Solid Phase Microextraction: Opportunities, Limitations, and Future Perspectives. *Analytica Chim. Acta* 984, 42–65. doi:10.1016/j.aca.2017.05.035
- Planche, C., Ratel, J., Mercier, F., Blinet, P., Debrauwer, L., and Engel, E. (2015). Assessment of Comprehensive Two-Dimensional Gas Chromatography-Time-Of-Flight Mass Spectrometry Based Methods for Investigating 206 Dioxin-like Micropollutants in Animal-Derived Food Matrices. *J. Chromatogr. A* 1392, 74–81. doi:10.1016/j.chroma.2015.02.054
- Poole, C. F. (2021). “Conventional Detectors for Gas Chromatography,” in *Gas Chromatography, A Volume in Handbooks in Separation Science*. Editor C. F. Poole (Amsterdam: Elsevier), 343–369. doi:10.1016/B978-0-12-820675-1.00001-0
- Prebhalo, S. E., Berrier, K. L., Freye, C. E., Bahaghighat, H. D., Moore, N. R., Pinkerton, D. K., et al. (2018). Multidimensional Gas Chromatography: Advances in Instrumentation, Chemometrics, and Applications. *Anal. Chem.* 90, 505–532. doi:10.1021/acs.analchem.7b04226
- Psillakis, E. (2017). Vacuum-assisted Headspace Solid-phase Microextraction: A Tutorial Review. *Analytica Chim. Acta* 986, 12–24. doi:10.1016/j.aca.2017.06.033
- Purcaro, G., Cordero, C., Liberto, E., Bicchì, C., and Conte, L. S. (2014). Toward a Definition of Blueprint of virgin Olive Oil by Comprehensive Two-Dimensional Gas Chromatography. *J. Chromatogr. A* 1334, 101–111. doi:10.1016/j.chroma.2014.01.067
- Qu, H., and Duan, X. (2019). Recent Advances in Micro Detectors for Micro Gas Chromatography. *Sci. China Mater.* 62, 611–623. doi:10.1007/s40843-018-9389-0
- Rasheed, D. M., Serag, A., Abdel Shakour, Z. T., and Farag, M. (2021). Novel Trends and Applications of Multidimensional Chromatography in the Analysis of Food, Cosmetics and Medicine Bearing Essential Oils. *Talanta* 223, 121710. doi:10.1016/j.talanta.2020.121710
- Ravia, A., Snitz, K., Honigstein, D., Finkel, M., Zirler, R., Perl, O., et al. (2020). A Measure of Smell Enables the Creation of Olfactory Metamers. *Nature* 588, 118–123. doi:10.1038/s41586-020-2891-7
- Rega, B., Guerard, A., Delarue, J., Maire, M., and Giampaoli, P. (2009). On-line Dynamic HS-SPME for Monitoring Endogenous Aroma Compounds Released during the Baking of a Model Cake. *Food Chem.* 112, 9–17. doi:10.1016/j.foodchem.2008.05.028
- Reichenbach, S. E., Zini, C. A., Nicolli, K. P., Welke, J. E., Cordero, C., and Tao, Q. (2019). Benchmarking Machine Learning Methods for Comprehensive Chemical Fingerprinting and Pattern Recognition. *J. Chromatogr. A* 1595, 158–167. doi:10.1016/j.chroma.2019.02.027
- Rocha, M. A. M., Coimbra, M. A., Rocha, S. M., and Nunes, C. (2021). Impact of Chitosan-Genipin Films on Volatile Profile of Wine along Storage. *Appl. Sci.* 11, 6294. doi:10.3390/app11146294
- Rocha, S. M., Rodrigues, F., Coutinho, P., Delgadillo, I., and Coimbra, M. A. (2004). Volatile Composition of Baga Red Wine. *Analytica Chim. Acta* 513, 257–262. doi:10.1016/j.aca.2003.10.009
- Rocha, S., Ramalheira, V., Barros, A., Delgadillo, I., and Coimbra, M. A. (2001). Headspace Solid Phase Microextraction (SPME) Analysis of Flavor Compounds in Wines. Effect of the Matrix Volatile Composition in the Relative Response Factors in a Wine Model. *J. Agric. Food Chem.* 49, 5142–5151. doi:10.1021/jf010566m
- Rodríguez-Bencomo, J. J., Muñoz-González, C., Martín-Álvarez, P. J., Lázaro, E., Mancebo, R., Castañé, X., et al. (2012). Optimization of a HS-SPME-GC-MS Procedure for Beer Volatile Profiling Using Response Surface Methodology: Application to Follow Aroma Stability of Beers under Different Storage Conditions. *Food Anal. Methods* 5, 1386–1397. doi:10.1007/s12161-012-9390-x
- Romero-Medina, A., Estarrón-Espinosa, M., Verde-Calvo, J. R., Lelièvre-Desmas, M., and Escalona-Buendía, H. B. (2020). Renewing Traditions: A Sensory and Chemical Characterisation of Mexican Pigmented Corn Beers. *Foods* 9, 1–24. doi:10.3390/foods9070886
- Rosso, M. C., Mazzucotelli, M., Bicchì, C., Charron, M., Manini, F., Menta, R., et al. (2020). Adding Extra-dimensions to Hazelnuts Primary Metabolome Fingerprinting by Comprehensive Two-Dimensional Gas Chromatography Combined with Time-Of-Flight Mass Spectrometry Featuring Tandem Ionization: Insights on the Aroma Potential. *J. Chromatogr. A* 1614, 460739. doi:10.1016/j.chroma.2019.460739

- Ruiz-Matute, A. I., Rodríguez-Sánchez, S., Sanz, M. L., and Soria, A. C. (2018). "Chromatographic Technique: Gas Chromatography (GC)," in *Modern Techniques for Food Authentication*. Editor D.-W. Sun (London: Academic Press), 415–458. doi:10.1016/B978-0-12-814264-6.00012-8
- Sahin, B., and Schieberle, P. (2019). Characterization of the Key Aroma Compounds in Yeast Dumplings by Means of the Sensomics Concept. *J. Agric. Food Chem.* 67, 2973–2979. doi:10.1021/acs.jafc.9b00556
- Salvador, Á. C., Rudnitskaya, A., Silvestre, A. J. D., and Rocha, S. M. (2016). Metabolomic-based Strategy for Fingerprinting of *Sambucus nigra* L. berry Volatile Terpenoids and Norisoprenoids: Influence of Ripening and Cultivar. *J. Agric. Food Chem.* 64, 5428–5438. doi:10.1021/acs.jafc.6b00984
- Salvador, Á. C., Silvestre, A. J. D., and Rocha, S. M. (2017). Unveiling Elderflowers (*Sambucus nigra* L.) Volatile Terpenic and Norisoprenoids Profile: Effects of Different Postharvest Conditions. *Food Chem.* 229, 276–285. doi:10.1016/j.foodchem.2017.02.037
- Santos, M. C., Nunes, C., Rocha, M. A. M., Rodrigues, A., Rocha, S. M., Saraiva, J. A., et al. (2015). High Pressure Treatments Accelerate Changes in Volatile Composition of sulphur Dioxide-free Wine during Bottle Storage. *Food Chem.* 188, 406–414. doi:10.1016/j.foodchem.2015.05.002
- Santos, M. C., Nunes, C., Rocha, M. A. M., Rodrigues, A., Rocha, S. M., Saraiva, J. A., et al. (2013). Impact of High Pressure Treatments on the Physicochemical Properties of a sulphur Dioxide-free white Wine during Bottle Storage: Evidence for Maillard Reaction Acceleration. *Innovative Food Sci. Emerging Tech.* 20, 51–58. doi:10.1016/j.ifset.2013.07.001
- Schieberle, P., and Hofmann, T. (2011). "Mapping the Combinatorial Code of Food Flavors by Means of Molecular Sensory Science Approach," in *Food Flavors: Chemical, Sensory, and Technological Properties*. Editor H. Jelen (Boca Raton, FL: CRC Press), 411–436.
- Schieberle, P., and Molyneux, R. J. (2012). Quantitation of Sensory-Active and Bioactive Constituents of Food: A Journal of Agricultural and Food Chemistry Perspective. *J. Agric. Food Chem.* 60, 2404–2408. doi:10.1021/jf2047477
- Schieberle, P. (1991). Primary Odorants of Pale Lager Beer. *Z. Lebensm. Unters. Forsch.* 193, 558–565. doi:10.1007/bf01190873
- Schmidberger, P. C., and Schieberle, P. (2017). Characterization of the Key Aroma Compounds in white alba Truffle (*Tuber magnatum* pico) and Burgundy Truffle (*Tuber uncinatum*) by Means of the Sensomics Approach. *J. Agric. Food Chem.* 65, 9287–9296. doi:10.1021/acs.jafc.7b04073
- Schoenauer, S., and Schieberle, P. (2019). Characterization of the Key Aroma Compounds in the Crust of Soft Pretzels by Application of the Sensomics Concept. *J. Agric. Food Chem.* 67, 7110–7119. doi:10.1021/acs.jafc.9b02601
- Seeley, J. V., and Seeley, S. K. (2013). Multidimensional Gas Chromatography: Fundamental Advances and New Applications. *Anal. Chem.* 85, 557–578. doi:10.1021/ac303195u
- Sekhon, R. K., Schilling, M. W., Phillips, T. W., Aikins, M. J., Hasan, M. M., Corzo, A., et al. (2010). Effects of Phosphine and Methyl Bromide Fumigation on the Volatile Flavor Profile and Sensory Quality of Dry Cured Ham. *Meat Sci.* 86, 411–417. doi:10.1016/j.meatsci.2010.05.026
- Shellie, R., Mondello, L., Marriott, P., and Dugo, G. (2002). Characterisation of Lavender Essential Oils by Using Gas Chromatography-Mass Spectrometry with Correlation of Linear Retention Indices and Comparison with Comprehensive Two-Dimensional Gas Chromatography. *J. Chromatogr. A* 970, 225–234. doi:10.1016/S0021-9673(02)00653-2
- Shirey, R. E. (2012). SPME Commercial Devices and Fibre Coatings. *Handb. Solid Phase Microextraction* 2012, 99–133. doi:10.1016/B978-0-12-416017-0.00004-8
- Siegmund, B., Urdl, K., Jurek, A., and Leitner, E. (2018). "More Than Honey": Investigation on Volatiles from Monovarietal Honeys Using New Analytical and Sensory Approaches. *J. Agric. Food Chem.* 66, 2432–2442. doi:10.1021/acs.jafc.6b05009
- Silva, I., Coimbra, M. A., Barros, A. S., Marriott, P. J., and Rocha, S. M. (2015). Can Volatile Organic Compounds Be Markers of Sea Salt? *Food Chem.* 169, 102–113. doi:10.1016/j.foodchem.2014.07.120
- Silva, I., Rocha, S. M., Coimbra, M. A., and Marriott, P. J. (2010). Headspace Solid-phase Microextraction Combined with Comprehensive Two-Dimensional Gas Chromatography Time-Of-Flight Mass Spectrometry for the Determination of Volatile Compounds from marine Salt. *J. Chromatogr. A* 1217, 5511–5521. doi:10.1016/j.chroma.2010.06.050
- Song, H., and Liu, J. (2018). GC-O-MS Technique and its Applications in Food Flavor Analysis. *Food Res. Int.* 114, 187–198. doi:10.1016/j.foodres.2018.07.037
- Souza-Silva, É. A., Gionfriddo, E., and Pawliszyn, J. (2015). A Critical Review of the State of the Art of Solid-phase Microextraction of Complex Matrices II. *Food Analysis. Trac Trends Anal. Chem.* 71, 236–248. doi:10.1016/j.trac.2015.04.018
- Spietelun, A., Marcinkowski, Ł., de la Guardia, M., and Namieśnik, J. (2013). Recent Developments and Future Trends in Solid Phase Microextraction Techniques towards green Analytical Chemistry. *J. Chromatogr. A* 1321, 1–13. doi:10.1016/j.chroma.2013.10.030
- Sterckx, F. L., Missiaen, J., Saison, D., and Delvaux, F. R. (2011). Contribution of Monophenols to Beer Flavour Based on Flavour Thresholds, Interactions and Recombination Experiments. *Food Chem.* 126, 1679–1685. doi:10.1016/j.foodchem.2010.12.055
- Sterckx, F. L., Saison, D., and Delvaux, F. R. (2010). Determination of Volatile Monophenols in Beer Using Acetylation and Headspace Solid-phase Microextraction in Combination with Gas Chromatography and Mass Spectrometry. *Analytica Chim. Acta* 676, 53–59. doi:10.1016/j.aca.2010.07.043
- Stilo, F., Segura Borrego, M. D. P., Bicchi, C., Battaglini, S., Callejón Fernández, R. M., Morales, M. L., et al. (2021). Delineating the Extra-virgin Olive Oil Aroma Blueprint by Multiple Headspace Solid Phase Microextraction and Differential-Flow Modulated Comprehensive Two-Dimensional Gas Chromatography. *J. Chromatogr. A* 1650, 462232. doi:10.1016/j.chroma.2021.462232
- Summerson, V., Gonzalez Viejo, C., Pang, A., Torrico, D. D., and Fuentes, S. (2021a). Assessment of Volatile Aromatic Compounds in Smoke Tainted Cabernet Sauvignon Wines Using a Low-Cost E-Nose and Machine Learning Modelling. *Molecules* 26, 5108. doi:10.3390/molecules26165108
- Summerson, V., Gonzalez Viejo, C., Torrico, D. D., Pang, A., and Fuentes, S. (2021b). Digital Smoke Taint Detection in Pinot Grigio Wines Using an E-Nose and Machine Learning Algorithms Following Treatment with Activated Carbon and a Cleaving Enzyme. *Fermentation* 7, 119. doi:10.3390/fermentation7030119
- Sýkora, M., Vítová, E., and Jelen, H. H. (2020). Application of Vacuum Solid-phase Microextraction for the Analysis of Semi-hard Cheese Volatiles. *Eur. Food Res. Technol.* 246, 573–580. doi:10.1007/s00217-020-03426-x
- Székelyhidi, R., Hanczné Lakatos, E., Sik, B., and Ajtony, Z. (2021). Development of New HS-SPME-GC-MS Technique to the Measurement of Volatile Terpenoid Profile of Milk. *Food Anal. Methods* 14, 2585–2596. doi:10.1007/s12161-021-02070-9
- Telikani, A., Tahmassebi, A., Banzhaf, W., and Gandomi, A. H. (2022). Evolutionary Machine Learning: A Survey. *ACM Comput. Surv.* 54, 1–35. in press. doi:10.1145/3467477
- The Future of Food and Farming: Challenges and choices for global sustainability (2011). Final Proj. Report. Gov. off. Sci. London, UK. Available at: <https://www.gov.uk/government/publications/future-of-food-and-farming>.
- Thibaud, F., Courregelongue, M., and Darriet, P. (2020). Contribution of Volatile Odorous Terpenoid Compounds to Aged Cognac Spirits Aroma in a Context of Multicomponent Odor Mixtures. *J. Agric. Food Chem.* 68, 13310–13318. doi:10.1021/acs.jafc.9b06656
- Topol, E. J. (2019). High-performance Medicine: the Convergence of Human and Artificial Intelligence. *Nat. Med.* 25, 44–56. doi:10.1038/s41591-018-0300-7
- Tranchida, P., Dugo, P., Dugo, G., and Mondello, L. (2004). Comprehensive Two-Dimensional Chromatography in Food Analysis. *J. Chromatogr. A* 1054, 3–16. doi:10.1016/j.chroma.2004.07.09510.1016/S0021-9673(04)01301-9
- Tranchida, P. Q., Aloisi, I., Giocastro, B., and Mondello, L. (2018). Current State of Comprehensive Two-Dimensional Gas Chromatography-Mass Spectrometry with Focus on Processes of Ionization. *Trac Trends Anal. Chem.* 105, 360–366. doi:10.1016/j.trac.2018.05.016
- Tranchida, P. Q., Purcaro, G., Maimone, M., and Mondello, L. (2016). Impact of Comprehensive Two-Dimensional Gas Chromatography with Mass Spectrometry on Food Analysis. *J. Sep. Sci.* 39, 149–161. doi:10.1002/jssc.201500379
- Uselmann, V., and Schieberle, P. (2015). Decoding the Combinatorial Aroma Code of a Commercial Cognac by Application of the Sensomics Concept and First Insights into Differences from a German Brandy. *J. Agric. Food Chem.* 63, 1948–1956. doi:10.1021/jf506307x
- van Den Dool, H., and Kratz, P. D. (1963). A Generalization of the Retention index System Including Linear Temperature Programmed Gas-Liquid Partition Chromatography. *J. Chromatogr. A* 11, 463–471. doi:10.1016/S0021-9673(01)80947-X

- van Gemert, L. J. (2011). *Odour Thresholds - Compilations of Odour Threshold Values in Air, Water and Other media*. Zeist, The Netherlands: Oliemans Punter & Partners BV.
- Vanderhaegen, B., Neven, H., Coghe, S., Verstrepen, K. J., Derdelinckx, G., and Verachtert, H. (2003a). Bioflavoring and Beer Refermentation. *Appl. Microbiol. Biotechnol.* 62, 140–150. doi:10.1007/s00253-003-1340-5
- Vanderhaegen, B., Neven, H., Coghe, S., Verstrepen, K. J., Verachtert, H., and Derdelinckx, G. (2003b). Evolution of Chemical and Sensory Properties during Aging of Top-Fermented Beer. *J. Agric. Food Chem.* 51, 6782–6790. doi:10.1021/jf034631z
- Vas, G., and Vékey, K. (2004). Solid-phase Microextraction: a Powerful Sample Preparation Tool Prior to Mass Spectrometric Analysis. *J. Mass. Spectrom.* 39, 233–254. doi:10.1002/jms.606
- Vesely, P., Lusk, L., Basarova, G., Seabrooks, J., and Ryder, D. (2003). Analysis of Aldehydes in Beer Using Solid-phase Microextraction with On-Fiber Derivatization and Gas Chromatography/mass Spectrometry. *J. Agric. Food Chem.* 51, 6941–6944. doi:10.1021/jf034410t
- Vichi, S., Pizzale, L., Conte, L. S., Buxaderas, S., and López-Tamames, E. (2003). Solid-Phase Microextraction in the Analysis of virgin Olive Oil Volatile Fraction: Modifications Induced by Oxidation and Suitable Markers of Oxidative Status. *J. Agric. Food Chem.* 51, 6564–6571. doi:10.1021/jf030268k
- Villamiel, M., Castillo, M. D., and Corzo, N. (2006). “Browning Reactions,” in *Food Biochemistry and Food Processing*. Editors Y. H. Hui, W. Nip, L. M. L. Nollet, G. Paliyath, and B. K. Simpson (Wiley-Blackwell), 71–100.
- Villière, A., Arvisenet, G., Lethuaut, L., Prost, C., and Sérot, T. (2012). Selection of a Representative Extraction Method for the Analysis of Odourant Volatile Composition of French Cider by GC-MS-O and GC×GC-TOF-MS. *Food Chem.* 131, 1561–1568. doi:10.1016/j.foodchem.2011.10.008
- Viswanathan, S. M., and Rajan, R. (2020). Digital Scent Technology-A Critical Overview. *Int. J. Trend Sci. Res. Dev.* 4, 218–221.
- Wang, C., Zhang, W., Li, H., Mao, J., Guo, C., Ding, R., et al. (2019). Analysis of Volatile Compounds in Pears by HS-SPME-GC×GC-TOFMS. *Molecules* 24, 1795. doi:10.3390/molecules24091795
- Wang, J., Yang, Z. J., Xu, L. Y., Wang, B., Zhang, J. H., Li, B. Z., et al. (2021). Key Aroma Compounds Identified in Cheddar Cheese with Different Ripening Times by Aroma Extract Dilution Analysis, Odor Activity Value, Aroma Recombination, and Omission. *J. Dairy Sci.* 104, 1576–1590. doi:10.3168/jds.2020-18757
- Weldegergis, B. T., Villiers, A. D., McNeish, C., Seethapathy, S., Mostafa, A., Górecki, T., et al. (2011). Characterisation of Volatile Components of Pinotage Wines Using Comprehensive Two-Dimensional Gas Chromatography Coupled to Time-Of-Flight Mass Spectrometry (GC×GC-TOFMS). *Food Chem.* 129, 188–199. doi:10.1016/j.foodchem.2010.11.157
- Welke, J. E., Hernandez, K. C., Nicolli, K. P., Barbará, J. A., Biasoto, A. C. T., and Zini, C. A. (2021). Role of Gas Chromatography and Olfactometry to Understand the Wine Aroma: Achievements Denoted by Multidimensional Analysis. *J. Sep. Sci.* 44, 135–168. doi:10.1002/jssc.202000813
- Welke, J. E., Zanús, M., Lazzarotto, M., and Alcaraz Zini, C. (2014). Quantitative Analysis of Headspace Volatile Compounds Using Comprehensive Two-Dimensional Gas Chromatography and Their Contribution to the Aroma of Chardonnay Wine. *Food Res. Int.* 59, 85–99. doi:10.1016/j.foodres.2014.02.002
- Whitener, M. E. B., Stanstrup, J., Panzeri, V., Carlin, S., Divol, B., Du Toit, M., et al. (2016). Untangling the Wine Metabolome by Combining Untargeted SPME-GC×GC-TOF-MS and Sensory Analysis to Profile Sauvignon Blanc Co-fermented with Seven Different Yeasts. *Metabolomics* 12, 1–25. doi:10.1007/s11306-016-0962-4
- Wong, J. W., Hayward, D. G., and Zhang, K. (2013). “Gas Chromatography-Mass Spectrometry Techniques for Multiresidue Pesticide Analysis in Agricultural Commodities,” in *Comprehensive Analytical Chemistry*. Editors I. Ferrer and E. M. Thurman (Oxford: Elsevier B.V.), 3–22. doi:10.1016/b978-0-444-62623-3.00001-0
- Xiao, Q., Yu, C., Xing, J., and Hu, B. (2006). Comparison of Headspace and Direct Single-Drop Microextraction and Headspace Solid-phase Microextraction for the Measurement of Volatile Sulfur Compounds in Beer and Beverage by Gas Chromatography with Flame Photometric Detection. *J. Chromatogr. A* 1125, 133–137. doi:10.1016/j.chroma.2006.06.096
- Xu, C.-H., Chen, G.-S., Xiong, Z.-H., Fan, Y.-X., Wang, X.-C., and Liu, Y. (2016). Applications of Solid-phase Microextraction in Food Analysis. *Trac Trends Anal. Chem.* 80, 12–29. doi:10.1016/j.trac.2016.02.022
- Yang, Y., Yu, P., Sun, J., Jia, Y., Wan, C., Zhou, Q., et al. (2022). Investigation of Volatile Thiol Contributions to Rapeseed Oil by Odor Active Value Measurement and Perceptual Interactions. *Food Chem.* 373, 131607. doi:10.1016/j.foodchem.2021.131607
- Y. H. Hui (Editor) (2010). *Handbook of Fruit and Vegetable Flavors* (New Jersey, United States of America: John Wiley & Sons).
- Zhao, C., Fan, W., and Xu, Y. (2021). Characterization of Key Aroma Compounds in Pixian Broad Bean Paste through the Molecular Sensory Science Technique. *Lwt* 148, 111743. doi:10.1016/j.lwt.2021.111743

Conflict of Interest: The authors declare that the research was conducted in the absence of any commercial or financial relationships that could be construed as a potential conflict of interest.

Publisher’s Note: All claims expressed in this article are solely those of the authors and do not necessarily represent those of their affiliated organizations, or those of the publisher, the editors, and the reviewers. Any product that may be evaluated in this article, or claim that may be made by its manufacturer, is not guaranteed or endorsed by the publisher.

Copyright © 2022 Rocha, Costa and Martins. This is an open-access article distributed under the terms of the Creative Commons Attribution License (CC BY). The use, distribution or reproduction in other forums is permitted, provided the original author(s) and the copyright owner(s) are credited and that the original publication in this journal is cited, in accordance with accepted academic practice. No use, distribution or reproduction is permitted which does not comply with these terms.



Speciation Study on O-Phosphorylethanolamine and O-Phosphorylcholine: Acid–Base Behavior and Mg^{2+} Interaction

Donatella Aiello¹, Massimiliano Cordaro^{2,3}, Anna Napoli¹, Claudia Foti² and Ottavia Giuffrè^{2*}

¹Dipartimento di Chimica e Tecnologie Chimiche, Università Della Calabria, Arcavacata di Rende (CS), Italy, ²Dipartimento di Scienze Chimiche, Biologiche, Farmaceutiche ed Ambientali, Università di Messina, Messina, Italy, ³CNR-ITAE, Messina, Italy

OPEN ACCESS

Edited by:

Paolo Oliveri,
University of Genoa, Italy

Reviewed by:

Valeria Marina Nurchi,
University of Cagliari, Italy
Daniela Piazzese,
University of Palermo, Italy

*Correspondence:

Ottavia Giuffrè
ogiufrè@unime.it

Specialty section:

This article was submitted to
Analytical Chemistry,
a section of the journal
Frontiers in Chemistry

Received: 28 January 2022

Accepted: 04 March 2022

Published: 28 March 2022

Citation:

Aiello D, Cordaro M, Napoli A, Foti C
and Giuffrè O (2022) Speciation Study
on O-Phosphorylethanolamine and O-
Phosphorylcholine: Acid–Base
Behavior and Mg^{2+} Interaction.
Front. Chem. 10:864648.
doi: 10.3389/fchem.2022.864648

In the present study, the acid–base behavior of compounds constituting the headgroups of biomembranes, O-phosphorylethanolamine (**PEA**), and O-phosphorylcholine (**PPC**) was investigated by potentiometric titrations in NaCl aqueous solutions at different temperatures ($15 \leq t/^{\circ}C \leq 37$) and ionic strength ($0.15 \leq I/\text{mol L}^{-1} \leq 1$) values. The complexation properties and the speciation of these ligands with Mg^{2+} were defined under different temperatures ($15 \leq t/^{\circ}C \leq 37$) and $I = 0.15 \text{ mol L}^{-1}$. The results evidenced the formation of three species for **PEA**, namely, MLH_2 , MLH , and ML and two species for **PPC**, namely, MLH and ML . 1H -NMR titrations were performed on solutions containing ligand and metal–ligand solutions at $t = 25^{\circ}C$ and $I = 0.15 \text{ mol L}^{-1}$. The estimated values of ligand protonation and complex formation constants and the speciation model are in accordance with the potentiometric data. The enthalpy changes were also determined at $t = 25^{\circ}C$ and $I = 0.15 \text{ mol L}^{-1}$ by the dependence of formation constants on the temperature, confirming the electrostatic nature of the interactions. Matrix-assisted laser desorption mass spectrometry (MALDI-MS) was applied for the characterization of Mg^{2+} -L systems (L = **PEA** or **PCC**). MS/MS spectra of free ligands and of Mg^{2+} -L species were obtained. The observed fragmentation patterns of both Mg^{2+} -L systems allowed elucidating the interaction mechanism that occurs via the phosphate group generating a four-membered cycle.

Keywords: Mg^{2+} , speciation, ligands of biological interest, sequestration, potentiometry, 1H -NMR spectroscopy, mass spectrometry, thermodynamic parameters

INTRODUCTION

Phospholipids can perform various biological functions (Takeda et al., 2019). For example, phosphatidylcholine plays a fundamental role in the absorption of dietary lipids (Kennelly et al., 2018), phosphatidylglycerol (PG) and phosphatidylinositol (PI) exert antiviral functions against respiratory syncytial virus infection (Numata et al., 2010; Numata et al., 2015; Takeda et al., 2019). More specifically, in mammalian liver cells, one of these two headgroups are contained in two-thirds of the lipids of the plasma membrane, nuclear membrane, mitochondria, microsomes, and Golgi (Woolf and Roux, 1994). The physical state of phospholipid bilayer membranes, as temperature and hydration level are varied, depends to a great extent on the properties of the polar headgroup (Woolf and Roux, 1994). Phospholipids constitute cell

membranes and also play other roles as cellular messengers and can perform various biological functions (Takeda et al., 2019). Phosphorylethanolamine (PEA) and phosphorylcholine (PPC) commonly constitute the headgroups of biological lipid membranes (Gennis, 1989; Woolf and Roux, 1994). PPC, a constituent of phosphatidylcholine, is considered as one of the fundamental metabolites in biological systems (Takeda et al., 2019). In mammals, it is synthesized from choline, which is absorbed from food (Fernandez-Botello et al., 2002). Alterations in PEA and/or PPC, as well as in glycerophosphocholine and glycerophosphoethanolamine, as measured by *in vivo* ^{31}P magnetic resonance spectroscopy in the cerebrospinal fluid (CSF) and subcortical and cortical regions are known to indicate neurodegenerative diseases (Weber-Fahr et al., 2013). In detail, an increase of the PPC level in the CSF was observed in patients with Alzheimer's compared to the normal value of $1.28\ \mu\text{M}$ (Walter et al., 2004). Increased PEA levels may indicate inhibition of choline and acetylcholine synthesis (The international standard for identifying health measurements, 2006). Biological membranes are in contact with physiological solutions containing different metal cations. The interactions of the headgroups of lipid membranes with these cations influence their structure and stability (Fukuma et al., 2007; Šegota et al., 2015). Metal complexation is also important in cation transport, lipoprotein formation, and several biochemical processes (Hendrickson and Fullington, 1965).

Among metal cations, magnesium is a main bioelement, together with calcium, sodium, and potassium. Magnesium and calcium are necessary to bind biological macromolecules by using negatively charged components (Nies, 2004). In 1926 Leroy was the first to describe the essential role played by Mg^{2+} in living organisms. The first investigation of its deficiency in humans was published in 1934 by Hirschfender and Haury (Vormann, 2004). In the following years the lack of Mg^{2+} has been linked with a series of diseases in humans (Flink, 1956). Since then, the role of magnesium in physiological processes has attracted increasing attention (Vormann, 2004). In biological systems, magnesium is present as Mg^{2+} , and being smaller than Ca^{2+} , it attracts water molecules more strongly (Saris et al., 2000). The large hydration shell of hydrated magnesium makes it difficult to enter biological membranes by passing through narrow channels (Vormann, 2004). It is the second most abundant cation within the cell. The intracellular free magnesium concentration is approximately $0.5\ \text{mmol L}^{-1}$. It is mainly bound to proteins, negatively charged phospholipids, ATP, and nucleic acids (Heaton, 1993). The concentration of magnesium in the plasma is in equilibrium with that adsorbed on the bone surface (Elin, 1994). The magnesium concentration in a healthy adult is as follows: in the erythrocytes, $2.5\ \text{mmol L}^{-1}$; in the blood, $0.7\text{--}1.1\ \text{mmol L}^{-1}$, of which 55% free, 32% bound primarily to albumin, and 13% bound to citrate, phosphate, etc; in the cerebrospinal fluid, $1.25\ \text{mmol L}^{-1}$ of which 55% free and 45% complexed; and

in the sweat, $0.3\ \text{mmol L}^{-1}$ (Shils, 1997; Weisinger and Bellorin-Font, 1998).

The excess magnesium present in the blood is excreted by the kidney. Precisely, the glomerular membrane of the kidney filters about 80% of the total serum magnesium (Quamme and de Rouffignac, 2000). Its high concentration inhibits its reabsorption, causing an increase in its loss from the human body (Dai et al., 2001). In adult humans, the dietary magnesium intake was set at 300–420 mg per day (The National Academies, 1997; Deutsche Gesellschaft für Ernährung, 2000). The main extracellular effects of the magnesium cation are represented by its ability to crosslink the negatively charged phospholipids in the membranes, stabilizing the latter and at the same time reducing their fluidity (Flatmann, 1993). One of the main features of Mg^{2+} is the high charge density, greater than other ions in the cells, so that its involvement with high negative charge density compounds, such as phosphate and pyrophosphate metabolites, prevails (Frausto da Silva and Williams, 2001).

In this study, the interaction between Mg^{2+} ions and two phosphoryl compounds present in biological membranes, i.e., PEA and PPC, represented in **Figure 1**, has been elucidated *via* a multidisciplinary approach. The aim was to evaluate the strength of the interaction by potentiometry and ^1H -NMR spectroscopy and to explain the mechanism by MALDI mass spectrometry and MS/MS. The determination of reliable thermodynamic data is necessary to simulate distribution of species in biological fluid conditions and, therefore, to assess biological phenomena such as transport through membranes but also for evaluating the possible use of these compounds in some application fields. Indeed, PPC is employed in biomaterials for clinical applications (Matsuura et al., 2016; Goda and Miyahara, 2018), and it is well known that the performance of these biomaterials can be affected by electrolytes (Wu et al., 2018; Díaz-Betancor et al., 2019). Therefore, the speciation studies can be crucial evaluating the performance of these compound-based biomaterials after interaction with Mg^{2+} .

MATERIALS AND METHODS

Materials

O-phosphorylethanolamine and O-phosphorylcholine chloride solutions were prepared by weighing and subsequent dissolution of the corresponding products (Sigma-Aldrich/Merck, Darmstadt, Germany). The purity of the ligands, determined by alkalimetric titration, was greater than 99%. Magnesium chloride solutions were prepared by weighing and dissolving the Fluka (Fluka/Honeywell, Charlotte, North Carolina, United States) product. These solutions were standardized using the EDTA (Ethylenediaminetetraacetic acid disodium salt, BioUltra, $\geq 99\%$) standard.

Sodium chloride solutions were obtained by weighing the salt (puriss., Sigma-Aldrich/Merck, Darmstadt, Germany), after drying at 110°C . The solutions of hydrochloric acid

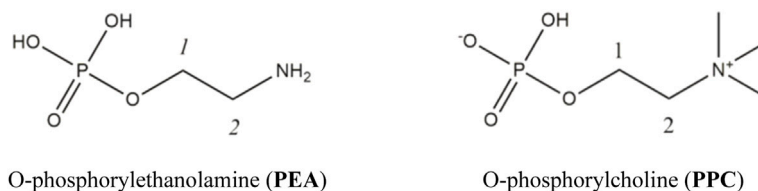


FIGURE 1 | Ligands under study.

and sodium hydroxide were obtained by diluting the Fluka (Fluka/Honeywell, Charlotte, North Carolina, United States) vials. Subsequently, they were standardized by titrations using sodium carbonate ($\geq 99.5\%$, Sigma-Aldrich/Merck, Darmstadt, Germany) and potassium acid phthalate ($\geq 99.5\%$, Sigma-Aldrich Merck, Darmstadt, Germany), respectively. These salts were previously dried in an oven at 110°C .

Potentiometric Apparatus and Procedure

Two distinct potentiometric systems were used for titrations. Each system has an identical configuration with a Metrohm model 809 Titrando potentiometer, an automatic dispenser Metrohm Dosino 800, and a Metrohm LL-Unitrode WOC combined glass electrode. A PC was connected to each potentiometric system to acquire experimental titration data by Metrohm TIAMO 2.2 software. Several parameters, such as the titrant delivery and e.m.f. stability, were controlled by this software. Estimated accuracies of these systems are $\pm 0.15\text{ mV}$ and $\pm 0.002\text{ ml}$ for e.m.f. and for titrant volumes, respectively.

For the ligand protonation, for each titration, volumes of the NaOH standard were added to 25 ml of the solution containing **PEA** or **PPC** at $C_L = 5\text{--}10\text{ mmol L}^{-1}$, $0.15 \leq I/\text{mol L}^{-1} \leq 1$ in NaCl at $t = 25^\circ\text{C}$, and $I = 0.15\text{ mol L}^{-1}$ at $t = 15, 37^\circ\text{C}$. For metal–ligand complexes, 25 ml of the solution containing Mg^{2+} and **PEA** or **PPC** at $C_M = 1\text{--}4\text{ mmol L}^{-1}$, $C_L = 2\text{--}4\text{ mmol L}^{-1}$, $C_M/C_L = 0.33\text{--}2$, and $I = 0.15\text{ mol L}^{-1}$ in NaCl was titrated by using the NaOH standard at $t = 15, 25$, and 37°C . All the solutions during the titrations were in glass jacket thermostated cells, under magnetic stirring and by bubbling pure N_2 . Independent titrations of HCl with standard NaOH were performed to obtain the values of the standard electrode potential E^0 and pK_w , under the same ionic strength and temperature conditions of the corresponding measurement.

NMR Apparatus and Procedure

A Varian NMR spectrometer 500 Mhz was used to process ^1H -NMR spectra. 1,4-dioxane was used as the internal reference ($\delta_{\text{CH}_2\text{dioxane}} = 3.70\text{ ppm}$), and all chemical shifts refer to tetramethylsilane (TMS). All measurements were carried out using the presaturation technique to reduce the water signal, in 9:1 $\text{H}_2\text{O}/\text{D}_2\text{O}$ solution at $t = 25^\circ\text{C}$. The spectra containing ligands **PEA** or **PPC** (at $C_L = 7\text{ mmol L}^{-1}$) and NaCl ($I = 0.15\text{ mol L}^{-1}$) solutions were recorded in a pH range between 2 and 11. The spectra containing **PEA** or **PPC** and Mg^{2+} ($C_M = 6\text{ mmol L}^{-1}$, C_L

$= 7\text{ mmol L}^{-1}$) and NaCl solutions were recorded in the same pH range of the free ligands.

Mass Spectrometric Apparatus and Procedure

All metal complexes were prepared, as published elsewhere (Chill  et al., 2020; Aiello et al., 2021a). Briefly, all ligands (1 or 2 mmol) were dissolved in 100 μL of water; the pH was adjusted to 8 with NaOH and then added to an aqueous solution (200 μL) of MgCl_2 (1 mmol). The resulting solutions were maintained under magnetic stirring, at room temperature for 2 h. MALDI mass spectrometry analysis was performed on a 1 μL portion of a premixed solution containing the reaction mixture and the matrix $\alpha\text{-CHCA}$ (0.3% in TFA), in a 2:10 (v:v) ratio.

All MS and MS/MS experiments were performed, as published elsewhere (Aiello et al., 2018; Imbrogno et al., 2019). All experiments were conducted using a 5800 MALDI-TOF/TOF analyzer (AB-SCIEX), supplied with a neodymium–yttrium–aluminum–garnet laser, operating at 349 nm. MS spectra were obtained with a mass accuracy of 5 ppm, by collecting 4,000 laser shots, applying a laser pulse rate of 400 Hz. A total of 5,000 laser shots, at a pulse rate of 1000 Hz and 1 kV of collision energy, were collected and averaged for each MS/MS experiment. Δppm of the MS/MS experiments was 20 ppm. MS/MS experiments were achieved using ambient air as the collision gas (10^{-6} Torr). Data Explorer (version 4.0) was used for handling all spectra.

Calculations

The STACO and BSTAC programs were employed to process the experimental potentiometric data. With their use, the protonation constants of the ligands, the formation constants of the complexes, and the parameters of the acid–base titration (the standard potential E^0 , junction potential, and analytical concentration of the reagents) were obtained. The LIANA program was used in processing experimental results at various ionic strengths and temperatures to obtain the dependence of protonation and formation constants on ionic strength and temperature. More information about BSTAC, STACO, and LIANA can be found in the reference (De Stefano et al., 1997). The speciation diagrams and the percentages of complex species were obtained using the HySS program (Alderighi et al., 1999). HypNMR software was used to process the observed experimental signals, assuming a fast mutual

TABLE 1 | Experimental values of protonation constants of PEA and PPC and formation constants of Mg^{2+} species obtained by potentiometry at different temperatures and ionic strength values in NaCl.

L	Species	$\log\beta^{\text{Ha}}$				
		$t = 15^\circ\text{C}$ $I = 0.15^{\text{b}}$	$t = 25^\circ\text{C}$ $I = 0.15^{\text{b}}$	$t = 25^\circ\text{C}$ $I = 0.5^{\text{b}}$	$t = 25^\circ\text{C}$ $I = 0.90^{\text{b}}$	$t = 37^\circ\text{C}$ $I = 0.15^{\text{b}}$
PEA	LH	10.381(2) ^c	10.141(2) ^c	10.071(4) ^c	10.087(2) ^c	9.836(7) ^c
	LH ₂	16.021(3)	15.731(4)	15.607(7)	15.551(4)	15.560(9)
	LH ₃	17.08(3)	16.69(3)	16.79(2)	16.45(4)	17.29(2)
	MLH ₂	17.78(4)	17.29(3)	—	—	16.96(9)
	MLH	12.61(2)	11.56(6)	—	—	11.65(7)
	ML	2.79(2)	2.66(3)	—	—	1.94(6)
PPC	LH	5.635(3) ^c	5.646(4) ^c	5.542(2) ^c	5.459(4) ^c	5.668(4) ^c
	LH ₂	—	6.53(3)	6.23(2)	6.12(3)	6.71(3)
	MLH	6.79(3)	7.46(3)	—	—	8.07(3)
	ML	1.62(2)	1.42(6)	—	—	2.24(3)
$\log K^{\text{Hd}}$						
PEA	LH	10.381	10.141	10.071	10.087	9.836
	LH ₂	5.640	5.590	5.536	5.464	5.724
	LH ₃	1.06	0.96	1.18	0.90	1.73
	MLH ₂	1.76	1.56	—	—	1.40
	MLH	2.23	1.41	—	—	1.81
	ML	2.79	2.66	—	—	1.94
PPC	LH	5.635	5.646	5.542	5.459	5.668
	LH ₂	—	0.88	0.69	0.66	1.04
	MLH	5.17	6.04	—	—	5.83
	ML	1.62	1.42	—	—	2.24

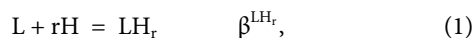
^aOverall protonation or formation constants.^bIn mol L⁻¹.^c≥95% of confidence interval.^dStepwise protonation or formation constants.

exchange in the NMR time scale (Frassinetti et al., 1995). With its use, the protonation constants of PEA and PPC, the formation constants of the complex species, and the individual chemical shifts of each species were calculated.

RESULTS AND DISCUSSION

Acid–Base Behavior, Complexation With Mg^{2+} , and Speciation Profiles

The protonation constants of the two ligands under study, PEA and PPC, necessary for the subsequent determination of the complexes with Mg^{2+} , were determined. The protonation reactions as overall formation constants (β) and stepwise formation constants (K) are as follows, where the charges are omitted for simplicity:



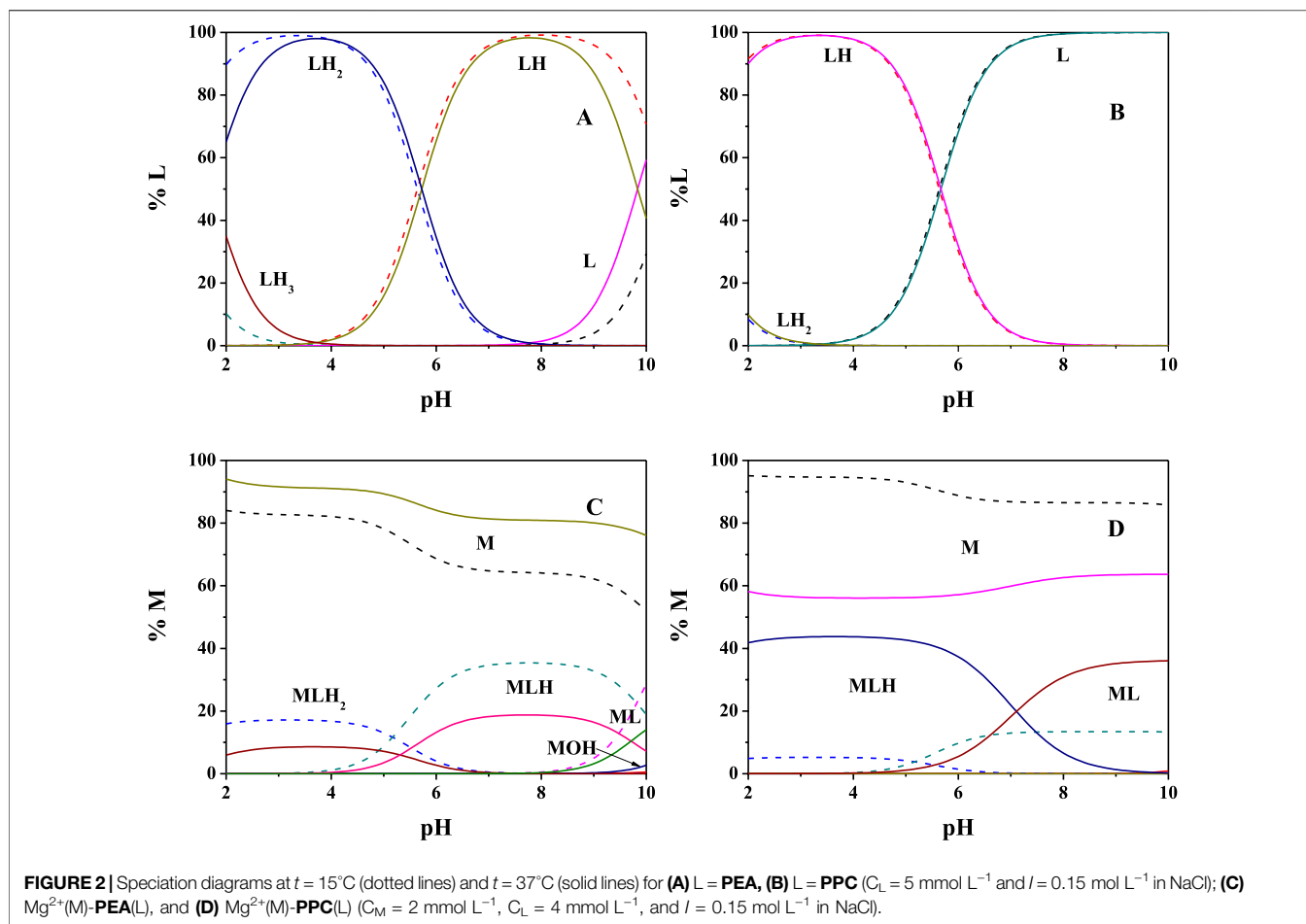
Protonation constant values obtained *via* potentiometric titrations under different temperature and ionic strength conditions are summarized in Table 1. The calculated values referred to PEA at $I = 0.15 \text{ mol L}^{-1}$ and $t = 25^\circ\text{C}$ ($\log K^{\text{LH}} = 10.141$, $\log K^{\text{LH}_2} = 5.590$) are similar to those reported by Mohan *et al.*, $\log K^{\text{LH}} = 10.12$, $\log K^{\text{LH}_2} = 5.52$ (at $I = 0.2 \text{ mol L}^{-1}$, $t = 25^\circ\text{C}$ in KNO_3) (Mohan and Abbott, 1978a; Mohan and Abbott, 1978b).

In a very recent study, the protonation constants of PEA at $t = 20^\circ\text{C}$ and $I = 0.1 \text{ mol L}^{-1}$ in KNO_3 were proposed ($\log K^{\text{LH}} = 10.41$, $\log K^{\text{LH}_2} = 5.70$) (Gabryel-Skrodzka et al., 2021). It is not possible to make other comparisons at other temperatures or ionic strengths since in the literature, there are only data up to 0.2 mol L^{-1} and $t = 20$ or 25°C (Datta and Grzybowski, 1959; Wozniak and Nowogrocki, 1979; May and Murray, 2001; Pettit and Powell, 2001; Martell et al., 2004). As far as we know, in the literature, there are no thermodynamic parameters on the protonation of PPC.

The species with Mg^{2+} were subsequently investigated. Both the protonation constants reported in this study and the hydrolysis constant of Mg^{2+} , reported in the Supplementary Table S1 under various conditions, were considered. Potentiometric experimental titrations were carried out at different metal/ligand ratios and different concentrations, to select the most reliable speciation model and to obtain the formation constants of the complex species. These $\text{Mg}^{2+}(\text{M})$ -ligand(L) formation constants are indicated as overall formation constants (β) or stepwise formation constants (K), based on the following reactions, where the charges are omitted for simplicity:



The choice of the speciation model that best reflects the system under study is made considering some requirements such as its



simplicity, goodness of statistical parameters (standard and mean deviations referring to the fit), percentages of formation of complex species, variance ratio between the chosen model, and others (Filella and May, 2005).

The obtained results, in terms of formation constants of $\text{Mg}^{2+}\text{-PEA}$ and $\text{Mg}^{2+}\text{-PPC}$ species at $I = 0.15 \text{ mol L}^{-1}$ in NaCl and $t = 15, 25$, and 37°C , are reported in **Table 1**. The speciation models include three species for the $\text{Mg}^{2+}\text{-PEA}$ system, namely, MLH_2 , MLH , and ML and two species for the $\text{Mg}^{2+}\text{-PPC}$ system, namely, MLH and ML . Mass spectrometry measurements will also highlight the formation of ML_2 species. Despite the excess ligand employed in the experimental potentiometric conditions ($\text{M:L} = 1:3$), the formation percentage of ML_2 species was negligible for both ligands. Therefore, this species was not considered in the speciation models. The speciation diagrams of the systems containing **PEA**, **PPC**, $\text{Mg}^{2+}\text{-PEA}$, and $\text{Mg}^{2+}\text{-PPC}$ are shown in **Figures 2A–D**. Under physiological conditions ($\text{pH} = 7.4$, $t = 37^\circ\text{C}$, and $I = 0.15 \text{ mol L}^{-1}$), considering **PEA** at $C_L = 5 \text{ mmol L}^{-1}$, formation percentages of L , LH , and LH_2 species are 0.3, 97.4, and 2.2, respectively. Under the same conditions, considering **PPC**, formation percentages of L and LH species are 98.3 and 1.7, respectively (**Figure 2B**). In the presence of Mg^{2+} , in the **PEA** system, MLH species achieves a significant formation

percentage of 18.6 (**Figure 2C**); in the **PPC** system, both MLH and ML species achieve significant formation percentages equal to 15.3 and 23.7, respectively (**Figure 2D**). More in detail, **Figure 2C**—referring to the $\text{Mg}^{2+}\text{-PEA}$ system—shows that in the acid pH range, the MLH_2 species is formed, reaching percentages of up to 10%. The main species is MLH with 20% in the pH range 6.5–9.0. ML species is formed at $\text{pH} > 9$. With regard to the $\text{Mg}^{2+}\text{-PPC}$ system, shown in **Figure 2D**, the observed complex species are much higher than those of **PEA** under the same conditions. MLH species exceeds 40% at $\text{pH} = 2\text{--}4$. ML species reaches almost 40% at $\text{pH} = 7\text{--}10$. In the literature, fairly close to our results of formation constants of Mg-PEA species at $I = 0.15 \text{ mol L}^{-1}$ and $t = 25^\circ\text{C}$ were reported by Hendrickson *et al.*, $\log K^{\text{ML}} = 2.20$ and $\log K^{\text{MLH}} = 1.48$ (at $I = 0.1 \text{ mol L}^{-1}$ in $(\text{C}_3\text{H}_7)_4\text{NI}$) and $t = 20^\circ\text{C}$) (Hendrickson and Fullington, 1965). Other values were obtained by Mohan *et al.*, $\log K^{\text{ML}} = 1.56$ and $\log K^{\text{MLH}} = 1.17$ (at $I = 0.2 \text{ mol L}^{-1}$ in KNO_3 and $t = 25^\circ\text{C}$) (Mohan and Abbott, 1978a; Mohan and Abbott, 1978b) and by Osterberg, $\log K^{\text{ML}} = 1.70$ and $\log K^{\text{MLH}} = 1.23$ (at $I = 0.15 \text{ mol L}^{-1}$ in KCl and $t = 25^\circ\text{C}$) (Osterberg, 1960). It was not possible to compare the results reported in this study on $\text{Mg}^{2+}\text{-PPC}$ species with those in the literature since as far as we know, the speciation patterns and the formation constants were not reported up to now.

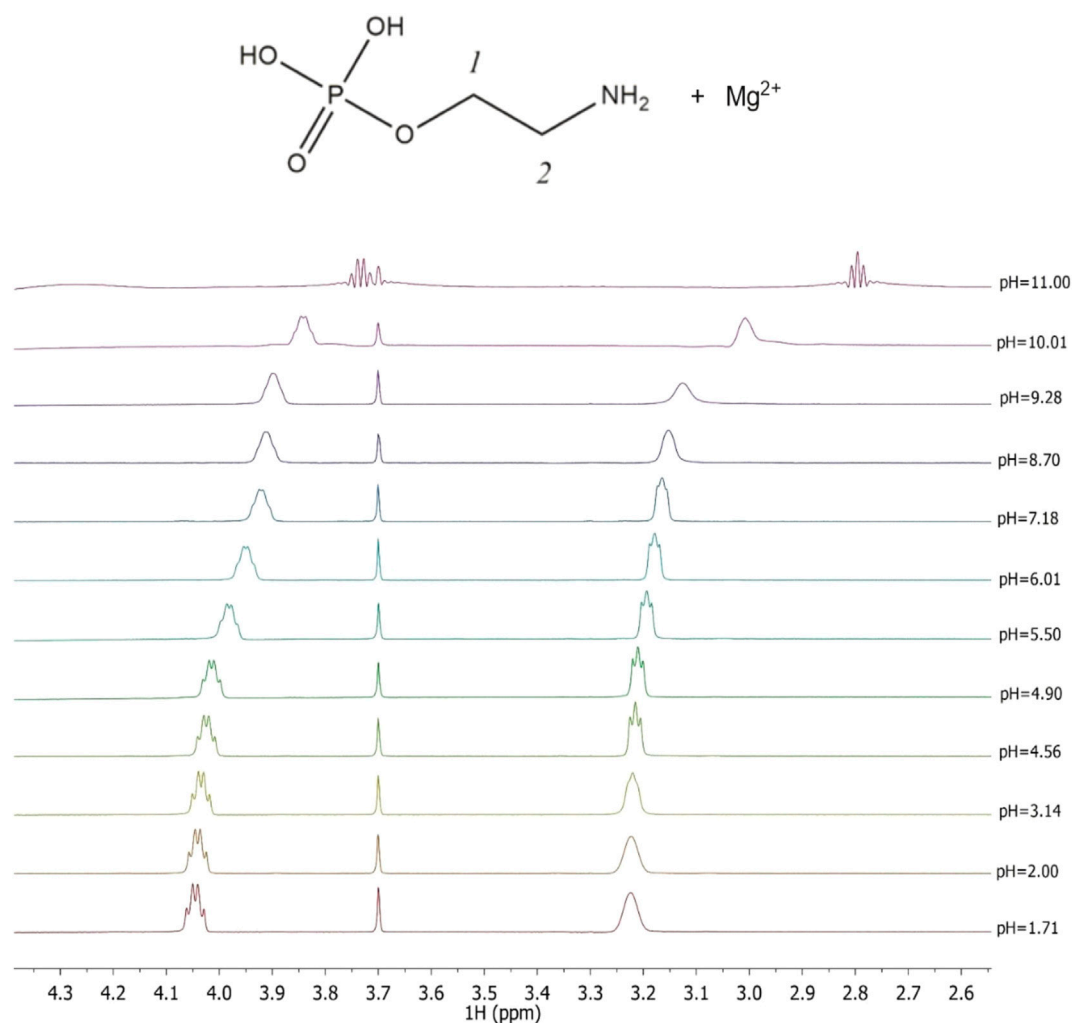


FIGURE 3 | Superimposed ^1H -NMR spectra of solutions containing $\text{Mg}^{2+}(\text{M})$ e **PEA**(L) at $C_M = 6 \text{ mmol L}^{-1}$, $C_L = 7 \text{ mmol L}^{-1}$, $t = 25^\circ\text{C}$, and $I = 0.15 \text{ mol L}^{-1}$ in NaCl, range of pH = 1.71–11.00.

^1H -NMR titrations were also carried out at $I = 0.15 \text{ mol L}^{-1}$ and $t = 25^\circ\text{C}$ both for the determination of the protonation constants of the ligands under study as well as of the complexes with Mg^{2+} , as already reported on other systems (Cardiano et al., 2011a; Cardiano et al., 2017). The Chemical shift and pattern of protons of the **PEA** solution are shown in **Supplementary Figure S1** at different pH values. Some noticeable signals can be identified for the two types of **PEA** protons: a doublet triplet (td) assignable to the CH_2 protons in position 1 showing $\Delta\delta = 0.28 \text{ ppm}$ from pH 1.67 to pH 11.00 and a triplet (t) assignable to the CH_2 protons in position 2 showing $\Delta\delta = 0.43 \text{ ppm}$ from pH 1.67 to pH 11.00. The solutions of **PEA** with Mg^{2+} were analyzed in the same pH range by the NMR technique, and the proton spectra are shown in **Figure 3**. The data collected indicate that the chemical shift values have the same trend as the values recorded for the free ligand, as evidenced in the graph showing small differences (**Supplementary Figure S2**).

Therefore, it can be assumed that the interaction between the metal and ligand occurs from the phosphoric moiety or by the electrostatic interaction of the negative oxygen atoms and the magnesium cation.

The chemical shift and pattern of protons of the **PPC** solution are shown in **Supplementary Figure S3** at different pH values. Some noticeable chemical shifts can be identified for the three types of **PPC** protons: a broad multiplet (m) assignable to the CH_2 protons in position 1 showing $\Delta\delta = 0.14 \text{ ppm}$ from pH 1.90 to pH 10.00, a triplet (t) assignable to the CH_2 protons in position 2 showing $\Delta\delta = 0.13 \text{ ppm}$ from pH 1.90 to pH 10.00, and a singlet of the nine methyl protons at 3.16 ppm, which does not have appreciable variations, in the pH range studied. The solutions of **PPC** with Mg^{2+} were analyzed by the NMR technique, and the proton spectra are shown in **Supplementary Figure S4**. Also, for **PPC** solutions, the chemical shift values of the free ligand and the ligand with magnesium are similar, evidencing small

TABLE 2 | Comparison between the experimental protonation constants of **PEA** and **PPC** and experimental formation constants of Mg^{2+} -**PEA** and Mg^{2+} -**PPC** species obtained via ^1H -NMR and potentiometry at $t = 25^\circ\text{C}$ and $I = 0.15 \text{ mol L}^{-1}$.

Ligand	Species	$\log\beta^a$	
		$^1\text{H-NMR}$	Potentiometry
PEA	LH	10.32(2) ^b	10.141
	LH ₂	15.88(5)	15.731
	LH ₃	16.69 ^c	16.69
	MLH ₂	17.29 ^c	17.29
	MLH	11.78(8)	11.56
	ML	2.85(6)	2.66
PPC	LH	5.64(1) ^b	5.646
	LH ₂	6.53 ^c	6.53
	MLH	7.36(4)	7.46
	ML	1.44(7)	1.42

^aOverall protonation constants.

^b≥95% of confidence interval.

^cThese values, obtained by potentiometry, were kept constant during the calculations with HypNMR.

differences, as shown in the graph (Supplementary Figure S5). A similar assumption on **PEA** and **PPC** could also interact through the phosphate group oxygen, and this would justify the lack of chemical shift of the protons on the aliphatic chain of the ligand in the presence of magnesium ions. The results listed in Table 2, together with those

obtained by potentiometry, were obtained from the processing of the measured chemical shifts. These results confirmed that the comparison between the results obtained with the two techniques, under the same experimental conditions, shows an excellent agreement both for the speciation model determined by potentiometry and for the values of the formation constants of the complexes, especially for **PPC**. Figure 4 highlights the excellent agreement between the experimental and the calculated chemical shift values over all pH ranges considered and therefore in the formation areas of the different species.

Simulation in Biological Fluids

One of the aims of this investigation is to be able to use the acquired thermodynamic information making simulations under real fluid conditions, such as biological ones. Just as an example, the composition of two biological fluids was considered with the aim of evaluating the significance of the complex species under study for the purposes of a characterization of the fluid itself. Among the biological fluids, the cerebrospinal fluid (CSF) and the extracellular fluid in the brain intracellular space were considered. The CSF is formed in the brain. It is an aqueous solution containing higher contents of magnesium, sodium, and chloride and lower concentrations of potassium, calcium,

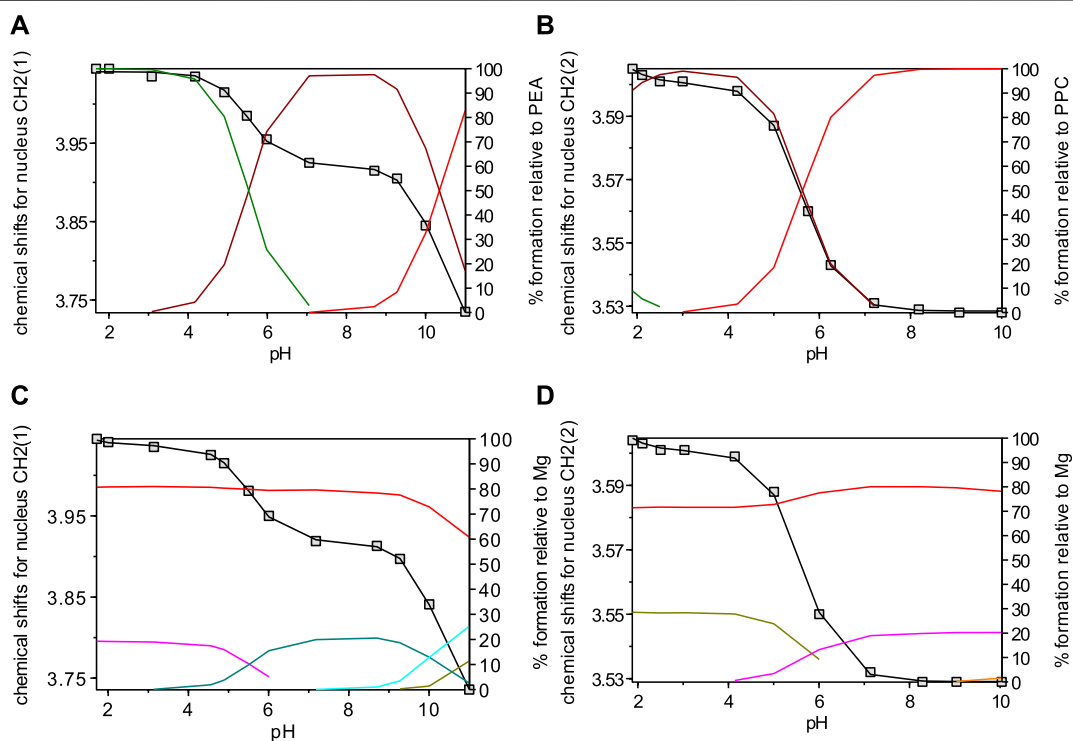


FIGURE 4 | Overlap of calculated (line) and observed (\square) chemical shifts with speciation diagrams obtained by HypNMR on solutions at $t = 25^\circ\text{C}$ and $I = 0.15 \text{ mol L}^{-1}$ containing: **(A)** PEA at $C_{\text{PEA}} = 7.6 \text{ mmol L}^{-1}$ (Lines: green, LH₂; brown, LH; red, L); **(B)** PPC at $C_{\text{PPC}} = 7 \text{ mmol L}^{-1}$ (Lines: green, LH₂; brown, LH; red, L); **(C)** Mg^{2+} -PEA at $C_{\text{M}} = 6 \text{ mmol L}^{-1}$ and $C_{\text{PEA}} = 7 \text{ mmol L}^{-1}$ (Lines: red, free M; violet, MLH₂; green, MLH; light blue, ML; dark green, MOH); **(D)** Mg^{2+} -PPC at $C_{\text{M}} = 6 \text{ mmol L}^{-1}$ and $C_{\text{PPC}} = 7 \text{ mmol L}^{-1}$ (Lines: red, free M; dark green, MLH; violet ML).

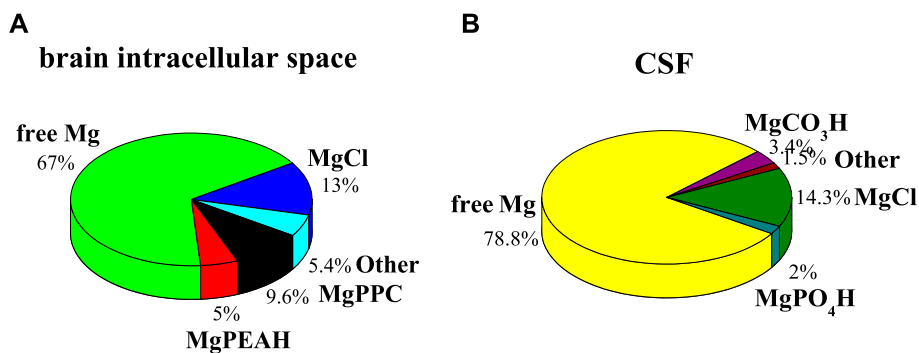


FIGURE 5 | Calculated percentages of Mg^{2+} -PEA and Mg^{2+} -PPC species in biological fluids at $\text{pH} = 7.4$, $t = 37^\circ\text{C}$, and $I = 0.15 \text{ mol L}^{-1}$. **(A)** Brain intracellular space conditions; **(B)** CSF conditions.

bicarbonate, and phosphate, with respect to the plasma in humans (Artru, 2010). The latter in the brain plays a role in multiple key functions, including non-synaptic neurotransmission. The extracellular space makes up about 15% of the total brain volume and is filled with an extracellular fluid whose electrolyte composition differs enough from that of the cerebrospinal fluid (Heinemann et al., 2009).

The complexes that they form with Mg^{2+} can be relevant and not negligible for the purposes of a characterization of the fluid itself. One example regards the calculation of the formation percentages of Mg^{2+} -PEA and -PPC species under CSF conditions ($C_{\text{Na}} = 141 \text{ mmol L}^{-1}$, $C_{\text{K}} = 2.9 \text{ mmol L}^{-1}$; $C_{\text{Ca}} = 1.25 \text{ mmol L}^{-1}$, $C_{\text{Mg}} = 1.2 \text{ mmol L}^{-1}$, $C_{\text{Cl}} = 124 \text{ mmol L}^{-1}$, $C_{\text{HCO}_3} = 21 \text{ mmol L}^{-1}$, $C_{\text{PO}_4} = 0.15 \text{ mmol L}^{-1}$, $C_{\text{PEA}} = 1.70 \text{ mmol L}^{-1}$, $C_{\text{PPC}} = 1.70 \text{ mmol L}^{-1}$, $t = 37^\circ\text{C}$, and $I = 0.15 \text{ mol L}^{-1}$) (Artru, 2010). All formation constants of the species taken into account in these simulations are listed in **Supplementary Table S3**. Under these conditions, none of the species containing PEA and PPC reaches significant formation percentages. Calculated percentages of Mg^{2+} -PEA and -PPC species in CSF conditions at $\text{pH} = 7.4$, $t = 37^\circ\text{C}$, and $I = 0.15 \text{ mol L}^{-1}$ are shown in **Figure 5B**. On the contrary, considering the conditions of the brain intracellular space, where PEA and PPC concentrations are higher than in the CSF and plasma ($C_{\text{Na}} = 155 \text{ mmol L}^{-1}$, $C_{\text{K}} = 3.0 \text{ mmol L}^{-1}$; $C_{\text{Ca}} = 1.6 \text{ mmol L}^{-1}$, $C_{\text{Mg}} = 1.2 \text{ mmol L}^{-1}$, $C_{\text{Cl}} = 135 \text{ mmol L}^{-1}$, $C_{\text{HCO}_3} = 21 \text{ mmol L}^{-1}$, $C_{\text{PO}_4} = 1.0 \text{ mmol L}^{-1}$, $C_{\text{PEA}} = 0.59 \text{ mmol L}^{-1}$, $C_{\text{PPC}} = 0.59 \text{ mmol L}^{-1}$, $t = 37^\circ\text{C}$, $I = 0.15 \text{ mol L}^{-1}$ (Klein et al., 1993; Eaton and Pooler, 2009; Barrett et al., 2013), the formation percentages, especially of the Mg^{2+} -PPC species, increase significantly. More in detail, free magnesium reaches 67%, MgCl 13%, MgPPC 9.6%, and MgPEAH 5%. Calculated percentages of Mg^{2+} -PEA and -PPC species, under the conditions of the extracellular fluid in the brain intracellular space, at $\text{pH} = 7.4$, $t = 37^\circ\text{C}$, and $I = 0.15 \text{ mol L}^{-1}$, are shown in **Figure 5A**. This result shows that the species MgPPC reaches a percentage not negligible, albeit not high. The availability of reliable thermodynamic constants makes simulation possible under the conditions of real fluids.

TABLE 3 | Protonation constants at infinite dilution and parameters for the dependence on ionic strength **Eq. 5**, of PEA and PPC species at $t = 25^\circ\text{C}$ in NaCl.

Ligand	Species	$\log\beta^{\text{a}}$	C
PEA	LH	10.59(3) ^b	0.33(5) ^b
	LH ₂	16.43(5)	0.36(9)
	LH ₃	17.5(1)	0.2(2)
PPC	LH	6.14(3) ^b	0.14(9) ^b
	LH ₂	7.27(3)	0.06(4)

^aOverall protonation constants.

^b≥95% of confidence interval.

TABLE 4 | Thermodynamic parameters of protonation of PEA and PPC and of formation of Mg^{2+} -PEA and Mg^{2+} -PPC species at $t = 25^\circ\text{C}$ and $I = 0.15 \text{ mol L}^{-1}$ in NaCl.

Ligand	Species	$\Delta G^{\text{a,b}}$	$\Delta H^{\text{a,b}}$	$T\Delta S^{\text{a,b}}$
PEA	LH	-57.9	-42(1) ^c	16
	LH ₂	-31.9	6(2)	38
	LH ₃	-5.5	54(5)	59
	MLH ₂	-8.9	-27(2)	36
	MLH	-8.0	-30(10)	38
	ML	-15.2	-67(10)	52
PPC	LH	-32.2	3(4) ^c	35
	LH ₂	-5.0	45(5)	50
	MLH	-34.5	96(3)	130
	ML	-8.1	50(8)	58

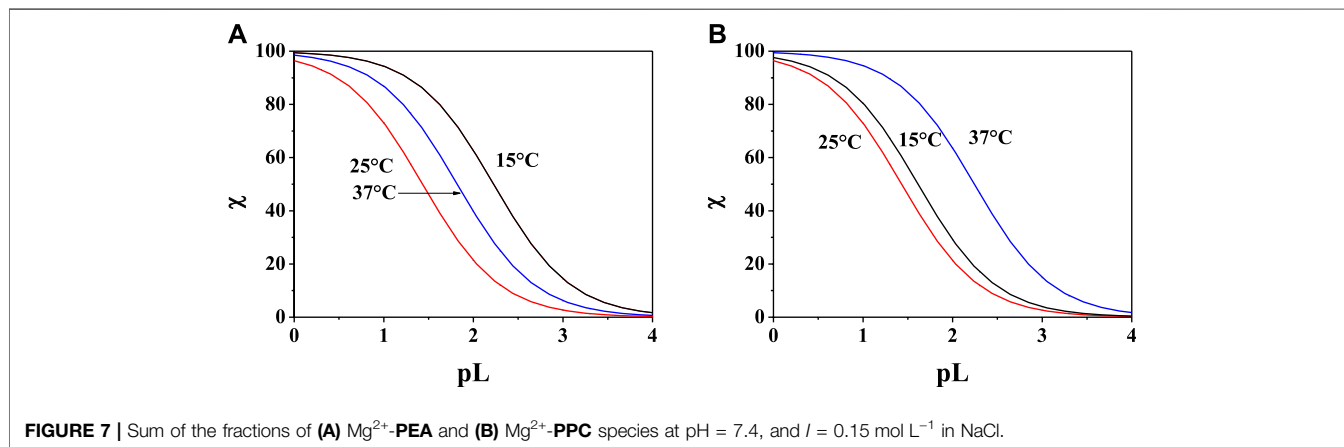
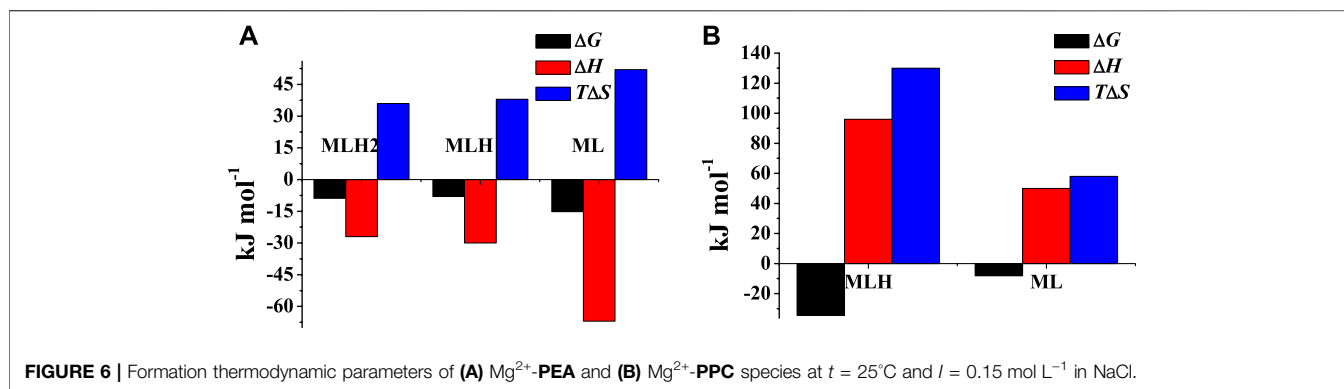
^aReferred to stepwise protonation and formation constants.

^bExpressed in kJ mol^{-1} .

^c≥95% of confidence interval.

Dependence of Formation Constants on Temperature and Ionic Strength

The dependence of protonation constants and formation constants on ionic strength was determined processing experimental measurements performed at different ionic strengths by considering the following Debye-Huckel equation, widely used in the $0 \leq I \leq 1 \text{ mol L}^{-1}$ range (Cardiano et al., 2018b; Chillè et al., 2018):



$$\log \beta = \log \beta^0 - 0.51 \cdot z^* \frac{\sqrt{I}}{1 + 1.5\sqrt{I}} + CI, \quad (5)$$

where β is the stability constant at a given ionic strength, β^0 is the stability constant at infinite dilution, $z^* = \Sigma(\text{charge})_{\text{reactants}}^2 - \Sigma(\text{charge})_{\text{products}}^2$, and C is an empirical parameter. Protonation constants at infinite dilution and C parameter values calculated by Eq. 5 for PEA and PPC species at $t = 25^\circ\text{C}$ in NaCl are listed in Table 3.

For the dependence on the temperature, the van't Hoff equation was used, as for other systems (Cordaro et al., 2019; Giuffrè et al., 2020):

$$\log \beta^T = \log \beta^0 + \Delta H (1/\theta - 1/T) R \ln 10, \quad (6)$$

where $\log \beta^T$ is the stability constant at a given ionic strength and temperature (in Kelvin), $\log \beta^0$ is the value at the reference temperature ($T = 298 \text{ K}$), and ΔH^0 is the formation enthalpy change expressed in kJ mol^{-1} at $T = 298.15 \text{ K}$ and $R = 8.314472 \text{ J K}^{-1} \text{ mol}^{-1}$.

The values of thermodynamic parameters, as formation enthalpy, entropy, and free energy changes, of the Mg^{2+} -PEA, and -PPC species are reported in Table 4. Formation thermodynamic parameters referring to reaction (4) are shown as a bar plot in Figure 6, to highlight the prevalent contribution of entropy or

enthalpy to free energy. As known for electrostatic interactions, the entropic term, related to the orientation disorder of the solvation water molecules, constitutes the main contribution to the free energy change. This behavior was found for most of the species, except for ML one formed by the PEA ligand.

Sequestering Ability

The sequestering capacity of a ligand in a solution correlates with the tendency of the ligand to form complexes with a given metal cation. The higher the stability of the complex species, the lower is the concentration of the free metal cation in the solution. To evaluate the sequestering ability of a ligand toward a specific metal cation, all equilibria in which both the ligand and the metal cation participate are considered, as metal ion hydrolysis, ligand protonation, and weak interactions with the ionic medium. The $\text{pL}_{0.5}$ empirical parameter, i.e., the co-logarithm of the ligand concentration which sequesters 50% of the metal cation in traces, was proposed. Traces of metal cations were considered as they represent the conditions of concentration with which many of them are generally present in natural fluids. The sequestering capacity of a ligand toward a metal cation can be evaluated by the following Boltzmann-type equation with asymptotes 0 for $\text{pL} \rightarrow 0$, 1 for $\text{pL} \rightarrow \infty$ (Cardiano et al., 2011b; Cardiano et al., 2018a):

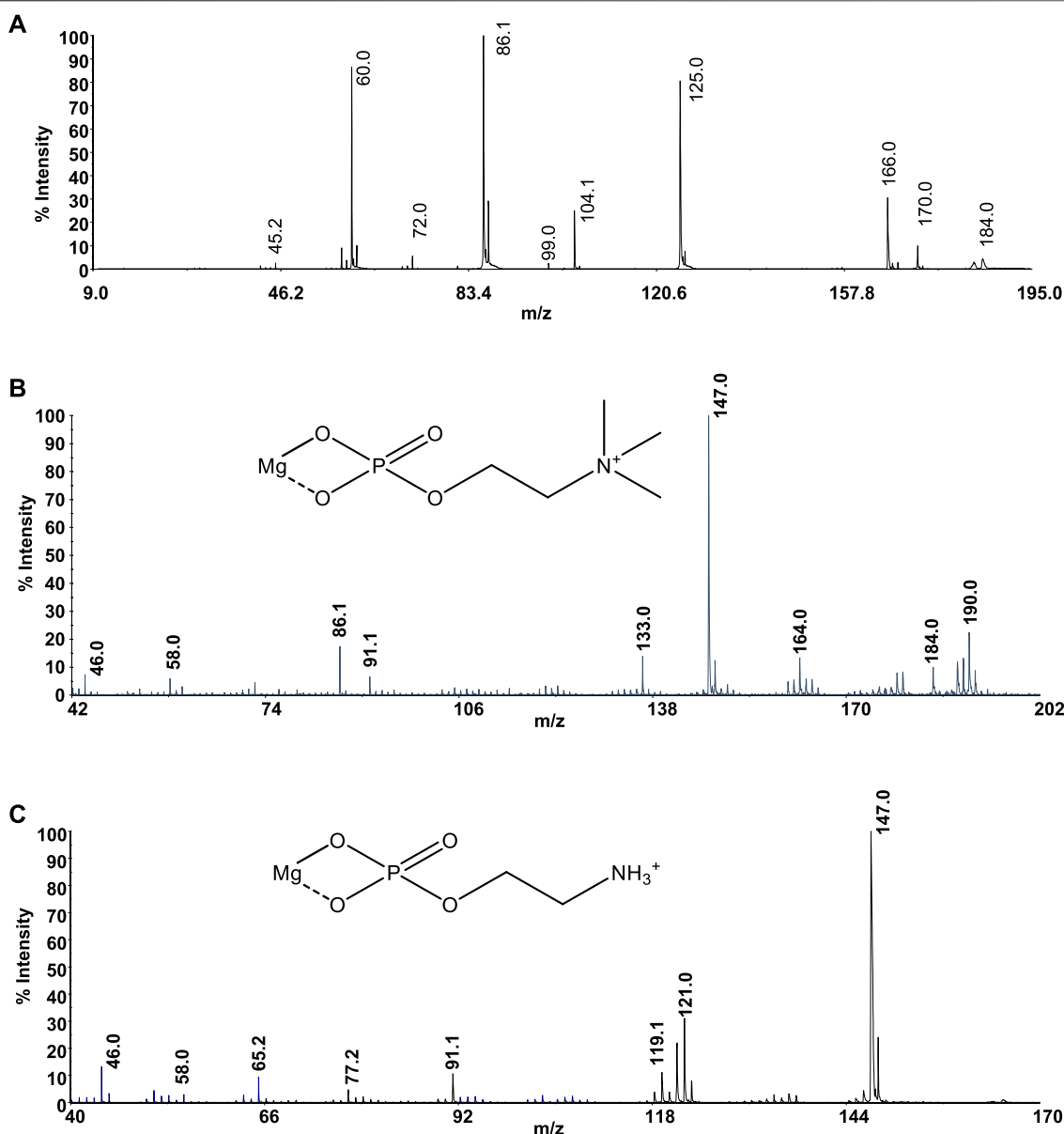


FIGURE 8 | Product-ion spectra of (A) $[\text{PPC}]^+$, (B) $[\text{MgPPC}]^+$, and (C) $[\text{MgPEA}]^+$.

$$\chi = \frac{1}{1 + 10^{(\text{pL} - \text{pL}_{0.5})}}, \quad (7)$$

where χ is the sum of the molar fractions of the metal–ligand species, and pL is the co-logarithm of the total ligand concentration. The sequestering ability strictly depends on pH, temperature, and ionic strength.

In order to evaluate the sequestering capacity of **PEA** and **PPC** toward Mg^{2+} , $\text{pL}_{0.5}$ values at different temperatures were calculated (Supplementary Table S4). Figures 7A,B show the comparison between the sequestering capacity of **PEA** and **PPC** under physiological conditions ($\text{pH} = 7.4$, and $I = 0.15 \text{ mol L}^{-1}$). The plot confirms that under these

conditions, **PPC** shows a slightly higher sequestering capacity than **PEA** toward Mg^{2+} .

Mass Spectrometry

Mass spectrometry measurements were used to elucidate the mechanism of **PPC** and **PEA** interactions. In turn, this aspect is very useful to understand some biological phenomena such as the mechanism transport through membranes but also for evaluating the possible use of these compounds in some application fields. Phosphorylcholine-based biomaterials are well studied due to their biocompatibility and being used in many clinical applications (Matsuura et al., 2016; Goda and Miyahara, 2018). The performance of these biomaterials can be affected by electrolytes.

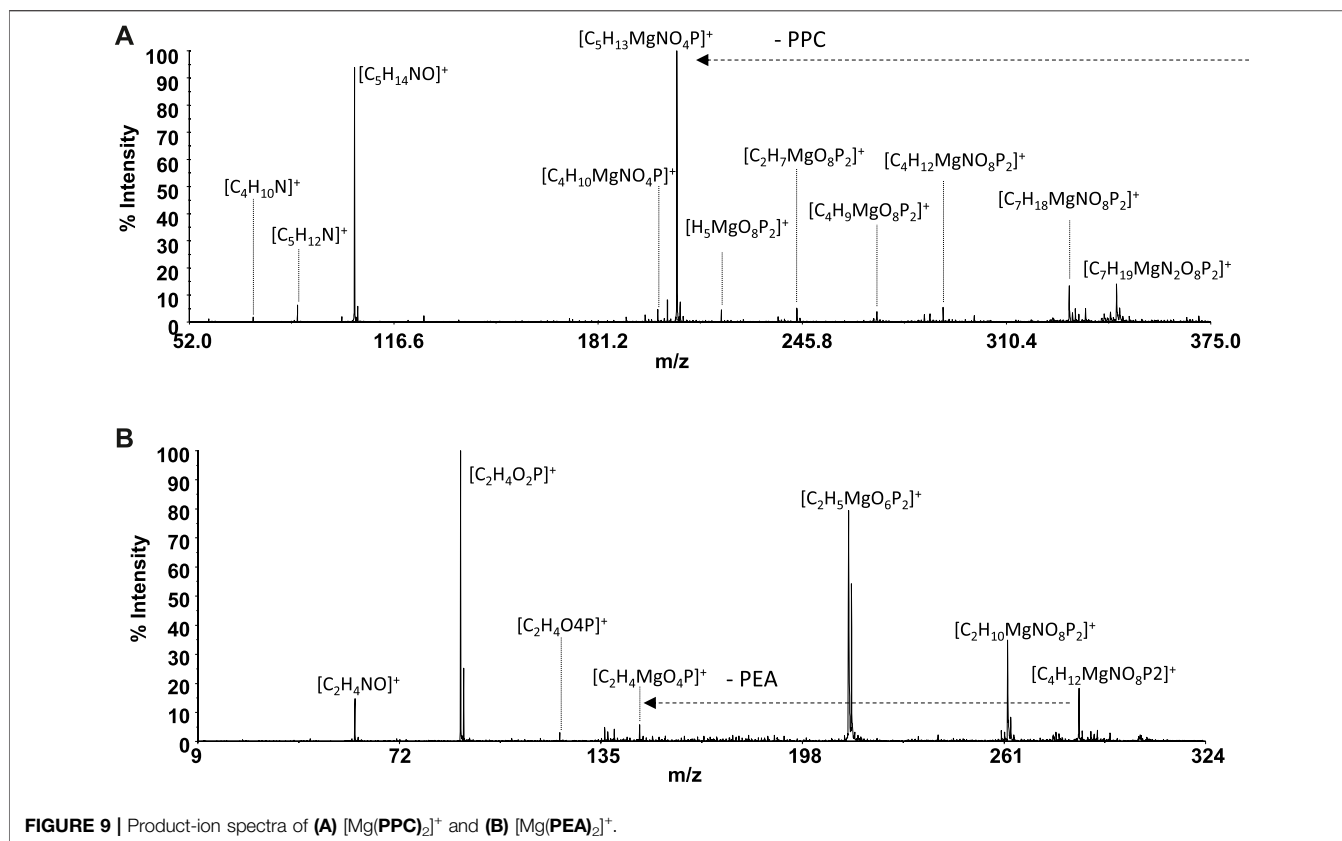
TABLE 5 | MS and MS/MS ion fragments of ligands and Mg^{2+} species.

PPC	Composition	Detected	PEA	Composition	Detected
	$[\text{C}_5\text{H}_{15}\text{NO}_4\text{P}]^+$	184.07	—	$[\text{C}_2\text{H}_9\text{NO}_4\text{P}]^+$	142.03
	$[\text{C}_4\text{H}_{13}\text{NO}_4\text{P}]^+$	170.06	—	$[\text{CH}_6\text{O}_4\text{P}]^+$	113.00
	$[\text{C}_5\text{H}_{13}\text{NO}_3\text{P}]^+$	166.06	—	$[\text{C}_2\text{H}_6\text{O}_4\text{P}]^+$	125.00
	$[\text{C}_2\text{H}_6\text{O}_4\text{P}]^+$	125.00	—	$[\text{H}_4\text{O}_4\text{P}]^+$	98.99
	$[\text{C}_5\text{H}_{14}\text{NO}]^+$	104.11	—	$[\text{H}_4\text{O}_3\text{P}]^+$	82.99
	$[\text{H}_4\text{O}_4\text{P}]^+$	98.99	—	—	—
	$[\text{C}_5\text{H}_{12}\text{N}]^+$	86.10	—	—	—
	$[\text{H}_4\text{O}_3\text{P}]^+$	82.99	—	—	—
	$[\text{C}_4\text{H}_{10}\text{N}]^+$	72.08	—	—	—
	$[\text{C}_3\text{H}_{10}\text{N}]^+$	60.08	—	—	—
MS $[\text{MgPPC}]^+$	$[\text{C}_5\text{H}_{13}\text{MgNO}_4\text{P}]^+$	206.04	MS $[\text{Mg(PPC)}_2]^+$	$[\text{C}_{10}\text{H}_{27}\text{MgN}_2\text{O}_8\text{P}_2]^+$	389.11
MS/MS	$[\text{C}_5\text{H}_{15}\text{NO}_4\text{P}]^+$	184.08	MS/MS	$[\text{C}_7\text{H}_{18}\text{MgNO}_8\text{P}_2]^+$	330.04
	$[\text{C}_2\text{H}_4\text{MgO}_4\text{P}]^+$	146.97	—	$[\text{C}_4\text{H}_9\text{MgO}_8\text{P}_2]^+$	270.97
	$[\text{C}_2\text{H}_7\text{MgNO}_4\text{P}]^+$	164.00	—	$[\text{C}_2\text{H}_6\text{MgNO}_7\text{P}_2]^+$	243.96
	$[\text{C}_5\text{H}_{14}\text{NO}]^+$	104.11	—	$[\text{H}_5\text{MgO}_8\text{P}_2]^+$	218.93
	$[\text{CH}_2\text{MgO}_4\text{P}]^+$	132.96	—	$[\text{C}_7\text{H}_{19}\text{MgN}_2\text{O}_8\text{P}_2]^+$	345.05
	$[\text{C}_5\text{H}_{12}\text{N}]^+$	86.10	—	$[\text{C}_4\text{H}_{12}\text{MgNO}_8\text{P}_2]^+$	287.99
	$[\text{C}_4\text{H}_{10}\text{N}]^+$	72.08	—	$[\text{C}_5\text{H}_{13}\text{MgNO}_4\text{P}]^+$	206.05
	$[\text{C}_3\text{H}_8\text{N}]^+$	58.08	—	$[\text{H}_3\text{MgO}_7\text{P}_2]^+$	200.92
	$[\text{C}_2\text{H}_8\text{N}]^+$	46.07	—	$[\text{C}_2\text{H}_6\text{O}_4\text{P}]^+$	125.00
	$[\text{C}_4\text{H}_9\text{MgNO}_4\text{P}]^+$	190.02	—	$[\text{C}_5\text{H}_{14}\text{NO}]^+$	104.11
	$[\text{CH}_4\text{MgO}_4\text{P}]^+$	134.97	—	$[\text{C}_5\text{H}_{12}\text{N}]^+$	86.10
	—	—	—	$[\text{C}_4\text{H}_{10}\text{N}]^+$	72.08
	—	—	—	$[\text{C}_3\text{H}_8\text{N}]^+$	58.08
MS $[\text{MgPEA}]^+$	$[\text{C}_2\text{H}_7\text{MgNO}_4\text{P}]^+$	164.00	MS $[\text{Mg(PEA)}_2]^+$	$[\text{C}_4\text{H}_{15}\text{MgN}_2\text{O}_8\text{P}_2]^+$	305.02
	$[\text{CH}_4\text{MgO}_4\text{P}]^+$	134.97	—	$[\text{C}_4\text{H}_{12}\text{MgNO}_8\text{P}_2]^+$	287.99
	$[\text{H}_2\text{MgO}_4\text{P}]^+$	120.96	—	$[\text{C}_2\text{H}_{10}\text{MgNO}_8\text{P}_2]^+$	261.98
	$[\text{C}_2\text{H}_4\text{MgO}_4\text{P}]^+$	146.97	—	$[\text{C}_2\text{H}_5\text{MgO}_6\text{P}_2]^+$	210.94
	$[\text{MgO}_3\text{P}]^+$	102.94	—	$[\text{C}_2\text{H}_4\text{MgO}_4\text{P}]^+$	146.97
	$[\text{H}_2\text{O}_3\text{P}]^+$	80.98	—	$[\text{C}_2\text{H}_4\text{O}_4\text{P}]^+$	122.99
	$[\text{C}_2\text{H}_4\text{O}_2\text{P}]^+$	91.00	—	$[\text{C}_2\text{H}_4\text{O}_2\text{P}]^+$	91.00
	$[\text{C}_2\text{H}_4\text{NO}]^+$	58.03	—	$[\text{C}_2\text{H}_4\text{NO}]^+$	58.03
	$[\text{C}_2\text{H}_8\text{N}]^+$	46.07	—	—	—

In fact, the zwitterionic nature of the phosphorylcholine groups may be changed into a cationic system introducing divalent cations that strongly interact with the phosphate group. Although it required the knowledge of the sequestering ability, the coordination mode of the natural ligand in local microenvironments helps to understand the potential activity of the biomaterials, and speciation studies are seldom reported (Gabryel-Skrodzka et al., 2021).

Mass spectrometry (MS) techniques are generally used for the highly sensitive analysis of metal ion complexes. The positive ion mode is usually the polarity for metal complex analysis by mass spectrometry (Aiello et al., 2017). Here, this selection was strengthened using ligands containing a quaternary nitrogen with a fixed positive charge. Therefore, the matrix-assisted laser desorption mass spectrometry (MALDI-TOF/TOF-MS) platform in the positive ion mode was adopted to study Mg^{2+} -L systems (L = **PPC** or **PEA**). This platform offers particular advantages in investigating biological systems (Aiello et al., 2021b). The most important peculiarities of MALDI MS-based methods rely in the rapid and sensitive detection of analytes (Aiello et al., 2020; Salvatore et al., 2020) and in obtaining the molecular profiling of complex mixtures. Finally, the structures of low molecular weight organic and organometallic compounds can be analyzed and

determined by tandem mass spectrometry (MS/MS) experiments (Falcone et al., 2013). The interaction of Mg^{2+} with **PPC** and **PEA** was explored by MALDI using α -CHCA as the matrix. Full-scan positive ion MS of Mg^{2+} -L systems (L = **PPC**, or **PEA**) displayed ion species indicating information on ML_n (n: 1, 2) species. The elemental composition of detected ML_n species, combined with the observed gas-phase fragmentation pathways, was used to identify the coordination sites and to ascribe the most probable structures of complexes. The isotope ratio patterns observed for all the Mg^{2+} /L complexes matched with those obtained from theoretical calculations, suggesting both ligands acting as a bidentate. The simplest systems, represented by free ligands, will first be discussed (**Figure 8A**). The MS/MS spectrum of $[\text{PPCH}]^+$ at 1 kV shows complementary fragment ion pairs of the m/z values 99/86 ($[\text{H}_4\text{O}_4\text{P}]^+ / [\text{C}_5\text{H}_{12}\text{N}]^+$), 81/104 ($[\text{H}_2\text{O}_3\text{P}]^+ / [\text{C}_5\text{H}_{14}\text{NO}]^+$), and 60/125 ($[\text{C}_3\text{H}_{10}\text{N}]^+ / [\text{C}_2\text{H}_6\text{O}_4\text{P}]^+$) as the most abundant fragment ions. **PPC** is an aliphatic ester of phosphoric acid; consequently, it preferentially forms the fragment of m/z 99 rather than the phosphate marker ion of m/z 81. Meanwhile, an intramolecular H transfer, involving the alkyl backbone of the **PPC** molecule, promotes the release of trimethylamine and the formation of the m/z 125



$[\text{C}_2\text{H}_6\text{O}_4\text{P}]^+$. MS and MS/MS ion fragments of ligands are listed in **Table 5**.

Direct MS analysis of solutions containing both Mg^{2+} and PPC at a final M:L ratio of 1:1, pH 8 as stated by speciation experiments, showed the formation of the ions of m/z 206 ($[\text{MgPPC}]^+$, $[\text{C}_5\text{H}_{13}\text{MgNO}_4\text{P}]^+$) and m/z 389 ($[\text{Mg}(\text{PPC})_2]^+$, and $[\text{C}_{10}\text{H}_{27}\text{MgN}_2\text{O}_8\text{P}_2]^+$). As shown in **Figure 8B** and **Table 5**, the product-ion spectrum of the $[\text{MgPPC}]^+$ (m/z 206) contains prominent ions of m/z 147 ($[\text{C}_2\text{H}_4\text{MgO}_4\text{P}]^+$) and m/z 91 ($[\text{C}_2\text{H}_4\text{O}_2\text{P}]^+$). The pathways proposed for formation of these two ions involve an initial loss of trimethylamine ($[\text{MgL}-59]$), followed by an additional loss of $\text{Mg}(\text{OH})_2$ (58 Da). Meanwhile, the observed daughter ion of m/z 191 ($[\text{C}_4\text{H}_{10}\text{MgNO}_4\text{P}]^+$), 177 ($[\text{C}_3\text{H}_8\text{MgNO}_4\text{P}]^+$), and 163 ($[\text{C}_2\text{H}_6\text{MgNO}_4\text{P}]^+$) arises from direct and consecutive loss of methyl groups matching typical fragmentation of the positively-charged head group. The gas-phase behavior of $[\text{Mg}(\text{PEA})\text{H}]^+$ matches that observed for Mg/PPC systems (**Figure 8C** and **Table 5**). The observed fragmentation patterns of both Mg systems enable us to design the most probable molecular structures, where the coordination occurs at the phosphate group generating a four-membered cycle.

Despite the experimental potentiometric conditions, the significant formation of MgL_2 species was not found; to complete this study, a solution containing Mg^{2+} :L (L = PPC or PEA), at a final ratio of 1:2, was analyzed by MALDI MS/MS spectrometry at different times, over 2 h. The experiments conducted allowed a better detection (% intensity of the total

ion current) of $[\text{MgL}_2]^+$ ions. The MALDI MS/MS spectrum of the $[\text{Mg}(\text{PPC})_2]^+$ (m/z 389 and $[\text{C}_{10}\text{H}_{27}\text{MgN}_2\text{O}_8\text{P}_2]^+$ **Figure 9A** and **Table 5**) revealed the formation of the cations $[\text{C}_5\text{H}_{13}\text{MgNO}_4\text{P}]^+$, $[\text{H}_3\text{MgO}_7\text{P}_2]^+$, $[\text{C}_2\text{H}_6\text{O}_4\text{P}]^+$, $[\text{C}_5\text{H}_{14}\text{NO}]^+$, $[\text{C}_5\text{H}_{12}\text{N}]^+$, $[\text{C}_4\text{H}_{10}\text{N}]^+$, and $[\text{C}_3\text{H}_8\text{N}]^+$, resulting from the initial loss of the ligand, followed by the additional fragmentations of $[\text{MgPPC}]^+$. Furthermore, the direct loss of trimethylamine $[\text{Mg}(\text{PPC})_2-59]$ (m/z 330), followed by the additional loss of trimethylamine $[\text{Mg}(\text{PPC})-118]^+$ (m/z 270) and/or ethylene (28) $[\text{Mg}(\text{PPC})_2-(145)]^+$ from the parent ion $[\text{Mg}(\text{PPC})_2]^+$, confirmed that the phosphate group to be involved in the coordination with Mg^{2+} . Interestingly, the loss of one ligand molecule from the $[\text{M}(\text{PPC})_2]^+$ species was observed. These data indicated that coordination of Mg^{2+} with PPC causes weakening of specific bonds which break upon collision. The gas-phase behavior of $[\text{Mg}(\text{PEA})_2]^+$ does not match that observed for Mg/PPC systems. For this species, the direct loss aminoethanol ($[\text{Mg}(\text{PEA})_2-60]$, m/z 244) followed by the additional loss of the methylamine ($[\text{Mg}(\text{PEA})_2-93]^+$, m/z 212) dominates the gas-phase fragmentation (**Figure 9B** and **Table 5**). The formation of $[\text{Mg}(\text{PEA})-17]^+$ suggests that coordination of Mg(II) with PEA is more rugged than PPC under MS/MS conditions. The ML and ML_2 complexes of Mg^{2+} with PEA features coordination modes which were very similar to those observed for the species containing PPC. For all species detected, mass spectra suggested a common

structure in which metal is coordinated to the phosphate group of the ligand frame.

CONCLUSION

The interactions between molecules constituting the headgroups of biological lipid membranes, such as **PEA** and **PCC** with metal cations present in biological fluids, are key factors as they can modify physicochemical properties, structure, and cell functioning. Any modification in membrane composition may significantly affect its physicochemical properties, structure, and cell function. As an example, modification in membrane composition in nerve cells is characteristic of neurodegenerative diseases. Therefore, the elucidation of the acid-base behavior of **PEA** and **PPC** and their complexing capacities toward cations of physiological relevance can assume crucial importance. As an example, the zwitterionic nature of the phosphorylcholine group in **PPC**-based biomaterials, employed in many clinical applications, can also be changed with the introduction of a metal cation. In particular, the coordination mode of **PPC** with metal cations contributes to understand the potential activity of the biomaterials. For all these reasons, a multidisciplinary study was undertaken to elucidate the interaction between **PEA** and **PPC** with Mg^{2+} , one of the main bioelements. The study described here offers useful information necessary for the interpretation of the nature of the metal-ligand interaction. Thanks to the assessment of reliable thermodynamic data, it was possible to calculate the sequestering ability of the ligands under study toward Mg^{2+} and also to make simulations under the conditions of biological fluids. For example, the results of simulations carried out under conditions of the extracellular fluid in the brain intracellular space showed that **MgPCC** achieves a non-negligible percentage of formation. MALDI-MS and MS/MS were employed for the characterization of the free **PPC** and **PEA** ligands and of their interactions with Mg^{2+} , both never investigated until now. The observed fragmentation pathways of both Mg^{2+} -L systems suggested a common interaction mechanism in which the metal is

coordinated to the phosphate group of the ligand frame, giving rise to a four-membered cycle.

DATA AVAILABILITY STATEMENT

The original contributions presented in the study are included in the article/**Supplementary Material**, further inquiries can be directed to the corresponding author.

AUTHOR CONTRIBUTIONS

OG planned the experiments, supervised, and organized the analysis, performed speciation calculations and simulations, and wrote the manuscript. CF contributed to conception, design of the study, analysis of the results, and manuscript revision. MC performed the ^1H NMR experiments and the qualitative analysis of the spectra and contributed to the ^1H NMR discussion. DA contributed to the experimental design of the study. DA and AN performed MALDI MS and MS/MS experiments and wrote mass spectrometry discussion. All authors contributed to manuscript revision, read, and approved the submitted version.

FUNDING

The authors OG and CF thank the University of Messina for FFABR 2020 funds.

SUPPLEMENTARY MATERIAL

The Supplementary Material for this article can be found online at: <https://www.frontiersin.org/articles/10.3389/fchem.2022.864648/full#supplementary-material>

REFERENCES

- Aiello, D., Cardiano, P., Cigala, R. M., Gans, P., Giacobello, F., Giuffrè, O., et al. (2017). Sequestering Ability of Oligophosphate Ligands toward Al^{3+} in Aqueous Solution. *J. Chem. Eng. Data* 62, 3981–3990. doi:10.1021/acs.jced.7b00685
- Aiello, D., Carnamucio, F., Cordaro, M., Foti, C., Napoli, A., and Giuffrè, O. (2021a). Ca^{2+} Complexation with Relevant Bioligands in Aqueous Solution: A Speciation Study with Implications for Biological Fluids. *Front. Chem.* 9, 640219. doi:10.3389/fchem.2021.640219
- Aiello, D., Giambona, A., Leto, F., Passarello, C., Damiani, G., Maggio, A., et al. (2018). Human Coelomic Fluid Investigation: a MS-based Analytical Approach to Prenatal Screening. *Sci. Rep.* 8, 10973. doi:10.1038/s41598-018-29384-9
- Aiello, D., Lucà, F., Siciliano, C., Frati, P., Fineschi, V., Rongo, R., et al. (2021b). Analytical Strategy for MS-Based Thanatochemistry to Estimate Postmortem Interval. *J. Proteome Res.* 20, 2607–2617. doi:10.1021/acs.jproteome.0c01038
- Aiello, D., Siciliano, C., Mazzotti, F., Di Donna, L., Athanassopoulos, C. M., and Napoli, A. (2020). A Rapid MALDI MS/MS Based Method for Assessing Saffron (*Crocus Sativus* L.) Adulteration. *Food Chem.* 307, 125527. doi:10.1016/j.foodchem.2019.125527
- Alderighi, L., Gans, P., Ienco, A., Peters, D., Sabatini, A., and Vacca, A. (1999). Hyperquad Simulation and Speciation (HySS): a Utility Program for the Investigation of Equilibria Involving Soluble and Partially Soluble Species. *Coord. Chem. Rev.* 184, 311–318. doi:10.1016/s0010-8545(98)00260-4
- Artru, A. A. (2010). “Cerebrospinal Fluid,” in *Cottrell's Neuroanesthesia*. Editors J. E. Cottrell and W. L. Young (San Francisco, CA: Mosby). doi:10.1016/b978-0-323-05908-4.10008-9
- Barrett, H. B. K., Boitano, S., and Barman, S. (2013). *Ganongs Review of Medical Physiology*. New York: McGraw-Hill Education.
- Cardiano, P., Cucinotta, D., Foti, C., Giuffrè, O., and Sammartano, S. (2011a). Potentiometric, Calorimetric and ^1H -NMR Investigation on Hg^{2+} -Mercaptocarboxylate Interaction in Aqueous Solution. *J. Chem. Eng. Data* 56, 1995–2004. doi:10.1021/je101007n
- Cardiano, P., De Stefano, C., Foti, C., Giacobello, F., Giuffrè, O., and Sammartano, S. (2018a). Sequestration of HEDPA, NTA and Phosphonic NTA Derivatives towards Al^{3+} in Aqueous Solution. *J. Mol. Liq.* 261, 96–106. doi:10.1016/j.molliq.2018.04.003
- Cardiano, P., Falcone, G., Foti, C., Giuffrè, O., and Sammartano, S. (2011b). Methylmercury(II)-sulphur Containing Ligand Interactions: a Potentiometric, Calorimetric and ^1H -NMR Study in Aqueous Solution. *New J. Chem.* 35, 800–806. doi:10.1039/c0nj00768d

- Cardiano, P., Foti, C., Giacobello, F., Giuffrè, O., and Sammartano, S. (2018b). Study of Al^{3+} Interaction with AMP, ADP and ATP in Aqueous Solution. *Biophys. Chem.* 234, 42–50. doi:10.1016/j.bpc.2018.01.003
- Cardiano, P., Giacobello, F., Giuffrè, O., and Sammartano, S. (2017). Thermodynamic and Spectroscopic Study on Al^{3+} -Polycarboxylate Interaction in Aqueous Solution. *J. Mol. Liq.* 232, 45–54. doi:10.1016/j.molliq.2017.02.047
- Chillè, D., Aiello, D., Grasso, G. I., Giuffrè, O., Napoli, A., Sgarlata, C., et al. (2020). Complexation of As(III) by Phosphonate Ligands in Aqueous Fluids: Thermodynamic Behavior, Chemical Binding Forms and Sequestering Abilities. *J. Environ. Sci. (China)* 94, 100–110. doi:10.1016/j.jes.2020.03.056
- Chillè, D., Foti, C., and Giuffrè, O. (2018). Thermodynamic Parameters for the Protonation and the Interaction of Arsenate with Mg^{2+} , Ca^{2+} and Sr^{2+} : Application to Natural Waters. *Chemosphere* 190, 72–79. doi:10.1016/j.chemosphere.2017.09.115
- Cordaro, M., Foti, C., Giacobello, F., Giuffrè, O., and Sammartano, S. (2019). Phosphonic Derivatives of Nitrilotriacetic Acid as Sequestering Agents for Ca^{2+} in Aqueous Solution: A Speciation Study for Application in Natural Waters. *ACS Earth Space Chem.* 3, 1942–1954. doi:10.1021/acsearthspacechem.9b00183
- Dai, L. J., Ritchie, G., Kerstan, D., Kang, H. S., Cole, D. E., and Quamme, G. A. (2001). Magnesium Transport in the Renal Distal Convoluted Tubule. *Physiol. Rev.* 81, 51–84. doi:10.1152/physrev.2001.81.1.51
- Datta, S. P., and Grzybowski, A. K. (1959). The Stability Constants of the Silver Complexes of Some Aliphatic Amines and Amino-Acids. *J. Chem. Soc.*, 1091–1095. doi:10.1039/jr9590001091
- De Stefano, C., Sammartano, S., Mineo, P., and Rigano, C. (1997). “Computer Tools for the Speciation of Natural Fluids,” in *Marine Chemistry - an Environmental Analytical Chemistry Approach*. Editors A. Gianguzza, E. Pelizzetti, and S. Sammartano (Amsterdam: Kluwer Academic Publishers), 71–83.
- Deutsche Gesellschaft für Ernährung (2000). *Referenzwerte Für die Nährstoffzufuhr D-A-CH*. Frankfurt: Deutsche Gesellschaft für Ernährung.
- Díaz-Betancor, Z., Bañuls, M.-J., Sanza, F. J., Casquel, R., Laguna, M. F., Holgado, M., et al. (2019). Phosphorylcholine-based Hydrogel for Immobilization of Biomolecules. Application to Fluorometric Microarrays for Use in Hybridization Assays and Immunoassays, and Nanophotonic Biosensing. *Microchimica Acta* 186, 570. doi:10.1007/s00604-019-3691-3
- Eaton, D. C., and Pooler, J. P. (2009). *Vanders's Renal Physiology*. New York: Mc Graw Hill Medical.
- Elin, R. J. (1994). Magnesium: the Fifth but Forgotten Electrolyte. *Am. J. Clin. Pathol.* 102, 616–622. doi:10.1093/ajcp/102.5.616
- Falcone, G., Foti, C., Gianguzza, A., Giuffrè, O., Napoli, A., Pettignano, A., et al. (2013). Sequestering Ability of Some Chelating Agents towards Methylmercury(II). *Anal. Bioanal. Chem.* 405, 881–893. doi:10.1007/s00216-012-6336-5
- Fernandez-Botello, A., Gomez-Coca, R. B., Holy, A., Moreno, V., and Sigel, H. (2002). Metal-ion Binding Properties of O-Phosphonomethylcholine (PMCh⁻). Effect of the Positive Charge of a Distant Trimethylammonium Group on the Coordinating Qualities of a Phosph(on)ate Group. *Inorg. Chim. Acta* 331, 109–116. doi:10.1016/s0020-1693(01)00763-0
- Filella, M., and May, P. M. (2005). Reflections on the Calculation and Publication of Potentiometrically-Determined Formation Constants. *Talanta* 65, 1221–1225. doi:10.1016/j.talanta.2004.08.046
- Flatmann, P. W. (1993). “The Role of Magnesium in Regulating Ion Transport,” in *Magnesium and the Cell*. Editor N. J. Birch (New York: Academic Press).
- Flink, E. B. (1956). Magnesium Deficiency in Man. *J. Am. Med. Assoc.* 160, 1406–1409.
- Frassinetti, C., Ghelli, S., Gans, P., Sabatini, A., Moruzzi, M. S., and Vacca, A. (1995). Nuclear Magnetic Resonance as a Tool for Determining Protonation Constants of Natural Polyprotic Bases in Solution. *Anal. Biochem.* 231, 374–382. doi:10.1006/abio.1995.9984
- Frausto da Silva, J. J. R., and Williams, R. J. P. (2001). “The Biological Chemistry of Magnesium: Phosphate Metabolism,” in *The Biological Chemistry of the Elements: The Inorganic Chemistry of Life*. Oxford University Press, 251–277.
- Fukuma, T., Higgins, M. J., and Jarvis, S. P. (2007). Direct Imaging of Lipid-Ion Network Formation under Physiological Conditions by Frequency Modulation Atomic Force Microscopy. *Phys. Rev. Lett.* 98, 106101. doi:10.1103/physrevlett.98.106101
- Gabryel-Skrodzka, M., Nowak, M., Stachowiak, K., Zabiszak, M., Ogawa, K., and Jastrzab, R. (2021). The Influence of pH on Complexation Process of Copper(II) Phosphoethanolamine to Pyrimidine Nucleosides. *Materials* 14, 4309. doi:10.3390/ma14154309
- Gennis, R. B. (1989). *Biomembranes: Molecular Structure and Function*. New York, NY: Springer-Verlag.
- Giuffrè, O., Aiello, D., Chillè, D., Napoli, A., and Foti, C. (2020). Binding Ability of Arsenate towards Cu^{2+} and Zn^{2+} : Thermodynamic Behavior and Simulation under Natural Water Conditions. *Environ. Sci. Process. Impacts* 22, 1731–1742. doi:10.1039/d0em00136h
- Goda, T., and Miyahara, Y. (2018). Specific Binding of Human C-Reactive Protein towards Supported Monolayers of Binary and Engineered Phospholipids. *Colloids Surf. B* 161, 662–669. doi:10.1016/j.colsurf.2017.11.036
- Heaton, F. W. (1993). “Distribution and Function of Magnesium within the Cell,” in *Magnesium and the Cell*. Editor N. J. Birch (London: Academic Press), 121–136.
- Heinemann, U., Angamo, E. A., and Liotta, A. (2009). “Non-synaptic Mechanisms: Modulation of Neuronal Excitability by Changes in Extracellular Ion Composition,” in *Encyclopedia of Basic Epilepsy Research*. Editor U. Heinemann (New York: Academic Press), 958–964. doi:10.1016/b978-012373961-2.00317-9
- Hendrickson, H. S., and Fullington, J. G. (1965). Stabilities of Metal Complexes of Phospholipids: Ca(II), Mg(II), and Ni(II) Complexes of Phosphatidylserine and Triphosphoinositide. *Biochemistry* 4, 1599–1605. doi:10.1021/bi00884a021
- Imbrogno, S., Aiello, D., Filice, M., Leo, S., Mazza, R., Cerra, M. C., et al. (2019). MS-based Proteomic Analysis of Cardiac Response to Hypoxia in the Goldfish (*Carassius auratus*). *Sci. Rep.* 9, 18953. doi:10.1038/s41598-019-55497-w
- Kennelly, J. P., van der Veen, J. N., Nelson, R. C., Leonard, K. A., Havinga, R., Buteau, J., et al. (2018). Intestinal De Novo Phosphatidylcholine Synthesis Is Required for Dietary Lipid Absorption and Metabolic Homeostasis. *J. Lipid Res.* 59, 1695–1708. doi:10.1194/jlr.m087056
- Klein, J., Gonzalez, R., Köppen, A., and Löffelholz, K. (1993). Free Choline and Choline Metabolites in Rat Brain and Body Fluids: Sensitive Determination and Implications for Choline Supply to the Brain. *Neurochem. Int* 22, 293–300. doi:10.1016/0197-0186(93)90058-d
- Martell, A. E., Smith, R. M., and Motekaitis, R. J. (2004). *Critically Selected Stability Constants of Metal Complexes*. Garthursburg, MD: National Institute of Standard Technology.
- Matsuura, R., Tawa, K., Kitayama, Y., and Takeuchi, T. (2016). A Plasmonic Chip-Based Bio/Chemical Hybrid Sensing System for the Highly Sensitive Detection of C-Reactive Protein. *Chem. Commun.* 52, 3883–3886. doi:10.1039/c5cc07868g
- May, P. M., and Murray, K. (2001). Database of Chemical Reactions Designed to Achieve Thermodynamic Consistency Automatically. *J. Chem. Eng. Data* 46, 1035–1040. doi:10.1021/jc000246j
- Mohan, M., and Abbott, E. (1978a). Metal Complexes of Amino Acid Phosphate Esters. *Inorg. Chem.* 17, 2203–2207. doi:10.1021/ic50186a036
- Mohan, M., and Abbott, E. (1978b). Metal Complexes of Biologically Occurring Aminophosphonic Acids. *J. Coord. Chem.* 8, 175–182. doi:10.1080/00958977808073092
- Nies, D. H. (2004). “Essential and Toxic Effects of Elements on Microorganisms,” in *Elements and Their Compounds in the Environment*. Editors E. Merian, M. Anke, M. Ihnat, and M. Stoeppeler (Weinheim, Germany: Wiley-WCH), 257–276.
- Numata, M., Chu, H. W., Dakhama, A., and Voelker, D. R. (2010). Pulmonary Surfactant Phosphatidylglycerol Inhibits Respiratory Syncytial Virus-Induced Inflammation and Infection. *Proc. Natl. Acad. Sci. USA* 107, 320–325. doi:10.1073/pnas.0909361107
- Numata, M., Kandasamy, P., Nagashima, Y., Fickes, R., Murphy, R. C., and Voelker, D. R. (2015). Phosphatidylinositol Inhibits Respiratory Syncytial Virus Infection. *J. Lipid Res.* 56, 578–587. doi:10.1194/jlr.m055723
- Osterberg, R. (1960). The Copper(II) Complexity of O-Phosphorylethanolamine. *Acta Chem. Scand.* 14, 471–485. doi:10.3891/acta.chem.scand.14-0471
- Pettit, L. D., and Powell, K. J. (2001). *IUPAC Stability Constants Database*. Otley, United Kingdom: IUPAC. Academic Software.

- Quamme, G. A., and de Rouffignac, G. (2000). Epithelial Magnesium Transport and Regulation by the Kidney. *Front. Biosci.* 5, D694–D711. doi:10.2741/quamme
- Salvatore, L., Gallo, N., Aiello, D., Lunetti, P., Barca, A., Blasi, L., et al. (2020). An Insight on Type I Collagen from Horse Tendon for the Manufacture of Implantable Devices. *Int. J. Biol. Macromol.* 154, 291–306. doi:10.1016/j.ijbiomac.2020.03.082
- Saris, N. E., Mervaala, E., Karppanen, H., Khawaja, J. A., and Lewensham, A. (2000). Magnesium. An Update on Physiological, Clinical and Analytical Aspects. *Clin. Chim. Acta* 294, 1–26. doi:10.1016/s0009-8981(99)00258-2
- Šegota, S., Vojta, D., Pletikapic, G., and Baranovic, G. (2015). Ionic Strength and Composition Govern the Elasticity of Biological Membranes. A Study of Model DMPC Bilayers by Force- and Transmission IR Spectroscopy. *Chem. Phys. Lipids* 2015, 17–29. doi:10.1016/j.chemphyslip.2014.11.001
- Shils, M. A. (1997). “Magnesium,” in *Handbook of Nutritionally Essential mineral Elements*. Editors B. J. O'Dell and R. Sunde (New York-Basel-Hong Kong: Marcel Dekker), 117–152.
- Takeda, H., Takahashi, M., Hara, T., Izumi, Y., and Bamba, T. (2019). Improved Quantitation of Lipid Classes Using Supercritical Fluid Chromatography with a Charged Aerosol Detector. *J. Lipid Res.* 60, 1365–1474. doi:10.1194/jlr.D094516
- The international standard for identifying health measurements (2006). *Phosphoethanolamine [Moles/volume] in Amniotic Fluid*. Indianapolis: Regenstrief Institute Inc., LOINC 27278–27271.
- The National Academies (1997). *Dietary Reference Intakes for Calcium, Phosphorus, Magnesium, Vitamine D, and Fluoride*. Washington D.C.: National Academies Press, 190–249. Institute of Medicine.
- Vormann, J. (2004). “Magnesium,” in *Elements and Their Compounds in the Environment*. Editors E. Merian, M. Anke, M. Ihnat, and M. Stoeppeler (Weinheim, Germany: Wiley-WCH), 587–596. doi:10.1002/9783527619634.ch23g
- Walter, A., Korth, U., Hilgert, M., Hartmann, J., Weichel, O., Hilgert, M., et al. (2004). Glycerophosphocholine Is Elevated in Cerebrospinal Fluid of Alzheimer Patients. *Neurobiol. Aging* 25, 1299–1303. doi:10.1016/j.neurobiolaging.2004.02.016
- Weber-Fahr, W., Englisch, S., Esser, A., Tunc-Skarka, N., Meyer-Lindenberg, A., Ende, G., et al. (2013). Altered Phospholipid Metabolism in Schizophrenia: A Phosphorus Nuclear Magnetic Resonance Spectroscopy Study. *Psychiatry Res. Neuroimaging* 214, 365–373. doi:10.1016/j.pscychres.2013.06.011
- Weisinger, J. R., and Bellorin-Font, E. (1998). Magnesium and Phosphorus. *Lancet* 352, 391–396. doi:10.1016/s0140-6736(97)10535-9
- Woolf, T. B., and Roux, B. J. (1994). Conformational Flexibility of O-Phosphorylcholine and O-Phosphorylethanolamine: A Molecular Dynamics Study of Solvation Effects. *Am. Chem. Soc.* 116, 5916–5920. doi:10.1021/ja00092a048
- Wozniak, M., and Nowogrocki, G. (1979). Acidites et complexes des acides (alkyl-et aminoalkyl-) phosphoniques-IV Acides aminoalkylphosphoniques $R_1R_2N(CH_2)_nCR_3R_4PO_3H_2$. *Talanta* 26, 1135–1141. doi:10.1016/0039-9140(79)80029-6
- Wu, J.-G., Wei, S.-C., Chen, Y., Chen, J.-H., and Luo, S.-C. (2018). Critical Study of the Recognition between C-Reactive Protein and Surface-Immobilized Phosphorylcholine by Quartz Engineering. *Mol. Biol. Rep.* 45, 2857–2867.

Conflict of Interest: The authors declare that the research was conducted in the absence of any commercial or financial relationships that could be construed as a potential conflict of interest.

Publisher's Note: All claims expressed in this article are solely those of the authors and do not necessarily represent those of their affiliated organizations, or those of the publisher, the editors, and the reviewers. Any product that may be evaluated in this article, or claim that may be made by its manufacturer, is not guaranteed or endorsed by the publisher.

Copyright © 2022 Aiello, Cordaro, Napoli, Foti and Giuffrè. This is an open-access article distributed under the terms of the Creative Commons Attribution License (CC BY). The use, distribution or reproduction in other forums is permitted, provided the original author(s) and the copyright owner(s) are credited and that the original publication in this journal is cited, in accordance with accepted academic practice. No use, distribution or reproduction is permitted which does not comply with these terms.



Comprehending Cardiac Dysfunction by Oxidative Stress: Untargeted Metabolomics of *In Vitro* Samples

Alan Gonçalves Amaral¹, Isabela Aparecida Moretto², Flávia da Silva Zandonadi³, Hans Rolando Zamora-Obando¹, Isabela Rocha¹, Alessandra Sussulini^{3,4}, André Alexandre de Thomaz⁵, Regina Vincenzi Oliveira⁶, Aline Mara dos Santos^{2*} and Ana Valéria Colnaghi Simionato^{1,4*}

¹Laboratory of Analysis of Biomolecules Tiselius, Department of Analytical Chemistry, Institute of Chemistry, State University of Campinas, Campinas, Brazil, ²Institute of Biology, Department of Structural and Functional Biology, State University of Campinas, Campinas, Brazil, ³Laboratory of Bioanalytics and Integrated Omics, Department of Analytical Chemistry, Institute of Chemistry, State University of Campinas, Campinas, Brazil, ⁴National Institute of Science and Technology for Bioanalytics—INCTBio, Institute of Chemistry, State University of Campinas, Campinas, Brazil, ⁵Institute of Physics “Gleb Wataghin”, State University of Campinas, Campinas, Brazil, ⁶Department of Chemistry, Federal University of São Carlos, São Carlos, Brazil

OPEN ACCESS

Edited by:

Eugenia Gallardo,
Universidade da Beira Interior,
Portugal

Reviewed by:

Nishikant Wase,
University of Virginia, United States
Haiyan Tan,
St. Jude Children’s Research Hospital,
United States

*Correspondence:

Ana Valéria Colnaghi Simionato
avsimionato@unicamp.br
Aline Mara dos Santos
alinems@unicamp.br

Specialty section:

This article was submitted to
Analytical Chemistry,
a section of the journal
Frontiers in Chemistry

Received: 15 December 2021

Accepted: 09 February 2022

Published: 08 April 2022

Citation:

Amaral AG, Moretto IA,
Zandonadi FdS, Zamora-Obando HR,
Rocha I, Sussulini A, Thomaz AAd,
Oliveira RV, Santos AMd and
Simionato AVC (2022)
Comprehending Cardiac Dysfunction
by Oxidative Stress: Untargeted
Metabolomics of *In Vitro* Samples.
Front. Chem. 10:836478.
doi: 10.3389/fchem.2022.836478

Cardiovascular diseases (CVDs) are noncommunicable diseases known for their complex etiology and high mortality rate. Oxidative stress (OS), a condition in which the release of free radical exceeds endogenous antioxidant capacity, is pivotal in CVC, such as myocardial infarction, ischemia/reperfusion, and heart failure. Due to the lack of information about the implications of OS on cardiovascular conditions, several methodologies have been applied to investigate the causes and consequences, and to find new ways of diagnosis and treatment as well. In the present study, cardiac dysfunction was evaluated by analyzing cells’ alterations with untargeted metabolomics, after simulation of an oxidative stress condition using hydrogen peroxide (H₂O₂) in H9c2 myocytes. Optimizations of H₂O₂ concentration, cell exposure, and cell recovery times were performed through MTT assays. Intracellular metabolites were analyzed right after the oxidative stress (oxidative stress group) and after 48 h of cell recovery (recovery group) by ultra-high-performance liquid chromatography coupled to mass spectrometry (UHPLC-MS) in positive and negative ESI ionization mode. Significant alterations were found in pathways such as “alanine, aspartate and glutamate metabolism”, “glycolysis”, and “glutathione metabolism”, mostly with increased metabolites (upregulated). Furthermore, our results indicated that the LC-MS method is effective for studying metabolism in cardiomyocytes and generated excellent fit (R²Y > 0.987) and predictability (Q² > 0.84) values.

Keywords: metabolomics, cardiovascular diseases, oxidative stress, LC-MS, cell culture

INTRODUCTION

Cardiovascular disease (CVD) refers to any sickness that affects the cardiovascular system and can be classified as heart, cerebral vascular, kidney, or peripheral arterial diseases. Their pathology is quite diverse, containing diseases such as cardiomyopathies, aneurysms, and others (Wilson et al., 1998; Kordalewska and Markuszewski, 2015). After the Second World War, such disorders became the leading cause of death in the world due to the lack of knowledge about the factors that would

contribute to their onset, progression, and development. Nowadays, despite still being one of the main causes of death annually, studies like the Framingham Heart Study have shown that CVDs are associated with risk factors such as smoking, sedentary lifestyle, obesity, and diabetes (Wilson et al., 1998; Dórea and Lotufo, 2001; Lotufo, 2008).

The main risk factors of CVDs increase the generation of reactive oxygen species (ROS), which are normally produced by a natural process of cellular metabolism. ROS are composed of neutral species, such as hydrogen peroxide (H_2O_2) and hypochlorous acid (HClO), and radical species, such as the superoxide anion radical ($\text{O}_2^{\cdot-}$). Although some of them are not very reactive, such as H_2O_2 , they can react with other molecules or enzymes to form species and radicals with higher oxidizing strength (Hunter and Chien, 1999; Zuo et al., 2015; Panth et al., 2016; Francisco et al., 2019). When these species are in excess in the body, due to an imbalance between them and antioxidant species, damage to important biological molecules occurs, resulting in tissue lesions and DNA damage. This condition is known as oxidative stress (Hermes-Lima et al., 1991; Meneghini, 1997; Rodrigo et al., 2013).

Several studies present the critical participation of ROS in the development of CVDs, such as higher production when therapeutic drugs (like doxorubicin) are administered (Ewer and Ewer, 2010; Clayton et al., 2020). However, the possible changes in metabolism and consequent effects on cardiac tissue have not been fully elucidated due to the complexity and diversity of molecular pathways. Such information is of paramount importance to find new markers and targets when devising new forms of diagnosis and treatments (Rebouças et al., 2016; Lee and Walsh, 2017; Tenreiro et al., 2021).

Within the methodologies currently used to explore the role of ROS in biological systems, metabolomics has gained considerable space as a powerful tool for understanding organisms at the molecular level (Zang et al., 2019). The goal of metabolomics is to study changes in the metabolome, which is composed of all biomolecules in a biological system of molecular mass up to 1,500 Da containing different chemical functions and variable concentration ranges found in a biological system (Fiehn, 2001; Barbosa et al., 2012; Viant et al., 2017). Several analytical platforms have been used for metabolomics analyses, such as gas chromatography–mass spectrometry (GC-MS) (Jonsson et al., 2004), liquid chromatography–mass spectrometry (LC-MS) (Cubbon et al., 2010), capillary electrophoresis–mass spectrometry (CE-MS) (Barbosa et al., 2013), and nuclear magnetic resonance (NMR) (Du et al., 2019), but LC-MS has been widely used for biological analysis and life science studies. Performing a metabolomics study in cellular culture (*in vitro* studies) avoids invasive techniques for obtaining biological samples. Moreover, *in vitro* systems have excellent advantages when compared with *in vivo* ones, such as the high metabolic homogeneity of the samples and its similarity to *in vivo* or *ex vivo* systems, which allows pre-test approaches to predict possible outcomes (Teng et al., 2009; Čuperlović-Culf et al., 2010; León et al., 2013).

The present study aims to perform an untargeted metabolomics investigation of differentiated cardiac cells of the

H9c2 lineage, divided into three groups: healthy cells (control group), cells after simulated oxidative stress by H_2O_2 (oxidative stress group), and cells after recovery from oxidative stress (recovery group) by LC-MS. The purpose of this work is to identify changes in metabolism between each pair of groups (oxidative stress vs. control; recovery vs. control; and recovery vs. oxidative stress). Therefore, a thorough comprehension of these systems, and evaluation of the simulated oxidative stress on the metabolism may be achieved.

MATERIALS AND METHODS

Chemicals and Materials

Ammonium formate (>99%), Dulbecco's Modified Eagle's Medium—high glucose (DMEM), sodium bicarbonate, Dulbecco's Phosphate Buffered Saline (DPBS), retinoic acid (RA), 3-[4,5-dimethyl-2-thiazolyl]-2,5-diphenyl-2-tetrazolium bromide (MTT), and 2-propanol PA 99% were acquired from Sigma Chemicals (St Louis, MO, United States). Penicillin/streptomycin antibiotic, fetal bovine serum (FBS), trypsin-EDTA, primary antibody (anti-paxillin), secondary antibody (Alexa Fluor-546-conjugated goat anti-rabbit), Alexa Fluor-647 phalloidin, and Prolong with DAPI were acquired from ThermoFisher (Waltham, MA, EUA). Hydrogen peroxide PA was acquired from Fmaia (Belo Horizonte, MG, Brazil). Hydrochloric acid 36.5%–38.0% was acquired from J.T. Baker (Mexico). Methanol and acetonitrile (HPLC grade) were acquired from Merck (Darmstadt, HE, Germany), formic acid (LC-MS grade) was acquired from Fluka (Buchs, Switzerland), and water was purified in a Milli-Q system (Millipore, São Paulo, SP, Brazil). The internal standard leucine enkephalin acetate salt was acquired from Cayman Chemical.

Cell Culture

H9c2 cell line, originally derived from ventricular myoblasts from rat embryos, was purchased from the American Type Culture Collection (ATCC). Cells were cultured in high-glucose DMEM supplemented with 3.7 g/L sodium bicarbonate, 10% FBS, and 1% penicillin/streptomycin solution at 37°C with 5% CO_2 atmosphere in a humidified incubator. Medium was changed every 2 days, and cells were trypsinized (Trypsin-EDTA) and split as soon as they reached approximately 70% confluence. Cells were counted using a Neubauer chamber to determine the appropriate seeding densities for each experiment. Experiments were performed on cells between passages 28 and 31.

Cell Differentiation

H9c2 cells were induced to cardiomyocyte differentiation through reduction of FBS content from 10 to 1% in the cell culture medium and addition of retinoic acid (RA) for 6 days. 10^6 cells were plated and, once they reached approximately 80% confluence, differentiation was initiated by changing the medium to high-glucose DMEM (same supplementation) but with 1% FBS and 10 nmol/L retinoic acid (RA), resulting in an increase in cardiac-like cells. The differentiation medium was changed every 2 days (Pereira et al., 2011; Suhaeri et al., 2015; Patten et al., 2017).

Cytotoxicity MTT Assay

In order to optimize the study parameters, two MTT assays were performed: (1) hydrogen peroxide (H_2O_2) concentration and exposure time to perform the oxidative stress; (2) cell recovery time. For the first assay, H9c2 undifferentiated cells were collected with trypsin, re-suspended, and seeded in 48-well multiplates. A total of 1.00×10^4 cells were plated per well, in triplicates, as previously described. After the differentiation protocol, cells were treated with increasing concentrations of H_2O_2 (25, 50, 75, 100, 200, 400, and $600 \mu\text{mol L}^{-1}$) and different times of exposure (1, 4, 8, 12, and 24 h) to define the optimum dose and treatment time (Kim et al., 2014; Ilavenil et al., 2015; Zhang et al., 2018; Wu et al., 2019).

After treatment, the medium was removed, each well was washed with sterile DPBS, and $250 \mu\text{L}$ of MTT (1 g/L) solution was added to the cell monolayer. After 3 h of reaction in the incubator, the solution was removed and the formazan crystals were solubilized by adding 2-propanol solution acidified with HCl (0.1 mol/L). The plate was transferred to a spectrophotometer for absorbance determination at a wavelength of 550 nm in a microplate reader (BioTek SynergyTM 2 multimode). The mean optical density (OD) of 3 wells in each group was used to calculate cell viability as follows:

$$\text{Cell Viability} = \frac{\text{OD}_{\text{treatment}} - \text{OD}_{\text{blank}}}{\text{OD}_{\text{control}} - \text{OD}_{\text{blank}}}$$

Addition of $500 \mu\text{mol L}^{-1}$ of H_2O_2 and 24 h of treatment were chosen for the next experiments.

For the second assay, a cell recovery test over 24 and 48 h was performed by replacing the culture medium containing H_2O_2 by a control one. Forty-eight hours of recovery was selected for this study.

Morphological Assessment

Undifferentiated H9c2 cells exhibit a fusiform morphology, i.e., elongated, with the ends narrower than the center, and mononucleated (Kimes and Brandt, 1976). After the differentiation process, their morphology becomes long with fine branching cardiomyocytes, and multinucleate. To follow the morphological change, an inverted microscope was used before differentiation and on days 2, 4, and 6 of differentiation. Changes after exposure to hydrogen peroxide were also captured after 24 h of oxidative stress, as well as at 24 and 48 h of recovery after oxidative stress (Pereira et al., 2011).

Immunofluorescence Staining and Microscopy Analysis

H9c2 cells were fixed with 4% paraformaldehyde, blocked, and permeabilized with 3% bovine serum albumin and 0.1% Triton-X in 0.1 mol L^{-1} DPBS on ice. Then, cells were incubated with anti-paxillin (1:200) or with anti- γH2AX (1:200) primary antibodies for 30 min at room temperature. Next, cells were labeled with Alexa Fluor-546-conjugated goat anti-rabbit (1:2,000) secondary antibody, and Alexa Fluor-647 phalloidin for 30 min at room temperature. Slides were then mounted with Prolong with 4',6-diamidino-2-phenylindole

TABLE 1 | Elution gradient of the chromatographic methods. B: Acetonitrile + 0.1% formic acid.

RPLC-MS (ESI+) and (ESI-)		HILIC-MS (ESI+) and (ESI-)	
Time (min)	B (%)	Time (min)	B (%)
0	1	0	99
3	2	3	98
10	20	10	70
15	60	15	40
18	85	18	15
20	90	20	10
25	95	20,1	1
30	95	22	1
31	99	22,1	99
33	99	25	99
33,1	1		
35	1		

(DAPI). Fluorescence images were acquired on a Zeiss Elyra PS.1 microscope. “Panoramic” images were examined by an EC Plan-Neofluar 10x/0.30 objective in the laser WideField mode. “Zoomed in” images were collected by a Plan-Apochromat 63x/1.4 Oil DIC objective in the 3D-SIM mode. 3D-SIM z stacks were projected on a single plane with summed intensities using the ImageJ-FIJI software.

Sample Preparation

Samples were divided into three groups: 3 samples of healthy cells (control group), 3 samples of cells that underwent oxidative stress with $500 \mu\text{mol L}^{-1}$ H_2O_2 for 24 h (oxidative stress group), and 3 samples of cells that recovered during 48 h from oxidative stress (recovery group). For cell metabolomics, the cardiomyoblasts were lightly scraped with a rubber cell scraper, and suspended in $800 \mu\text{L}$ of ice-cold methanol (MeOH) extraction solvent. Samples were subjected to three freeze-thaw cycles for complete cell disruption. For this purpose, samples were placed in liquid nitrogen for 10 min for rapid freezing and thawed in an ice bath for 10 min. The supernatant was recovered by centrifugation at $5,725 \times g$ for 5 min at 4°C ; the cell pellet was extracted once with $400 \mu\text{L}$ of MeOH and combined with the previous supernatant. Samples were stored at -80°C until analysis. For quality control samples (QCs), $200 \mu\text{L}$ from each of the samples was aliquoted, pooled, and separated into equal volumes (Dettmer et al., 2011; Mastrangelo et al., 2016).

LC-MS Analysis

RPLC-MS and HILIC-MS analysis were conducted on an Agilent UHPLC system (model 1,260 Infinity II, Agilent Technologies, California, EUA). Separations were performed on an Ascentis Express C18 column ($2.7 \mu\text{m}$, $150 \text{ mm} \times 2.1 \text{ mm}$, Supelco Inc., Missouri, EUA) for RPLC, an Atlantis Silica column ($1.7 \mu\text{m}$, $100 \text{ mm} \times 2.1 \text{ mm}$, Waters, Massachusetts, EUA) for HILIC in positive ionization mode, and an ACQUITY BEH Amide column ($1.7 \mu\text{m}$, $100 \text{ mm} \times 2.1 \text{ mm}$, Waters, Massachusetts, EUA) for HILIC in negative ionization mode, both kept at 15°C during analyses. For RPLC in both ionization modes and HILIC in negative ionization mode, the mobile phase was composed of the following: A—water + 0.1% formic acid, and B—acetonitrile +

0.1% formic acid. For HILIC in positive ionization mode, the mobile phase was composed of the following: A—ammonium formate 100 mmol/L, and B—acetonitrile + 0.1% formic acid. Injection volumes of 2.0 μ l and a flow rate of 400 μ L/min were used. The gradients applied in the two separation modes are shown in **Table 1**.

Mass spectra were acquired using an Impact HD QTOF™ (Bruker Daltonics, Bremen, Germany) mass spectrometer with ESI ionization. The MS was operated in positive and negative ESI modes. The following parameters were used to register mass spectra: capillary voltage: 3600 V; end plate offset: 450 V; nebulizer gas: 4.0 bar; drying gas flow rate: 8.0 L/min; drying gas temperature: 180°C; collision cell energy: 5.0 eV; MS range (full scan): 50.0–1,300.0 Da.

In addition, 3 μ g/ml leucine enkephalin acetate salt ($C_{28}H_{37}N_5O_7$) was used as internal standard for RPLC and HILIC, presenting exact mass of 556.2765 Da ($[M + H]^+$) in positive ionization mode, and 554.2609 Da ($[M-H]^-$) in negative ionization mode. The mass spectrometer was programmed to perform data acquisition in data-dependent acquisition (DDA) mode.

Data Processing

Raw data files were calibrated automatically by application of DataAnalysis 4.2 (Bruker Daltonics, Bremen, Germany). The mzXML files were pre-processed by application of MZmine 2.53 (Pluskal et al., 2010), and the parameters present in **Supplementary Table S1** have been applied for MS and MS/MS scans.

Statistical Analysis

The resulting data matrix has been exported as a .csv file. Features with at least 30% of RSD of the QCs, peak detection ratio less than 70%, and/or at least 5% of blank contribution were removed. Further data pre-processing was performed with MetaboAnalyst 5.0 (Pang et al., 2021), using Log transformation and auto scaling normalization for RPLC-ESI(+)-MS, RPLC-ESI(-)-MS, and HILIC-ESI(+)-MS, while auto scaling was used on HILIC-ESI(-)-MS. Multivariate analyses (PCA and PLS-DA) were applied to check trends, VIP scores indicated significant features for group separation, while unpaired *t*-test with false discovery rate (FDR) showed which of the features were statistically significant. From the PLS-DA model, a cross-validation was performed to evaluate the R^2Y (goodness of fit) and Q^2 (goodness of prediction) values, and a permutation test was carried out (2000 permutations).

Metabolite Annotation and Pathway Analysis

Statistically significant metabolites, i.e., $FDR < 0.05$, p value < 0.05 and VIP score > 1.0 , were searched in the CEU Mass Mediator (Gil-de-la-Fuente et al., 2019) tool in order to perform a tentative identification using their m/z values from MS1 spectra. Kyoto Encyclopedia of Genes and Genome (KEGG) (Kanehisa et al., 2019), Human Metabolome Database (HMDB) (Wishart et al., 2018), LipidMaps (www.lipidmaps.org), and PubChem (Kim

et al., 2021) public databases were used for identification with a maximum error of 10 ppm. For the possible adducts, $[M + H]^+$, $[M + Na]^+$, $[M + K]^+$, $[M + NH_4]^+$, $[2M + H]^+$, $[M + 2H]^{2+}$, $[M + 2Na]^{2+}$, $[M + 2K]^{2+}$, $[M + H + Na]^{2+}$, $[M + H + K]^{2+}$, $[M + H + NH_4]^{2+}$, $[M + 2Na-H]^+$, $[M + 2K-H]^+$, $[M + H-H_2O]^+$, and $[M + H-2H_2O]^+$ were considered for positively charged adducts, while $[M-H]^-$, $[M + Cl]^-$, $[M-H-H_2O]^-$, $[2M-H]^-$, $[M-2H]^{2-}$, $[M + Na-2H]^-$, $[M + K-2H]^-$, and $[M + FA-H]^-$ were considered for negatively charged ones. In an attempt to validate the annotated features using the MS² spectra acquired by DDA, a comparison was performed with literature MS² spectra available in the PubChem chemical information library (Kim et al., 2021). MetaboAnalyst 5.0 Pathway Analysis tool provided the impact on metabolic pathways, and the possible connections of these changes with oxidative stress-related CVDs.

RESULTS

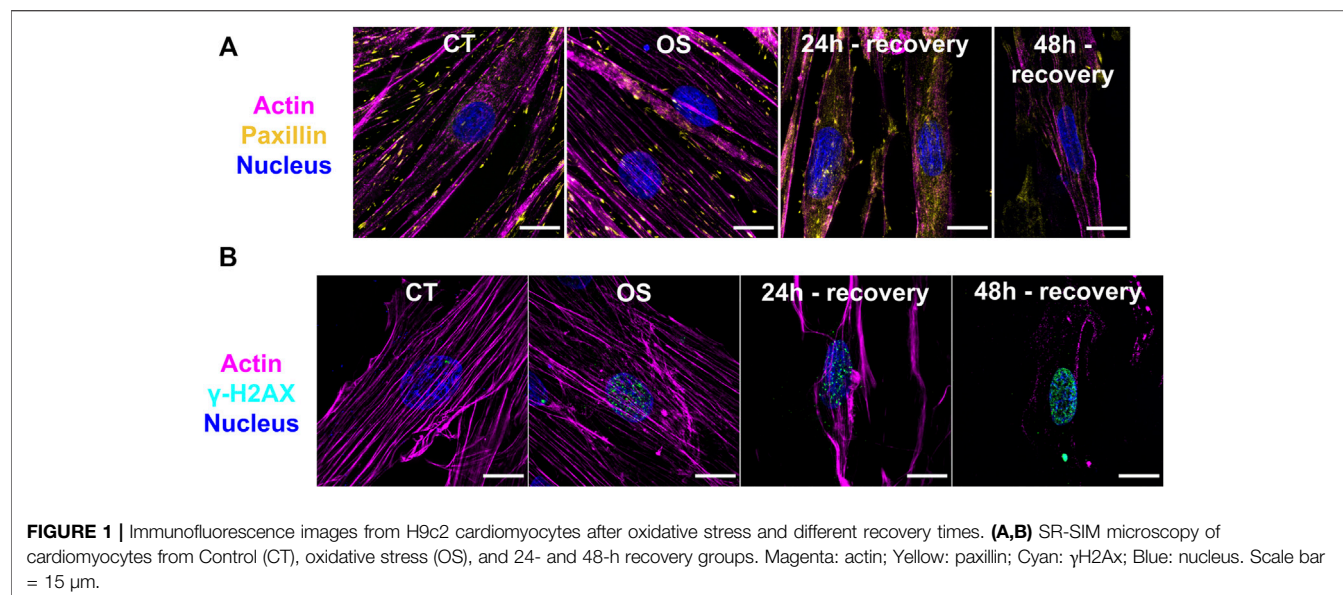
Cytotoxicity MTT Assay

In order to obtain information regarding cell viability against H_2O_2 treatment, MTT assays were performed. Our data showed a general decrease in cell viability with the increment of H_2O_2 concentration after 12 and 24 h of exposure (**Supplementary Figure S1A**), although 4 and 8 h resulted in an increase in cell viability that reached higher values than the control samples. Myocytes exposed to H_2O_2 for 24 h presented a gradual reduction in cell viability, reaching approximately 50% when treated with 400 and 600 μ mol/L of H_2O_2 . Thus, 24 h was chosen as the optimal time of cell exposure for the proposed experimental design. Since cell viability was similar for 400 and 600 μ mol/L of H_2O_2 , according to standard deviations (0.544 ± 0.015 for the former, and 0.471 ± 0.059 for the latter), 500 μ mol/L intermediate value was used in the present study.

The recovery time assay showed that after 24 h of recovery, there was 80% reduction in the cardiomyocyte viability. A possible reactivation of cell proliferation was also noted after 48 h recovery time, since the viability value reached the same value of the control (**Supplementary Figure S1B**).

Morphological Assessment and Immunofluorescence Staining

The differentiated cardiomyocytes were morphologically elongated and multinucleated, while the undifferentiated cells showed a polygonal shape (**Supplementary Figure S2A**). Morphological damages were observed in the oxidative stress group and in cells after recovery for 24 and 48 h (**Supplementary Figure S2B**). Triple-labeled fluorescence super-resolution microscopy showed control cells with an extensive cytoplasm, preserved actin filaments, and focal adhesions sites (**Figure 1A**, **Supplementary Figure S3**). Few DNA damage sites were confirmed in control cells by the low number of γ H2AX foci (**Figure 1B**). Cells submitted to oxidative stress showed a similar morphology; however, a substantial increase of DNA damage sites were observed, as expected (**Figure 1B**). On the other hand, myocytes recovered for 24 h presented cytoplasm retraction and



disassembly of the cytoskeleton accompanied by large DNA damage increase. Cells recovered for 48 h of oxidative stress had a smaller number of focal adhesions, cytoplasm retraction, paxillin accumulation on the cytosol, and extensive DNA damage (**Figures 1A,B**). Paxillin was also accumulated on distinct points of the extracellular matrix, probably coming from cell debris. These findings indicate that the generation of ROS had a negative effect in the H9c2 cardiomyocyte architecture and metabolism.

LC-MS Analysis

The analysis of the intracellular metabolome was performed after completion of the cell growth and stress stages. The data were processed by MZmine software version 2.53 resulting in 704 (RPLC-ESI(+)-MS), 327 (RPLC-ESI(-)-MS), 427 (HILIC-ESI(+)-MS), and 811 (HILIC-ESI(-)-MS) molecular features. After data filtering with RSDs of QC samples and blank contribution, 101 (RPLC-ESI(+)-MS), 85 (RPLC-ESI(-)-MS), 198 (HILIC-ESI(+)-MS), and 430 (HILIC-ESI(-)-MS) features remained. Principal component analysis (PCA) was used to check data integrity (**Figure 2A**), showing a good pattern of grouping among the samples and clustered QCs, which indicates the instrumental variation was lower than the biological one.

PLS-DA models were also built without the QC samples to maximize the discrimination between groups since it is a supervised method (**Figure 2B**). Cross-validation results shows the performance parameters, R^2Y and Q^2 (**Table 2**), indicating that the models had an excellent goodness of fit ($R^2Y \approx 1$) and a good prediction ($Q^2 > 0.84$). The statistical significance of Q^2 was evaluated by means of a permutation test using 2,000 random permutations. The p -values < 0.05 show that Q^2 is statistically significant (**Table 2**).

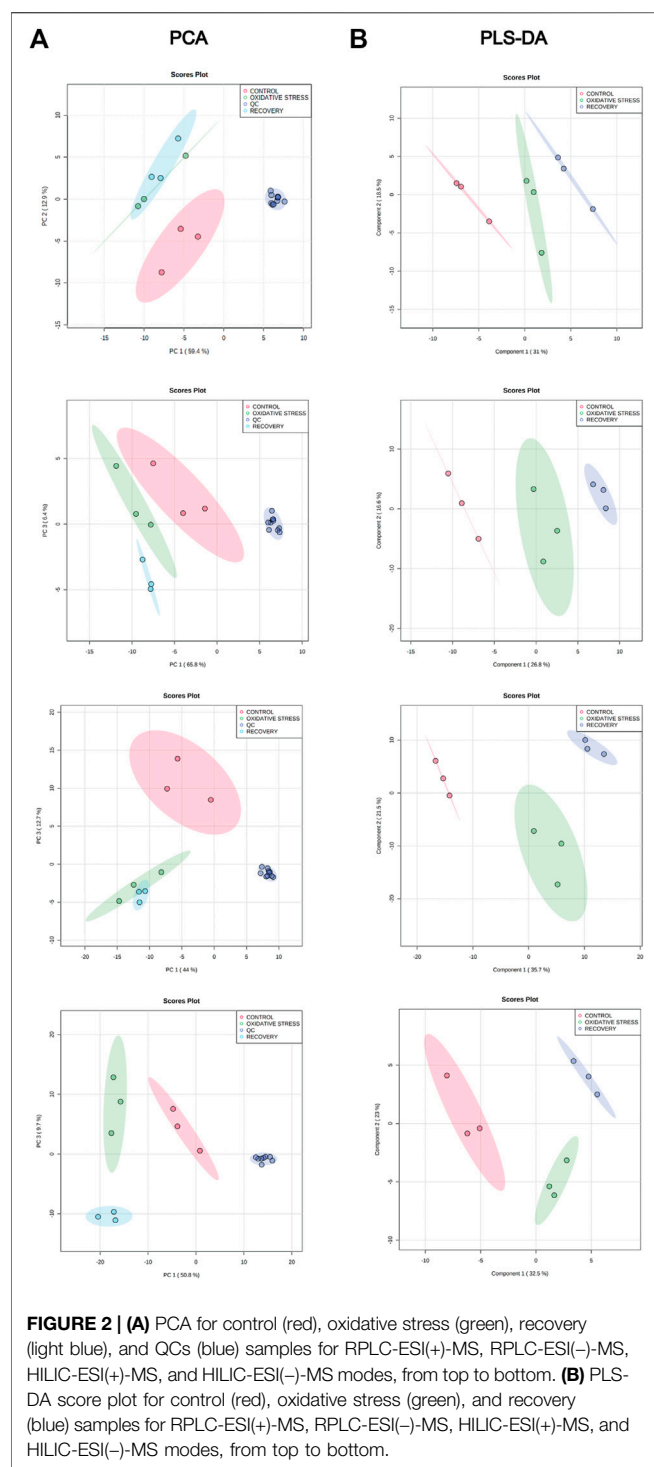
Metabolite Annotation and Pathway Analysis

To perform biological interpretation of the results obtained from LC-MS analyses, metabolite annotation was performed. Thirty-

four metabolites from the OS group were compared to the control one, while 69 metabolites from the 48-h recovery group were used for the same comparison (**Supplementary Tables S2, S3**). Twenty-three metabolites in recovery vs. OS group (**Supplementary Table S4**) were significantly altered. Pathway Analysis tool of MetaboAnalyst 5.0 revealed 7 pathways significantly altered (p value < 0.05) in OS, 12 in recovery, and 3 in recovery vs. OS (**Table 3** and **Supplementary Figure S4**). Next, the up- and downregulated metabolites of the major pathways were compared using pie charts (**Figure 3**). In the OS group, 19 metabolites were upregulated and 7 were downregulated, within the pathways “alanine, aspartate and glutamate metabolism”, “pyrimidine biosynthesis”, “arginine biosynthesis”, “arginine biosynthesis”, and “purine biosynthesis”. Moreover, only upregulated metabolites were identified in the pathways “sphingolipid metabolism”, “aminoacyl-tRNA metabolism”, and “histidine metabolism” in the cells exposed to hydrogen peroxide.

Interestingly, 35 metabolites were upregulated and 3 were downregulated after 48 h of cell recovery, with only downregulated metabolites found in “pyrimidine biosynthesis” and “aminoacyl-tRNA metabolism”. Among the upregulated metabolites, “alanine, aspartate and glutamate metabolism” stands out, with 7 altered metabolites. Furthermore, comparisons of pathways related to oxidative stress and recovery after 48-h groups, despite not indicating a large number of alterations, pointed to “glutathione metabolism”, an important pathway for intracellular antioxidant activity and for maintaining cellular homeostasis.

Metabolites of “alanine, aspartate and glutamate metabolism” were upregulated (i.e., L-Aspartate, L-Asparagine, L-Glutamate, L-Glutamine, N-Acetyl-L-aspartate, and N-Acetylglutamate) in both OS and after recovery for 48-h groups (**Figure 4A** and **Supplementary Figure S5A**). The only downregulated metabolite of this pathway was N-(L-Arginine)succinate in the OS group, being an



intermediate of the “arginine biosynthesis” and “urea cycle” (Figure 4A). Several studies on this pathway show a connection with oxidative stress due to the intracellular production of nitric oxide (NO) (Rochette et al., 2013).

A pathway identified by its significant metabolites is “anaerobic glycolysis”, represented by increased Glucose-6-phosphate, Glycerol-3-phosphate, and Lactate under all

TABLE 2 | R^2Y , Q^2 , and permutation (p) values for the evaluation of statistical significance.

	R^2Y	Q^2Y	Permutation test (p)
RPLC-ESI(+)-MS	0.9915	0.8405	$<5 \times 10^{-4}$
RPLC-ESI(-)-MS	0.9952	0.8428	$<5 \times 10^{-4}$
HILIC-ESI(+)-MS	0.9871	0.8847	0.011
HILIC-ESI(-)-MS	0.9995	0.8855	0.0335

conditions (Figure 4B and Supplementary Figure S5B). This pathway stands out for energy production in the form of ATP inside the cells, but in oxidative stress situations, species such as Lactate promote cellular defense mechanisms (Tauffenberger et al., 2019). By altering Glucose-6-phosphate and Lactate, alterations in “pentose phosphate pathway” are detected, supported by the presence of Gluconate-6-phosphate downregulated in the OS group. This pathway is directly related to “pyrimidine biosynthesis” and “purine biosynthesis” due to the formation of phosphoribosyl pyrophosphate (PRPP), an important metabolite in both pathways. Although PRPP was not altered, Uridine 5'-diphosphate (UDP), Uridine 5'-triphosphate (UTP), and Cytidine 5'-diphosphate (CDP) were downregulated, and Cytidine was upregulated in OS and recovery groups (Figure 4C and Supplementary Figure S5C).

Glutathione levels were upregulated in the control group when compared to the recovery one. On the other hand, the OS group showed a downregulation pattern when compared to the recovery one. Among other altered metabolites from “glutathione metabolism”, L-Cysteinylglycine and 5-Oxoproline were downregulated, while L-Cystathionine was upregulated in recovery vs. OS groups (Figure 4D and Supplementary Figure S5D). Additionally, other relevant metabolites showed significant changes, although they did not necessarily appear in significant pathways. Sphingosine 1-phosphate and the metabolism it participates in, “sphingolipid metabolism”, were significant in all conditions, presenting upregulated. Additionally, carnosine was upregulated in OS; taurine was slightly upregulated and adenosine 5'-monophosphate (AMP) was downregulated in the recovery group; carnitine was upregulated and All-trans-4-oxoretinoic acid was downregulated in recovery vs. OS group (Supplementary Figure S5E). Afterwards, features validation was performed by obtaining the MS^2 spectra, and the following metabolites were identified: L-Aspartate, L-Asparagine, Glycerol 3-phosphate, CDP, L-Cystathionine, Taurine, AMP, L-Carnosine, and L-Carnitine (Supplementary Figure S6–13).

DISCUSSION

Oxidative stress (OS) has shown to play an important role in the pathophysiology of CVDs. A balance between the levels of reactive oxygen species (ROS) and the antioxidant defenses is

TABLE 3 | Statistically significant metabolic pathways (p value < 0.05) altered in H9c2 cardiomyocytes upon H_2O_2 -induced oxidative stress. * p value < 0.01.

Pathways (OS vs. Control)	p value	FDR	Impact	Metabolites up	Metabolites down
Alanine, aspartate, and glutamate metabolism	$6.7111 \cdot 10^{-5}$	0.0056	0.4070	4 (21.05%)	1 (14.29%)
Pyrimidine metabolism	$3.4662 \cdot 10^{-4}$	0.0146	0.0912	2 (10.53%)	3 (42.86%)
Arginine biosynthesis	0.0014	0.0378	0.1168	2 (10.53%)	1 (14.29%)
Sphingolipid metabolism	0.0046	0.0958	0.0284	3 (15.79%)	0 (0.00%)
Aminoacyl-tRNA biosynthesis	0.0073	0.1232	0.1667	4 (21.05%)	0 (0.00%)
Purine metabolism	0.0210	0.2940	0.0230	2 (10.53%)	2 (28.57%)
Histidine metabolism	0.0281	0.3373	0.0902	2 (10.53%)	0 (0.00%)
Pathways (Recovery vs. Control)	p value	FDR	Impact	Metabolites Up	Metabolites Down
Alanine, aspartate and glutamate metabolism	$1.915 \cdot 10^{-5}$	0.0016	0.6691	7 (17.07%)	0 (0.00%)
Pyrimidine metabolism	0.0013	0.0561	0.0963	3 (7.32%)	3 (75.00%)
Cysteine and methionine metabolism	0.0037	0.0841	0.1220	5 (12.20%)	0 (0.00%)
Aminoacyl-tRNA biosynthesis	0.0040	0.0841	0.1667	5 (12.20%)	1 (25.00%)
Arginine biosynthesis	0.0095	0.1536	0.1168	3 (7.32%)	0 (0.00%)
Histidine metabolism	0.0139	0.1536	0.0492	3 (7.32%)	0 (0.00%)
Nitrogen metabolism	0.0146	0.1536	0.0	2 (4.88%)	0 (0.00%)
D-Glutamine and D-glutamate metabolism	0.0146	0.1536	0.5	2 (4.88%)	0 (0.00%)
Glyoxylate and dicarboxylate metabolism	0.0189	0.1767	0.0741	2 (4.88%)	0 (0.00%)
Sphingolipid metabolism	0.0294	0.2469	0.0284	3 (7.32%)	0 (0.00%)
Pentose phosphate pathway	0.0385	0.2942	0.1126	3 (7.32%)	0 (0.00%)
Glycolysis/Gluconeogenesis*	0.0590	0.4131	0.0425	3 (7.32%)	0 (0.00%)
Pathways (Recovery vs. OS)	p value	FDR	Impact	Metabolites Up	Metabolites Down
Glutathione metabolism	0.0036	0.2425	0.3199	0 (0.00%)	3 (60.00%)
Cysteine and methionine metabolism	0.0058	0.2425	0.0221	2 (66.67%)	1 (20.00%)
Sphingolipid metabolism	0.0235	0.6575	0.0243	1 (33.33%)	1 (20.00%)

essential for cell health (Rodrigo et al., 2013; van der Pol et al., 2019; Alkadi, 2020). Moderated concentration of ROS has important roles in cell signaling, whereas excessive levels of ROS cause damage to macromolecules such as protein, lipids and DNA, which can trigger cell death (Meneghini, 1997; Poljsak et al., 2013; Alkadi, 2020). Although several signaling pathway studies and functional *in vivo* experiments have demonstrated the effects of ROS production in CVD, scarce information is available about measurable changes in the metabolomic profile of cardiomyocytes undergoing oxidative stress. In the current study, PCA and PLS-DA analyses allowed identification of the predominant metabolites and pathways modulated by OS in cardiomyocytes H9c2.

Our results showed that a key pathway to be activated under oxidative stress was the alanine, aspartate, and glutamate metabolism. Specifically, we found that the L-aspartate and L-Asparagine were upregulated 2.5- and 1.56-fold, respectively, while the N-(L-Arginino)succinate was downregulated 1.76-fold in cardiomyocytes exposed to H_2O_2 over control cells (Figure 4A), probably due to increased utilization or decreased synthesis. Although we cannot firmly distinguish between these possibilities, it is likely that N-(L-Arginine) succinate is depleted because of increased utilization. L-aspartate is converted into N-(L-Arginine)succinate, which may be converted into L-arginine, the substrate of nitric oxide (NO) synthase. NO is a potent anti-hypertensive agent, produced when L-arginine is converted to citrulline (Hou et al., 2017). Under oxidative stress, the increased ROS concentrations reduce

the amount of bioactive NO by chemical inactivation to form the peroxynitrite anion ($ONOO^-$), resulting in both oxidation and nitration of proteins and in lipid peroxidation (Toyokuni, 2008; Rochette et al., 2013). This pathway was also upregulated in the cardiomyocytes recovered for 48 h after oxidative stress.

The observed upregulation of the “aspartate metabolism” under OS may also affect related pathways including “glycolysis”, “gluconeogenesis”, “citric acid cycle”, “amino acids biosynthesis”, and “pyrimidine and purine biosynthesis” (Bielarczyk et al., 1986; Darvey, 2000; Weckmann et al., 2018). Interestingly, upon 48-h recovery of OS, we observed an upregulation of the glycolysis metabolites such as Glucose-6-phosphate (2.01-fold), Glycerol-3-phosphate (0.8-fold), and Lactate (1.59-fold) (Figure 4B), which indicated that the energy metabolism shifts to anaerobic glycolysis as an adaptive response to oxidative stress in cardiomyocytes H9c2. We also identified a modest accumulation in citrate levels (0.48-fold) and an upregulation of amino acid biosynthesis pathways (Figure 3), indicating a dysfunction of the citric acid cycle and a shift towards amino acids biosynthesis (Mullarky et al., 2015). Scientific literature have reported the action of the factor HIF-1 α during oxidative stress in mediation of gene expression involved in shifting the metabolism towards anaerobic glycolysis without requirement of a hypoxic condition (Shi et al., 2009; Frezza et al., 2011). HIF-1 α upregulates the expression of Glut1 and glycolytic enzymes increasing the anaerobic glycolysis pathway (Fulda and Debatin, 2007). Moreover, HIF-1 α has shown to limit the conversion of pyruvic acid to acetyl-CoA in the mitochondria,

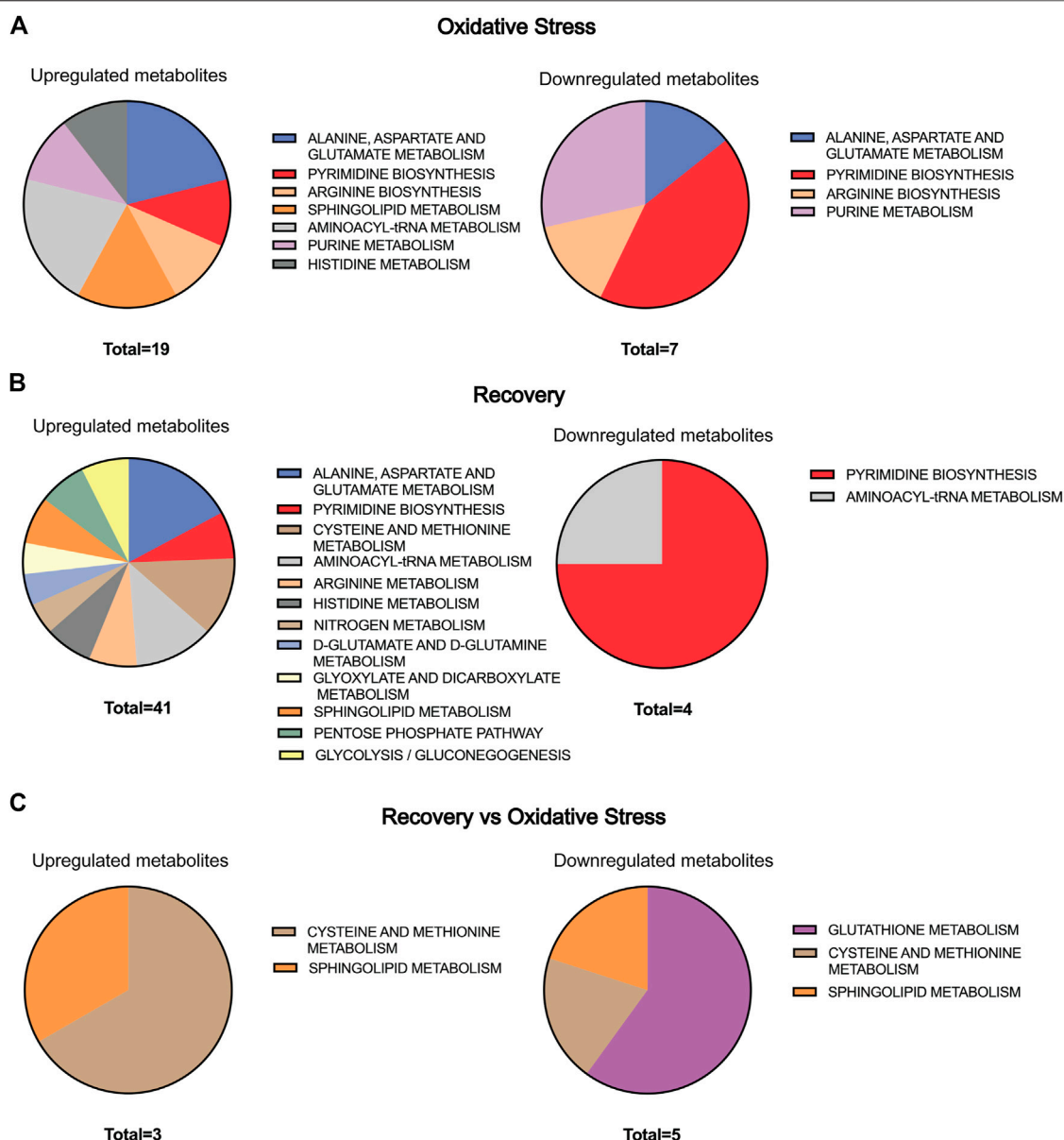
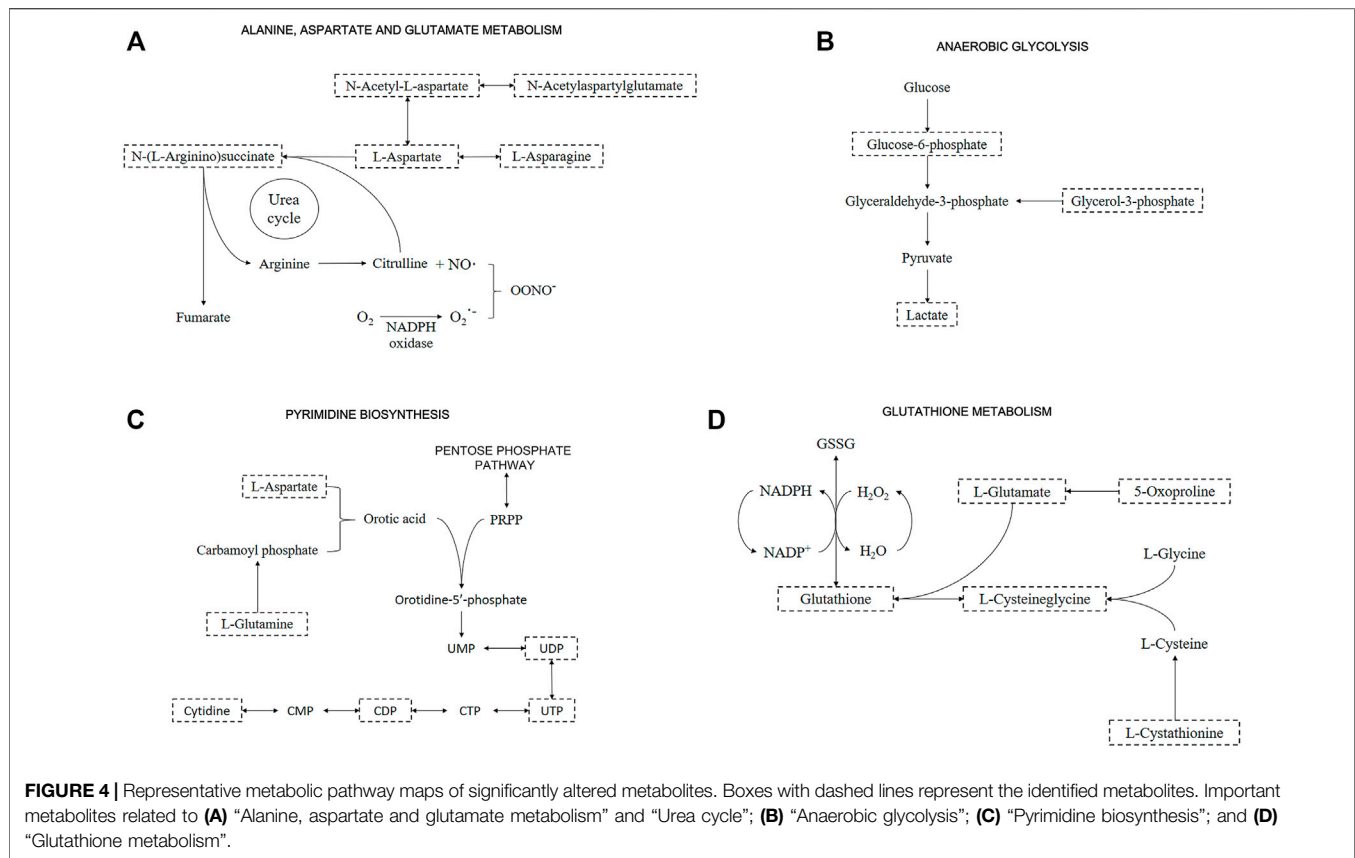


FIGURE 3 | Pie chart representation of the statistically significant metabolic pathway present in **Table 3** for **(A)** oxidative stress, **(B)** recovery, and **(C)** recovery vs. oxidative stress. The size of the pie chart is represented by the number of up- and downregulated metabolites in each group.

impairing the citric acid cycle activity as a strategy to couple to oxidative stress (Kim et al., 2006; Papandreou et al., 2006; Weckmann et al., 2018).

The metabolite L-carnitine was also upregulated (1.9-fold) in cardiomyocytes under oxidative stress. This metabolite facilitates the long-chain fatty acids transport into the mitochondrial matrix in order to be degraded by beta oxidation. The fatty acids conjugated to coenzyme A are transferred to carnitine by the enzyme carnitine acyltransferase I, resulting in the production of fatty acid acyl-carnitine. This metabolite is transported across the inner mitochondrial membrane *via* carnitine translocase, which exchanges long-chain acyl-carnitine for carnitine. Inside the

mitochondria, the acyl group from fatty acyl-carnitine is transferred to coenzyme-A by carnitine acyltransferase II. Then, the long-chain acyl-CoA enters beta-oxidation pathway, which results in the production of acetyl-CoA, a substrate for citric acid cycle. Studies suggest that L-carnitine protects cardiomyocytes from oxidative stress and toxic myocardial injury, such as by doxorubicin exposure (Wang et al., 2018). In this case, upregulation of L-carnitine may be related to a reduction in intra-mitochondrial acetyl-CoA in response to the mitochondria oxidative damage, leading to stimulation of pyruvate dehydrogenase, enhancing anaerobic glycolysis, and reducing beta oxidation (Mate et al., 2010).



We also demonstrated a regulation of the “pyrimidine and purine biosynthesis” in cardiomyocytes under oxidative stress (Figure 4C). Interestingly, although the upstream metabolites L-glutamine (1.56-fold), L-aspartate (2.5-fold), and cytidine (1.86-fold) were upregulated, the products UDP, CDP, and AMP of the pyrimidine and purine metabolism were strongly downregulated. The metabolites UDP and CDP were downregulated 3.28- and 3.49-fold in the OS group and 2.47- and 4.5-fold in the recovery group, respectively. We also identified a downregulation in the AMP levels (3.61-fold) in the recovery group. The downregulation of AMP without alterations in the ATP levels increases the ATP/AMP ratio and inhibits AMPK, the main sensor of cellular energy status in eukaryotic cells (Garcia and Shaw, 2017; Lin and Hardie, 2018). AMPK inhibits anabolic pathways to avoid wasting energy through the inhibition of mTORC1, under stressful conditions. The kinase mTORC1 regulates key cellular functions, which promotes cell growth and survival (Hardie, 2014; Saxton and Sabatini, 2017; González et al., 2020; Ling et al., 2020). In general, our results suggest that oxidative stress induces a metabolic adaptation mechanism that allows cell survival and the reactivation of the anabolic pathways in cardiomyocytes recovered from the oxidative stress condition.

A significant alteration of glutathione occurred after cardiomyocytes recovered from oxidative stress. The main function of glutathione is to avoid oxidative stress, reducing the deleterious effects of ROS on the cardiomyocytes,

constituting the most abundant cellular antioxidant (Matuz-Mares et al., 2021). Glutathione acts on redox equilibrium on its reduced form, trapping ROS, and preventing the inactivation of compounds such as NO (Ceconi et al., 2000; Guerra, 2001; Pompella et al., 2003; Matuz-Mares et al., 2021). Within glutathione consumption, it is easily replaced if the amino acids L-glutamate, L-cysteine, and L-glycine are available, as provided by DMEM medium. Usually, cysteine is found in lower amounts and is one of the limiting factors for glutathione synthesis. In such cases, dipeptides such as cystathionine (1.35-fold) can be precursors of cysteine through the transsulfuration pathway, which is even more favored under oxidative conditions (Finkelstein, 1998; Mosharov et al., 2000). Therefore, our data suggest that glutathione is consumed to promote protection to cardiomyocytes after oxidative stress, as a defense mechanism against ROS.

The all-trans-4-oxoretinoic acid, a derivative of retinoic acid (which was used in the cell differentiation process), showed a slight fold change. Choudhary et al. (2008) showed that retinoic acid is a potential inhibitor of ROS generation, protecting cardiomyocytes from apoptosis generated by mechanical stress and Angiotensin II. In contrast, data about all-trans-4-oxoretinoic acid formation suggests that it inactivates growth and differentiation pathways (Pijnappel et al., 1993). Such results would account for the loss of the differentiated phenotype visualized in Figure 1 and Supplementary Figure S2B.

Another metabolite that was upregulated in cardiomyocytes under oxidative stress was Carnosine (1.48-fold). It is a dipeptide, composed of L-histidine and β -alanine amino acids, with roles in muscle cells regulating the calcium metabolism and protecting against ROS (Boldyrev et al., 2013). Carnosine functions as a chelant to sequester heavy metal ions. In cardiomyocytes, carnosine can buffer the intracellular medium during anaerobic glycolysis, protecting the cells from apoptosis by maintaining a constant acidity. Anaerobic glycolysis increases the production of lactic acid, which is dissociated in protons (H^+) and lactate ions, and carnosine can sequester these protons, attenuating the acidosis (Baye et al., 2016; Zhao et al., 2019). In hypertrophic and failing hearts, carnosine levels are depleted, suggesting its role against cardiac injury. Recent studies also indicate an interaction of carnosine with highly toxic lipid peroxidation products, such as 4-hydroxy-trans-2-nonenal and acrolein, which avoids damage and promotes cell protection in infarcted mouse hearts (Zhao et al., 2019). Therefore, the upregulation of carnosine may be protective for cardiomyocytes under OS, acting as a pro-survival metabolite.

Metabolites involved in the sphingolipid metabolism were mostly upregulated, such as sphingosine 1-phosphate (2.65-fold) and phytosphingosine (2.31-fold) in the recovery group. *In vivo* studies suggest that changes in sphingolipid metabolism may occur as a consequence of increased utilization or decreased synthesis on failing or hypertrophic hearts. For example, sphingosine can be used on ceramide synthesis, which is increased on failing or hypertrophic hearts. Furthermore, extensive changes on lipid metabolism were also associated with myocardial decompensation (Sansbury et al., 2014). Interestingly, sphingolipids can accumulate on tissues under conditions of cellular stress, causing the activation of some sphingolipid metabolizing enzymes, such as sphingomyelinases. Sphingosine 1-phosphate is a ceramide metabolite that can induce the generation of more oxygen reactive species and propagate inflammation (Nikolova-Karakashian and Reid, 2011). Studies also connect ceramides to heart failure, showing that it can lead to cardiomyocyte apoptosis by acting on the mitochondrial membranes, inducing ROS formation and promoting release of cytochrome c to initiate apoptosis. The upregulation of the sphingolipid metabolism demonstrated the persistence of the OS deleterious effects in the 48-h recovery cardiomyocytes.

CONCLUSION

For the first time, data from a metabolomics study using differentiated H9c2 cardiomyocytes cultured *in vitro* were presented to analyze intracellular changes after oxidative stress, followed by cell recovery upon restoring initial culture medium composition. Our results show that the analysis of the intracellular metabolome by LC-MS and morphological assays can discriminate healthy cells from those suffering oxidative damage. This is an indication of a confident model to understand the effects of oxidative stress on the cardiovascular

system and possible therapeutic targets. At the same time, the use of two LC-MS modes (RPLC and HILIC) with positive and negative ionization modes brought complementary information that could not be obtained using only one methodology, showing the importance of multiplatform analyses in untargeted metabolomics approaches.

DATA AVAILABILITY STATEMENT

The datasets presented in this study can be found in online repositories. The names of the repository/repositories and accession number(s) can be found in the article/Supplementary Material.

AUTHOR CONTRIBUTIONS

AA, AdS, and AVS conceived the research. AA, AdS, AVS, IM, and IR designed the experiments. AA, IM, and IR performed cell culture and differentiation. AA, AS, and FZ performed the MTT assays. AA, HZ-O, and RO performed LC-MS experiments. AA, AdT, AdS, and IM performed the immunofluorescence experiment. AA and HZ-O analyzed the LC-MS data. AA, AdS, and IM performed the biological interpretation and wrote. AA, AdT, AdS, AVS, FZ, and IM wrote and edited the manuscript.

FUNDING

This research was supported by the Agency for the Improvement of Higher Education Personnel (CAPES) (Finance Code 001), the National Council for Scientific and Technological Development (CNPq) (grant numbers 406064/2018-05 and 42.3228/2018-8), and São Paulo Research Foundation (FAPESP) (grant numbers 2014/50244-6, 2018/07383-6 and 2020/05965-8).

ACKNOWLEDGMENTS

We thank the access to equipment and assistance provided by the National Institute of Science and Technology on Photonics Applied to Cell Biology (INFABIC) at the State University of Campinas; INFABIC is co-funded by São Paulo Research Foundation (FAPESP) (2014/50938-8) and National Council for Scientific and Technological Development (CNPq) (465699/2014-6). HZ-O would like to thank the University of Costa Rica for the scholarship (OAI-159-2019).

SUPPLEMENTARY MATERIAL

The Supplementary Material for this article can be found online at: <https://www.frontiersin.org/articles/10.3389/fchem.2022.836478/full#supplementary-material>

REFERENCES

- Alkadi, H. (2020). A Review on Free Radicals and Antioxidants. *Iddt* 20 (1), 16–26. doi:10.2174/1871526518666180628124323
- Barbosa, C. G., Gonçalves, N. S., Bechara, E. J. H., and Assunção, N. A. (2013). Potential Diagnostic Assay for Cystinuria by Capillary Electrophoresis Coupled to Mass Spectrometry. *J. Braz. Chem. Soc.* 24 (4), 534–540. doi:10.5935/0103-5053.20130085
- Barbosa, E. D., Vidotto, A., Polachini, G. M., Henrique, T., de Marqui, A. B. T., and Tajara, E. H. (2012). Proteômica: metodologias e aplicações no estudo de doenças humanas. *Rev. Assoc. Med. Bras.* 58 (3). doi:10.1590/s0104-42302012000300019
- Baye, E., Ukropcova, B., Ukropec, J., Hipkiss, A., Aldini, G., and de Courten, B. (2016). Physiological and Therapeutic Effects of Carnosine on Cardiometabolic Risk and Disease. *Amino Acids* 48, 1131–1149. doi:10.1007/s00726-016-2208-1
- Bielarczyk, H., Lysiak, W., and Szutowicz, A. (1986). Synthesis of Glutamate and Aspartate in Rat Brain Synaptosomes. *Acta Biochim. Pol.* 33, 239–251. PMID: 2881415.
- Boldyrev, A. A., Aldini, G., and Derave, W. (2013). Physiology and Pathophysiology of Carnosine. *Physiol. Rev.* 93 (4), 1803–1845. doi:10.1152/physrev.00039.2012
- Cecconi, C., Bernocchi, P., Boraso, A., Cargnoni, A., Pepi, P., Curello, S., et al. (2000). New Insights on Myocardial Pyridine Nucleotides and Thiol Redox State in Ischemia and Reperfusion Damage. *Cardiovasc. Res.* 47 (3), 586–594. doi:10.1016/s0008-6363(00)00104-8
- Choudhary, R., Baker, K. M., and Pan, J. (2008). All-trans Retinoic Acid Prevents Angiotensin II- and Mechanical Stretch-Induced Reactive Oxygen Species Generation and Cardiomyocyte Apoptosis. *J. Cel. Physiol.* 215 (1), 172–181. doi:10.1002/jcp.21297
- Clayton, Z. S., Brunt, V. E., Hutton, D. A., VanDongen, N. S., D'Alessandro, A., Reisz, J. A., et al. (2020). Doxorubicin-Induced Oxidative Stress and Endothelial Dysfunction in Conduit Arteries Is Prevented by Mitochondrial-specific Antioxidant Treatment. *JACC: CardioOncology* 2 (3), 475–488. doi:10.1016/j.jacc.2020.06.010
- Cubbon, S., Antonio, C., Wilson, J., and Thomas-Oates, J. (2010). Metabolomic Applications of HILIC-LC-MS. *Mass. Spectrom. Rev.* 29 (5), 671–684. doi:10.1002/mas.20252
- Čuperlović-Culfi, M., Barnett, D. A., Culfi, A. S., and Chute, I. (2010). Cell Culture Metabolomics: Applications and Future Directions. *Drug Discov. Today* 15 (15–16), 610–621. doi:10.1016/j.drudis.2010.06.012
- Darvey, I. G. (2000). Does the Transport of Oxaloacetate across the Inner Mitochondrial Membrane during Gluconeogenesis Require Carrier Proteins Other Than Those Used in the Malate-Aspartate Shuttle? *Biochem. Educ.* 28, 80–82. PMID: 10722937. doi:10.1111/j.1539-3429.2000.tb00025.x
- Dettmer, K., Nünberger, N., Kaspar, H., Gruber, M. A., Altmstetter, M. F., and Oefner, P. J. (2011). Metabolite Extraction from Adherently Growing Mammalian Cells for Metabolomics Studies: Optimization of Harvesting and Extraction Protocols. *Anal. Bioanal. Chem.* 399 (3), 1127–1139. doi:10.1007/s00216-010-4425-x
- Dórea, E. L., and Lotufo, P. A. (2001). Framingham Heart Study e a teoria Do contínuo de Pickering: duas contribuições da epidemiologia para a associação entre pressão arterial e doença cardiovascular. *Rev. Bras. Hipertens.* 8 (2), 195–200. ID: lil-313906.
- Du, Z., Wen, R., Liu, Q., Wang, J., Lu, Y., Zhao, M., et al. (2019). 1H NMR-Based Dynamic Metabolomics Delineates the Therapeutic Effects of Baoyuan Decoction on Isoproterenol-Induced Cardiac Hypertrophy. *J. Pharm. Biomed. Anal.* 163, 64–77. doi:10.1016/j.jpba.2018.09.049
- Ewer, M. S., and Ewer, S. M. (2010). Troponin I Provides Insight into Cardiotoxicity and the Anthracycline-Trastuzumab Interaction. *Jco* 28 (25), 3901–3904. doi:10.1200/JCO.2010.30.6274
- Fiehn, O. (2001). Combining Genomics, Metabolome Analysis, and Biochemical Modelling to Understand Metabolic Networks. *Comp. Funct. Genomics* 2 (3), 155–168. doi:10.1002/cfg.82
- Finkelstein, J. D. (1998). The Metabolism of Homocysteine: Pathways and Regulation. *Eur. J. Pediatr.* 157 (Suppl. 2), S40–S44. doi:10.1007/pl00014300
- Francisco, A., and Castilho, R. F. (2019). *Radicais livres e estresse oxidativo*. Editors A. Célula, H. F. Carvalho, and S. M. Recco-Pimentel (Paulo, SP: Manole), 583–594.
- Frezza, C., Zheng, L., Tennant, D. A., Papkovsky, D. B., Hedley, B. A., Kalna, G., et al. (2011). Metabolic Profiling of Hypoxic Cells Revealed a Catabolic Signature Required for Cell Survival. *PLoS One* 6 (9), e24411. doi:10.1371/journal.pone.0024411
- Fulda, S., and Debatin, K.-M. (2007). HIF-1-Regulated Glucose Metabolism: A Key to Apoptosis Resistance? *Cell Cycle* 6 (7), 790–792. doi:10.4161/cc.6.7.4084
- Garcia, D., and Shaw, R. J. (2017). AMPK: Mechanisms of Cellular Energy Sensing and Restoration of Metabolic Balance. *Mol. Cel* 66 (6), 789–800. doi:10.1016/j.molcel.2017.05.032
- Gil-de-la-Fuente, A., Godzien, J., Saugar, S., Garcia-Carmona, R., Badran, H., Wishart, D. S., et al. (2019). CEU Mass Mediator 3.0: A Metabolite Annotation Tool. *J. Proteome Res.* 18 (2), 797–802. doi:10.1021/acs.jproteome.8b00720
- González, A., Hall, M. N., Lin, S.-C., and Hardie, D. G. (2020). AMPK and TOR: The Yin and Yang of Cellular Nutrient Sensing and Growth Control. *Cel Metab.* 31 (3), 472–492. doi:10.1016/j.cmet.2020.01.015
- Guerra, J. I. E. (2001). Oxidation, between Life and Disease. *Med. Interna.* 18 (1), 1–4. PMID: 11387837. doi:10.4321/s0212-71992001000600010
- Hardie, D. G. (2014). AMPK-sensing Energy while Talking to Other Signaling Pathways. *Cel Metab.* 20 (6), 939–952. doi:10.1016/j.cmet.2014.09.013
- Hermes-Lima, M., Pereira, B., and Bechara, E. J. H. (1991). Are Free Radicals Involved in lead Poisoning? *Xenobiotica* 21 (8), 1085–1090. doi:10.3109/00498259109039548
- Hou, E., Sun, N., Zhang, F., Zhao, C., Usa, K., Liang, M., et al. (2017). Malate and Aspartate Increase L-Arginine and Nitric Oxide and Attenuate Hypertension. *Cel Rep.* 19 (8), 1631–1639. doi:10.1016/j.celrep.2017.04.071
- Hunter, J. J., and Chien, K. R. (1999). Signaling Pathways for Cardiac Hypertrophy and Failure. *N. Engl. J. Med.* 341 (17), 1276–1283. doi:10.1056/NEJM199910213411706
- Ilavenil, S., Kim, D. H., Jeong, Y.-I., Arasu, M. V., Vijayakumar, M., Prabhu, P. N., et al. (2015). Trigonelline Protects the Cardiocyte from Hydrogen Peroxide Induced Apoptosis in H9c2 Cells. *Asian Pac. J. Trop. Med.* 8 (4), 263–268. doi:10.1016/S1995-7645(14)60328-X
- Jonsson, P., Gullberg, J., Nordström, A., Kusano, M., Kowalczyk, M., Sjöström, M., et al. (2004). A Strategy for Identifying Differences in Large Series of Metabolomic Samples Analyzed by GC/MS. *Anal. Chem.* 76 (6), 1738–1745. doi:10.1021/ac0352427
- Kanehisa, M., Sato, Y., Furumichi, M., Morishima, K., and Tanabe, M. (2019). New Approach for Understanding Genome Variations in KEGG. *Nucleic Acids Res.* 47 (D1), D590–D595. doi:10.1093/nar/gky962
- Kim, D.-E., Kim, B., Shin, H.-S., Kwon, H. J., and Park, E.-S. (2014). The Protective Effect of Hispidin against Hydrogen Peroxide-Induced Apoptosis in H9c2 Cardiomyoblast Cells through Akt/GSK-3 β and ERK1/2 Signaling Pathway. *Exp. Cel Res.* 327 (2), 264–275. doi:10.1016/j.yexcr.2014.07.037
- Kim, J.-w., Tchernyshyov, I., Semenza, G. L., and Dang, C. V. (2006). HIF-1-mediated Expression of Pyruvate Dehydrogenase Kinase: A Metabolic Switch Required for Cellular Adaptation to Hypoxia. *Cel Metab.* 3 (3), 177–185. doi:10.1016/j.cmet.2006.02.002
- Kim, S., Chen, J., Cheng, T., Gindulyte, A., He, J., He, S., et al. (2021). PubChem in 2021: New Data Content and Improved Web Interfaces. *Nucleic Acids Res.* 49 (D1), D1388–D1395. doi:10.1093/nar/gkaa971
- Kimes, B., and Brandt, B. (1976). Properties of a Clonal Muscle Cell Line from Rat Heart. *Exp. Cel Res.* 98 (2), 367–381. doi:10.1016/0014-4827(76)90447-x
- Kordalewska, M., and Markuszewski, M. J. (2015). Metabolomics in Cardiovascular Diseases. *J. Pharm. Biomed. Anal.* 113, 121–136. doi:10.1016/j.jpba.2015.04.021
- Lee, R. T., and Walsh, K. (2017). The Future of Cardiovascular Regenerative Medicine. *Circulation* 133 (25), 2618–2625. doi:10.1161/CIRCULATIONAHA.115.019214
- León, Z., García-Cañaveras, J. C., Donato, M. T., and Lahoz, A. (2013). Mammalian Cell Metabolomics: Experimental Design and Sample Preparation. *Electrophoresis* 34 (19), a–n. doi:10.1002/elps.201200605
- Lin, S.-C., and Hardie, D. G. (2018). AMPK: Sensing Glucose as Well as Cellular Energy Status. *Cel Metab.* 27 (2), 299–313. doi:10.1016/j.cmet.2017.10.009
- Ling, N. X. Y., Kaczmarek, A., Hoque, A., Davie, E., Ngoei, K. R. W., Morrison, K. R., et al. (2020). mTORC1 Directly Inhibits AMPK to Promote Cell

- Proliferation under Nutrient Stress. *Nat. Metab.* 2 (1), 41–49. doi:10.1038/s42255-019-0157-1
- Lotufo, P. A. (2008). O escore de risco de Framingham para doenças cardiovasculares. *Rev. Med. (São Paulo)* 87 (4), 232–237. doi:10.11606/issn.1679-9836.v87i4p232-237
- Mastrangelo, A., Panadero, M. I., Pérez, L. M., Gálvez, B. G., García, A., Barbas, C., et al. (2016). New Insight on Obesity and Adipose-Derived Stem Cells Using Comprehensive Metabolomics. *Biochem. J.* 473 (14), 2187–2203. doi:10.1042/BCJ20160241
- Mate, A., Miguel-Carrasco, J. L., and Vázquez, C. M. (2010). The Therapeutic Prospects of Using L-Carnitine to Manage Hypertension-Related Organ Damage. *Drug Discov. Today* 15 (11–12), 484–492. doi:10.1016/j.drudis.2010.03.014
- Matuz-Mares, D., Riveros-Rosas, H., Vilchis-Landeros, M. M., and Vázquez-Meza, H. (2021). Glutathione Participation in the Prevention of Cardiovascular Diseases. *Antioxidants* 10 (8), 1220. doi:10.3390/antiox10081220
- Meneghini, R. (1997). Iron Homeostasis, Oxidative Stress, and DNA Damage. *Free Radic. Biol. Med.* 23 (5), 783–792. doi:10.1016/s0891-5849(97)00016-6
- Mosharov, E., Cranford, M. R., and Banerjee, R. (2000). The Quantitatively Important Relationship between Homocysteine Metabolism and Glutathione Synthesis by the Transsulfuration Pathway and its Regulation by Redox Changes. *Biochemistry* 39 (42), 13005–13011. doi:10.1021/bi001088w
- Mullarky, E., Cantley, L. C., Nakao, K., Minato, N., and Uemoto, S. (2015). *Innovative Medicine: Basic Research and Development*. Tokyo: Springer. [Internet]. doi:10.1007/978-4-431-55651-0_1Diverting Glycolysis to Combat Oxidative Stress
- Nikolova-Karakashian, M. N., and Reid, M. B. (2011). Sphingolipid Metabolism, Oxidant Signaling, and Contractile Function of Skeletal Muscle. *Antioxid. Redox Signaling* 15 (9), 2501–2517. doi:10.1089/ars.2011.3940
- Pang, Z., Chong, J., Zhou, G., de Lima Morais, D. A., Chang, L., Barrette, M., et al. (2021). MetaboAnalyst 5.0: Narrowing the gap between Raw Spectra and Functional Insights. *Nucleic Acids Res.* 49 (W1), W388–W396. doi:10.1093/nar/gkab382
- Panth, N., Paudel, K. R., and Parajuli, K. (2016/2016). Reactive Oxygen Species: A Key Hallmark of Cardiovascular Disease. *Adv. Med.* 2016, 9152732. doi:10.1155/2016/9152732
- Papandreou, I., Cairns, R. A., Fontana, L., Lim, A. L., and Denko, N. C. (2006). HIF-1 Mediates Adaptation to Hypoxia by Actively Downregulating Mitochondrial Oxygen Consumption. *Cel. Metab.* 3 (3), 187–197. doi:10.1016/j.cmet.2006.01.012
- Patten, V. A., Chabaesele, I., Sishi, B., and van Vuuren, D. (2017). Cardiomyocyte Differentiation: Experience and Observations from 2 Laboratories. *SA Heart J.* 14 (2), 96–107. doi:10.24170/14-2-2498
- Pereira, S. L., Ramalho-Santos, J., Branco, A. F., Sardão, V. A., Oliveira, P. J., and Carvalho, R. A. (2011). Metabolic Remodeling during H9c2 Myoblast Differentiation: Relevance for *In Vitro* Toxicity Studies. *Cardiovasc. Toxicol.* 11 (2), 180–190. doi:10.1007/s12012-011-9112-4
- Pijnappel, W. W. M., Hendriks, H. F. J., Folkers, G. E., van den Brink, C. E., Dekker, E. J., Edelenbosch, C., et al. (1993). The Retinoid Ligand 4-Oxo-Retinoic Acid Is a Highly Active Modulator of Positional Specification. *Nature* 366, 340–344. doi:10.1038/366340a0
- Pluskal, T., Castillo, S., Villar-Briones, A., and Orešič, M. (2010). MZmine 2: Modular Framework for Processing, Visualizing, and Analyzing Mass Spectrometry-Based Molecular Profile Data. *BMC Bioinform.* 11. doi:10.1186/1471-2105-11-395
- Poljsak, B., Šuput, D., and Milisav, I. (2013). Achieving the Balance between ROS and Antioxidants: When to Use the Synthetic Antioxidants. *Oxid. Med. Cel. Longev.* 2013, 956792. doi:10.1155/2013/956792
- Pompella, A., Visvikis, A., Paolicchi, A., Tata, V. D., and Casini, A. F. (2003). The Changing Faces of Glutathione, a Cellular Protagonist. *Biochem. Pharmacol.* 66 (8), 1499–1503. doi:10.1016/s0006-2952(03)00504-5
- Rebouças, J. S., Santos-Magalhães, N. S., and Formiga, F. R. (2016). Regeneração cardíaca com fatores de crescimento: avanços e desafios. *Arq Bras Cardiol.* 107 (3), 271–275.
- Rochette, L., Lorin, J., Zeller, M., Guillard, J.-C., Lorgis, L., Cottin, Y., et al. (2013). Nitric Oxide Synthase Inhibition and Oxidative Stress in Cardiovascular Diseases: Possible Therapeutic Targets? *Pharmacol. Ther.* 140 (3), 239–257. doi:10.1016/j.pharmthera.2013.07.004
- Rodrigo, R., Libuy, M., Feliú, F., and Hasson, D. (2013). Molecular Basis of Cardioprotective Effect of Antioxidant Vitamins in Myocardial Infarction. *Biomed. Res. Int.* 2013, 1–15. doi:10.1155/2013/437613
- Sansbury, B. E., DeMartino, A. M., Xie, Z., Brooks, A. C., Brainard, R. E., Watson, L. J., et al. (2014). Metabolomic Analysis of Pressure-Overloaded and Infarcted Mouse Hearts. *Circ. Heart Fail.* 7 (4), 634–642. doi:10.1161/CIRCHEARTFAILURE.114.001151
- Saxton, R. A., and Sabatini, D. M. (2017). mTOR Signaling in Growth, Metabolism, and Disease. *Cell* 168 (6), 960–976. doi:10.1016/j.cell.2017.02.004
- Shi, D.-y., Xie, F.-z., Zhai, C., Stern, J. S., Liu, Y., and Liu, S.-l. (2009). The Role of Cellular Oxidative Stress in Regulating Glycolysis Energy Metabolism in Hepatoma Cells. *Mol. Cancer* 8 (32), 32. doi:10.1186/1476-4598-8-32
- Suhaeri, M., Subbiah, R., Van, S. Y., Du, P., Kim, I. G., Lee, K., et al. (2015). Cardiomyoblast (H9c2) Differentiation on Tunable Extracellular Matrix Microenvironment. *Tissue Eng. A* 21 (11–12), 1940–1951. doi:10.1089/ten.TEA.2014.0591
- Tauffenberger, A., Fiumelli, H., Almustafa, S., and Magistretti, P. J. (2019). Lactate and Pyruvate Promote Oxidative Stress Resistance through Hormetic ROS Signaling. *Cell Death Dis* 10, 653. doi:10.1038/s41419-019-1877-6
- Teng, Q., Huang, W., Collette, T. W., Ekman, D. R., and Tan, C. (2009). A Direct Cell Quenching Method for Cell-Culture Based Metabolomics. *Metabolomics* 5, 199–208. doi:10.1007/s11306-008-0137-z
- Tenreiro, M. F., Louro, A. F., Alves, P. M., and Serra, M. (2021). Next Generation of Heart Regenerative Therapies: Progress and Promise of Cardiac Tissue Engineering. *Npj Regen. Med.* 6 (30). doi:10.1038/s41536-021-00140-4
- Toyokuni, S. (2008). Molecular Mechanisms of Oxidative Stress-Induced Carcinogenesis: from Epidemiology to Oxygenomics. *IUBMB Life* 60 (7), 441–447. doi:10.1002/iub.61
- van der Pol, A., van Gilst, W. H., Voors, A. A., and van der Meer, P. (2019). Treating Oxidative Stress in Heart Failure: Past, Present and Future. *Eur. J. Heart Fail.* 21 (4), 425–435. doi:10.1002/ehf.1320
- Viant, M. R., Kurland, I. J., Jones, M. R., and Dunn, W. B. (2017). How Close Are We to Complete Annotation of Metabolomes? *Curr. Opin. Chem. Biol.* 36, 64–69. doi:10.1016/j.cbpa.2017.01.001
- Wang, Z.-Y., Liu, Y.-Y., Liu, G.-H., Lu, H.-B., and Mao, C.-Y. (2018). l-Carnitine and Heart Disease. *Life Sci.* 194 (1), 88–97. doi:10.1016/j.lfs.2017.12.015
- Weckmann, K., Diefenthaler, P., Baeken, M. W., Yusifli, K., Turck, C. W., Asara, J. M., et al. (2018). Metabolomics Profiling Reveals Differential Adaptation of Major Energy Metabolism Pathways Associated with Autophagy upon Oxygen and Glucose Reduction. *Sci. Rep.* 8, 2337. doi:10.1038/s41598-018-19421-y
- Wilson, P. W. F., D'Agostino, R. B., Levy, D., Belanger, A. M., Silbershatz, H., and Kannel, W. B. (1998). Prediction of Coronary Heart Disease Using Risk Factor Categories. *Circulation* 97 (18), 1837–1847. doi:10.1161/01.cir.97.18.1837
- Wishart, D. S., Feunang, Y. D., Marcu, A., Guo, A. C., Liang, K., Vázquez-Fresno, R., et al. (2018). HMDB 4.0: the Human Metabolome Database for 2018. *Nucleic Acids Res.* 46 (1), D608–D617. doi:10.1093/nar/gkx1089
- Wu, H., Gao, H., Gao, S., Lei, Z., Dai, L., Wang, X., et al. (2019). A Chinese 4-herb Formula, Yiqi-Huoxue Granule, Alleviates H2O2-Induced Apoptosis by Upregulating Uncoupling Protein 2 in H9c2 Cells. *Phytomedicine* 53, 171–181. doi:10.1016/j.phymed.2018.09.031
- Zang, Z., and Yu, B. (2019). In *Metabolomics, Proteomics and Genomics: An Introduction to a Clinician* in *Biomarkers in Cardiovascular Disease*. Editor V. Nambi (Amsterdam, Netherlands: Elsevier, 159–170. doi:10.1016/B978-0-323-54835-9.00015-6
- Zhang, H., Zhang, X., and Zhang, J. (2018). MiR-129-5p Inhibits Autophagy and Apoptosis of H9c2 Cells Induced by Hydrogen Peroxide via the PI3K/AKT/mTOR Signaling Pathway by Targeting ATG14. *Biochem. Biophysical Res. Commun.* 506 (1), 272–277. doi:10.1016/j.bbrc.2018.10.085
- Zhao, J., Posa, D. K., Kumar, V., Hoetker, D., Kumar, A., Ganesan, S., et al. (2019). Carnosine Protects Cardiac Myocytes against Lipid Peroxidation Products. *Amino Acids* 51 (1), 123–138. doi:10.1007/s00726-018-2676-6

Zuo, L., Zhou, T., Pannell, B. K., Ziegler, A. C., and Best, T. M. (2015). Biological and Physiological Role of Reactive Oxygen Species - the Good, the Bad and the Ugly. *Acta Physiol.* 214 (3), 329–348. doi:10.1111/apha.12515

Conflict of Interest: The authors declare that the research was conducted in the absence of any commercial or financial relationships that could be construed as a potential conflict of interest.

Publisher's Note: All claims expressed in this article are solely those of the authors and do not necessarily represent those of their affiliated organizations, or those of

the publisher, the editors, and the reviewers. Any product that may be evaluated in this article, or claim that may be made by its manufacturer, is not guaranteed or endorsed by the publisher.

Copyright © 2022 Amaral, Moretto, Zandonadi, Zamora-Obando, Rocha, Sussulini, Thomaz, Oliveira, Santos and Simionato. This is an open-access article distributed under the terms of the Creative Commons Attribution License (CC BY). The use, distribution or reproduction in other forums is permitted, provided the original author(s) and the copyright owner(s) are credited and that the original publication in this journal is cited, in accordance with accepted academic practice. No use, distribution or reproduction is permitted which does not comply with these terms.



Chromatography Conditions Development by Design of Experiments for the Chemotype Differentiation of Four *Bauhinia* Species

Amanda J. Aquino¹, Edenir R. Pereira-Filho², Regina V. Oliveira^{1*†} and Quezia B. Cass^{1*†}

¹Separare—Núcleo de Pesquisa em Cromatografia, Departamento de Química, Universidade Federal de São Carlos, São Carlos, Brazil, ²Grupo de Análise Instrumental Aplicada (GAIA), Departamento de Química, Universidade Federal de São Carlos, São Carlos, Brazil

OPEN ACCESS

Edited by:

Zhenbin Zhang,
Ningbo University, China

Reviewed by:

Mohammad Sharif Khan,
Cargill, United States
Zhixin Wang,
University of Florida, United States

*Correspondence:

Regina V. Oliveira
oliveirav@ufscar.br
Quezia B. Cass
qcass@ufscar.br

[†]These authors have contributed
equally to this work and share last
authorship

Specialty section:

This article was submitted to
Analytical Chemistry,
a section of the journal
Frontiers in Chemistry

Received: 23 October 2021

Accepted: 25 April 2022

Published: 23 May 2022

Citation:

Aquino AJ, Pereira-Filho ER,
Oliveira RV and Cass QB (2022)
Chromatography Conditions
Development by Design of
Experiments for the Chemotype
Differentiation of Four
Bauhinia Species.
Front. Chem. 10:800729.
doi: 10.3389/fchem.2022.800729

The extensive use of medicinal herbs to traditionally treat disease persists for generations, and scientific evidence on plant-derived extracts has indicated their numerous biological activities. The *Bauhinia*, popular known as cow's paw ("pata de vaca"), with more than 60 native species, are extensively used in Brazilian popular medicine for the control of diabetes. Therefore, in 2009, *B. forficata*, *B. variegata* and/or *B. affinis* were included in the Brazilian National List of Medicinal Plants of Interest to SUS (RENISUS - Brazil). In this context, this work reports the results of the chemical differentiation of *B. forficata*, *B. variegata*, *B. longifolia*, and *B. affinis* using liquid chromatography coupled to high-resolution mass spectrometry and unsupervised chemometric tools. Chromatographic conditions were optimized by using the design of experiments (DoE) and chromatographic knowledge. Furthermore, the chemical profile of the studied species was analyzed by principal component analysis (PCA) and hierarchical cluster analysis that differentiated the four species of *Bauhinia*, and 55 compounds were also inferred by MS2 experiments, some of them for the first time in *B. affinis*. In this manner, this work provides important information that could be used in quality control, development of new pharmaceuticals, and food products based on *Bauhinia* leaves, as well as to explain ethnomedicinal properties, pharmacological and toxicological actions.

Keywords: HRMS, hierarchical cluster analysis, *Bauhinia*, chemotype differentiation, dereplication, design of experiments

INTRODUCTION

Widely used by the Brazilian population for the treatment and prevention of diabetes, plants of the genus *Bauhinia* Linnaeus (*Bauhinia* L.) are popularly known as cow's paw ("pata de vaca") or ox nail ("unha de boi") because of its bilobed leaves (Henrique Domingos & Capellari Júnior, 2016).

The therapeutic properties of the cow's paw leaf extracts are attributed to the presence of flavonoids that may act as hypoglycemic agents mainly in type 2 diabetes mellitus (de Souza et al., 2018). For instance, several biological studies have shown the antidiabetic activity attributed mainly to flavonoid glycosides, in particular kaempferitrin (kaempferol-3,7-di-O- α -L-rhamnopyranoside), a

chemical marker reported for *B. forficata* leaves (da Cunha et al., 2010; De Sousa et al., 2004; Silva et al., 2002).

In Brazil, approximately more than 60 native species of *Bauhinia* are found (Cechinel Filho, 2009; Vaz et al., 2010). Teas of *Bauhinia* leaves or other plant-derived preparations have been widely used for the treatment of several illnesses, especially diabetes. Because of its high empirical use for medicinal purposes and the high interest in research with this plant species, the genus *Bauhinia* (*B. forficata*, *B. variegata* and/or *B. affinis*) was included in the RENISUS—National Relation of Medicinal Plants of Interest to the Unified Health System, Brazil, whose purpose is to foster research and development of monographs for quality control of herbal medicine (BRASIL, 2009).

The crescent commercial interest and therapeutic properties of herbal medicines undoubtedly require pharmacovigilance in the herbal medicinal products industry. Therefore, the monitoring of herbal medicines has become a major concern to both national health authorities and the public (Who, 2013). An effective regulation of plant-derived products must be established to improve their quality and avoid adverse reactions due to adulterations, misidentification of the medicinal plant species, inadequate quality control during the manufacturing, and/or poor-quality herbal preparations. For the protection of consumers and the development of relevant industries, authentication of medicinal plants represents a critical issue.

Usually, a medicinal herb contains hundreds of chemical constituents, so sophisticated separation and detection methods with high sensitivity and selectivity are required. Liquid chromatography coupled to high-resolution mass spectrometry (LC-HRMS) is widely used in the qualitative and quantitative analysis of natural product extracts since it provides a rapid and reliable picture of the plant's chemical content. In the literature, several studies have been described for the characterization of chemical markers in natural products by liquid chromatography coupled to quadrupole time-of-flight mass spectrometry (LC-QTOF) for quality control, authentication/standardization, and differentiation of plant species (Xiao et al., 2013; Zhang et al., 2015; Chang et al., 2017; Xu et al., 2018).

Liquid chromatography (LC) is the analytical technique of choice for the analysis of diverse compounds in complex matrices. An effective analytical method development involves evaluating and optimizing different parameters to comply with the goals of the method. LC analytical methods are usually developed using the one-factor-at-a-time (OFAT) approach, in which one chromatographic parameter is varied in consecutive experiments until a satisfactory chromatographic resolution is obtained (Tome et al., 2019). The disadvantage of this strategy relies on the increased number of experiments and longer development time, especially when many parameters are affecting the separation. To circumvent this, the use of the design of experiments (DoE) analytical approaches, which systematically vary multiple key variables (e.g., pH, temperature, organic modifier, stationary phase, among others) simultaneously to obtain suitable experimental conditions with a minimum number of experiments (Tome et al., 2019;

Thorsteinsdóttir & Thorsteinsdóttir, 2021). Screening and response-surface experimental designs allow the identification of significant factors, and the factor–response relationship is described by mathematical models, which can predict the optimal response. Multivariate combinations of key factors responsible for chromatographic performance promote reliable results for analytical method optimization and robustness.

Besides, new column technologies have furnished innovative stationary phase bonding chemistries and sub-2 μm fully porous and core-shell particles to mitigate some of the common problems associated with the traditional 5 μm and C18 associated with silica as solid support (Lopez et al., 2020). As a result, these new analytical opportunities provide faster LC analyzes with a gain of efficiency and chromatographic resolution. Moreover, significant advances have also been presented in the detection technologies, such as high-resolution mass spectrometers (HRMS) and nuclear magnetic resonance (NMR), making possible the comprehensive differentiation of isobaric or diastereomeric compounds (Wolfender et al., 2015).

This study describes the achievements of a high-efficiency LC method employing a three-step strategy for fingerprinting ethanolic extracts of *B. forficata* leaves, a specie recognized as a true cow's-paw. In addition, the use of DoE for chromatographic separation and optimization, LC-HRMS analysis, and unsupervised statistical tools (principal component analysis, PCA and hierarchical cluster analysis, HCA) were carried out to classify four *Bauhinia* species (*B. forficata*, *B. variegata*, *B. longifolia*, and *B. affinis*) that are widely distributed in Brazil, being three of them already used as herbal medicines and *B. longifolia* was complementary selected to add to its phytochemistry database (Aquino et al., 2019). In this regard, 33 compounds were inferred as responsible for *Bauhinia* species chemical profiling, providing important information that could be used in quality control of these species, development of new pharmaceuticals and food products based on *Bauhinia* leaves, as well as to explain ethnomedicinal properties, pharmacological, and toxicological actions.

MATERIALS AND METHODS

Chemicals

Methanol (HPLC grade) was used in all experiments and purchased from J.T. Baker (Philipsburg, United States). Formic acid (LC-MS grade) was acquired from Fluka (Buchs, Switzerland). Water was purified in a Milli-Q system (Millipore, São Paulo, Brazil).

Plant Material

Leaves of *B. forficata* were obtained from the Multidisciplinary Research Center on Biological and Agricultural Chemistry—CPQBA—SP—Brazil (22.79° S, 47.11° W; 22.86° S, 47.07° W). The leaves of *B. longifolia* (22.87° S, 47.07° W; 22.86° S, 47.08° W) and *B. variegata* (22.98° S, 47.88° W; 22.70° S, 46.98° W; 22.70° S, 47.98° W) were obtained of the Agronomic Institute of Campinas—IAC—SP—Brazil. *B. forficata*, *B. variegata*, and *B.*

longifolia were collected by V. A. P. e Carvalho (Carvalho, 2011). The leaves of *B. affinis* were obtained from the environmental preservation area—APA of the Ponta do Araçá—Porto Belo—Brazil—SC (27.13° S, 48.52° W) and collected by A. N. da Silva (Federal University of Santa Catarina). All species were identified by the Ph.D. researcher A. S. de F. Vaz, from the Research Institute of the Botanical Garden of Rio de Janeiro, Brazil. The specimen of *B. forficata* (755, 8333), *B. longifolia* (8325, 8330), and *B. variegata* (1112, 7655, 7658) was deposited in the herbarium of the Federal University of São Carlos (SPSC) and *B. affinis* (1884) was deposited in the herbarium of the botanical garden of Rio de Janeiro (JBRJ) and in the herbarium of the Botany Department of the Federal University of Santa Catarina (UFSC—FLOR61387). The collected samples have also been registered at SisGen Brazilian platform of Genetic Heritage and Associated Traditional Knowledge under the number A99450F. These vegetal samples were dried in a forced-air circulation drying oven set at 40°C for 7 days. For appropriated storage, the dried material was ground to a fine powder (60 Mesh).

Sample Preparation

Powdered and dried samples (500 mg) were weighed and soaked with 5 ml of ethanol (LC grade) in conical tubes (50 ml) using an Ultraturrax® homogenizer (IKA®, T18 basic model) set at speed 6 for 5 min. After grinding, the samples were centrifuged using a Jouan® centrifuge (model, BR4i) for 10 min at 10,000 rpm and the supernatant (S1) was isolated. The S1 was evaporated using a Speed-Vac® (Savant®, model SPD131DDA) set at 45°C overnight. The dried extracts obtained from the S1 fraction were labeled, weighed, and diluted to 50 mg/ml (D1) in MeOH:H₂O (85:15; v/v).

The diluted extracts (D1) were cleaned up to eliminate chlorophylls. To this end, SPE cartridges (C18 end-capped, 100 mg, Varian®) with a volume capacity of 1 ml and a 20-port vacuum manifold system coupled to a Tecnal® vacuum pump (model TE-058) were used. Initially, the SPE cartridge was activated with 2 ml of methanol (MeOH), equilibrated with 2 ml of MeOH:H₂O (85:15; v/v), and then loaded with 500 µL of the D1. The eluate was collected, dried in a Speed-Vac® set at 45°C overnight, and resuspended in MeOH:H₂O (85:15; v/v) to yield a final concentration required for LC-HRMS analyzes. Before analysis, the samples were centrifuged at 9300 g for 10 min.

Chromatographic Conditions

The UHPLC system (model Nexera®, Shimadzu) consisted of two quaternary LC-30AD pumps, a DGU-20A5R degasser, a SIL-30AC autoinjector, an SPD-M30A diode arrangement detector, a CTO-20AC furnace, a six-column selector valve, and a system Nexera Scouting Solution® was used for the method development and sequence setup. All equipment units were controlled by a CBM 20A interface. The LabSolutions® workstation software was used for operation of all modules and for data analysis and processing. The chromatographic columns selected were: Kinetex® Biphenyl (100 mm × 2.1 mm × 2.7 µm) (Phenomenex, Torrance, CA, United States), Raptor® Biphenyl (100 mm × 2.1 mm × 2.7 µm) (Restek, Bellefonte, PA,

United States), Ascentis® Express F5 (100 mm × 2.1 mm × 2.7 µm), and Ascentis® Express C18 (100 mm × 2.1 mm × 2.7 µm) from Supelco (Bellefonte, PA, United States).

To calculate the number of chromatographic bands, the automatic integration parameters consisting of the same criteria were used for all samples to promote the highest number of bands in the chromatogram. The integration parameters were as follow: 1) width: 3 s; slope: 1,000 uV/min, drift: 0 uV/min, T.DBL (time required to double the peak width): 1,000 min; minimum area/weight: 1,000 counts; signal to noise ≥10, and the wavelength was fixed at 254 nm due to the solvent cutoff at different pH levels and the molar absorptivity of the compounds present in the plant matrices.

Design of Experiments

The design of experiments (DoE), executed in three stages, was elaborated to produce the optimal chromatographic condition with a maximum number of chromatographic bands. Step 1 was carried out considering a full factorial design with all possible combination of high and low levels for all factors for three experimental critical factors: chemistry of the stationary phase, pH and organic modifier.

Initially, 51 experiments were carried out, of which 21 experiments were replicates run to estimate the confidence interval at the center point. Additionally, the gradient time and the column temperature were set at 10 min and 40°C, respectively. Next step (Step 2), the best chromatographic conditions obtained from Step 1 were selected and eight additional experiments were performed using a linear gradient of 30 min. The best condition of Step 2 was used in Step 3, in which the flow rate and the column temperature were modified to reduce the analysis time. For the calculation of the numbers of chromatographic bands, an automatic integration was applied to all chromatograms using the same criteria. The detection wavelength was set at 254 nm. The computational programs used for calculations were Excel® (v.2019) and Matlab® (v. R2013b 8.2.0.701).

Liquid Chromatography Coupled to High-Resolution Mass Spectrometry Analysis

For the principal component analysis of 4 *Bauhinia* ssp, a liquid chromatography separation was obtained with a Kinetex® Biphenyl column (100 mm × 2.1 mm; 2.7 µm) (Phenomenex, Torrance, CA, United States) equipped with a guard-column. The solvents used were 100 µmol/L of formic acid in water (solvent A) and 100 µmol/L of formic acid in methanol (solvent B) as mobile phase, flow rate of 0.7 ml/min, and temperature set at 50°C. Gradient elution of 25 min run time was carried out using the following steps: 0 min, 5% B; 0–20 min, 5%–70% B; 20.1–25 min, 100% B for column cleaning and a conditioning time of 5 min with 5% B. The injection volume was 0.5 µl (sample concentration: 30 mg/ml).

The UHPLC (Nexera, Shimadzu) system, previously described, was coupled to an Impact HD QTOF mass

spectrometer (quadrupole time-of-flight mass spectrometry—Bruker Daltonics, Bremen, Germany) equipped with an electrospray (ESI) interface operating in the positive or negative ion mode. Negative ionization mode was chosen for promoting better sensitivity for a higher number of metabolites under the analytical conditions tested (Liigand et al., 2017). A flow splitter was placed between the LC column exit and the MS, and the flow rate arriving at the MS was set at 118 μ L/min. The optimal mass spectrometer parameters were set as follows: capillary voltage, 4000 V; endplate offset, 500 V; nebulizer, 1 bar; dry heater temperature, 250°C; dry gas flow, 8 L/min; collision cell energy, 5 eV, and full-MS scan range, m/z 50–1500.

For characterization of the secondary metabolites, the mass spectrometer was programmed to perform acquisition in Auto MS/MS mode (number of precursors 5) and MS/MS experiments were performed using different collision energies of 10, 20, 25, 30, 35, 40, 45, or 50 eV for all m/z interval range. Data acquisition and processing were performed using Data Analysis[®] and Profile Analysis[®] v.2.1 software (Bruker Daltonics GmbH, Bremen, Germany). Structural chemical characterization was established based on MS/MS fragmentation pattern, accurate mass, and comparison to spectral library (CompoundCrawler[™], MetFrag, and SmartFormula[™] from Bruker Daltonics GmbH, Bremen, Germany) and public databases structure search based on formula (<http://mona.fiehnlab.ucdavis.edu/>; <http://www.massbank.eu/>; <https://metlin.scripps.edu/>) to enable the creation of annotations at increasing levels of specificity and confidence. Molecular formulas of the identified compounds were calculated using an accurate mass error <10 ppm. The identified compounds were searched in the literature to check if they were present in the *Bauhinia* spp and examined using the HMDB database (<http://www.hmdb.ca/>) to learn if they were in the plant kingdom and/or in the Fabaceae family, as previously published for *B. longifolia* (Aquino et al., 2019).

RESULTS AND DISCUSSION

Analytical Development by Design of Experiments

The analytical method development and optimization were performed through a design of experiment (DoE) study by modifying simultaneously multiple critical method parameters (CMPs), which can affect critical method attributes (CMAs) such as resolution (R_s), peak tailing (T), and selectivity (α) (Lloyd R. Snyder & Dolan, 2013).

The plant extract chosen for the LC method development was the ethanolic extract of *B. forficata* leaves. The reverse mode of elution was used due to the properties of the analytes present in plant matrices being of medium polarity to non-polar, and for the same reasons, the use of ionic pairing was not considered as a variable. The orthogonality values for the pre-selected stationary phases were obtained from the results of F_s described on the website of the American Pharmacopoeia, which is based on the theory of hydrophobic subtraction developed by Snyder and collaborators (USP, 2005; Snyder & Dolan, 2013; Cass, 2015; Lloyd R.).

Thus, the Kinetex[®] biphenyl ($F_s = 0$) column was compared to three other columns: the Ascentis[®] Express F5, Ascentis[®] Express C18, and the Raptor[®] biphenyl, being considered orthogonal only to the Ascentis[®] Express F5 and the Ascentis[®] Express C18 columns with an $F_s > 10$ (USP, 2005).

The organic modifier was selected according to Snyder-Rohrshneider's selectivity triangle which considers the different chemical interactions of the organic modifiers—acidity, basicity, and dipole interactions (L. R. Snyder et al., 1993). In this work, only the use of methanol and acetonitrile were investigated because of the incompatibility of tetrahydrofuran with modern LC equipment.

Initially, a full factorial design was carried out (DoE—Step 1), in which all variables, their interactions, and levels were considered in the calculations. This design allows the screening of a high number of factors with fewer experiments and can also be used for robustness or ruggedness testing (Thorsteinsdóttir & Thorsteinsdóttir, 2021). To meet this end, three critical method parameters that mainly affect chromatographic selectivity were considered: 1) chemistry of the stationary phase (column); 2) type of organic modifier, and 3) pH values. All CMPs and levels are shown in **Table 1**.

Thus, three main steps were considered for the development and optimization of the chromatographic separation: 1) screening of the variables that most impact the selectivity—stationary phase, pH, and organic modifier; 2) fine adjustment of peak capacity by using the best conditions from Step 1 and applying a different gradient time; 3) optimization of analysis time by keeping the chromatographic resolution without losing selectivity. To this end, higher flow rate and temperature were considered.

The results encoded variables and levels of DoE—Step 1 are shown in **Supplementary Table S1**, and the results of the analysis of variance (ANOVA) are shown in **Supplementary Table S2**. It was verified that the regression model selected was an adequate fit to the data using an F test, where the mean square regression (MSR) and regression mean residual (MS_{residual}) were statistically significant, with an $F_{\text{calculated}} > F_{\text{critical}}$ at 95% confidence level. These results produced a mathematical model, where a second-order equation (Eq. 1) describes the results obtained from DoE—Step 1:

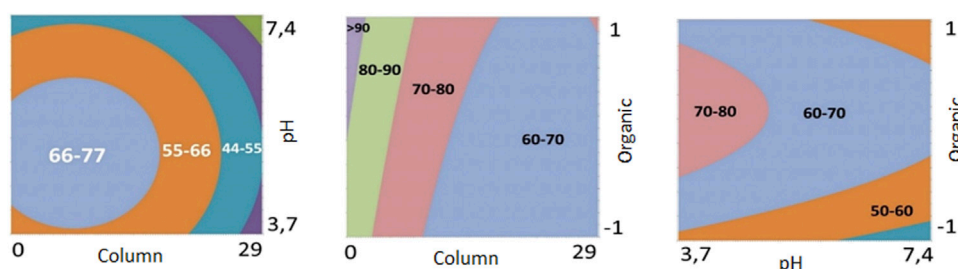
$$y = 67.86 - 12.14 C - 6.22 pH + 4.29 O + 10.63 C^2 - 11.99 pH^2 \\ (\pm 6.9) \quad (\pm 3.6) \quad (\pm 3.7) \quad (\pm 2.8) \quad (\pm 6.1) \quad (\pm 7.7) \quad (1)$$

Where y is the dependent variable that accounts for the number of chromatographic bands, C is the column type, pH is the acidity/basicity value of the aqueous mobile phase, and O is the type of organic modifier used.

The results obtained for DoE—Step 1 showed that the Kinetex[®] Biphenyl column promoted a higher number of chromatographic bands when used at lower pH levels. Also, the contour plots (**Figure 1**) for the Kinetex[®] biphenyl column demonstrate these findings, and it was the chromatographic column selected for further experiments. Therefore, different levels for pH (3–5), organic modifier (methanol and acetonitrile), and a linear gradient time of 10 and 30 min,

TABLE 1 | Critical method parameters (CMPs) and levels used in the development of the chromatographic conditions in Step 1.

Selectivity factor (F_s)	Column	Column levels	Organic modifiers (OM)	OM levels	pH effective	pH levels
0	Kinetex [®] biphenyl (100 mm × 2.1 mm); 2.7 μ m	−1	Methanol (MeOH)	1	3.7	Ammonium formate 10 mM
9	Raptor [®] Biphenyl (100 mm × 2.1 mm); 2.7 μ m	−0.3791	Acetonitrile (MeCN)	−1	4.2	Formic acid 200 μ M
20	Ascentis [®] Express F5 (100 mm × 2.1 mm); 2.7 μ m	0.3791			5.3	Ammonium acetate 10 mM
29	Ascentis [®] Express C18 (100 mm × 2.1 mm); 2.7 μ m	1			7.4	Ammonium bicarbonate 10 mM

**FIGURE 1** | Contour plots obtained in DoE—Step 1 of the experimental design.**TABLE 2** | Variables used in DoE—Step 2.

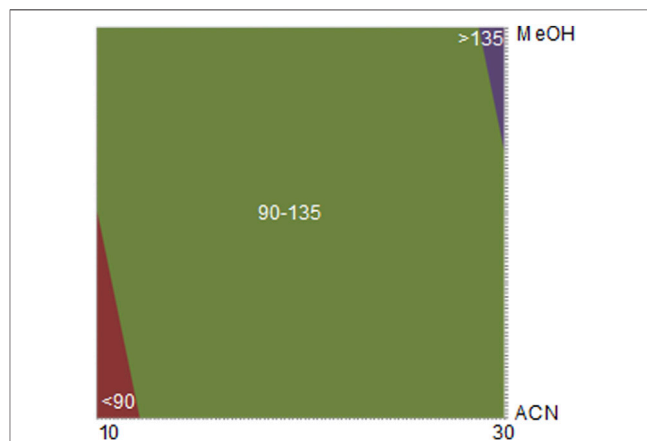
Time (min)	Organic modifier	Aqueous pH
30	MeOH	3.7
10	MeCN	4.2
		5.3

*Fixed condition: Kinetex[®] biphenyl column, temperature 40°C, and flow rate 0.5 ml/min.

Table 2, were used as the next critical factors during the DoE—Step 2 of the chromatographic optimization. Therefore, eight more analyzes were performed, with 2 replicates, using the Kinetex[®] biphenyl column, temperature 40°C, and flow rate of 0.5 ml/min.

The results obtained from DoE—Step 2 (Table 2) were also analyzed using ANOVA and Student's t-test (with 4 degrees of freedom), and it was verified that the pH value showed no significant effect in the studied value range (pH 3–5), then it was fixed in pH 4.2 using 200 μ M of formic acid in the mobile phase for further experiments. The results obtained when using pH 4.2 promoted higher signal intensities for the detected ions in the negative ionization mode.

Because replicated experiments have been carried out ($n = 2$), the residual component from the total variation was assembled from the lack of fit (LoF) component and a component due to pure experimental error (Tome et al., 2019). In our results, the square mean of lack of adjustment (MS_{LoF}) and the square mean of the pure error (MS_{PE}) was statistically equal with an $F_{2calculated} < F_{2critical}$ indicating that the model did not lack of fit. In addition, the mean

**FIGURE 2** | Contour plot obtained in DoE—Step 2. [* The values in the contour chart refer to the number of chromatographic bands. ** Fixed condition: Kinetex[®] Biphenyl column, pH 4.2 (formic acid 200 μ M), temperature 40°C, and flow rate 0.5 ml/min X axis (time—minutes) and Y axis organic modifier.

square regression (MSR) and regression mean residual ($MS_{residual}$) were statistically different. Therefore, the model was statistically significant with $F_{1calculated} > F_{1critical}$ and the coefficient of determination (R^2) equal to 0.97, also indicating an adequate adjustment of the model to the observed responses at a confidence level of 95%. For a full list of the parameters used from the DoE—Step 2 refer to **Supplementary Table S3**.

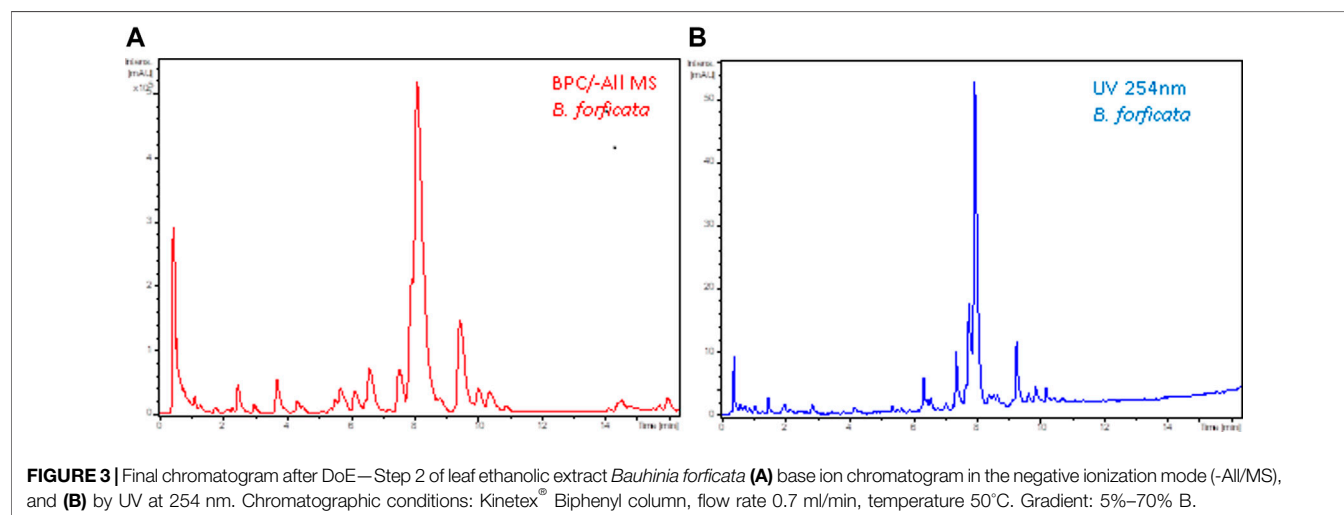


FIGURE 3 | Final chromatogram after DoE—Step 2 of leaf ethanolic extract *Bauhinia forficata* (A) base ion chromatogram in the negative ionization mode (-All/MS), and (B) by UV at 254 nm. Chromatographic conditions: Kinetex[®] Biphenyl column, flow rate 0.7 ml/min, temperature 50°C. Gradient: 5%–70% B.

After applying the Student's *t*-test (with 12 degrees of freedom), both gradient slope (I) and organic modifier (O) were statistically significant. Thus, with Eq. 2, the contour plot was constructed and displayed in Figure 2, showing that when using longer analysis time and methanol as an organic modifier, the highest number of resolved chromatographic bands is obtained.

$$y = 111.56 + 21.85 I + 4.32 O \quad (2)$$

(±5.4) (±3.4) (±3.6)

The Kinetex[®] biphenyl stationary phase and methanol as the organic modifier showed the highest resolution for a larger number of chromatographic bands. This could be justified due to the presence of many phenolic compounds in these species (Aquino et al., 2019).

In DoE—Step 3, chromatographic adjustments were made to decrease the analysis time but to preserve the same number of chromatographic bands and resolution. The flow rate of 0.5 ml/min and temperature 40°C were increased to 0.7 ml/min and 50°C, respectively. The final chromatographic condition in the LC-HRMS and LC-UV is shown in Figure 3.

Dereplication of the Four *Bauhinia* Species

The previously developed chromatographic conditions were used for the analysis of the ethanolic extracts of *B. forficata*, *B. variegata*, *B. longifolia*, and *B. affinis* by LC-HRMS to identify the compounds that could differentiate these species. The obtained chromatograms and MS survey spectra (SV) are shown in Figure 4. The MS survey view displays the density data of the selected chromatogram analysis by recording the retention time and the *m/z* value. The intensity values that correspond to the retention time—*m/z* pairs are expressed by a color code, where darker blue means more intense MS signals.

The data evaluation of the MS data using statistical techniques was carried out using the Profile Analysis software (Bruker Daltonics), which calculate the molecular features by using numerical values obtained from the grouping of ions by retention time (*t_R*) and isotope pattern, and by unifying *m/z*

of the same ion (different charged ions, adducts or clusters). This preprocessing bucketing method performs a data reduction by grouping highly similar spectra, after which each bucket can be represented by a single consensus spectrum (Bittremieux et al., 2021). Moreover, ion intensities were normalized by the sum of the values of the buckets, and these were tabulated. As a result, 541 buckets (S/N 5^a) were obtained from the selection parameters described in Supplementary Table S4.

The explained variance plot, obtained by plotting the percentage of the variance explained by the extracted PC, was used to identify the ideal number of principal components (PCs) and the resulting curve profile used to determine the cut-off point by decreasing the slope observed, which in this case was the third principal component. Three PCs were selected, which explained 93.7% of the total data variation. The principal component 1 (PC1) was responsible for 61.2% of the original data variance, whereas PC2 and PC3 corresponded to 25.3% and 7.2%, respectively.

The obtained MS data were evaluated to further contribute to the phytochemical studies of the genus *Bauhinia*. The dereplication of the compounds was feasible due to manually comparison of the exact masses, MS/MS fragmentation patterns, and isotopic contribution pattern with those data reported in the literature or already deposited in spectral libraries online (<http://mona.fiehnlab.ucdavis.edu/>; <http://www.massbank.eu/>; <https://metlin.scripps.edu/>), and data acquired in LC-MS systems equipped with an ESI source and fragmentation through collision-induced dissociation (CID). Furthermore, the identified compounds were searched in the literature to verify if they were present in the *Bauhinia* spp, consulted in the HMDB database (<http://www.hmdb.ca/>) to know if they were present in the plant kingdom and/or in the Fabaceae family. The compounds were inferred by excluding those ions which were fragment ions of the precursor, adducts, and clusters at the same retention time. Supplementary Table S5 illustrates the 55 compounds inferred by dereplication and listed in numerical order according to their retention time. The LC-HRMS spectra data is also presented in the Supplementary Material, Section 1. Supplementary Table S6 shows the presence of the 55 compounds in the ethanolic extracts (*n* =

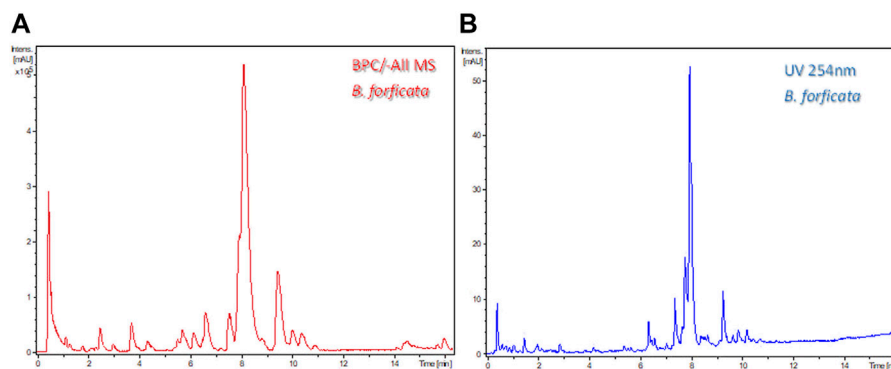


FIGURE 4 | Survey view (SV) and base peak chromatograms (BPC) in negative ionization mode (-All/MS) for *B. forficata* (1a and 1b), *B. variegata* (2a and 2b), *B. affinis* (3a and 3b), and *B. longifolia* (4a and 4b).

2) of *B. forficata*, *B. variegata*, *B. longifolia*, and *B. affinis* leaves, at the experimental conditions evaluated for sample extraction and analysis.

Differentiation of the *Bauhinia* Species Using Chemometric Tools

The inferred compounds from the molecular characteristics table (Supplementary Table S5) were used for species classification and differentiation using the unsupervised pattern recognition, cluster analysis (HCA), and principal component analysis (PCA) methods. In the dendrogram obtained with the HCA (Figure 5) it was possible to see four large groups formed based on the existing similarities in relation to the analyzed variables, indicating clear differences between the *Bauhinia* species.

To get a better understanding of the compounds that differentiate the species, PCA was applied. The explained variance plot, obtained by plotting the percentage of the variance explained by the extracted PC, was used to identify the ideal number of principal components (PCs) and the resulting curve profile used to determine the cut-off point by decreasing the slope observed, which in this case was the third principal component. Three PCs were selected, which explained 98.7% of the total data variation. The principal component 1 (PC1) was responsible for 80.0% of the original data variance, whereas PC2 and PC3 corresponded to 12.3% and 6.0%, respectively (Supplementary Figure S1).

The samples of each species were grouped in scores graphs (PC1 vs. PC2), Figure 6A, with differentiation between the species *Bauhinia longifolia* and *Bauhinia affinis*, while grouping *Bauhinia forficata* and *Bauhinia variegata*. In the loading graphs (PC2 vs. PC3) (Figure 6B) it was possible to verify the separation of *Bauhinia forficata*, *Bauhinia variegata*, and *Bauhinia affinis*.

Secondary Metabolites Chemical Characterization by Liquid Chromatography Coupled to High-Resolution Mass Spectrometry

The compounds 2, 9–12, 15–18, 25, 26, 28, 31, 33, 41, 42, 44, 46, 50–52, and 55 listed in Supplementary Table S5 have been

previously inferred by the authors for *Bauhinia longifolia* extract (Aquino et al., 2019), while the discussion and spectra of the other metabolites annotated in this article are disclosed in the Supplementary Material.

Additionally, it was not possible to verify the presence of kaempferitrin, the alleged chemical marker of *Bauhinia forficata*. For that, we searched the data using the ion extracted chromatograms (EIC), considering the deprotonated molecular ion m/z 577.1552 ($M-H$)[−], adducts such as $[(M-AF)]^{-}$, $(M-H_2O-H)^{-}$, and $(2M + AF-H)^{-}$, and their respective fragment ions. Our data corroborate with those previously published by Ferreres et al. (2012), in which kaempferitrin was not detected in *B. forficata* Link subsp. *Pruinosa* (Vogel) Fortunato & Wunderlin.

Bauhiniastatin 2 is present in all species studied in this work. This compound has been reported in *B. purpurea* and its medicinal properties are related to anticancer activities (Pettit et al., 2006), which demonstrates the potential of *Bauhinia* species for this purpose.

In all species studied, a wide variety of phenolic compounds were identified, however, to date, no results of biological and toxicological activities have been reported for the plant-derived extractions of *B. affinis* and very few for *B. longifolia*.

CONCLUSION

The use of DoE for the LC method development using extracts of *Bauhinia forficata* as a model, allowed a rapid and efficient method development since multiple CMPs were simultaneously evaluated. The DoE approach also provided an increased selectivity for a complex mixture of compounds in a natural product matrix. The obtained chromatograms promoted a satisfactory number of resolved bands and the LC coupling to HRMS and further data analysis by principal component analysis allowed the dereplication of a series of compounds and differentiation of the four studied *Bauhinia* species.

Bauhiniastatin 2 is herein reported for the four species, as well as a wide variety of phenolic compounds providing important information to the herbal medicine industry; however, it is important to highlight, that up to date, no results of biological

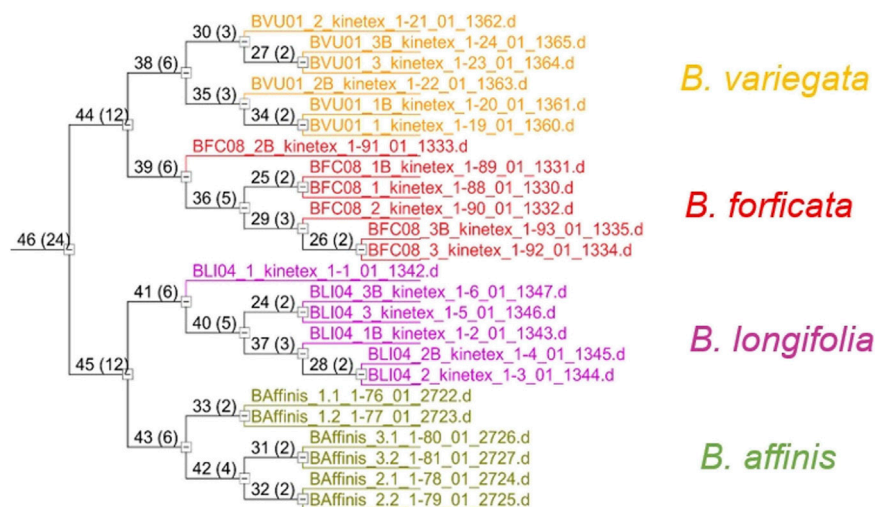


FIGURE 5 | Hierarchical clustering analysis of the 4 studied *Bauhinia* species.

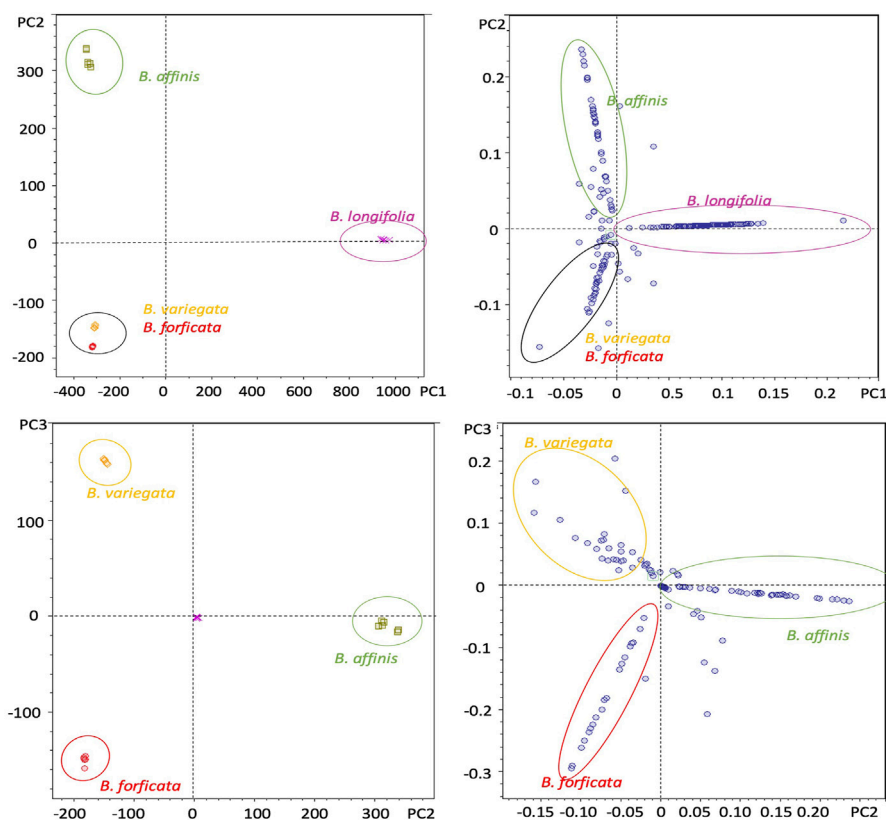


FIGURE 6 | Principal component analysis (PCA) of *B. forficata*, *B. variegata*, *B. longifolia*, and *B. affinis*. Upper: PC1 vs. PC2 (Score graphs). Bottom: PC2 vs. PC3 (loading graphs).

and/or toxicological activities have been reported for *B. affinis* and very scarce results are presented for *B. longifolia*. Thus, further studies are needed for their safe plant medicinal use.

The presented work demonstrated that the use of DoE for method development of plant-derived extracts and analytical approaches by LC-HRMS associated with unsupervised chemometric methods is a

powerful tool for the chemical differentiation of plant species and can be further used in plant authentication, especially in Brazil where there is a growth in the use of herbal medicines for the Brazilian population through the Unique Health System (SUS).

DATA AVAILABILITY STATEMENT

The original contributions presented in the study are included in the article/**Supplementary Material**, further inquiries can be directed to the corresponding authors.

AUTHOR CONTRIBUTIONS

AA and QC conceived the study design. AA and EP-F performed the DoE and chemometric studies and analyzed the data. AA, QC, and RO performed the LC and HRMS studies, formal analysis, and interpretation of the data. RO and QC resources, funding acquisition, supervision of the work. AA, QC, and RO wrote the manuscript, while all authors gave significant contributions in discussion and revision. All authors agreed with the final version.

REFERENCES

- Aquino, A. J., da C. AlvesAlves, T. T., Oliveira, R. V., Ferreira, A. G., and Cass, Q. B. (2019). Chemical Secondary Metabolite Profiling of *Bauhinia Longifolia* Ethanolic Leaves Extracts. *Industrial Crops Prod.* 132 (January), 59–68. doi:10.1016/j.indcrop.2019.01.040
- Bittremieux, W., Laukens, K., Noble, W. S., and Dorrestein, P. C. (2021). Large-scale Tandem Mass Spectrum Clustering Using Fast Nearest Neighbor Searching. *Rapid Commun. Mass Spectrom.* 2021, e9153. doi:10.1002/rcm.9153
- BRASIL (2009). Relação de Plantas Medicinais de Interesse ao SUS. Portal Saúde - Ministério Da Saúde. Availablehttp://bvsms.saude.gov.br/bvs/sus/pdf/marco/ms_relacao_plantas_medicinais_sus_0603.pdf (Accessed May 15, 2018).
- Carvalho, V. A. P. (2011). *Caracterização química por cromatografia líquida e análise quimiométrica de espécies vegetais de Bauhinia com aplicação em controle de qualidade de amostras comerciais de pata-de-vaca*. Universidade Federal de São Carlos.
- Cass, Q. B. (2015). "Ortogonalidade no modo reverso de eluição," in *Cromatografia líquida: Novas tendências e aplicações*. 1st ed. (Elsevier), 1–17.
- Chang, X., Zhang, J., Li, D., Zhou, D., Zhang, Y., Wang, J., et al. (2017). Nontargeted Metabolomics Approach for the Differentiation of Cultivation Ages of Mountain Cultivated Ginseng Leaves Using UHPLC/QTOF-MS. *J. Pharm. Biomed. Analysis* 141, 108–122. doi:10.1016/J.JPBA.2017.04.009
- da Cunha, A. M., Menon, S., Menon, R., Couto, A. G., Bürger, C., and Biavatti, M. W. (2010). Hypoglycemic Activity of Dried Extracts of *Bauhinia Forficata* Link. *Phytomedicine* 17 (1), 37–41. doi:10.1016/j.phymed.2009.06.007
- De Sousa, E., Zanatta, L., Seifriz, I., Creczynski-Pasa, T. B., Pizzolatti, M. G., Szpoganicz, B., et al. (2004). Hypoglycemic Effect and Antioxidant Potential of Kaempferol-3,7-O-(α)-Dirhamnoside from *Bauhinia Forficata* Leaves. *J. Nat. Prod.* 67 (5), 829–832. doi:10.1021/np030513u
- de Souza, B. V. C., Moreira Araújo, R. S. D. R., Silva, O. A., Faustino, L. C., Gonçalves, M. F. B., Dos Santos, M. L., et al. (2018). *Bauhinia Forficata* in the Treatment of Diabetes Mellitus: a Patent Review. *Expert Opin. Ther. Pat.* 28 (Issue 2), 129–138. doi:10.1080/13543776.2018.1409208
- Ferreiras, F., Gil-Izquierdo, A., Vinholes, J., Silva, S. T., Valentão, P., and Andrade, P. B. (2012). *Bauhinia Forficata* Link Authenticity Using Flavonoids Profile: Relation with Their Biological Properties. *Food Chem.* 134 (2), 894–904. doi:10.1016/j.foodchem.2012.02.201
- Filho, V. C. (2009). Chemical Composition and Biological Potential of Plants from the genus *Bauhinia*. *Phytother. Res.* 23, 1347–1354. doi:10.1002/ptr.2756

FUNDING

This work was supported by the São Paulo Research Foundation (FAPESP) with the research grants 2013/01710-1 and 2014/50244-6. The research grants (140469/2013-3, 302557/2018-0, and 406064/2018-0) from the National Council for Scientific and Technological Development (CNPq) and the Finance Code 001 from CAPES (Agency for the Improvement of Higher Education Personnel) are also acknowledged.

ACKNOWLEDGMENTS

The authors thank for the financial support of FAPESP, CNPq, and CAPES.

SUPPLEMENTARY MATERIAL

The Supplementary Material for this article can be found online at: <https://www.frontiersin.org/articles/10.3389/fchem.2022.800729/full#supplementary-material>

- Henrique Domingos, A., and Capellari Júnior, L. (2016). *Plantas Medicinais: Pata-de-Vaca*, Piracicaba: ESALQ - Divisão de Biblioteca.
- Liigand, P., Kaupmees, K., Haav, K., Liigand, J., Leito, I., Girod, M., et al. (2017). Think Negative: Finding the Best Electrospray Ionization/MS Mode for Your Analyte. *Anal. Chem.* 89, 5665–5668. doi:10.1021/acs.analchem.7b00096
- Lopez, D. A., Green, A., and Bell, D. S. (2020). What Is on Your HPLC Particle? A Look at Stationary Phase Chemistry Synthesis. *LCGC N. Am.* 38 (9), 488–493.
- Pettit, G. R., Numata, A., Iwamoto, C., Usami, Y., Yamada, T., Ohishi, H., et al. (2006). Antineoplastic Agents. 551. Isolation and Structures of Bauhinistatins 1–4 from *Bauhinia Purpurea*. *J. Nat. Prod.* 69 (3), 323–327. doi:10.1021/np058075+
- Silva, F. R., Szpoganicz, B., Pizzolatti, M. G., Willrich, M. A., and De Sousa, E. (2002). Acute Effect of *Bauhinia Forficata* on Serum Glucose Levels in Normal and Alloxan-Induced Diabetic Rats. *J. Ethnopharmacol.* 83 (1–2), 33–37. doi:10.1016/S0378-8741(02)00193-9
- Snyder, L. R., Carr, P. W., and Rutan, S. C. (1993). Solvatochromically Based Solvent-Selectivity Triangle. *J. Chromatography A* 656, 537–547. doi:10.1016/0021-9673(93)80818-S
- Snyder, L. R., and Dolan, J. W. (2013). Optimizing Selectivity during Reversed-phase High Performance Liquid Chromatography Method Development: Prioritizing Experimental Conditions. *J. Chromatogr. A* 1302, 45–54. doi:10.1016/j.chroma.2013.05.082
- Thorsteinsdóttir, U. A., and Thorsteinsdóttir, M. (2021). Design of Experiments for Development and Optimization of a Liquid Chromatography Coupled to Tandem Mass Spectrometry Bioanalytical Assay. *J. Mass Spectrom.* 56 (9). doi:10.1002/jms.4727
- Tome, T., Žigart, N., Časar, Z., and Obreza, A. (2019). Development and Optimization of Liquid Chromatography Analytical Methods by Using AQbD Principles: Overview and Recent Advances. *Org. Process Res. Dev.* 23, 1784–1802. doi:10.1021/acs.oprd.9b00238
- USP (2005). The USP Approach for Selecting Columns of Equivalent Selectivity. *Pharmacopeial Forum* 31 (2), 637–645. <http://www.usp.org/resources/pqri-approach-column-equiv-tool>.
- Vaz, A. M. S. d. F., Bortoluzzi, R. L. d. C., and Silva, L. A. E. d. (2010). Checklist of *Bauhinia* *Sensu Stricto* (Caesalpinaceae) in Brazil. *Plecevo* 143 (2), 212–221. doi:10.5091/plecevo.2010.391
- WHO (2013). WHO traditional medicine strategy: 2014–2023. Available at: <https://www.who.int/publications/i/item/9789241506096> (Accessed May 15, 2018).
- Wolfender, J.-L., Marti, G., Thomas, A., and Bertrand, S. (2015). Current Approaches and Challenges for the Metabolite Profiling of Complex Natural Extracts. *J. Chromatogr. A* 1382, 136–164. doi:10.1016/J.CHROMA.2014.10.091

- Xiao, X., Hou, Y., Liu, Y., Liu, Y., Zhao, H., Dong, L., et al. (2013). Classification and Analysis of Corn Steep Liquor by UPLC/Q-TOF MS and HPLC. *Talanta* 107, 344–348. doi:10.1016/j.talanta.2013.01.044
- Xu, M., Heidmarsson, S., Thorsteinsdottir, M., Kreuzer, M., Hawkins, J., Omarsdottir, S., et al. (2018). Authentication of Iceland Moss (*Cetraria Islandica*) by UPLC-QToF-MS Chemical Profiling and DNA Barcoding. *Food Chem.* 245, 989–996. doi:10.1016/j.foodchem.2017.11.073
- Zhang, X., Lv, H., Li, Z., Jiang, K., and Lee, M.-R. (2015). HPLC/QTOF-MS/MS Application to Investigate Phenolic Constituents from *Ficus pandurata* H. Aerial Roots. *Biomed. Chromatogr.* 29 (6), 860–868. doi:10.1002/bmc.3366

Conflict of Interest: The authors declare that the research was conducted in the absence of any commercial or financial relationships that could be construed as a potential conflict of interest.

Publisher's Note: All claims expressed in this article are solely those of the authors and do not necessarily represent those of their affiliated organizations, or those of the publisher, the editors and the reviewers. Any product that may be evaluated in this article, or claim that may be made by its manufacturer, is not guaranteed or endorsed by the publisher.

Copyright © 2022 Aquino, Pereira-Filho, Oliveira and Cass. This is an open-access article distributed under the terms of the Creative Commons Attribution License (CC BY). The use, distribution or reproduction in other forums is permitted, provided the original author(s) and the copyright owner(s) are credited and that the original publication in this journal is cited, in accordance with accepted academic practice. No use, distribution or reproduction is permitted which does not comply with these terms.

Advantages of publishing in Frontiers



OPEN ACCESS

Articles are free to read
for greatest visibility
and readership



FAST PUBLICATION

Around 90 days
from submission
to decision



HIGH QUALITY PEER-REVIEW

Rigorous, collaborative,
and constructive
peer-review



TRANSPARENT PEER-REVIEW

Editors and reviewers
acknowledged by name
on published articles

Frontiers

Avenue du Tribunal-Fédéral 34
1005 Lausanne | Switzerland

Visit us: www.frontiersin.org

Contact us: frontiersin.org/about/contact



REPRODUCIBILITY OF RESEARCH

Support open data
and methods to enhance
research reproducibility



DIGITAL PUBLISHING

Articles designed
for optimal readership
across devices



FOLLOW US

@frontiersin



IMPACT METRICS

Advanced article metrics
track visibility across
digital media



EXTENSIVE PROMOTION

Marketing
and promotion
of impactful research



LOOP RESEARCH NETWORK

Our network
increases your
article's readership